Evolution and decay of peneplains in the northern Lhasa terrane, Tibetan Plateau

Revealed by low-temperature thermochronology, U-Pb geochronology, provenance analyses, and geomorphometry

DISSERTATION

zur Erlangung des mathematisch-naturwissenschaftlichen Doktorgrades
"Doctor rerum naturalium"
der Georg-August-Universität Göttingen
im Promotionsprogramm Geowissenschaften / Geographie der Georg-August University School of Science (GAUSS) vorgelegt von

Viktoria L. Haider
aus Waldneukirchen
(Österreich)

Göttingen
Mai, 2014

BETREUUNGSAUSSCHUSS:

Prof. Dr. Hilmar von Eynatten
Abteilung für Sedimentologie und Umweltgeologie
Geowissenschaftliches Zentrum der Georg-August-Universität Göttingen

Dr. István Dunkl
Abteilung für Sedimentologie und Umweltgeologie
Geowissenschaftliches Zentrum der Georg-August-Universität Göttingen

MITGLIEDER DER PRÜFUNGSKOMMISSION:

Referent:	**Prof. Dr. Hilmar von Eynatten** Abteilung für Sedimentologie und Umweltgeologie Geowissenschaftliches Zentrum der Georg-August-Universität Göttingen
1. Korreferent:	**Dr. István Dunkl** Abteilung für Sedimentologie und Umweltgeologie Geowissenschaftliches Zentrum der Georg-August-Universität Göttingen
2. Korreferent:	**Prof. Dr. Jonas Kley** Abteilung für Strukturgeologie and Geodynamik Geowissenschaftliches Zentrum der Georg-August-Universität Göttingen

WEITERE MITGLIEDER DER PRÜFUNGSKOMMISSION:

Prof. Dr. Bent T. Hansen
Abteilung für Isotopengeologie
Geowissenschaftliches Zentrum der Georg-August-Universität Göttingen

Prof. Dr. Gerhard Wörner
Abteilung für Geochemie
Geowissenschaftliches Zentrum der Georg-August-Universität Göttingen

Dr. Bianca Wagner
Abteilung für Angewandte Geologie
Geowissenschaftliches Zentrum der Georg-August-Universität Göttingen

TAG DER MÜNDLICHEN PRÜFUNG: 1. JULI 2014

Hiermit erkläre ich an Eides statt, die vorliegende Arbeit selbstständig angefertigt zu haben und dabei keine anderen als die von mir angegebenen Quellen und Hilfsmittel bnutzt zu haben. Ferner erkläre ich, dass ich nicht anderweitig versucht habe, eine Dissertation einzureichen.

Göttingen, Mai 2014

Viktoria L. Haider

“The only real voyage of discovery
consists not in seeking new landscapes,
but in having new eyes.”

by Marcel Proust

Abstract

The key issue of this thesis is the evolution and decay of peneplains, which are distinctive geomorphological structures in the southern area of the Tibetan Plateau. Additionally, evidence concerning the uplift history and sediment dispersion patterns of the southern Tibetan Plateau was attained. These processes are, still not well understood but heavily debated and especially crucial for the understanding of the geodynamic and paleoclimatologic evolution of Asia.

The concept of peneplains exists since the end of the 19^{th} century, and its definition and genesis are controversially discussed by the geomorphological community. Neither has a standardized definition for peneplains been developed yet, nor an established procedure to identify well preserved peneplains using geospatial methods.

In this thesis, representative peneplains are understood as elevated geomorphological features with a plain top and a hillside, although most of the existing peneplains are actually disturbed due to tilting in the process of tectonic activity or intersected by linear erosional features.

Highly elevated and well-preserved peneplains are characteristic geomorphic features of the Tibetan Plateau. The area under investigation of this thesis is located in the northern Lhasa terrane, north-northwest of *Nam Co*, one of the highest lakes in the world. Here the peneplains were carved into granitoids and into their metasedimentary host formations.

The post-emplacement thermal history of the granitoids was constrained by applying a multi-method geochronology including zircon U-Pb, zircon (U-Th)/He apatite (U-Th)/He, and apatite fission track dating. Additionally, these investigation methods provided a good benchmark for the rate of final exhumation of the peneplains. U-Pb geochronology of zircons yields two narrow age groups for the intrusions at around 118 Ma and 85 Ma, and a third group shows Paleocene igneous activity (63 - 58 Ma).

Abstract

Thermal modeling based on zircon and apatite (U-Th)/He, and apatite fission track data indicates cooling and exhumation of the granitoids between ca. 75 and ca. 55 Ma. and a rapid decline in the exhumation rate from about 300 m/m.y. during the above mentioned period to $\sim$ 10 m/m.y. in the subsequent period between ca. 55 and ca. 45 Ma. Cosmogenic nuclide data gained by our co-operation partner at the University of Münster yield a low local and catchment-wide erosion rates of 6 - 11 and 11 - 16 m/m.y. in the last 10,000 years and indicate an ongoing period of stability for the geomorphic feature of the peneplain.

During the prolonged phase of erosion and planation, between 3 and 6 km of rock layer were removed from the peneplain region until ca. 45 Ma. The ablated rock material transformed to sediments and was most probably transported towards the ocean by existing rivers. This can be assumed by the lack of huge amounts of sediments on the Lhasa block. These facts as well as the performed provenance analysis lead to the conclusion that peneplanation and subsequent erosion proceeded at low elevation, most probably near sea level. This leveling process was stopped by the collision of the India plate and the Asian continent. Crustal thickening and related surface uplift transported the peneplains onto the “roof of the world”. Due to dry climatic conditions the peneplains could be preserved until present day.

The second part of the thesis deals with the establishment of a robust geospatial method to detect and analyze peneplains. Since digital elevation models (DEM) with same resolutions and quality are available worldwide, it is possible to analyze and characterize the morphology of the Earth’s surface in a representative way and to a significant extend. DEM offers an excellent opportunity to map distinctive peneplains.

For this purpose, a new unbiased DEM-based numerical fuzzy-logic approach was developed for the delineation of peneplains, merely from a morphological point of view. The approach is based on a morphometrical analysis of 90 arcsec Shuttle Radar Topography Mission (SRTM) - DEM of the field area at the central Tibetan Plateau. A model involving the critical parameters of (I) slope, (II) curvature, (III) terrain ruggedness index, and (IV) relative height was implemented in a geographic information system (GIS). These parameters turned out to be valuable for the correct description and calculation of peneplains. In order to verify the applied method, peneplains,

which already had been described in the literature, were delineated in different regions around the world with various geological settings. The obtained results from the Appalachian Mountains, the Andes, the Massif Central, and New Zealand confirm the robustness of the proposed approach.

Kurzfassung

Diese Dissertation befasst sich mit der Entwicklung von “Fastebenen”, die im Weiteren einheitlich als “Peneplains” bezeichnet werden, sowie dem Zerfall dieses markanten geomorphologischen Erscheinungsbildes im südlichsten Teil des tibetischen Plateau dem sogenannten Lhasa Block. Im Zuge dieser Arbeit konnten neue Erkenntnisse über die Hebungsgeschichte und der Sedimentverteilung in diesem Untersuchungsgebiet gewonnen werden. Diese Ergebnisse tragen zu einem besseren Verständnis der geodynamischen Entwicklung Asiens bei, die bis heute viele Fragen aufwirft.

Ende des 19. Jahrhunderts wurden Peneplains als metastabile geomorphologische Formen angesehen, die im Zuge großflächiger Erosion entstehen. Die Bezeichnung *Peneplain* und das dahinter stehende Konzept werden seitdem von der geomorphologischen Gemeinschaft jedoch kontrovers diskutiert. Bis heute gibt es keine standardisierte bzw. repräsentative Definition für das nicht zu übersehende landschaftsbildende Phänomen der Peneplains. Dementsprechend gibt es auch nur wenige Ansätze zu Modellierungen oder Berechnungen mit Geoinformationssystemen. Hier, in dieser Dissertation, werden idealisierte Peneplains als erhöhte, gleichmäßige und großflächige Ebenen mit abfallenden Hängen verstanden, auch wenn sich landschaftsbildende Peneplains oft gekippt darstellen und durch tektonische Prozesse gestört bzw. bereits durch fortschreitende Erosionsprozesse angegriffen sind.

Gut erhaltene Peneplains sind speziell für das Gebiet um den höchstgelegenen See der Welt, dem *Nam Co*, im nördlichen Teil des Lhasa Blocks im Hochland von Tibet charakteristisch. Die Peneplains zerschneiden das dort vorkommende viel ältere und vorwiegend granitische Gestein sowie die angrenzenden Metasedimente.

Zur Bestimmung der Abkühl- und Hebungsalter der Granite wurden geo- und thermochrono-

logische Methoden wie Zirkon U-Pb, Zirkon (U-Th)/He, Apatit (U-Th)/He und Apatit-Spaltspuren-Datierung angewendet. Neben der Hebungsrate konnte auch die Freilegung des granitischen Gesteines ermittelt werden. Mit der Methode zur Bestimmung des U-Pb-Zirkonalters konnten zwei Intrusionsgruppen, um 118 Ma und 85 Ma, festgestellt werden. Ebenso wurden vulkanische Aktivitäten nachgewiesen und auf einen Zeitraum zwischen 63 Ma und 58 Ma datiert.
Thermische Modelle, aufbauend auf Zirkon- und Apatit-(U-Th)/He-Datierungen sowie auf Apatit-Spaltspuren-Daten der untersuchten Granitoide, ergeben einen Hebungs- und Abkühlungszeitraum von 75 Ma bis 55 Ma mit einer Hebungsrate von 300 m/Ma, welche im Zeitfenster zwischen 55 Ma und 45 Ma stark abfällt auf 10 m/Ma. Die Auswertung der Messdaten unserer Kooperationspartner an der Universität Münster zu kosmogenen Nukliden zeigen sehr niedrigen Erosionsraten von 6-11 m/Ma und 11-16 m/Ma, in den letzten 10.000 Jahren die in den einzelnen Einzugsgebieten ermittelt wurden. Diese Daten zeugen von einer noch immer andauernden Periode der Stabilität und tragen zur Erhaltung der Peneplains bei.
Während der anhaltenden Phase der Erosion und Einebnung sind vor ungefähr 45 Ma in der untersuchten Region zwischen 3 km und 6 km Gestein abgetragen und weg transportiert worden. Es ist naheliegend, dass das abgetragene Material als Sediment über das vorhandene Flusssystem fast vollständig in die heute bestehenden Ozenane transportiert wurde. Im Lhasa Block können nur verhältnismäßig wenig Sedimente aus dieser Zeit nachgewiesen werden. Alle bisherigen Untersuchungsergebnisse sowie die durchgeführte Sediment-Herkunftsanalyse untermauern die Theorie, dass die Peneplainbildung und ihre Erosionsprozesse in niedriger Höhe - höchstwahrscheinlich auf Meeresniveau - stattgefunden haben muss. Dieser Prozess wurde durch die Kollision des indischen Kontinents mit Asien gestoppt. Die resultierende Krustenverdickung führte zu einer Hebung der Landschaft mit den Peneplains, von Meeresniveau auf 5.000 bis 7.000 Höhenmeter. Die auf dem "das Dach der Welt" vorherrschenden idealen Klimabedingungen haben anschließend für die fast vollständige Erhaltung der Peneplains gesorgt.

Der zweite Teil der Dissertation befasst sich mit der Entwicklung einer robusten Methode Peneplains anhand digitale Höhenmodelle (DEM) zu berechnen bzw. zu kartieren. Frei zugängliche DEMs machen es möglich, Erdoberflächen repräsentativ mathematisch und statistisch zu analysieren und zu charakterisieren. Diese Analysemethode stellt eine ausgezeichnete Möglichkeit dar, die Peneplains mittels aussagekräftiger Algorithmen zu charakterisieren und digital zu kartieren. Um Peneplains algorithmisch von der Umgebung klar abgrenzen zu können, wurde ein komplett neuer Ansatz der Fuzzylogik angewandt. Als DEM-Basis wurde ein 90 arcsec-DEM der Shuttle Radar Topography Mission (SRTM) verwendet. Mithilfe eines Geoinformationssystems (GIS) wurden Algorithmen geschrieben, die vier verschiedene kritische Parameter zur Beschreibung von Peneplains berücksichtigen: (I) Gefälle, (II) Kurvigkeit, (III) Geländerauhigkeit und (IV) Relative Höhe. Um die Eignung der Methode zu prüfen, wurde auf Basis der SRTM-DEM weltweit kartiert und mit schon in der Literatur beschriebenen Peneplains verglichen. Die dabei erhaltenen Ergebnisse von den Appalachen, den Anden, dem Zentralmassif und Neuseeland bestätigen dass ein Einsatz des Modells, weltweit und unabhängig von der Höhenlage möglich ist.

Preface

The present PhD thesis was carried out in the context of the DFG-funded project No. DU373/5 of the priority programme 1372 entitled "Tibetan Plateau: Formation- Climate Ecosystem". The focus lies on the extensive investigation of peneplains in the southern part of the Tibetan Plateau near the lake *Nam Co* between 29°30'N and 31°30'N latitude and 89°30'E and 92°00'E longitude.

The thesis deals with three key issues related to the peneplains: (I) When and under which conditions developed the peneplains; (II) what happened with the surface material ablated away by erosion from the peneplains, and (III) how can peneplains be determined representatively and quantitatively by a geospatial analysis tool.
For this purpose, fieldtrips were performed of a total duration of 10 weeks in autumn 2008 and 2009. During the campaigns, samples were collected in the area of the peneplains and in the surrounding Tertiary basins for further geo-, thermochronological and sedimentological research. Thermochronological and sedimentological investigations were fully performed at the GZG, Göttingen. Zircon U-Pb dating were carried out in cooperation with Dirk Frei at the Geological Survey of Denmark and Greenland (GEUS) in Copenhagen. The foundation of the ArcGis "PAT" ("Peneplain Analysis Tool") script for the determination of peneplains with geomorphometrical methods was laid during a visit at Dresden University of Technology in prolific teamwork with Jan Kropáček (Institute for Cartography).

The thesis is set up as cumulative work and incorporates five publications in form of single chapters. The introduction provides an overview on insights into the topic of peneplains, the geomorphometrical methods to detect peneplains, automatic mapping of digital elevation models, and the background of the following publications.

Chapter 1 primarily gives a comprehensive introduction into the current state of knowledge on peneplains and the investigated field on the southern Tibetan Plateau near *Nam Co*. Special attention will be given to aspects such as as the present state of the peneplains, their geology, applied methods, and geomorphometry. While in the first chapter the used analytical methods are only treated roughly, more details are given in the following chapters.

Chapter 2a corresponds to the manuscript entitled “Peneplain formation in southern Tibet predates the India-Asia collision and plateau uplift” that was published with Geology in October 2011, Volume 39, Page 983-986. The manuscript is authored by R. Hetzel, I. Dunkl, V. Haider, M. Strobl, H. von Eynatten, L. Ding, and D. Frei. It discusses the evolution of the peneplain in context of the tectonic evolution of the Tibetan Plateau. Geo- and thermochronological data, as well as cosmogenic nuclide data analysis constrain the crystallization and exhumation ages, and erosion rate of the peneplain. My main contributions to this manuscript were the performance of geochronological (zircon U-Pb) and thermochronological (zircon (U-Th)/He, apatite (U-Th)/He, and apatite fission track) data analyses.

Chapter 2b corresponds to the manuscript entitled “FORUM Reply: Peneplain formation in southern Tibet predates the India-Asia collision and plateau uplift” that was published with Geology in March 2013, Volume 41, Page e297-e298. It is authored by: R. Hetzel, I. Dunkl, V. Haider, M. Strobl, H. von Eynatten, L. Ding, and D. Frei. The manuscript deals with the reply to a comment published by Tian et al. in 2013. Tian and his co-authors question the scenario predicted by R. Hetzel et al. (see chapter 2a) that peneplains had already existed before the uplift. Instead, they offer an alternative option according to which peneplains developed after the uplift of the Tibetan Plateau. Our response to the arguments claimed by Tian et al. (2013) outlines why the presented alternative hypothesis is untenable.

Chapter 3 presents the manuscript entitled “Cretaceous to Cenozoic evolution of the northern

Lhasa terrane and the Early Paleogene development of peneplains at Nam Co, Tibetan Plateau" that was published with the Journal of Asian Earth Science in July 2013, Volume 70-71, Page 79-98. It was authored by V. L. Haider, I. Dunkl, H. von Eynatten, L. Ding, D. Frei, and L. Zhang. The manuscript as well as this chapter deal extensively with the evolution of the peneplain between the time of emplacement of igneous rocks and the time of the uplift. With geo- and thermochronological data, several time constrains where modeled around Nam Co, and a new sensitivity test of the thermal modeling procedure was established. Besides writing the manuscript, I did all the analysis, except of the Al-in-amphibole geobaromety.

Chapter 4 is the sedimentological part of the thesis and is similar to the manuscript entitled "Assessment of single-grain age signature from sediments and their potential source rocks: provenance of post-Jurassic sediments from northern Lhasa Terrane, Tibetan Plateau". The manuscript is close to be submitted in an international journal and will be authored by: V. L. Haider, I. Dunkl, H. von Eynatten, L. Ding and D. Frei. This part of the thesis deals with the sediments next to the peneplains. Provenance analysis of detrital apatite and zircon grains with geo- and thermochronological methods from Jurassic to Cenozoic sediments reveal insights into the sediment dispersion patterns in the area of the peneplains. I did all geochronological, thermochronological and provenance analyses. Together with I. Dunkl and H. von Eynatten, I wrote the manuscript and interpreted the data.

Chapter 5 focuses on geomorphometry and is similar to the manuscript entitled "Identification of peneplains by multiparameter assessment of digital elevation models" that was submitted to the journal Earth Surface Processes and Landforms in September 2013. The manuscript is authored by: V. L. Haider, J. Kropáček, I. Dunkl, B. Wagner and H. von Eynatten. This part of the thesis concerns with the geomorphometrical aspect of peneplains. A new geospatial analysis tool was developed to map peneplains on digital elevation models quantitatively and independently of their location and elevation. Besides writing the manuscript, I developed the peneplain analysis tool, and defined all thresholds and fuzzy logic settings. I also evaluated generated metadata of the models with contributions from the co-authors.

Chapter 6 summarizes all the new facts gained throughout the single chapters and gives an overall picture about the development of the peneplains at the southern Tibet Plateau. This overall view is completed by outlining new scientific findings and already established knowledge. Subsequently, a sketchy outlook is given for possible starting points of advanced research related to the complex but highly fascinating topic of peneplains.

Contents

List of Figures

List of Tables

List of Abbreviations

ASTER	Advanced Spaceborne Thermal Emission and Reflection Radiometer
AFT	Apatite Fissiontrack
AHe	Apatite (U-Th)/He
Ap	Apatite
CIAT	Compagnie Industrielle d'Applications Thermiques (International Center for Tropical Agriculture)
CN5	corning glass dosimeter 5
CRONUS	Cosmic Ray produced Nuclides
cu	curvature
DEM	Digital Elevation Model
DRC	dynamic reaction cell
FT	Fissiontrack
GDEM	Global Digital Elevation Model
GEUS	Geological Survey of Denmark and Greenland
GIS	Geographic Information System
GOF	Goodness Of Fit
GOF_f	Goodness Of Fit_fission track age
GOF_h	Goodness Of Fit_AHe data
GOF_t	Goodness Of Fit_track length
ICP-MS	Inductively Coupled Plasma - Mass Spectrometry
ID-TIMS	Isotope Dilution Thermal Ionization Mass Spectrometry
IYSZ	Indus-Yarlung Suture Zone
JLP	Jet Propulsion Laboratory
LA-SF-ICP-MS	Laser Ablation - Single Collector Magnetic Sectorfield - ICP-MS
LT	Lhasa Terrane
METI	Ministry of Economy, Trade, and Industry (of Japan)
MTL	Mean Track Length
NASA	National Aeronautics and Space Administration (US)

NERC	Natural Environment Research Council
NIGL	NERC Isotope Geosciences Laboratory
PAT	Peneplain Analyzing Tool
PP	Peneplain
PRZ	Partial Retention Zone
rh	relative height
SF-ICP-MS	see LA-SF-ICP-MS
sl	slope
SRTM	Shuttle Radar Topography Mission
SS	Sandstone
TP	Tibetan Plateau
tri	terrain ruggedness index
UTM	Universal Transverse Mercator
WGS84	World Geodetic System 1984
ZHe	Zircon (U-Th)/He
Zrn	Zircon

1 Introduction

1.1 Scope

The main topic of this thesis is the investigation of the evolution and the decay of the peneplains in the northern Lhasa terrane . This landforming feature is understood as geomorphologic structure with a characteristic, almost featureless plain delimited by steep slopes. Its evolution and appearance are complex, still not well understood, and heavily discussed in the geomorphological community. Peneplains can be found in the Lhasa terrane, on the southern Tibetan Plateau, where this distinctive geomorphologic structure was studied extensively. The present thesis deals with different methodical issues in order to better understand the history and characteristics of the peneplains in the Lhasa terrane. Approaches involving geo- and thermochronological methods such as zircon U-Pb age, zircon (U-Th)/He age, apatite (U-Th)/He age, and apatite fission track age were used to decipher the development of peneplains. Models based on the above mentioned methods outline a congruent and interpretable age - exhumation - subsidence path of the investigated peneplains. The analysis of cosmogenic nuclide data to decipher the erosion rate of the peneplain was performed by our cooperation partners at the University of Münster (cf. Hetzel et al., 2011; Strobl et al., 2012) and are considered in this thesis. Detrital zircon geochronology of surrounding young sediments were used to investigate the erosion of the Peneplains and the related sediment dispersion patterns. The predominant methodical approach deals with the establishment of a geospatial analysis method to define, detect, and analyze peneplains around the world. FIGURE 1.1 visualizes assumptions published on peneplains, different aspects of peneplains, all methods used in this thesis, and how they are linked to each other.

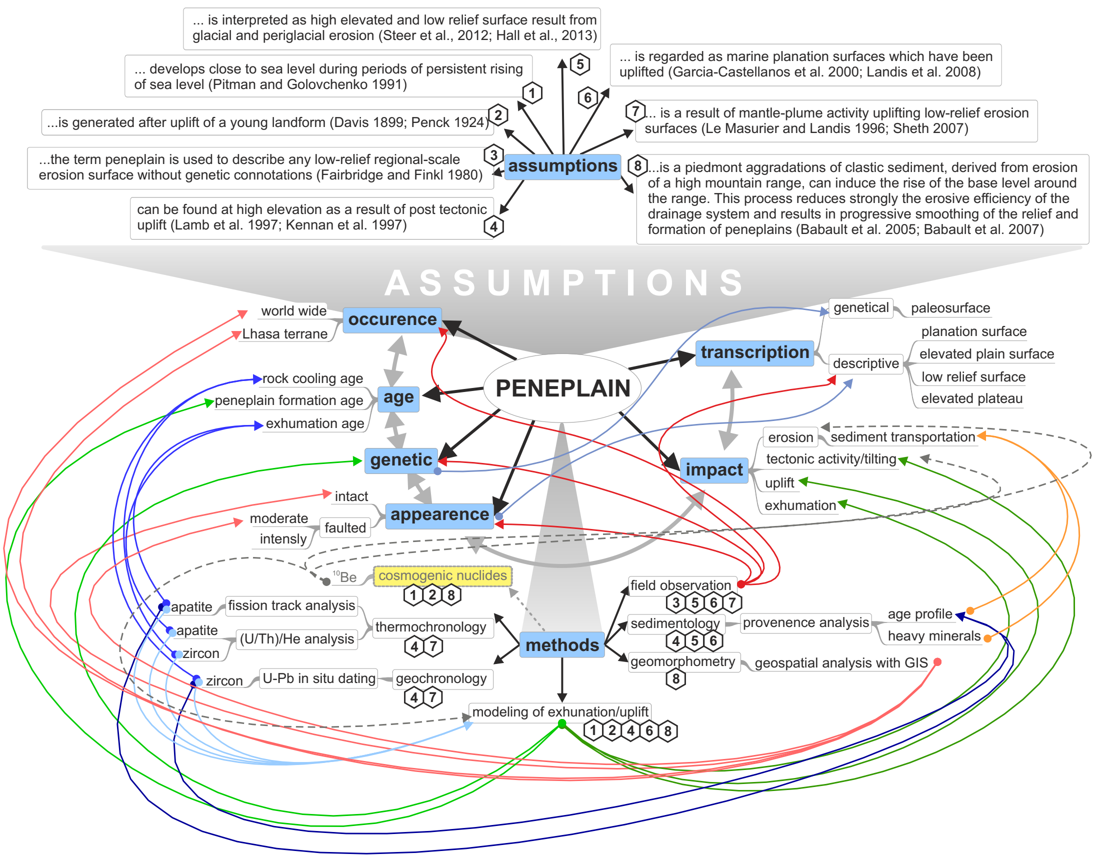

Figure 1.1: Six different aspects as occurrence, age, genetic, appearance, transcription, and impact are pointed out between the published assumptions and the methods to characterize or describe peneplains. The gray curved arrows and the numbers in the hexagons emphasizes that all aspects are linked together. Colored arrows starting from *methods* link to each aspect which can be solved by the used method. The *Cosmogenic nuclides* marked in yellow, was carried out by M. Strobl and R. Hetzel at the University of Münster.

1.2 Overview and location of the study area

The study area is located in the very southern part of the Tibetan Plateau (FIGURE 1.2A) in Central Asia between 89°30' E and 92°00' E longitude and 29°30' N and 31°30' N latitude (FIGURE 1.2B). It comprises an area of about 150 × 100 km with an elevation range between 4,530 and 5,600 m. The southern border of the field is the Nyainqentanghla Range which is aligned north-east. This mountain range forms a natural border between the rough topography with a high density of rivers in the south and the very smooth landscape with lakes in the north (FIGURE 1.2B). Immediately north of the mountain range and in the center of the lake area one of the biggest and highest elevated brackish lake *Nam Co* (translated: *Heavenly Lake*) is located. The area of interest is located predominantly north and northwest of Nam Co.

1.3 Geology

1.3.1 Tectonic setting of the Tibetan Plateau

The Tibetan Plateau is a unique and fascinating plane realm in central Asia with a size of about two and a half million square kilometers at an unusually high elevation of around 5,000 m (FIGURE 1.2A). This largest plateau on Earth is remarkably flat and has a relief of less than 1,000 m of a wavelength of about 100 km (Fielding et al., 1994). The massive Himalayan range in the south, the Kunlun Range in the north and the Qilian Range in the northeast enclose the Tibetan Plateau. The "roof of the world" is sometimes also named as the third pole (Qiu, 2008) as it is predominated by permafrost (Qiu, 2008). Brackish lakes accumulate in the southern part of the plateau.

The plateau results from the amalgamation and uplift of several terranes during the collision between the northward moving Indo-Australian Plate and the southern margin of the Eurasian Plate during Mesozoic time (Dewey et al., 1988). Four terranes, the Kunlun-Qilian, Songpan-Ganze, Qiangtang and Lhasa terrane, were located in the Tethys Oceans and shifted east-west, trending against the Eurasian Plate one after another. The suture zones can be followed across the entire plateau (cf. e. g. DeCelles et al., 2002; Leier et al., 2007a, FIGURE 1.3).

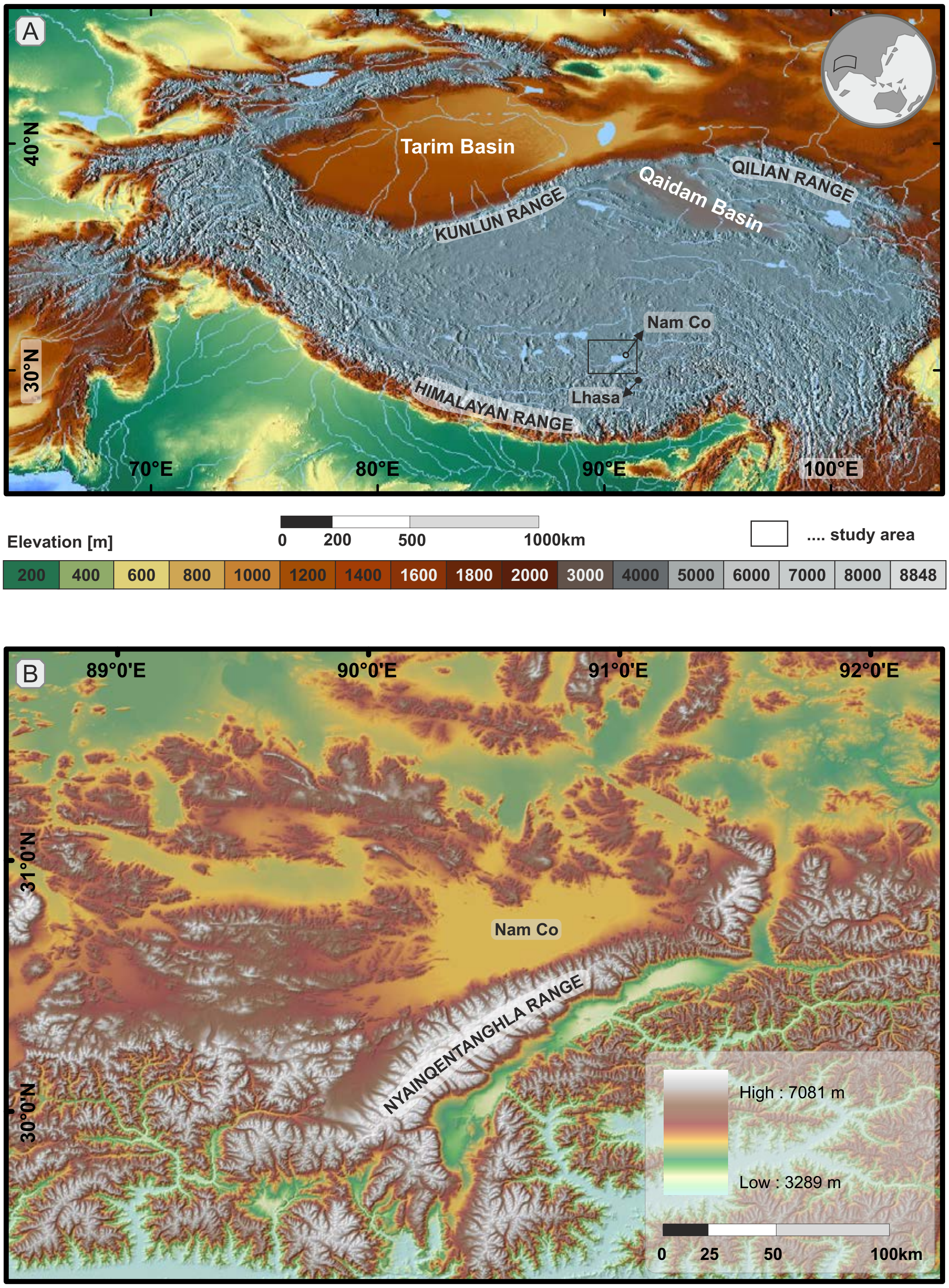

Figure 1.2: Elevation maps of the Tibetan Plateau with the biggest lakes and rivers [A] (Modified content from http://maps-for-free.com/). Map [B] outlines the area of interest north of the Nyainqentanghla range.

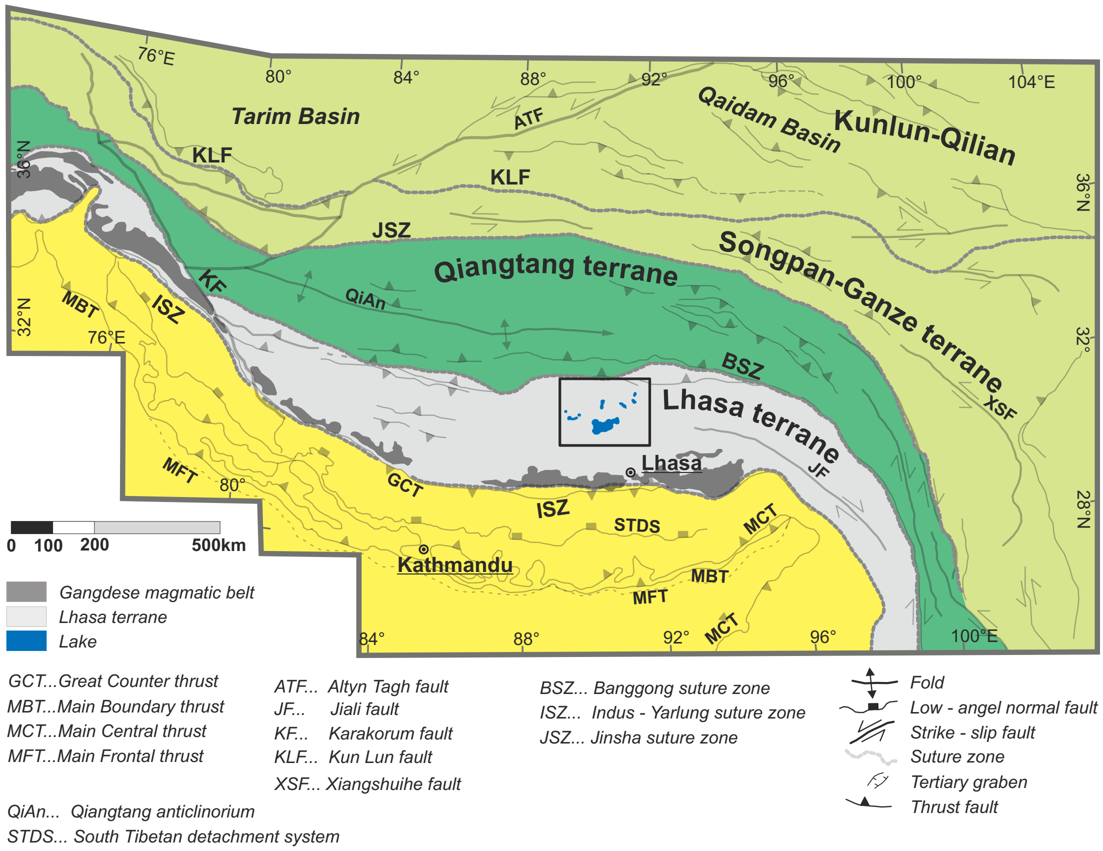

Figure 1.3: Tectonic map showing terranes of the Tibetan Plateau.

1.3.2 Mesozoic to Cenozoic evolution of the Lhasa terrane

The Lhasa terrane is the southernmost of the Tibetan terranes accreted to the Eurasian Plate (FIGURE 1.3; FIGURE 1.4). It is interpreted as the southern continental margin of Eurasia during the northward subduction of the Neotethyan Ocean in the Cretaceous (Murphy et al., 1997; Yin and Harrison, 2000).

In Late Triassic, the Neotethyan oceanic crust of the northwards drifting Lhasa terrane subducted under the Eurasian Plate (FIGURE 1.4). Around 150 to 140 Ma, in Late Jurassic time, the Lhasa terrane came into collision with the Qiangtang terrane to the north (Chen et al., 2002). The Neotethyan Ocean developed between the Lhasa terrane and the Indian-Australian Plate caused by rifting (Tapponnier et al., 1981). During Cretaceous, in the period of closing the Neotethyan Ocean, the Himalaya started folding by the subduction of the northern margin of the Indo-Australian Plate beneath the southern continental margin of Eurasia (Tapponnier et al., 1981; Murphy et al., 1997; Yin and Harrison, 2000). About 50 Ma years ago, the subduction of the northward moving Indian Plate closed the Neotethyan Ocean completely. The Banggong suture zone (BSZ) in the north separates the Lhasa terrane from the Qiangtang terrane and from the Indo-Australian Plate to the south by the Indus-Yarlung suture zone (IYSZ; Allegre et al., 1984; Yin and Harrison, 2000; FIGURE 1.3; FIGURE 1.4). As a consequence of the tectonic activity described above, the Tibetan Plateau rapidly moved upward behind the folding Himalaya range.

The geology of Meso- to Cenozoic plutonic and volcanic activity shapes the Lhasa terrane (Xu et al., 1985; Debon et al., 1986; Miller et al., 2000; Schwab et al., 2004; Kapp et al., 2005a; Volkmer et al., 2007). North of the IYSZ, the over 2,500 km long calc-alkaline magmatic Gangdese belt is exposed (Tapponnier et al., 1981; Allegre et al., 1984, FIGURE 1.3). The arc-shaped mountain belt is a large chain of mainly I-type batholiths forms the southern rim of the Lhasa terrane. It mainly comprises two intrusive stages of Early Cretaceous and Paleogene age (Debon et al., 1986; Copeland et al., 1987). The Gangdese magmatic arc comprehends the youngest magmatism of the Lhasa terrane, ranging between ca. 25 and 10 Ma (Allegre et al., 1984; Dewey et al., 1988; Yin and Harrison, 2000; Lee et al., 2009). The occurring of the Linzizong Potassic volcanism in the Gangdese belt (He et al., 2007; Mo et al., 2008; Lee et al., 2009) and sporadical also in the northern part of the Lhasa terrane (Lee et al., 2009; Pan et al., 2004) has been proposed in either Eocene (e. g. DeCelles et al., 2002; Chung et al., 2005) or the Oligocene-Miocene (e. g. Miller et al., 1999; Aitchison et al., 2007). Both, the Gangdese magmatic arc and the Linzizong Potassic volcanism are linked to the closure of the Neotethyan Ocean and the subsequent intracontinental collision (Allegre et al., 1984; Dewey et al., 1988, FIGURE 1.4). Early Cretaceous magmas (between 140 and 110 Ma) are spread over the whole Lhasa terrane (e. g. Xu et al., 1985; Murphy et al., 1997; Liang et al., 2008; Chiu et al., 2009) and forms the central plutonic belt. Its emplacement was connected to the closure of the Neotethyan Ocean between Greater India and the Lhasa terrane (Yin and Harrison, 2000, FIGURE 1.4). Predominantly strongly foliated orthogneisses with Jurassic protolith age are exposed in the Amdo basement (FIGURE 1.2B), south of the Banggong suture (Guynn et al., 2006).

Besides the granitic and volcanic rocks, Paleozoic to Mesozoic sedimentary rocks are widely exposed across the Lhasa terrane (Pan et al., 2004). According to the sediments, the Lhasa terrane can be divided in two geological provinces (Jixiang et al., 1988; Zhang et al., 2011). Jurassic to Cenozoic sedimentary strata scatter sporadically in the southern province with the dominating Gangdese Belt and the Cretaceous to Cenozoic igneous rock (Jixiang et al., 1988; Pan et al., 2004). In the northern part of the Lhasa terrane Upper Paleozoic to Cretaceous sedimentary sequences are exposed (Jixiang et al., 1988; Leeder et al., 1988; Pan et al., 2004). The Jurassic strata of the central and northern Lhasa terrane are typically very low-grade metamorphosed gray shales and fine-grained sandstones, partly associated with ophiolitic assemblages (Coward et al., 1988; Leeder et al., 1988; Yin et al., 1988). There are different approaches concerning the deposition of the Cretaceous strata which Zhang et al. (2011) summarize as follows. So the strata can be deposited within

(I) a Gangdese retroarc foreland basin (approach represented by e. g. England and Searle, 1986; DeCelles et al., 2007),

(II) a back-arc extensional basin (Zhang et al., 2004),

(III) a peripheral foreland basin (Leeder et al., 1988; Kapp et al., 2005b, 2007a; Leier et al., 2007c), or

(IV) a composite foreland basin (Ding et al., 2003).

Miocene E-W extension was accommodated by a series of generally N-S trending rift valleys throughout southern Tibet reflecting an orogenic collapse that likely follows an attainment of maximum elevation of the area (Molnar and Tapponnier, 1978; Dewey et al., 1988; England and Houseman, 1989; Yin and Harrison, 2000; Tapponnier et al., 2001). The development of these graben systems marks a significant shift in the state of stress within the Tibetan crust (Harris et al., 1988). There is evidence for an E-W extension in southern Tibet dating back to $\sim$ 19 Ma (Williams et al., 2001). It is assumed that the onset of normal faulting has been induced in southern Tibet about 14 Ma ago (Coleman and Hodges, 1995), and that these structures were reactivated about 8 Ma ago (Harrison et al., 1995). Central Tibet bears evidence for even younger significant E-W extension and normal faulting about 4 Ma ago (Harrison et al., 1995; Yin et al., 1999).

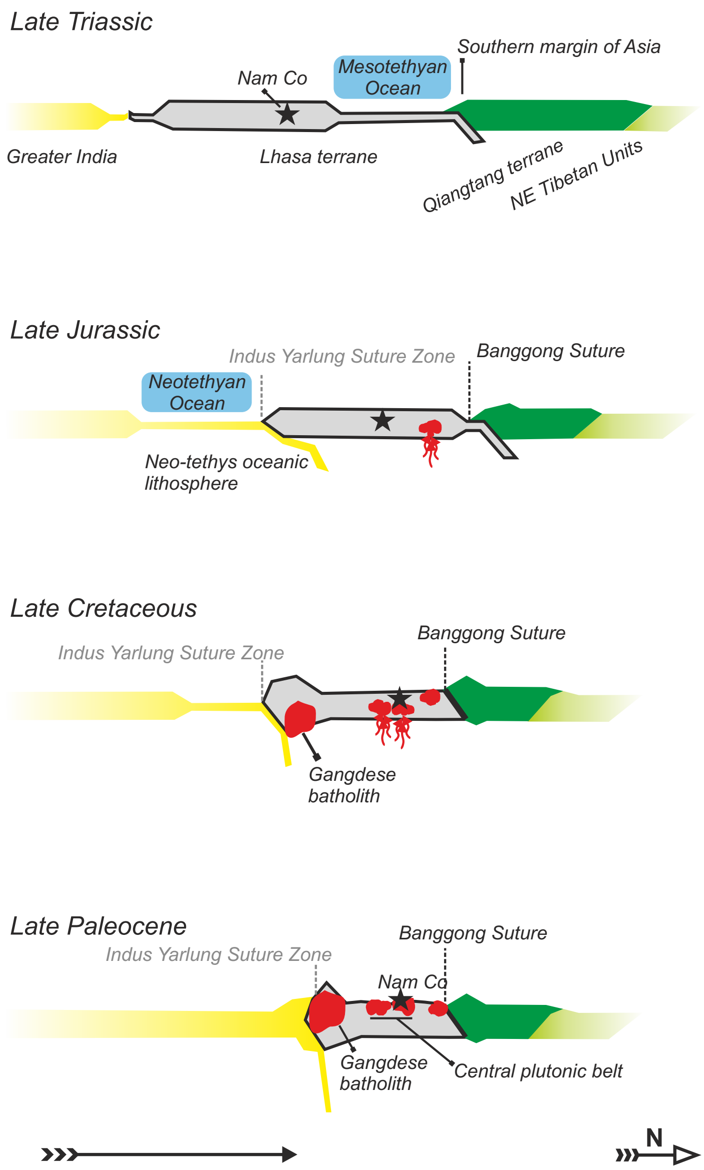

Figure 1.4: Schematic illustrations showing tectonic evolution at continent-scale between the northern margin of India and the southern Tibetan terranes (modified after Leier et al., 2007b). The Lhasa terrane (marked in gray) is especially emphasized, and details about plutonic events are shown. The colors of the terranes match with those in (FIGURE 1.3). The asterisk indicates the presumed position of the study area at Nam Co.

1.3.3 Stratigraphy of the northern part of the Lhasa terrane

Yin et al. (1988) describe in detail the stratigraphy of the northern part of the Lhasa terrane, dividing the area into two sub regions (FIGURE 1.5). The southern sub region *Doilungdeqen - Lhunzhub* involves the stratigraphy in the Lhasa area south of the Nyainqentanghla Range, whereas the northern Bangoin Nam Co sub region comprises the area between the Nyainqentanghla Range and the Banggong Suture.

In the southern sub region (FIGURE 1.5) first Mesozoic sediment deposition is recorded for the Middle Jurassic time. The *Quesangwenquan Formation* incorporated sandstone, volcanic conglomerate and shelly limestone which implied the deposition of sediments in an unstable shallow-water environment. Late Jurassic, the *Duodigou Formation* sedimented embracing argillaceous limestone with interbedded shale, shelly limestone, and fine sandstone. From Late Jurassic to Cretaceous, the *Linbuzong Formation*, characterized by siltstones with thin-bedded limestones, was deposited. The *Chumulong Formation* is part of the lower Cretaceous strata. It is composed of mainly terrestrial quartzose sandstone, conglomerate, some irregularly distributed andesites and ignimbrites. At the end of Early Cretaceous, the thick *Takena Formation* started to deposit and the formation process went on until Late Cretaceous. This formation consists of two members, the Early Cretaceous Penbo Member with basal limestone, and the overlain Late Cretaceous *Lhunzhub Member* implying fluvial red beds. (Yin et al., 1988; Leier et al., 2007c). The occurrence of fossils in the limestone beds of the *Penbo Member* indicates the deposition between Aptian and Late Albian time (Leier et al., 2007c).

In the northern sub region (FIGURE 1.5), the *Qusongbo Formation* is the northern equivalent to the *Quesangwenquan Formation* comprising Middle to Late Jurassic terrestrial sandstone and conglomerate. The *Duba Formation* is deposited during Early Cretaceous and it is dominated by red/green siltstone, mudstone of floodplain environment, and some conglomerate units. Scattered throughout are feldspathic sandstones and pebbly sandstones originating from sheet-flood (Leeder et al., 1988; Yin et al., 1988; Leier et al., 2007b,c). The conglomerate beds were deposited in shallow marine and meandering river environments. The *Langshan Formation* consists of limestone deposited during Early Cretaceous before Late Cretaceous fluvial red beds from the

Takena Formation overlaid the limestone. The general lithologic progression from lower carbonate to upper clastic red beds remains the same as in the southern sub region. After forming the *Takena Formation* a gap in sedimentation is recorded in both subregions until the end of Cretaceous. The *Linzizong Formation* with the volcanic strata partly covered the northern part of the Lhasa terrane Paleogene (e. g. DeCelles et al., 2002; Pan et al., 2004; Chung et al., 2005; Lee et al., 2009).

1.3.3.1 Mesozoic to Cenozoic Geodynamic Evolution of the Nam Co area

Between Triassic and Cretaceous, nearly continuous sedimentation took place (FIGURE 1.5). Smaller outcrops of Triassic strata can be found west of Nam Co and north of Bam Co (FIGURE 1.6), embedded mostly in limestone and basalts (Coward et al., 1988; Pan et al., 2004). The Jurassic lithology with the typically very low-grade metamorphosed gray shales and fine-grained sandstones are proven in the eastern and northern part of the study area (Leeder et al., 1988; Yin et al., 1988).

During Cretaceous time, a belt of felsic intrusions was emplaced, representing the prevalent lithologies of the Nam Co area: Biotite-hornblende granodiorite, leucogranite, monzogranite and tonalite (Xu et al., 1985; Harris et al., 1990). In the eastern part of the study area, the granitoids of the Bangoin batholith complex (FIGURE 1.6) intruded into the slightly folded Jurassic sequences and generated contact metamorphic zones. In Late Cretaceous, the Bangoin batholith complex was penetrated by andesitic-dacitic dikes (Xu et al., 1985; Coulon et al., 1986; Harris et al., 1990; Pan et al., 2004). During the time of intrusion and volcanic activity, Cretaceous sediments were deposited especially southern of the Bangoin batholith complex (Pan et al., 2004; Leier et al., 2007b). The sediments consist primarily of Carboniferous sandstone, metasandstone, shale and phyllite, and less frequent sequences bearing Ordovician, Silurian, and Permian limestone (Leeder et al., 1988; Yin et al., 1988; Pan et al., 2004; Leier et al., 2007b). Shallow marine limestone of Aptian to Cenomanian age (Zhang, 2000) overlies the Lower Cretaceous clastic units and is widely exposed further south and southwest of the study area (Yin et al., 1988). Fluvial arkosic sandstone and mudstone are characteristic for the Upper Cretaceous strata in the Lhasa terrane (*Takena Formation*; Leier et al., 2007a). The sources of the Upper Cretaceous clastic formations

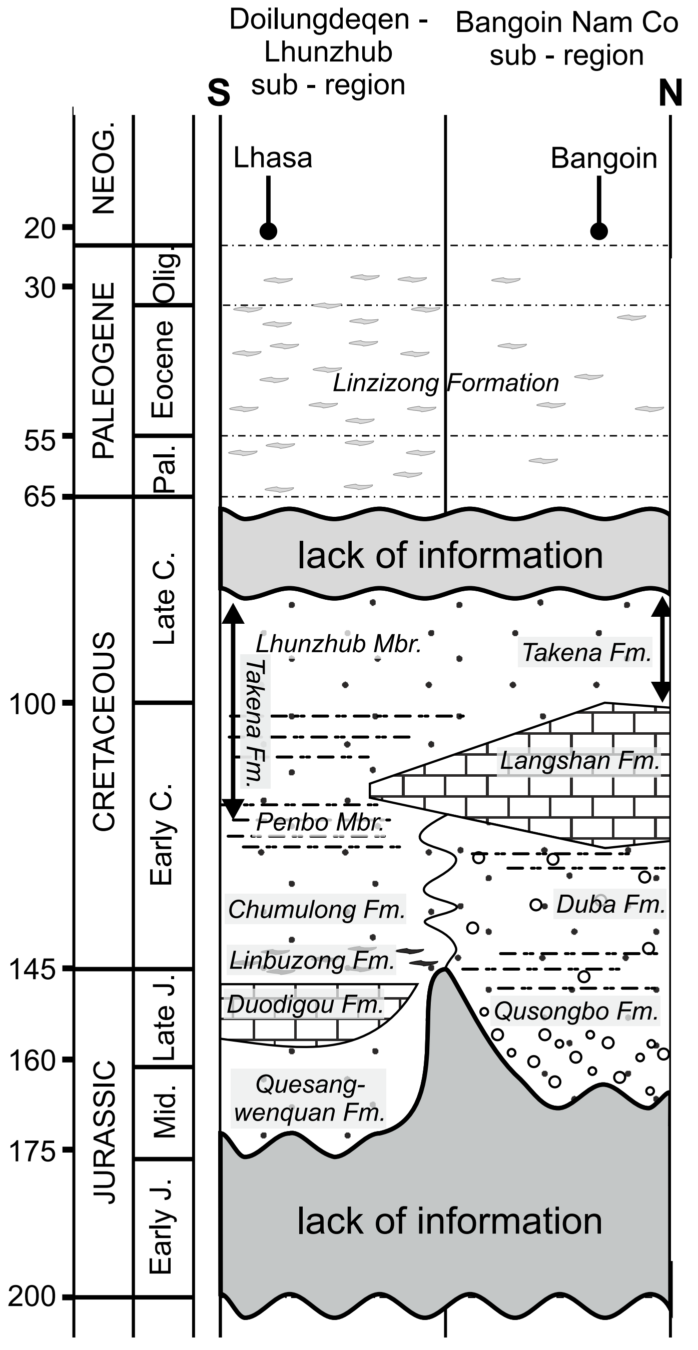

Figure 1.5: Stratigraphy of the northern Lhasa terrane (set up after Yin et al., 1988)

were volcanic rocks, granitoids of Early Cretaceous age, and sedimentary strata eroded from the northern Lhasa and southern Qiangtang terranes (Leier et al., 2007a,b). Jurassic to Cretaceous sediments are present mainly in the eastern part of the study area, north of Nam Co (Coward et al., 1988; Pan et al., 2004).

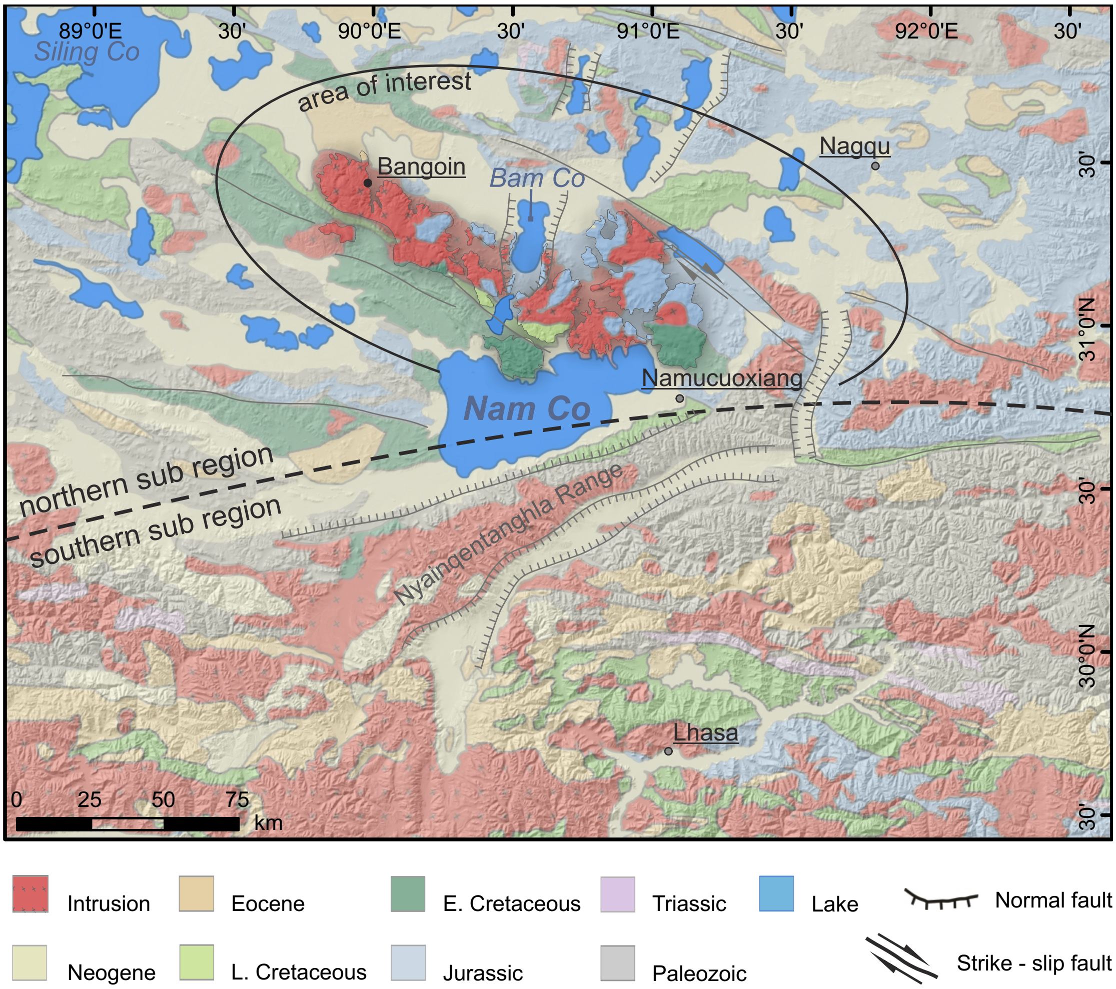

Figure 1.6: Geological map with peneplains. The peneplains north of Nam Co are highlighted by darker colors. The dashed line shows the boundary of the stratigraphical sub regions. Note that the widespread volcanic rocks scattering over the area are not emphasized in this geological map.

Eocene continental red-beds are widespread in the northern part of the study area (FIGURE 1.6; FIGURE 1.7), especially north of Bangoin city. The sediments are interpreted as marginal, mainly alluvial fan facies equivalents of the *Niubao Formation* of the Lunpola basin (FIGURE 1.2B) situated further north of the Nam Co area (Xu and Lee, 1984; Taner and Meyerhoff, 1990;

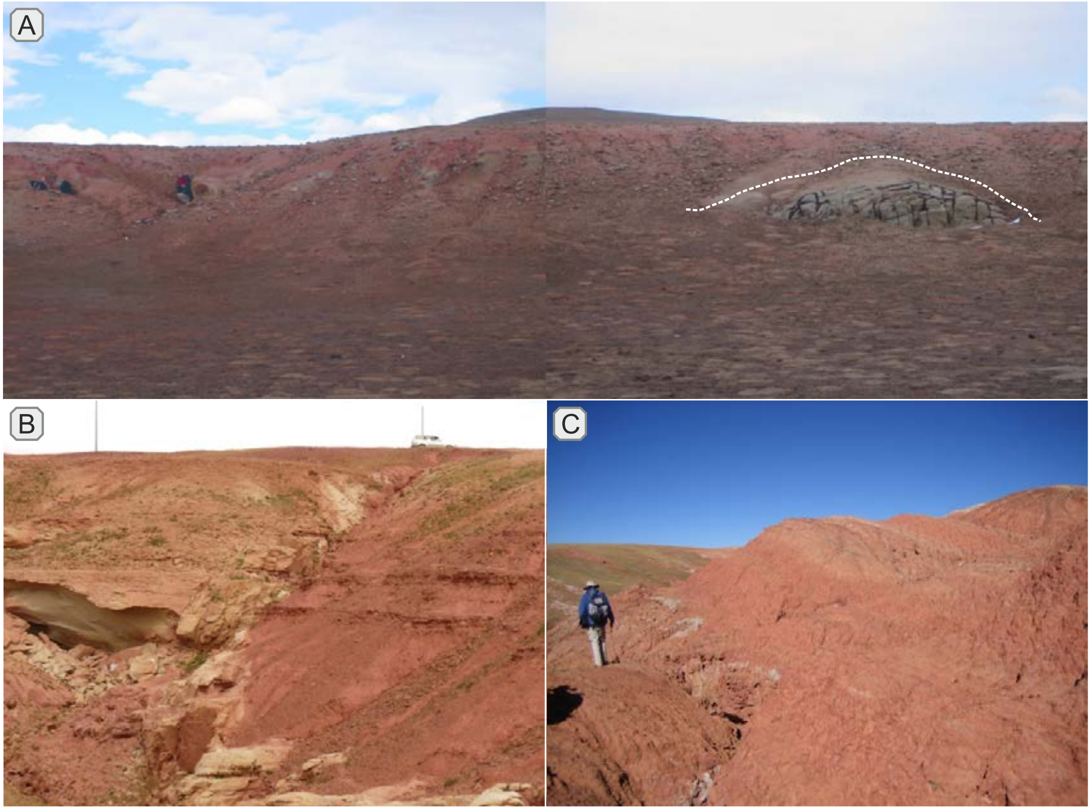

Figure 1.7: The panorama image [A] shows an example of continental red beds overlying basement rocks (right side of the image) of the Bangoin batholith complex. The typical red Eocene sediments [B-C] are present north of the peneplain area.

DeCelles et al., 2007). Sand- and siltstone dominate in the Eocene strata of the area, but there are also fractional conglomerate, pelite and sometimes gypsum-bearing strata as well as fragments and incrustations of hematite-rich tropical duricrusts can be found. The index composition of sandstones is dominated by monocrystalline quartz, metapelitic lithic fragments, and feldspar grains. The basal beds of the siliciclastic sequences are rich in coarse feldspar crystals indicating short sediment transport. Most probably, their provenance are the Bangoin batholith complex and low-grade Jurassic metapelites. The strata overlies the northern part of the Bangoin batholith complex but it is not directly exposed (FIGURE 1.7A). Granitoid clasts found in the arenites and the results of mapping expeditions (e. g. profiles in the 1:250,000 geological map H45C001004) support an onlap geometry of the clastic sequences onto the Bangoin batholith complex. The Eocene sediments are mostly sub-horizontal with an observed tilt of less than 15° towards N-NE. Neogene/Quaternary deposits dominate the sediment cover south of Nam Co and north of the

Bangoin batholith complex. Terraces with varying heights can be observed in the gravel banks of the lake margins and reflect diverse Pleistocene to Holocene lake levels. They are also carved in the basement rocks in several tens of meters above the current levels of the lakes. Although they sometimes are remarkable features, these flat geomorphological objects are typically of minor extent. Moreover, they are only localized in the lowest levels of the depressions.

1.4 Peneplains

The concept and term "peneplain" is used and discussed since the end of the 19th century, long before plate tectonics was discovered. William Davis introduced this term in the article "The geographic cycle" to explain the concept of denudation of mountains to base level (Davis, 1899). Independently, and at the same time Penck (1894) developed a similar scenario (cf. Penck, 1924). Both scientists applied genetic definitions and understood peneplains as the youngest geomorphological feature before mountains are completely planated to base level. With their paradigm, they started a broad discussion in the geoscientist community. Since gaining an understanding of the permanent movement of the Earth's crust and the wide-spread acceptance of plate tectonics in the 1960's (e. g. Runcorn, 1965; Korgen, 1995) Davis' seemed to be no longer valid and peneplains came out of focus. Coltorti and Pieruccini (2000) paraphrase peneplains as planation surfaces and state that the topic is outdated in geomorphology. In sense of landforms, a peneplain is understood as a low-relief plain representing the final stage of fluvial erosion during times of extended tectonic stability (Phillips, 2002), or in other words, as "a polygenetic surface of low relief" (Fairbridge and Finkl 1980). The recently increased attention paid to topic shows that peneplains are still a valid concept (e. g. Babault et al., 2005; Hetzel et al., 2011; Steer et al., 2012; Hall et al., 2013).

Some authors tried to clarify the genesis and definition of peneplains using different approaches (see also FIGURE 1.1) which are presented in the following:

(I) Peneplains are generated after the uplift of a young landform (Davis, 1899; Penck, 1924);

(II) Peneplains develop close to sea level during periods of persistently rising of sea level (Pitman and Golovchenko 1991);

(III) They can be found at high elevations as a result of post tectonic uplift (Lamb et al., 1996; Kennan et al., 1997);

(IV) They are regarded as marine planation surfaces which have been uplifted (Garcia-Castellanos et al., 2000; Landis et al., 2008) ;

(V) Peneplains interpreted as high elevated and low relief surface result from glacial and periglacial erosion (Steer et al., 2012; Hall et al., 2013);

(VI) Piedmont aggradations of clastic sediment, originating from erosion of a high mountain range, can induce the rise of the base level around the range. This process strongly reduces the erosive efficiency of the drainage system and results in a progressive smoothing of the relief and the formation of peneplains (Babault et al., 2005, 2007);

(VII) Peneplains are the result of mantle-plume activity uplifting low-relief erosion surfaces (LeMasurier and Landis, 1996; Sheth, 2007); or

(VIII) The term peneplain is used to describe any low-relief regional-scale erosion surface without genetic connotations as suggested by Fairbridge and Finkl Jr. (1980).

Peneplains and related features termed “low-relief surfaces” or “paleosurfaces” are described around the world. They can be found on every continent and in many mountain belts such as the Klamath Region in California (e. g. Anderson, 1902; Aalto, 2006), the Rocky Mountains (e. g. Lindgren and Livingston, 1918; McMillan et al., 2006), the Andes (e. g. Kummel, 1948; Jordan et al., 1989; Hoke and Garzione, 2008; Schildgen et al., 2009; Allmendinger and González, 2010), the Pyrenées (e. g. Babault et al., 2005; Gunnell et al., 2009), Scandinavia (e. g. Strøm, 1948; Lidmar-Bergström, 1999; Sturkell and Lindström, 2004), Africa (e. g. Willis, 1933; Dixey, 1939; Coltorti et al., 2007), Himalaya (e. g. Cui et al., 1997; Liu-Zeng et al., 2008; Van der Beek et al., 2009), Australia/New Zealand (e. g. Mulcahy et al., 1972; Stirling, 1991; Landis et al., 2008), and Antarctica (e. g. LeMasurier and Landis, 1996).
Most peneplains around the world were described prior to 1960’s. By this time, the information/data was derived from field observations and topographical maps. Later, many scientists adopted the maps relying mostly on the knowledge gained during first half of the last century.

Since the last decade, new techniques are used to investigate peneplains such as thermo- and geochronological tools (e. g. Jordan et al., 1989; Lamb et al., 1996; Gunnell et al., 2009), cosmogenic nuclides (e. g. Jackson et al., 2002; Hetzel et al., 2011; Strobl et al., 2012) or geospatial data analysis (e. g. Babault et al., 2005; Hoke and Garzione, 2008; Strobl et al., 2010).

Nevertheless, until yet there is no concept established for the unambiguously definition of Peneplains. Focusing onto the descriptive point of view, the only common denominator of all above mentioned studies, regardless of geological history and age, is the observation of distinctive elevated and flat surfaces delimited by steep slope (FIGURE 1.8). Ideal peneplains are rare due to tectonic activity and incipient erosion. The plane top of peneplains can be tilted to a greater extend and effected by erosion. It is not necessarily the highest geomorphological structure in its realm. If there is more than one peneplain in one region, the elevation can vary . Tectonic activity and proceeding erosion can deface peneplains beyond recognition.

Peneplains situated at different elevations are documented from all over the world they are described either from a genetic or a morphologic point of view. Existing definitions of peneplain are diffuse and still intensely discussed. As a consequence, it is nearly impossible to outline peneplains in a reproducible way. Thus it is inevitable to redefine this remarkable geomorphological structure descriptively in order to enable their unbiased identification and to foster a deeper understanding of the multifaceted origin of peneplains.

1.4.1 Peneplains in the study area

Peneplains in the field area can be found north and north-west of Nam Co (FIGURE 1.6A). The sizes of the planated surfaces are between one and ca. 100 km^2. The elevation varies between 4,600 and 5,600 m. They are the dominant geomorphological features in the study area. Peneplains are carved in granitoids and in their metasedimentary host formations. Some are fully intact (FIGURE 1.9A-C) but the greater part is already intersected, tilted, or faulted (FIGURE 1.9D-F; FIGURE 1.10A-B). The randomly positioned blocks on top of intersected peneplains (FIGURE 1.10C-D) do not feature any marks of movements. Where the top is sheltered against the wind, vegetation grows between the blocks and smooths the surface (FIGURE 1.10D).

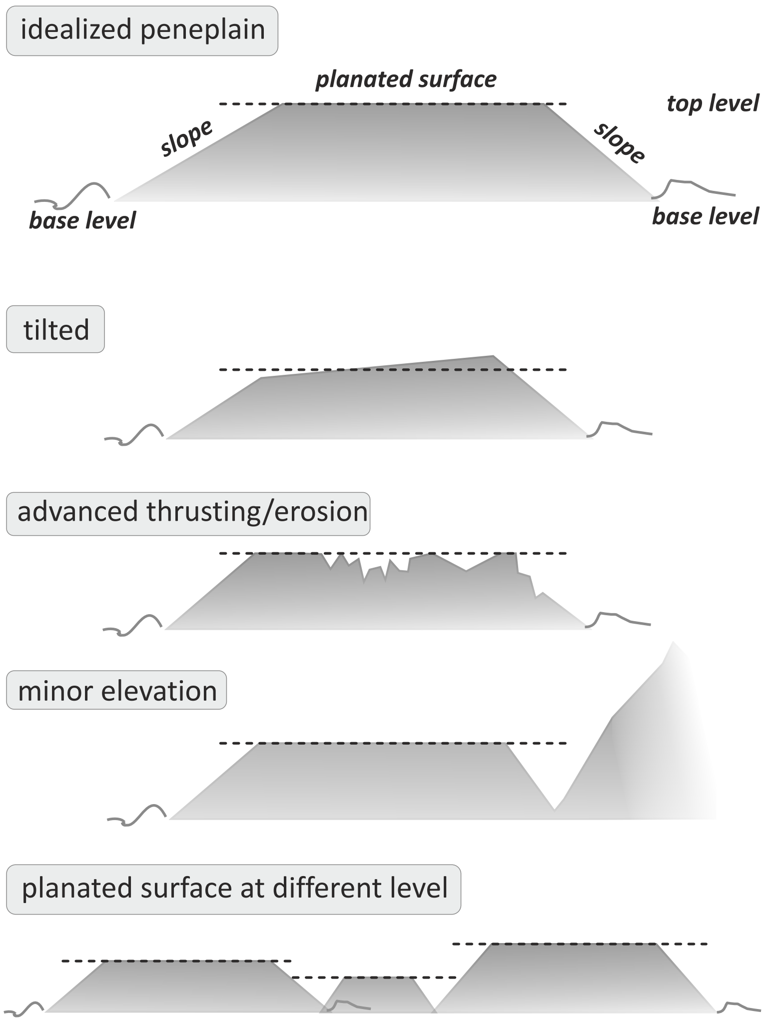

Figure 1.8: The sketches show different characteristics of peneplains. While the uppermost drawing shows an ideal peneplain, the drawings beneath shows typical peneplains influenced by post-planation tectonics or erosion.

1.5 Methodology

1.5.1 Sample preparation

Rock samples were crushed using a jaw crusher. Heavy mineral fractions, including zircons and apatite, were pre-concentrated by separating of the fine sieve fraction ($< 250\,\mu m$) on a Wilfley table. The heavy minerals were further concentrated by separation using heavy liquid sodium-polytungstate (ρ=2.86 g/cm^3). Before the next treating step, an untreated aliquot was picked from each sample for the semi-quantitative heavy mineral analysis. From the other part, ferromagnetic

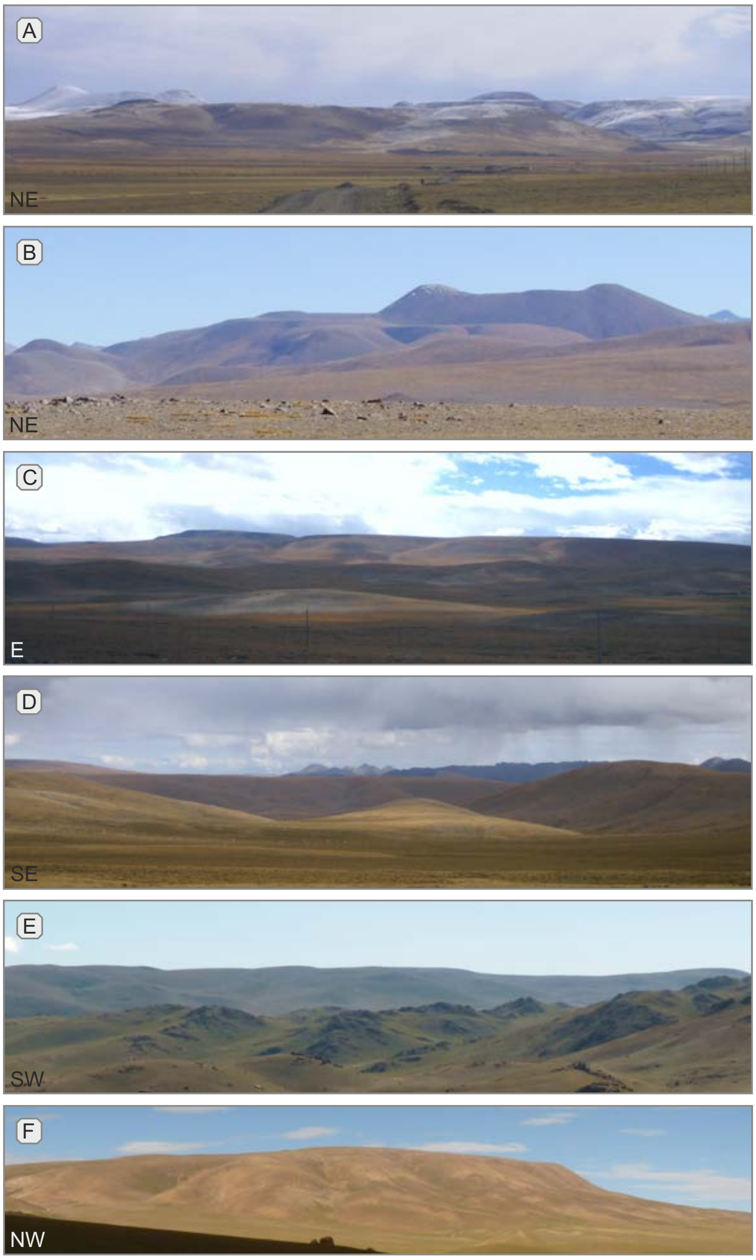

Figure 1.9: Compilation of photographs showing the field area and the characteristic peneplains. It gives a good overview about the diversity of peneplains in the study area. [A] Characteristic peneplains east of Nam Co with flat surfaces but varying elevations; [B] Photograph taken from the top of a peneplain towards peneplains further east in the eastern Nam Co area. The image was taken by M. Strobl; [C] Peneplains are typical and landscape forming around Nam Co. The image shows a giant peneplain behind an already lowered surface north of Nam Co; [D] Behind the huge peneplain, the ridge of Nyainqentanghla range can be seen. Nam Co lays in between but is not visible in the image; [E] Peneplains decayed by spheroidal weathering to a rugged hilly landscape forming corestones. Behind this incised, alterated area, a still intact peneplain is visible. The image shows such a surface in front of another massive and intact peneplain north-west of Nam Co. [F] This peneplain represents peneplains with smooth but inclined surface. It inclines towards SW. Image [E] and [F] were taken by I. Dunkl.

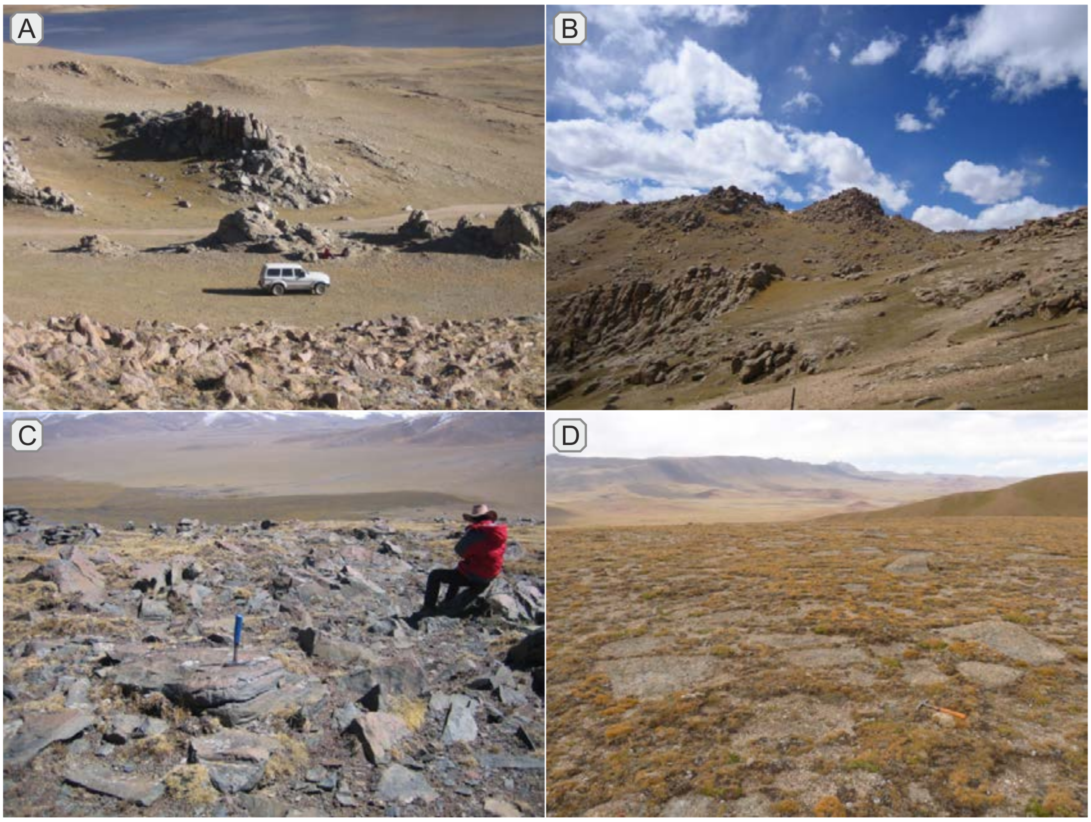

Figure 1.10: Photographs [A] and [B] represent examples of remaining corestones of strongly alterated peneplains. The images [C] and [D] present typical tops of the peneplain. [D] Mostly the surfaces are broken open to smaller blocks and sometimes fixed by existing vegetation. Image [D] was taken by I. Dunkl.

minerals were removed from the heavy mineral concentrates by using a common hand magnet. The dia- and paramagnetic fractions were treated by isodynamic magnetic separation. For this purpose, four to six different magnetic fractions were produced by applying a stepwise increasing current from 0.5 to 1.7 Amps at 10° side tilt of the magnet. High quality zircons and apatite concentrate were produced by a treatment with 1.7 Amps. The washed and dried zircon-apatite substrate was further processed by removing the zircons (ρ=4.6 g/cm^3) from the lighter apatite (ρ=3.2 g/cm^3) in two different ways: either by panning it in alcohol or by applying another gravity separation using diiodomethane (ρ=3.33 g/cm^3).

1.5.2 Geo- and thermochronological methods

Time constrains at different stages of development are necessary to comprehend and model the evolution of the peneplain. Therefore, in-situ U-Pb dating on zircons was performed to (I) determine the emplacement age of the Bangoin batholith complex (CHAPTER 2A; CHAPTER 3) and (II) obtain findings about the provenance of the sediments (CHAPTER 4). Zircon and apatite (U-Th)/He data from the Bangoin batholith complex shed light on the exhumation rate (CHAPTER 2A; CHAPTER 3). In combination with apatite fission track data and cosmogenic nuclides data, the exhumation of the Lhasa terrane and the rate of erosion were reconstructed (CHAPTER 2A; CHAPTER 3). Further, apatite fission track data of detrital apatite grains gives valuable insights about provenance and sediment transport (CHAPTER 4).

1.5.2.1 Introduction

Geologists nowadays are in the very lucky position of having the possibility to receive absolute age numbers of dated rock. Especially the radioactive isotopes ^{238}U (99.28 % occurrence) and ^{235}U (0.715 % occurrence) decaying to ^{206}Pb and ^{207}Pb (Jaffey et al., 1971, TABLE 1.1) are very valuable due to the alpha-decays, the spontaneous fission of ^{238}U, and the continuously emitting helium nuclei that delivered by multifaceted chronometers with different sensitivities. Tapping the full potential of the uranium decay delivers many time marks to constrain geodynamic processes.

Table 1.1: Parent-daughter pairs and the emitted α particles (^{4}He) within the chain.

Decay route	$^{4}He_{emitted}$	$t_{1/2}$, Ga	Decay const. λ, yr^{-1}	References
$^{238}U \rightarrow {}^{206}Pb$	8	4.47	1.55125×10^{-10}	Jaffey et al. (1971)
$^{235}U \rightarrow {}^{207}Pb$	7	0.704	9.8485×10^{-10}	Jaffey et al. (1971)
$^{232}Th \rightarrow {}^{208}Pb$	6	14.01	0.49475×10^{-10}	Jaffey et al. (1971)
$^{147}Sm \rightarrow {}^{143}Nd$	1	106	6.54×10^{-10}	Lugmair and Marti (1978)

1.5.2.2 U-Pb chronology

Several positive features of U-Pb decay make this isotope system to a unique and important tool for geochronology:

(I) there are two complex U-Pb alpha decay chains

(II) different decay constants (λ) are known (TABLE 1.1), and

(III) of the four stable lead isotopes, ^{204}Pb, ^{206}Pb, ^{207}Pb, and ^{208}Pb, only ^{204}Pb is non - radiogenic. ^{208}Pb is the final decay product of ^{232}Th which can also be used for dating but was ignored for this project.

These attributes provide the basis for the most precise and versatile chronometers. Due to the high closure temperature of U-rich accessory minerals such as zircon, U-Pb is mainly applied for dating of magmatic rocks, high temperature stages of metamorphic rocks, or old detrital components in sedimentary rocks (Müller, 2003). Zircon U-Pb systems have a very high closure temperature of about 900 °C (Dahl, 1997; Cherniak and Watson, 2001, TABLE 1.2). Before the mother isotopes ^{238}U, ^{235}U, and ^{232}Th decay to the stable daughter isotopes ^{206}Pb, ^{207}Pb, and ^{208}Pb, they give rise to several other radioactive isotopes. Step by step the mother isotope decays to the metastable daughter isotopes. While most of these are stable for less than thousand years, some only for few seconds (e. g. ^{219}Rn), and others can have half life times of up to ca. 250 thousands of years (e. g. ^{234}U). The mother isotopes (^{234}U, ^{232}Th, ^{235}U, and ^{247}Sm) are many times more stable than the intermediate daughter isotopes (TABLE 1.1). It is supposed that, in view of the length of geological time, the radioactive chain reaches a stationary state where the content of all the intermediate radioactive isotopes remains constant, the so called secular equilibrium (e. g. Dickin, 2005).

Table 1.2: Summary of used geo- and thermochronometers and closure temperatures (assembled by Reiners et al., 2005)

Decay system	Mineral	AP*	CT**	AE***	References
(U-Th)/Pb	zircon	1-2	>900	550	Cherniak et al. (1991); Cherniak and Watson (2001)
Fission track	apatite	8	90-120	190	Jaffey et al. (1971)
(U-Th)/He	zircon	3-4	160-200	170	Jaffey et al. (1971)
(U-Th)/He	apatite	3-4	55-80	140	Lugmair and Marti (1978)

*Approximate precision (%,1σ); **Closure temperature (°C); ***Activation energy (kJ/mol)

1.5.2.2.1 Laboratory procedure of U-Pb geochronology

About 35 zircon crystals from igneous samples and about 250 zircon crystals from sediment samples were randomly picked for in-situ age dating. The selected crystals were fixed in grain mounts with epoxy resin, ground down (diamond suspensions of 9 μm) to expose their internal textures in longitudinal section, and polished (diamond suspensions of 3 and 1 μm) until the zircons were exposed and had a plain surface so that they were suitable for Cathodoluminescence (CL) mapping and laser ablation ICP-MS isotopic measurements. The CL images served as a base for the selection of laser spots to minimize the bias caused by ablation of heterogeneous zones. In-situ U-Pb dating was performed by laser ablation-single collector-magnetic sectorfield inductively coupled plasma mass spectrometry (LA-SF-ICP-MS) at the Geological Survey of Denmark and Greenland (GEUS) in Copenhagen. A Thermo Finnigang Element 2 mass spectrometer coupled to a NewWave UP213 laser ablation system was used. All age data presented in this thesis were obtained by single spot analyses with a spot diameter of 30 μm) and a crater depth of approximately 15 to 20 μm). The laser was fired at a repetition rate of 5 Hz and at nominal laser energy output of 50 %. He and Ar were used as sample carrier gases. Analytes of ^{238}U, ^{232}Th, ^{208}Pb, ^{207}Pb. ^{206}Pb and ^{204}Pb were measured with SF-ICP-MS. Further details about the used methods are given by Frei and Gerdes (2009); Gerdes and Zeh (2006). The age calculation was based on the standard-sample bracketing using the GJ-I zircon standard (Jackson et al., 2004). For further validation the Plešovice standard (Sláma et al., 2008) was analyzed. The age results of the standards were consistently within 1σ of the published ID-TIMS values. Drift corrections and data reductions of the raw data were performed by using the PepiAGE data reduction software (Dunkl et al., 2008). Depending on the trend detected through the measurement session of the ICP-MS, the drift was corrected by linear, logarithmic, or 2nd order polynomial regression. No common lead correction was required. ^{206}Pb/^{238}U ratios with a concordance (^{206}Pb/^{238}U vs. ^{207}Pb/^{235}U) between 90 and 105 % were used for the geological interpretation. Tukey's Biweight method was used to determine the robust mean age using Isoplot/Ex 3.0 (Ludwig, 2003). The probability plots for the provenance study were generated with an algorithm which had been programmed with the *R* software.

1.5.2.3 (U-Th)/He thermochronology

Besides the decay of ^{238}U, ^{235}U, and ^{232}Th, ^{147}Sm emit ^{4}He after every single decay. For dating, the alpha particles originating from samarium are less important. While U-Th produce 21 ^{4}He within a half life time of < 4.47 Ga, the ^{147}Sm produce only one alpha particle holding a half life time of 106 Ga (Jaffey et al., 1971; Lugmair and Marti, 1978, TABLE 1.1). Since the diffusive loss of He in crystals is comprehensible (Zeitler et al., 1987), the helium amount can be quantified. The determined He age is suitable to constrain cooling through very low temperature (Braun et al., 2006) in the range between 55 and 200 °C (Reiners et al., 2004; Farley, 2000). Therefore, it is of interest for determining near-surface cooling and attractive for many other geomorphological approaches. The effective closure temperature strongly depends on the cooling rate and the size of the analyzed crystal (Wolf et al., 1996; Farley, 2000, FIGURE 1.11). The partial retention zone (PRZ) temperature is a widely used parameter to describe the range of the closure temperature. While the PRZ of zircon is at ∼160-200 °C (Reiners et al., 2004), the PRZ of apatite is at ∼55-80 °C (Farley, 2000, TABLE 1.2). Step heating experiments reveal the closure temperature as a function of the cooling rate (Reiners, 2005, and references therein; FIGURE 1.11).

1.5.2.3.1 (U-Th)/He dating procedure

Usually four apatite and four zircon crystal aliquots from each sample were carefully handpicked under the binocular with precision tweezers. Under 250x magnification and cross-polarized light, the crystals were extensively checked. Only euhedral, clear, intact, and inclusion-free crystals with a minimum diameter of 70 μm were selected. For the calculation of the alpha ejection correction factor (Farley et al., 1996), several microphotographs were taken to determine shape parameters like width, total length, and length of prismatic section. Each crystal was wrapped in platinum capsules with a diameter of about 1 mm and prepared for the measurement chain: (I) measuring the mass of He and (II) measurement of the parents isotopes (^{238}U, ^{235}U, ^{232}Th, ^{147}Sm). For this purpose, the filled capsules were degassed in high vacuum by heating them with an infrared laser that was provided at the Thermochronology Laboratory at Geoscience Center, University of Göttingen (GÖochronology). A SAES Ti-Zr getter at 450 °C purified

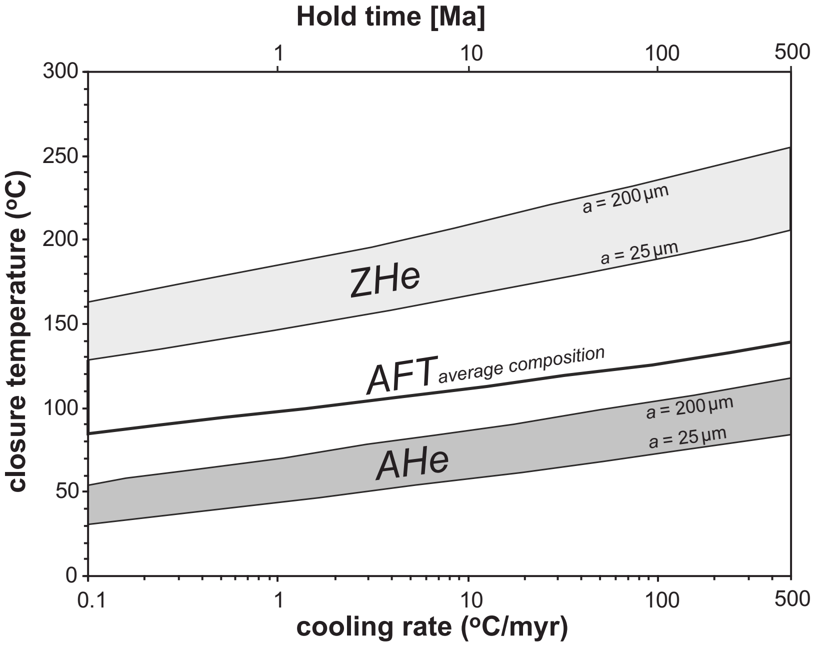

Figure 1.11: The effective closure temperature or partial retention zone temperature is a function of cooling rate and in case of (U-Th)/He method, additionally size of crystal. (modified and assembled after Reiners, 2005).

the gas extracted from the crystals and a Hiden®triple-filter quadrupole mass spectrometer equipped with a positive-ion-counting detector measured the helium content. For each crystal, a re-extraction was performed to double-check the degree of the first degassing. For the detection of the α-emitting elements (uranium, thorium, and samarium), the degassed crystals were spiked with calibrated ^{230}Th and ^{233}U solutions. Zircons were dissolved in pressurized Teflon bombs using distilled 48 % HF + 65 % HNO_3 during five days at 220 °C, while apatites were dissolved in 2 % HNO_3 at room temperature in an ultrasonic bath. The actinide concentrations were determined by the isotope dilution method and the Sm by an external calibration method, using a Perkin Elmer Elan DRC II ICP-MS equipped with an APEX micro-flow nebulizer. Data reduction was performed with MASsoft (software of the mass spectrometer) and the PEPITA freeware (Dunkl et al., 2008).

1.5.2.4 Apatite fission track thermochronology

The ^{238}U naturally decays by spontaneous fission. The two new nuclei fly with high energy 7 μm antipodally (e. g. Fleischer and Price, 1964; Naeser and Faul, 1969) and create a so called latent fission track in the mineral lattice. Such damage can be shown on plain mineral surfaces (FIGURE 1.12) through acid etching because to the fact that the acid preferentially attacks damaged areas at a higher dissolution rate. The number of countable fission tracks correlates with the cooling age of the crystal after passing a defined temperature windows. The advantage of knowledge that (I) the ratio between ^{238}U/^{235}U is assumed as a constant value (137.8; Steiger and Jäger, 1977) and (II) induced fission of ^{235}U isotope can be produced under laboratory conditions, make fission track dating a well controllable chronometer in the low temperature sector (TABLE 1.2). The susceptibility of fission tracks to thermal re-setting, which was used to be a disadvantage, has been put to a very good use as a measure of cooling, uplift and burial processes (Dickin, 2005).

Fission tracks have an initial length of 15 to 16 μm (e. g. Fleischer and Price, 1964; Reiners and Brandon, 2006) and react very sensitive against reheating (see also FIGURE 1.13). The damaged crystal lattice slowly heals and the tracks continuously fade by exceeding a certain temperature boundary (e. g. Silk and Barnes, 1959; Ketcham et al., 1999). Hence, they have a smaller probability of intersecting the exposed mineral surface. That's why, fewer tracks become etched and the apparent track density decreases (e. g. Laslett et al., 1982). The track length distribution can be used to decipher the thermal evolution of the host rock (Gallagher et al., 1998, FIGURE 1.13). The closure temperature in apatite ranges between 90 and 120 °C (Laslett et al., 1982; Ketcham et al., 1999). The annealing behavior of apatite is not only controlled by temperature but also by the chemical composition of the crystal and etching procedures (Green et al., 1986; Donelick et al., 2005). Fluorine and chlorine secondary anions in the lattice of apatite influence the annealing kinetics of the tracks (Gleadow et al., 1986; Green et al., 1986). Therefore, kinetic parameters are required (e. g. Ketcham et al., 1999; Donelick et al., 2005; Tagami and O'Sullivan, 2005). D_{par}, the mean etch pit of outcropping fission tracks parallel to the crystallographic c-axis (FIGURE 1.2) is representative of the kinetics of the annealing of fission tracks (Carlson et al., 1999; Ketcham et al., 1999).

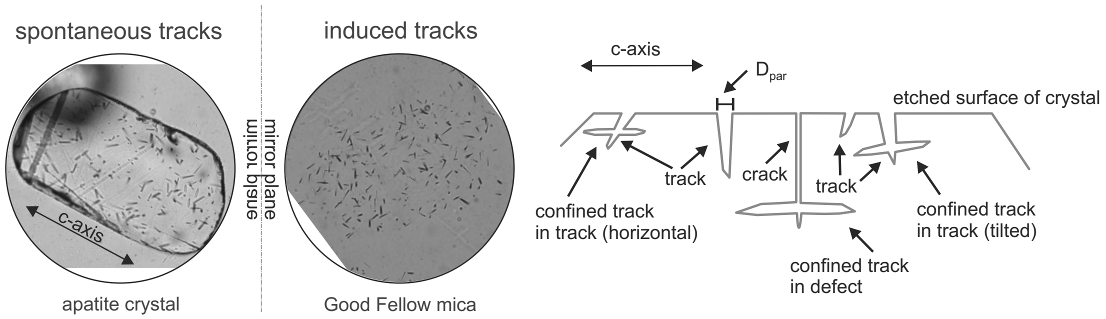

Figure 1.12: The photographs on the left show a polished crystal with spontaneous fission tracks (left) and the associated Good Fellow mica print with induced tracks (right). The schematic on the right illustrates a section through a polished apatite crystal with D_{par} tracks and confined tracks (adapted from Gallagher et al., 1998).

1.5.2.4.1 Fission track dating procedure

Aliquots of the highly enriched apatite concentrates were dispersed randomly onto a sticky tape. The strew slides were fixed in grain mounts by thin epoxy resin blocks (*Araldite brand #2020*), ground down in two steps to expose their internal textures in longitudinal section, and polished plain (diamond suspensions of 3 and 1 μm) until the bulk of apatites were exposed. After etching with 5.5 N HNO_3 for 20 sec at 21 °C (Donelick et al., 1999) the mounts were ready for the apatite fission track (AFT) analysis with the external detector method according to Gleadow (1981). The apatite grain compounds with the etched spontaneous tracks were covered with freshly cleaved muscovite sheets (Goodfellow mica) serving as external track detectors and irradiated with thermal neutrons in the research reactor of the TU Munich in Garching. The requested neutron fluence was 5×10^{15} n/cm^2. A corning glass dosimeter (CN5) was used to monitor the neutron fluence. After irradiation the tracks in the external detectors were revealed by etching in 40 % HF for 40 min at 21 °C. Both grain mount and corresponding mica detectors were fixed side by side on a glass slide. The spontaneous and induced fission tracks were counted under 1,000× magnification using a Zeiss Axioskop microscope equipped with computer-controlled stage system (Dumitru, 1993). Only apatite crystals with well polished surfaces parallel to the crystallographic c-axis and free from dislocations were counted. From the igneous samples, fission tracks of only 25 grains were counted, while from the sediment samples, 100 apatite grains were considered for provenance analyses. Additionally the D_{par} values were recorded for each dated apatite crystal. If confined tracks (FIGURE 1.12) were available, between 60 to 100 horizontal confined tracks (only track in track) were measured in most of these samples, considering the c-axis of the crystal (Donelick et al., 1999). Apatite fission track ages were calculated using the zeta (ζ) age calibration method (Hurford and Green, 1982) with the standards listed in Hurford (1998). For fission track dating in this study, $\zeta = 324.74 \pm 6.09$ Ma were used. Data processing and plotting was performed with the TRAKKEY software (Dunkl, 2002); errors were calculated using double Poisson dispersion including Ns, Ni, and Nd as described in Green (1981).

1.5.2.5 Thermal modeling

For modeling thermal histories, a complex data set is necessary including information which are now available such as AFT, AHe and ZHe apparent ages, track length distributions, D_{par} values, apatite and zircon crystal dimensions, U content, zircon U-Pb age data and kinetic parameters. The HeFTy program (Ketcham, 2005) was used to run thermal history models of selected samples. The program uses a Monte Carlo algorithm with a multi-kinetic annealing model (Ketcham et al., 1999). The algorithm generates a large number of time-temperature paths, and it calculates the apparent age and the synthetic track length distribution which are tested with respect to the measured data. Before starting the modeling, HeFTy is fed step by step with five major types of input data:

(I) apatite fission track single-grain ages with the counted track number and the corresponding kinetic parameter (here: D_{par}; Carlson et al., 1999),

(II) the length of confined horizontal fission tracks and their angle to the crystallographic c-axis,

(III) parameters from (U-Th)/He apatite analysis such as U, Th, and Sm contents, the calculated equivalent sphere radius for each crystal, and the measured and uncorrected AHe age,

(VI) the same parameters from (U-Th)/He zircon analysis, and

(V) the available additional constraints of the time-temperature history, i. e. the annual mean temperature (5 °C in the region), the emplacement age of the dated intrusions and surface temperature in Eocene (between 55 and 35 Ma) when the plateau forming igneous formations were exhumed to the surface and covered by the Paleogene sediments.

The modeling was performed using minor limitation factors (in nearly unsupervised mode). The only fixed constraints that were used were (I) the emplacement age of the Bangoin batholith complex (120 ± 80 Ma), (II) a mean surface temperature of 5 °C and (III) a time interval for the deposition of the Eocene red beds of 50 to 40 Ma with a near-surface temperature of 15-20 °C for this time because the red beds were deposited at tropical latitude (see CHAPTER 2A). The annealing models used for AFT, AHe and ZHe thermochronology are described in Farley (2000); Reiners et al. (2004); and Ketcham et al. (2007). A temperature of 200 °C and an age of 200 Ma were set as maximum values for modeling the thermal history. In order to estimate the reliability of the modeled thermal paths, systematic tests were made to determine the influence of variable single-grain (U-Th)/He ages on the HeFTy modeling (see CHAPTER 3).

1.5.3 Geomorphometry

Geomorphometry is the science of topographic quantification. Its operational focus is the extraction of land-surface parameters and objects from digital elevation models (Pike et al., 2009). For the quantification of peneplains, digital elevation models (DEMs) generated by Shuttle Radar Topography Mission (SRTM) were used and processed with the *ArcGis 9.3.1 Info* graphic information system software and analyzed with the “R 2.15.1” statistical software. As a result of this approach, many new understandings were gained and a manuscript was published (chapter 5). The publication describes a compact form of multi-parameter assessment of digital elevation models and the application of this method in other areas. Nevertheless, the expatiate data processing has high potential for further development. Therefore, this section aims to describe the workflow and data processing at great length to allow for an easier reproduction.

1.5.3.1 SRTM digital elevation model

A digital elevation model (DEM) was acquired by the mission of the Endeavour Space Shuttle in February 2000. The Shuttle scanned the entire land mass of the earth between latitudes 60°N

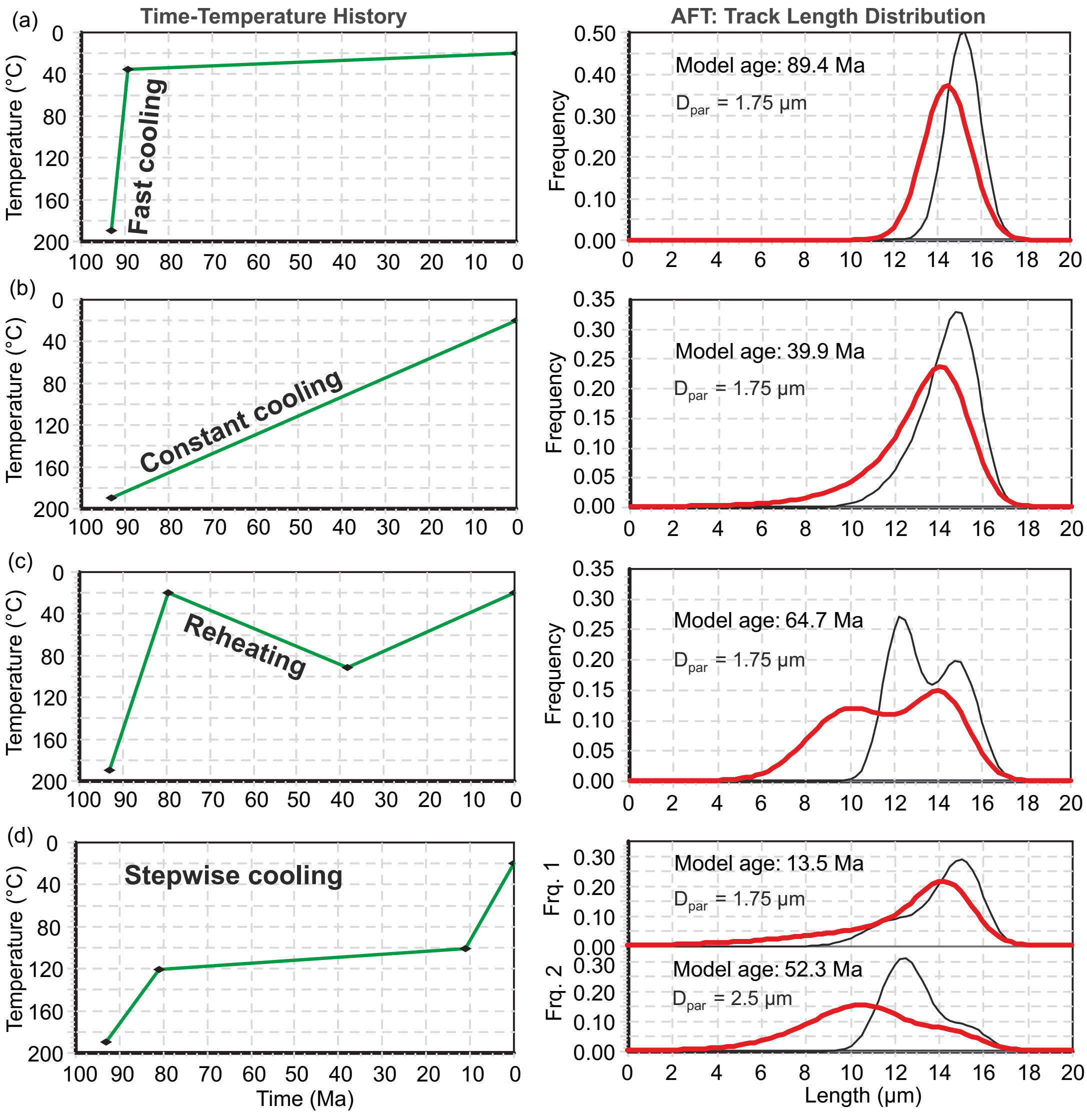

Figure 1.13: Example fission-track length distributions (right column) for various time-temperature scenarios (left column) and apatite kinetics. The bold red line in the length distributions reflects unprojected lengths while the thin black curve stands for the c-axis projected lengths. Scenario (d) demonstrates that kinetic variability can yield different bimodal length distributions depending on the kinetics of the crystal. While the upper model represents a bimodal length distribution with the same kinetic as the other scenarios (D_{par} = 1.75 μm), the lower model has a larger D_{par} of 2.5 μm. (adapted and modified from Ketcham, 2005).

and 57°S by single path radar interferometry at C-band. The SRTM has a pixel resolution of 3 arc second and 90 m, converted in SI unit. The high quality DEMs are provided for the international community and can be downloaded for free (http://www2.jpl.nasa.gov/srtm/). The original SRTM DEM assembled by the Jet Propulsion Laboratory (JPL) contains a certain amount of gaps in areas of radar shadows and low coherency. Therefore the already filled up version denoted as SRTM version 4 (Reuter et al., 2007; Jarvis et al., 2008) is used which is provided by CIAT (http://srtm.jrc.ec.europa.eu/). This version is ready to be used for geomorphological analysis and formed the basis for all purposes in this thesis.

1.5.3.2 Geographic information system (GIS)

To display, analyze, or manipulate raster images (FIGURE 1.14), a specially designed system from the Geographic information system is necessary. For this aim, ArcGis Info 9.3.1 by Esri ArcGis was used, which provides several toolboxes as extensions for special objects. For the approach presented in this thesis, three toolboxes are crucial for processing data and developing models for peneplains: (I) Spatial analyst, (II) Conversion tool and (III) Data Management tool. Additionally ArcGis implemented a very useful application to process and execute single manipulation as a compact model. The so called ModelBuilder allows to batch all single algorithms to a complete model, it gives a good overview and it makes models reproducible. It simplifies the repeats of runs with different datasets and conditions. Successfully run models can be converted easily to an independent ad-in tool and be provided for the geomorphometric community. In this project, the ModelBuilder was used to calculate possible peneplains from DEM. The new toolbox was named as “Peneplain Analyzing Tool” (PAT).

1.5.3.3 Key characteristics of peneplains

As already discussed in SECTION 1.4, peneplains have a characteristic appearance. An ideal peneplain sticks out of the scenery and has an elevated but leveled plain surface with a steep slope. Peneplains are mostly faulted by tectonic activity and attacked by erosion (FIGURE 1.8). Some are bordered by higher elevated mountain ranges.
The following three characteristic and geomorphological criteria are capable of fully describing

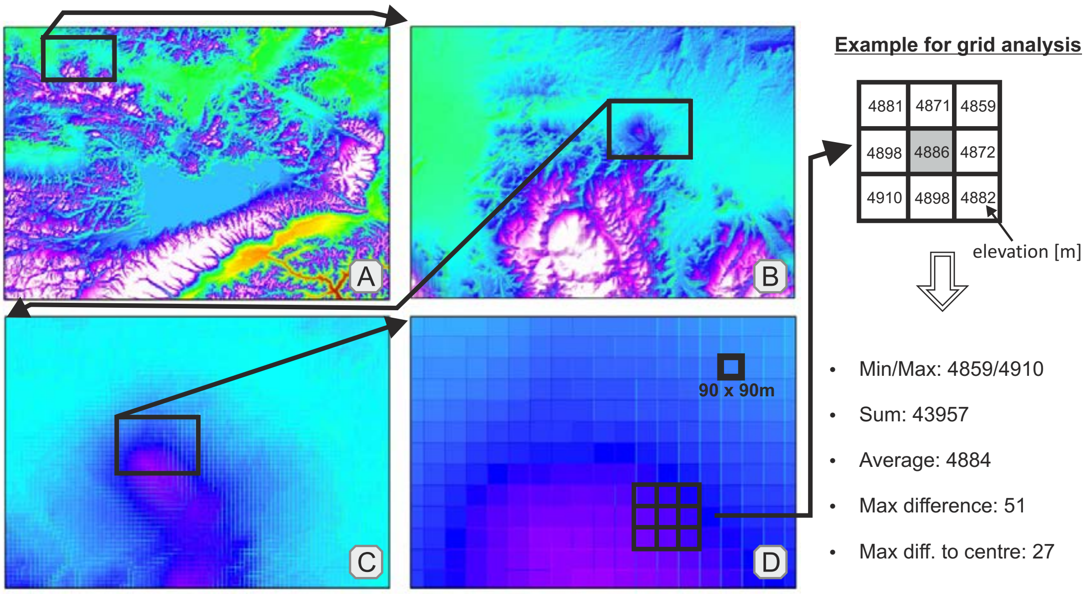

Figure 1.14: Example for the structure of raster data (3 arc second DEM). Stepwise zoom-in from image [A] to [D] until each pixel is clearly visible. Every pixel contains information about the elevation (see the grid at the right hand side). Generally, a spatial analyst tool works with a moving grid sized 3 by 3. The grid is moving pixel by pixel over the complete model, evaluating and comparing the pixel in the center (in our example the gray shaded grid box) with the eight adjacent pixels. Depending on the aim of a DEM mapping project, different algebraic functions can be calculated. The elevation number of a pixel is replaced by the newly calculated value. Simple examples are given below the model grid as minimum/maximum, sum, average, maximum difference and maximum difference to the center. Of course, there is the possibility to change the size and movement of the grid randomly.

and calculating peneplains with geospatial methods: slope inclination, curvature, and terrain ruggedness index. A fourth criterion, relative height makes the elevation of peneplains independent of the absolute elevation. These four significant criteria are illustrated in FIGURE 1.15 in a schematic landscape from the sea to the mountains. The erosion level is defined as the currently lowest possible level of the realm derived from the bottom of a river or stream channel. Interpolation between the erosion levels generates the erosional base level. The local base level represents the base level which the local surface attempts to reach by erosion. The sea level is the ultimate base level and the lowest level of continental denudation.

High values of slope indicate a steep gradient (FIGURE 1.15) and low slopes represent smooth surfaces for example an area near the sea, near lakes, and on top of peneplains. Slope inclination in DEMs describes the maximum rate of change between the centered pixel cell and its eight

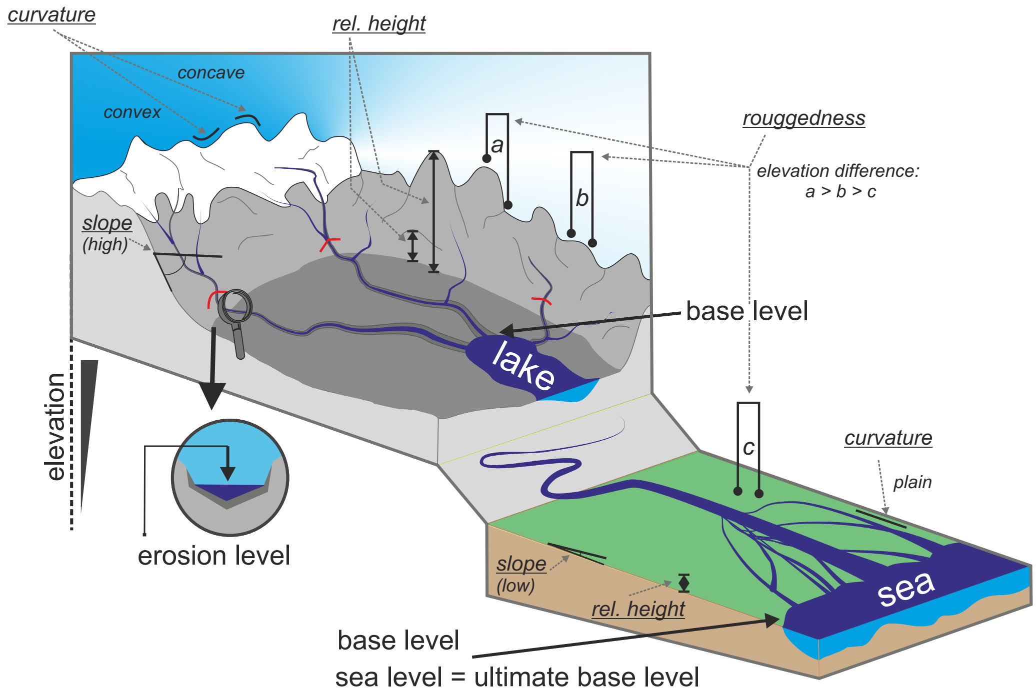

Figure 1.15: This scheme summarizes a low level area and a high level surface. Significant geomorphometrical criteria and their behavior are outlined in both realms. Further details are given in the text.

adjacent cells (FIGURE 1.16A). For the calculation standard algorithms established by Burrough and McDonnell (1998) were used. Besides the flanks of hills, a relatively plain surface can be characterized by slope as well. Therefore the slope can be used to identify the plain top of peneplains. However, slope inclination alone is insufficient to distinguish potential peneplains from lakes or other plain surfaces such as alluvial basins. Hypothetically, the threshold of slope is 0 and 90°. For the peneplain detection involving also slightly tilted peneplains, slopes between 0 and 30° are relevant.

A plain, convex, or concave behavior of the land surface is described as curvature. While mountainous realms have a high curvature, flat areas are of course, plain (FIGURE 1.15). Expressed mathematically, curvature describes the second derivate of the surface. ArcGis uses an algorithm batch by Peckham (2011) and Zevenbergen and Thorne (1987, FIGURE 1.15A). While zero values represent plain surfaces, negative values indicate concave, and positive values convex curves. Curvature is a great geomorphometrical criterion to distinguish and analyze different erosion zones in DEMs. Curvatures are important for characterizing peneplains because (I) values near zero describe the top surface and (II) curvature zones along mountain crests can be excluded. A big advantage of curvature is the possible identification of flat areas even if the DEM rough data are slightly biased by noise. While values ranging from -1 to +1 can indicate potential peneplains, all other values exclude this geomorphometrical structure.

The terrain ruggedness index (TRI) developed by Riley et al. (1999) expresses the ruggedness of the potential area (FIGURE 1.15). To yield the TRI, the difference between the basis pixel and each of the adjacent pixels are calculated. Each of the eight results is squared, the squares are added together and finally the root is extracted (FIGURE 1.16B). High TRI values reflect very rugged surfaces as mountainous realms and young erosion surfaces while plain areas, for example peneplains, nearly featureless surfaces, and lakes have a very small TRI of ideally zero.

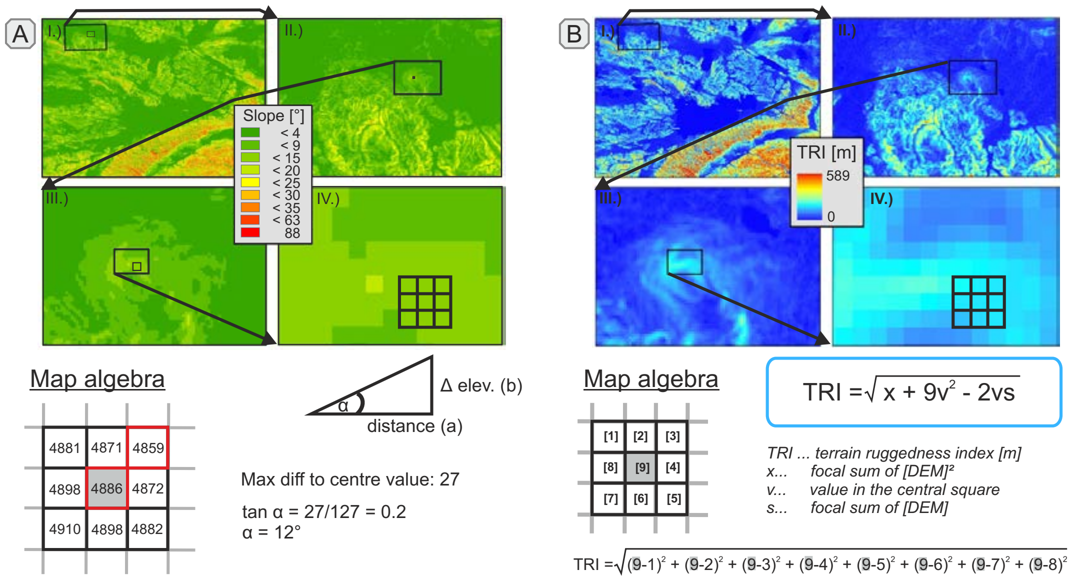

Figure 1.16: [A] Scheme of slope with a sample calculation. [B] Terrain ruggedness index developed by Riley et al. (1999)

The criterion "relative height" is a theoretical criterion reflecting the elevation difference between local base level and the surface line (FIGURE 1.15). With the introduction of relative height into the model, it is possible to eliminate plain surfaces near local erosional base level. It makes the mapping of peneplains more dynamical and independent of the elevation of the base level. To model the relative height with DEM, a drainage system was calculated. Interpolation between the branches reproduces the erosional base level. The relative height is calculated by subtracting the base level from the DEM surface (FIGURE 1.17B). Peneplains usually stick out from the surroundings. Here it is assumed that peneplains can be found on relative heights from 100 to 2000 m of relative height. Nevertheless, the modeling of many different areas showed that the relative height of potential peneplains range predominantly between 100 and 600 m. To unify all four criteria fuzzy logic is introduced. For this purpose, the data sets are evaluated and weighted. Further details about thresholds, algorithms, and the peneplain detection set criterion are given in CHAPTER 5.

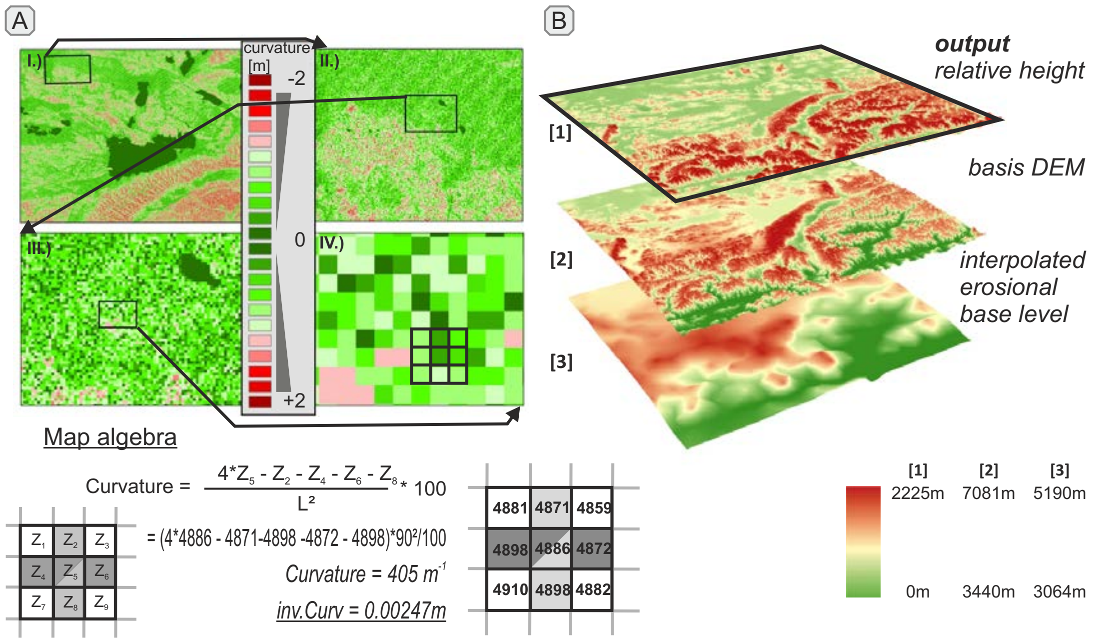

Figure 1.17: Model of [A] curvature calculated with the model after Peckham (2011) and Zevenbergen and Thorne (1987). [B] The interpolated erosional base level [3] subtracted from the basis DEM [2] gives the relative height [1].

1.5.3.4 Structure of the Peneplain analyzing tool (PAT)

Several individual operations with ArcGis are necessary before peneplains are detected by the spatial analysis tool (FIGURE 1.18).

The new *Fill* DEM is the base raster for calculating the four algorithm batches individually

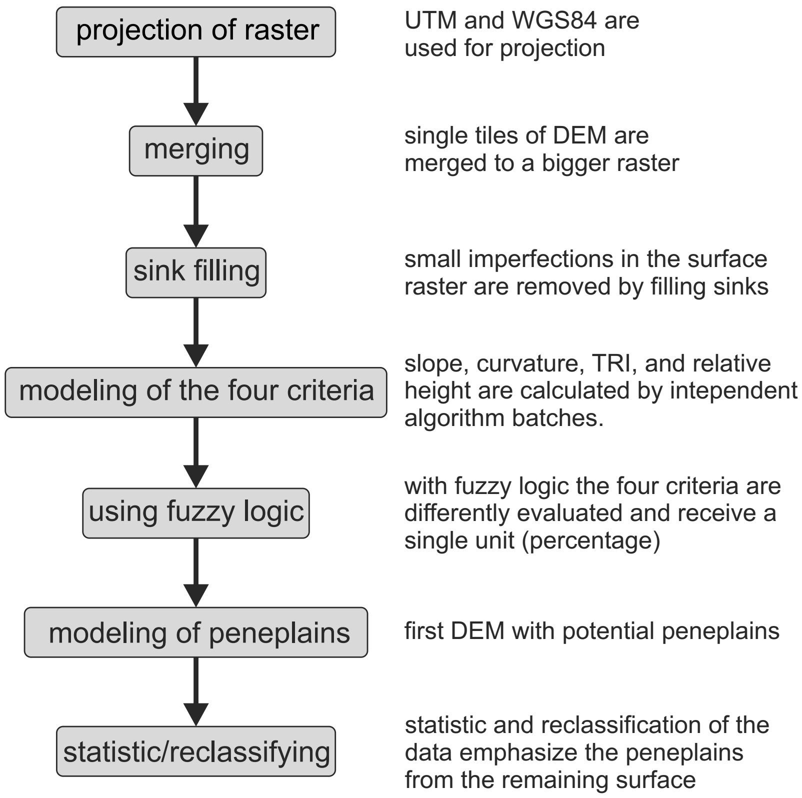

Figure 1.18: Flowchart sketching the way of DEM until peneplains are identified

(FIGURE 1.19). Curvature *(cu)* and slope *(sl)* are calculated with the ArcGis's own algorithm batch (producing raster *cu1* and *sl1*). To prepare the results, the absolute values were evaluated and converted to percentage by using fuzzy logic (→ *cu2* and → *sl2*). For the algorithm batch of the terrain ruggedness index *(tri)*, some more intermediate steps were necessary to solve the equation of Riley et al. (1999, FIGURE 1.16B) to get the raster based on the terrain ruggedness index. First, the DEM *Fill* was summed by focal statistics (over 3x3 square neighborhoods) to receive *tri1*. As a next step, *Fill* was multiplied by itself (→ *tri2*). On the one hand, *tri2* were used to get a sum with focal statistics (again over 3x3 square neighborhoods; → *tri3*) and on the other hand, *tri2* were multiplied by 9 (→ *tri4*). The *Fill* raster was multiplied by *tri1* (→ *tri5*) times two (→ *tri6*). The intermediary result *tri7* is an addition between *tri3* and *tri4*. In the next calculation, *tri7* is subtracted from *tri6* (→ *tri8*). As last step before performing fuzzy logic, the square root of *tri8* is calculated (→ *tri9*). Fuzzy logic executed on *tri9* converts TRI to percentage (→ *tri10*). To receive the modeled DEM for the "relative height" *(rh)*, several algorithms are necessary as well. After calculating the flow direction (→ *rh1*) and flow accumulation (→ *rh2*), the first threshold is set to receive a solid drainage system expressing the erosion base level (→ *rh3*). Before converting the remaining pixel values of the raster to a shape file (→ *rh5*), the raster is resized to the original DEM size (→ *rh4*). With the "Natural Neighbor" function, the surface between the solid drainage system is interpolated to gain the erosion base level (→ *rh6*). The relative height (→ *rh7*) is produced by subtracting *rh6* from *Fill*. As last step, fuzzy logic was performed to evaluate the data and align the relative height with the other raster (→ *rh8*). The four final rasters, *sl2*. *cu2*, *tri10*, and *rh8* were multiplied (→ *tim03*) and the resolution of the data set with focal statistics was adjusted. As last step, the data set is reclassified to receive a map outlining potential peneplains. The algorithms of the used fuzzy logic are described and discussed in detail in CHAPTER 5. The comprehensive script about the model written in Python is provided in the appendix of this thesis (SECTION A.4).

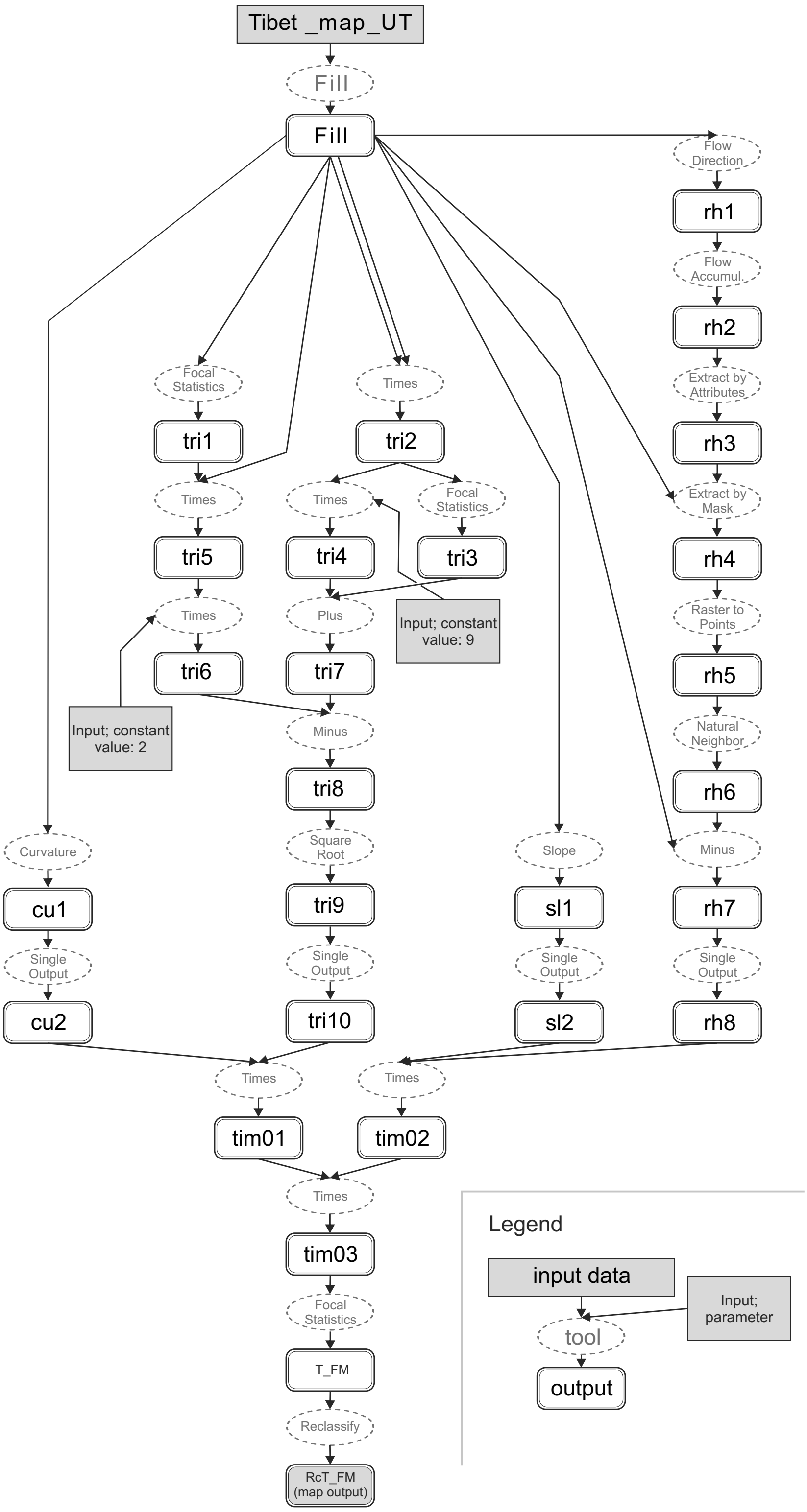

Figure 1.19: Flowchart of the PAT developed with the powerful ArcGis ModelBuilder tool.

2a Peneplain formation in southern Tibet predates the India-Asia collision and plateau uplift

This chapter is similar to the manuscript entitled: "Peneplain formation in southern Tibet predates the India-Asia collision and plateau uplift" that is published with Geology in October 2011, Volume 39, Page 983-986.

Authored by: R. Hetzel, I. Dunkl, V. Haider, M. Strobl, H. von Eynatten, L. Ding and D. Frei.

2a.1 Abstract

The uplift history of Tibet is crucial for understanding the geodynamic and paleoclimatologic evolution of Asia; however, it remains controversial whether Tibet attained its high elevation before or after India collided with Asia $\sim$50 m.y. ago. Here we use thermochronologic and cosmogenic nuclide data from a large bedrock peneplain in southern Tibet to shed light on the timing of the uplift. The studied peneplain, which was carved into Cretaceous granitoids and Jurassic metasediments, is located in the northern Lhasa block at an altitude of $\sim$5300 m. Thermal modeling based on (U-Th)/He ages of apatite and zircon, and apatite fission track data, indicate cooling and exhumation of the granitoids between ca. 70 and ca. 55 Ma, followed by a rapid decline in exhumation rate from $\sim$300 m/m.y. to $\sim$10 m/m.y. between ca. 55 and ca. 48 Ma. Since then, the peneplain has been a rather stable geomorphic feature, as indicated by low local and catchment-wide erosion rates of 6-11 m/m.y. and 11-16 m/m.y., respectively,

which were derived from cosmogenic ^{10}Be concentrations in bedrock, grus, and stream sediment. The prolonged phase of erosion and planation that ended ca. 50 Ma removed 3-6 km of rock from the peneplain region, likely accomplished by laterally migrating rivers. The lack of equivalent sediments in the northern Lhasa block and the presence of a regional unconformity in the southern Lhasa block indicate that the rivers delivered this material to the ocean. This implies that erosion and peneplanation proceeded at low elevation until India's collision with Asia induced crustal thickening, surface uplift, and long-term preservation of the peneplain.

2a.2 Introduction

The growth of the Tibetan Plateau, the highest plateau on Earth, with a mean elevation of 5 km above sea level (Fielding et al., 1994), has long been attributed to India's collision with Asia (Argand, 1924; Dewey et al., 1988; Tapponnier et al., 2001), which started ca. 50 Ma (Patriat and Achache, 1984; Rowley, 1996; Najman et al., 2010). However, the preceding accretion of continental terranes to Asia (e. g. Dewey et al., 1988) raises the possibility that crustal thickening, and hence surface uplift, occurred much earlier. It has been argued that the collision between the Lhasa block and the Qiantang terrane (FIGURE 2A.1A, INSET) resulted in crustal shortening, which may have raised southern Tibet to an elevation of 3-4 km during the Cretaceous (Murphy et al., 1997; Kapp et al., 2005b, 2007a). However, the following observations suggest that crustal shortening in several regions of the Lhasa block and the Qiangtang terrane does not necessarily imply that southern Tibet as a whole reached a high elevation and remained high until the onset of the India-Asia collision. First, marine limestones document that many regions of southern Tibet remained close to sea level until the Albian (ca. 100 Ma) or Cenomanian (ca. 95 Ma; Marcoux et al., 1987; Leeder et al., 1988; Yin et al., 1988). Second, thrust fault systems interpreted to have caused considerable north-south shortening in the Lhasa block and the Qiangtang terrane at long 85°E are crosscut by undeformed granitoids dated at ca. 99 Ma, ca. 113 Ma, and ca. 153 Ma (Murphy et al., 1997). Likewise, shortening at 87°E occurred before ca. 118 Ma and there is no evidence for deformation between the Cenomanian (ca. 95 Ma) and the early Tertiary (Kapp et al., 2007a). Hence, the thickened crust was subject to erosion for tens of millions of years before the collision of India, which may have reduced the crustal thickness substantially before the India-Asia collision started. The detritus derived from the erosion of the Early Cretaceous orogen is partly preserved in the mid-Cretaceous Takena Formation of the Lhasa block (Dewey et al., 1988; Leeder et al., 1988), but was also transported farther south and deposited in the Xigaze forearc basin (Dürr, 1996) located just north of the Indus - Yarlung suture (FIGURE 2A.1A, INSET).

Here we apply an independent approach to constrain the early uplift of southern Tibet, which is based on quantifying the age and geomorphic evolution of a large bedrock peneplain using low-temperature thermochronology and cosmogenic nuclides. We use the term peneplain to denote a nearly featureless, gently undulating land surface of considerable area, which has been produced by erosion almost to base level (cf. Jackson, 1997)

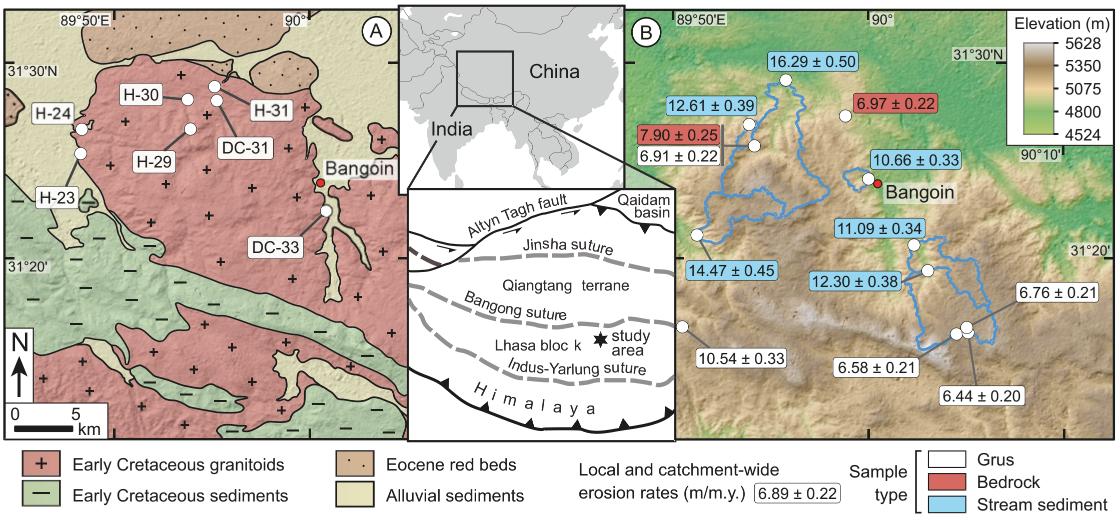

Figure 2a.1: (A:) Geologic map of peneplain region in northern Lhasa block near town of Bangoin and sample locations. U-Pb dating and thermochronology performed on granitoid samples revealed their intrusion ages and their subsequent cooling history. Inset maps show continental terranes of Tibetan Plateau, bounded by suture zones, and depict their location in Central Asia. (B:) Digital elevation model (30 m resolution) of study area with local and catchment-wide erosion rates (m/m.y.) quantified from concentrations of cosmogenic. ^{10}Be in quartz. Peneplain is in brown.

2a.3 Study area

The investigated bedrock peneplain is located in the northern Lhasa block (FIGURE 2A.1, INSET) and was carved into Cretaceous granitoids and very low grade metamorphic sediments of Jurassic age. Field investigations and the analysis of digital elevation models show that originally the peneplain extended for at least ~ 150 km east-west and ~ 75 km north-south. Streams that incised the original erosion surface have generated a local relief of as much as a few hundred meters and divide the peneplain into different well-preserved parts that are at similar elevations of ~ 5,200 m to ~ 5,400 m (Strobl et al., 2010). The best preserved portion of the original planation surface occurs near the town of Bangoin, where it was eroded into granitoids that intruded Early Cretaceous sediments (FIGURE 2A.1; SECTION 2A.3.1). Locally, the granitoids underneath the peneplain are overlain by continental red beds of Eocene age (Qu et al., 2003) along a gently dipping unconformity (FIGURE 2A.1). These red beds contain abundant granitic detritus, indicating that the granitoids had been exhumed to the surface by Eocene time. Field observations show that the peneplain exposes bedrock or is covered by block fields generated by frost weathering of the granitoids (FIGURE 2A.3). Where present, the soil between the blocks is thin (< 30 cm) and contains large amounts of granite grus.

2a.3.1 Geomorphology of the bedrock peneplain

The bedrock peneplain in the northern Lhasa block is best preserved in the vicinity of the town Bangoin. To illustrate the morphology of the landscape in this region we present a digital elevation model (FIGURE 2A.2A) and a figure that combines the spatial distribution of local slope angles with the local elevation (FIGURE 2A.2B). In addition, we show three field photographs of the peneplain region (FIGURE 2A.3B-C).

2a.4 Methods and results

We dated the emplacement age and the cooling history of the granitoids in the Bangoin region with U-Pb geochronology and low-temperature thermochronological methods (TABLE 2A.2; TABLE A.1 – TABLE A.5). Five U-Pb ages reveal that the granitoids intruded their sedimentary host rock between ca. 120 and ca. 110 Ma. The subsequent cooling history is constrained by seven pairs of zircon and apatite (U-Th)/He ages and seven apatite fission track ages that demonstrate that the rocks cooled from ~ 180 °C to ~ 60 °C between 90 and 75 Ma and ca. 55 Ma

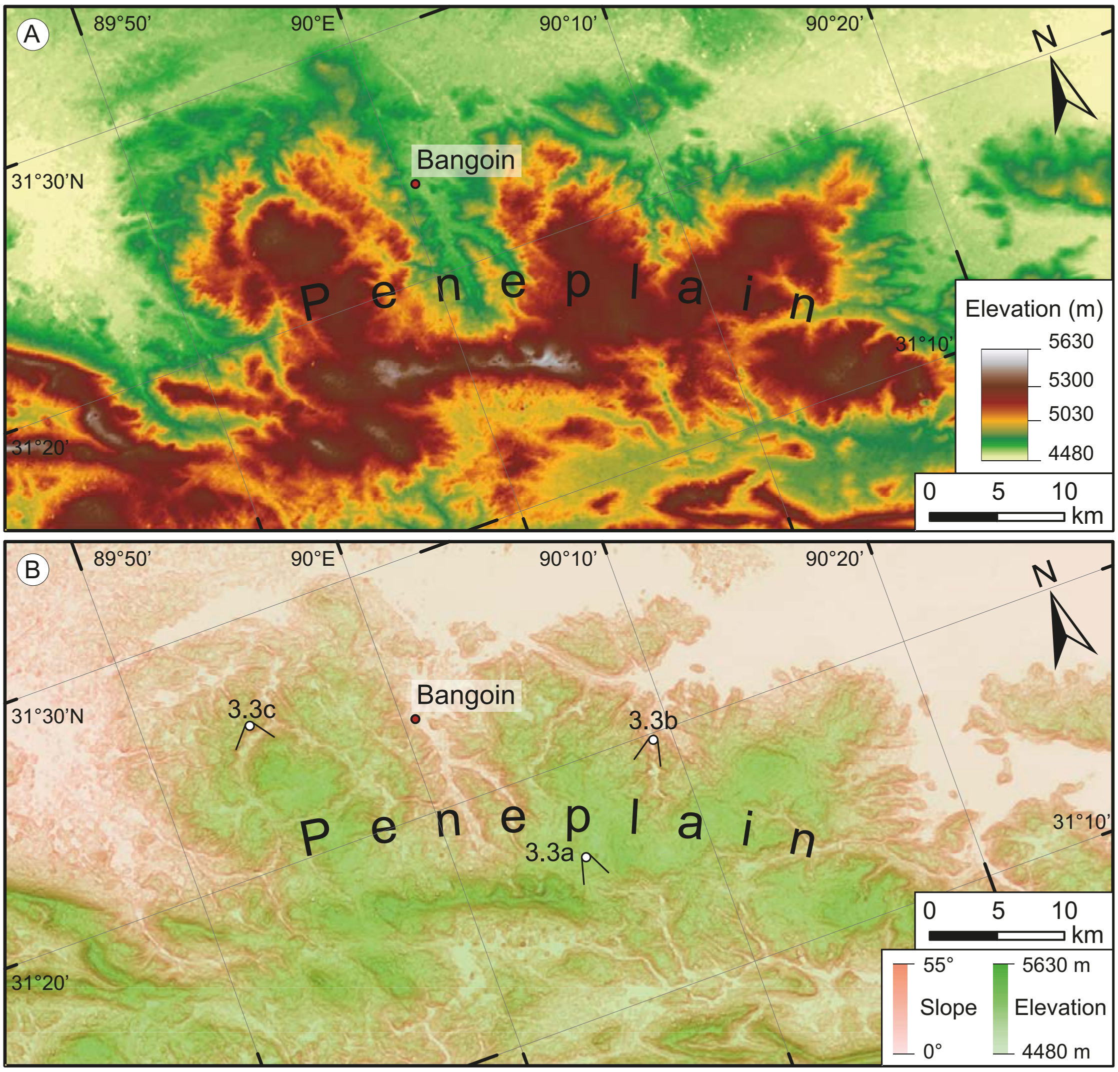

Figure 2a.2: (A:) Digital elevation model of the peneplain region near the town Bangoin. The peneplain surface, which is at an elevation of ∼5300 m, appears in brownish colors. The digital elevation model is based on a Global Digital Elevation Model (GDEM) derived from ASTER GDEM data with a spatial resolution of ∼30 m. (B:) Map of the region shown in (A) illustrating spatial variations in slope angle and elevation. Note that slope angles in the valleys dissecting the peneplain increase towards lower elevation. White circles mark the positions from which the photographs shown in FIGURE 2A.3 were taken (black lines mark the view direction).

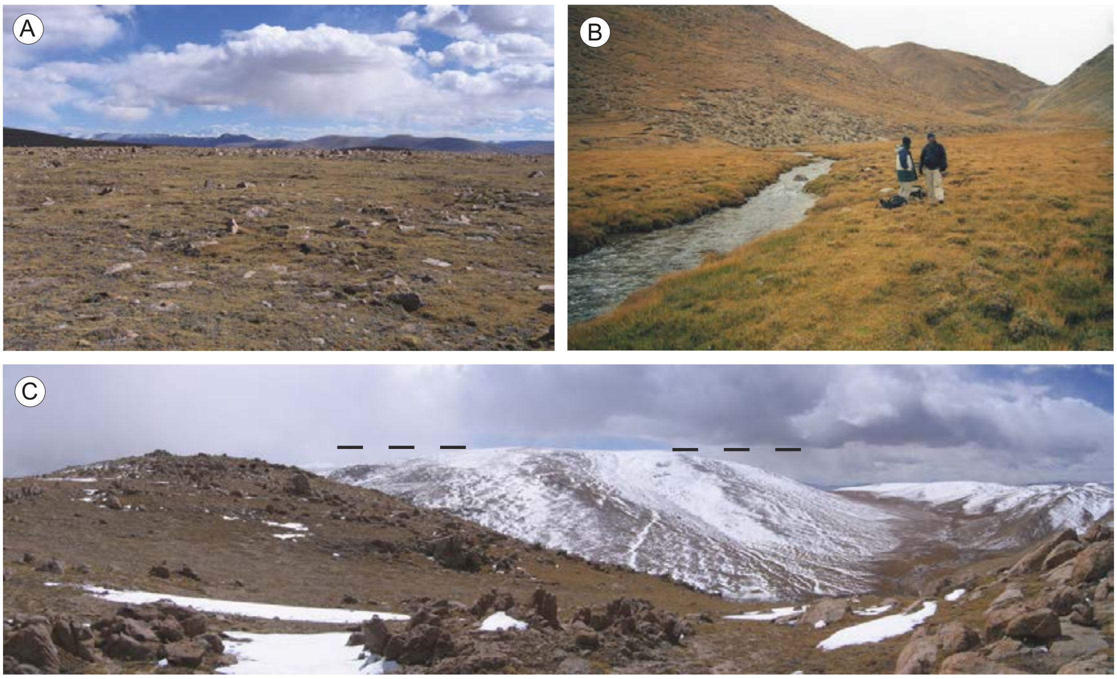

Figure 2a.3: Field photographs of the peneplain region (for location and view direction see FIGURE 2A.1). (A:) A well-preserved part of the flat peneplain southeast of Bangoin with granite blocks and a thin veneer of intervening soil. (B:) Small valley east of Bangoin that was incised into the peneplain by a stream flowing to the north. (C:) The peneplain - indicated by the dashed line - west of Bangoin where it has been incised by a river flowing to the northeast.

(TABLE 2A.2). Thermal modeling based on apatite fission track data, (U-Th)/He constraints, and the Eocene age of the red beds overlying the granitoids demonstrates a rapid cooling from $\sim 130\,^{\circ}$C to near-surface temperatures between ca. 65 and ca. 48 Ma (FIGURE 2A.1, for further details, see SECTION 2A.4.1.1), reflecting the exhumation of the granitoids forming the peneplain. We infer that the planation process was synchronous with the waning stage of exhumation and was completed ca. 50 Ma.

To evaluate the stability of the peneplain we determined erosion rates from concentrations of in situ-produced cosmogenic ^{10}Be (TABLE 2A.3; TABLE A.9). We used granite grus and bedrock samples for quantifying local erosion rates, whereas spatially integrated erosion rates for six catchments were derived from sediment samples taken in streams that are incising and eroding headward into the peneplain (FIGURE 2A.1B; FIGURE 2A.3B-C). All samples except one yield local erosion rates of only 6-8 m/m.y. (TABLE 2A.3), demonstrating that the bedrock peneplain

Table 2a.1: Location and lithology of geochronological samples

Sample number	Latitude (°N)	Longitude (°E)	Lithology
H-23	31.4227	89.8048	Granodiorite
H-24	31.4434	89.8054	Granodiorite
H-29	31.4433	89.8982	Biotite granite
H-30	31.4685	89.8959	Leucogranite
H-31	31.4797	89.9194	Leucogranite
DC-31	31.4677	89.9208	Biotite granite
DC-33	31.3733	90.0143	Granodiorite

constitutes a stable landform. The catchment-wide erosion rates are only slightly higher than the local erosion rates, i. e., 11-16 m/m.y., indicating that incision of the peneplain by the small streams proceeds at low rates. We note that erosion rates measured with cosmogenic nuclides integrate over the time that is needed to remove $\sim$ 60 cm of rock (Lal, 1991), i. e., a period of 40-90 k.y. for our samples. As this time scale roughly spans the last glacial - interglacial cycle, we consider the erosion rates to be representative for the Quaternary Period. Extrapolation further back in time is more uncertain, because climate conditions during the Tertiary, and hence erosion rates, were presumably different from those today. On the flat peneplain, where a thin veneer of soil is present between bedrock blocks in most areas, a warmer and more stable climate in the Tertiary may have caused soils to be thicker than today. Since the soil production rate (i. e., the rate at which bedrock is transformed to soil by processes such as freeze-thaw or burrowing) decreases with increasing soil thickness (Heimsath et al., 1997), erosion in the Tertiary may have proceeded at a lower rate compared to the Quaternary. However, since it is not possible to quantify the effect of a warmer climate, we assume that the local erosion rates of 6-8 m/m.y. are at least roughly representative for the past 50 m.y. This suggests that the peneplain was lowered by 300 - 400 m during that period.

Table 2a.2: U-Pb and thermochronological age data

Sample Nr.	**U-Pb age♦✠ (Ma)**	**(U-Th)/He zircon age§ (Ma)**	**Apatite fission track age§ (Ma)**	**(U-Th)/He apatite age§ (Ma)**
H-23	117.0± 2.8	77.1± 7.9	59.4± 2.3	56.2± 0.9
H-24		80.2± 5.0	58.5± 3.3	56.3± 0.7
H-29	111.7± 1.6	75.1± 6.6	56.8± 2.8	53.6± 1.2
H-30	112.8± 2.3	94.1± 9.1	58.2± 3.0	59.0± 3.6
H-31		66.7± 3.2	68.4± 3.9	55.4± 5.7
DC-31	117.5± 3.9	85.1± 4.7	58.8± 3.0	55.1± 3.3
DC-33	111.6± 0.5	74.8± 1.7	59.6± 2.4	52.0± 0.2

♦ Age were obtained using laser inductively coupled plasma - mass spectrometry dating of zircon.
✠ Reported error limits are 2σ.
§ Reported error limits are 1σ.

2a.4.1 Description of the geochronological investigations

2a.4.1.1 U-Pb dating and low-temperature thermochronology

Zircon and apatite crystals were concentrated by standard mineral separation processes (crushing, sieving, gravity and magnetic separation). U-Pb age data were acquired by laser ablation - single collector magnetic sectorfield - inductively coupled plasma - mass spectrometry (LA-SF-ICP MS) at the Geological Survey of Denmark and Greenland in Copenhagen employing a Thermo Finnigan Element 2 mass spectrometer coupled to a NewWave UP213 laser ablation system. All age data were obtained by single spot analyses with a spot diameter of 30 μm and a crater depth of approximately 15 - 20 μm. Cathodoluminescence imaging of each zircon was used to study internal structure and avoid ablation of heterogeneous zones. The methods employed for analysis and data processing are described in Frei and Gerdes (2009) and Gerdes and Zeh (2006). For quality control, the Plešovice (Sláma et al., 2008) and M127 (Nasdala et al., 2008) zircon standards were analyzed. The results were consistently within 1σ of the published ID-TIMS ages. U-Pb ages were calculated with Isoplot/46 Ex 3.0 (Ludwig, 2003).

Apatite crystals for fission track analysis were irradiated at the research reactor of the Technical University of Munich (Garching). The external detector method (Gleadow, 1981) was used. After irradiation the induced fission tracks in the mica detectors were revealed by etching in 40 % HF for

Table 2a.3: Erosion rates from cosmogenic ^{10}Be

Sample number	**^{10}Be concentration†**	**Erosion rate‡ (m/m.y.)**
Grus samples		
08T10	912 ± 27	6.58 ± 0.21
08T12	906 ± 27	6.76 ± 0.21
08T13	951 ± 29	6.44 ± 0.20
08T20	534 ± 16	10.54 ± 0.33
08T24	838 ± 25	6.91 ± 0.22
Bedrock samples		
08T16	714 ± 21	6.97 ± 0.22
08T25	709 ± 21	7.90 ± 0.25
Stream sediment samples		
08T21	346 ± 10	16.29 ± 0.50
08T23	487 ± 15	10.66 ± 0.33
08T26	441 ± 13	12.61 ± 0.39
09T21	408 ± 12	14.47 ± 0.45
09T26	479 ± 14	12.30 ± 0.38
09T27	522 ± 16	11.09 ± 0.34

† Blank-corrected ^{10}Be concentrations with 1σ error limits.
‡ Erosion rates reported with 1σ error limits (internal uncertainty) were calculated with the CRONUS-Earth ^{10}Be - ^{26}Al web calculator, version 2.2.1 (http://hess.ess.washington.edu), using the constant production rate scaling model of Lal (1991) and Stone (2000).

40 min at 21 °C. Tracks were counted with a Zeiss-Axioskop microscope . computer-controlled stage system (Dumitru, 1993), with 1000× magnification. The fission track ages were determined by the zeta method (Hurford and Green, 1983) using age standards listed in Hurford (1998). Errors were calculated using double Poisson dispersion (Green, 1981). Calculations and plots were made with the program TRACKKEY (Dunkl, 2002).

For (U-Th)/He thermochronology only clear, intact, euhedral apatite and zircon single crystals were used. The shape parameters for the alpha ejection correction (Farley et al., 1996) were determined by multiple microphotographs. The crystals were wrapped in ca. 1 × 1 mm - sized platinum capsules and degassed in high vacuum by heating with an infrared laser in the Thermochronology Laboratory at Geoscience Center, University of Göttingen. The extracted gas was purified by a Ti - Zr getter and the He content was measured by a Hiden®triple-filter quadrupol mass spectrometer. Following degassing, samples were retrieved from the gas extraction line and spiked with calibrated ^{230}Th and ^{233}U solutions. Zircons were dissolved in pressurized teflon bombs using distilled 48 % HF + 65 % HNO_3 in five days at 220 °C, while apatites were dissolved in 2 % HNO_3 at room temperature in an ultrasonic bath. The concentrations of alpha - emitting elements (actinides and Sm) were determined by ICP-MS using isotope dilution.

The thermal histories of the samples were modeled with the HeFTy program (Ketcham, 2005). The modeling is based on AFT, AHe and ZHe apparent ages, track length distributions, Dpar values, apatite and zircon crystal dimensions, and U content. We have tested both multiple and averaged AHe grain data for the thermal modeling. As the average grain parameters gave more consistent results, we used the unweighted arithmetic mean of the ages, grain radii, and U and Th concentrations for thermal modeling. The annealing models used for AFT, AHe, and ZHe are described in Ketcham et al. (2007); Farley (2000); Reiners et al. (2004), respectively. The thermal modeling was performed basically in "unsupervised mode". As fixed constraints we only used (I) the emplacement age the Bangoin intrusives (120 ± 10 Ma), (II) a mean surface temperature of 5 °C, and (III) a time interval for the deposition of the Eocene red beds of 50 to 40 Ma with a near - surface temperature of 15-20 °C for this time, because the red beds were deposited at tropical latitude. Note that the 50-40 Ma time constraint used for sediment deposition is a conservative approach because the red beds contain intercalated fine-grained tuffs, which are presumably related to the main phase of Linzizong volcanism around 50 Ma. Assuming a shorter age range near ∼ 50 Ma would lead to an even higher rate of cooling and exhumation.

2a.4.1.2 Determination of erosion rates from cosmogenic ^{10}Be

Before we describe the determination of the erosion rates from concentrations of cosmogenic ^{10}Be in quartz (Lal, 1991), we note that we use the term erosion to describe the surface lowering of a landscape. Strictly speaking, ^{10}Be concentrations record the rate of denudation, i. e. the sum of physical erosion and chemical weathering (Riebe et al., 2003). To quantify local erosion rates on the peneplain we used granitic bedrock samples and samples consisting of granite grus. The latter were taken over areas of 10 - 50 m^2 and amalgamate thousands of grains that record individual rock erosion histories, thus providing representative average erosion rates (Hancock and Kirwan, 2007; Meyer et al., 2010). To quantify catchment-wide erosion rates (Granger et al., 1996) we took sediment samples from small streams.

After crushing of the grus and bedrock specimens, all samples were 92 washed, sieved, and the 9 non-magnetic part of the 250 - 500 μm grain size fraction was used for further purification. Samples were leached once in 6 M HCl and three to four times in a mixture of 1 % HF and 1 % HNO_3 at 80 °C in an ultrasonic bath. After addition of ~0.3 mg of Be carrier, the pure quartz samples were dissolved and Be was separated by successive anion and cation exchange columns. The Be in the eluate was precipitated as $Be(OH)_2$ at a pH of 8-9, rinsed, dried, and transformed to BeO at ~1000 °C. Finally, the BeO was mixed with copper powder and analyzed by accelerator mass spectrometry at ETH Zürich. The accelerator mass spectrometry measurements at ETH Zürich were normalized to the standards S555 and S2007, which have $^{10}Be/^{9}Be$ ratios of 95.5×10^{-12} and 30.8 x 10^{-12}, respectively (Kubik and Christl, 2010), and are calibrated against the primary BEST433 standard (Hofmann et al., 1987). The ^{10}Be erosion rates were calculated with the CRONUS-Earth ^{10}Be - ^{26}Al calculator (Balco et al., 2008), version 2.2.1 (http://hess.ess.washington.edu), using the constant production rate scaling model of Lal (1991) and Stone (2000). The calculator uses a ^{10}Be half-life of 1.387 Ma (Chmeleff et al., 2010; Korschinek et al., 2010) and corrects for the different standards and Be half - life used at ETH Zürich. The erosion rates - given with internal and external uncertainties - are maximum rates as no correction for snow shielding was made (Lal, 1991).

2a.5 Discussion and conclusions

The amount of rock that was removed during the exhumation of the granitoids and the generation of the peneplain in the Bangoin area can be estimated from the mean cooling rate of ~10 °C/m.y. between 65 and 50 Ma, a rate derived from the time-temperature history (FIGURE 2A.4). Combining this cooling rate with a conservative estimate for the paleogeothermal gradient of 25 - 50 °C/km yields an exhumation rate of 200 - 400 m/m.y. Thus, within 15 m.y., ~3 - 6 km of rock was removed from the peneplain region, which requires an efficient agent of erosion able to erode bedrock uniformly over a large area (> 10,000 km^2). We infer that erosion

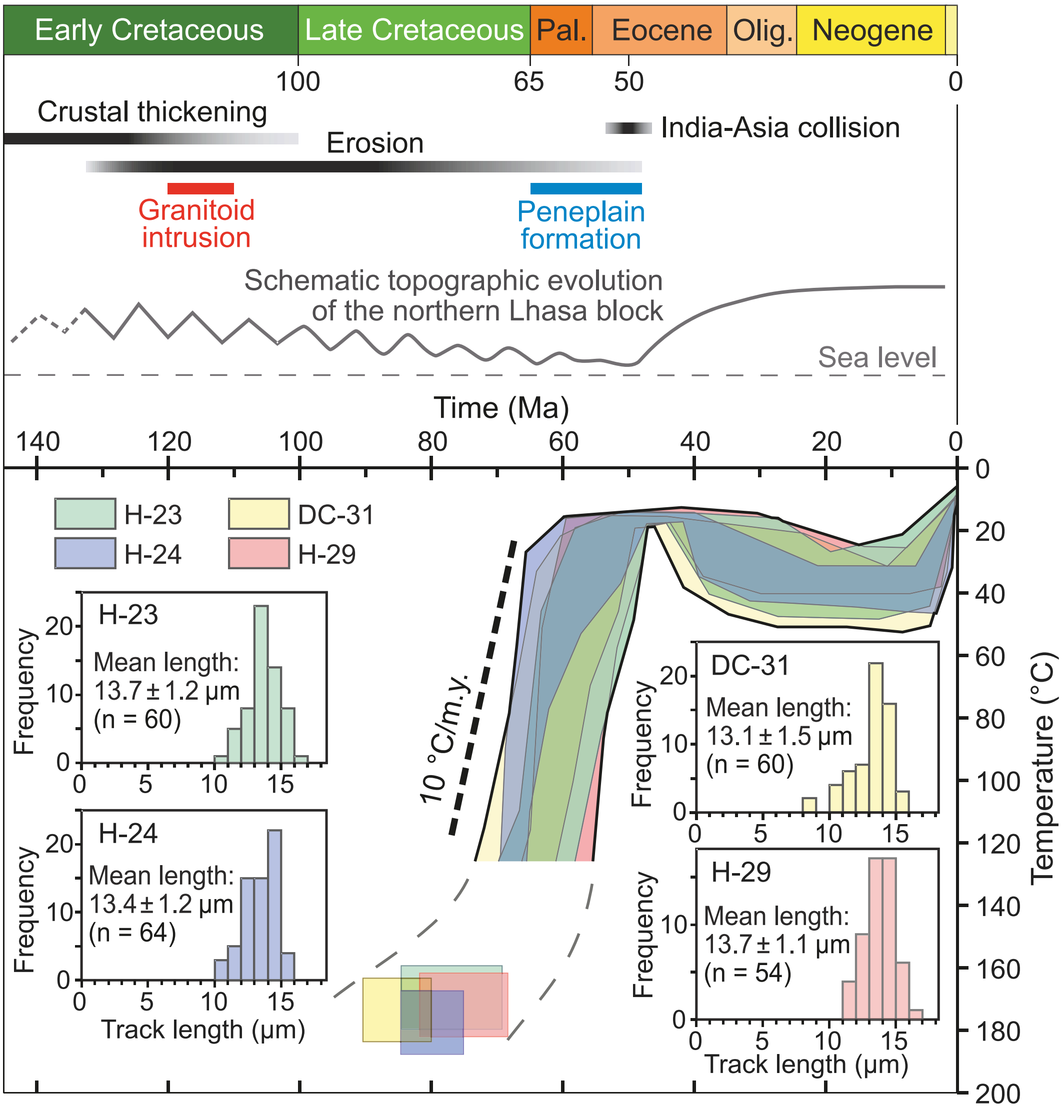

Figure 2a.4: Cooling history of Cretaceous granitoids forming peneplain and geologic events in southern Tibet. Lower part of figure shows cooling histories of four samples based on thermal modeling of zircon and apatite (U-Th)/He ages, apatite fission track data, age of Bangoin intrusives, and Eocene age of overlying red beds. Boundaries of mutual cooling path encompass all path envelopes of acceptable fit obtained for four samples using merit value of 0.05 in HeFTy software (Ketcham, 2005). Boxes are defined by zircon (U-Th)/He ages of samples and their respective closure temperatures (calculated with software CLOSURE; Ehlers et al., 2005). Box size represents 1σ errors. Inset diagrams depict track length distributions and numbers of confined fission tracks in apatite from the four granitoid samples. Upper part of figure illustrates timing of important geologic events in southern Tibet, shown by horizontal bars below geologic time scale (Pal.-Paleocene; Olig.-Oligocene). Grey line sketches topographic evolution of northern Lhasa block through time. After period of crustal thickening during Early Cretaceous (Murphy et al., 1997; Kapp et al., 2005b, 2007a) and intrusion of granitoids (red bar), crust was thinned by erosion in Late Cretaceous and Paleocene. Exhumation of granitoids and formation of bedrock peneplain (blue bar) ended ca. 50 Ma with onset of India-Asia collision. Subsequent underthrusting of Indian continental crust beneath Lhasa block is thought to be responsible for rapid surface uplift, and by ca. 35 Ma southern Tibet had reached an elevation of at least $\sim$4 km (Tapponnier et al., 2001; Rowley and Currie, 2006; Van der Beek et al., 2009)

and exhumation of the granitoids were accomplished by major rivers that migrated laterally over the future peneplain area.

Two arguments suggest that the large volumes of sediment that were produced during exhumation and peneplain formation were not deposited on the Lhasa block, but were transported to a basin near global base level. First, siliciclastic sediments of Paleocene to Early Eocene age (65 - 48 Ma) are scarce in the Lhasa block (e. g. Leeder et al., 1988). Second, in the southern Lhasa block an erosional unconformity extends for $\sim$ 1,000 km east-west and $\sim$200 km north-south at the base of the Linzizong Formation (Burg et al., 1983; Lee et al., 2009). This regional unconformity separates folded Early Cretaceous sediments from nearly undeformed volcanic rocks of the Linzizong Formation (Burg et al., 1983; Lee et al., 2009), erupted mainly between ca. 60 and ca. 40 Ma (Yin and Harrison, 2000; Wen et al., 2008; Lee et al., 2009). As the deformed Cretaceous rocks must have undergone a phase of erosion before the deposition of the Linzizong Formation, the southern Lhasa block was not able to act as a depocenter for the clastic sediments produced in the peneplain region. Hence, these sediments were presumably transported to the ocean by large rivers. At least a part of the erosional debris may be preserved in the Late Paleocene to Eocene Qiuwu Formation (Qian, 1985; Einsele et al., 1994), which was deposited at the southern margin of the Lhasa block and originally had a much larger extent (Einsele et al., 1994). Alternatively, the sedimentary material from the peneplain region may have been transported northward and deposited at the northern margin of the Qiangtang terrane, where there are sedimentary basins with Paleocene and Eocene sediments (Liu and Wang, 2001; Spurlin et al., 2005).

We prefer the former interpretation, because the topography produced by the collision between the Lhasa and Qiantang terranes in the Early Cretaceous may still have been partly preserved, which would have prevented a northward flow of rivers originating in the peneplain region. Future provenance studies using fission track and U-Pb dating of detrital apatite and zircon will likely identify the source areas of early Tertiary deposits in Tibet and adjacent regions and decipher the pathways of the material removed from the peneplain region. If our preferred interpretation is correct and the rivers draining the northern Lhasa block were connected to the sea, the peneplain must have formed at rather low elevation, because otherwise the rivers would have merely incised the bedrock, and lateral migration and erosion over large distances (required for peneplanation) would have been inhibited. Although it is difficult to quantify the paleoelevation of the northern Lhasa block, we suggest that the peneplain formed at least 3-4 km beneath its current elevation of $\sim$5,300 m. Taken together, our results indicate that the formation of the peneplain at low elevation was completed by ca. 50 Ma and that the resistant bedrock surface has undergone only very slow erosion since then. Combined with the results of previous studies, which used paleoaltimetry (Rowley and Currie, 2006), geomorphology and thermochronology (Van der Beek et al., 2009), and geologic data (Tapponnier et al., 2001) to show that southern Tibet had reached an elevation of at least 4 km by ca. 35 Ma, this implies that the Tibetan Plateau grew rapidly in height between ca. 50 and ca. 35 Ma, i. e., early in the ongoing history of the India-Asia collision, and retained its high elevation (Spicer et al., 2003; Rowley and Currie, 2006; DeCelles et al., 2007).

Our study demonstrates that the age and geomorphic evolution of bedrock peneplains can be deciphered using a combination of thermochronologic and cosmogenic nuclide analyses. Dating the formation of these remarkable features has hitherto been a major obstacle, hampering their use as geomorphic markers tracking the uplift of mountains through space and time. If peneplains are developed in resistant bedrock, they can be preserved for tens of millions of years, even at high altitude, and may provide important constraints on the paleoelevation history of Cenozoic mountain belts.

2b Forum reply to “Peneplain formation in southern Tibet predates the India-Asia collision and plateau uplift”

This chapter is similar to the manuscript entiteled: “FORUM Reply: Peneplain formation in southern Tibet predates the India-Asia collision and plateau uplift” that is published with Geology in March 2013, Volume 41, Page e297-e298
Authored by: R. Hetzel, I. Dunkl, V. Haider, M. Strobl, H. von Eynatten, L. Ding and D. Frei.

Tian et al. (2013) challenge our interpretation that peneplain formation in the Lhasa terrane occurred prior to plateau uplift, when the region was still at low elevation and externally drained. Instead, they suggest an internal drainage at high elevation already in the late Cretaceous-Paleogene. As the timing of plateau uplift is crucial for understanding the evolution of Tibet, we thank Tian et al. for the opportunity to elaborate on these conflicting interpretations.

We first address the question how much shortening occurred in the Lhasa terrane prior to ~ 50 Ma. A close inspection of the study by Kapp et al. (2007b), who inferred > 230 km of shortening in the southern Lhasa terrane between ca. 90 and 53 Ma, raises severe doubts on this huge amount of shortening, because it is based on the restoration of a cross section constructed from a simplified geological map and the postulation of two detachments. The restoration implies > 150 km of slip on the hypothetical upper detachment with almost no hanging wall deformation (Kapp et al., 2007b). We regard this scenario as very unlikely and argue that the surface geology can be explained with considerably less shortening. Moreover, the northern margin of the thrust belt does not extend into the studied peneplain region but ends farther south. Whether deformation did propagate to the peneplain area is an open question. A second study cited by Tian et al. (2013) describes the development of a thrust belt in the Nima area (northern Lhasa terrane) during the accretion of the Lhasa block to Asia (Kapp et al., 2007a). The reported total shortening since the Early Cretaceous is >58 km, but this value includes a post-Eocene shortening of >25 km (Kapp et al., 2007b), which reduces the early-mid Cretaceous shortening to >33 km. We stress that the age of shortening given as "ca. 100-50 Ma" by Tian et al. (2013) is incorrect. Instead, Kapp et al. (2007a) infer an age of ~ 125 to ~ 95 Ma and write (p. 927-928): "Geologic relations provide no evidence for significant deformation in the Nima area subsequent to Cenomanian time and prior to the onset of non-marine sedimentation during the late Oligocene". The ~ 50 Ma depositional hiatus mentioned by Tian et al. does not necessarily imply shortening. It may simply reflect isostatic uplift during long-lasting erosion of the mountains created along the Bangong suture in the early-mid Cretaceous. Furthermore, shortening in the Lhasa terrane may have varied significantly along strike. For example, Kapp et al. (2005a) estimated that Cretaceous shortening declines from 150 km (at 84°E) to 70 km in the Nima area (at 87°E). In the peneplain region, ~ 250 km farther east at 90°E, shortening may be even less. Hence, extrapolating geological data from 2D profiles over hundreds of kilometers along strike into three dimensions - as done by Tian et al. (2013) in their figure 1B, which shows east-west mountain ranges acting as barriers for sediment transport at infinity - is speculative and not supported by data.

The other points raised by Tian et al. (2013) are related to the paleogeography inferred from provenance studies and the question whether the northern Lhasa terrane was internally or externally drained during late Cretaceous-Paleogene time. Our thermochronologic data indicate the removal of 3-6 km of rock between ~ 65 and ~ 50 Ma (see chapter 2a). Given the vast extent of the peneplain (150×75 km), we consider the proposition of Tian et al. that the material was "deposited locally in terrestrial basins within the northern Lhasa terrane" as unreasonable. If - in the Paleocene - an internal drainage had already existed, the Lhasa terrane would have been largely covered by sediments from the eroding mountains farther north and south - similar to what is happening in the Qaidam Basin since the Pliocene (Métivier et al., 1998). Tian et al. (2013) argue that the provenance of sediments in basins adjacent to the Gangdese arc (e. g. Liuqu -, Xigaze -, Takena formation) indicates an internal drainage of the northern Lhasa terrane. The Liuqu formation consists of coarse clastic deposits with rapid lateral facies changes that accumulated in relatively small elongated oblique-slip basins (Davis et al., 2002). Such basins typically receive detritus from local sources and are therefore not very informative with respect to large-scale drainage systems. However, although provenance and detrital zircon data indicate mainly local sources for the Liuqu formation, it is evident that a minor contribution may in fact be derived from the northern Lhasa terrane (see Wang et al. (2010), their figure 5). Likewise, zircon U-Pb and Hf isotopic data show that the Early Cretaceaous granitoids of the northern Lhasa terrane may also be one of the sources for the Xigaze flysch (Wu et al., 2010). Thus, a complete absence of material from the northern Lhasa terrane - as required for the internal-drainage hypothesis - is incompatible with the available data. The presence of fluvial sediments in the foreland basin north of the Gangdese arc (i. e. Lhunzhub member of the Takena formation) is also insufficient to prove an internal drainage. As evident from the Hexi corridor - the presently active foreland basin of the Qilian Shan (Métivier et al., 1998) - major rivers may still leave such basins. Based on these considerations we retain our interpretation that the peneplain region was not internally drained. The rivers that left the area may have formed direct, though widely spaced, gateways across the Gangdese arc to the Neotethys, or alternatively may have flowed from the Lhasa terrane eastward before delivering their sediment to the Bengal Basin (cf. Najman et al., 2008). Even a northward drainage to the Hoh Xil and Tarim basins is possible (cf. Bosboom et al., 2011; Dai et al., 2012). Finally, we would like to highlight that the lack of evidence for tectonic denudation requires the erosive exhumation of the study area to explain our thermochronologic data. This, in turn, requires a high precipitation and run-off, which is supported by the paleo-position of Eocene "Tibet" at tropical to subtropical latitudes (Lippert et al., 2011). Internal drainage of such a huge system at high elevation would require long-lasting effective barriers on all sides of the eroded and finally planated region, despite the coeval existence of basins at or near sea level farther south and north. Thus, we consider the scenario suggested by Tian et al. (2013) highly unlikely.

3 Cretaceous to Cenozoic evolution of the northern Lhasa terrane and the Early Paleogene development of peneplains at Nam Co, Tibetan Plateau

This chapter is similar to the manuscript entitled: "Cretaceous to Cenozoic evolution of the northern Lhasa terrane and the Early Paleogene development of peneplains at Nam Co, Tibetan Plateau" that is published with the Journal of Asian Earth Science in July 2013, Volume 70-71, Page 79 -98.
Authored by: V. L. Haider, I. Dunkl, H. von Eynatten, L. Ding, D. Frei and L. Zhang

3.1 Abstract

Highly elevated and well-preserved peneplains are characteristic geomorphic features of the Tibetan plateau in the northern Lhasa terrane, north-northwest of Nam Co. The peneplains were carved in granitoids and in their metasedimentary host formations. We use multi-method geochronology (zircon U-Pb and (U-Th)/He dating and apatite fission track and (U-Th)/He dating) to constrain the post-emplacement thermal history of the granitoids and the timing and rate of final exhumation of the peneplain areas. LA-ICP-MS U-Pb geochronology of zircons yields two narrow age groups for the intrusions at around 118 Ma and 85 Ma, and a third group records Paleocene volcanic activity (63-58 Ma) in the Nam Co area. The low-temperature thermochronometers indicate common age groups for the entire Nam Co area: zircon (U-Th)/He ages cluster around

75 Ma, apatite fission track ages around 60 Ma and apatite (U-Th)/He ages around 50 Ma. Modeling of the thermochronological data indicates that exhumation of the basement blocks took place in latest Cretaceous to earliest Paleogene time. By Middle Eocene time the relief was already flat, documented by a thin alluvial sediment sequence covering a part of the planated area. The present-day horst and graben structure of the peneplains is a Late Cenozoic feature triggered by E-W extension of the Tibetan Plateau. The new thermochronological data precisely bracket the age of the planation to Early Eocene, i. e. between ca. 55 and 45 Ma., The erosional base level can be deduced from the presence of Early Cretaceous zircon grains in Eocene strata of Bengal Basin. The sediment generated during exhumation of the Nam Co area was transported by an Early Cenozoic river system into the ocean, suggesting that planation occurred at low elevation.

3.2 Introduction

The Tibetan Plateau is the highest and with ca. 2 million km^2 area the largest plateau on Earth. More than 90 % of the plateau has a mean elevation of ca. 5,000 m (Fielding et al., 1994). The collision of India and Asia was the major process generating the thickened crust of Tibet, however the timing and the mechanism of the thickening and the crustal structure is heavily debated (e. g. Aitchison et al., 2007; Ali and Aitchison, 2008; Molnar and Tapponnier, 1975; Patriat and Achache, 1984). The onset of collision took place in the Paleocene - Early Eocene, most probably between 56 and 50 Ma (Patriat and Achache, 1984; Zhang et al., 2012), but several authors have suggested ages between ca. 65 Ma (Ding et al., 2005; Najman et al., 2010; Willems et al., 1996) and ca. 34 Ma (Aitchison et al., 2007). Currently the intense deformation due to ongoing India-Asia collision is accommodated mainly along the margins of the Tibetan Plateau (Kirby and Ouimet, 2011; Aitchison et al., 2002; Allegre et al., 1984). This results in the immense contrast in relief and topography of the plateau and the bordering mountain chains (e. g. Himalayas).

This study focuses on the Lhasa terrane, which is located in the central - southern part of the Tibetan Plateau (FIGURE 3.1A). The study area is situated N-NW of Nam Co close to the northern margin of the Lhasa terrane in central Tibet. This region is not drained by major rivers and belongs to the giant central Asian endorheic basin system (FIGURE 3.1B). The local relief is

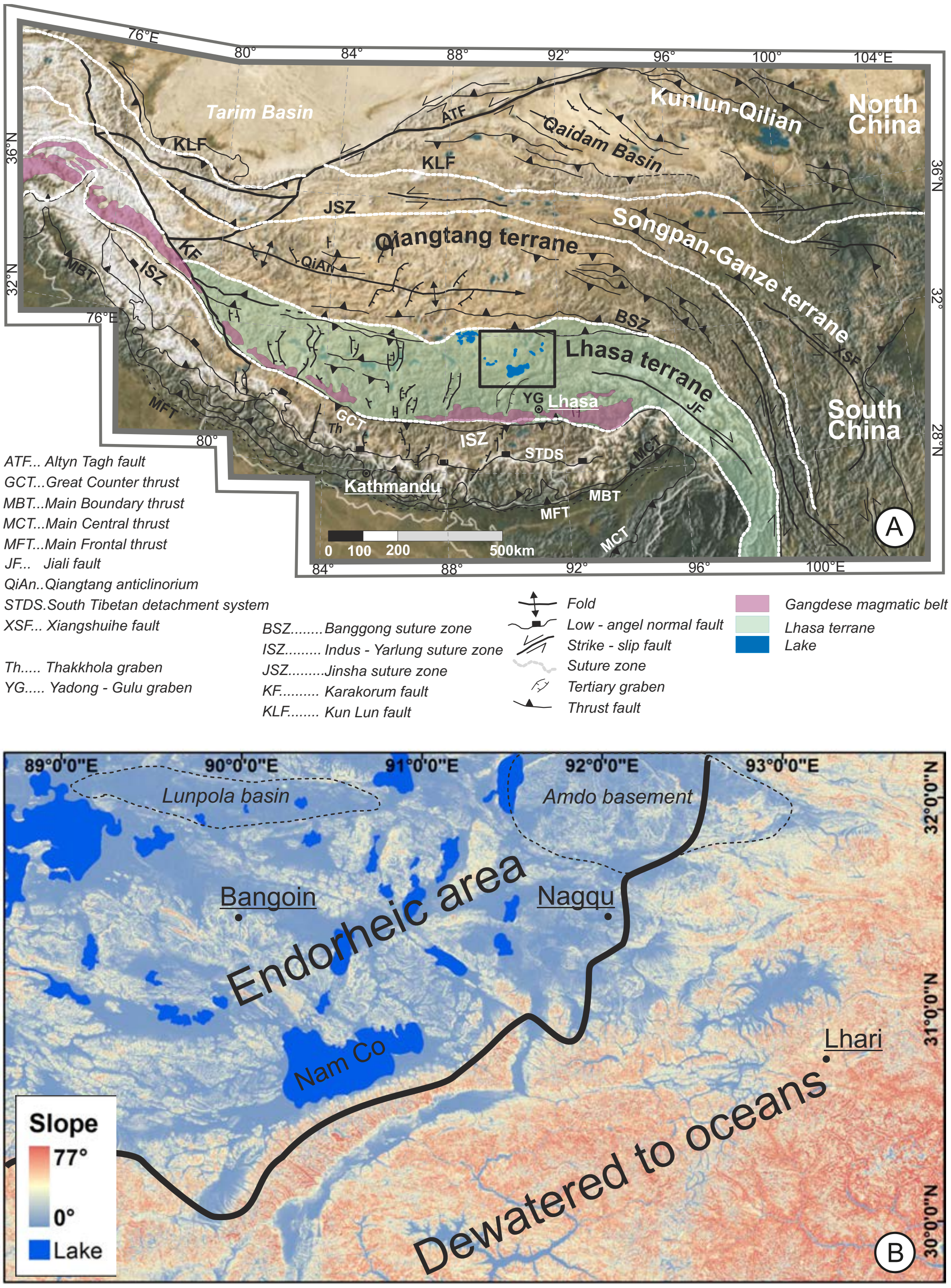

Figure 3.1: A: Tectonic map of the Tibetan plateau modified after DeCelles et al. (2002). The base map is a composite Landsat satellite image (www.landsat.org/ortho/index.php). The boundaries of the major accreted terranes are indicated by white lines. Our study area is situated in the northern part of the Lhasa Terrane. The black rectangle indicates position of the geological map in FIGURE 3.4 and the topography of the study area below. B: On the slope map (generated from the digital elevation model) the endorheic plateau area is highly contrasting when compared to the areas that are dewatered to the Indian and Pacific oceans. The black line marks the border between the two dewatering systems. (source of DEM: www.cigiar-csi.org, Jarvis et al., 2008)

relatively moderate and can be classified in three major types.

(I) High (> 6,000 m), steep, rugged and usually glaciated mountain chains mark the zones of active tectonic movements (e. g. Nyainqentanghla Range).

(II) Local shallow basins filled by lakes or alluvial plains with typical elevations between 4,600 and 4,850 m. These minor depressions were developed in several cases in the graben structures generated by the Late Miocene to Holocene extensional tectonics (Yin and Harrison, 2000).

(III) Mountains with flat top; the typical altitude of these elevated planation surfaces range between 4,900 and 5,400 m.

These flat geomorphological forms are carved in basement rocks and their evolution constitutes the target of our study.
Before reviewing the details of former studies and presenting the new results of our study, we discuss the nomenclature used for "flat-top mountains". Typically the following terms are used: paleosurface, plateau, planation surface and peneplain (e. g. Danišík et al., 2010; Davis, 1902; Penck, 1924; Rohrmann et al., 2012; Schildgen et al., 2009; Widdowson, 1997). In order to avoid confusion in terminology, we should first specify our criteria defining a peneplain. In this study, we consider peneplain.

(I) a flat-top area of the mountains that forms a positive relief landform elevated relatively to the surrounding areas,

(II) the surface of a peneplain can be slightly undulating, but this region does not contain well developed and incised river network,

(III) it is typically bordered by a sharp morphological breaks, which separates the flat (slowly eroding, presumably old) central landscape from the surrounding hilly lowlands (where modern typically linear erosion is dominant and responsible for the decay of the marginal zones of peneplain), and

(IV) the flat-top character is not the consequence of sub-horizontal stratification of the substrate lithology or the sedimentary cover (i. e. the horizontal surface cross-cuts older geological formations and older structures).

3.2.1 Planation process: thoughts on driving forces and paleo-elevation

Flat-top mountains have fascinated geologists and geomorphologists for long time. Davis (1899, 1902) described at first in the Colorado Front Range that mountain building orogens tend to flatten their topography down to base level. Post orogenic tectonic processes are then responsible for the uplift of the planation surface to high elevation. Later streams can dissect the elevated low relief surface, forming summits and valley systems and cause a new cycle of denudation until the formation of a stable, slightly undulating, low level land surface. This concept argues for peneplain formation at low elevation near base level and followed by uplift. This hypothesis is highly debated and has been extensively discussed (e. g. Molnar and England, 1990; Gregory and Chase, 1994; Bognar, 2001; Babault et al., 2007; Bishop, 2007; Ebert, 2009; Gunnell et al., 2009).

Opposing concepts suggested that peneplanation can occur significantly above the ultimate base level, because of extensive piedmont-type sedimentation in foreland basins causing significant rise of the base level for mountain belt erosion (e. g. Babault et al., 2007; Baldwin et al., 2003; Carretier and Lucazeau, 2005).

Three conditions for rock and surface uplift are most widely accepted;

(I) organic crustal thickening generally induced by orogenesis, i. e. convergence and continent-continent collision,

(II) magmatic underplating (Furlong and Fountain 1986), and

(III) thinning or heating of the lithosphere caused by slab breakoff, mantle delamination, melting or by combinations thereof (Gunnell et al., 2009).

The collision of India with Asia obviously impacts the uplift of the Tibetan Plateau to recent height (Dewey et al., 1988; Tapponnier et al., 2001) but it's still controversial whether Tibet Plateau reached its high elevation before or after collision. Several arguments support that southern Tibet had a thickened crust and reached elevated topography already at Cretaceous time due to crustal shortening (e. g. Burg et al., 1983; Kapp et al., 2003, 2005b, 2007a; Murphy et al., 1997; Ratschbacher et al., 1992). Hence Lhasa and Qiangtang terranes have merged and reached the present-day high elevation of the Tibetan Plateau before collision with India. Other studies postulate that the area was generally near global base level before India collides with Asia requiring thinned continental crust at that time (e. g. Dewey et al., 1988; Tapponnier et al., 2001; Zhang, 2000; Zhang et al., 2004). Such scenario suggests that the uplift of Tibetan Plateau started after the collision ca. 50 Ma ago.

3.2.2 Dating geomorphological processes and their rates in the central Tibetan Plateau

For the indirect dating of peneplain formation the application of thermochronological methods can serve time constraints. The apatite fission track and apatite and zircon (U-Th)/He techniques (later these methods are abbreviated as AFT, AHe and ZHe, respectively) describe the cooling history of the basement in which the peneplain was carved. Closure temperatures of these *"low-temperature"* thermochronometers are around 180 °C, 110 °C and 60 °C (ZHe, AFT and AHe, respectively; Farley, 2000; Reiners et al., 2004). The combination of thermochronometers allows for constraining both timing and rates of the near-surface exhumation processes. It is important to note that by the dating of cooling we actually get time constraints for subsurface processes that precede peneplain formation. The periods of active exhumation and erosional removal of a thick cover lid results in relatively rapid cooling, which is then manifested by close-by thermochronological ages from methods having different closure temperature. For the removal of thick covers (i. e. datable by thermochronology) active erosional processes must be assumed implying a rugged and mountainous surface (FIGURE 3.2). Thus the periods of rapid cooling and exhumation actually exclude contemporaneous peneplain formation. During waning and finally cessation of vertical orogenic movements the mountainous morphology decays and the landscape transforms gradually via hilly landscape to a low relief, more-or-less *"flat"* landscape approximating the global base level. The development of such well-leveled erosional surface requires a longer period of tectonic quiescence. Clift et al. (2009) estimated that the duration of a planation process can be as long as ~ 100 My. Since exhumation is significantly slowed down towards the end of the active tectonic period, different thermochronometers converge towards similar ages. This age refers to the end of active exhumation and can be interpreted as maximum age for the peneplain formation.

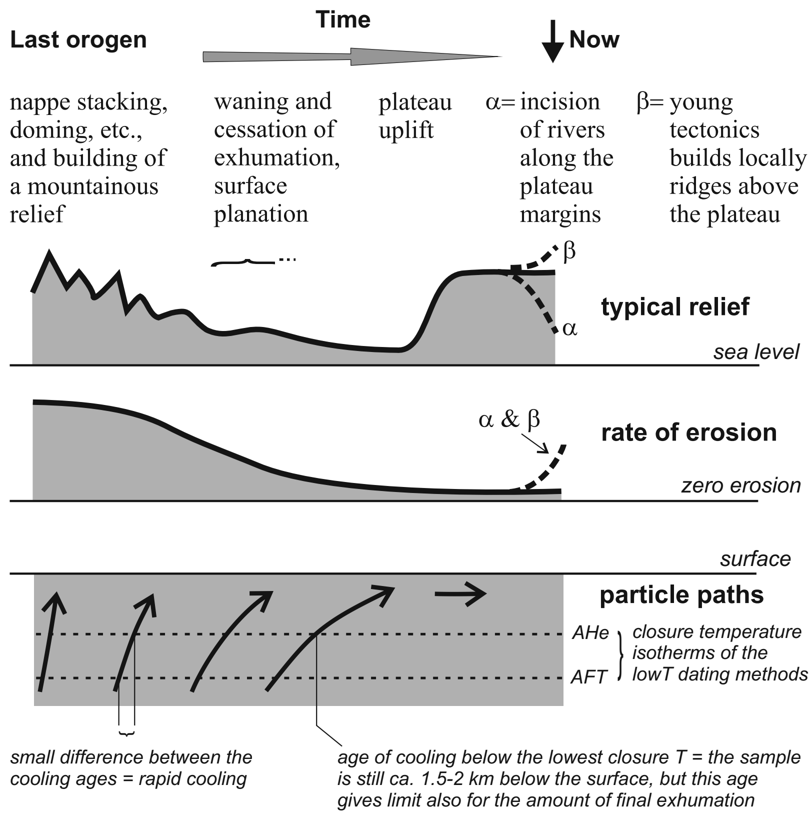

Figure 3.2: Schematic cartoon showing the relationship between the development of relief and the rate of erosion/exhumation as well as the thermochronological constraints expressing the exhumation rate. Note that regional uplift has no effect on the rate of erosion of already planated areas. While scenario reflects typical late stage dissection of the peneplains (like currently along the eastern margin of the Tibetan Plateau), scenario is specific for inner parts of the TP reflecting young tectonics.

From the central part of the Tibetan Plateau only few thermochronological data are available (Hetzel et al., 2011; Rohrmann et al., 2012; Wang et al., 2008; Jiang et al., 2002 and sporadic unpublished apatite fission track ages of Ding Lin). Apatite fission track, apatite (U-Th)/He and zircon (U-Th)/He data near Bangoin City indicate cooling events in Cretaceous and Eocene time (Hetzel et al., 2011). Rohrmann et al. (2012) studied thermochronologic data ($^{40}Ar/^{39}Ar$, AFT, AHe) from many sites of the central Tibetan Plateau. They interpreted the thermochronological results by a scenario of plateau growth that began locally in central Tibet during the Late Cretaceous and expanded to encompass most of central Tibet by 45 Ma. These apatite fission track and (U-Th)/He data indicate cooling events in Cretaceous and Eocene time, although Wang et al. (2008) reported also Miocene apparent AFT ages. First approaches of thermal history modeling from the western Tibetan plateau (Deosai plateau) were reported by (Van der Beek et al., 2009) focusing on exhumation after continental collision and proving very low denudation rate for the past 35 Ma.

According to Cretaceous low-temperature cooling ages reported by former studies in the interior of the Tibetan Plateau the elevated peneplains are actually archives of the pre-Himalyan evolution. We use this archive to reveal the pre-Miocene igneous events, as well as the tectonic and geomorphologic evolution of the Nam Co area in central Tibet. We present an extensive set of U-Pb, ZHe, AFT, and AHe data. The applied geo- and thermochronometers record the ages of magma emplacements and are sensitive to shallow crustal to near surface exhumation events in the northern Lhasa terrane. The new data presented in here allow for (I) reconstructing the exhumation history of the Lhasa terrane, and (II) bracketing the timing of the planation process.

3.3 Geology

3.3.1 Major domains of the Tibetan Plateau and their evolution

The Tibetan Plateau is build up of several terranes accreted together in the course of northward moving of the Indian continent during Mesozoic time (Dewey et al., 1988). The terranes are bordered by E-W trending suture zones that can be followed across the entire plateau (e. g. DeCelles et al., 2002; Leier et al., 2007a). Four east-west trending terranes can be defined from south to north: Lhasa, Qiangtang, Songpan-Ganze and Kunlun-Qilian Terrane (Dewey et al., 1988, see FIGURE 3.1).

The Lhasa Terrane is interpreted as the southern continental margin of Eurasia during the northward subduction of the Neotethyan Ocean in the Cretaceous (Murphy et al., 1997; Yin and Harrison, 2000). Before the India-Asia collision the Lhasa terrane came into collision with the Qiangtang terrane to the north along the Bangong suture zone during Late Jurassic time (around

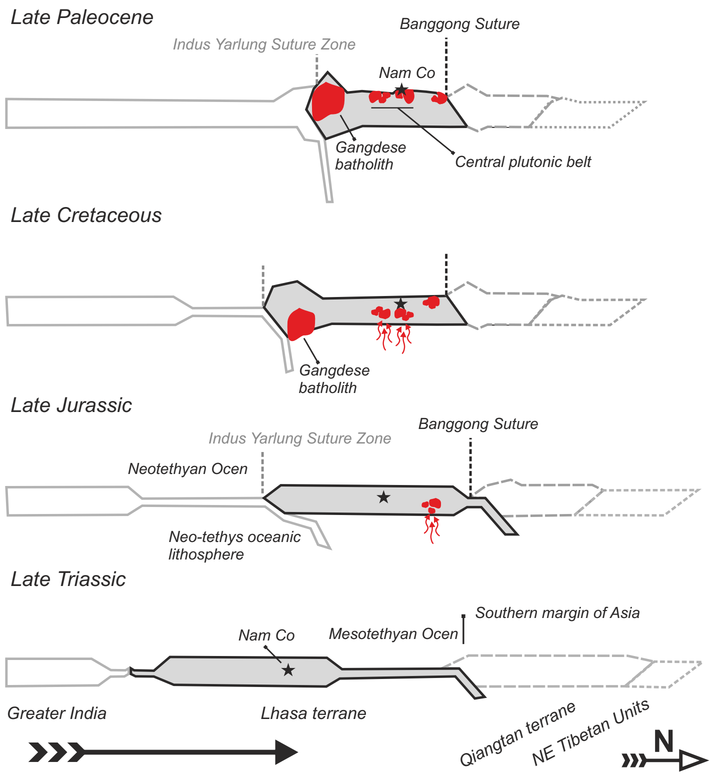

Figure 3.3: Schematic continent-scale evolution between India and the southern margin of Asia adapted from Leier et al. (2007b) with a special focus on the Lhasa Terrane (marked in gray). The asterisk represents the presumed position of the study area at Nam Co.

150 to 140 Ma, Chen et al., 2002; see also FIGURE 3.3). Igneous activity is omnipresent in the Lhasa terrane (Debon et al., 1986; Kapp et al., 2005a; Miller et al., 2000; Schwab et al., 2004; Volkmer et al., 2007; Xu et al., 1985). Cambrian intrusions and predominantly strongly foliated orthogneisses with Jurassic protolith age of around 160 Ma are present in the Amdo basement (see FIGURE 3.1B) south of the Bangong suture zone (Guynn et al., 2006). The over 2500 km long calc-alkaline magmatic Gangdese belt (FIGURE 3.1A), a large chain of mainly I-type batholiths next to the Indus-Yarlung suture forms the southern rim of the Lhasa terrane and comprises mainly two intrusive stages of Early Cretaceous and Paleogene age (Copeland et al., 1987; Debon et al., 1986). The Gangdese belt results from subduction of Neotethyan crust beneath the southern margin of the Lhasa terrane (Allegre et al., 1984; Dewey et al., 1988). The central plutonic belt (FIGURE 3.3) intruded between 130 and 110 Ma and spreads over the Lhasa terrane up to the Bangong suture zone (Kapp et al., 2005b; Leier et al., 2007b; Murphy et al.,

1997; Xu et al., 1985). The Linzizong Potassic volcanism erupted across the southern Lhasa terrane from Eocene to Oligocene in the Gangdese belt (He et al., 2007; Lee et al., 2009; Mo et al., 2008) and has been related to northward subduction of the Neotethyan oceanic slab beneath southern Asia (Lee et al., 2009). Miocene E-W extension has been accommodated by a series of generally N-S trending rift valleys throughout southern Tibet reflecting orogenic collapse that likely follows attainment of maximum elevation of the area (Dewey et al., 1988; England and Houseman, 1989; Molnar and Tapponnier, 1978; Tapponnier et al., 2001; Yin and Harrison, 2000). Development of these graben systems marks a significant shift in the state of stress within the Tibetan crust (Harris et al., 1988). There is evidence for E-W extension in southern Tibet dating back to $\sim$ 19 Ma (Williams et al., 2001). It is assumed that the onset of normal faulting has been induced in southern Tibet about 14 Ma ago (Coleman and Hodges, 1995), and these structures were reactivated about 8 Ma ago (Harrison et al., 1995). Central Tibet bears evidence for even younger significant east-west extension and normal faulting about 4 Ma ago (Harrison et al., 1995; Yin et al., 1999).

3.3.2 Geology of the Nam Co area

Nam Co area is located in the northern part of the Lhasa terrane, north to northwest of the Tibetan holy lake Nam Co. The dominant geological unit of the study is the Bangoin batholith complex (FIGURE 3.4A). The prevalent lithologies are biotite-hornblende granodiorite, leucogranite, monzogranite and tonalite (Harris et al., 1990; Xu et al., 1985). This central plutonic belt intruded during Cretaceous time and is widespread over the Lhasa terrane. Andesitic-dacitic dikes penetrate the Bangoin batholith complex (FIGURE 3.4A) in Late Cretaceous (Coulon et al., 1986; Harris et al., 1990; Pan et al., 2004; Xu et al., 1985). The granitoid bodies are surrounded by Phanerozoic sedimentary rocks consisting primarily of Carboniferous sandstone, metasandstone, shale and phyllite, and less frequent sequences bearing Ordovician, Silurian, and Permian limestone (Leeder et al., 1988; Leier et al., 2007b; Pan et al., 2004; Yin et al., 1988). Triassic formations, mostly bedded limestones and basalts, play a minor role and are exposed west of Nam Co and north of Bam Co only. Jurassic to Cretaceous sediments are present mainly in the eastern part of the study area, north of Nam Co (Coward et al., 1988;

Pan et al., 2004). The Jurassic strata of the central and northern Lhasa terrane are typically very low-grade metamorphosed gray shales and fine-grained sandstones, partly associated with ophiolitic assemblages (Coward et al., 1988; Leeder et al., 1988; Yin et al., 1988). Especially in the eastern part of the study area the granitoids of Bangoin batholith complex intruded into the slightly folded Jurassic sequences, and generated contact metamorphic zones. Lower Cretaceous strata (Duba Formation) of the study area consist of sandstone, mudstone and some conglomerate units (Yin et al., 1988; Leier et al., 2007a,b). The conglomerate beds were deposited in shallow marine and meandering-river environments. Shallow marine limestone of Aptian to Cenomanian age (Zhang, 2000) overlies the Lower Cretaceous clastic units and is widely exposed further south and southwest of the study area (Yin et al., 1988). Fluvial arkosic sandstone and mudstone are characteristic for the Upper Cretaceous strata in the Lhasa terrane (Takena Formation; Leier et al., 2007a). The sources of the Upper Cretaceous clastic formations were volcanic rocks, granitoids of Early Cretaceous age, and sedimentary strata eroded from the northern Lhasa and southern Qiangtang terranes (Leier et al., 2007a,b).

In the northern part of the study area Eocene continental red-beds are widespread (FIGURE 3.4A). These deposits are probably the marginal, mainly alluvial fan facies equivalents of the Niubao Formation of the Lunpola basin (FIGURE 3.1B) situated north of the Nam Co area (DeCelles et al., 2007; Taner and Meyerhoff, 1990; Xu and Lee, 1984). The outcrops of this sequence are relatively small and can be found mainly in little gorges. However, a stepped pyramid-shaped erosional remnant of total height of 140 m exposes well the alternating sandstone-siltstone sequence (FIGURE 3.1A AND B). The Eocene sediments are dominated by sandstone and siltstone, but some conglomerate, pelite and sometimes gypsum-bearing strata are also present. Fragments and incrustations of hematite-rich tropical duricrusts are also common. The framework composition of sandstones is dominated by monocrystalline quartz, metapelitic lithic fragments and feldspar grains. The basal beds of the siliciclastic sequences are rich in coarse feldspar crystals. This composition indicates provenance mainly from local sources, i. e. granitoids of the Bangoin batholith complex and low-grade Jurassic metapelites. The strata are mainly sub-horizontal, the observed maximum tilt is ca. 15 °C towards N-NE. The immediate onlap of the Eocene siliciclastic sequence on the Bangoin batholith complex is not exposed, but the granitoid clasts in

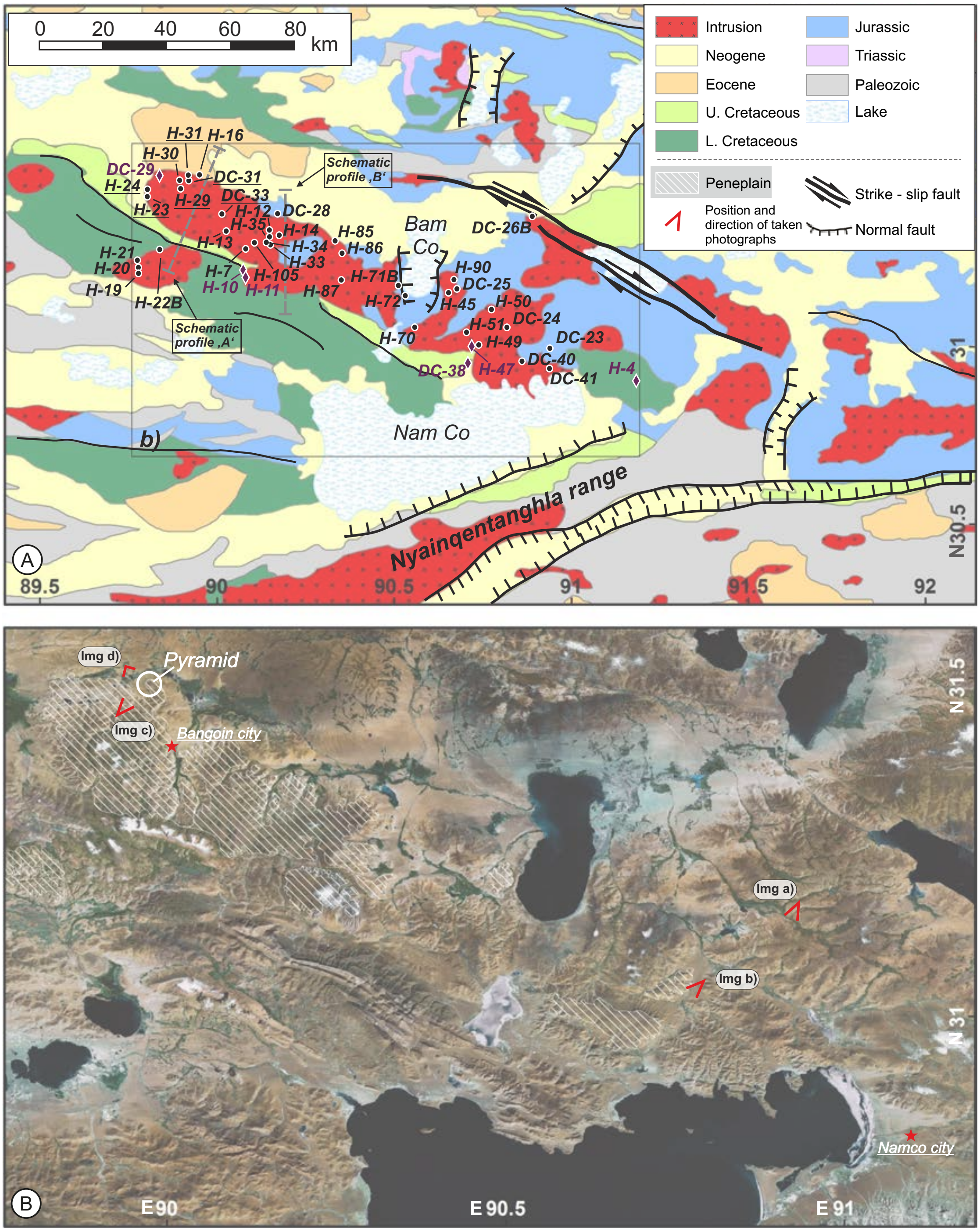

Figure 3.4: A: Geological map of the study area with the sample sites (based on Pan et al. (2004) with simplifications). The intrusions in the rectangle comprise the Bangoin batholith complex. White circles mark the samples taken from intrusions (underlined sample code indicates 7 samples from the northwesternmost area close to the city of Bangoin already published in Hetzel et al. (2011); see chapter 2a), purple diamonds refer to volcanic and green crosses refer to sedimentary samples B: Landsat image (from METI and NASA) of the area north of Nam Co were the peneplains were studied. Well preserved peneplains are outlined by white striped signature. The red v-shaped signs indicate position and direction of landscape photographs presented in FIGURE 3.5A, D.

the arenites and the results of mapping expeditions (e. g. profiles in the 1:250,000 geological map H45C001004) call for an onlap geometry of the clastic sequence onto the granitoids. We assume that a significant part of the granitoid area was covered by the Eocene red-bed sequence.

Especially north of the Bangoin batholith complex, Quaternary deposits dominate the sediment coverage of the Lhasa terrane. The depressions are the local sediment traps and they were filled with sediments with short transport distance. Terraces in several heights can be observed in the gravel banks of the lake margins reflecting Pleistocene to Holocene lake level variations, and they are also carved in the basement rocks in several 10 m above the current levels of the lakes. Although sometimes they are well remarkable features, the extent of these flat geomorphological objects are typically minor and they are localized only in the lowest levels of the depressions.

3.3.3 Peneplains on the study area

Peneplains are prominent geomorphologic features in the Bangoin batholith complex (FIGURE 3.5A - B). These highly elevated surfaces with steep hillsides and planar or slightly undulating top surfaces with a slope $< 15°$ can be found in an area of ca. 150 km east-west and ca. 75 km north-south extent in the central Lhasa terrane at different elevations between 4,800 m and 5,600 m (Hetzel et al., 2011). Along the marginal zones creeks and wadis incise the peneplains and create rugged erosion surfaces (Strobl et al., 2010). Such degraded or ruined peneplain remnants typically surround the more-or-less preserved peneplain areas.

The peneplains were carved into bedrocks, mostly in granitoids, however in the southern area some peneplains were formed in the Jurassic low-grade metamorphic siltstone-sandstone sequences and also in the Cretaceous ignimbrite complex. The top of the intact peneplains are predominantly covered by a few cm thin layers of very immature soil, chiefly composed of granule-sized granitic detritus, and permafrost generated block fields. In some zones especially to the north the decay of peneplains has already started to decay, and the slightly rugged hilly landscape is dominated by corestones and woolsack structures (FIGURE 3.5E - F).

A NW-SE trending fault zone is splitting the study area south of the Bangoin batholith complex (FIGURE 3.4A). Some shortening accommodated along this reverse fault system and generated a crest that is emerging above the peneplains. The geology of the two sides of the fault zone differs;

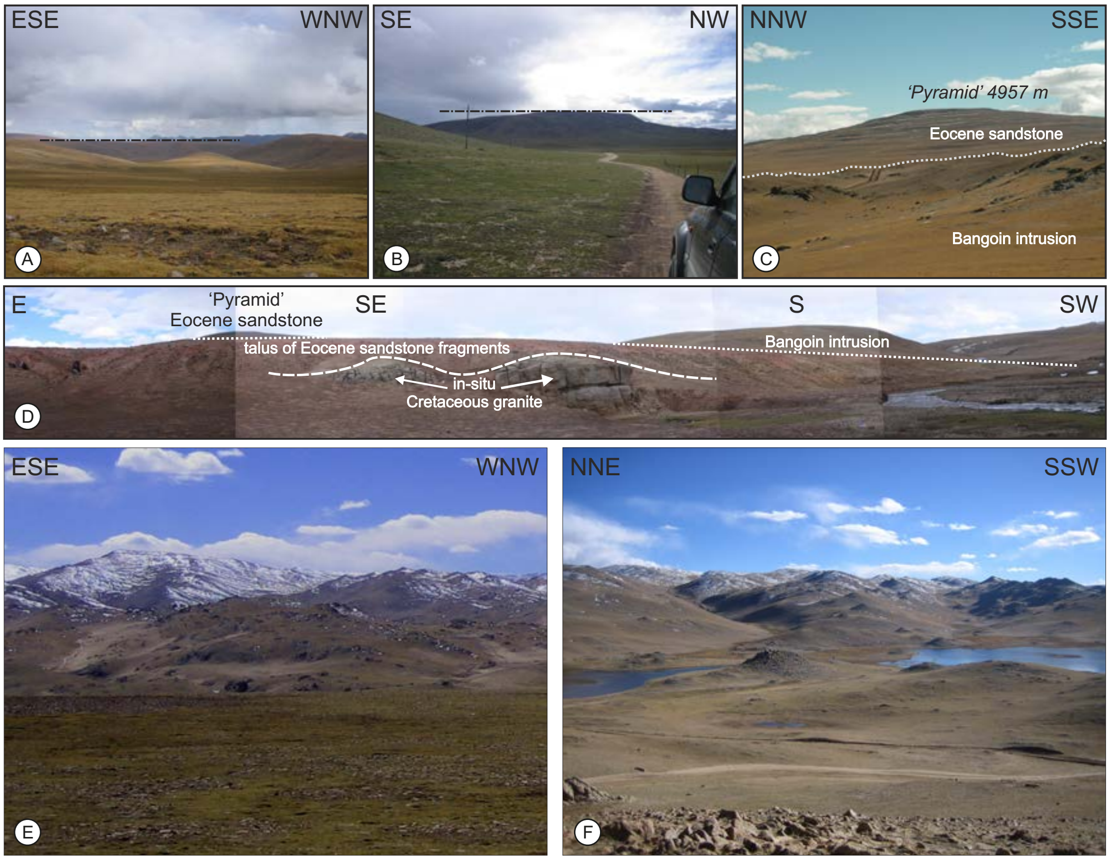

Figure 3.5: Landscape photographs from the Bangoin area. Images A: and B: illustrate different intact peneplains with flat top. Image C: shows the Eocene sandstone forming a *"pyramid"* onlapping onto the Bangoin intrusive complex. Image D: gives a sight from Bangoin intrusion complex towards the area covered by Eocene sediments. The pyramid-shaped hill is composed of dominantly from sandstone that onlaps the granitoide basement belonging to Bangoin intrusive complex. Images E: and F: North of the intact planation surface (flat-top hill) the former peneplain decayed to a rugged hilly landscape with corestone forming wollsack structures.

thus we distinguish a north-eastern and a south-western block. The more extended and better preserved peneplains are in the northeastern block.

3.4 Samples and methods

The geological map of Pan et al. (2004) was used for field work. We have collected 46 igneous samples, predominantly from granitoids, and 5 samples were taken from effusive and ignimbritic formations. The samples were shattered to nut-sized pieces before crushing by jaw crusher. Sieve fractions smaller than 250 μm were processed on a Wilfley table and the pre-concentrated heavy mineral-rich fractions were gravity separated by sodium-polytungstate solution (density set to 2.86 g/cm^3). Ferromagnetic minerals were removed with hand magnet from the heavy mineral concentrates and the dia- and paramagnetic fractions were treated by isodynamic magnetic separation; 4 to 6 "magnetic fractions" having different susceptibilities were produced from each sample. Further zircon-rich concentrates were separated from apatite by panning in alcohol or by gravity separation using diiodomethane (ρ=3.33 g/cm^3).

3.4.1 U-Pb zircon geochronology

From 22 igneous samples typically 35 zircon crystals were randomly selected for in-situ age dating. The crystals were picked and fixed in grain mounts by epoxy resin. After polishing procedure (using diamond suspensions of 9 μm, 3 μm and 1 μm grade) the internal structure of the crystals were studied by cathodoluminescence imaging. These photographs were the base for the selection of laser spots to minimize the bias caused by ablation of heterogeneous zones. In-situ U-Pb dating was performed at the Geological Survey of Denmark and Greenland (GEUS) in Copenhagen by laser ablation-single collector-magnetic sectorfield inductively coupled plasma mass spectrometry (LA-SF-ICP-MS). A Thermo Finnigan Element 2 mass spectrometer coupled to a NewWave UP213 laser ablation system was used. All age data presented here were obtained by single spot analyses with a spot diameter of 30 μm and a crater depth of approximately 15 to 20 μm. The laser was fired at a repetition rate of 5 Hz and at nominal laser energy output of 50 %. He and Ar were used as sample carrier gas. Analytes of ^{238}U, ^{232}Th, ^{208}Pb, ^{207}Pb, ^{206}Pb and ^{204}Pb were measured by the ICP-MS. The methods employed for analysis are described in detail by Frei and Gerdes (2009); Gerdes and Zeh (2006). The age calculation is based on the standard-sample bracketing using GJ-1 zircon standard (Jackson et al., 2004). For further control the Plešovice standard (Sláma et al., 2008) was analysed. The age results of the standards were consistently within 1σ of the published ID-TIMS values. Drift corrections and data reductions of the raw data were performed by the software Pepita (Dunkl et al., 2008). No common lead correction was required. Tukey's Biweight method was used to determine the robust mean age using Isoplot/Ex 3.0 (Ludwig, 2003).

3.4.2 Apatite fission track thermochronology

For AFT analysis the external detector method was used (Gleadow, 1981). Highly enriched apatite concentrates were embedded in epoxy resin (Araldite brand #2020); then they were polished in five steps down to 1 μm and etched by 5.5 N HNO_3 solution for 20 sec at 21 °C (Donelick et al., 1999). The apatite grain mounts with the etched spontaneous tracks were covered with freshly cleaved muscovite sheets *(Goodfellow mica)* as external track detectors and irradiated with thermal neutrons in the research reactor of the TU Munich in Garching. The requested neutron flux was 5×10^{15} n/cm^2. Corning glass dosimeter (CN5) was used to monitor the neutron fluence. After irradiation the tracks in the external detectors were revealed by etching in 40 % HF for 40 min at 21 °C. Both grain mount and corresponding mica detector were fixed side by side on a glass slide. Spontaneous and induced fission tracks were counted under 1000x magnification using a Zeiss Axioskop microscope equipped with computer-controlled stage system (Dumitru, 1993). Only apatite crystals with well polished surface parallel to the crystallographic c-axis were counted. From each igneous sample a minimum of 25 grains were counted. Additionally the Dpar values were measured in each dated apatite crystal and around 60 horizontal confined tracks were measured in most of the samples. AFT ages were calculated using the zeta age calibration method (Hurford and Green, 1982) with the standards listed in Hurford (1998). Data processing and plotting were performed with the TRAKKEY software (Dunkl, 2002) while errors were calculated using the classical procedure described in Green (1981).

3.4.3 Apatite and zircon (U-Th)/He thermochronology

Usually four crystals per samples from 51 apatite and 20 zircon concentrates were selected. Euhedral crystals were inspected for inclusions under 250x magnification and cross-polarized light. Only inclusion-free grains that exceeded 70 μm diameters were selected. To calculate the alpha ejection correction factor (Farley et al., 1996) microphotographs were taken for determining shape parameters like width, total length, and length of prismatic section. After proper documentation, each crystal were wrapped in platinum capsules and degassed in high vacuum by heating with an infrared laser in the Thermochronology Laboratory at Geoscience Center, University of

Göttingen *(GÖochronology)*. A SAES Ti-Zr getter purified the gas extracted from the crystals and a Hiden®triple-filter quadrupole mass spectrometer measured the ^{4}He content. For the detection of the alpha-emitting elements (uranium, thorium and samarium) the degassed crystals were spiked with calibrated ^{230}Th and ^{233}U solutions. Zircons were dissolved in pressurized Teflon bombs using distilled 48 % HF + 65 % HNO_3 in five days at 220 °C, while apatites were dissolved in 2 % HNO_3 at room temperature in an ultrasonic bath. The actinide concentrations were determined by isotope dilution method and the Sm by external calibration method, using a Perkin Elmer Elan DRC II ICP-MS equipped with an APEX micro-flow nebulizer.

3.5 Results

3.5.1 U-Pb results

For calculation of the weighted sample mean U-Pb ages the single grain ages with ^{206}Pb/^{238}U - ^{207}Pb/^{235}U concordance lower than 90 % and reverse concordance higher than 103 % were not considered. Furthermore, concordant, but extremely old ages that are obviously derived from inherited cores of the zircon grains were also eliminated from the averaging procedure. The weighted mean ages are summarised in TABLE 3.1, and analytical details can be found in chapter A. The U-Pb ages of the granitoids range between 127 Ma and 84 Ma, while the ages of volcanic formations range between 130 Ma and 58 Ma. The areal distribution of the U-Pb ages is presented in FIGURE 3.6.

3.5.2 Low-temperature thermochronological results

A synopsis of the ages obtained by low-temperature thermochronometers is given in TABLE 3.1, while detailed fission track and (U-Th)/He data are listed in TABLE A.23 – TABLE A.22 of the data repository. Zircon (U-Th)/He ages range between 91 and 62 Ma while apatite fission track and (U-Th)/He thermochronology yield tight age groups around 60 Ma and 50 Ma (FIGURE 3.7). Fission track length measurements of all AFT dated samples give a mean length around 13.6 μm and typically unimodal distributions with left-sided asymmetry indicating rather simple cooling histories. No significant trend can be observed on the areal distribution of low-temperature

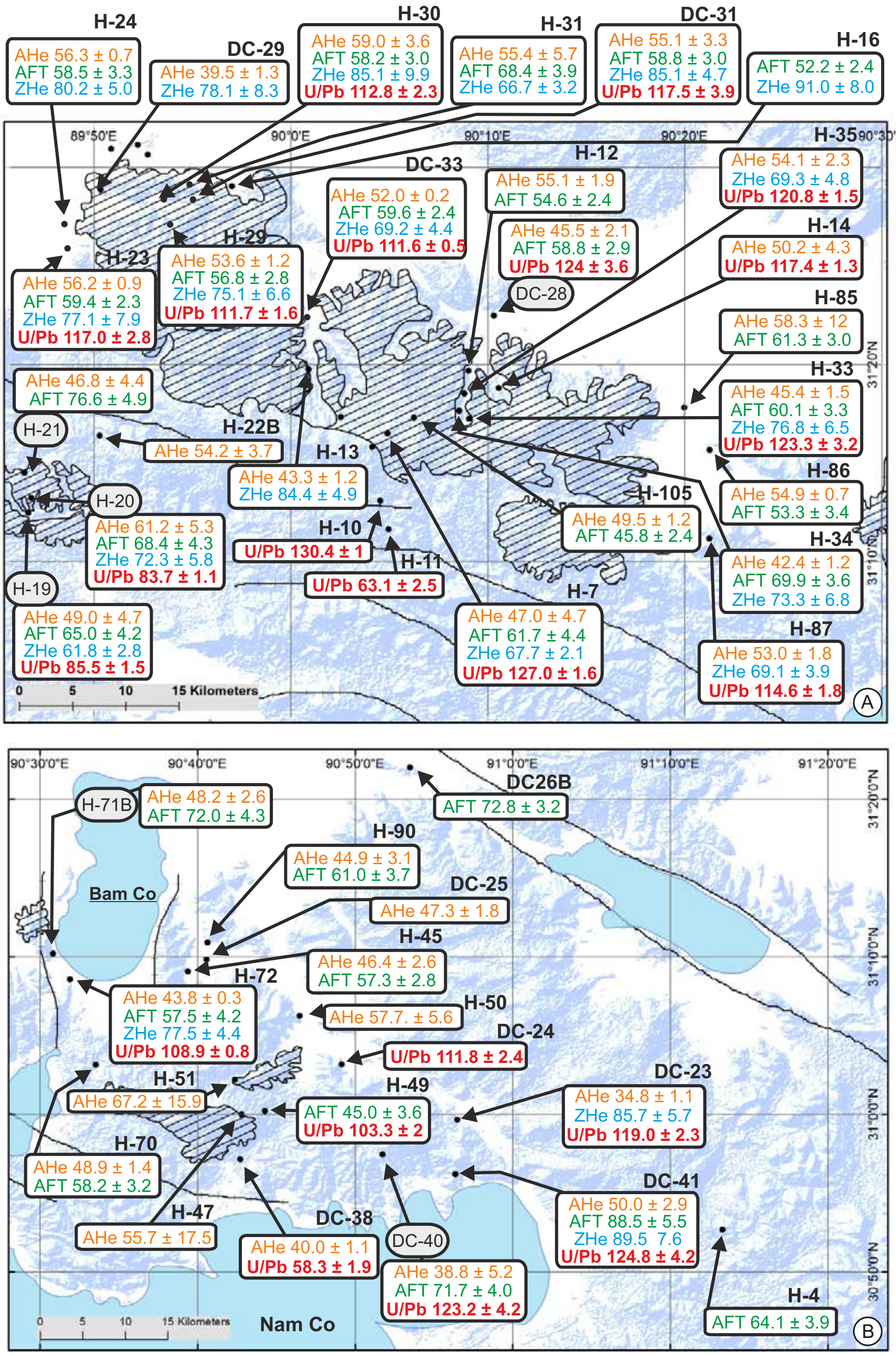

Figure 3.6: Maps of the western (A) and eastern (B) part of the study area with the outlines of the well-preserved peneplains (striped signature) and with the new geochronological data. gray labeled samples were used for the modeling of the thermal history. Black lines represent the major faults.

Table 3.1: Summary of geochronological results obtained on the igneous formations of the Nam Co - Bangoin area. Details of the analyses can be found in the appendix

Sample	Lithology	Lat [°]	Long [°]	Elev. [m]	$^{206}Pb/^{238}U$ age*[1)]	*N***	ZHe age[2)]	*N***
	Granitoids in the northeastern block							
DC-23	granite	30.9944	90.9415	4801	119.0 ± 2.3	19	85.7 ± 5.7	3
DC-24	granite	31.0530	90.8194	4830	111.8 ± 2.4	20		
DC-25	granite	31.1641	90.6762	4699				
DC-26B	granite	31.3668	90.8914	4812				
DC-28	granite	31.3746	90.1720	4680	124.0 ± 3.6	19		
DC-31	Bt granite	31.4677	89.9208	4824	117.5 ± 3.9	25	85.1 ± 4.7	5
DC-33	granite	31.3733	90.0143	4733	111.6 ± 0.5	30	69.2 ± 4.4	3
DC-40	granite	30.9579	90.8623	4955	123.3 ± 4.2	22		
DC-41	granite	30.9366	90.9395	4845	124.8 ± 4.2	20	89.5 ± 7.6	3
H-7	Bt granite	31.2753	90.0820	5350	127.0 ± 1.6	28	67.7 ± 2.1	3
H-12	Bt granite	31.3281	90.1504	4750				
H-13	sand (local, granitic)	31.3293	90.0153	4714			84.4 ± 6.9	3
H-14	Hb granite	31.3136	90.1761	4830	117.4 ± 1.3	25		
H-16	granite	31.4844	89.9504	4700			91.0 ± 8.0	2
H-23	granite	31.4227	89.8048	4630	117.0 ± 2.8	28	77.1 ± 7.9	3
H-24	granite	31.4434	89.8054	4610			80.2 ± 5.0	3
H-29	granite	31.4433	89.8982	4970	111.7 ± 1.6	25	75.1 ± 6.6	3
H-30	granite	31.4685	89.8959	4750	112.8 ± 2.3	28	85.1 ± 9.9	2
H-31	leucogranite	31.4797	89.9194	4770			66.7 ± 3.2	3
H-33	granite	31.2879	90.1510	5020	123.3 ± 3.2	21	76.8 ± 6.5	5
H-34	monzonite	31.2944	90.1428	5001			73.3 ± 6.8	3
H-35	Bt granite	31.3090	90.1469	4926	120.8 ± 1.5	25	69.3 ± 4.8	4
H-45	Bt granite	31.1510	90.6566	4700				
H-49	granite	31.0037	90.7381	4876	103.3 ± 2.0	25		
H-50	Bt granite	31.1043	90.7746	4831				
H-51	granite	31.0367	90.7063	5062				
H-70	diorite	31.0527	90.5591	4841				
H-71B	diorite	31.1702	90.5139	4693				
H-72	Bt diorite	31.1430	90.5319	4603	108.9 ± 0.8	25	77.5 ± 4.4	3
H-85	Bt granite	31.2970	90.3332	4640				
H-86	Bt granite	31.2613	90.3545	4664				
H-87	granite	31.1861	90.3544	4998	114.6 ± 1.8	22	69.1 ± 3.9	3
H-90	Bt granite	31.1817	90.6772	4770				
H-105	diorite	31.2885	90.1044	5333				
	Granitoids in the southwestern block							
H-19	granite	31.2078	89.7781	4830	85.5 ± 1.5	29	61.8 ± 2.8	2
H-20	granite	31.2208	89.7804	5070	83.7 ± 1.1	28	72.3 ± 5.8	2
H-21	granite	31.2419	89.7747	5180				
H-22B	Bt granite	31.2734	89.8383	5050				
	Volcanic rocks							
DC-29	andesite	31.2889	89.5034	4733			78.1 ± 8.3	2
DC-38	dacite	30.9527	90.7118	4770	58.3 ± 1.9	17		
H-4	ignimbrite	30.878	91.222	5050				
H-10	dacite	31.2182	90.0758	5080	130.4 ± 1.0	32		
H-11	ignimbrite	31.1943	90.0828	5100	63.1 ± 2.5	28		
H-47	ignimbrite	31.0002	90.7132	5390				

Sample	Lithology	Lat [°]	Long [°]	Elev. [m]	AFT age	*N***	MTL 3)	*N****	AHe age 2)	*N***
	Granitoids in the northeastern block									
DC-23	granite	30.9944	90.9415	4801					34.8 ± 1.1	4
DC-24	granite	31.0530	90.8194	4830						
DC-25	granite	31.1641	90.6762	4699					47.3 ± 1.8	4
DC-26B	granite	31.3668	90.8914	4812	72.8 ± 3.2	30				
DC-28	granite	31.3746	90.1720	4680	58.8 ± 2.9	30	13.8 ± 1.3	60	45.5 ± 2.1	2
DC-31	Bt granite	31.4677	89.9208	4824	58.8 ± 3.0	24	13.1 ± 1.5	60	55.1 ± 3.3	5
DC-33	granite	31.3733	90.0143	4733	59.6 ± 2.4	28	13.3 ± 1.6	60	52.0 ± 0.2	4
DC-40	granite	30.9579	90.8623	4955	71.7 ± 4.0	25	14.1 ± 0.9	60	38.8 ± 5.2	3
DC-41	granite	30.9366	90.9395	4845	88.5 ± 5.5	25	13.6 ± 1.2	63	50.0 ± 2.9	3
H-7	Bt granite	31.2753	90.0820	5350	61.7 ± 4.4	23			47.0 ± 4.7	5
H-12	Bt granite	31.3281	90.1504	4750	54.6 ± 2.4	30	13.2 ± 1.4	65	55.1 ± 1.9	3
H-13	sand (local, granitic)	31.3293	90.0153	4714					43.3 ± 1.2	3
H-14	Hb granite	31.3136	90.1761	4830					50.2 ± 4.3	4
H-16	granite	31.4844	89.9504	4700	52.2 ± 2.1	27	13.1 ± 1.3	61		
H-23	granite	31.4227	89.8048	4630	59.4 ± 2.3	24	13.7 ± 1.2	60	56.2 ± 0.9	5
H-24	granite	31.4434	89.8054	4610	58.5 ± 3.3	23	13.4 ± 1.2	64	56.3 0.7	3
H-29	granite	31.4433	89.8982	4970	56.8 ± 2.8	26	13.7 ± 1.1	54	53.6 ± 1.2	3
H-30	granite	31.4685	89.8959	4750	58.2 ± 3.0	32	13.6 ± 1.6	60	59.0 ± 3.6	3
H-31	leucogranite	31.4797	89.9194	4770	68.4 ± 3.9	23	13.3 ± 1.3	40	55.4 ± 5.7	2
H-33	granite	31.2879	90.1510	5020	60.1 ± 3.3	31	14.5 ± 1.6	57	45.4 ± 1.5	6
H-34	monzonite	31.2944	90.1428	5001	66.9 ± 3.6	30			42.4 ± 1.2	8
H-35	Bt granite	31.3090	90.1469	4926					54.1 ± 2.3	7
H-45	Bt granite	31.1510	90.6566	4700	57.3 ± 2.8	30	13.5 ± 1.3	60	46.4 ± 2.6	4
H-49	granite	31.0037	90.7381	4876	45.0 ± 3.6	31	13.5 ± 1.6	54		
H-50	Bt granite	31.1043	90.7746	4831					57.7 ± 5.6	3
H-51	granite	31.0367	90.7063	5062					67.2 ± 15.9	2
H-70	diorite	31.0527	90.5591	4841	58.2 ± 3.2	30	14.6 ± 0.9	53	48.9 ± 1.4	4
H-71B	diorite	31.1702	90.5139	4693	72.0 ± 4.3	40	13.6 ± 1.5	60	48.2 ± 2.6	5
H-72	Bt diorite	31.1430	90.5319	4603	57.5 ± 4.2	17			43.8 ± 0.3	3
H-85	Bt granite	31.2970	90.3332	4640	61.3 ± 3.0	30	13.9 ± 1.0	60	58.4 ± 11.9	2
H-86	Bt granite	31.2613	90.3545	4664	53.3 ± 3.4	30	13.3 ± 1.4	60	54.9 ± 0.7	2
H-87	granite	31.1861	90.3544	4998					53.0 ± 1.8	2
H-90	Bt granite	31.1817	90.6772	4770	61.0 ± 3.7	30			44.9 ± 3.1	2
H-105	diorite	31.2885	90.1044	5333	45.8 ± 2.4	30			49.5 ± 1.2	4
	Granitoids in the southwestern block									
H-19	granite	31.2078	89.7781	4830	65.0 ± 4.2	30	13.5 ± 1.3	27	49.0 ± 4.7	1
H-20	granite	31.2208	89.7804	5070	68.4 ± 4.3	30	13.9 ± 1.1	60	61.2 ± 5.3	2
H-21	granite	31.2419	89.7747	5180	76.6 ± 4.9	30	13.7 ± 1.3	42	46.8 ± 4.4	4
H-22B	Bt granite	31.2734	89.8383	5050					54.2 ± 3.7	3
	Volcanic rocks									
DC-29	andesite	31.2889	89.5034	4733					39.5 ± 1.3	5
DC-38	dacite	30.9527	90.7118	4770					40.0 ± 1.1	4
H-4	ignimbrite	30.878	91.222	5050	64.1 ± 3.9	30				
H-10	dacite	31.2182	90.0758	5080						
H-11	ignimbrite	31.1943	90.0828	5100						
H-47	ignimbrite	31.0002	90.7132	5390					55.7 ± 17.5	2

Bt and Hb indicate that the major mafic mineral is biotite or hornblende, respectively
*: Zircon LA-ICP-MS ages
**: Number of measured/counted grains
***: Number of measured track lengths
1) Uncertainty in 2σ.
2) Uncertainty in 1σ.
3) Mean track lengths

thermochronological ages (FIGURE 3.6).

The samples were collected from elevations between ca. 4,600 m and ca. 5,400 m. This elevation range covers actually the maximum contrast in relief available from the study area. This ca. 800 m range is rather low for an age-elevation study (first applied by Wagner et al., 1977), but it is noteworthy that the apatite thermochronometric ages and the mean track length data do not show significant vertical trends (FIGURE 3.8).

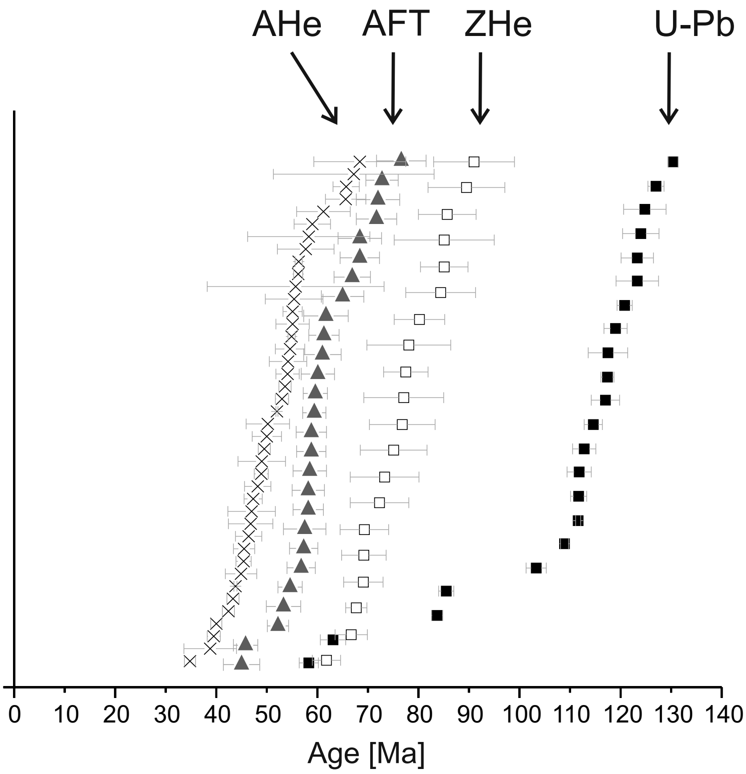

Figure 3.7: Compilation of the new geochronological data: zircon U-Pb ages and all low-temperature thermochronological ages are presented on a cumulative probability plot. Note that each symbol reflects a mean age of a sample, not individual grain ages.

3.6 Discussion

3.6.1 Zircon U-Pb ages of the igneous bodies of the Nam Co area

The major mass of the granitoids of the study area between Nam Co and Bangoin belongs to the oldest, Early Cretaceous magmatic period (130 to 103 Ma see FIGURE 3.9). Beyond the

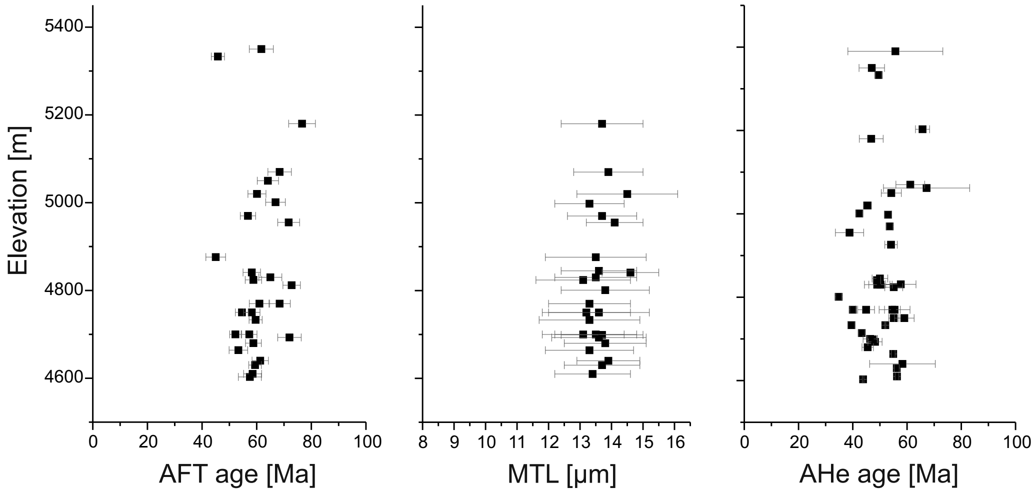

Figure 3.8: Age - elevation plots of apatite thermochronological and track length data of the Nam Co area. The total contrast in elevation of the lowest and highest sample sites is ca. 800 m. Note that thermochronological data show not any trend with elevation.

granitoids one volcanic sample yields a similar Early Cretaceous age TABLE 3.1. This oldest magma-forming event in the Early Cretaceous was connected to the intense crustal thickening during the northward movement and thrusting of Lhasa terrane beneath the Qiangtang terrane (Kapp et al., 2005b, 2007a; Murphy et al., 1997, FIGURE 3.3).

Late Cretaceous U-Pb ages 85.5 to 83.7 Ma; TABLE 3.1 were determined on a granitoid body that intruded south of the major Bangoin batholith complex into Lower Cretaceous sediments (see FIGURE 3.4A). This intrusion took place probably before the final closing of the Bangong suture. The youngest U-Pb ages were detected in felsic volcanic rocks along the southern margin of the study area and scatter around 60 Ma (FIGURE 3.6; TABLE 3.1). This volcanism can be related to the Linzizong volcanic sequence comprising Paleogene to Eocene igneous rocks especially in the southern part of the Lhasa terrane (He et al., 2007; Lee et al., 2009; Mo et al., 2008).

We have compiled all available U-Pb ages from the study area and from the Lhasa terrane (Chen et al., 2002; Chiu et al., 2009; Chu et al., 2006; He et al., 2007; Hou et al., 2004, and references therein; Kapp et al., 2005a, 2003, 2007a; Lee et al., 2009; Liang et al., 2008, McDermid et al., 2002, and references therein; Miller et al., 2000; Schwab et al., 2004; Wen et al., 2008; Xu et al., 1985). The zircon U-Pb ages from the entire Lhasa terrane show a much wider distribution than

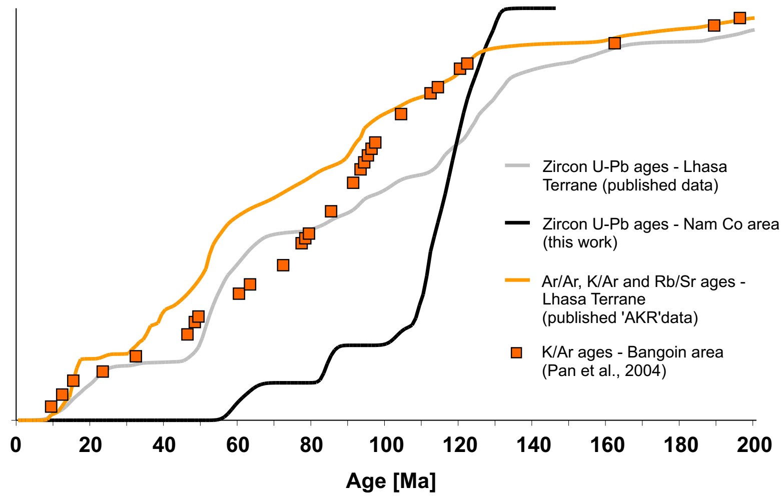

Figure 3.9: Compilation of the high-temperature geochronological data from the Lhasa terrane obtained on the igneous rocks of the Bangoin area, shown as cumulative frequency plot. See list of sources of the data in the text.

our new U-Pb ages from the Nam Co area (FIGURE 3.9). The prominent ca. 110 to 125 Ma age group of the Nam Co area plays a rather subordinate role in the magmatic suites of the entire Lhasa terrane. We could not find traces of the igneous units with ages around 20 Ma and older than 130 Ma in Nam Co area (FIGURE 3.9).

In order to determine of the depth of emplacement we have performed Al-in-amphibole geobarometry on euhedral amphibole crystals of an Early Cretaceous granitoid body from the well preserved Bangoin peneplain (see sample H-14 in FIGURE 3.4). The amphibole crystals have rather low Al-content (7.2 to 7.9 wt % Al_2O_3; see details of the electron microprobe analysis in appendix, TABLE A.28). According to (Ridolfi and Renzulli, 2012, their equation 1b) the Al-in-amphibole geobarometer indicates 1.3 ± 0.1 kb crystallization pressure corresponding to 4.0 ± 0.2 km depth when assuming the typical density of continental crust.

3.6.2 Low-temperature thermal history of the Nam Co area

While the zircon U-Pb ages refer the age of emplacement of igneous bodies, the low-temperature thermochronological data carry crucial information on the post-magmatic exhumation history of the study area. The areal distribution of the samples and the new ages are presented in FIGURE 3.6, while FIGURE 3.6 shows a compilation of all ages in a cumulative frequency plot. The ZHe, AFT and AHe ages are considerably younger than the emplacement ages of the major granitoid bodies of the Bangoin complex. There is a characteristic, ca. 40 My long lag time between the Early Cretaceous U-Pb crystallization ages detected in the northeastern block and the zircon (U-Th)/He ages, which are typically younger than 85 Ma.

According to the amphibole geobarometry the intrusions of the ca. 120 Ma old Bangoin complex were emplaced in a rather shallow position (ca. 4 km depth, see above). These plutons thus crystallized above the usual depth of the closure temperature of the ZHe thermochronometer, which is ca. 7 km in the continental crust (assuming a "normal" geothermal gradient). The results of thermal modeling of the cooling of plutons indicate that after the emplacement of an intrusion of ca. 10 km diameter the relaxation of the isotherms takes only a few million years (e. g. Steenken et al., 2002). Therefore the lag time of approximately 40 My between the U-Pb ages and the ZHe ages reflecting cooling below the closure temperature (ca. 180 °C) of the ZHe thermochronometer cannot be explained by a simple post-emplacement cooling. Instead we have to assume a conductive, rather rapid cooling after the Early Cretaceous magmatic period and a later total thermal reset of the ZHe thermochronometer triggered by re-heating in Late Cretaceous time. We relate this younger heating event (>180 °C) to Late Cretaceous magmatism. The product of this magmatic event is present in the form of a ca. 25 km long granitoid body intruded in the southwestern block, dated at around 85 Ma (see above). The observed wide contact zones with coarse-grained marbles and skarn mineralization document its significant local thermal effect and the regional effect can be deduced from its big size. During this igneous period at around 85 Ma the increased heat flow modified the thermal structure of the entire Nam Co area and triggered the regional reset of the ZHe ages. Thus, ZHe thermochronometer lost the complete memory for the pre-85 Ma history.

The post-80 Ma thermal history is well mirrored in the AFT and AHe ages. The apparent ages cover the cooling history between the closure temperatures in the time span of ca. 65 to 45 Ma (FIGURE 3.7). If we neglect very few ages in the tails of the distributions the offset between the data sets of AFT and AHe ages is approximately 8 to 10 My. There are traces of igneous activity in the region in this time interval, but the ca. 60 Ma old Paleocene magmatism is represented by thin dikes and ash layers only. Their volume is rather small and we assume that their thermal impact was very minor and thus the influence on AFT and AHe ages was negligible in the Nam Co area. Consequently, we interpret the low-temperature thermochronological data as cooling ages generated by regional exhumation. In order to reveal the details of the evolution of the region the thermal data have to be modeled.

3.6.2.1 Modeling of the thermal history

For thermal modeling we use a complex data set that included, beyond the AFT and AHe ages, confined track length distributions and kinetic parameters. modeling runs of thermal histories of selected samples were carried out by the HeFTy software (Ketcham, 2005). The program uses a Monte Carlo algorithm with a multikinetic annealing model (Ketcham et al., 1999). The algorithm generates a large number of time-temperature paths, calculates the apparent age and the synthetic track length distribution, which are tested with respect to the input data. Before starting modeling, HeFTy is fed step by step with five major types of input data:

(I) apatite fission track single-grain ages with the number of track counted and the corresponding kinetic parameter (in our case Dpar; Carlson et al., 1999),

(II) the length of confined horizontal fission tracks and their angle to the crystallographic c-axis,

(III) parameters from (U-Th)/He apatite analysis such as U, Th, and Sm contents, calculated equivalent sphere radius for each crystal and measured uncorrected AHe age,

(IV) the same parameters from (U-Th)/He zircon analysis, and

(V) the available additional constraints of the time-temperature history, which are the annual mean temperature (5 °C in the region), the age of the emplacement of the dated intrusions and surface temperature in Eocene (between 55 and 35 Ma), when the plateau forming igneous formations were exhumed to surface and covered by the Paleogene sediments.

The modeling was performed using minor limitation factors (in nearly unsupervised mode). The annealing models used for AFT, AHe and ZHe thermochronometers are described in Farley

(2000); Reiners et al. (2004); Ketcham et al. (2007). Temperature of 200 °C and age of 200 Ma were set as maximum values for modeling of the thermal history.

3.6.2.2 Sensitivity test of the thermal modeling procedure

Numerous ZHe, AFT and AHe data are available now from the Nam Co area. However for the reconstruction of the thermal history we have considered also the available independent geological constraints and this data set is extremely poorish. The samples mainly derive from uncovered basement areas without evidence on age and magnitude of burial or tectonic activity.

In order to estimate the reliability of the modeled thermal paths we made systematic tests to determine the influence of variable single-grain (U-Th)/He ages on the HeFTy modeling. The usually wide range of single-grain (U-Th)/He ages is a well known phenomenon. The spread is mainly caused by zoning of actinide elements, different grain sizes, and the impurities of the grains (e. g. Fitzgerald et al., 2006). Furthermore, accumulating alpha-recoil tracks modify the crystal lattice, which in turn impacts the closure temperature and thus the apparent He age (Shuster et al., 2006) modeling of the thermal history was performed in four different ways, considering:

(I) the averaged single-grain AHe data with the error calculated by the standard deviation of the ages measured in the sample, or by the maximum error defined as the spread of ages (see equation above),

(II) the oldest single-grain AHe data,

(III) the youngest single-grain AHe data, and

(VI) all AHe single grain data with the individual parameters like age, equivalent sphere radii and actinide content with the observed zonation.

A compact formula for spatial analysis:

$$as = \frac{(age_{max} + sd_{max}) - (age_{min} - sd_{min})}{2}$$

where

as: age spread
age_{max}: oldest single-grain age
sd_{max}: standard deviation of oldest single-grain age
age_{min}: youngest single-grain age
sd_{min}: standard deviation of youngest single-grain age

For the sensitivity tests we assume two scenarios: with or without re-burial of the granitoids by Eocene continental sediments. Although at the northern margin of the exposed granitoid bodies of Bangoin complex the onlap of the Eocene sequence is obvious we should consider that sediment cover may have not been complete on the entire peneplain area. In this case the southern part of the study area was not exposed to the surface in Eocene time and the exhumation lasted longer. Thus the two scenarios are:

(I) Considering no onlap of Eocene sediments: in this case no additional time-temperature constraint is used between the Cretaceous high temperature (deeply buried) initial conditions and the present surface temperature.

(II) Considering exhumation to the surface until ca. 45 Ma, and in this case we add one invariable time-temperature constraint for the exhumation close to the surface in Eocene time when the continental red beds were deposited on the granitoids.

The results of the sensitivity tests are presented using sample H-33 as example, because this sample is well constrained by 6 AHe ages and 5 ZHe ages (TABLE 3.1). The modeled thermal histories performed by the above outlined ways in treating AHe data (cases I to IV), for each of the two scenarios *A* and *B*, are actually rather similar with strong overlap between the cooling paths (FIGURE 3.10). Interestingly, the time-temperature constraint that forces the cooling to surface temperature in Eocene (scenario *B*) hardly causes any detectable difference relative to the results of *"unsupervised" modeling* (scenario *A*). The first row in FIGURE 3.10; *case I* shows modeling results based on averaged AHe data. In case II the oldest single grain AHe age is used which is close to or even older than the AFT age. Thus modeling based on the oldest AHe ages results in low degree of fit and very steep cooling gradients. It is well known that AHe ages are primarily biased towards old ages (Fitzgerald et al., 2006). Using the youngest single-grain AHe data (case III in FIGURE 3.10) the modeling gave a high degree of well-fitted t-T-paths, but the age of the low temperature cooling is slightly younger compared to all the other methods. The modeled thermal paths using the youngest AHe datum are characterized by remarkable sharp turns. Selecting exclusively the youngest age and considering it as the most meaningful for the thermal modeling, however, seems to force the data in an exaggerative manner towards young and pronounced cooling events. Theoretically the thermal modeling with consideration of all individually single-grain AHe data should yield the most reliable results (case IV). However, such modeling often failed or resulted in comparatively bad fit. The reason for the high degree of misfits is that multi-grain aliquots contain too many parameters to be fitted. A single thermal path can not fulfill all optimizing criteria and, thus, the overall performance of this modeling procedure is typically low. We conclude that the modeling based on the average AHe data leads to most robust results. Therefore, we used this modeling procedure (case I, see equation above) for the interpretation of the Nam Co data.

3.6.2.3 Exhumation history of the Bangoin batholith complex and the age of the planation process

Six robust cooling paths modeled on samples from different parts of the Bangoin complex are illustrated in FIGURE 3.11. The thermal histories deliver well-constrained information from the temperature range between 40 and 125 °C, where the AFT and AHe systems are the most sensitive thermochronometers. The high temperature range (above ca. 125 °C) is properly constrained in samples H-19 and H-20 only, where zircon (U-Th)/He ages are available. For the other samples modeling is based solely on apatite measurements which do not provide information on temperatures above 125 °C. Furthermore, results give only weak hints in the temperature range below ca. 40 °C, where annealing of fission tracks and He diffusion are very slow processes.

The modeled thermal histories have basically similar characters; the studied samples experienced

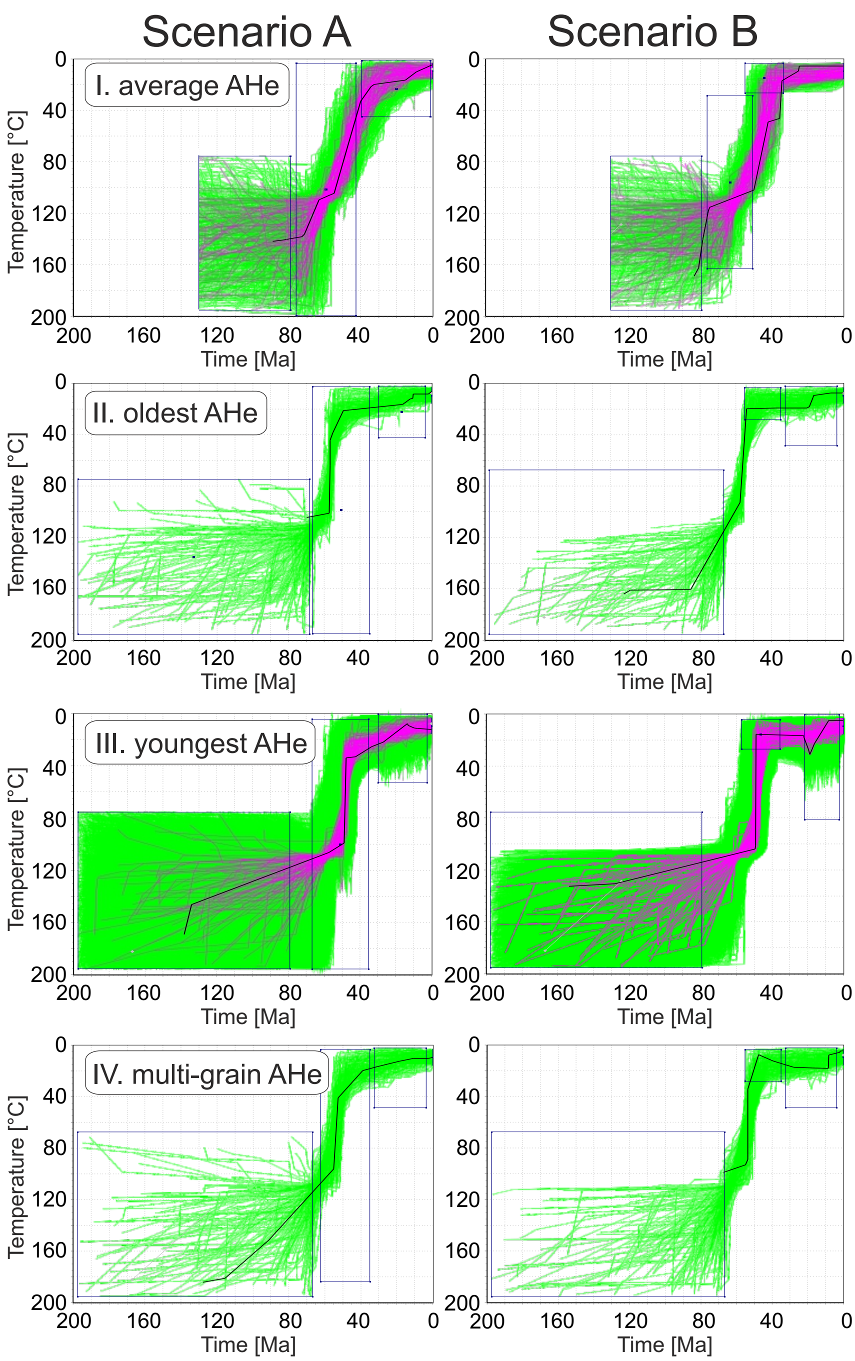

Figure 3.10: Time-temperature plots showing the raw results of the modeling series performed on sample H-33 in order to estimate the sensitivity on the input data. The modeling was performed by software HeFTy (Ketcham, 2005). The green lines represent all the acceptable time-temperature histories while magenta lines represent well constrained t-T histories with good fit to the analytical results. The left column contains the results of practically unsupervised modeling runs (no any constraints were considered between the emplacement of the intrusions and present surface temperature). The right column includes an invariable t-T field at around 45 Ma, forcing the model to reach the surface in Eocene time. See explanation in text.

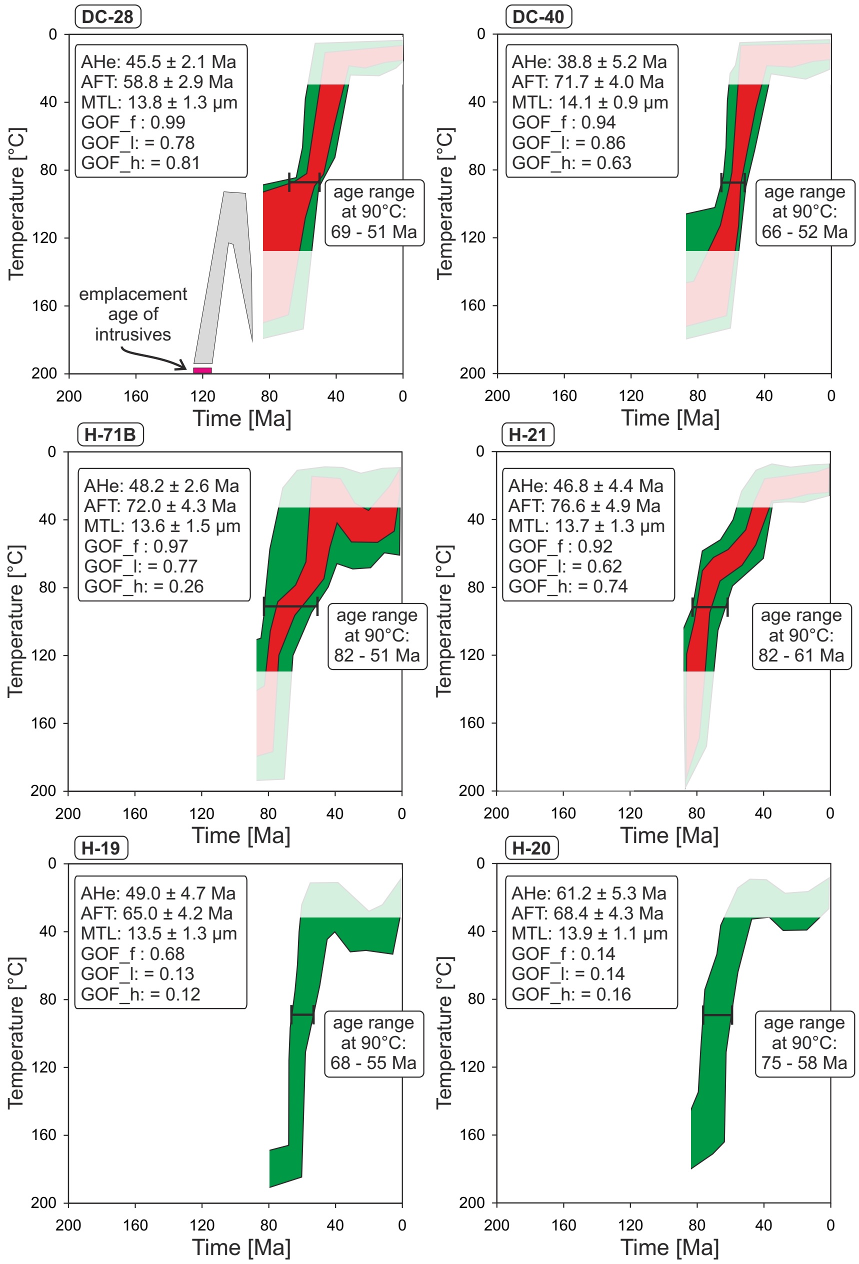

Figure 3.11: Modeled thermal histories of six samples from the Nam Co area. The green and red fields represent the smoothed envelopes of time-temperature histories with acceptable and good fit, respectively. Pale color marks the temperature ranges, where the modeling is less sensitive. GOF_f, GOF_l and GOF_h: goodness of fit of the fission track age, track length and AHe data, respectively. Samples DC-28, DC-40 and H-71B represent Early Cretaceous granitoids from the northeastern block, while samples H-19 to H-21 represent Late Cretaceous granitoids of the southwestern block. The selected samples cover nearly the entire Bangoin complex: DC-40 derives from the SE and DC-28 from NW of the Nam Co area and the maximum distance between sample sites exceeds 120 km. The gray band in DC-28 represents the inferred Cretaceous thermal history for the intrusives of the northeastern block. Another four modeled thermal histories from the NW part of the study area yield very similar cooling histories (see samples H-23, H-24, H-29 and DC-31 in FIGURE 2A.2.

rapid cooling from ca. 125 down to ca. 40 °C in the time interval from ca. 70 to ca. 50 Ma. The cooling trends detected in the different parts of the Bangoin batholith complex are very similar the cooling history of the northwestern part of the study area constrained by our earlier work (Hetzel et al., 2011, CHAPTER 2A). The onset of the period of cooling can be determined by the age range at which the all modeled acceptable cooling paths passes the 90 °C temperature (FIGURE 3.11). We have chosen this temperature threshold empirically because the modeled thermal paths indicate obviously the beginning of the major cooling phase in this temperature. This age range provides an interval for the onset of the well-constrained cooling period was between the latest Cretaceous in Campanian and Late Paleocene. The cooling rates vary between 5 and 15 °C/Ma. In the Early Cretaceous intrusions of the northeastern block the primary, post-emplacement cooling took place before the thermal reset in Late Cretaceous, thus ZHe, AFT and AHe thermochronometers can not refer the pre- 85 Ma history. A suggested Cretaceous thermal path is indicated on the plot for sample DC-28 (FIGURE 3.11). In the Late Cretaceous intrusion of the southwestern block the cooling was monotonous since the emplacement of 85 Ma (samples H-19 to H-21 in FIGURE 3.11).

Although the thermochronometers are only faintly sensitive below 40 °C, the cessation of the period of rapid cooling is well constrained to Early to Middle Eocene, because (I) onlapping red beds on the Bangoin complex are of Eocene age (e. g. Xu and Lee, 1984; Qu et al., 2003), and (II) unsupervised thermal modeling (see above) yields thermal histories that indicate cooling to surface temperature at around 50 Ma, too. The modeled thermal histories yield insignificant burial temperature for the post-Eocene time. This is supported by the style of grain contacts observed in thin sections of the Eocene sandstones indicating minor compression and, thus, only shallow burial. Sample H-71B, however, shows a weak, but detectable post-Eocene thermal overprint FIGURE 3.11. Because this is the only exception, it seems unlikely that this part of the Bangoin complex was buried by the continental red bed sequences much deeper than the other areas. The sample was collected along the western normal faults of the N-S depression at Bam Co (FIGURE 3.4 and FIGURE 3.6). This extensional feature reflects one of the youngest and most significant tectonic processes affecting the Tibetan Plateau (Yin and Harrison, 2000). Hydrothermal fluids may have ascended along the normal faults and caused local perturbations of the isotherms. It is plausible to assume that such process is detected by the low-temperature thermochronometers for sample H-71B. Active hot springs are quite common in Tibet and -e. g. along the Nyainqentanghla faults hot springs- indicate thermal anomalies situated at relatively shallow depth. The inferred cooling history of the Nam Co area results from the integrated effect of (I) post-emplacement dispersion of magmatic heat after the Late Cretaceous intrusions by conduction and (II) exhumation to the surface.

The post-magmatic cooling is restricted to a few million years after plutonic emplacement. Thus cooling of the intrusives can not be responsible for the detected period of rapid cooling and to near-surface temperatures around 50 Ma. Instead, exhumation is necessary to explain the observed data. The average AHe ages cluster around 55 Ma, meaning that the presently exposed sample sites were still below the surface at this time, somewhere in the partial retention zone of the apatite (U-Th)/He thermochronometer.

The waning stage and final cessation of the exhumation was followed by a planation period producing the flat topography of the peneplains, close to the erosional base. The position of the Lhasa terrane at tropical to subtropical latitudes in Eocene time (Lippert et al., 2011), and further the abundance of ferricrust fragments found in the Eocene sequence suggest a tropical probably wet climate that triggered rapid weathering and erosion of the granitoids. The age of the planation is actually bracketed by the period of rapid exhumation on one side (70 to 50 Ma), and cessation of exhumation and the onlap of the Eocene sequence on the already established peneplains on the other side (50 to 40 Ma). Therefore, planation should took place between ca. 55 and 45 Ma.

3.6.3 Post-Jurassic evolution of the Nam Co area

The following post-Jurassic evolution of the Nam Co area is based on

(I) the available geological maps,

(II) formerly published geochronological data,

(III) the new geochronological and thermochronological results presented herein, and

(IV) our own field observations.

We present the major stages of the evolution in five time slices from Early Cretaceous to Present (FIGURE 3.12). The geology of the peneplains and the adjacent fault zone is slightly different NW and SE from Bangoin, thus the illustration is separated in two idealized cross sections (*A'* and *B'* in FIGURE 3.4 and FIGURE 3.12). Further we have to distinguish the northeastern and southwestern blocks (see above), because they were separated and experienced different evolution before Late Cenozioc fault activity (separated in SW and NE blocks in the Eocene and older scenarios in FIGURE 3.12).

3.6.3.1 Early Cretaceous, ca. 120 Ma

The northeastern block was intruded by different granitoids of the Bangoin complex (Harris et al., 1990) and the host rocks of the plutons (Paleozoic and Jurassic sequences) experienced contact metamorphism. The plutons are crosscutted by several trachyandesitic to rhyolitic dikes, suggesting that the area was partly covered by a stratovolcanic complex. In the southeastern part of the study area (east of Nam Co) even thick sequences of Lower Cretaceous ignimbrite layers have been preserved. In the southwestern block marine, partly carbonatic sedimentation took place (Zhang et al., 2004) at that time. One ignimbrite sample yields ca. 130 Ma old U-Pb age TABLE 3.1, thus the deposition of pyroclastic material reached also this region (FIGURE 3.12E).

3.6.3.2 Late Cretaceous, ca. 85 Ma

A siliciclastic sequence was deposited on the eroded surface of the northeastern block (Takena Fm.; Leeder et al., 1988). Its areal extent in Late Cretaceous time is not known, but at least the southern margin of the Bangoin batholith complex was covered. The detrital components are mainly derived from (meta-)sedimentary rocks, but Cretaceous magmatitic detritus was also detected (Leier et al., 2007b). This indicates that between ca. 120 and ca. 85 Ma the volcanic/volcanoclastic edifice was removed by erosion, as well as parts of the host rocks and, probably from the Bangoin batholith complex itself. At that time the level of the later peneplain was still deeply buried below the closure temperature isotherm of the zircon (U-Th)/He thermochronometer. In the southwestern block the emplacement of the Late Cretaceous granitoid intrusion(s) took place. This magmatic period had a significant thermal effect; heat flow was high and led to reset of the low-T thermochronometers, and partial reset of Ar and Sr geochronometers in both blocks (FIGURE 3.12D).

3.6.3.3 Paleocene, ca. 60 Ma

Rapid Paleogene exhumation characterizes the northeastern block. The thermochronological data indicates high erosion rate, but at that time the level of the later peneplain was still in the depth of the partial annealing zone of apatite fission track thermochronometer (60-100 °C). Rapid exhumation and erosion usually generate a rugged and mountainous relief. The perturbed isotherms caused by the high heat flow of the Late Cretaceous magmatism are probably relaxed at this time. Similarly, thermal modeling indicates a cooling period for the southwestern block in Paleocene time. The total erosion, however, was less compared to the adjacent northeastern block, because a part of the Lower Cretaceous volcanoclastic sequence has been preserved. Deposition of a Paleocene ignimbrite layer found in the southwestern block also indicates less erosion, thus we conclude that Paleocene relief was less rugged than in the northeastern block (FIGURE 3.12C).

3.6.3.4 Middle Eocene, ca. 45 Ma

Significant exhumation removed approximately 3 - 6 km of rock since the Early Paleocene, but the rate of exhumation was slowing down for the Eocene. The waning stages of exhumation were accompanied by the onset of planation. The peneplains were well developed already by Middle Eocene time. Continental red beds were deposited on the northern part of the northeastern block. It is possible that the entire peneplain area was covered by this siliciclastic sequence. The latter scenario would have contributed to the good preservation of the peneplains. In the southwestern block a peneplain is carved in the Late Cretaceous granite (FIGURE 3.12B).

3.6.3.5 Post-Eocene development, present situation

The tectonic pattern of the fault zone separating the two blocks in 1:250,000 scale geological maps is a post-Eocene compressional feature. Not any constraints are available for a more precise age of the displacements, but the locally steep morphology and the elongated scarps indicate a rather young age. Along this reverse fault zone the southwestern block was thrusted on the northeastern block, which contains the well developed, extended peneplains. Thus, at present the peneplains are not the highest elements of the region, but the narrow crest, which formed the hanging wall above the reverse fault zone. South of the thrust zone the peneplains are less preserved (FIGURE 3.12A).

The Eocene red beds experienced significant erosion and the sequence is preserved in the northern parts of the study area only, especially in the *"Pyramid"*. E-W extension generates local grabens (such as Bam Co) between the uplifted peneplain areas. These grabens strike sub-parallel to the profiles, thus their presentation via normal faults in FIGURE 3.12 is rather symbolic.

3.6.4 The base level for the planation process in central Tibet

As outlined above the thermochronological data and the modeled cooling histories only indirectly date the age of planation process. The period of rapid cooling of the level of the present peneplain surfaces is well constrained for the time span of Late Cretaceous (from Campanian) until Early Eocene. The cooling was associated with significant amount of exhumation. In this time interval the Nam Co area developed a rugged mountainous relief. The intense weathering under tropical climate was contributing to the development of the flat landscape after the cessation of the rapid exhumation. The planation process is bracketed between the end of rapid exhumation in earliest Eocene and onlapping Eocene sediments.

Similar cooling data and exhumation patterns were described by Rohrmann et al. (2012) in a several hundreds of km wide area in central Tibet. Thus, a huge area was affected by the Late Cretaceous to Paleocene erosion and this process necessarily resulted in a big amount of sediment. The geographic and geodynamic position of the final depositional site of sediment generated and removed from the cover of the later peneplains is the key for estimating the elevation at which the planation process occurred. For the deposition of this huge sediment mass we see two possibilities: (I) in the south and east (ocean) or (II) in the central Asian intracontinental basins located predominantly to the north.

If the sediment was transported to the south or east and deposited in an oceanic foreland basin, then the relevant base level was the global sea level and the planation took place at low elevation (Hetzel et al., 2011). If the sediment was transported towards north, then the material derived

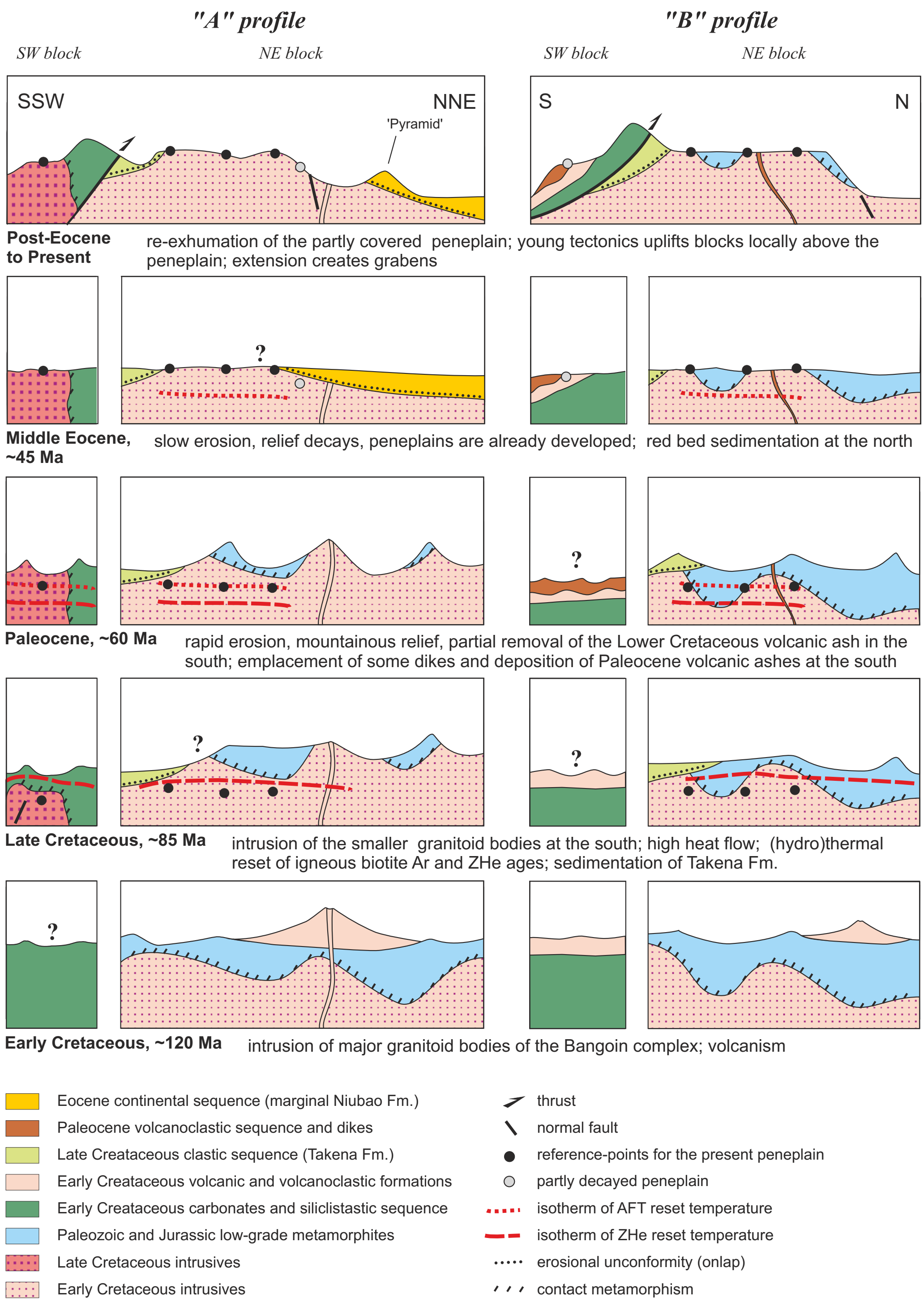

Figure 3.12: Schematic profiles to illustrate the major steps of Early Cretaceous to Recent development of Nam Co area. The traces of the profiles A' and B' are shown in FIGURE 3.4. See text for explanation and discussion.

from the northern Lhasa terrane may have contributed to the filling of the Lunpola, Hoh Xil and Tarim basins (Yang et al., 1975; Yi et al., 2008). Internal drainage of such a huge system at high elevation would require long-lasting effective barriers over several hundreds to thousand of kilometers on all sides of the intensely eroded and finally planated region. This is an unlikely scenario especially if we consider the results of facies and paleontological studies from the Tarim basin: this large basin system was close to or connected to the global sea level in Paleocene to early Eocene time (Burtman, 2000; Wang et al., 2008; Bosboom et al., 2011). Thus both the northern and the southern provenance scenarios suggest that the related base level was at low elevation at the time of the decay of the Late Cretaceous relief, and the uplift of the Tibetan Plateau postdates the planation process.

For a further evaluation of the two scenarios we can use provenance indicators from the Eocene sediments of the Himalayan foreland basin and the northern Tibetan Lunpola and Hoh Xil basins. The Bangoin complex of the Nam Co area and the continuation of this belt in central Tibet are dominated by the ca. 120 Ma old igneous suite that should have delivered zircon grains with a very characteristic U-Pb age signature during erosion of the northern Lhasa terrane. Both, the southern foreland as well as the northern intracontinental basins contain zircon crystals with ca. 120 Ma ages in early Paleogene time (Dai et al., 2012; Najman et al., 2008). This age component is crucial although present only in subordinate proportions in both dispersal systems. It indicates that the Lhasa terrane was dewatered to both directions in Early Paleocene and Early Eocene times, and this is interpreted to reflect a phase of change in the paleotopography. For the Late Cretaceous Leier et al. (2007b) sketched a drainage system that dewatered the southern to central part of the present Tibetan Plateau towards north. This situation however, has changed by Early Eocene, when the detritus of the Early Cretaceous magmatic suite is appearing in the Bengal basin (Najman et al., 2008). The southward draining major river systems thus already reached the igneous belt of the northern Lhasa terrane, which were mainly planated already at that time in the Nam Co area. This indicates that the removal of the eroded sediment was performed by rivers connect to the global base level, i. e. at low elevation. The uplift of the assumed *"proto-Tibetan Plateau"* south of Hoh Xil basin (Dai et al., 2012) occurred significantly later, because the paleoaltimetric constraints of Rowley and Currie (2006); Polissar et al. (2009) were determined on Late Eocene and Oligocene strata.

3.7 Conclusions

The flat-top mountains in Central Tibet, north of Nam Co are surrounded by more rugged areas including locally steep slopes, where mainly fluvial erosion has generated the recent landscape. The pronounced contrast between these two landscapes allows for distinguishing peneplains (i. e. elevated flat areas) from the areas dominated by modern erosion. Cosmogenic isotope studies have proven extremely slow erosion rates of the peneplains at least for the last ca. one million years. These peneplains constitute slightly modified palesosurfaces and, thus, serve as archives of the early development of the Central Tibetan region.

Geochronological-thermochronological methods are used in order to constrain the timing of evolution of these paleosurfaces. New zircon U-Pb ages of the Bangoin batholith complex indicate two major pulses of granitoid emplacement at around 118 Ma and 85 Ma. Argon and strontium-based geochronometers widely scatter and are typically younger than the U-Pb emplacement ages due to the (hydro-)thermal effect of the intrusions and later Paleocene volcanic activity. Zircon (U-Th)/He cooling ages cluster around 75 Ma and are interpreted to result from Late Cretaceous ($\sim$ 85 Ma) igneous activity leading to overall reset in the entire study area. Apatite fission track and (U-Th)/He ages also show rather tight clusters around 60 Ma and 50 Ma, respectively. The confined track length data are typically uniform, and the mean track length is around 13.6 μm.

Modeling of the thermal evolution was performed under different conditions, including a detailed sensitivity test. The high number of thermochronological data allows for drawing robust conclusions on the exhumation history of the present-day peneplains. Cooling of the basement took place in latest Cretaceous to Early Eocene. The intense vertical movement practically precludes existence or formation of flat landscape at this time. Thus, the dying of the cooling period in Late Paleocene to Early Eocene time sets a bench-mark for the onset of the planation process. The other bracketing constraint is the onlap of Eocene continental deposits onto already planated surfaces, which is still preserved at the northern margin of the Bangoin batholith complex. Consequently, planation had to happen in Early Eocene time, i. e. between ca. 55 and 45 Ma. The burial and exhumation history as well as surface development of different blocks of the Nam Co area can be reconstructed in five time slices (FIGURE 3.12).

The connection of the northern Lhasa terrane to the ocean is documented by the presence of zircon grains having a characteristic Early Cretaceous U-Pb age signature in Eocene strata of the Bengal Basin that probably originates from the Bangoin intrusive complex. When these zircons appeared in the ocean basin exhumation of the Nam Co area has already slowed down or even ceased. In conclusion, Nam Co area has formed a flat landscape at low elevation in Early Eocene time, shortly before or around the time of India-Asia collision.

4 Assessment of single-grain age signature from sediments

This chapter is similar to the manuscript entitled: "Assessment of single-grain age signature from sediments and their potential source rocks: provenance of post-Jurassic sediments from northern Lhasa Terrane, Tibetan Plateau" that will be soon submitted to an international journal.
Authored by: V. L. Haider, I. Dunkl, H. von Eynatten, L. Ding, D. Frei

4.1 Abstract

The center of the Lhasa terrane, southern Tibet, is predominated by Cretaceous to Cenozoic siliciclastic formations and some exposed granitoids in the Bangoin area. This study is intended to improve understanding the provenance of the Cretaceous to Tertiary strata of the central Lhasa terrane. Therefore, twenty four sandstones and two claystones were sampled and detrital zircon U-Pb analysis, apatite fission track thermochronology (AFT), and semi-quantitative heavy mineral analysis were performed. Basement zircon U-Pb ages from the Tibetan Plateau were obtained. Additionally, robust statistical tests (t-Test and Kolmogorov-Smirnoff test) were applied to the newly gained zircon U-Pb-data in order to explain the relation between each sedimentary sequences. This available referenced zircon U-Pb data set is used as a potential detrital data set to compare the detrital zircon age distribution detected in the sedimentary formations. The newly gained data contribute to the reconstruction of the origin and dispersal of the sedimentary rocks as well as the paleogeographic situation during their formation.

The detrital zircon U-Pb age spectrum of the Jurassic sandstone yields various age clusters between 500 and 1500 Ma with the most pronounced age group around 900 Ma. The heavy mineral assemblages of the two Lower Cretaceous sandstones are rather similar, but their U-Pb age spectra are highly different.

The data set of all samples younger than Lower Cretaceous were summarized, due to their similarity of the heavy mineral composition (high amount of euhedral zircon crystals) and the detrital zircon U-Pb age spectra. Abundant granitoid-derived lithic fragments are observed which implies that a significant part of the sediments has been transported over short distances and locally derived from the granitoid complexes of the northern Lhasa terrane. The bundled detrital zircon age spectrum shows one dominant cluster in Cretaceous time and one pre-Cretaceous age cluster. About 70% of all Upper Cretaceous to Eocene detrital zircons fall into the distinct age cluster < 160 Ma, hence must have derived mostly from the granitoids of the Lhasa terrane. In samples from the Eocene, a well defined 51 Ma age component could be detected which is most likely derived from the Linzizong volcanics exposed in the south of the study area. The summarized remaining age spectra (> 160 Ma) yield isolated age components between ~ 340 and ~ 1800 Ma. Whilst the pronounced Triassic age component (237 ± 32 Ma) is interpreted as sediments sourced from the northern terranes as Kunlun, Songpan-Gaze and Qiangtang, the possible source of the Carboniferous age component (342 ± 28 Ma) is the Kunlun terrane. The Cambrian age component (515 ± 75 Ma) and the 911 ± 110 Ma age cluster are most likely derived from the Lhasa terrane. The oldest age groups (1220 ± 90 Ma and 1790 ± 135 Ma) can be sourced either from the Lhasa terrane or from the Songpan-Ganze and South Qiangtang terranes. Additionally the age cluster < 160 Ma was statistically analyzed and no differences were found between Upper Cretaceous and Eocene samples.

The AFT age data from onlapping sediments onto the Bangoin granitoid complex emphasize the assumption of distal sources of the Upper Cretaceous to Eocene sediments. Compared to the AFT cooling age spectrum in the granitoids, the age dataset contains a high amount of older single grain AFT ages.

4.2 Introduction

The Tibetan Plateau was formed by the amalgamation of several terranes, wedged and uplifted between the southern margin of Asia and the northern margin of the northward drifting Indian plate (Burg et al., 1983; Allegre et al., 1984; Dewey et al., 1988; Yin and Harrison, 2000). Roughly E-W trending suture zones separating the terranes can be found across the plateau. Kunlun terrane is the northernmost continental terrane accreted directly to Asia and is followed southward by the Songpan - Ganze and Qiangtang terranes. Lhasa terrane, between Qiangtang terrane in the north and the Himalayas in the south (FIGURE 4.1A), is interpreted as the southern continental margin of Asia during the northward subduction of the Neotethyan Ocean in the Cretaceous (Murphy et al., 1997; Yin and Harrison, 2000).

The information stored in pre-, syn-, and postcollisional sedimentary strata plays a prominent role in reconstructing the development of the Tibetan Plateau. Sedimentary facies, age, composition and specific provenance indicators are integrated in the current image on the plateau formation through time (e. g. Leeder et al., 1988; Leier et al., 2007a,b,c; Dai et al., 2012, and references therein). Nevertheless, many open questions exist regarding the exhumation of the different terranes and structural blocks, their sediment yield and drainage patterns, as well as basin subsidence and inversion, which are discussed intensely (e. g. DeCelles et al., 2001; Hetzel et al., 2011; Gehrels et al., 2011; Rohrmann et al., 2012; Wang et al., 2014)

In this study we intend to improve understanding of the provenance of Cretaceous to Cenozoic siliciclastic formations of Lhasa terrane in central Tibet. Results are based on heavy mineral analysis, detrital zircon U-Pb geochronology, and detrital apatite fission track thermochronology performed on several stratigraphic levels of the non-metamorphosed basin fill deposited in the surroundings of Nam Co (FIGURE 4.1C). These new data allow for reconstructing the origin and dispersal of the sedimentary rocks as well as the paleogeographic situation during their formation. Beyond this regional provenance study we address some pestering methodological questions regarding statistical treatment of zircon U-Pb data. Multiple sampling from the same stratigraphic horizons along with high number of single-grain zircon U-Pb ages ($n = 2026$) allow for detailed comparison and robust statistical tests in order to strictly elucidate the relations between sedimentary sequences. Moreover, the available reference zircon U-Pb data set from the adjacent basement area offers a unique opportunity to process the numerous zircon U-Pb ages from the basement like a detrital data set and to perform comparison with the distributions detected in the sedimentary formations.

4.3 Geologic Framework

Along the Bangong Suture, the Lhasa Terrane came into collision with the Qiangtang Terrane during Late Jurassic time around 150 - 140 Ma prior to the India - Asia collision (Chen et al., 2002). The Amdo basement near the Bangong suture zone substitute metamorphic formations of Cambrian and older protolites, predominantly composed of strongly foliated orthogneisses with Jurassic metamorphic ages of around 160 Ma (Guynn et al., 2006). Several igneous province dominate the Lhasa terrane that represent intense magmatic activity between 170 and 20 Ma (Xu et al., 1985; Debon et al., 1986; Kapp et al., 2005a; Volkmer et al., 2007). The over 2,500 km long calc-alkaline Gangdese belt, a large I-type composite batholith next to the Indus-Yarlung suture forms the southern province of the Lhasa Terrane and comprises dominantly two intrusive stages largely Late Cretaceous and Paleogene in age (Debon et al., 1986; Copeland et al., 1987). The Linzizong potassic volcanism erupted across the southern Lhasa Terrane from Eocene to Oligocene in the Gangdese belt (He et al., 2007; Mo et al., 2008; Lee et al., 2009) has been related to northward subduction of the Neotethyan oceanic slab beneath southern Asia (Lee et al., 2009). The central plutonic belt intruded between 130 and 110 Ma and spreads over the remaining Lhasa Terrane limited at the north by the Bangong-Nujiang suture (Xu et al., 1985; Murphy et al., 1997; Kapp et al., 2005a; Leier et al., 2007b).
Our study area is located around the Tibetan holy lake Nam Co in the central part of the Lhasa Terrane. The dominant geological unit north of the lake is the Bangoin batholith complex with an age ranging between 130 and 100 Ma (Haider et al., 2013). The Bangoin batholith complex intruded mainly into a folded, low-grade Jurassic pelitic-arenitic sequence, but contact metamorphic zones were formed also in some places along the host Lower Cretaceous limestones (Yin et al., 1988; Leier et al., 2007a). At the northern part the Bangoin batholith is covered by

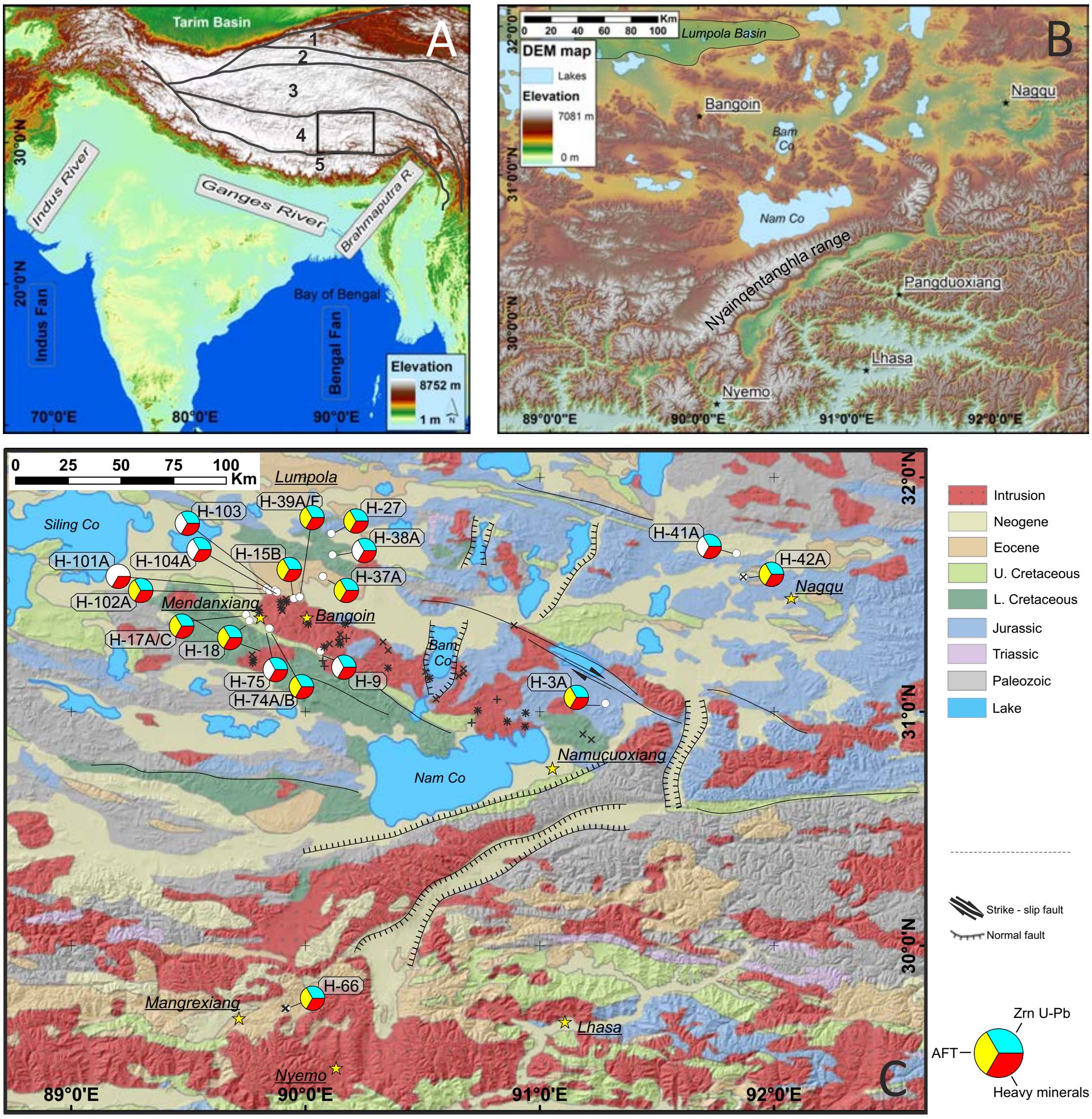

Figure 4.1: (A) Digital elevation map including the position of the study area in the Tibetan Plateau with outlined terranes (1 = Kunlun terrane, 2 = Songpan - Ganze terrane, 3 = Qiangtang terrane, 4 = Lhasa terrane) and the Himalaya (5). (B) Detailed DEM image of the study area with the lake Nam Co in the centre. (C) Geological map (Pan et al., 2004) and the position of the samples coded with the applied analytical methods. The symbol + marks the basement sample sites with available U-Pb data, x indicates AFT data, and * denotes Zrn U-Pb and AFT data (published in Hetzel et al., 2011; Haider et al., 2013).

Eocene sediments, while in the southern part pre- and post-intrusion Cretaceous sediments are present.

4.3.1 Stratigraphy

Paleozoic sedimentary strata in the Lhasa terrane consist predominantly of Carboniferous sandstone, metasandstone, shale and phylite. Ordovician, Silurian and Permian limestone appears occasionally (Leeder et al., 1988; Yin et al., 1988; Leier et al., 2007c). Triassic strata in the Lhasa terrane is rare and most prevalent along the southern margin of the terrane (Leeder et al., 1988; Leier et al., 2007c). The Triassic rocks include inter-bedded limestone and basaltic volcanic units (Leeder et al., 1988).

4.3.1.1 Jurassic strata

The Jurassic stata in the northern part of the Lhasa terrane differ from the southern part of the terrane (Leeder et al., 1988; Yin et al., 1988; Leier et al., 2007c, FIGURE 4.2). Mostly, the Jurassic gray, pelitic, and partly sandy sequences experienced weak metamorphism and folding. They are still scarcely investigated and described (Yin et al., 1988).

North: The Jurassic strata consist primarily of deepwater sandstone and shale, and in many places are associated with ophiolitic assemblages (Leeder et al., 1988; Yin et al., 1988; Leier et al., 2007c). The described *Qusongbo Formation* consists of terrestrial sandstone and conglomerate (Yin et al., 1988).

South: The Jurassic deposits are predominantly composed of marine limestone and mudstone (Yin et al., 1988). The described *Quesangwenquan Formation* (sandstone, volcanic conglomerate and shelly limestone) in the southern part imply deposition in an unstable shallow-water environment and is the oldest non-metamorphosed formation of the area (Yin et al., 1988, FIGURE 4.2). The *Duodigou Formation* deposited Late Jurassic and consists of argillaceous limestone interbedded with shale, shelly limestone, and fine sandstone (Yin et al., 1988).

4.3.1.2 Lower Cretaceous strata

The sediments of the Lower Cretaceous time and younger are better studied, (e. g. Yin et al., 1988; Leeder et al., 1988; Zhang et al., 2004; Leier et al., 2007a,c). Yin et al. (1988) gave a detailed facies description and the detrital U-Pb age spectra were also documented (Leier et al., 2007a). Lower Cretaceous strata consist of clastic mudstone, sandstone and local conglomerate units (Yin et al., 1988; Leier et al., 2007a)

North: The *Duba Formation* consists of terrestrial beds with marine intercalations and is overlaid by the *Langshan Formation*, a Cretaceous limestone composed of neritic carbonates (Ma Xiaoda 1981, Wang Naiwen 1984 cited in Yin et al., 1988).

South: Siltstones with thin-bedded limestones are characteristic for the *Linbuzong Formation*. The *Chumulong Formation* composes mainly of terrestrial quartzose sandstone, conglomerate, some irregularly distributed andesites, and andesitic ignimbrites (Yin et al., 1988). In the south, the *Penbo Member* starts its deposition in the middle of Early Cretaceous. This Member consists of basal limestone and is the older part of the *Takena Formation*, a marginal-marine strata, (Yin et al., 1988; Leier et al., 2007a).

4.3.1.3 Upper Cretaceous strata

The younger part of the *Takena Formation* is the *Lhunzhub Member* and consists of fluvial red beds (Yin et al., 1988; Leier et al., 2007a). The occurrence of fossils of these shallow marine limestone beds narrows the deposition down to Aptian and late Albian time (Leier et al., 2007a). Biostratigraphic evidence indicates the deposition over a longer duration between Barremian and Cenomanian (Zhang et al., 2004; Leier et al., 2007a).

4.3.1.4 Paleogene strata

In Paleogene only the *Linzizong Formation* is recorded, a Late Cretaceous - Early Tertiary volcanic strata (Yin et al., 1988).

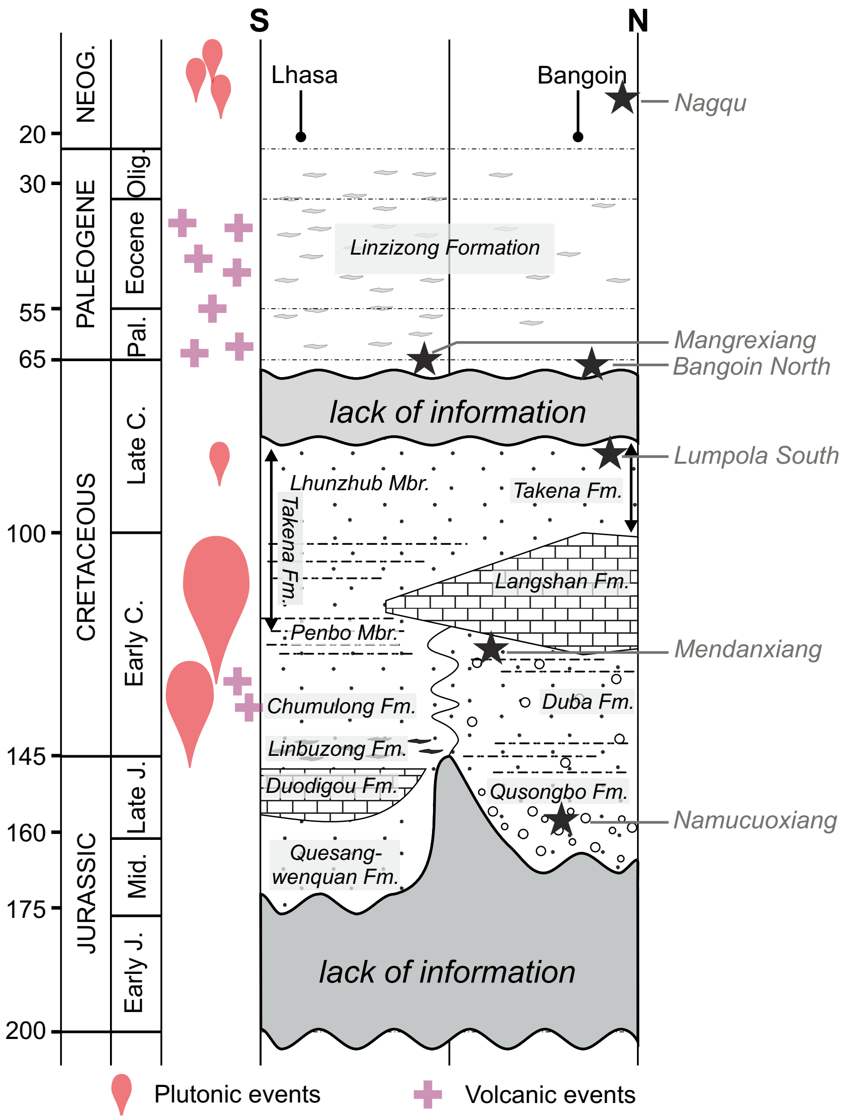

Figure 4.2: Simplified stratigraphy of the study area including the different volcanic and plutonic events of the region (modified after Yin et al., 1988; Leier et al., 2007a,b). Black stars outline schematically the sample positions labeled at the right side of the figure.

4.3.2 U-Pb age pattern of the Tibetan Plateau

Before the evaluation of the obtained zircon U-Pb age distributions we should review briefly the available basement ages of the Tibetan Plateau, because these age patterns form the base for the interpretation of the new detrital age data set.
We collected the available zircon U-Pb ages of igneous rocks from the literature, evaluated, and plot them onto the tectonic map of the Tibetan Plateau (FIGURE 4.3, FIGURE 4.4). The plot gives as a good insight about the U-Pb age distribution onto the Tibetan Plateau and its terranes. While onto the Kunlun terrane mainly Palaeozoic ages were measured, the age distribution become younger towards south. In the Qiangtang terrane the Triassic magmatites are common (Roger et al., 2003; Reid et al., 2005; Dai et al., 2012; Zhai et al., 2012). The youngest, Cenozoic ages components were detected along the Gangdese belt at the southern part of the Lhasa terrane. In the northern - central part of the Lhasa terrane, predominantly Cretaceous ages were measured and it is noticeable that this component is less abundant in the other terranes. The cumulative probability plot of the zircon U-Pb ages of the different terranes revealed unique signatures (FIGURE 4.3).

4.4 Samples and methods

We sampled Jurassic to Miocene sandstones around Nam Co with a special focus on the north-eastern part of the area (FIGURE 4.1C, TABLE 4.1). At the selection of the sample sites we aimed also to study the internal heterogeneity of the formations, thus we took more samples both from the Lower and from the Upper Cretaceous siliciclastic sequences. The sandstones were crushed down to grit with jaw crusher. The fraction smaller than 250 μm were sieved from remaining material and treated by shaking table in order to pre-concentrate the heavy minerals. Accessory minerals were separated from Qtz, Fsp and other low-density lithic fragments with sodium-polytungstate (ρ =2.86 g/cm^3). Ferromagnetic minerals where removed with hand magnet and the other dia- and paramagnetic mineral fractions were separated by Frantz magnet in five steps. The apatite and zircon rich, less magnetic fractions (yield at 1.7 amperes at 10° tilt) used for thermo- and geochronological analysis. Further the Zrn were separated from Ap by

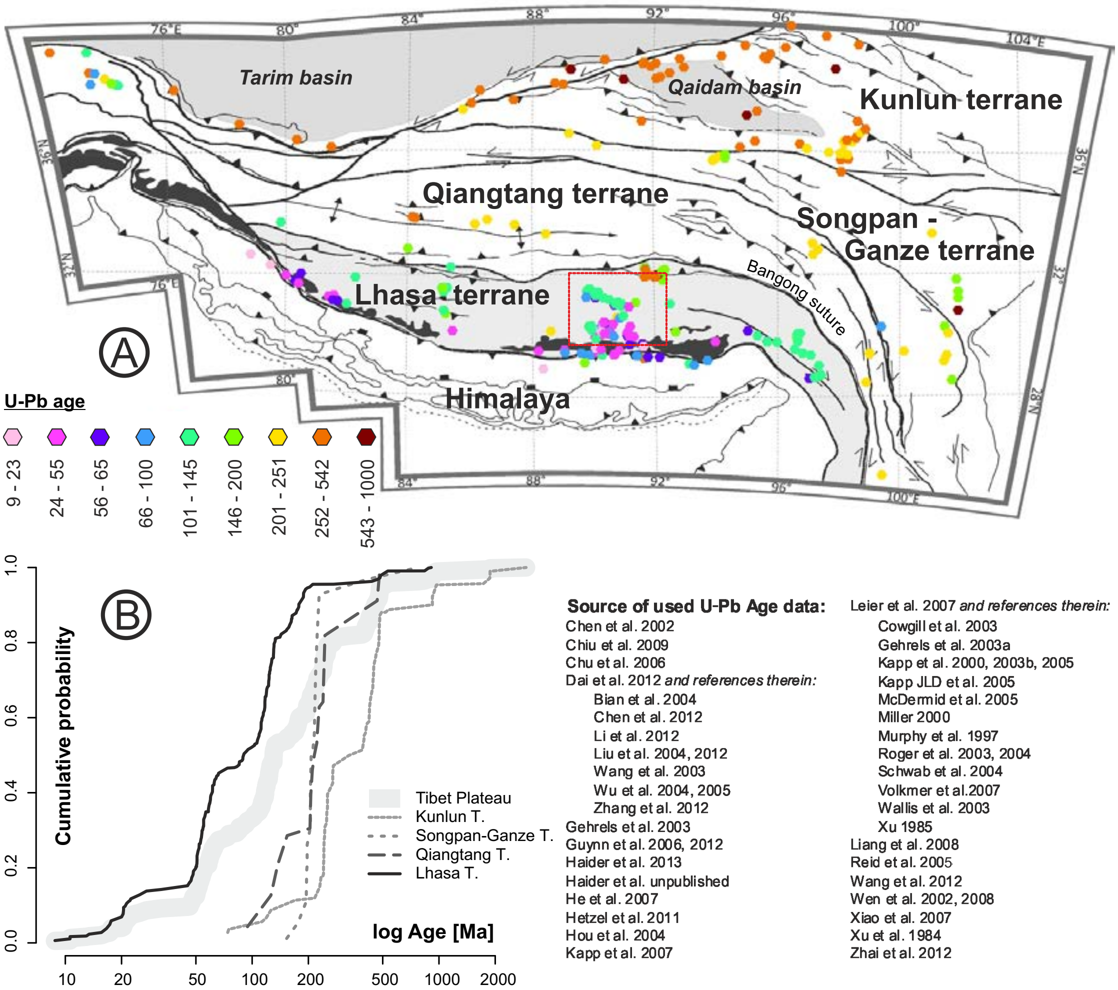

Figure 4.3: (A) Tectonic map of the Tibetan plateau (modified after DeCelles et al., 2002) containing a compilation of already published U-Pb zircon data. The Lhasa terrane is outlined in light gray. The dark gray patterns represent basins. (B) Compilation of 279 basement zircon U-Pb age data from the literature and own data. The cumulative probability curves are grouped by terranes.

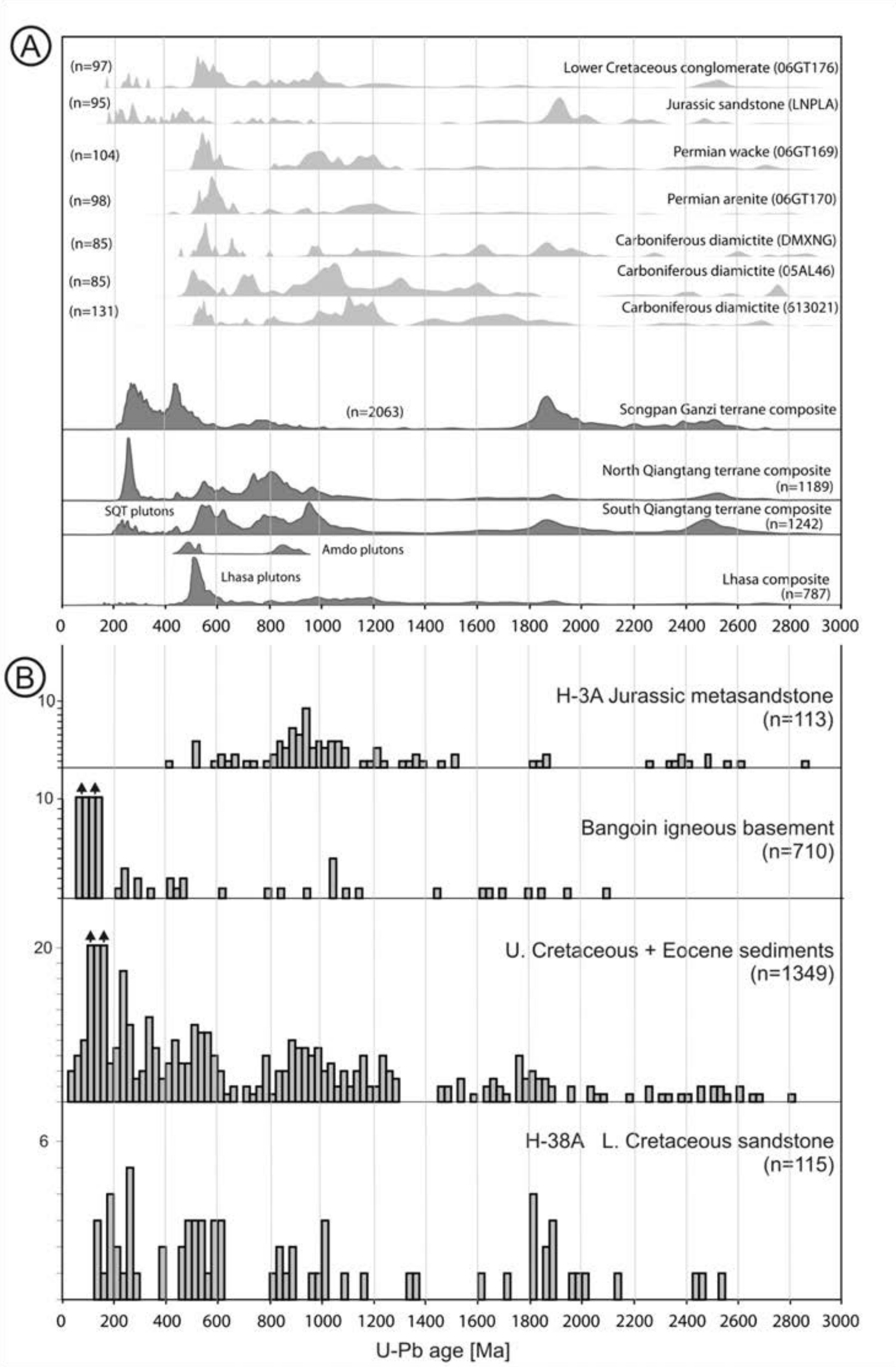

Figure 4.4: (A) Age distributions of potential source units: probability density plots of U-Pb ages from different terranes of the Tibetan Plateau (from the compilation of Gehrels et al., 2011). (B) Binned age spectra of new U-Pb ages from the studied sediments and compiled zircon U-Pb ages of the igneous rocks of Bangoin batholith complex (from Hetzel et al., 2011; Haider et al., 2013). Eocene siliciclastic formations in the Nam Co area and the age components fitted by PopShare algorithm.

diiodomethane (ρ=3.33 g/cm^3).

Table 4.1: Geographic co-ordinates of the sedimentary samples, their stratigraphic age according to the available geological maps and the list of analyses performed on the samples.

U-Pb	AFT	HM	sample number	latitude (°N)	longitude (°E)	elevation (m)	stratigraphy	area	lithology *(ss = sandstone)*
H-3A		x	H-3A	31.0369	91.2804	5030	Jurassic	Namucuoxiang	ss
H-9		x	H-9	31.2587	90.0650	5360	U. Cretaceous	Mendanxiang	ss
		x	H-15A	31.4844	89.9504	4700	Eocene	Bangoin north	ss gray
H-15B		x	H-15B	31.4844	89.9504	4700	Eocene	Bangoin north	ss gray
H-17A	H-17A	x	H-17A	31.4153	89.7464	4620	U. Cretaceous	Mendanxiang	ss red (congl. seq.)
	H-17C	x	H-17C	31.4153	89.7464	4620	U. Cretaceous	Mendanxiang	ss red (congl. seq.)
H-18	H-18	x	H-18	31.3871	89.7607	4680	U. Cretaceous	Mendanxiang	ss red
H-27	H-27	x	H-27	31.7611	90.1111	4770	L. Cretaceous	Lumpola south	ss red
H-37A	H-37A	x	H-37A	31.5790	90.0751	4777	Eocene	Bangoin north	ss brown-red
		x	H-37B	31.5790	90.0751	4777	Eocene	Bangoin north	clay gray
		x	H-37C	31.5790	90.0751	4777	Eocene	Bangoin north	ss gray
H-38A		x	H-38A	31.6704	90.1150	4957	L Cretaceous	Lumpola south	ss red
		x	H-38B	31.6704	90.1150	4957	L Cretaceous	Lumpola south	ss red
H-39A	H-39A	x	H-39A	31.4901	89.9765	4937	Eocene	Bangoin north	ss gray
H-39F		x	H-39F	31.4901	89.9765	4937	Eocene	Bangoin north	ss gray
H-41A		x	H-41A	31.6756	91.8392	4615	Miocene	Nagqu	ss gray
H-42A	H-42A	x	H-42A	31.6756	91.8392	4615	Miocene	Nagqu	ss red (green comp)
H-66	H-66	x	H-66	29.7329	89.9189	4513	Eocene	Mangrexian	ss red
	H-74A	x	H-74A	31.3543	89.8488	4753	U. Cretaceous	Mendanxiang	ss red
H-74B		x	H-74B	31.3543	89.8488	4753	U. Cretaceous	Mendanxiang	ss red
H-75		x	H-75	31.3568	89.8461	4763	U. Cretaceous	Mendanxiang	ss metamorphic
		x	H-101A	31.5275	89.8351	4668	Eocene	Bangoin north	ss red
		x	H-101B	31.5275	89.8351	4668	Eocene	Bangoin north	clay gray (tuff)
H-102A	H-102A	x	H-102A	31.5159	89.8482	4693	Eocene	Bangoin north	ss
H-103		x	H-103	31.5192	89.8707	4731	Eocene	Bangoin north	ss
H-104A		x	H-104A	31.5109	89.8791	4698	Eocene	Bangoin north	ss

4.4.1 Zircon U-Pb geochronology

For the in-situ age analyses 250 zircon crystals were randomly handpicked from about 16 samples. The crystals were fixed in grain mounts by epoxy resin. After polishing procedure (using 9, 3, and 1 μm diamond) and CL imaging the in-situ U-Pb dating was performed at the Geological Survey of Denmark and Greenland (GEUS) in Copenhagen (Denmark) following the method of Gerdes and Zeh (2006); Frei and Gerdes (2009). Drift corrections and data reductions of the raw data were performed by using PepiAGE/UranOS data reduction software (Dunkl et al., 2008). Depending on the detected trend through the measurement session of the ICP-MS, the drift was corrected by liner, logarithmic or 2nd order polynomial regression. No common lead correction was required. ^{206}Pb/^{238}U ratios with a concordance (^{206}Pb/^{238}U vs. ^{207}Pb/^{235}U) between 90 and 105% were used for the geological interpretation; the probability plots were generated by setting up own algorithm with the statistic software package R (R Core Team 2013). The identification of age components were performed by the PopShare software (Dunkl and Székely, 2002).

4.4.2 Apatite fission track geochronology (AFT)

For AFT analysis the external detector method was used (Gleadow, 1981). An apatite enriched concentrate of each sample were embedded in epoxy resin (Araldite 2020), stepwise polished down to 1 μm and etched by 5.5 N HNO_3 solution for 20 sec at 21 °C (Donelick et al., 1999). The grain mounts with the etched spontaneous tracks were covered with freshly cleaved muscovite sheets (Goodfellow™ mica) as external track detectors and irradiated with thermal neutrons in the research reactor of the Technical University of Munich in Garching. Requested neutron fluence was 5*1015 n/cm^2. Corning glass dosimeter (CN-5) was used to monitor the neutron fluence. After irradiation the tracks in the external detectors were revealed by etching in 40% HF for 40 min at 21 °C. Spontaneous and induced fission tracks were counted with 1000x magnification with a Zeiss - Axioskop microscope equipped with computer - controlled stage system (Dumitru, 1993). Only apatite crystals with polished surface oriented parallel to the crystallographic c-axis were counted. Additionally, D_{par} in each counted apatite crystal and track length of around 60 horizontal confined tracks were measured in most of the samples. The AFT ages were calculated using the ζ-age calibration method (Hurford and Green, 1982) with the standards described in (Hurford, 1998). Data processing and plotting were performed with the TRACKKEY software (Dunkl, 2002), while errors were calculated by using classical procedure described in (Green, 1981).

4.4.3 Heavy minerals

Before the magnetic separation, an untreated aliquot was selected from each sample for semi-quantitative heavy mineral analysis. The relative proportions of the most abundant heavy minerals rutile, tourmaline, zircon, apatite, epidote, and garnet were classified in six categories with values from 0 (not present) to 5 (predominant, $>60\%$).

4.5 Results

4.5.1 Framework of characterization and heavy minerals in the samples

All siliclastic samples were studied in thin sections. In the composition of the sandstones the monocrystalline quartz and lithic fragments are dominating, the feldspars have subordinate role. The lithic fragments are mainly low-grade metapelites but some volcanic and granophyric grains are also present (FIGURE 4.5). North of Bangoin in the coarse sand to fine-grained conglomerate members of the Eocene sequence subangular granitoid grains were recognisable. Leier et al. (2007c) performed a detailed study mainly on Jurassic and Lower Cretaceous sediments on the Lhasa terrane, and detected that in our study area the Upper Cretaceous and Eocene strata have similar framework compositions. The intense subaerial tropical weathering is responsible for the decomposition of feldspars and these weathering conditions etched also the surface of apatite grains and generated the iron-oxide crust associated with the sediments.

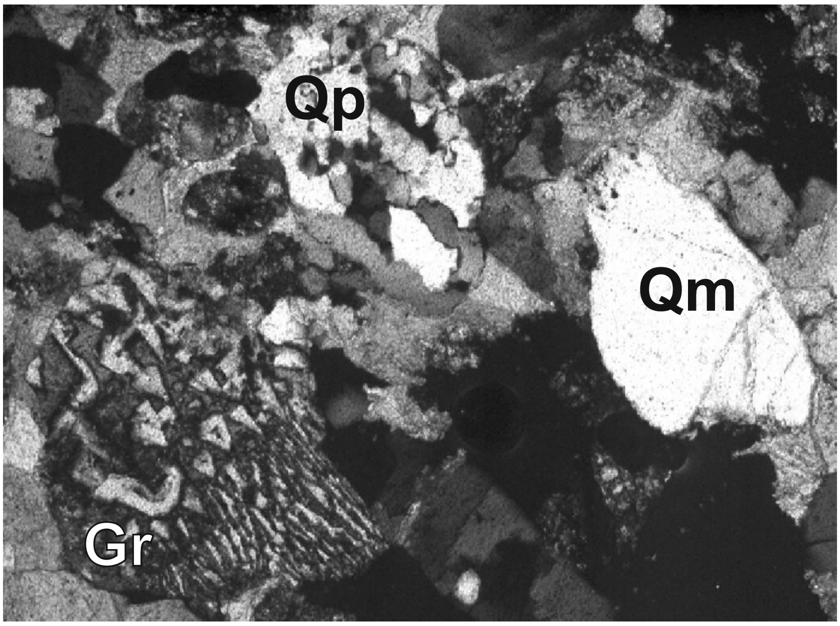

Figure 4.5: Microphotograph of some characteristic components of the Eocene sandstones. Qm: monocrystalline quartz (vast majority of the grains), Qp: polycrystalline quartz (in minor amounts, typically associated with low-grade metapelitic fragments), Gr: granophyric grain (< 1%, but diagnostic because similar microtextures were observed in many granitoids of the Bangoin batholith complex). Cross-polarized light, longer side of the image is 1.2 mm.

Semi-quantitative heavy mineral data of selected samples are summarized in (TABLE 4.2). The most frequent heavy minerals in nearly every sample are tourmaline and zircon. Apatite and rutile are also common while epidote and garnet are less abundant or completely absent. Polycrystalline, bluish anatas grains occur in some samples, too. Sample H-42A from Miocene has an anomalous composition with garnet being the major heavy mineral and tourmaline present only in traces. Zircon crystals are either dominantly euhedral or show similar amounts of euhedral and rounded shapes. Rounded grains, however, prevail in samples H-27, H-38A and H-39F. Apatite crystals are mainly rounded while prismatic faces are recognized in minor proportions only. The surface of apatite grains frequently show chemical corrosion.
The Jurassic metasandstone sample H-3A is distinct from all the others, because this sequence actually has experienced metamorphism and forms part of the sediment-supplying basement. Except for the exclusively rounded shape of the zircon grains the heavy mineral assemblage of this sample does not contain any characteristic feature that can be used to identify provenance from this sequence. The high tourmaline content is typical for low-grade metapelites, but its occurrence is not source-diagnostic, because tourmaline is also present in the granitoids of the region, and both units show mainly euhedral-shaped tourmaline.

4.5.2 Detrital zircon U-Pb age

2026 single-grain U-Pb ages from 16 samples were determined. The proportions of ages between 95 - 105%, and 90 - 105% concordance are 75% and 90%, respectively (for details see TABLE A.29 - TABLE A.62 in SECTION A.3). The calculated ages range from ca. 37 Ma to 3 Ga. In order to get a clear-cut visual comparison we present the entire age distributions by probability density curves (FIGURE 4.6). The post-Jurassic U-Pb age spectra are rather uniform and typically show tight age components having mean ages between 140 and 110 Ma, and low proportions of U-Pb ages older than 160 Ma ranging between 5 and 83% (average = 36%). However, one Lower Cretaceous and one Miocene sandstone sample yield rather complex age spectra with high proportions of > 160 Ma ages (97 - 100%). Notably, the dominant Early Cretaceous age component in the Upper Cretaceous and Eocene sandstones are not identical. Zooming into the post-Jurassic time interval reveals that most of the samples show characteristic differences (see

Table 4.2: Sample overview and summary of semi-quantitative heavy mineral composition of the studied sandstones. Indicative heavy minerals are outlined as Rt: rutile; Tur: tourmaline; Zrn: zircon; Ap: apatite; Ep: epidote; Grt: garnet. Dark gray fields highlight the dominating mineral(s) and white fields indicate the absence of a given mineral species. Asterisk indicates that the Later Cretaceous depositional age (based on the available maps) is re-interpreted as Eocene according to the new U-Pb data

Sample	U-Pb	lithology (ss = sandstone)	Rt	Tur	Zrn	Ap	Ep	Grt
North								
Miocene (NAGQU)								
H-41A	x	ss gray	2	4	3	0	0	0
H-42A	x	ss red	2	0	2	3	0	4
Eocene (BANGOIN NORTH)								
H-15A		ss gray	2	4	3	0	0	1
H-15B	x	ss gray	1	5	2	0	0	0
H-37A	x	ss brown-red	3	2	3	1	1	1
H-37B		clay gray	0	2	3	4	0	0
H-37C		ss gray	2	4	3	0	0	2
H-39A	x	ss gray	2	3	3	1	1	1
H-39F	x	ss gray	2	4	3	1	1	0
H-101A		ss red	0	3	3	2	1	1
H-101B		clay gray	2	3	2	2	3	0
H-102A	x	ss	1	4	3	1	1	2
H-103	x	ss	1	5	2	2	0	1
H-104A	x	ss	2	4	3	1	0	2
Upper Cretaceous (MENDANXIANG)								
H-9	x	ss	0	0	1	1	5	0
H-17A	x	ss red	3	0	4	3	0	0
H-17C		ss red	2	3	3	2	1	0
H-18	x	ss red	1	3	3	2	1	2
H-74A*		ss red	1	3	4	2	1	1
H-74B*	x	ss red	2	4	3	2	0	1
H-75*	x	ss metamorphic	1	5	1	2	1	1
Lower Cretaceous (LUMPOLA SOUTH)								
H-27	x	ss red	2	3	3	1	0	1
H-38A	x	ss red	2	4	3	2	0	0
H-38B		ss red	2	4	3	2	1	0
Jurassic (NAMUCUOXIANG)								
H-3A		ss	0	4	3	2	2	0
South								
Eocene (MANGREXIANG)								
H-66	x	ss red	0	3	4	3	2	0

0%	0	absence
<2%	1	in trace
2-20%	2	minor
20-40%	3	moderate
40-60%	4	major
>60%	5	predominate

FIGURE 4.7).

4.5.3 Apatite fission track age

488 single-grain apatite fission track ages were determined from 10 sandstone samples (FIGURE 4.8; further details are in SECTION A.3, TABLE A.64 - TABLE A.74). The age distributions are rather similar, with a broad Cretaceous to Tertiary age range and high dispersion (0.15 to 0.5). The chi-square test fails in 8 out of 10 dated samples indicating complex distributions composed of several components FIGURE 4.8.

Table 4.3: Apatite fission track data

				spontaneous		induced		dosimeter		chi-sq[d]	disp.[e]	Central	error	U	U		
Sample	Location	Stratigr.	Cry.	Rho[a]	(N)[b]	Rho[a]	(N)[b]	Rho[c]	(N)[c]	P (%)		Age	± 1σ	ppm	rel %	Dpar	sd
H-42A	Nagqu	Miocene	52	5.2	609	8.8	1036	6.8	6083	0	0.33	67.4	4.9	16	69	2.4	0.3
H-37A	Bangoin north	Eocene	49	13.3	1213	17.7	1617	7.2	6925	0	0.32	89.2	5.8	32	78	2.1	0.3
H-39A	Bangoin north	Eocene	21	16.2	515	26.2	836	7.0	6083	0	0.42	82.9	9.4	45	88	1.9	0.3
H-102A	Bangoin north	Eocene	51	16.2	1312	26.3	2133	7.1	6925	0	0.34	78.8	5.2	42	84	2.2	0.4
H-17A	Mendanxiang	Upper Cret.	68	11.1	1277	21.9	2516	7.3	6925	0	0.35	65.6	4	39	90	2.3	0.4
H-17C	Mendanxiang	Upper Cret.	50	14.3	1329	22.1	2053	6.8	6083	10	0.13	73.1	3.4	44	101	2.4	0.4
H-18	Mendanxiang	Upper Cret.	16	12.6	343	28.5	773	7.1	6925	15	0.15	52.7	4.2	49	73	2	0.2
H-74A	Mendanxiang	Upper Cret.	50	19.9	1024	50.1	2581	7.1	6433	0	0.33	47.7	3.1	91	73	3.3	0.6
H-27	Lumpola south	Lower Cret.	31	9.6	678	14.0	997	6.6	6433	0	0.50	73.3	7.9	32	106	3.3	0.9
H-66	Mangrexian	Eocene	100	10.7	2569	16.7	4009	7.0	6433	3	0.16	74.5	2.7	32	95	3.1	0.4

Age calculations based on a zeta value of 329.4 ± 1.6 (1σ)
Stratigr. = Stratigraphy, Cry. = Crystals
[a] Track densities (Rho) are as measured (x10^5 tr/cm^2).
[b] Number of tracks counted is shown in brackets.
[c] Rho and N are track densities of the CN5 detector.
[d] Chi-square P(%): probability obtaining Chi-square value for n degree of freedom (where n = no. crystals – 1).
[e] Dispersion was determined according to Galbraith and Laslett (1993).

4.6 Discussion

Geologic and petrographic evidences (see SECTION 4.6.1) clearly point to the Bangoin batholith complex (and related volcanic formations) as the major source area. In order to a complex source-to-sink evaluation we should consider the single-grain zircon U-Pb ages obtained by our former study on the Bangoin area. Before the detailed discussion of the new detrital ages we outline first the data set measured on the basement formations.

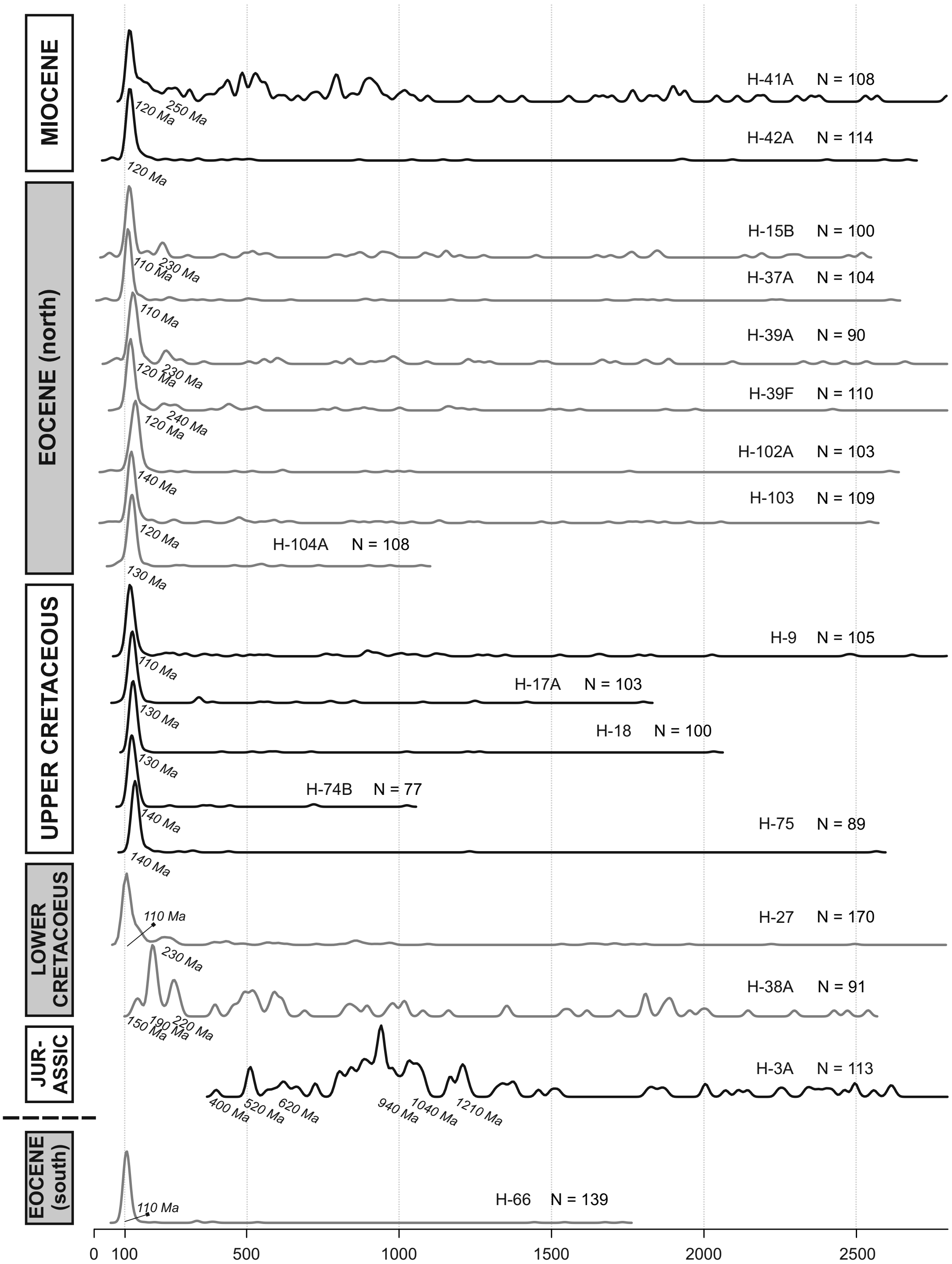

Figure 4.6: Zircon U-Pb age distribution of each single sample displayed as probability density curve. Ages typed in italics are the mean age of the major populations.

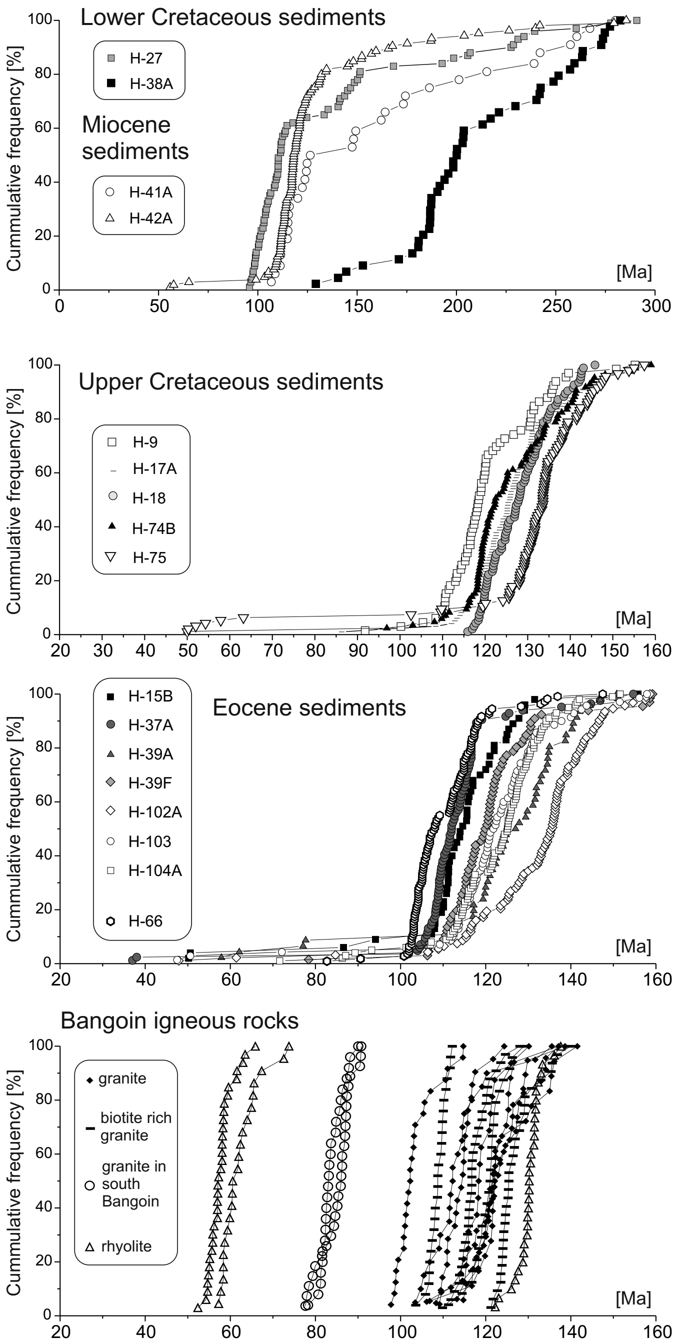

Figure 4.7: Cumulative plots of the younger parts of the U-Pb age data (the subdivision of the results into age groups follows the stratigraphy indicated on the maps used at the sampling; the re-interpretation of stratigraphic ages is discussed in the text). The selected intervals are different; the normalization to 100% was performed to 300 Ma in case of Lower Cretaceous and Miocene samples, while the Upper Cretaceous and Eocene samples are normed until 160 Ma. In these samples the older single-grain ages do not form well pronounced groups in the individual samples; their compilation is presented in FIGURE 4.4B. At the bottom the single-grain U-Pb age distributions of the different igneous formations of the adjacent Bangoin hills is presented for comparison data from Haider et al. (2013).

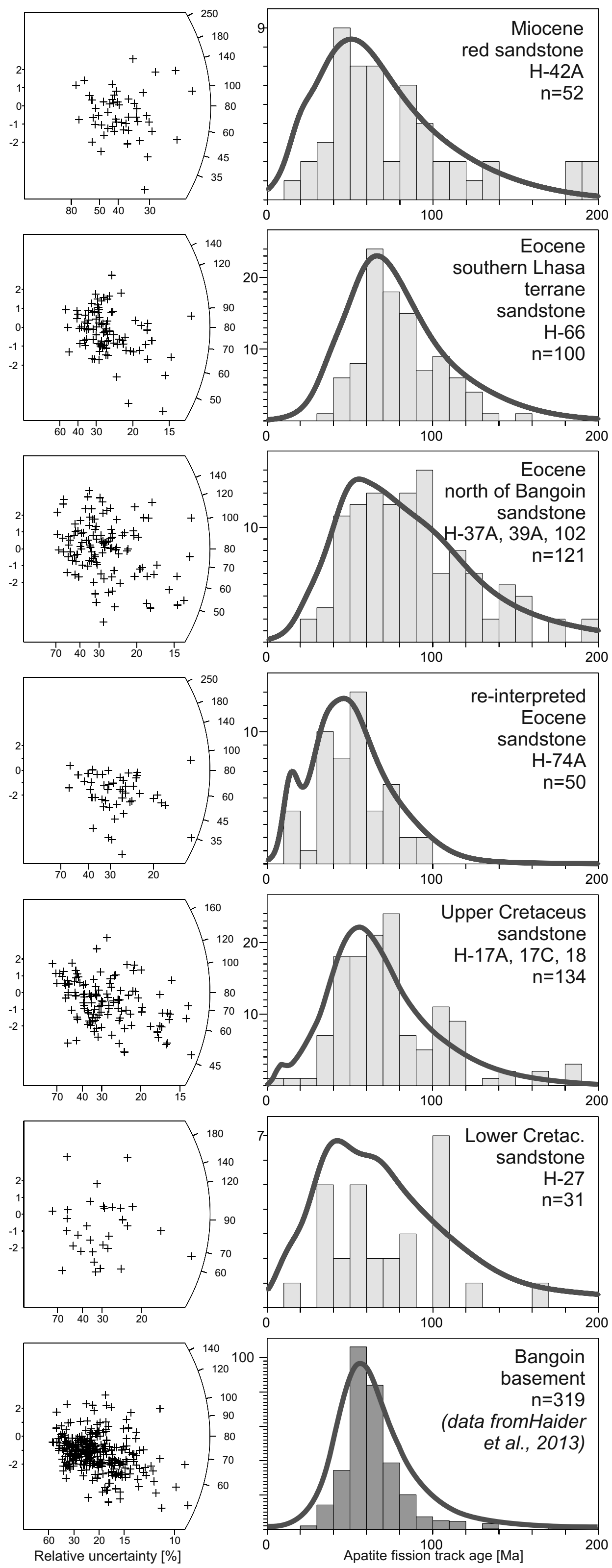

Figure 4.8: Radial plots, binned frequency diagrams and probability density plots generated from the apatite fission track ages.

4.6.1 Reference U-Pb age data from the Bangoin batholith complex

In previous studies we have determined 710 zircon single-grain U-Pb ages from 22 igneous samples from the adjacent Bangoin batholith complex (Hetzel et al., 2011; Haider et al., 2013, see FIGURE 4.7 and detailed data in SECTION A.3). We thus have an outstanding possibility to directly compare the single-grain age distributions of the largely batholith-sourced sedimentary formations to the single-grain age distributions detected in the igneous rocks of the Bangoin complex. The apparently simple provenance relations along with the comprehensive data base of both source rocks and sedimentary rocks allow for evaluating possible bias in the comparison of single-grain age distributions generated in provenance and igneous studies. Single-grain ages from igneous rocks that are considerably older than the magmatic activity are actually by-products of the determination of the emplacement ages and are usually ignored or even not presented. These ages are typically not tightly grouped, because the in-situ dating procedures for igneous rocks usually place the analytical spots in the outermost zones of the crystals showing magmatic features. Thus the older inherited ages occur accidentally. Further, mixed ages of inherited cores and igneous rims are likely and foster a broad and “noisy” pre-magmatic age pattern. In provenance studies, however, the analytical spots are typically positioned in the “mantle” of the grain, i.e. in the thickest homogeneous zones, which represents the main mass of the crystals, avoiding the usually thin outermost rim. Consequently, a potential bias is expected between zircon U-Pb age distributions of igneous rocks and directly related sedimentary rocks that largely stems from the selection of spot positions resulting from generally different aims in studying these rocks. In our case, additional bias due to different operators and different analytical facilities can be excluded.

4.6.2 Jurassic sandstone sample

A single Jurassic sandstone was analyzed in order to gather criteria for the possible re-cycling of detritus from the metasedimentary Jurassic sequence. The heavy mineral composition of sample H-3A is dominated by tourmaline and well-rounded zircon grains, while apatite and epidote are minor constituents and rutile and garnet are absent TABLE 4.2. The detrital zircon U-Pb age spectrum (N = 113) yields a complex pattern; most single-grain ages (76%) are between 500 and 1500 Ma (FIGURE 4.6, FIGURE 4.7). The most pronounced age group scatter around 900 Ma. This age component is also present in the age distribution determined by Leier et al. (2007c) in the Jurassic formations in the region, but in their sample the < 500 Ma ages and a tight age component around 1900 Ma have much higher proportions compared to the ca. 900 Ma age component.

4.6.3 Lower Cretaceous sandstone samples

The Lower Cretaceous sandstone samples were collected from the northernmost zone of the Lhasa terrane, close to the Bangong suture (FIGURE 4.1C). Early Cretaceous samples were included to trace possible recycling from the Lower Cretaceous Duba formation into the younger Takena formation. The two samples were derived from petrographically similar successions the only difference is the higher lithic fragment content in H-27, relatively to H-38A. The heavy mineral assemblages of the two Lower Cretaceous samples are rather similar.
In contrast, the U-Pb age spectra of the two samples are highly different (FIGURE 4.6, FIGURE 4.7). In H-27 two well-constrained late Mesozoic age components (106 ± 7 Ma and 144 ± 5 Ma) can be isolated by the PopShare software (Dunkl and Székely, 2002) while the pre-Mesozoic ages (28%) yield high scatter and no distinct groups. In sample H-38A (I) the proportion of pre-Mesozoic ages is much higher (73%), (II) the youngest ages are significantly older and scatter around the Jurassic/Cretaceous boundary (i.e. the late Early Cretaceous age component is completely missing), and (III) the mean of Mesozoic age component (189 ± 14 Ma) is significantly older than the typical Early Cretaceous ages of the Bangoin batholith complex as detected in sample H-27. A late Permian age component (259 ± 19 Ma) was isolated in sample, too. The presence of the ca. 140 Ma age component is the only common feature of these two samples. Remarkably, this ca. 140 Ma old age component is reported also for Lower Cretaceous sedimentary samples by Leier et al. (2007c), although relative proportions are higher in their study. These authors also recognised a high variability between the age distributions in their Lower Cretaceous samples. In the northern Lhasa terrane the formations mapped as Lower Cretaceous strata thus contain highly different single-grain U-Pb age spectra. According to the variable and

partly minor presence of Cretaceous zircon ages (which are dominant in the Lhasa terrane) we can conclude that either (I) the two samples containing contrasting Cretaceous age components (ca. 140 Ma and ca. 110 Ma) derive from the base (H-38A) and from the uppermost part (H-27) of the Lower Cretaceous sequence (it is maybe even Upper Cretaceous), or (II) the depositional ages are similar, but the provenance of this basin fill was complex receiving sediments from different directions, including the north. This is because the ca. 190 Ma age component in sample H-38A may be related to ages detected in the basement of the Amdo region and further to the northeast. The ages around 1.9 Ga may also give some hints for northern provenance because such ages were reported from the Songpan-Ganzi terrane and from the southern Qiangtan terrane (see compilation by Gehrels et al., 2011, and FIGURE 4.4).

4.6.4 Upper Cretaceous and Eocene sandstone samples

The Upper Cretaceous and Eocene sedimentary successions are the principal targets of our provenance study. We sampled these strata mainly in the surroundings of the Bangoin batholith complex (FIGURE 4.1C). Additionally a single Eocene sample was collected south of the Nyainqentanghla range close to the city of Magrexiang (H-66, FIGURE 4.1C). The heavy mineral assemblages are all rather similar (predominance of tourmaline and zircon; TABLE 4.2) except for sample H-37B, which is high in apatite and relatively low in tourmaline and lacks rutile, and H-17A which lacks tourmaline completely. Similarly, the U-Pb ages obtained on Late Cretaceous and Eocene samples show strong analogies and are obviously composed of two parts: the majority of the U-Pb ages cluster in Cretaceous time - obviously indicating the origin from the granitoids of the Lhasa terrane-, while pre-Cretaceous ages are less frequent and form less pronounced age components. Based on these striking similarities we jointly evaluate the Late Cretaceous and Eocene U-Pb results. We discuss the two main parts of the age distributions (Early Cretaceous distinct age group and pre-Cretaceous diffuse age groups) separately - split at a frequency minimum around 160 Ma. The pre-160 Ma ages will be compared to published data compiled from the Tibetan Plateau and thus serve as large-scale provenance indicator, while the post-160 Ma ages will be treated as local provenance indicators. Furthermore, the < 160 Ma age data are suited for the direct comparison to the age distributions recorded in the adjacent Bangoin batholith complex.

4.6.4.1 Pre-160 Ma zircon U-Pb ages in the Upper Cretaceous and Eocene strata

The proportion of > 160 Ma ages constitutes ca. 31% of all Upper Cretaceous and Eocene age spectra. These ages do not form well-defined age components in the individual samples. Therefore all > 160 Ma data are integrated and evaluated en bloc. The isolated age components are: 237 ± 32 Ma, 342 ± 28 Ma, 515 ± 75 Ma, 911 ± 110 Ma, 1220 ± 90 Ma and 1790 ± 135 Ma (FIGURE 4.4B). These components are first compared to the pre-Cretaceous ages detected in the Bangoin igneous rocks FIGURE 4.4B. Around 9% of the zircon single-grain ages of the Bangoin igneous rocks are significantly older than the emplacement age, but the total number of ages measured in the cores of igneous zircons is not sufficient for a robust statistical analysis. However a striking feature is that the > 160 Ma age components of the sediments correspond well to the ages of the old zircons of the Bangoin batholith complex (clustering around 300, 500, 1000 and 1800 Ma). The plate tectonic significance of the origin of these inherited cores is not the task of the current study, but we can declare that a part of the pre-Cretaceous ages detected in the sediments derived from the Cretaceous igneous formations of Lhasa terrane.

The U-Pb age spectra of the Jurassic metasandstone sample (H-3A) is dominated by an age component broadly scattering around 900 Ma (FIGURE 4.4B). This age component is observed in the Upper Cretaceous to Eocene sediments, too.

Beyond local sources, there are striking analogues to the dominant ages in other terranes of the Tibetan Plateau. The pronounced Triassic age component (237 ± 32 Ma) call for a significant contribution from northern provenance because the Kunlun (Chen et al., 2002; Dai et al., 2012), Songpan-Ganze (Roger et al., 2003; Xiao et al., 2007; Dai et al., 2012, especially the northern Qiangtang) and Qiangtang terranes (Roger et al., 2003; Reid et al., 2005; Zhai et al., 2012) contain similar Triassic zircon age signatures (see compilation in FIGURE 4.3). Minor contribution of Triassic ages from recycled Jurassic may be possible because Leier et al. (2007c) reported such ages from Jurassic sedimentary rocks from the north of the Lhasa terrane, however, our sample does not show such ages. Possible source units for the less pronounced Carboniferous age component (342 ± 28 Ma) are rare but such ages were detected sporadically in the Kunlun terrane

(Cowgill et al., 2003; Schwab et al., 2004; Dai et al., 2013). The Cambrian age component (515 ± 75 Ma) forms a significant part of the pre-Cretaceous ages. Such ages are common in the Lhasa terrane, both in the plutons and also as re-worked zircon grains in Permo-Carboniferous sequences (e. g. Gehrels et al., 2011). The ca. 900 Ma age component (FIGURE 4.4B) is also a common part in the Late Paleozoic sequences of the Lhasa terrane. Ages similar to the Mesoproterozoic, ca. 1120 Ma and the Paleoproterozoic, ca. 1800 Ma age components were detected in the Paleozoic and Mesozoic sediments of the Lhasa terrane further in the Songpan-Ganze and South Qiangtang terranes.

4.6.4.2 Post 160 Ma zircon U-Pb ages in the Upper Cretaceous and Eocene strata

4.6.4.2.1 Bulk evaluation of post 160 Ma zircon U-Pb ages

The cumulative age plots of the < 160 Ma ages (n=945) from Upper Cretaceous and Eocene sandstones are similar at first glance (FIGURE 4.7). Each distribution has a dominant Early Cretaceous group of ages and old and young "tails". We do not consider the "old tails" as significant because the splitting at 160 Ma of the discussed age interval is somehow arbitrary. Furthermore, the igneous zircons do contain inherited cores, and the laser spot sometimes may have partly covered the cores. Thus a diffuse transition towards the next well developed age cluster (237 ± 32 Ma) does not need further discussion. The "young tails" of the distribution, however, can have high significance and is discussed below. The dominant Early Cretaceous age components are quite different when looking in detail, with some samples showing only minor overlap in ages (FIGURE 4.7). Both t-Test (performed using ORIGIN by OriginLab) and Kolmogorov-Smirnoff test (J. Guynn, University of Arizona) were applied to express numerically the similarities/differences of the Early Cretaceous U-Pb age distributions. We performed the tests both on the entire < 160 Ma age interval and also on the selected "steep" interval on the cumulative curve, between the lower and upper inflexion points. The isolation of the "steep" intervals was performed by the Grubbs and IQR (interquartile range) tests using the software Out?Lier (http://www.sediment.uni-goettingen.de/staff/dunkl/software). The results for all Upper Cretaceous and Eocene samples are illustrated in textsctable 4.4. The two basically different procedures yield mainly similar results: while a part of the age distributions is statistically

Table 4.4: Comparison of single grain age distributions of Upper Cretaceous and Eocene sandstone samples. The upper panel presents the results of t-Test; "D" denotes when the compared samples significantly differ at 0.05 level and "=" denotes when the two means are not significantly different. The lower panel presents the results of comparison using the P values of the Kolmogorov-Smirnoff test. Gray background emphasizes the statistically indistinguishable sample pairs ($P \geq 0.05$). The lower left fields of the panels show the test results when all ages < 160 Ma were considered, while the upper right fields show the test results when only the "steep" intervals of the cumulative spectra were compared -see text for details of the isolation of the tested age ranges.

Means compared by t-Test

		U. Cretaceous					Eocene					
		H-9	H-17A	H-18	H-74B	H-75	H-15B	H-37A	H-39A	H-39F	H-102A	H-103
U. Cretaceous	H-9		D	D	D	D	=	D	D	D	D	D
	H-17A	D		D	D	D	D	D	D	D	D	D
	H-18	D	=		=	D	D	D	=	D	D	D
	H-74B	D	=	=		D	D	D	=	D	D	D
	H-75	D	=	=	=		D	D	D	D	D	D
Eocene	H-15B	=	D	D	D	D		D	D	=	D	D
	H-37A	D	D	D	D	D	=		D	D	D	D
	H-39A	=	=	=	=	=	D	D		D	=	D
	H-39F	=	D	D	=	D	=	D	=		D	=
	H-102A	D	D	=	D	=	D	D	D	D		D
	H-103	=	D	D	=	D	=	D	=	=	D	

Tested by K-S method

		U. Cretaceous					Eocene					
		H-9	H-17A	H-18	H-74B	H-75	H-15B	H-37A	H-39A	H-39F	H-102A	H-103
U. Cretaceous	H-9		0.00	0.00	0.00	0.00	**0.17**	0.00	0.00	0.00	0.00	0.00
	H-17A	0.00		0.00	0.00	0.00	0.00	0.00	0.00	0.00	0.00	**0.14**
	H-18	0.00	**0.22**		**0.11**	0.00	0.00	0.00	**0.72**	0.00	0.00	0.00
	H-74B	0.00	**0.19**	0.01		0.00	0.00	0.00	**0.59**	0.00	0.00	0.00
	H-75	0.00	0.00	0.00	0.00		0.00	0.00	0.00	0.00	0.02	0.00
Eocene	H-15B	0.03	0.00	0.00	0.00	0.00		0.01	0.00	**0.06**	0.00	0.00
	H-37A	0.00	0.00	0.00	0.00	0.00	**0.05**		0.00	0.00	0.00	0.00
	H-39A	0.00	**0.22**	**0.21**	**0.52**	0.00	0.00	0.00		0.00	0.01	0.00
	H-39F	**0.44**	0.00	0.00	0.01	0.00	0.03	0.00	0.00		0.00	**0.40**
	H-102A	0.00	0.00	0.00	0.00	**0.13**	0.00	0.00	0.00	0.00		0.00
	H-103	0.03	**0.08**	0.00	**0.20**	0.00	0.00	0.00	0.03	**0.27**	0.00	

indistinguishable, other distributions are significantly different. - This results is independent from stratigraphic age and implies that there is no significant difference between the zircon U-Pb age distributions of Upper Cretaceous and Eocene sandstone samples.

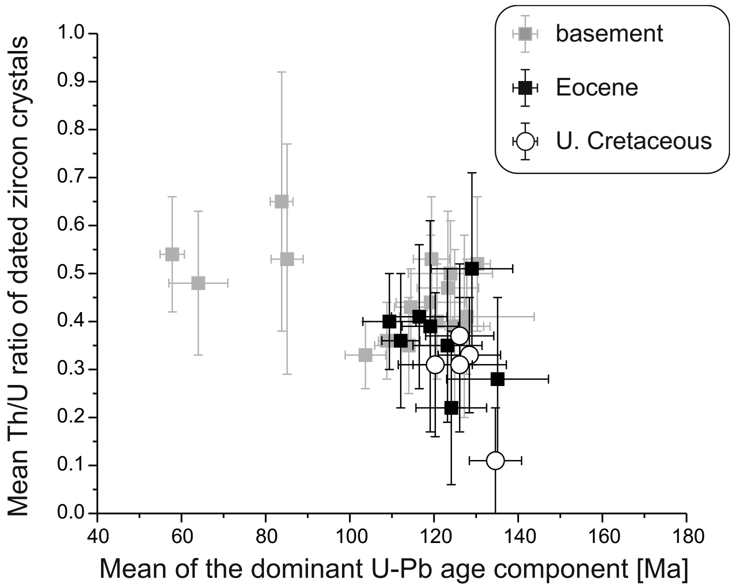

Figure 4.9: Comparison of the composition and age of the dated zircon crystals from the Bangoin basement and the adjacent sedimentary formations

The Th/U ratio may add age-independent information for zircon provenance (FIGURE 4.9). The Eocene, but especially the Upper Cretaceous detrital zircons differ via lower Th/U rations from the major cluster of the Early Cretaceous zircons from Bangoin batholith complex. Basically the provenance of the Early Cretaceous zircons from the Lhasa terrane is not a question, but this plot suggests that beyond the well studied Bangoin batholith complex other Early Cretaceous igneous formations with low Th/U ratios also contributed to the Upper Cretaceous to Eocene sediments.

4.6.4.2.2 Component identification in the post 160 Ma zircon U-Pb ages

The youngest age data in a detrital single-grain age population may provide valuable constraints for the age of deposition. This is especially the case in continental sedimentary successions where biostratigraphic information is typically rare. In our understanding, however, it needs rather an age component (i.e. isolated by statistical procedures like, e. g., PopShare) than a single youngest grain age to be conclusively interpreted as, for instance, maximum age of deposition (von Eynatten and Dunkl, 2012) . The best example for an obvious post-Cretaceous age component is sample H-75 (FIGURE 4.10) which is assigned to the Cretaceous according to the geologic map. This age component (51 ± 3 Ma) suggests an Eocene age and an aeolic or fluvially transported contribution from the Linzizong volcanic suite situated south of the study area (He et al., 2007; Lee et al., 2009). Alternatively, but less likely, Eocene zircons may reflect local sources from minor Palaeogene magmatism in the Bangoin batholith complex, although these ages are on average slightly older (Haider et al., 2013). Sample H-74B contains just a single zircon crystal yielding Eocene age (49.9 ± 0.9 Ma at 97% concordance). This alone has low diagnostic value, but sample locality is pretty close to H-75 and both samples yield altogether 7 Paleocene to Eocene zircon U-Pb ages. Consequently, the geological map must be improved towards presence of Eocene strata along the SW boundary of the Bangoin batholith complex, too (see localities of samples H-75 and H-74B in FIGURE 4.1).

Similar, early Cenozoic ages were detected in five Eocene samples and in a Miocene sandstone (see below). The youngest age component at ca. 38 Ma was detected in sample H-37A (FIGURE 4.10). This component consists of two crystals only, however, it is well separated from the rest of the age distribution of this sample (FIGURE 4.7) and both ages are highly consistent (i.e. ^{206}Pb/^{238}U and ^{207}Pb/^{235}U ages are equal within 2 sigma errors (38.0 and 37.0 Ma vs. 40.0 and 37.8 Ma, respectively); thus we infer a late Eocene maximum age of deposition for sample H-37A.

A similarly small group of ages scatter between 95 and 75 Ma (FIGURE 4.7, FIGURE 4.10B). These grains likely derive from the southern part of the Bangoin batholith complex, where voluminous intrusions yield similar zircon U-Pb ages (Haider et al., 2013, FIGURE 4.10C;). These age components are clearly separated from the Lower Cretaceous age components.

The Early Cretaceous age components range from approximately 140 to 105 Ma and fully reflect the age range observed for the vast majority of the Cretaceous Bangoin batholith complex. The small (< 10%) older (Jurassic) components are negligible because they most likely reflect mixed ages of inherited cores (see SECTION 4.6.4.1) and Cretaceous magmatism (i.e. laser spot integrates over core and mantle/rim of the grains). The Early Cretaceous ages, however, do not form a single widespread distribution. Instead, it is possible to isolate major Early Cretaceous

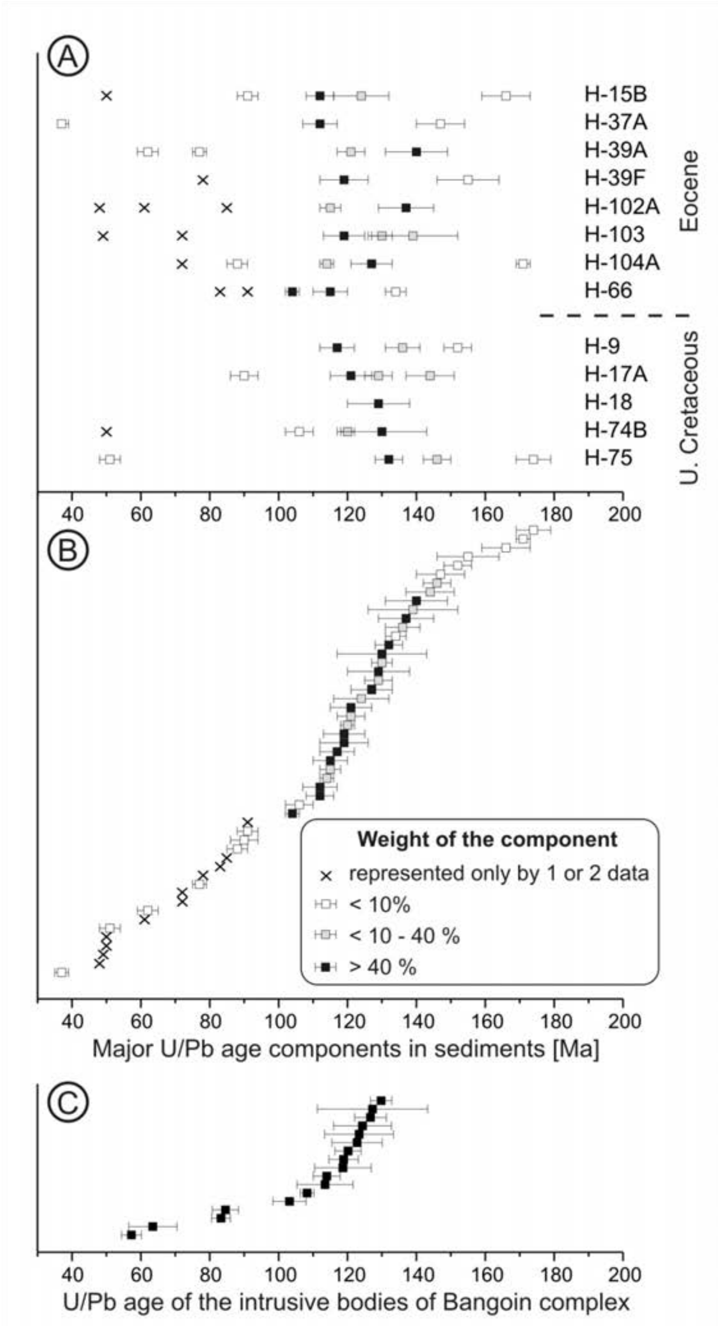

Figure 4.10: (A) Zircon U-Pb age components isolated by PopShare software for the Upper Cretaceous and Eocene sedimentary samples. Color coding of the mean values emphasizes the weight of the age component. (B) Cumulative distribution of all isolated components. The dominant components are in Early Cretaceous time (140 to 105 Ma). The older ones have probably no explicit geological meaning, but the younger ones can be related to volcanic periods in the Lhasa terrane. (C) For comparison the U-Pb single-grain distributions and mean values determined in the igneous bodies of the Bangoin complex are also plotted. Error bars represent 1 s.d.

age components in each sandstone sample (FIGURE 4.7, FIGURE 4.10; see also TABLE A.63 in SECTION A.3) and to assign each sandstone layer to one, two or three distinct phases of magmatism of the Lhasa terrane.

This statement can be validated by comparing the standard deviations of the age components observed in igneous single-grain age distributions with the standard deviations of the age components isolated from the sedimentary rocks. The average s.d. of the igneous data set is 5.1 Ma while the major age components (i.e. >40% of the ages of the respective distribution) in the sediment samples yield an average s.d. of 6.3 Ma (TABLE A.29 - TABLE A.62). Thus the scatter of major age components of the detrital single-grain data is similar to the empirical scatter detected in the igneous units, implying that the zircon composition of sandstones still mirror individual igneous bodies and thus indicates the minor sizes of the catchment areas.

Sample H-66 was collected far from the other Eocene samples in the southern Lhasa terrane (FIGURE 4.1). Its zircon U-Pb age distribution does not differ significantly from all the samples (both sedimentary and igneous) collected in the surroundings of the Bangoin hills, at the northernmost part of the Lhasa terrane. This suggests a rather uniform provenance and drainage pattern across the Lhasa terrane in Late Cretaceous to Early Tertiary time.

4.6.5 Miocene sandstone samples

Along highway G109, northwest of Nagqu two Miocene samples were collected, according to the available geological map (Pan et al., 2004): a grayish, well-sorted sandstone (H-41A) and a reddish, poorly sorted sandstone sample (H-42A) containing green components. The heavy mineral composition of the two samples is highly different: tourmaline and zircon are the prevailing minerals of the grayish sandstone, while the reddish sandstone lacks tourmaline and is dominated by garnet and apatite (TABLE 4.2). Similarly, the zircon U-Pb age distributions of the two Micoene samples are very different (FIGURE 4.6, FIGURE 4.7). The typical signature of the Lhasa terrane (i.e. ages < 140 Ma) is of minor relevance for H-41A (16%) but predominant in H-42A (86%). The pre-Mesozoic single-grain age distribution in H-41A shows striking similarity to the Lower Cretaceous sample H-38A (FIGURE 4.6). This tentatively suggests a northern provenance, like for sample H-38A (see SECTION 4.6.3). The dominance of the typical Early

Cretaceous zircon U-Pb Lhasa-terrane ages in sample H-42A apparently contrasts to the untypical heavy mineral composition dominated by garnet. This discrepancy most likely implies a strong contribution from a garnet-rich but zircon-poor source unit, probably rich in micaschists. The results from the two Miocene samples are contrasting and, moreover, their absolute depositional ages are poorly constrained and their relative stratigraphic position is not known. However, we can deduce that these strata indicate more distal (likely northern) sources compared to the Eocene strata.

4.6.6 Apatite fission track and (U-Th)/He ages

The sedimentary and tectonic overburden as well as the long-lasting magmatic activity of the region generated some local reset in the apatite FT system. Thus in several samples the AFT ages have no any significance on the provenance. Together with the higher relative uncertainty of single-grain AFT ages, the AFT data are less diagnostic in terms of sediment provenance compared to the zircon U-Pb ages in our study.

Only one of the Lower Cretaceous samples yields apatite crystals in passably amount and proper quality (H-27; FIGURE 4.7). The AFT age distribution has an extremely wide scatter (dispersion = 0.5) and the central age (73 $\pm$ 8 Ma) is younger than the assumed depositional age. In this case late and/or post-Cretaceous tectonics (e. g. Harrison et al., 1992; Chung et al., 1998, 2005; Mo et al., 2008) are responsible for the thermal reset of the AFT system, and the data thus cannot be used for the detection of provenance.

One out of 3 Upper Cretaceous samples (H-18) yields a Paleogene AFT central age (ca. 53 Ma), which is considerably younger than Late Cretaceous (FIGURE 4.7). It is located below the thrust south of the Bangoin batholith complex thus a post-depositional thermal reset is reasonable. Two Upper Cretaceous samples yield central ages at the young end of the possible range of depositional ages (65.6 and 73.1 Ma in samples H-17A and 17C, respectively). Because of the uncertainty in depositional age these AFT ages are difficult to interpret. Therefore, to assess possible post-depositional thermal overprint as obviously detected for sample H-18 we performed preliminary apatite (U-Th)/He thermochronology (AHe) on sample H-17A (see TABLE A.75). The average AHe age of three apatite aliquots is 50 $\pm$ 4 Ma, and clearly proves a post-depositional thermal overprint that could have slightly modified the original, detrital AFT ages. That is why we can not relate provenance significance to the apatite fission track ages, as they possibly experienced some rejuvenation.

The sedimentary site south of the Bangoin intrusion that is Upper Cretaceous according to the map but includes Paleogene U-Pb ages (H-74A; see SECTION 4.6.4.2) and yields 48 ± 3 Ma AFT central age (TABLE 4.3, FIGURE 4.7). This AFT age is within error similar to the youngest U-Pb age component (51 ± 3 Ma), and is thus consistent with a largely detrital signature in the AFT data:

The Eocene strata north of the Bangoin batholith complex yield an integrated apatite FT central age of 83 ± 4 Ma that is much older than the AFT ages measured in the H-74A sample from the southern side of the Bangoin hills and even older than the AFT ages in Upper Cretaceous siliciclastics. They are even older then the cooling ages of the Bangoin batholith complex that was intensively studied by Hetzel et al. (2011); Haider et al. (2013): the average of the central ages of 29 granitoid samples is 61 Ma (see FIGURE 4.7 for comparison). The Eocene strata are onlapping onto the Bangoin batholith complex along the northern margin, and large parts or even the entire basement was covered (Haider et al., 2013). The fact that the AFT ages in the cover sequence are older by ca. 20 My than in the basement makes probable that the igneous formations in the currently exhumed part of the northern Lhasa terrane (Bangoin hills s. s.) were not, or only minor contributors to the Eocene siliciclastic sediments in the northern area.

Remarkably, the Eocene pilot sample from the distal southern area yields an AFT age distribution similar to the Eocene samples from the north (H-66 in FIGURE 4.1 and FIGURE 4.8). The Miocene sample (H-42A) shows a more complex AFT age distribution. The age components can not be identified at a high level of significance, but the detected broad distribution is likely composed of two major age components: 52 ± 8 Ma and 81 ± 37 Ma (FIGURE 4.1, TABLE A.69).

4.7 Conclusion

The conclusions are subdivided into two parts, according to the twofold character of the study, and focus on (I) new constraints to the provenance of the Cretaceous to Tertiary strata of the

Lhasa terrane, and (II) methodological aspects on the evaluation of detrital zircon U-Pb age distributions with complex igneous source rock units.

4.7.1 Provenance model of post Jurassic strata of the central Lhasa terrane

(I) The continuous presence of granitoid-derived lithic fragments and euhedral zircon crystals, and the predominance of Early Cretaceous zircon U-Pb ages in the Upper Cretaceous and Eocene strata implies that a significant part of the sediments is derived from the granitoid complexes of the northern Lhasa terrane (FIGURE 4.11). The dominant host rocks of the granitoids in the Bangoin area are Jurassic low-grade metapelites and subordinate metasandstones. Corresponding lithic fragments are abundant in the Cretaceous and Eocene sandstones, which underlines short transport from sources in the northern Lhasa terrane. Due to the typically fine-grained character of the metasediments the heavy mineral yield from erosion of the Jurassic sequence is low compared to the heavy mineral yield from the granitoids of the Bangoin batholith complex. Thus we infer that the Jurassic metasediments (and probably also the Permo-Carboniferous strata) contributed mainly to the framework composition (i.e. metapelitic lithoclasts) of the post-Jurassic sandstones while the igneous units delivered most of the heavy minerals, especially the lion-share of the zircons.

(II) The Early Cretaceous zircon U-Pb ages are rather variable and no systematic difference between the age distributions of Upper Cretaceous vs. Eocene sandstones has been recognized. The statistical tests further show that some samples show identical distributions while the majority differs significantly from each other. This is interpreted to reflect local provenance of sediments deposited as alluvial fans of small creeks having minor catchment areas that drain only single or related intrusive bodies of the Bangoin batholith complex.

(III) The igneous detritus of the Eocene sediments is derived directly from the granitoid basement. The variable and heterogeneous character of the U-Pb age distributions precludes re-working from Lower and/or Upper Cretaceous strata, because the latter would obviously produce assimilation of age distributions across different Eocene samples.

(IV) More distal sources have also contributed to the Late Cretaceous and especially the Eocene strata, because: (i) the sequence onlaps the northern margin of the batholith complex and presumably the entire Bangoin hills were covered by Eocene sediments, (ii) AFT data from these onlapping sediments contain contribution of older ages than the AFT cooling ages in the adjacent/underlying granitoids of the Bangoin hills, (iii) the low Th/U ratios detected in some Late Cretaceous and Eocene samples has not yet been identified in the Bangoin complex, and (iv) the well defined 51 Ma age component from an Eocene sample (Late Cretaceous according to the map) south of the Bangoin hills is suggested to derive from the Linzizong volcanics exposed to the south of the study area.

The youngest U-Pb ages give a ca. 38 Ma bench-mark for the maximum age of deposition in the studied Eocene strata. On the other hand we could not detect any Oligo-Miocene zircon U-Pb ages, which are characteristic in the air-born ash layers and sandstones of the adjacent Lunpola basin (Kapp et al., 2007a; He et al., 2012). Thus there is no evidence that the depositional ages of the studied continental sediments are younger than Eocene.

(I) Assuming that the > 160 Ma ages derived from other terranes of the Tibetan plateau than the synthese of Gehrels et al. (2011); Ding et al. (2013) and our compilation (FIGURE 4.3, FIGURE 4.4) offer well established patterns for searching analogues. In this case the Triassic (237 $\pm$ 32 Ma), and older (ca. 510 Ma, 910 Ma, 1200 Ma and 1800 Ma) age components can be related dominantly to the terranes situated north of the Lhasa terrane (see simplified provenance pattern in FIGURE 4.11). Due to the characteristic local provenance with short transport and minor mixing (as it was deduced from the < 160 Ma zircon ages) a very remote transport e. g. from the Kunlun terrane is not probable. However, the similarities to the Qiangtang and Songpan-Ganze terranes is remarkable and Leier et al. (2007b) concluded also a sediment transport also from the north for the northern margin of the Lhasa terrane during Early Cretaceous times.

(II) Another plausible scenario is the origin of the pre-Cretaceous U-Pb ages from the Lhasa terrane, by re-cycling from Jurassic and Paleozoic siliciclastic formations. This would

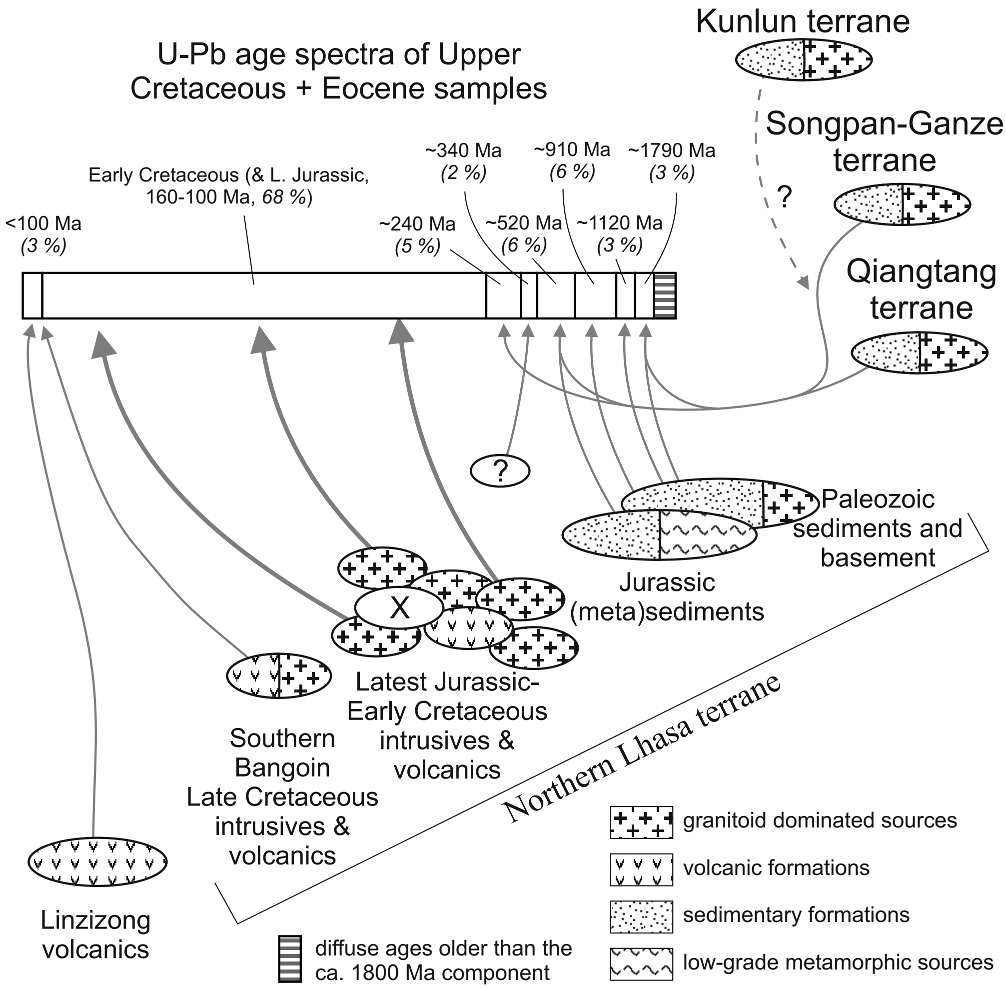

Figure 4.11: Schematic provenance pattern of the zircon grains of the Late Cretaceous and Eocene sediments of the northern Lhasa terrane. The arrangement of the possible sources roughly follows their geographic north-south positions. The latest Jurassic-Early Cretaceous igneous formations are represented as multiple, individual bodies, because in the sedimentary samples the origin from distinct units was recognized. “X” represents the currently exposed part of the Lhasa magmatites in the Bangoin batholith complex that was covered in Eocene times and did not emit zircon and apatite grains.

support the exclusively southern provenance scenario, because in this way the source area and the transport direction of the igneous-derived sediment and the recycled sediment would be the same.

(III) The distribution of inherited ages detected in the cores of the crystals of the Bangoin magmatites is similar to the major pre-Cretaceous age clusters of the sediments and it also shows similarities to the major age clusters on the entire Tibetan plateau. The old, inherited ages detected in the zircons by the dating of the Bangoin batholith complex (ca.9% of the total data) rises that at least a part of the pre-Cretaceous ages derives from the Early Cretaceous magmatites themselves. In this way of course we can not explain the entire (ca. 31%) contribution of pre-Cretaceous ages, but we should keep it in mind, especially at the interpretation of minor and diffuse age groups in the sedimenary samples.

The origin of the Carboniferous age component (342 $\pm$ 28 Ma) is not trivial, such ages are relatively scarce in the Tibetan plateau.

4.7.2 Methodical conclusions

In case of complex igneous source-rock units characterized by multiple episodes of melt ascent, magma mixing and crystallization, which may lead to complex areal pattern of igneous bodies with distinct age signatures, a thorough characterization of the variability in zircon U-Pb age distributions of the source rocks is crucial for a detailed characterization of sediment provenance. In such settings the following points should be considered in sample analysis and evaluation:

(I) Data acquisition should apply the same analytical protocol regarding grain selection criteria, laser spot positioning, and data processing for source rocks (basement formations) and sedimentary rocks.

(II) Sample evaluation (both source vs. sediment and sediment vs. sediment) should rely on comparing the entire age distributions by applying suitable statistical tests, as well as the identification of individual age components in source rocks and/or sediments that may be related to each other or not. Mean and standard deviation (s.d.) of the age components allow for constraining (i) the reliability of the observed age components in the sediments (i.e., s.d. of age components in the sediment should not be smaller than s.d. of age components observed for the entire igneous complex), and (ii) source-to-sink relations such as relative catchment size with respect to the pattern of heterogeneity in the igneous complex.

(III) In case of well-defined (detrital) age components with similar s.d. compared to age components in the source rocks and inferred small catchment size, the age data can neither be used for regional correlation nor for, e. g., estimations of relative sediment yield. The evaluation and comparison of such samples would frequently result in statistically significant dissimilarity, although the samples were derived from the same source rock complex.

(IV) Beyond zircon age distribution, trace element characteristics such as Th/U-ratios provide efficient additional information on sediment provenance and source-to-sink relations.

5 Identification of peneplains by multi-parameter assessment of digital elevation models

This chapter is similar to the manuscript entitled: "Identification of peneplains by multi-parameter assessment of digital elevation models" that is submitted to the journal Earth Surface Processes and Landforms
Authored by: V. L. Haider, J. Kropáček, I. Dunkl, B. Wagner and H. von Eynatten

5.1 Abstract

The concept of peneplains has existed since the end of the 19^{th} century. Typical peneplains are elevated geomorphological features with a low relief surface on top. They may be tilted due to tectonic activity or intersected by evolving erosion. Until now, there exists neither a standardized definition for peneplains, nor an established procedure to identify and quantify well preserved peneplains as prominent landforms. At present the global availability of homogeneous digital elevation models (DEM) provides an accurate characterization of the morphology of the Earth surface. In this study, a new unbiased DEM-based numerical fuzzy-logic approach is developed for the delineation of peneplains solely from morphological perspective. The approach is based on morphometric analysis of the 90-arcsec Shuttle Radar Topography Mission (SRTM) digital elevation model. We employ four critical parameters which are implemented within a geographic information system (GIS). The parameters for the correct and unambiguous description of a "flat

top mountain" are: (I) slope, (II) curvature, (III) terrain ruggedness index, and (IV) relative height. The approach was developed using a test area in the central Tibetan Plateau that is characterized by representative and well preserved peneplains and for which field data is available. In order to verify the method, peneplains were delineated in different regions with various geological settings for which peneplains were already described in the literature. The results from the Appalachian Mountains, Andes, Massif Central, and New Zealand confirm the robustness of the proposed approach.

5.2 Introduction

Flat-top mountains have always fascinated geologists and geomorphologists. The existence of peneplains and the planation as a geomorphological process is discussed controversially due to missing clear definitions and the fact that peneplains are metastable landforms. Deposition of cover sediments or uplift and erosion affect them, thus they can be found at different elevations and in different stages of decay. Neither the habitus nor the origin are fully understood. The term peneplain is inconsistently and cautiously used. Various theories about genesis and formation of these distinctive geomorphological features were already developed, published and discussed. Eight different approaches are established to provide clarity regarding genesis and definition of peneplains.

(I) Peneplains are generated after uplift of a young landform (Davis, 1899; Penck, 1924).

(II) Peneplains develop close to sea level during periods of persistent rising of sea level (Pitman and Golovchenko, 1991).

(III) They can be found at high elevation as a result of post tectonic uplift (Lamb et al., 1996; Kennan et al., 1997).

(IV) They are regarded as marine planation surfaces which have been uplifted (Garcia-Castellanos et al., 2000; Landis et al., 2008).

(V) Peneplains interpreted as high elevated and low relief surface result from glacial and periglacial erosion (Steer et al., 2012; Hall et al., 2013).

(VI) Piedmont aggradations of clastic sediment, derived from erosion of a high mountain range, can induce the rise of the base level around the range. This process reduces strongly the erosive efficiency of the drainage system and results in progressive smoothing of the relief and formation of peneplains (Babault et al., 2005, 2007).

(VII) Peneplains are the result of mantle-plume activity uplifting low-relief erosion surfaces (LeMasurier and Landis, 1996; Sheth, 2007) or

(VIII) the term peneplain is used to describe any low-relief regional-scale erosion surface without genetic connotations as suggested by Fairbridge and Finkl Jr. (1980).

Peneplains and related features termed low-relief surfaces or paleosurfaces are discussed on every continent and in many mountain belts such as the Klamath Region in California (e. g. Anderson, 1902; Aalto, 2006), the Rocky Mountains (e. g. Lindgren and Livingston, 1918; McMillan et al., 2006), the Andes (e. g. Kummel, 1948; Jordan et al., 1989; Hoke and Garzione, 2008; Schildgen et al., 2009; Allmendinger and González, 2010), Pyrenées (e. g. Babault et al., 2005; Gunnell et al., 2009), Scandinavia (e. g. Strøm, 1948; Gjessing, 1967; Lidmar-Bergström, 1999; Sturkell and Lindström, 2004; Steer et al., 2012), Africa (e. g. Willis, 1933; Dixey, 1939; Coltorti et al., 2007), Himalaya (e. g. Cui et al., 1997; Liu-Zeng et al., 2008; Van der Beek et al., 2009), Australia/New Zealand (e. g. Mulcahy et al., 1972; Stirling, 1991; Landis et al., 2008), and Antarctica (e. g. LeMasurier and Landis, 1996).

Most peneplains were described prior to 1960's and derive solely from field observations and topographical maps. Mainly in the last two decades, new techniques are used to investigate peneplains such as thermo- and geochronological tools (e. g. Jordan et al., 1989; Lamb et al., 1996; Gunnell et al., 2009), cosmogenic nuclides (e. g. Jackson et al., 2002; Hetzel et al., 2011; Strobl et al., 2012) or geospatial data analysis (e. g. Babault et al., 2005; Hoke and Garzione, 2008; Strobl et al., 2010).

What is common in all above mentioned studies is the observation of distinctive elevated and flat surfaces, regardless of their geological history and age. Existing definitions of peneplain are diffuse and still intensely discussed. As a consequence, it is nearly impossible to outline peneplains in a reproducible way. It is thus inevitable to redefine this remarkable geomorphological structure in order to enable their unbiased identification and to foster a deeper understanding of the peneplains and the multiple possibilities for their origin.

In this study, peneplain is used as a descriptive term in contrast to the controversially discussed definition of Davis (1899) as a genetic term. Until yet the minimum uplift of peneplains relatively to their surrounding landscape is not defined. We focus onto peneplains which is uplifted relatively to their surrounding landscape by at least of 100 m. The minimum specification is not a sharp number so we assume the likelihood decreases continuously with decreasing relative elevation towards zero.

Peneplain is referred to a distinctively elevated landform having almost plain top with a slope less than 15°. It might be slightly tilted or incised due to tectonic activity and/or advanced erosion. To a certain degree, erosion may degrade the plain surface, but no well developed valley system or intersecting river system can be found on an intact peneplain. It is not necessarily the highest geomorphological unit in a mountain range; young tectonics or volcanism may create local heights above a peneplain. In this study we look at peneplains from the perspective of surface morphology. We characterize peneplains as distinct morphological units which can be defined by geomorphometric parameters. This allowed us to develop a simple and general model for delineation of peneplains using parameters derived from a digital elevation models (DEM). For the definition of the morphological criteria we use data for the central part of the Tibetan Plateau for which ground observations are available. Validity and reproducibility of this geospatial approach is tested in various geological settings in different parts of the world by comparison with peneplains described in literature.

5.3 Geological setting and characterization of the peneplains north of Nam Co, central Tibet

The central Tibetan Plateau near Nam Co is dominated by well developed and preserved peneplains we could confirm during our field investigations (FIGURE 5.1). We have developed the peneplain identification method in this area, thus we give a brief description of the geology and geomorphology of the region.

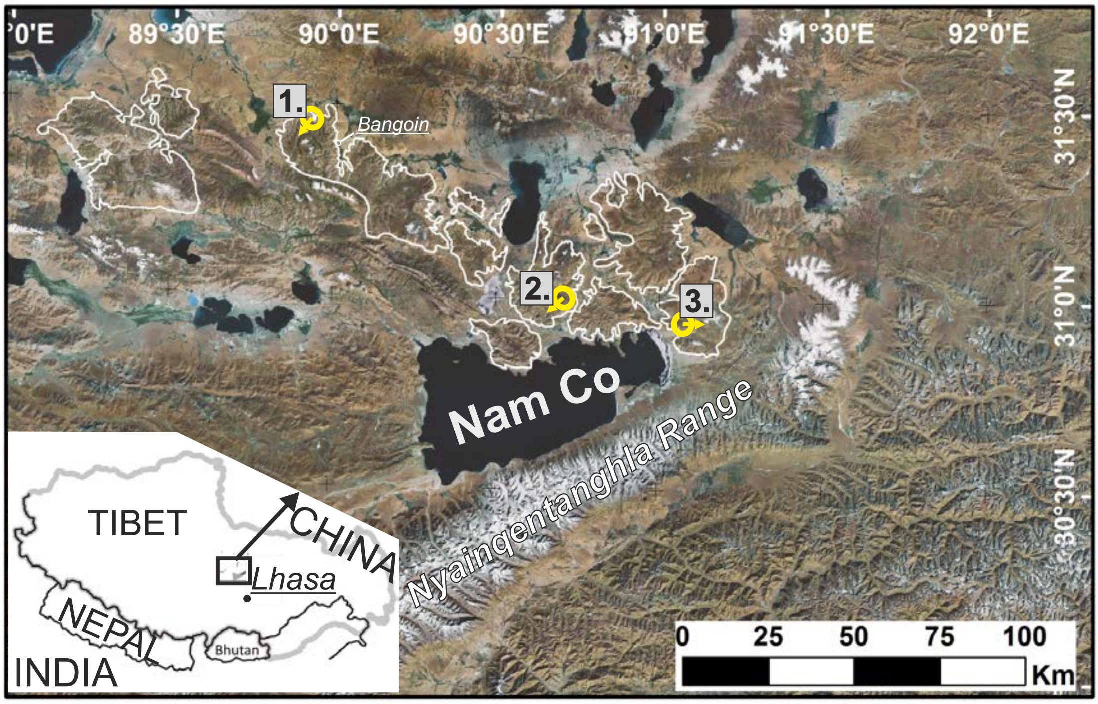

Figure 5.1: Landsat map showing land surface of the study area in central Tibet, the assumed peneplains (contoured with white line North and North West of Nam Co) and flag of taken images as examples of evidenced peneplains (yellow circles with streaks showing the directions of images of FIGURE 5.2). The assumed peneplains were determined by field observation and by the rough analysis of the available topographic maps.

The Tibetan Plateau is the highest and with $\sim$ 2 million km^2 the largest plateau on Earth. More than 90 % of the plateau has an elevation between 4,800 m and 5,400 m, and a relief of less than 1 km at a wavelength of about 100 km (Fielding et al., 1994). An internal drainage system is progressively filling the intramontane basins by sediments eroded from the adjacent mountains (e. g. Métivier et al., 1998; Liu-Zeng et al., 2008). The highly uplifted Tibetan Plateau is the result of collision of India and Asia that generated the thickened crust (Patriat and Achache, 1984).

The study area is situated in Central Tibet, along the northern boundary of the southernmost accreted terrane, the Lhasa terrane. We studied the landscape north of Nyainqentanghla mountain range near lake Nam Co, where elevated flat surfaces (FIGURE 5.1, FIGURE 5.2) with low relief are carved into mostly granitic bedrock (Clark et al., 2004; Strobl et al., 2010, FIGURE 5.3). The elevation of this area is generally above 4,600 m. The Nyainqentanghla mountain range is bordering the area in the south (FIGURE 5.2). South to south-east of this mountain range, the Tibetan Plateau is highly dissected and a well developed river system drains the area towards the ocean. Thus the general geomorphological features of the area south-east and north-west of Nyainqentanghla range are highly different: young and steep topography in the south with a high density of river network and old, passive, and smooth topography with lakes in the north (FIGURE 5.2). The peneplains are carved mainly in a Cretaceous granitoid suite and in Jurassic metasediments (Jixiang et al., 1988; Leeder et al., 1988; Leier et al., 2007a). Peneplains west of the study area are carved also in Paleozoic metasediments (Pan et al., 2004).

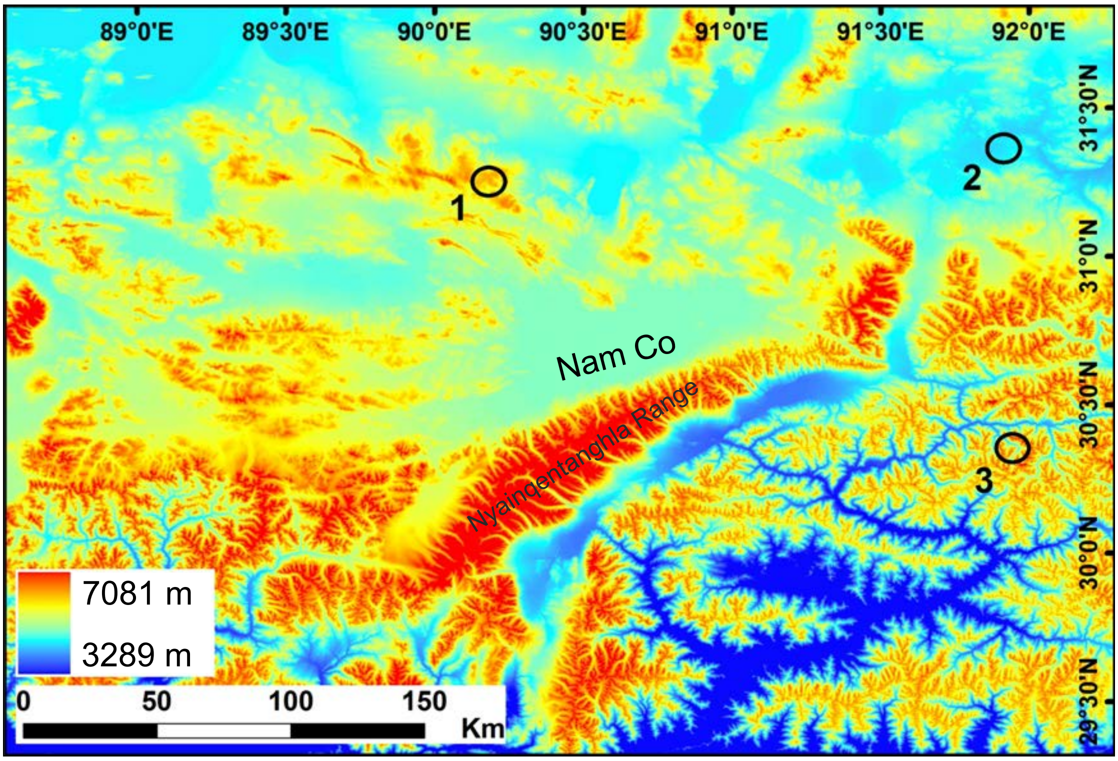

Figure 5.2: SRTM raster image used for modeling of the topography; the elevation of the area is ranging from 3,300 m to nearly 7,100 m. The black circles represent areas, which were sampled for detailed DEM analysis. All three circles have the same size of 10737 data points and represent three different geomorphologic areas; circle 1: "peneplain", circle 2: "average plateau", circle 3: "steep and dissected area". We used the metadata from these circles for detailed statistical analysis (see FIGURE 5.5, FIGURE 5.8).

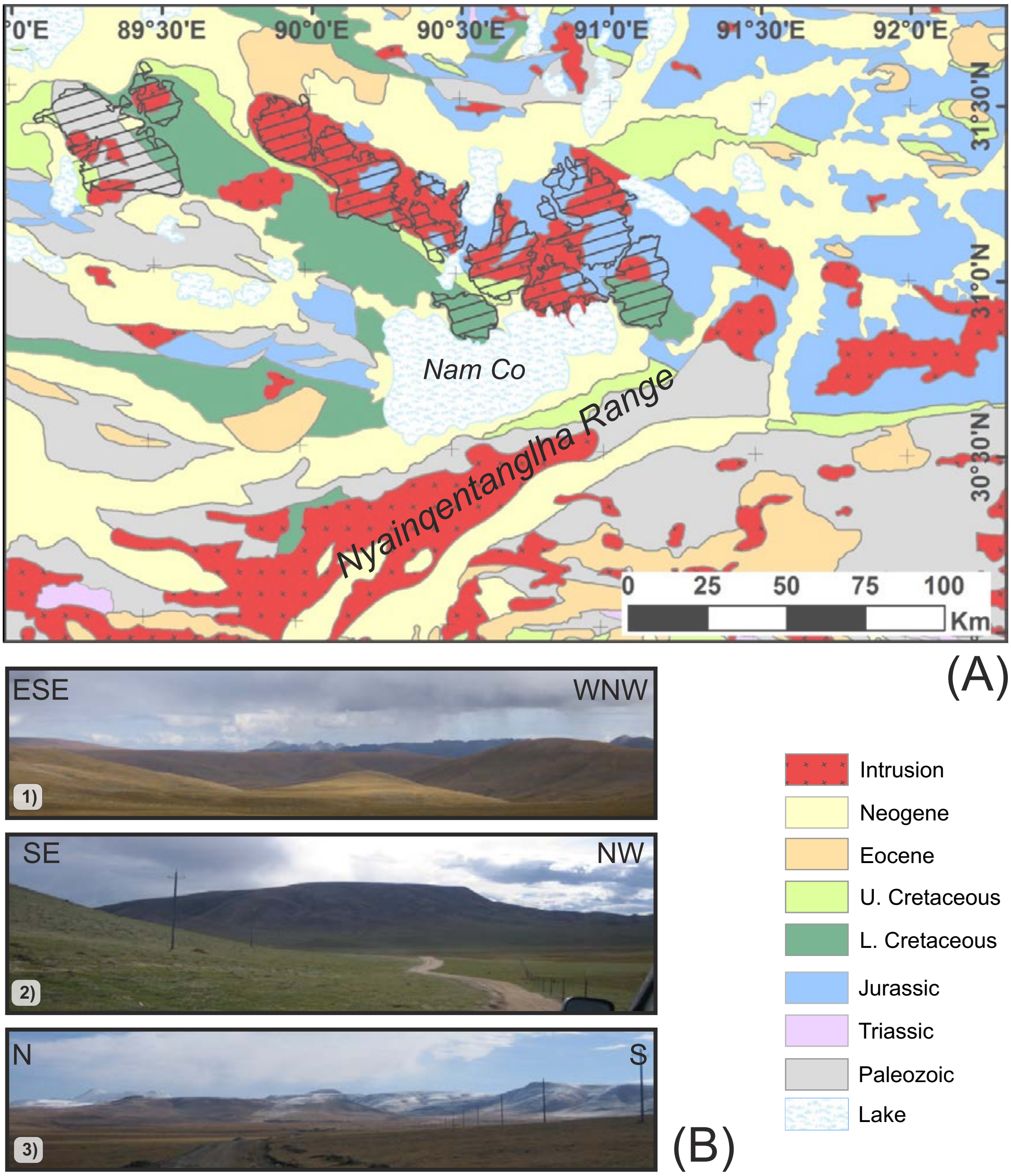

Figure 5.3: A: Assumed peneplains (hatched areas) plotted on the geological map of the study area. The local geology does not have impact on the development of peneplains; they are formed both in granitoids and in (meta-) sedimentary formations. B: Landscape photographs of peneplains from three different areas of the field; see locations in FIGURE 5.1. Images **1** and **2** display peneplains carved into Cretaceous granitoids while image **3** shows peneplains formed in Cretaceous volcano-sedimentary sequence.

5.4 Materials and Methods

5.4.1 The Shuttle Radar Topography Mission (SRTM) DEM

The SRTM provides digital elevation model of unprecedented quality for the international community (Farr and Kobrick, 2001; Farr et al., 2007). The data was acquired during an 11 days mission of Endeavor Space Shuttle in February 2000. The single path radar interferometry at C-band recorded the topography of the Earth between latitudes 60°N and 57°S. The data is freely available on the Internet. The original SRTM DEM denoted commonly as SRTM version 3 which was assembled by Jet Propulsion Laboratory contains a certain amount of gaps in areas of radar shadows and low. In this study, we used the gap-filled version denoted as SRTM version 4 (Reuter et al., 2007; Jarvis et al., 2008). The SRTM is available at a pixel resolution of 3 arc seconds (90 m at the equator).

5.4.2 Processing of the SRTM data: The Peneplain Analyzing Tool (PAT)

We perform the GIS analyses using ArcGis Info 9.3 and Arc Tool Spatial Analyst. As spatial reference system, we use UTM projection and WGS84 datum. Depending on the size of analyzed area, we assemble several image tiles into a single mosaic. In the following step we fill-up the basin-like artifacts using a standard procedure of ArcGis where the tool iterates until all sinks are filled (Tarboton, 1997). This procedure is necessary to enable an automatic and representative identification of drainage structure in the following step (FIGURE 5.4A). The pixel resolution of 3 arc seconds persists through the complete modeling procedure.

We implement the new PAT based on derivation of multi-assessment parameters in an interactive environment of ArcGis Modelbuilder. FIGURE 5.4A displays a schematic overview about the structure of PAT. We always perform the raster analysis using the smallest floating window namely three by three pixels to keep the high resolution of the original DEM through the complete modeling procedure. Only at the focal statistics in the last step of the modeling procedure the floating window size is expanded to 55 by 55 pixels. This results in compact areas that are needed for visualization of possible peneplains in the final map.

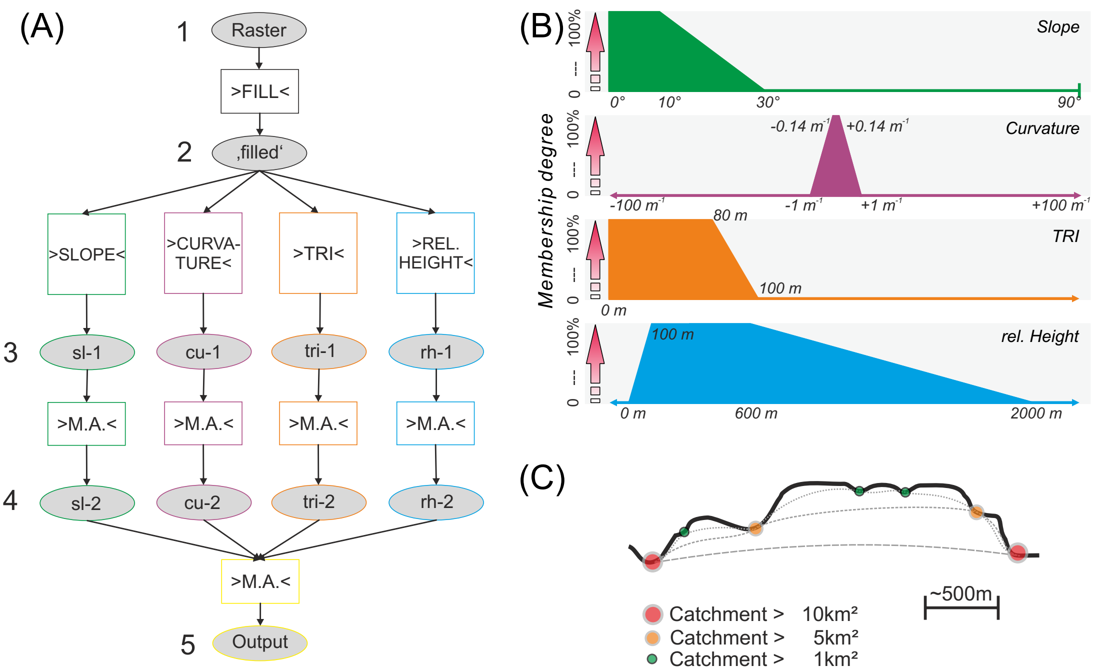

Figure 5.4: (A) Schematic workflow chart developed for the identification of peneplains. 1. input, 2. closure of the erroneous small pixel holes and gaps in raster, 3. meta output of four calculation strings (slope, curvature, terrain ruggedness index, and relative height), 4. converting meta output to appropriate raster set with fuzzy logic method and map algebra (>M.A.<), 5. output of final map after multiplication of all four meta raster with map algebra. (B) Fuzzy logic chart of each single calculation string. Y-axis represents membership degree in percentage; the maximum value of each curve is one hundred percent, the minimum value is zero. The dashed gray lines in relative height chart represent the alternative fuzzy logic settings used for some models cutting at thresholds of 50 m and 100 m. (C) Schematic sketch outlining the effect of different threshold settings of the valley system for calculating catchments and thus calculating erosional base level (gray dashed lines). While interpolation between catchment of 10 km^2 cuts huge amount of information off, interpolation between catchment 1 km^2 has higher resolution.

5.4.3 Characterization of peneplains by geomorphometric parameters

We hypothesize that peneplains can be characterized by a set of parameters describing the morphology of a flat-top mountain. These parameters would allow us to identify peneplains in an unbiased way regardless of their genesis, geology, and geographic locationparameters. For identification of planation surfaces, we tested various morphological parameters derived from the DEM data. We searched for suitable parameters for construction of conditions in form of simple thresholds and ranges of values. Finally, we selected following four parameters : (I) slope inclination, (II) curvature, (III) terrain ruggedness index (TRI), and (IV) relative height.

We calculate all four parameters on a pixel-by-pixel basis in a floating window. None of these parameters alone can describe sufficiently the morphology of a 'flat-top' mountain. For a joint evaluation, the four parameters have to be normalized and they should be given a weight. This was accomplished using fuzzy logic (e. g. Zadeh, 1968; Santos, 1970; Biacino and Gerla, 2002). Therefore we used fuzzy logic in order to convert the magnitude of the parameters to membership degree that a pixel under consideration belongs to a peneplain. Fuzzy logic allow us to define the transition of belonging-not belonging to peneplain class by a smooth transition rather than by a hard threshold which better respect the character of the peneplain definition.
To set up the parameters, which characterize peneplains in a complete and unbiased manner, we analyze three representative test areas from basically different landscapes. Each area contains 10737 pixels sampled in a circle. In each of these three areas we select one circular sample on a well-developed peneplain, another one on a typical plateau and the third one on an area characterized by rugged mountainous relief and rapid erosion - called below as "steep and dissected area" (FIGURE 5.2). Density scatterplots show the different behavior of the datasets from the different test areas (FIGURE 5.5). While the dataset of "steep and dissected area" scatters nearly over the whole diagram, the datasets of "peneplain" and "average plateau" occupy small areas on the plots. Scatterplots of curvature versus relative height show the major difference between "peneplain" and "average plateau". With fuzzy logic it is possible to capture all data belonging to peneplains and to exclude all other data points. Fuzzy logic weights the values of each parameter individually and converts the different magnitudes into likelihood (membership degree; FIGURE 5.4B). The following geomorphometric parameters appear to be the most useful for the characterization of peneplains: slope, curvature, terrain ruggedness index and relative height.

5.4.4 Implementation of the criteria in the GIS environment

5.4.4.1 Slope (sl)

Slope inclination results as a maximum rate of change between each cell and its eight neighbor cells at the DEM. We calculate the slope inclination with standard tools (Burrough and McDonnell,

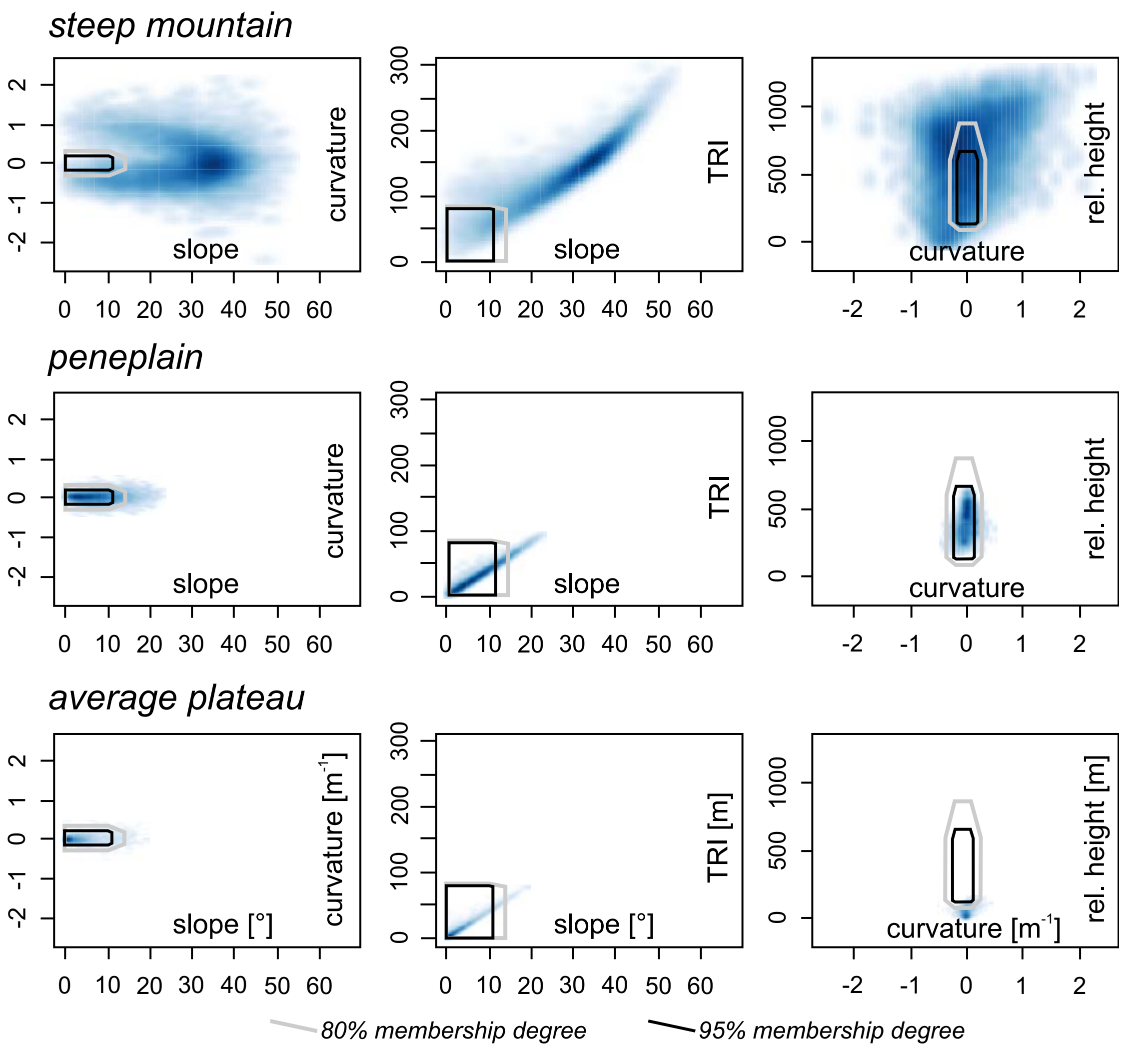

Figure 5.5: Density scatterplots from the metadata of three different areas marked in FIGURE 5.2. In each plot was generated from 10737 DEM pixels of the selected areas. Scatterplots of the upper row concerns to "steep and dissected area", while middle row represent results of "peneplain" and the lower row apply to "average plateau". Gray and black shapes in the plots outline the "high likelihood parameter field" used at fuzzy logic (see text for explanation). Data points plotting in the gray shapes have a membership degree of > 80 %, while datapoints inside the black rimed "high likelihood parameter field" hold a membership degree of > 95 %.

1998). Nevertheless, slope solely is not sufficient for detection potential peneplains because lakes and other flat areas, as e. g. alluvial basins, have low slope inclination.

Theoretically slope can vary between 0 and 90°. At the identification of peneplains primarily the low angle slope data are relevant. However, peneplains can be tilted by tectonic activity. Therefore it is unfeasible to set an explicit boundary between “still being a peneplain” and “definitely not a peneplain”. With increasing slope the likelihood of a possible presence of a peneplain decrease. Peneplains with a slope up to 10° are highly possible and becoming continuously implausible towards slope > 30° (FIGURE 5.5). Such situation can be well treated in the fuzzy logic approach. If an elevated planar surface is tilted more than 15°, it is clearly not matching any criterion considered until now at the definition of a peneplain and such surface can be disregarded.

Thus we set the fuzzy logic criteria as follows: > 30° are set 0 %; 0 - 10° are set 100 % and values from 10 to 30° change continuously from 100 to 0 % (FIGURE 5.4B). With this fuzzy logic criteria the likelihood of a peneplain with a slope of 14° is 80 %.

5.4.4.2 Curvature (cu)

Curvature for any direction is the second derivate of the surface or in other words, a function “slope of a slope” described by Peckham (2011) and Zevenbergen and Thorne (1987) and Peckham (2011). Profile and plan curvature can be calculated which are related to the concavity (negative values) and convexity (positive values) of the surface (Olaya, 2009). Zero value describes a plain surface independently of inclination. Curvature is broadly used in terrain analysis in hydrology and soil erosion studies (Zevenbergen and Thorne, 1987; Olaya, 2009; Peckham, 2011; Hurst et al., 2013). As potential parameter for PAT, curvature distinguish planar surfaces and excludes zones along mountain crests which cannot be distinguished by the parameter slope. Curvature correlates to slope in flat areas ($\sim$ 0 m^{-1} versus $\sim$ 0° slope) while the characteristics can diverge in steep realms (FIGURE 5.5). The excluded areas are generally small and easy to distinguish from potential peneplains in the final model. Additionally, it appeared that curvature is insensitive to noise of DEM data, thus it can be well used for the identification of flat areas.

Curvature characterizes peneplains with values near zero. The curvature can be high only at the rim of the peneplain, along the transition zone towards rugged, eroding areas. For the calculation of curvature we use the standard tool implemented in ArcGIS involving combined plan and profile curvature, which calculates an inverse curvature range between -100 and +100 m^{-1}. The fuzzy logic criteria: < -1.0 and > 1.0 m^{-1} are set 0 %; < -0.14 and > 0.14 m^{-1} are set 100 % and -0.14 - -1.0 m^{-1} and 0.14 - 1.0 m^{-1} respectively change linear from 100 to 0 % (FIGURE 5.4B).

5.4.4.3 Terrain ruggedness index (TRI)

The Terrain ruggedness index is the sum change in elevation between a grid cell and its eight neighbor grid cells Riley et al. (1999). It was developed to characterize surface ruggedness and quantify topographic heterogeneity such as steep and dissected area and undulating surface. We adopted the following formula for calculation of the TRI:

A compact formula for spatial analysis:

$$TRI = \sqrt{x + 9v^2 - 2vs}$$

where

x: focal sum of [DEM]$^($2)
v: focal value
s: focal sum in the floating window 3 by 3 raster cells

The active and rapid erosion is typically localized along the decaying margins of the peneplains and the internal, flat part remain intact for a longer time period, thus these areas are characterized by low TRI values. Together with curvature and slope, TRI exclude areas with surface undulations. Both, curvature and TRI behave similar in plain realms with values ranging near zero. The more rugged the topographical surface become, the higher is the variance of TRI and curvature value due to increasing TRI independently of the curvature (FIGURE 5.5).

The parameter TRI provides an opportunity to distinguish between rough geomorphology (typically the result young incision) from a flat or hilly and nearly featureless surface. While a high TRI value is characteristic to mountainous areas, flat landscapes yield low TRI numbers. The calculated TRI value can vary from zero to several hundreds of meters. We set the threshold for values involving peneplains empirically by testing different value range and analyzing the scatterplots of datasets. See discussion of this parameter in SECTION 5.4.3 and in FIGURE 5.5. The fuzzy logic criteria: Values between 0 and 80 m are accepted to describe parts of peneplains. Higher 100 m is set to 0. Between 80 and 100 m, the membership degree gradually decreases from 100 to 0 % (FIGURE 5.4B).

5.4.4.4 Relative height (rh)

Since we focus on peneplains which are uplifted relatively to their surrounding landscape by at least of 100 m we needed a suitable parameter to describe this relative height. We defined such parameter called further simply 'relative height' as elevation above local erosional base level represented by main branches of the drainage system. The erosional base level was obtained by interpolation of elevation between the branches which were detected automatically as streams with high flow accumulation. Here we used standard hydrological tools in Spatial Analyst. The purpose to introduce the "relative height" into our model is primarily to eliminate plain surfaces near local erosional base level to delimit potential peneplains. The first step in calculation of the relative height is determination of flow direction for each raster cell, which is a theoretical direction in that water, would flow out of the cell. Based on this new dataset the accumulation area can be determined for each cell by the summation of the upstream cells. In other words, it is the catchment area, which drains to the cell under examination. The next step is the calculation of a drainage system (valley network) applying a threshold for the catchment area. The erosional base level is a computed, undulating surface resulted by interpolation between the calculated drainage systems (FIGURE 5.6). It is obvious that the considered drainage network highly influences the erosional base level. The erosional base level would "follow" the surface and the relative height would be low, if we use a too detailed drainage network for interpolation. If the interpolation between the branches of the drainage system is too rough -only tributaries considered with large catchment area- then the interpolated erosional surface would remain at low elevation and in this way the large and complex peneplain areas can be well detected (FIGURE 5.4C). The resolution of the drainage system defines the size of valleys that will be considered. The more developed the drainage system, the higher is the number of accumulation in each single affected cell. With cutting out the accumulated cell numbers of the DEM smaller than 1000, 5,000, 10,000 and

50,000 corresponding to catchment areas of 8.1, 40.5, 81, and 405 km^2, a solid drainage system for further interpolations were tested. Catchment area threshold at 5,000 DEM pixels is too detailed to interpolate representative erosional base level, while using 50,000 DEM pixels cuts out to much information and smoothed the erosional base level too much (FIGURE 5.7). The threshold of 10,000 pixels resulted in the most applicable erosional base level in our test runs, thus this empirically determined value of the catchment area is used for interpolation. Relative height allows distinguishing peneplains that are elevated above their surroundings- from other flat landscapes like lakes, swamps, sedimentary basins, and low-angle alluvial fans because these are always at the erosional base level or only slightly above it.

The relative height is the vertical difference between the surface and the envelope of the erosional base level calculated according to the considered valley bottoms of the studied area. It can range between several meters and theoretically 8,848 m -the highest point of Earth. After evaluating different settings empirically, we set a threshold as follows: between 100 and 600 m, 100 %; lower 0 and higher 2,000 m, 0 %; between 100 and 0 m and between 600 and 2,000 m the membership degree change linear from 100 to 0 % (FIGURE 5.4B). This relatively high set parameter practically excludes geomorphological domains only slightly elevated above their surroundings. The reason of selecting such high threshold values derives from the geomorphology of our primary study area. In central Tibet the young brittle, extensional tectonics generated well developed “horst-and-graben” landscape, where the elevated peneplains are situated typically by a few hundreds meter above the alluvial filled basin areas. The PAT system is flexible and allows that on other areas the threshold for fuzzy logic can be set for lower values according to the intensity of young erosional or tectonic differentiation of the surface.

5.4.4.5 Evaluation of the test areas using the fuzzy logic thresholds

According to the fuzzy logic thresholds the areas of > 80 % and > 95 % likelihood are outlined on the different projection planes represented by the scatterplots of FIGURE 5.5. While most of the data of “Peneplain” test area fit into the high membership degree parameter field of all scatterplots, the relative height cut out the data of “average plateau”. Most of the dataset of “steep and dissected area” test area scatters outside of the high membership degree parameter

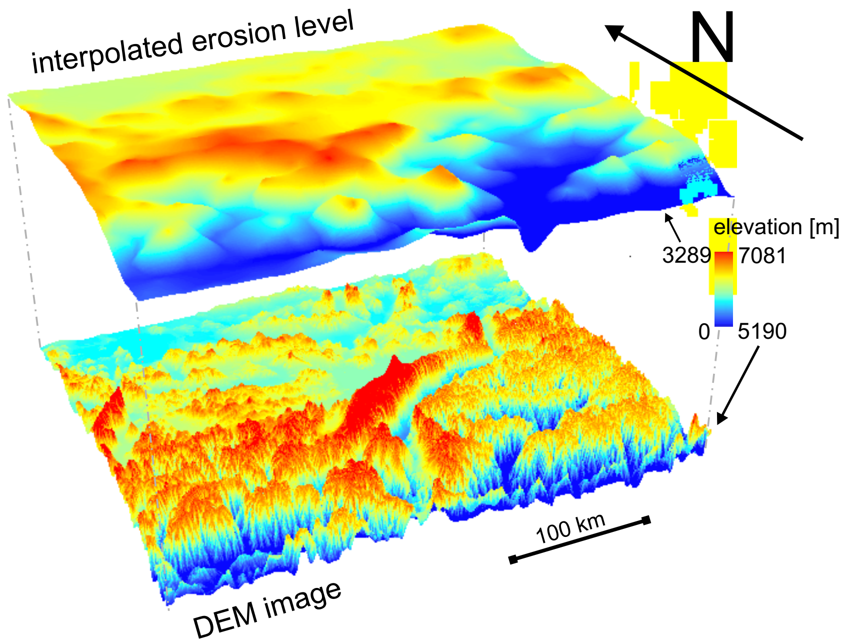

Figure 5.6: The relative height results from subtraction of interpolated erosional base level from DEM. For better visualization both layers are 20 times vertically exaggerated. The result from this specific example is given in FIGURE 5.7C, see more explanations over there.

field. After applying fuzzy logic and multiplication of all four parameters, we plot the analyzed data from the three test areas as bar plot (FIGURE 5.8). The diagram shows the membership degree of the three, geomorphologically different test areas belonging to a peneplain. The data of "steep and dissected area" spreads over the whole membership degree scale but more than 95 % have a membership degree less than 60 % and the majority of the data have a membership degree between 0 and 20 %. The data of "average plateau" has a membership degree lower than 50 % with the highest frequency at 10 %. More than 95 % of data of "Peneplain" have a higher membership degree than 80 % and the majority of the data is even above 95 %. This matching of peneplain data and the obvious misfit of the points derived from the test areas of "steep and dissected area" and "average plateau" emphasize the robustness of the above outlined DEM-based automatic identification scheme of peneplains.

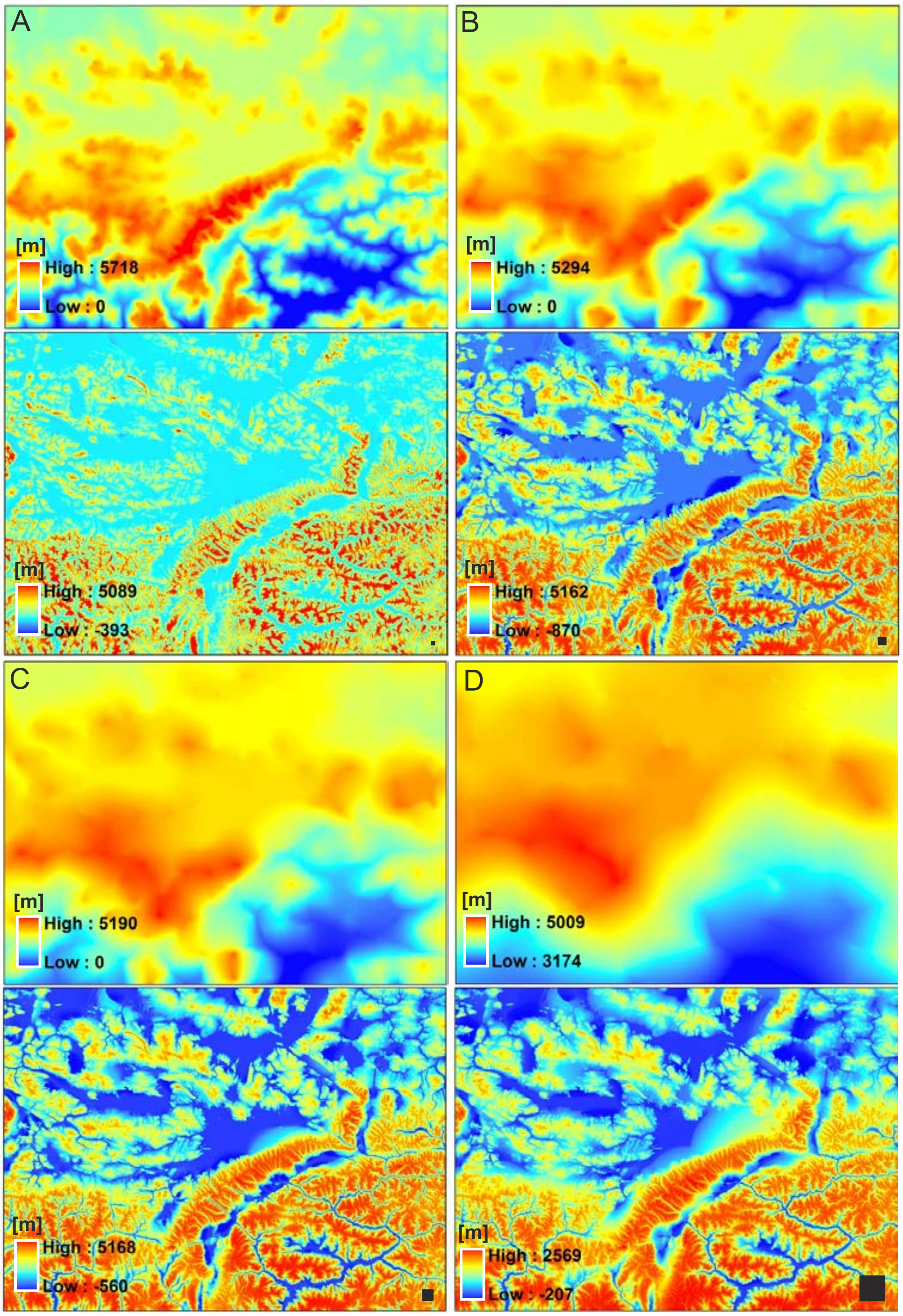

Figure 5.7: Series of images show the impact of the calculated erosional base level on the relative height (the area is introduced in FIGURE 5.1). The upper image of each set shows the erosional base level resulted by interpolation between rivers with different threshold settings. The lower image of each set shows the relative height calculated by subtraction of the interpolated erosional base level from the original SRTM digital elevation raster (FIGURE 5.1). The black square at the bottom right corner symbolizes the size of catchment area (A = 1,000, B = 5,000, C = 10,000, D = 50,000 DEM pixels) used as threshold at the determination of the drainage system for the calculation of erosional base level.

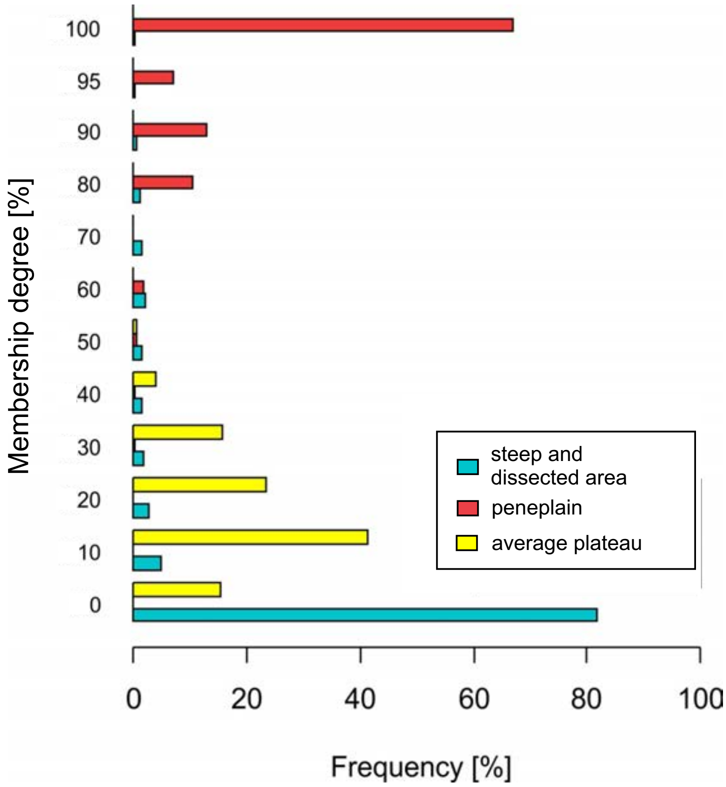

Figure 5.8: Barplot showing the membership degree distribution of the pixels of the selected circular test areas (see their position in FIGURE 5.2). The membership degree to be a peneplain is calculated by the fuzzy logic multiplication of the four parameters (further discussed in the text). The high score of "peneplain" test area and the very low score of the "high mountains" test area is obvious.

5.5 Result

5.5.1 Peneplains identified in Nam Co area in Central Tibet

Beyond the selected test areas (FIGURE 5.2), we perform the peneplain identification procedure on the entire Nam Co area, where we have been working in three field seasons and gathered geomorphological observations. Neither the single parameters, (FIGURE 5.9; upper panels), nor the fuzzy logic applied to the single parameters (FIGURE 5.9; lower panels) identify peneplains optimally. FIGURE 5.10 presents the integration of the four parameters in a single map. The final result is a map that shows the likelihood expressed as membership degree that a given area can be considered as a peneplain. Focusing on calculated peneplains with a membership degree $> 80\,\%$ in the study area, they coincide with observed peneplains in the field (see inset in FIGURE 5.10).

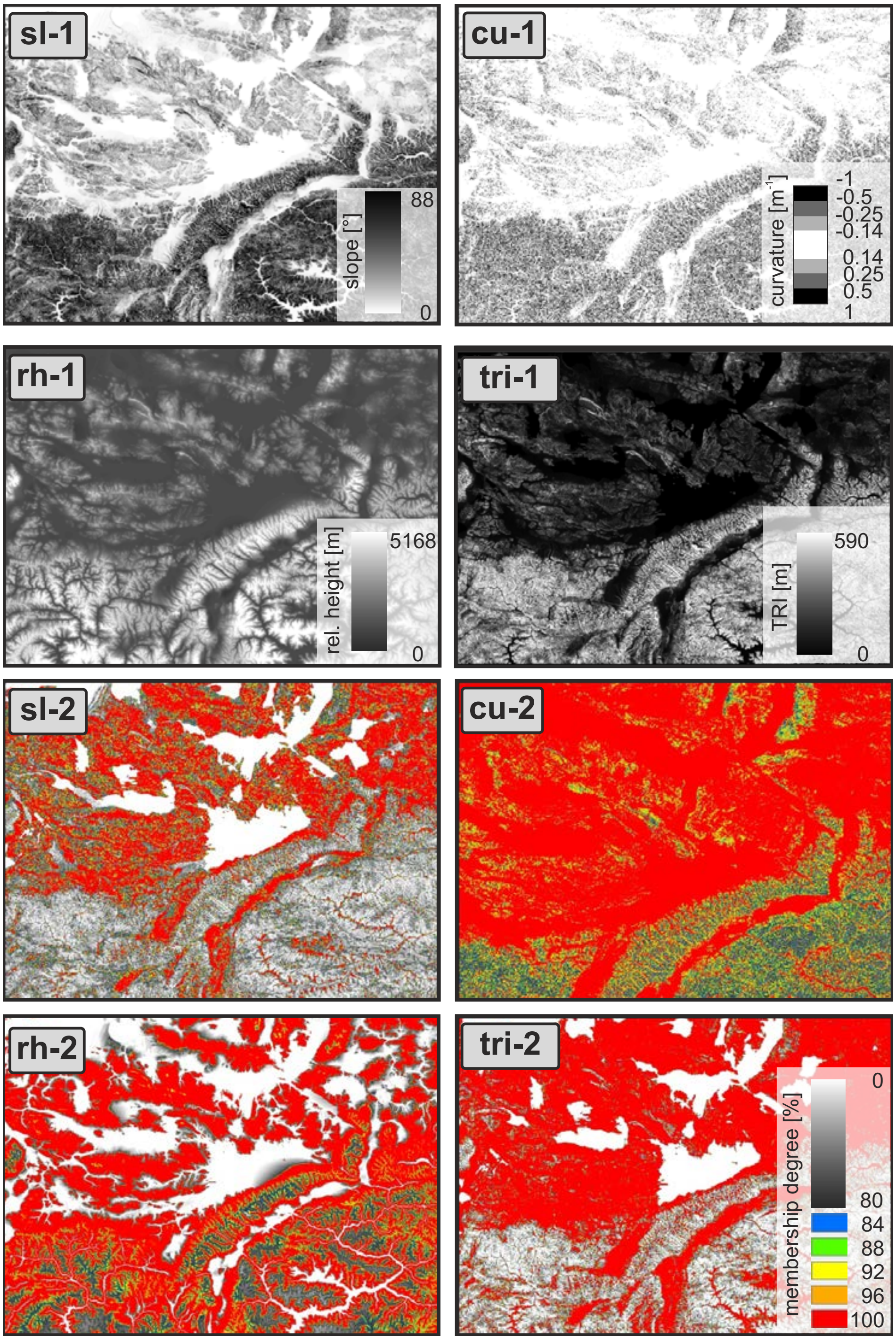

Figure 5.9: The upper panel shows the four parameters: slope (sl), curvature (cu), rel. height (rh), and terrain ruggedness index (tri) calculated for the Nam Co area -see geological map and topography of the area in FIGURE 5.1 and FIGURE 5.2. The colored maps in the lower panel present the membership degree after fuzzy logic conversion (only membership degree above 80 % are colored, the lower values remained gray-scaled).

The fuzzy logic based map of peneplains shows occurrence of peneplains not only north of Nam Co, but also in the Amdo Basement (FIGURE 5.10; right top corner). Along the Nyainqentanghla range and south of it no significant areas of peneplain character could be detected except a few small spots. In the inset image of FIGURE 5.10 the known peneplains of Nam Co are shown in detail and are compared to the rough contour of the previously assumed extent of the peneplains. The latter coincides well with the automatically identified peneplains.

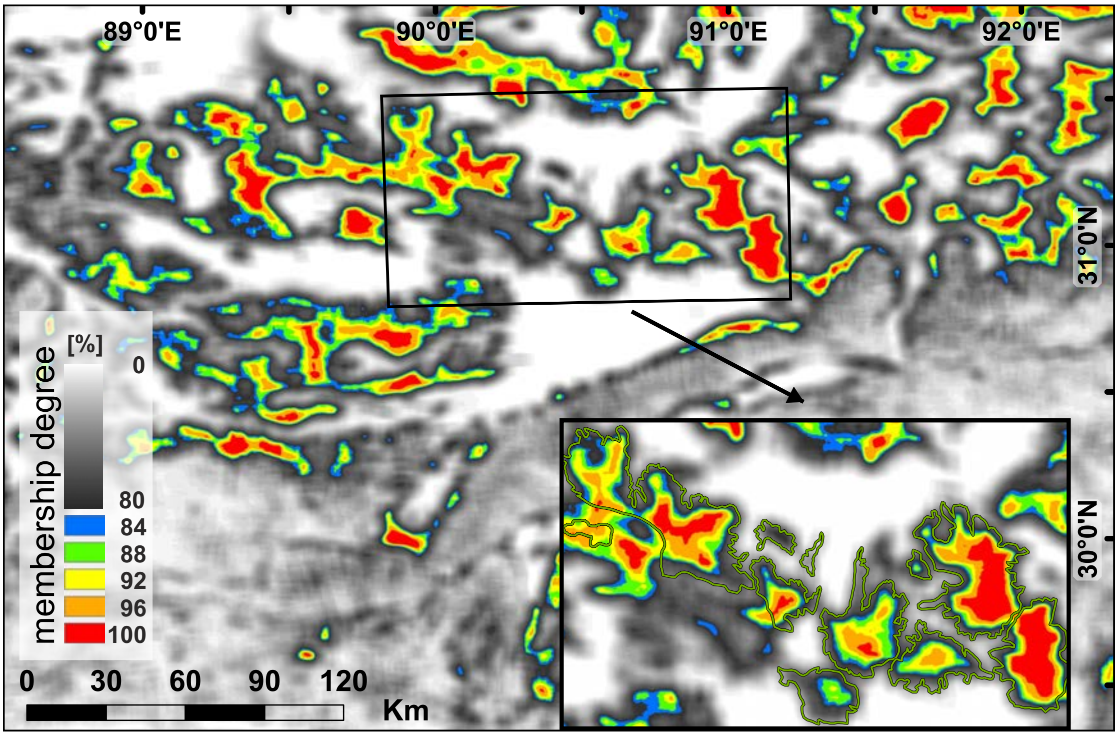

Figure 5.10: Map of the peneplains of the Nam Co area identified by the fuzzy logic integration of the four parameters (presented individually in FIGURE 5.9). Areas with a higher membership degree than 80 % are colored while the others are kept in shades of gray. The main peneplain area is zoomed in the inset (lower right). The inset shows also the preliminary contour of the peneplain (green line) according to our field observations and the evaluation of the available topographic information.

5.5.2 Verification of PAT on peneplains identified and mapped in previous studies by various authors

We tested the proposed approach at four independent areas located in the Andes, Appalachian Mountains, Pyrenees, and Southern New Zealand (FIGURE 5.11, FIGURE 5.12) where peneplains have already been identified and discussed by different authors. The same parameter settings were used for modeling of these areas that were applied in the Tibetan Plateau.

5.5.2.1 Andes

In the Central Andes in the region of the Altiplano numerous publications mention peneplains or elevated planation surfaces or paleosurfaces. In the northern area peneplains were described by e. g. Kummel (1948) and Campbell et al. (2006), while examples in the south are given by e. g. Jordan et al. (1989) and Hoke and Garzione (2008). In the Central Andes in northern Chile and Bolivia, Lamb et al. (1996) mentioned, among others, peneplains in the Eastern Cordillera around Juan de Oro Basin. Kennan et al. (1997) also studied the Eastern Cordillera and used for the observed geomorphology the expression “highly elevated plain surface”. Hoke et al. (2007) mentioned pediments and paleosurfaces. Further south in Sierras Pampeanas Jordan et al. (1989) studied peneplains from thermochronological point of view. Galli-Olivier (1967) and Muñoz et al. (2008) investigated peneplains in the Tarapacá Region (N-Chile), whereas Galli-Olivier (1967) interpreted the observed geomorphology as pediplain. Allmendinger and González (2010) started the modern deformation cycle with a long period of erosion that culminated in a regional surface as the Tarapacá peneplain.
PAT detects peneplains along the coast and also in several spots in the highly elevated parts of the orogen (FIGURE 5.11A). Peneplains along the coast outline the ramp-like piedmont areas between the Western Andean Escarpment and the Coastal Cordillera in northern Chile and southern Peru (e. g. Wörner et al., 2002; Schildgen et al., 2009). Notably, peneplains on the Altiplano typically scatter around the basins. A well-studied peneplain is the Tarapacá Peneplain between Altiplano and Atacama Desert (FIGURE 5.11A), which is also clearly identified by PAT. Using PAT in the Andes gives a good example for gaining additional valuable information. The intramontane basins and big lakes as Lake Titicaca are correctly classified as non-peneplain although they share many characteristics (slope, ruggedness and curvature) with peneplains. However, the relative height is low in these geomorphological domains, thus PAT classifies the intramontane basins in the Altiplano or in the Atacama area with a very low membership degree (around zero percent).

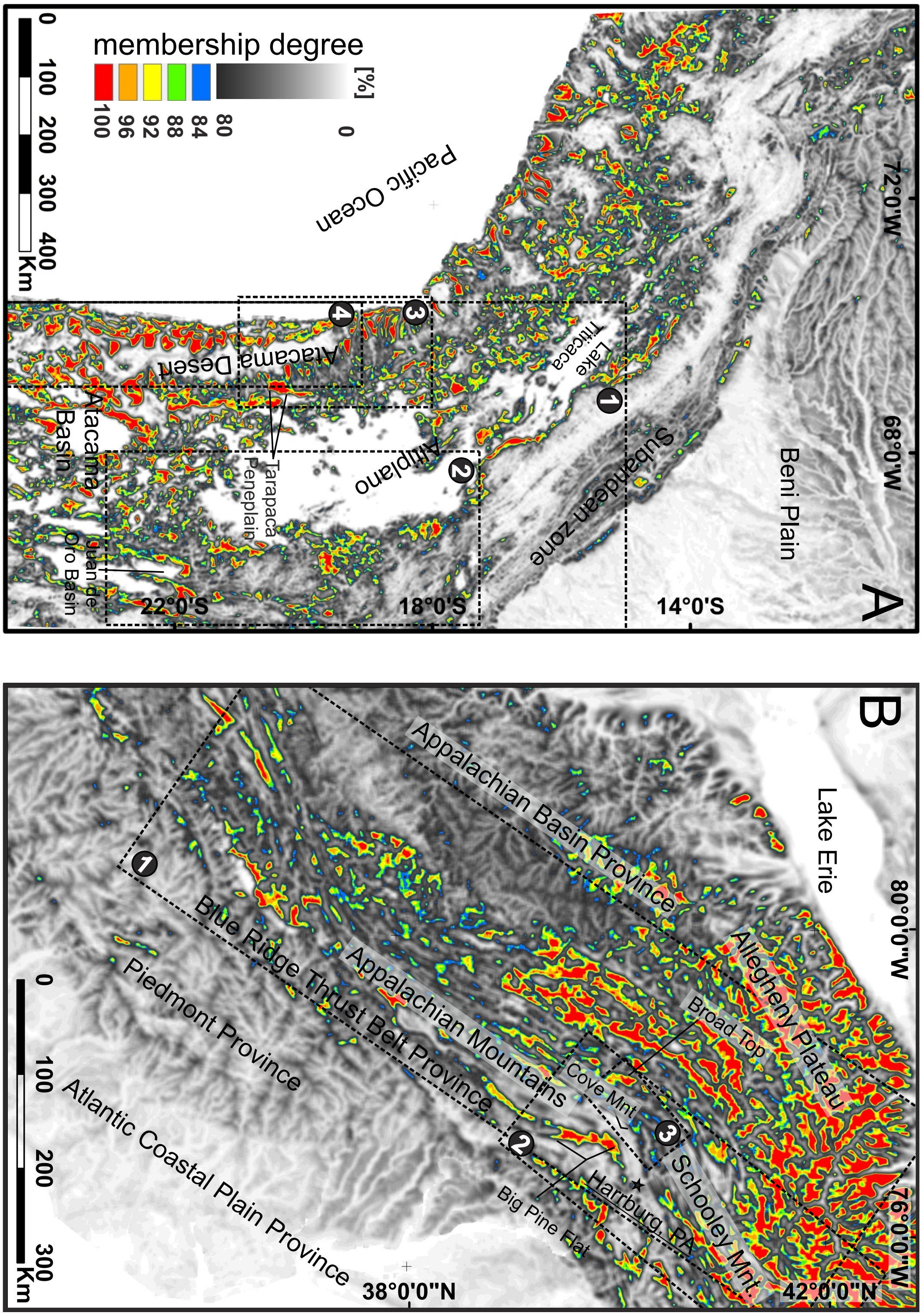

Figure 5.11: Peneplains and their membership degree identified by the PAT method in the Andes (A) and in the Appalachian Mountains (B). Rectangles with dotted lines allocate the formerly studied peneplain-bearing areas by different authors. Andes: **(1)** Lamb et al. (1996), **(2)** Kennan et al. (1997), **(3)** Allmendinger and González (2010), **(4)** Muñoz et al. (2008). Appalachian Mountains: **(1)** Davis (1899); White (2009), **(2)** Stose (1940), **(3)** Bethune (1948)

5.5.2.2 Appalachian Mountains

William Davis studied intensely the morphology of Appalachian Mountains before introducing the term peneplain the first time (Davis, 1899, 1902). He investigated his Geographical Cycle and peneplains in the whole Appalachian Mountains but focused mainly on the northern part. Therefore we selected this area to test our new model (FIGURE 5.11B). The Appalachian Mountains cross the eastern part of USA from NNE to SSW. Allegheny Mountain forms the northwestern part of the Appalachian Mountains bordering to the Appalachian Basin Province and the Allegheny Plateau. In this area many studies were performed about peneplains in the first half of the twentieth century (e. g. Fridley and Nölting Jr., 1931; Cole, 1934; Smith, 1935). The Schooley Mountains are the northeastern part of Appalachian Mountains. Peneplains from this area were described by many studies (Hou et al., 2004; Stose, 1940, and references therein; Bethune, 1948; Hack, 1975; Sevon et al., 1983; White, 2009). Stose (1940) discussed the age of peneplains in Schooley Mountains. Bethune (1948) did not study peneplains actively but accepted the peneplains as part of the Schooley Mountains and part of the Davisian Cycle. He proposed the hypothesis that the Appalachian drainage was substantially reorganized at the time of uplift of the "Schooley peneplain". Hack (1975) evaluated the theory of Davis (1899) in the Appalachian Mountains around Harrburg and studied the principle of dynamic equilibrium in multiple erosion cycles forming landscape features. Hack (1975) challenges the peneplain concept as genetic expression and accepts it as definition of true erosion in a broader understanding of Earth surface processes.

We use PAT to identify the peneplains in the Appalachian Mountains. Several peneplains especially on the northwestern rim of the Appalachian Mountains and some near the border to the Blue Ridge Thrust Belt Province in the east were detected. PAT spots the highest density of peneplains in the northern part of Allegheny Mountains. The well studied Schooley peneplains are considered as remnants of old peneplains (e. g. Stose, 1940; Hack, 1975; White, 2009). PAT recognizes all distinctive peneplains with a minimum relative elevation of 80 m in this area (FIGURE 5.11B; RECTANGLE NR. 3). The main reason for rare detection of peneplains compared to the published observations is the high threshold setting of relative height in the PAT.

Nearly leveled peneplains with an elevation lower than 80 m are not considered in this PAT in first instance. The possible impact on the results of the different relative height threshold is discussed at the case study from New Zealand (see below).

5.5.2.3 West Europe

For identification of peneplains we also selected an area in western Europe (FIGURE 5.12A) because of (I) the controversial discussions on the development of the peneplains in the Pyrenees (Babault et al., 2005, 2007; Gunnell et al., 2009; Sinclair et al., 2009), and (II) the presence of well developed peneplains in the Massif Central, France (e. g. Simon-Coinçon et al., 1997).
The Massif Central forms an exhumed part of the European Variscan basement. After erosion to a peneplain and a marine transgression the area was reactivated during Alpine orogeny (Zeyen et al., 1997). Baulig (1957) and Simon-Coinçon et al. (1997) discussed the occurrence of peneplains as paleosurface from Tertiary time. Beneath the Massif Central mantle plume activity was detected (Granet et al., 1995), which is considered responsible for the continuous uplift of the Massif Central. Our PAT analysis detects several potential peneplains in the area of the Massif Central (FIGURE 5.12A).Further potential peneplains were detected south of the Ebro basin.
In the Pyrenees peneplains were described by DeSitter (1952); Babault et al. (2005); Gunnell et al. (2009) and Sinclair et al. (2009). Babault et al. (2005) considered peneplanation in the highly elevated areas of Pyrenees as a result of long-term erosion processes that smooth relief even at high elevation. Gunnell et al. (2009) related the highly elevated flat topography in the E-Pyrenees to “the resurrection of a mountain belt which prior to the $\sim$ 12 Ma was a low-relief landscape, or peneplain, beveling eroded stumps of the Pyrenean compressional orogen”.
Our modeling using PAT could not detect proper developed peneplains in the Pyrenees. It identifies only some minor areas with a membership degree mostly less than 92 %. Those can be eventually discussed as remnants of old peneplains.

5.5.2.4 South New Zealand

Peneplains in the south of New Zealand belong to the most studied peneplains worldwide. Several authors described and investigated peneplains directly or indirectly in the southern part of New

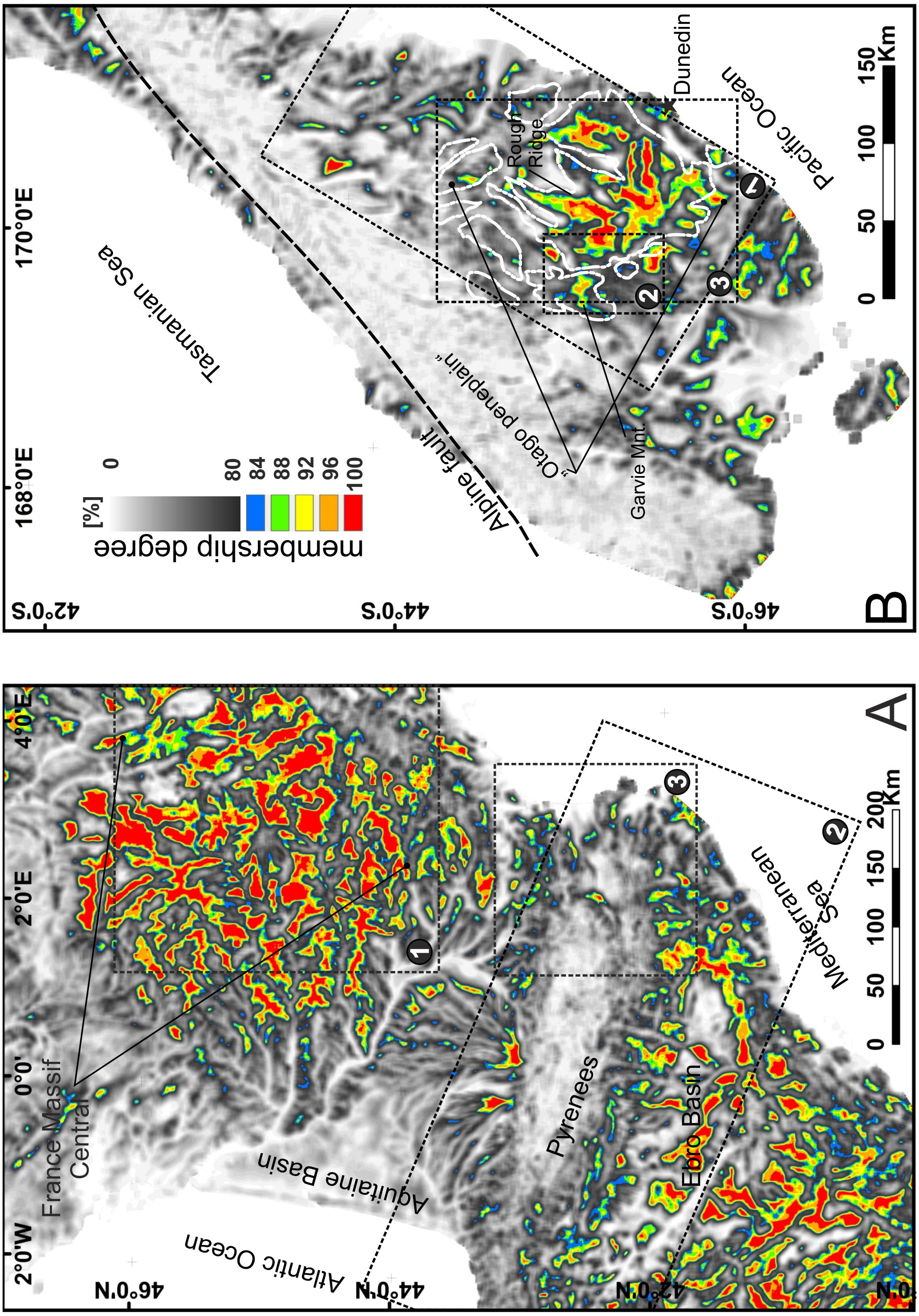

Figure 5.12: Peneplains and their membership degree identified by the PAT method in north-eastern Iberia and in the Massif Central (A), and in the southern part of New Zealand (B). White lines highlight the peneplains mapped by Jackson et al. (1996). Rectangles with dotted lines show the peneplains discussed by other authors. North-eastern Iberia and Massif Central in France: **(1)** Simon-Coinçon et al. (1997), **(2)** Babault et al. (2005), **(3)** Gunnell et al. (2009). New Zealand: **(1)** Adams (1980), **(2)** Stirling (1991), **(3)** Jackson et al. (1996). Color scale is shown in FIGURE 5.5

Zealand in the region of Otago (e. g. Coombs et al., 1960; Adams, 1980; Stirling, 1991; Jackson et al., 1996; Markley and Norris, 1999; Jackson et al., 2002; Landis et al., 2008). According to Coombs et al. (1960); Stirling (1991) the peneplains developed in Late Tertiary, which occurs as a low-relief surface in Central Otago. The authors examined also the degree to which the peneplain has been modified by non-tectonic processes. Adams (1980) identified and outlined Otago peneplain as still visible geomorphological feature. Jackson et al. (1996) mapped peneplains in S-New Zealand.

With PAT we recognize very distinctive areas that were already classified as peneplains (FIGURE 5.12B). The calculated peneplains coincide with the roughly outlined peneplains after Adams (1980). PAT reproduces very well area-wide peneplains as it was mapped by Jackson et al. (1996, FIGURE 5.12B). Peneplains described at Rough Ridge (Jackson et al., 2002) and Garvie Mountains (Stirling, 1991) are well recognizable also in the generated peneplain-likelihood map.

5.6 Discussion and Conclusions

It was demonstrated that the peneplains identified in the study area of the central Tibetan Plateau correspond to our field observations as shown in the FIGURE 5.10. The newly developed PAT method confirms already described peneplains also in other areas such as the Massif Central (France), the central Andes, the Appalachian Mountains, and in the southern part of New Zealand. PAT was not able to identify the intensely discussed peneplains in the Pyrenees. The most likely reason is the method of allocation of peneplains in the Pyrenees. While PAT exclusively focuses on the geometry of the landscape, the peneplain-like geomorphologic domains in the Pyrenees which are controversially discussed in the literature were described fully from a genetic point of view (e. g. Babault et al., 2005; Gunnell et al., 2009).

The thresholds for three of the four criteria determined in our study can be fixed and used universally for the identification of peneplains (slope, curvature, and terrain ruggedness index). "Relative height" based on the calculated drainage system has a high potential to be adjust to calculate lower elevated peneplains or peneplains with a certain spectrum of relative elevation. Furthermore any anomalies as for example interfering depression of the DEM can be computed

(e. g. Nobre et al., 2011 and therein). Nevertheless many models were developed to simulate hydrological processes using DEMs (e. g. Tarboton, 1997; Curkendall et al., 2003; Nobre et al., 2011) and these tools provide different ways to suppress disturbing interference (e. g. O'Callaghan and Mark, 1984; Garbrecht and Martz, 1997; Jones, 2002; Nobre et al., 2011). Compared to these hydrologically relevant models our model operates at a considerably larger scale with a minimum area of around 2,000 km^2. Cell interferences at high resolution have no significant impact on our method to calculate the "relative height" and to delineate the peneplains.

However, the parameter "relative height" is sensitive and can be tuned in several cases according to the depth of modern incision and the typical relief of the region and of course the definition of the minimum height of peneplains.

There are two possibilities of the manipulation of relative height. (I) The drainage network can be set to be coarse or fine which results in a smooth/flat or undulating base level, respectively. Using fine drainage network (considering also small catchments) the calculated erosional base level "follows" well the topography and, thus, the relative height remains always small. Using a coarse drainage network (only the well developed branches of the drainage system) the relative height increases and the elevated surfaces become easier to identify (see also FIGURE 5.7). (II) The second possibility. i. e. adjusting the "relative height" criteria to the typical local relief (to the altitude of peneplain relatively to the regional erosion level), is to set the 100 % acceptance of the fuzzy logic. The most robust acceptance value that was determined in central Tibet is the range of 100 to 600 m and this range works well in several other settings worldwide. However, when the peneplain experienced only minor uplift the acceptance range should be reduced. Our applications of the PAT method in different areas worldwide show that it is possible to set the thresholds in such a way, that the regional characteristics are accounted for and the peneplains are successfully identified.

We conclude that it is possible to set up a representative criteria system to identify peneplains using solely morphometric parameters derived from a digital elevation data. It appears that only a coincidence of multiple criteria can lead to a successful delineation of geomorphological features, which can be classified as peneplains. The global availability of the homogeneous DEM allows the application of this approach on the regional scale independently of the geographical location.

The peneplains identified by the fuzzy logic model in various geological settings appear to be in a good accordance with the findings described in the literature. This strongly corroborates our assumption that peneplains can be characterized in a uniform way regardless of their age, elevation or geographical location. However this approach can lead to certain mis-match with peneplains described in the literature in cases when purely genetic criteria were employed for their identification. A favorable side effect of modeling with PAT is the additional highlighting of extensive intramontane basins (see FIGURE 5.11A). The PAT method was shown to be a robust new approach to identify and validate peneplains. An unbiased definition and delineation of peneplains is a fundamental step that allows for further systematic investigating peneplains with respect to their genesis, age, and geological structure on the regional scale. The proposed method can thus contribute to better understanding of this intensely discussed geomorphological phenomenon.

6 Summary

This thesis has discussed the formation and decay of the peneplains in the central part of the Tibetan plateau. The main objective was the usage of thermochronological methods such as AHe and AFT to set up an exhumation model and gain insights into the formation of these peneplains. The investigations also involved the sediments overlying and surrounding peneplains in order to receive additional information about the decay of this geomorphological, instable formation. Since its first description in the literature, a lot of discussions have been going on about the definition of the concept of peneplains. Therefore, a geospatial approach was developed to define peneplains objectively from a geomorphometrical point of view.

Geochronological investigations of the Bangoin batholith complex reveal two major granitoid emplacement periods at around 118 Ma and 85 Ma. Zircon (U-Th)/He cooling ages cluster around 75 Ma and are interpreted to result from Late Cretaceous (~ 85 Ma) igneous activity leading to an overall reset in the entire study area. Apatite fission track ages between 60 Ma and 50 Ma and (U-Th)/He ages clustering between 40 Ma and 60 Ma show rather tight clusters. The confined track length data are typically uniform, and the mean track length is around $13.6\ \mu m$. Provenance analyses on detrital zircons reveal that (I) post-Jurassic sediments around the peneplains predominantly derive from the terrane itself, and (II) the continental deposits derived from small catchments.

The high density of geo- and thermochronological data of the Bangoin batholith complex and the superposed sediments with consideration of the erosion rates derived from cosmogenic nuclides studies deliver benchmarks to reproduce the evolution of the peneplains. The modeling of the thermal evolution was performed under different conditions, including a detailed sensitivity test. A performed sensitivity test of the thermal modeling procedure demonstrated that the most robust results were generated by using average age values of AHe and ZHe age data with a maximum of errors. Thermal modeling considering of all individual single grain AHe and ZHe data failed or produced unreliable or very bad fits. An unsupervised modeling confirmed the burial of the surface by Eocene sediments. The model yields a mean cooling rate of about 10°C/m.y between 65 and 50 Ma. Assuming conservative cooling rates of the paleo-geothermal-gradient of 25 to 50°C/km yields an exhumation rate of 200 - 400 m/m.y. or in other words, 0.2 mm/year. Within 15 m.y., 3 to 6 km of rock were ablated in an area bigger than 10,000 km^2. More than 30,000 km^3 were removed during this period of time. This rapid erosion and intense vertical movement practically precludes the existence or formation of a flat landscape at this time. Therefore, the period from Late Paleocene to Eocene time sets a benchmark for the onset of the planation of surfaces which are still preserved in the northern Lhasa terrane. Two arguments support the theory of a massive sediment transport out of the Lhasa terrane: (I) the lack of massive siliciclastic sediment of Paleocene to Early Eocene age (65 - 48 Ma) in the Lhasa terrane (e. g. Leeder et al., 1988; Pan et al., 2004), and (II) the erosional unconformity in the southern Lhasa block at the base of the Linzizong formation (Burg et al., 1983; Lee et al., 2009), extending about 1,000 km E-W and $\sim$ 200 km S-W. This regional unconformity separates the folded Early Cretaceous sediments from the nearly undeformed volcanic rocks of the Linzizong formation (Burg et al., 1983; Lee et al., 2009), that erupted mainly between ca. 60 and ca. 40 Ma (Yin and Harrison, 2000; Wen et al., 2008; Lee et al., 2009). As the deformed Cretaceous rocks had undergone a phase of erosion before the deposition of the Linzizong formation, the southern Lhasa block could not absorb the clastic sediments released in the peneplain region. Most probably, the sediments were transported to the ocean by large but shallow rivers. Besides the fact that peneplanation processes such as migration over large distances and erosion would have been interrupted, the rivers merely incised the bedrock at high elevation. This supports the idea that peneplains developed at low elevation, presumably near sea level but supposed at least less than 1,500 m. Low local and catchment-wide erosion rates of 6-11 and 11-16 m/m.y. within the last 100,000 years substantiate the idea of a still ongoing period of stability of the peneplain.

For the purpose of characterizing and quantifying the peneplains from the Nam Co area, a spatial method was developed to describe peneplains representatively on digital elevation models. Sequences of complex algorithms describing four critical parameters were implemented within a geographic information system. Besides (I) slope inclination and (II) curvature, (III) the criteria terrain ruggedness index (Riley et al., 1999) and (IV) relative height were implemented. This newly developed PAT method (Peneplain Analyzing Tool) is able to identify the peneplains in the Nam Co area in a reliable way; the results correspond to the field observations. As a side benefit, PAT shows good results in the detection of the sediment basins. The four chosen criteria are well suited to identify peneplains around the world within the area of SRTM. Under the same condition, PAT was also successfully tested in areas where peneplains at different elevation levels and in different realms were already under discussion. Analyses in the Massif Central (France), the central Andes, the Appalachian Mountains and in the southern part of New Zealand show a good sensitivity of the PAT.

7 Outlook

Even after a complex and extensive research, the peneplain still bears a lot of interesting and rewarding aspects to be explored for investigation.

[1] Extensive provenance analyses (detrital zircon dating, quantitative heavy mineral analysis, geochemistry) and thermochronology of the Eocene sediments north of Nagqu and south of the Nyainqentanghla range are promising concerning the investigation of sediment dispersion patterns.

[2] North of the Nam Co area the Amdo basement next to the Bangong suture zone is an interesting spot. It is still not clear in terms of the exhumation history, whether the Amdo basement is part of the Lhasa terrane or if it already belongs to the northern Qingtang terrane. A thermochronological approach would shed light onto the evolution of the Amdo basement in post-Jurassic time and could have potential to answer the question whether the suture zone is situated south or north of the Amdo basement.

[3] Peneplains were observed further west as well as northeast of the study area. Geo- and thermochronological investigation in these realms could give a more sensitive benchmark on the evolution of the peneplains.

[4] After the first run, it can be stated that PAT is a reliable tool to detect peneplains worldwide. For this study, PAT was only tested in 3 arcsec SRTM DEM. It is necessary to also test digital elevation models with a higher resolution. Further, areas north of 60°N latitude and south of

57°S latitude were excluded from this study due to the fact that SRTM were only recorded within these latitudes. Scandinavia with its old land surface is well known for featuring peneplains and it is an excellent area to test and fine-tune the tool. Additionally PAT has to be prepared for a stand alone tool in ArcGis to provide it the geomorphological and geomorphometrical community.

[5] As soon as the PAT runs out of the box, peneplains can be detected, quantified, and newly classified around the world. The PAT has potential to deliver new ideas about the evolution of peneplains in general and to provide strong starting points for new approaches.

8 Bibliography

Aalto, K. R. (2006). The Klamath peneplain: A review of J. S. Diller's classic erosion surface. *The Geological Society of America*, Geological studies in the Klamath Mountains province, California and Oregon. A volume in honor of William P. Irwin: Boulder, Colorado:451–464.

Adams, J. (1980). Contemporary uplift and erosion of the Southern Alps, New Zealand. *Geological Society of America Bulletin*, 91(1 Part II):1–114.

Aitchison, J. C., Ali, J. R., and Davis, A. M. (2007). When and where did India and Asia collide. *Journal of Geophysical Research*, 112(B5):2156–2202.

Aitchison, J. C., Davis, A. M., Badengzhu, and Luo, H. (2002). New constraints on the India-Asia collision: the lower Miocene Gangrinboche conglomerates, Yarlung Tsangpo suture zone, SE Tibet. *Journal of Asian Earth Sciences*, 21(3):251–263.

Ali, J. R. and Aitchison, J. C. (2008). Gondwana to Asia: plate tectonics, paleogeography and the biological connectivity of the Indian sub-continent from the Middle Jurassic through latest Eocene (166–35 Ma). *Earth-Science Reviews*, 88:145–166.

Allegre, C. J., Courtillot, V., Tapponnier, P., Hirn, A., Mattauer, M., Coulon, C., Jaeger, J. J., Achache, J., Schaerer, U., and Marcoux, J. (1984). Structure and evolution of the Himalaya–Tibet orogenic belt. *Nature*, 307(5946):17–22.

Allmendinger, R. W. and González, G. (2010). Invited review paper: Neogene to Quaternary tectonics of the coastal Cordillera, northern Chile. *Tectonophysics*, 495(1):93–110.

Anderson, F. M. (1902). The physiographic features of the Klamath Mountains. *The Journal of Geology*, 10(2):144–159.

Argand, E. (1924). La Tectonique de l'Asie. *13th International Geological Congress Proceedings*, 7:171–372.

Babault, J., Bonnet, S., Driessche, J. V. D., and Crave, A. (2007). High elevation of low–relief surfaces in mountain belts: does it equate to post–orogenic surface uplift? *Terra Nova*, 19(4):272–277.

Babault, J., van Den Driessche, J., Bonnet, S., Castelltort, S., and Crave, A. (2005). Origin of the highly elevated Pyrenean peneplain. *Tectonics*, 24(2):1944–9194.

Balco, G., Stone, J. O., Lifton, N. A., and Dunai, T. J. (2008). A complete and easily accessible means of calculating surface exposure ages or erosion rates from ^{10}Be and ^{26}Al measurements. *Quaternary Geochronology*, 3(3):174–195.

Baldwin, J. A., Whipple, K. X., and Tucker, G. E. (2003). Implications of the shear stress river incision model for the timescale of postorogenic decay of topography. *Journal of Geophysical Research*, 108(B3):2156–2202.

Baulig, H. (1957). Peneplains and pediplains. *Geological Society of America Bulletin*, 68(7):913–930.

Bethune, P. F. (1948). Geomorphic studies in the Appalachians of Pennsylvania. *American Journal of Science*, 246(1):1–22.

Biacino, L. and Gerla, G. (2002). Fuzzy logic, continuity and effectiveness. *Archive for Mathematical Logic*, 41(7):643–667.

Bishop, P. (2007). Long term landscape evolution: linking tectonics and surface processes. *Earth Surface Processes and Landforms*, 32(3):329–365.

Bognar, A. (2001). Criticism of Teory about Geomorphological Cycles by William Morris Davis. *Hrvatski geografski glasnik*, 63(1):183–201.

Bosboom, R. E., Dupont-Nivet, G., Houben, A. J. P., Brinkhuis, H., Villa, G., Mandic, O., Stoica, M., Zachariasse, W. J., Guo, Z., and Li, C. (2011). Late Eocene sea retreat from the Tarim

Basin (west China) and concomitant Asian paleoenvironmental change. *Palaeogeography, Palaeoclimatology, Palaeoecology*, 299(3-4):385–398.

Braun, J., van der Beek, P., and Batt, G. (2006). *Quantitative thermochronology: numerical methods for the interpretation of thermochronological data*. Cambridge University Press.

Burg, J. P., Proust, F., Tapponnier, P., and Chen, G. M. (1983). Deformation phases and tectonic evolution of the Lhasa block (southern Tibet, China). *Eclogae Geologicae Helvetiae*, 76(3):643–665.

Burrough, P. A. and McDonnell, R. A. (1998). Creating continuous surfaces from point data. *Principles of Geographic Information Systems. Oxford University Press, Oxford, UK*.

Burtman, V. S. (2000). Cenozoic crustal shortening between the Pamir and Tien Shan and a reconstruction of the Pamir–Tien Shan transition zone for the Cretaceous and Palaeogene. *Tectonophysics*, 319(2):69–92.

Campbell, K. E., Frailey, C. D., and Romero-Pittman, L. (2006). The Pan-Amazonian Ucayali Peneplain, late Neogene sedimentation in Amazonia, and the birth of the modern Amazon River system. *Palaeogeography, Palaeoclimatology, Palaeoecology*, 239(1-2):166–219.

Carlson, W. D., Donelick, R. A., and Ketcham, R. A. (1999). Variability of apatite fission-track annealing kinetics; I, Experimental results. *American Mineralogist*, 84(9):1213–1223.

Carretier, S. and Lucazeau, F. (2005). How does alluvial sedimentation at range fronts modify the erosional dynamics of mountain catchments? *Basin Research*, 17(3):361–381.

Chen, W., Zhang, Y., Ji, Q., Wang, S., and Zhang, J. (2002). Magmatism and deformation times of the Xidatan rock series, East Kunlun Mountains. *Science in China Series B: Chemistry*, 45(1):20–27.

Cherniak, D. J., Lanford, W. A., and Ryerson, F. J. (1991). Lead diffusion in apatite and zircon using ion implantation and Rutherford backscattering techniques. *Geochimica et Cosmochimica Acta*, 55(6):1663–1673.

Cherniak, D. J. and Watson, E. B. (2001). Pb diffusion in zircon. *Chemical Geology*, 172(1):5–24.

Chiu, H. Y., Chung, S. L., Wu, F. Y., Liu, D., Liang, Y. H., and Lin, I. (2009). Zircon U-Pb and Hf isotopic constraints from eastern Transhimalayan batholiths on the precollisional magmatic and tectonic evolution in southern Tibet. *Tectonophysics*, 477(1-2):3–19.

Chmeleff, J., von Blanckenburg, F., Kossert, K., and Jakob, D. (2010). Determination of the ^{10}Be half-life by multicollector ICP-MS and liquid scintillation counting. *Nuclear Instruments and Methods in Physics Research Section B: Beam Interactions with Materials and Atoms*, 268(2):192–199.

Chu, M. F., Chung, S. L., Song, B., Liu, D., O'Reilly, S. Y., Pearson, N. J., Ji, J., and Wen, D. J. (2006). Zircon U-Pb and Hf isotope constraints on the Mesozoic tectonics and crustal evolution of southern Tibet. *Geology*, 34(9):745–748.

Chung, S. L., Chu, M. F., Zhang, Y., Xie, Y., Lo, C. H., Lee, T. Y., Lan, C. Y., Li, X., Zhang, Q., and Wang, Y. (2005). Tibetan tectonic evolution inferred from spatial and temporal variations in post-collisional magmatism. *Earth-Science Reviews*, 68(3–4):173 – 196.

Chung, S. L., Lo, C. H., Lee, T. Y., Zhang, Y., Xie, Y., Li, X., Wang, K. L., and Wang, P. L. (1998). Diachronous uplift of the Tibetan plateau starting 40 Myr ago. *Nature*, 394(6695):769–773.

Clark, M. K., Schoenbohm, L. M., Royden, L. H., Whipple, K. X., Burchfiel, B. C., Zhang, X., Tang, W., Wang, E., and Chen, L. (2004). Surface uplift, tectonics, and erosion of eastern Tibet from large-scale drainage patterns. *Tectonics*, 23(1):1–20.

Clift, P. D., Vannucchi, P., and Morgan, J. P. (2009). Crustal redistribution, crust–mantle recycling and Phanerozoic evolution of the continental crust. *Earth-Science Reviews*, 97(1):80–104.

Cole, W. S. (1934). Identification of erosion surfaces in eastern and southern Ohio. *The Journal of Geology*, 42(3):285–294.

Coleman, M. and Hodges, K. (1995). Evidence for Tibetan plateau uplift before 14 Myr ago from a new minimum age for east-west extension. *Nature*, 374(6517):49–52.

Coltorti, M., Dramis, F., and Ollier, C. D. (2007). Planation surfaces in Northern Ethiopia. *Geomorphology*, 89(3-4):287–296.

Coltorti, M. and Pieruccini, P. (2000). A late Lower Pliocene planation surface across the Italian Peninsula: a key tool in neotectonic studies. *Journal of Geodynamics*, 29(3-5):323–328.

Coombs, D. S., White, A. J. R., Hamilton, D., and Couper, R. A. (1960). Age relations of the Dunedin volcanic complex and some paleogeographic implications – Part II. *New Zealand Journal of Geology and Geophysics*, 3(4):572–579.

Copeland, P., Harrison, T. M., Kidd, W. S. F., Ronghua, X., and Yuquan, Z. (1987). Rapid early Miocene acceleration of uplift in the Gangdese Belt, Xizang (southern Tibet), and its bearing on accommodation mechanisms of the India-Asia collision. *Earth and Planetary Science Letters*, 86(2):240–252.

Coulon, C., Maluski, H., Bollinger, C., and Wang, S. (1986). Mesozoic and Cenozoic volcanic rocks from central and southern Tibet: ^{39}Ar-^{40}Ar dating, petrological characteristics and geodynamical significance. *Earth and Planetary Science Letters*, 79(3-4):281–302.

Coward, M. P., Butler, R. W. H., Chambers, A. F., Graham, R. H., Izatt, C. N., Khan, M. A., Knipe, R. J., Prior, D. J., Treloar, P. J., and Williams, M. P. (1988). Folding and Imbrication of the Indian Crust during Himalayan Collision [and Discussion]. *Philosophical Transactions of the Royal Society of London. Series A, Mathematical and Physical Sciences*, 326(1589):89–116.

Cowgill, E., Yin, A., Harrison, T. M., and Xiao-Feng, W. (2003). Reconstruction of the Altyn Tagh fault based on U–Pb geochronology: Role of back thrusts, mantle sutures, and heterogeneous crustal strength in forming the Tibetan Plateau. *Journal of Geophysical Research: Solid Earth (1–28)*, 108(B7).

Cui, Z., Gao, Q., Liu, G., Pan, B., and Chen, H. (1997). The initial elevation of palaeokarst and planation surfaces on Tibet Plateau. *Chinese Science Bulletin*, 42(11):934–939.

Curkendall, D. W., Fielding, E. J., Cheng, T., and Pohl, J. M. (2003). A computational-grid based system for continental drainage network extraction using SRTM digital elevation models.

In *International Conference on: Parallel Processing Workshops, 2003. Proceedings.*, pages 181–190.

Dahl, P. S. (1997). A crystal-chemical basis for Pb retention and fission-track annealing systematics in U-bearing minerals, with implications for geochronology. *Earth and Planetary Science Letters*, 150(3):277–290.

Dai, J., Wang, C., Hourigan, J., and Santosh, M. (2013). Multi-stage tectono-magmatic events of the Eastern Kunlun Range, northern Tibet: insights from U-Pb geochronology and (U-Th)/He thermochronology. *Tectonophysics*, 599:97–106.

Dai, J., Zhao, X., Wang, C., Zhu, L., Li, Y., and Finn, D. (2012). The vast proto-Tibetan Plateau: New constraints from Paleogene Hoh Xil Basin. *Gondwana Research*, 22(2):434–446.

Danišík, M., Migoń, P., Kuhlemann, J., Evans, N. J., Dunkl, I., and Frisch, W. (2010). Thermochronological constraints on the long-term erosional history of the Karkonosze Mts., Central Europe. *Geomorphology*, 117(1):78–89.

Davis, A. M., Aitchison, J. C., Luo, H., and Zyabrev, S. (2002). Paleogene island arc collision-related conglomerates, Yarlung–Tsangpo suture zone, Tibet. *Sedimentary Geology*, 150(3):247–273.

Davis, W. M. (1899). The geographical cycle. *Geographical Journal*, 14(5):481–504.

Davis, W. M. (1902). Baselevel, grade and peneplain. *The Journal of Geology*, 10(1):77–111.

Debon, F., Le Fort, P., Sheppard, S. M. F., and Sonet, J. (1986). The four plutonic belts of the Transhimalaya-Himalaya: A chemical, mineralogical, isotopic, and chronological synthesis along a Tibet-Nepal section. *Journal of Petrology*, 27(1):219–250.

DeCelles, P. G., Quade, J., Kapp, P., Fan, M., Dettman, D. L., and Ding, L. (2007). High and dry in central Tibet during the Late Oligocene. *Earth and Planetary Science Letters*, 253(3-4):389–401.

DeCelles, P. G., Robinson, D. M., Quade, J., Ojha, T. P., Garzione, C. N., Copeland, P., and Upreti, B. N. (2001). Stratigraphy, structure, and tectonic evolution of the Himalayan fold-thrust belt in western Nepal. *Tectonics*, 20(4):487–509.

DeCelles, P. G., Robinson, D. M., and Zandt, G. (2002). Implications of shortening in the Himalayan fold-thrust belt for uplift of the Tibetan Plateau. *Tectonics*, 21(6):1062–1086.

DeSitter, L. U. (1952). Pliocene uplift of Tertiary mountain chains. *American Journal of Science*, 250(4):297–307.

Dewey, J. F., Shackleton, R. M., Chengfa, C., and Yiyin, S. (1988). The tectonic evolution of the Tibetan Plateau. *Philosophical Transactions of the Royal Society of London. Series A, Mathematical and Physical Sciences*, 327(1594):379–413.

Dickin, A. P. (2005). *Radiogenic isotope geology*. Cambridge University Press, 2nd edition.

Ding, L., Kapp, P., and Wan, X. (2005). Paleocene–Eocene record of ophiolite obduction and initial India–Asia collision, south central Tibet. *Tectonics*, 24(3):1–18.

Ding, L., Kapp, P., Zhong, D., and Deng, W. (2003). Cenozoic volcanism in Tibet: Evidence for a transition from oceanic to continental subduction. *Journal of Petrology*, 44(10):1833–1865.

Ding, L., Yang, D., Cai, F. L., Pullen, A., Kapp, P., Gehrels, G. E., Zhang, L. Y., Zhang, Q. H., Lai, Q. Z., and Yue, Y. H. (2013). Provenance analysis of the Mesozoic Hoh–Xil–Songpan–Ganzi turbidites in northern Tibet: Implications for the tectonic evolution of the eastern Paleo–Tethys Ocean. *Tectonics*, 32(1):34–48.

Dixey, F. (1939). The Early Cretaceous Valley-floor Pene-Plain of the Lake Nyasa Region and its Relation to Tertiary Rift Structures. *Quarterly Journal of the Geological Society*, 95(1-4):75–108.

Donelick, R. A., Ketcham, R. A., and Carlson, W. D. (1999). Variability of apatite fission-track annealing kinetics; II, Crystallographic orientation effects. *American Mineralogist*, 84(9):1224–1234.

Donelick, R. A., O'Sullivan, P. B., and Ketcham, R. A. (2005). Apatite fission-track analysis. *Reviews in Mineralogy and Geochemistry*, 58(1):49–94.

Dumitru, T. A. (1993). A new computer-automated microscope stage system for fission-track analysis. *International Journal of Radiation Applications and Instrumentation. Part D. Nuclear Tracks and Radiation Measurements*, 21(4):575–580.

Dunkl, I. (2002). Trackkey: a Windows program for calculation and graphical presentation of fission track data* 1. *Computers & Geosciences*, 28(1):3–12.

Dunkl, I., Mikes, T., Simon, K., and von Eynatten, H. (2008). Brief introduction to the Windows program Pepita: data visualization, and reduction, outlier rejection, calculation of trace element ratios and concentrations from LAICPMS data. *Mineralogical Association of Canada, Short Course*, 40:334–340.

Dunkl, I. and Székely, B. (2002). Component analysis with visualization of fitting; PopShare, a Windows program for data analysis. *Geochimica et Cosmochimica Acta*, 66:201.

Dürr, S. B. (1996). Provenance of Xigaze fore-arc basin clastic rocks (Cretaceous, south Tibet). *Bulletin of the Geological Society of America*, 108(6):669–684.

Ebert, K. (2009). Terminology of long-term geomorphology: a Scandinavian perspective. *Progress in Physical Geography*, 33(2):163–182.

Ehlers, T. A., Chaudhri, T., Kumar, S., Fuller, C. W., Willett, S. D., Ketcham, R. A., Brandon, M. T., Belton, D. X., Kohn, B. P., and Gleadow, A. J. W. (2005). Computational tools for low-temperature thermochronometer interpretation. *Reviews in Mineralogy and Geochemistry*, 58(1):589–622.

Einsele, G., Liu, B., Dürr, S., Frisch, W., Liu, G., Luterbacher, H. P., Ratschbacher, L., Ricken, W., Wendt, J., and Wetzel, A. (1994). The Xigaze forearc basin: evolution and facies architecture (Cretaceous, Tibet). *Sedimentary Geology*, 90(1-2):1–32.

England, P. and Houseman, G. (1989). Extension during continental convergence, with application to the Tibetan Plateau. *Journal of Geophysical Research*, 94(B12):17561–17579.

England, P. and Searle, M. (1986). The Cretaceous-Tertiary deformation of the Lhasa block and its implications for crustal thickening in Tibet. *Tectonics*, 5(1):1–14.

Fairbridge, R. W. and Finkl Jr., C. W. (1980). Cratonic erosional unconformities and peneplains. *The Journal of Geology*, 88(1):69–86.

Farley, K. A. (2000). Helium diffusion from apatite: General behavior as illustrated by Durango fluorapatite. *Journal of Geophysical Research*, 105(B2):2903–2914.

Farley, K. A., Wolf, R. A., and Silver, L. T. (1996). The effects of long alpha-stopping distances on (U-Th)/He ages. *Geochimica et Cosmochimica Acta*, 60(21):4223–4229.

Farr, T. and Kobrick, M. (2001). The shuttle radar topography mission. *Eos Transactions AGU*, 82:47.

Farr, T. G., Rosen, P. A., Caro, E., Crippen, R., Duren, R., Hensley, S., Kobrick, M., Paller, M., Rodriguez, E., Roth, L., Seal, D., Shaffer, S., Shimada, J., Umland, J., Werner, M., Oskin, M., Burbank, D., and Alsdorf, D. (2007). The Shuttle Radar Topography Mission. *Reviews of Geophysics*, 45(2):1–33.

Fielding, E., Isacks, B., Barazangi, M., and Duncan, C. (1994). How flat is Tibet? *Geology*, 22(2):163–167.

Fitzgerald, P. G., Baldwin, S. L., Webb, L. E., and O'Sullivan, P. B. (2006). Interpretation of (U-Th)/He single grain ages from slowly cooled crustal terranes: A case study from the Transantarctic Mountains of southern Victoria Land. *Chemical Geology*, 225(1-2):91–120.

Fleischer, R. L. and Price, P. B. (1964). Techniques for geological dating of minerals by chemical etching of fission fragment tracks. *Geochimica et Cosmochimica Acta*, 28(10):1705–1714.

Frei, D. and Gerdes, A. (2009). Precise and accurate in situ U-Pb dating of zircon with high sample throughput by automated LA-SF-ICP-MS. *Chemical Geology*, 261(3-4):261–270.

Fridley, H. M. and Nölting Jr., J. P. (1931). Peneplains of the Appalachian Plateau. *The Journal of Geology*, 39(8):749–755.

Gallagher, K., Brown, R., and Johnson, C. (1998). Fission track analysis and its applications to geological problems. *Annual Review of Earth and Planetary Sciences*, 26(1):519–572.

Galli-Olivier, C. (1967). Pediplain in northern Chile and the Andean uplift. *Science*, 158(3801):653–655.

Garbrecht, J. and Martz, L. W. (1997). The assignment of drainage direction over flat surfaces in raster digital elevation models. *Journal of Hydrology*, 193(1–4):204–213.

Garcia-Castellanos, D., Cloetingh, S., and van Balen, R. (2000). Modelling the Middle Pleistocene uplift in the Ardennes–Rhenish Massif: thermo-mechanical weakening under the Eifel? *Global and Planetary Change*, 27(1):39–52.

Gehrels, G., Kapp, P., DeCelles, P., Pullen, A., Blakey, R., Weislogel, A., Ding, L., Guynn, J., Martin, A., and McQuarrie, N. (2011). Detrital zircon geochronology of pre–Tertiary strata in the Tibetan–Himalayan orogen. *Tectonics*, 30(5):1–20.

Gerdes, A. and Zeh, A. (2006). Combined U-Pb and Hf isotope LA-(MC-) ICP-MS analyses of detrital zircons: Comparison with SHRIMP and new constraints for the provenance and age of an Armorican metasediment in Central Germany. *Earth and Planetary Science Letters*, 249(1-2):47–61.

Gjessing, J. (1967). Norway's paleic surface. *Norsk Geografisk Tidsskrift*, 21(2):69–132.

Gleadow, A. J. W. (1981). Fission-track dating methods: What are the real alternatives? *Nuclear Tracks*, 5(1-2):3–14.

Gleadow, A. J. W., Duddy, I. R., Green, P. F., and Lovering, J. F. (1986). Confined fission track lengths in apatite: a diagnostic tool for thermal history analysis. *Contributions to Mineralogy and Petrology*, 94(4):405–415.

Granet, M., Wilson, M., and Achauer, U. (1995). Imaging a mantle plume beneath the French Massif Central. *Earth and Planetary Science Letters*, 136(3):281–296.

Granger, D. E., Kirchner, J. W., and Finkel, R. (1996). Spatially averaged long-term erosion rates measured from in situ-produced cosmogenic nuclides in alluvial sediment. *The Journal of Geology*, 104(3):249–257.

Green, P. F. (1981). A new look at statistics in fission-track dating. *Nuclear Tracks*, 5(1):77–86.

Green, P. F., Duddy, I. R., Gleadow, A. J. W., Tingate, P. R., and Laslett, G. M. (1986). Thermal annealing of fission tracks in apatite: 1. A qualitative description. *Chemical Geology: Isotope Geoscience Section*, 59:237–253.

Gregory, K. M. and Chase, C. G. (1994). Tectonic and climatic significance of a late Eocene low-relief, high-level geomorphic surface, Colorado. *Journal of Geophysical Research*, 99(B10):20141–20160.

Gunnell, Y., Calvet, M., Brichau, S., Carter, A., Aguilar, J. P., and Zeyen, H. (2009). Low long-term erosion rates in high-energy mountain belts: insights from thermo-and biochronology in the Eastern Pyrenees. *Earth and Planetary Science Letters*, 278(3-4):208–218.

Guynn, J. H., Kapp, P., Pullen, A., Heizler, M., Gehrels, G., and Ding, L. (2006). Tibetan basement rocks near Amdo reveal "missing" Mesozoic tectonism along the Bangong suture, central Tibet. *Geology*, 34(6):505–508.

Hack, J. T. (1975). Dynamic equilibrium and landscape evolution. *Theories of landform development*, 1:87–102.

Haider, V. L., Dunkl, I., von Eynatten, H., Ding, L., Frei, D., and Zhang, L. (2013). Cretaceous to Cenozoic evolution of the northern Lhasa Terrane and the Early Paleogene development of peneplains at Nam Co, Tibetan Plateau. *Journal of Asian Earth Sciences*, 70:79–98.

Hall, A. M., Ebert, K., Kleman, J., Nesje, A., and Ottesen, D. (2013). Selective glacial erosion on the Norwegian passive margin. *Geology*, 41(12):1203–1206.

Hancock, G. and Kirwan, M. (2007). Summit erosion rates deduced from ^{10}Be: Implications for relief production in the central Appalachians. *Geology*, 35(1):89–92.

Harris, N. B. W., Holland, T. J. B., and Tindle, A. G. (1988). Metamorphic rocks of the 1985 Tibet Geotraverse, Lhasa to Golmud. *Philosophical Transactions of the Royal Society of London. Series A, Mathematical and Physical Sciences*, 327(1594):203–213.

Harris, N. B. W., Inger, S., and Ronghua, X. (1990). Cretaceous plutonism in Central Tibet: an example of post-collision magmatism? *Journal of Volcanology and Geothermal Research*, 44(1-2):21–32.

Harrison, T., Copeland, P., Kidd, W. S. F., and Yin, A. (1992). Raising Tibet. *Science*, 255(5052):1663.

Harrison, T. M., Copeland, P., Kidd, W. S. F., and Lovera, O. M. (1995). Activation of the Nyainqentanghla shear zone: Implications for uplift of the southern Tibetan Plateau. *Tectonics*, 14(3):658–676.

He, H., Sun, J., Li, Q., and Zhu, R. (2012). New age determination of the cenozoic lunpola basin, central tibet. *Geological Magazine*, 149(1):141–145.

He, S., Kapp, P., DeCelles, P. G., Gehrels, G. E., and Heizler, M. (2007). Cretaceous-Tertiary geology of the Gangdese Arc in the Linzhou area, southern Tibet. *Tectonophysics*, 433(1-4):15–37.

Heimsath, A. M., Dietrich, W. E., Nishiizumi, K., and Finkel, R. C. (1997). The soil production function and landscape equilibrium. *Nature*, 388(6640):358–361.

Hetzel, R., Dunkl, I., Haider, V., Strobl, M., von Eynatten, H., Ding, L., and Frei, D. (2011). Peneplain formation in southern Tibet predates the India-Asia collision and plateau uplift. *Geology*, 39(10):983–986.

Hofmann, H. J., Beer, J., Bonani, G., von Gunten, H. R., Raman, S., Suter, M., Walker, R. L., Wölfli, W., and Zimmermann, D. (1987). ^{10}Be: Half-life and AMS-standards. *Nuclear Instruments and Methods in Physics Research Section B: Beam Interactions with Materials and Atoms*, 29(1-2):32–36.

Hoke, G. D. and Garzione, C. N. (2008). Paleosurfaces, paleoelevation, and the mechanisms for the late Miocene topographic development of the Altiplano plateau. *Earth and Planetary Science Letters*, 271(1-4):192–201.

Hoke, G. D., Isacks, B. L., Jordan, T. E., Blanco, N., Tomlinson, A. J., and Ramezani, J. (2007). Geomorphic evidence for post-10 Ma uplift of the western flank of the central Andes 18°30'–22°S. *Tectonics*, 26(5):1–17.

Hou, Z. Q., Gao, Y. F., Qu, X. M., Rui, Z. Y., and Mo, X. X. (2004). Origin of adakitic intrusives generated during mid-Miocene east–west extension in southern Tibet. *Earth and Planetary Science Letters*, 220(1):139–155.

Hurford, A. J. (1998). Zeta: the ultimate solution to fission-track analysis calibration or just an interim measure. *Advances in Fission-Track Geochronology*, 80:19–32.

Hurford, A. J. and Green, P. F. (1982). A users' guide to fission track dating calibration. *Earth and Planetary Science Letters*, 59(2):343–354.

Hurford, A. J. and Green, P. F. (1983). The zeta age calibration of fission-track dating. *Chemical Geology*, 41:285–317.

Hurst, M. D., Mudd, S. M., Yoo, K., Attal, M., and Walcott, R. (2013). Influence of lithology on hillslope morphology and response to tectonic forcing in the northern Sierra Nevada of California. *Journal of Geophysical Research: Earth Surface*, 118(2):832–851.

Jackson, J., Norris, R., and Youngson, J. (1996). The structural evolution of active fault and fold systems in central Otago, New Zealand: evidence revealed by drainage patterns. *Journal of Structural Geology*, 18(2):217–234.

Jackson, J., Ritz, J. F., Siame, L., Raisbeck, G., Yiou, F., Norris, R., Youngson, J., and Bennett, E. (2002). Fault growth and landscape development rates in Otago, New Zealand, using in situ cosmogenic ^{10}Be. *Earth and Planetary Science Letters*, 195(3):185–193.

Jackson, J. A. (1997). *Glossary of geology*. American Geological Institute, Alexandria and Virginia, fourth edition.

Jackson, S. E., Pearson, N. J., Griffin, W. L., and Belousova, E. A. (2004). The application of laser ablation-inductively coupled plasma-mass spectrometry to in situ U-Pb zircon geochronology. *Chemical Geology*, 211(1-2):47–69.

Jaffey, A. H., Flynn, K. F., Le Glendenin, t Bentley, W. C., and Essling, A. M. (1971). Precision Measurement of Half-Lives and Specific Activities of ^{235}U and ^{238}U. *Physical Review C*, 4(5):1889–1906.

Jarvis, A., Reuter, H. I., Nelson, A., and Guevara, E. (2008). Hole-filled SRTM for the globe Version 4. *available from the CGIARCSI SRTM 90 m Database*, 2007(June 15).

Jiang, Z., Wu, W., Zhang, Z., and Wu, S. (2002). Dating of typical basin and range tectonics in the central Qinghai-Xizang Plateau, China. Diqiu Xuebao. *Acta Geoscientia Sinica*, 23(4):289–294.

Jixiang, Y., Juntao, X., Chengjie, L., and Huan, L. (1988). The Tibetan plateau: regional stratigraphic context and previous work. *Philosophical Transactions of the Royal Society of London. Series A, Mathematical and Physical Sciences*, 327(1594):5–52.

Jones, R. (2002). Algorithms for using a DEM for mapping catchment areas of stream sediment samples. *Computers & Geosciences*, 28(9):1051–1060.

Jordan, T. E., Zeitler, P., Ramos, V., and Gleadow, A. J. W. (1989). Thermochronometric data on the development of the basement peneplain in the Sierras Pampeanas, Argentina. *Journal of South American Earth Sciences*, 2(3):207–222.

Kapp, J. L. D., Harrison, T. M., Kapp, P., Grove, M., Lovera, O. M., and Ding, L. (2005a). Nyainqentanglha Shan: a window into the tectonic, thermal, and geochemical evolution of the Lhasa block, southern Tibet. *Journal of Geophysical Research*, 110(B8):1–23.

Kapp, P., DeCelles, P. G., Gehrels, G. E., Heizler, M., and Ding, L. (2007a). Geological records of the Lhasa-Qiangtang and Indo-Asian collisions in the Nima area of central Tibet. *Geological Society of America Bulletin*, 119(7-8):917–932.

Kapp, P., DeCelles, P. G., Leier, A. L., Fabijanic, J. M., He, S., Pullen, A., Gehrels, G. E., and Ding, L. (2007b). The Gangdese retroarc thrust belt revealed. *GSA today*, 17(7):4–9.

Kapp, P., Murphy, M. A., Yin, A., Harrison, T. M., Ding, L., and Guo, J. (2003). Mesozoic and Cenozoic tectonic evolution of the Shiquanhe area of western Tibet. *Tectonics*, 22(4):1029–1038.

Kapp, P., Yin, A., Harrison, T. M., and Ding, L. (2005b). Cretaceous-Tertiary shortening, basin development, and volcanism in central Tibet. *Bulletin of the Geological Society of America*, 117(7-8):865–878.

Kennan, L., Lamb, S. H., and Hoke, L. (1997). High-altitude palaeosurfaces in the Bolivian Andes: evidence for late Cenozoic surface uplift. *Special Publication - Geological Society of London*, 120:307–323.

Ketcham, R. A. (2005). Forward and inverse modeling of low-temperature thermochronometry data. *Reviews in Mineralogy and Geochemistry*, 58(1):275–314.

Ketcham, R. A., Carter, A., Donelick, R. A., Barbarand, J., and Hurford, A. J. (2007). Improved modeling of fission-track annealing in apatite. *American Mineralogist*, 92(5-6):799–810.

Ketcham, R. A., Donelick, R. A., and Carlson, W. D. (1999). Variability of apatite fission-track annealing kinetics; III, Extrapolation to geological time scales. *American Mineralogist*, 84(9):1235–1255.

Kirby, E. and Ouimet, W. (2011). Tectonic geomorphology along the eastern margin of Tibet: Insights into the pattern and processes of active deformation adjacent to the Sichuan Basin. *Geological Society, London, Special Publications*, 353(1):165–188.

Korgen, B. J. (1995). A Voice From the Past: John Lyman and the Plate Tectonics Story. *Oceanography: the official magazine of the Oceanography Society*, 8(1):19–20.

Korschinek, G., Bergmaier, A., Faestermann, T., Gerstmann, U. C., Knie, K., Rugel, G., Wallner, A., Dillmann, I., Dollinger, G., and von Gostomski, C. L. (2010). A new value for the half-life of ^{10}Be by Heavy-Ion Elastic Recoil Detection and liquid scintillation counting. *Nuclear Instruments and Methods in Physics Research Section B: Beam Interactions with Materials and Atoms*, 268(2):187–191.

Kubik, P. W. and Christl, M. (2010). ^{10}Be and ^{26}Al measurements at the Zurich 6 MV Tandem AMS facility. *Nuclear Instruments and Methods in Physics Research Section B: Beam Interactions with Materials and Atoms*, 268(7-8):880–883.

Kummel, B. (1948). Geological reconnaissance of the Contamana region, Peru. *Geological Society of America Bulletin*, 59(12):1217–1266.

Lal, D. (1991). Cosmic ray labeling of erosion surfaces: in situ nuclide production rates and erosion models. *Earth and Planetary Science Letters*, 104(2-4):424–439.

Lamb, S., Hoke, L., Kennan, L., and Dewey, J. (1996). Cenozoic evolution of the Central Andes in Bolivia and northern Chile. *Special Publication - Geological Society of London*, 121:237–264.

Landis, C. A., Campbell, H. J., Begg, J. G., Mildenhall, D. C., Paterson, A. M., and Trewick, S. A. (2008). The Waipounamu Erosion Surface: questioning the antiquity of the New Zealand land surface and terrestrial fauna and flora. *Geological Magazine*, 145(2):173–197.

Laslett, G. M., Kendall, W. S., Gleadow, A. J. W., and Duddy, I. R. (1982). Bias in measurement of fission-track length distributions. *Nuclear Tracks and Radiation Measurements (1982)*, 6(2):79–85.

Lee, H. Y., Chung, S. L., Lo, C. H., Ji, J., Lee, T. Y., Qian, Q., and Zhang, Q. (2009). Eocene Neotethyan slab breakoff in southern Tibet inferred from the Linzizong volcanic record. *Tectonophysics*, 477(1-2):20–35.

Leeder, M. R., Smith, A. B., and Jixiang, Y. (1988). Sedimentology, palaeoecology and palaeoenvironmental evolution of the 1985 Lhasa to Golmud Geotraverse. *Philosophical Transactions of the Royal Society of London. Series A, Mathematical and Physical Sciences*, 327(1594):107–143.

Leier, A. L., DeCelles, P. G., Kapp, P., and Ding, L. (2007a). The Takena Formation of the Lhasa terrane, southern Tibet: The record of a Late Cretaceous retroarc foreland basin. *Geological Society of America Bulletin*, 119(1-2):31–48.

Leier, A. L., DeCelles, P. G., Kapp, P., and Gehrels, G. E. (2007b). Lower Cretaceous strata in the Lhasa Terrane, Tibet, with implications for understanding the early tectonic history of the Tibetan Plateau. *Journal of Sedimentary Research*, 77(10):809–825.

Leier, A. L., Kapp, P., Gehrels, G. E., and DeCelles, P. G. (2007c). Detrital zircon geochronology of Carboniferous-Cretaceous strata in the Lhasa terrane, southern Tibet. *Basin Research*, 19(3):361–378.

LeMasurier, W. E. and Landis, C. A. (1996). Mantle-plume activity recorded by low-relief erosion surfaces in West Antarctica and New Zealand. *Geological Society of America Bulletin*, 108(11):1450–1466.

Liang, Y. H., Chung, S. L., Liu, D., Xu, Y., Wu, F. Y., Yang, J. H., Wang, Y., and Lo, C. H. (2008). Detrital zircon evidence from Burma for reorganization of the eastern Himalayan river system. *American Journal of Science*, 308(4):618–638.

Lidmar-Bergström, K. (1999). Uplift histories revealed by landforms of the Scandinavian domes. *Geological Society, London, Special Publications*, 162(1):85–91.

Lindgren, W. and Livingston, D. C. (1918). The Idaho peneplain (discussion). *Economic Geology*, 13(6):486–492.

Lippert, P. C., Zhao, X., Coe, R. S., and Lo, C. H. (2011). Palaeomagnetism and ^{40}Ar/^{39}Ar geochronology of upper Palaeogene volcanic rocks from Central Tibet: implications for the Central Asia inclination anomaly, the palaeolatitude of Tibet and post–50 Ma shortening within Asia. *Geophysical Journal International*, 184(1):131–161.

Liu, Z. and Wang, C. (2001). Facies analysis and depositional systems of Cenozoic sediments in the Hoh Xil basin, northern Tibet. *Sedimentary Geology*, 140(3-4):251–270.

Liu-Zeng, J., Tapponnier, P., Gaudemer, Y., and Ding, L. (2008). Quantifying landscape differences across the Tibetan plateau: Implications for topographic relief evolution. *Journal of Geophysical Research*, 113(F4):1–26.

Ludwig, K. R. (2003). User's manual for Isoplot 3.00: a geochronological toolkit for Microsoft Excel. *Berkeley Geochronology Center Special Publication*, 4:1–70.

Lugmair, G. W. and Marti, K. (1978). Lunar initial ^{143}Nd/^{144}Nd: Differential evolution of the lunar crust and mantle. *Earth and Planetary Science Letters*, 39(3):349–357.

Ma, X. (1981). Cretaceous marine sediments of central xizang. *J. Strat.*, 5:133–138.

Marcoux, J., Girardeau, J., Fourcade, E., Bassoullet, J. P., Philip, J., Jaffrezo, M., Xuchang, X., and Chengfa, C. (1987). Geology and biostratigraphy of the Jurassic and Lower Cretaceous series to the north of the Lhasa Block (Tibet, China). *Geodinamica Acta*, 1(4-5):313–325.

Markley, M. and Norris, R. J. (1999). Structure and neotectonics of the Blackstone Hill Antiform, Central Otago, New Zealand. *New Zealand Journal of Geology and Geophysics*, 42(2):205–218.

McDermid, I. R. C., Aitchison, J. C., Davis, A. M., Harrison, T. M., and Grove, M. (2002). The Zedong terrane: a Late Jurassic intra-oceanic magmatic arc within the Yarlung-Tsangpo suture zone, southeastern Tibet. *Chemical Geology*, 187(3-4):267–277.

McMillan, M. E., Heller, P. L., and Wing, S. L. (2006). History and causes of post-Laramide relief in the Rocky Mountain orogenic plateau. *Geological Society of America Bulletin*, 118(3-4):393–405.

Métivier, F., Gaudemer, Y., Tapponnier, P., and Meyer, B. (1998). Northeastward growth of the Tibet plateau deduced from balanced reconstruction of two depositional areas: The Qaidam and Hexi Corridor basins, China. *Tectonics*, 17(6):823–842.

Meyer, H., Hetzel, R., Fügenschuh, B., and Strauss, H. (2010). Determining the growth rate of topographic relief using in situ-produced ^{10}Be: A case study in the Black Forest, Germany. *Earth and Planetary Science Letters*, 290(3-4):391–402.

Miller, C., Schuster, R., Klötzli, U., Frank, W., and Grasemann, B. (2000). Late Cretaceous-Tertiary magmatic and tectonic events in the Transhimalaya batholith (Kailas area, SW Tibet). *Schweizerische Mineralogische und Petrographische Mitteilungen*, 80(1):1–20.

Miller, C., Schuster, R., Klötzli, U., Frank, W., and Purtscheller, F. (1999). Post-collisional potassic and ultrapotassic magmatism in SW Tibet: geochemical and Sr–Nd–Pb–O isotopic constraints for mantle source characteristics and petrogenesis. *Journal of Petrology*, 40(9):1399–1424.

Mo, X., Niu, Y., Dong, G., Zhao, Z., Hou, Z., Zhou, S., and Ke, S. (2008). Contribution of syncollisional felsic magmatism to continental crust growth: A case study of the Paleogene Linzizong volcanic Succession in southern Tibet. *Chemical Geology*, 250(1-4):49–67.

Molnar, P. and England, P. (1990). Late Cenozoic uplift of mountain ranges and global climate change: chicken or egg? *Nature*, 346(6279):29–34.

Molnar, P. and Tapponnier, P. (1975). Cenozoic tectonics of Asia: effects of a continental collision. *Science*, 189(4201):419–426.

Molnar, P. and Tapponnier, P. (1978). Active tectonics of Tibet. *Journal of Geophysical Research*, 83(B11):5361–5375.

Mulcahy, M. J., Churchward, H. M., and Dimmock, G. M. (1972). Landforms and soils on an uplifted peneplain in the Darling Range Western Australia. *Soil Research*, 10(1):1–14.

Müller, W. (2003). Strengthening the link between geochronology, textures and petrology. *Earth and Planetary Science Letters*, 206(3):237–251.

Muñoz, V., Hérail, G., and Farías, M. (2008). Nature of a topographic height in the Tarapacá pediplain, Northern Chile. *Journal of Hydrology*, 404 (1):13–29.

Murphy, M. A., Yin, A., Harrison, T. M., and Durr, S. B. (1997). Did the Indo-Asian collision alone create the Tibetan plateau? *Geology*, 25(8):719–722.

Naeser, C. W. and Faul, H. (1969). Fission track annealing in apatite and sphene. *Journal of Geophysical Research*, 74(2):705–710.

Najman, Y., Appel, E., Boudagher-Fadel, M., Bown, P., Carter, A., Garzanti, E., Godin, L., Han, J., Liebke, U., and Oliver, G. (2010). Timing of India-Asia collision: Geological, biostratigraphic, and palaeomagnetic constraints. *Journal of Geophysical Research*, 115(B12):1–18.

Najman, Y., Bickle, M., Boudagher-Fadel, M., Carter, A., Garzanti, E., Paul, M., Wijbrans, J., Willett, E., Oliver, G., and Parrish, R. (2008). The Paleogene record of Himalayan erosion: Bengal Basin, Bangladesh. *Earth and Planetary Science Letters*, 273(1):1–14.

Nasdala, L., Hofmeister, W., Norberg, N., Martinson, J. M., Corfu, F., Dörr, W., Kamo, S. L., Kennedy, A. K., Kronz, A., and Reiners, P. W. (2008). Zircon M257-a homogeneous natural reference material for the ion microprobe U-Pb analysis of zircon. *Geostandards and Geoanalytical Research*, 32(3):247–265.

Nobre, A. D., Cuartas, L. A., Hodnett, M., Rennó, C. D., Rodrigues, G., Silveira, A., Waterloo, M., and Saleska, S. (2011). Height Above the Nearest Drainage–a hydrologically relevant new terrain model. *Journal of Hydrology*, 404(1):13–29.

O'Callaghan, J. F. and Mark, D. M. (1984). The extraction of drainage networks from digital elevation data. *Computer Vision, Graphics, and Image Processing*, 28(3):323–344.

Olaya, V. (2009). Basic land-surface parameters. *Developments in Soil Science*, 33:141–169.

Pan, G., Ding, J., Yao, D., and Wang, L. (2004). Geological map of Qinghai-Xizang (Tibet) Plateau and Adjacent Areas (1: 1,500,000).

Patriat, P. and Achache, J. (1984). India–Eurasia collision chronology has implications for crustal shortening and driving mechanism of plates. *Nature*, 311(5987):615–621.

Peckham, S. D. (2011). Profile, Plan and Streamline Curvature: A Simple Derivation and Applications. *International Geomorphometry 2011*, pages 27–30.

Penck, A. (1894). *Morphologie der Erdoberflache*. Bibliothek Geographischer Handbücher. Engelhorn, Stuttgart.

Penck, W. (1924). *Die morphologische Analyse. Ein Kapital der physikalischen Geologie.* Engelhorn, Stuttgart.

Phillips, J. D. (2002). Erosion, isostatic response, and the missing peneplains. *Geomorphology*, 45(3-4):225–241.

Pike, R. J., Evans, I. S., and Hengl, T. (2009). Geomorphometry: A brief guide. *Developments in Soil Science*, 33:3–30.

Pitman, W. C. and Golovchenko, X. (1991). The Effect of Sea Level Changes on the Morphology of Mountain Belts. *Journal of Geophysical Research*, 96(B4):6879–6891.

Polissar, P. J., Freeman, K. H., Rowley, D. B., McInerney, F. A., and Currie, B. S. (2009). Paleoaltimetry of the Tibetan Plateau from D/H ratios of lipid biomarkers. *Earth and Planetary Science Letters*, 287(1):64–76.

Qian, D. Y. (1985). A discussion on the age of the Qiuwu coal measures and the preliminary correlation of the molasse formation at the Ladakh–Gangdise marginal mountain chain. *Contributions to the Geology of the Qinghai-Xizang (Tibet) Plateau*, 16:229–241.

Qiu, J. (2008). China: The third pole. *Nature News*, 454(7203):393–396.

Qu, Y., Wang, Y., Duan, J., Zhang, S., Wang, Z., and Lu, P. (2003). Geological map of the Duoba district; scale 1:250 000.

R Core Team (2013). *R: A Language and Environment for Statistical Computing*. R Foundation for Statistical Computing, Vienna, Austria.

Ratschbacher, L., Frisch, W., Chen, C., and Pan, G. (1992). Deformation and motion along the southern margin of the Lhasa block (Tibet) prior to and during the India-Asia collision. *Journal of Geodynamics*, 16(1-2):21–54.

Reid, A. J., Fowler, A. P., Phillips, D., and Wilson, C. J. L. (2005). Thermochronology of the Yidun Arc, central eastern Tibetan Plateau: constraints from $^{40}Ar/^{39}Ar$ K-feldspar and apatite fission track data. *Journal of Asian Earth Sciences*, 25(6):915–935.

Reiners, P. W. (2005). Zircon (U-Th)/He thermochronometry. *Reviews in Mineralogy and Geochemistry*, 58(1):151–179.

Reiners, P. W. and Brandon, M. T. (2006). Using thermochronology to understand orogenic erosion. *Annual Review Earth and Planetary Science*, 34:419–466.

Reiners, P. W., Ehlers, T. A., and Zeitler, P. K. (2005). Past, present, and future of thermochronology. *Reviews in Mineralogy and Geochemistry*, 58(1):1–18.

Reiners, P. W., Spell, T. L., Nicolescu, S., and Zanetti, K. A. (2004). Zircon (U-Th)/He thermochronometry: He diffusion and comparisons with 40Ar/39Ar dating. *Geochimica et Cosmochimica Acta*, 68(8):1857–1887.

Reuter, H. I., Nelson, A., and Jarvis, A. (2007). An evaluation of void–filling interpolation methods for SRTM data. *International Journal of Geographical Information Science*, 21(9):983–1008.

Ridolfi, F. and Renzulli, A. (2012). Calcic amphiboles in calc-alkaline and alkaline magmas: thermobarometric and chemometric empirical equations valid up to 1,130°C and 2.2 GPa. *Contributions to Mineralogy and Petrology*, 163(5):877–895.

Riebe, C. S., Kirchner, J. W., and Finkel, R. C. (2003). Long-term rates of chemical weathering and physical erosion from cosmogenic nuclides and geochemical mass balance. *Geochimica et Cosmochimica Acta*, 67(22):4411–4427.

Riley, S. J., DeGloria, S. D., and Elliot, R. (1999). A terrain ruggedness index that quantifies topographic heterogeneity. *intermountain Journal of sciences*, 5(1-4):23–27.

Roger, F., Arnaud, N., Gilder, S., Tapponnier, P., Jolivet, M., Brunel, M., Malavieille, J., Xu, Z., and Yang, J. (2003). Geochronological and geochemical constraints on Mesozoic suturing in east central Tibet. *Tectonics*, 22(4):1–20.

Rohrmann, A., Kapp, P., Carrapa, B., Reiners, P. W., Guynn, J., Ding, L., and Heizler, M. (2012). Thermochronologic evidence for plateau formation in central Tibet by 45 Ma. *Geology*, 40(2):187–190.

Rowley, D. B. (1996). Age of initiation of collision between India and Asia: A review of stratigraphic data. *Earth and Planetary Science Letters*, 145(1):1–13.

Rowley, D. B. and Currie, B. S. (2006). Palaeo-altimetry of the late Eocene to Miocene Lunpola basin, central Tibet. *Nature*, 439(7077):677–681.

Runcorn, S. K. (1965). Palaeomagnetic Comparisons between Europe and North America. *Philosophical Transactions of the Royal Society of London. Series A, Mathematical and Physical Sciences*, 258(1088):1–11.

Santos, E. S. (1970). Fuzzy algorithms. *Information and control*, 17(4):326–339.

Schildgen, T. F., Ehlers, T. A., Whipp, D. M., van Soest, M. C., Whipple, K. X., and Hodges, K. V. (2009). Quantifying canyon incision and Andean Plateau surface uplift, southwest Peru: A thermochronometer and numerical modeling approach. *Journal of Geophysical Research*, 114(F4):1–22.

Schwab, M., Ratschbacher, L., Siebel, W., McWilliams, M., Minaev, V., Lutkov, V., Chen, F., Stanek, K., Nelson, B., and Frisch, W. (2004). Assembly of the Pamirs: Age and origin of magmatic belts from the southern Tien Shan to the southern Pamirs and their relation to Tibet. *Tectonics*, 23(4):1–31.

Sevon, W. D., Potter, N., and Crowl, G. H. (1983). Appalachian peneplains: An historical review. *Earth Sciences History*, 2(2):156–164.

Sheth, H. C. (2007). Plume-related regional prevolcanic uplift in the Deccan Traps: Absence of evidence, evidence of absence. *Geological Society of America Special Papers*, 430:785–813.

Shuster, D. L., Flowers, R. M., and Farley, K. A. (2006). The influence of natural radiation damage on helium diffusion kinetics in apatite. *Earth and Planetary Science Letters*, 249(3-4):148–161.

Silk, E. C. H. and Barnes, R. S. (1959). Examination of fission fragment tracks with an electron microscope. *Philosophical Magazine*, 4(44):970–972.

Simon-Coinçon, R., Thiry, M., and Schmitt, J. M. (1997). Variety and relationships of weathering features along the early Tertiary palaeosurface in the southwestern French Massif Central and the nearby Aquitaine Basin. *Palaeogeography, Palaeoclimatology, Palaeoecology*, 129(1):51–79.

Sinclair, H. D., Gibson, M., Lynn, G., and Stuart, F. (2009). The evidence for a Pyrenean resurrection: a response to Babault et al.(2008). *Basin Research*, 21(1):143–145.

Sláma, J., Košler, J., Condon, D. J., Crowley, J. L., Gerdes, A., Hanchar, J. M., Horstwood, M. S. A., Morris, G. A., Nasdala, L., Norberg, N., Schaltegger, U., Schoene, B., Tubrett, M. N., and Whitehouse, M. J. (2008). Plešovice zircon—A new natural reference material for U–Pb and Hf isotopic microanalysis. *Chemical Geology*, 249(1-2):1–35.

Smith, G. H. (1935). The relative relief of Ohio. *Geographical Review*, 25(2):272–284.

Spicer, R. A., Harris, N. B. W., Widdowson, M., Herman, A. B., Guo, S., Valdes, P. J., Wolfe, J. A., and Kelley, S. P. (2003). Constant elevation of southern Tibet over the past 15 million years. *Nature*, 421(6923):622–624.

Spurlin, M. S., Yin, A., Horton, B. K., Zhou, J., and Wang, J. (2005). Structural evolution of the Yushu-Nangqian region and its relationship to syncollisional igneous activity, east-central Tibet. *Geological Society of America Bulletin*, 117(9-10):1293–1317.

Steenken, A., Siegesmund, S., Heinrichs, T., and Fügenschuh, B. (2002). Cooling and exhumation of the Rieserferner Pluton (Eastern Alps, Italy/Austria). *International Journal of Earth Sciences*, 91(5):799–817.

Steer, P., Huismans, R. S., Valla, P. G., Gac, S., and Herman, F. (2012). Bimodal Plio-Quaternary glacial erosion of fjords and low-relief surfaces in Scandinavia. *Nature Geoscience*, 5(9):635–639.

Steiger, R. and Jäger, E. (1977). Subcommission on geochronology: convention on the use of decay constants in geo-and cosmochronology. *Earth and Planetary Science Letters*, 36(3):359–362.

Stirling, M. W. (1991). Peneplain modification in an alpine environment of Central Otago, New Zealand. *New Zealand Journal of Geology and Geophysics*, 34(2):195–201.

Stone, J. O. (2000). Air pressure and cosmogenic isotope production. *Journal of Geophysical Research*, 105(B10):23753–23759.

Stose, G. W. (1940). Age of the Schooley peneplain. *American Journal of Science*, 238(7):461–476.

Strobl, M., Hetzel, R., Ding, L., Zhang, L., and Hampel, A. (2010). Preservation of a large-scale bedrock peneplain suggests long-term landscape stability in southern Tibet. *Zeitschrift für Geomorphologie*, 54(4):453–466.

Strobl, M., Hetzel, R., Niedermann, S., Ding, L., and Zhang, L. (2012). Landscape evolution of a bedrock peneplain on the southern Tibetan Plateau revealed by in situ-produced cosmogenic ^{10}Be and ^{21}Ne. *Geomorphology*, 153-154:192–204.

Strøm, K. M. (1948). The geomorphology of Norway. *The Geographical Journal*, 112(1/3):19–23.

Sturkell, E. and Lindström, M. (2004). The target peneplain of the Lockne impact. *Meteoritics & Planetary Science*, 39(10):1721–1731.

Tagami, T. and O'Sullivan, P. B. (2005). Fundamentals of fission-track thermochronology. *Reviews in Mineralogy and Geochemistry*, 58(1):19–47.

Taner, I. and Meyerhoff, A. A. (1990). Petroleum at the roof of the world: The geological evolution of the Tibet (Qinghai–Xizang) Plateau Part I. *Journal of Petroleum Geology*, 13(2):157–177.

Tapponnier, P., Mercier, J. L., Armijo, R., Tonglin, H., and Ji, Z. (1981). Field evidence for active normal faulting in Tibet. *Nature*, 294(5840):410–414.

Tapponnier, P., Zhiqin, X., Roger, F., Meyer, B., Arnaud, N., Wittlinger, G., and Jingsui, Y. (2001). Oblique stepwise rise and growth of the Tibet Plateau. *Science*, 294(5547):1671–1677.

Tarboton, D. G. (1997). A new method for the determination of flow directions and upslope areas in grid digital elevation models. *Water Resources Research*, 33(2):309–319.

Tian, Y., Kohn, B. P., Gleadow, A. J. W., and Hu, S. (2013). Peneplain formation in southern Tibet predates the India-Asia collision and plateau uplift: Comment. *Geology*, 41(9):e295–e296.

van der Beek, P., van Melle, J., Guillot, S., Pêcher, A., Reiners, P. W., Nicolescu, S., and Latif, M. (2009). Eocene Tibetan plateau remnants preserved in the northwest Himalaya. *Nature Geoscience*, 2(5):364–368.

Volkmer, J. E., Kapp, P., Guynn, J. H., and Lai, Q. (2007). Cretaceous-Tertiary structural evolution of the north central Lhasa terrane, Tibet. *Tectonics*, 26(6):1–18.

von Eynatten, H. and Dunkl, I. (2012). Assessing the sediment factory: The role of single grain analysis. *Earth-Science Reviews*, 115(1):97–120.

Wagner, G. A., Jäger, G. M., and Reimer, E. (1977). Cooling ages derived by apatite fission track, mica Rb-Sr and K-Ar dating: the uplift and cooling history of the Central Alps. *Mem. Ist. Geol. Mineral. Univ. Padova*, 31:1–27.

Wang, C., Dai, J., Zhao, X., Li, Y., Graham, S. A., He, D., Ran, B., and Meng, J. (2014). Outward-growth of the Tibetan Plateau during the Cenozoic: A review. *Tectonophysics*, 621(0):1–43.

Wang, C., Zhao, X., Liu, Z., Lippert, P. C., Graham, S. A., Coe, R. S., Yi, H., Zhu, L., Liu, S., and Li, Y. (2008). Constraints on the early uplift history of the Tibetan Plateau. *Proceedings of the National Academy of Sciences*, 105(13):4987–4992.

Wang, J. G., Hu, X. M., Wu, F. Y., and Jansa, L. (2010). Provenance of the Liuqu Conglomerate in southern Tibet: A Paleogene erosional record of the Himalayan–Tibetan orogen. *Sedimentary Geology*, 231(3):74–84.

Wang, N. (1984). Development of the mesozoic formations in the lake region, north tibet and its plate tectonic implications. *Contribution to the geology of the Qinghai-Xizang (Tibet) plateau*, 8:29–40.

Wen, D. R., Liu, D., Chung, S. L., Chu, M. F., Ji, J., Zhang, Q., Song, B., Lee, T. Y., Yeh, M. W., and Lo, C. H. (2008). Zircon SHRIMP U-Pb ages of the Gangdese Batholith and implications for Neotethyan subduction in southern Tibet. *Chemical Geology*, 252(3-4):191–201.

White, W. B. (2009). The evolution of Appalachian fluviokarst: competition between stream erosion, cave development, surface denudation, and tectonic uplift. *Journal of Cave and Karst Studies*, 71(3):159–167.

Widdowson, M. (1997). *Palaeosurfaces: Recognition, Reconstruction and Palaeoenvironmental Interpretation*, volume 120 of *Geological Society Special Publication*. Geological Society.

Willems, H., Zhou, Z., Zhang, B., and Gräfe, K. U. (1996). Stratigraphy of the Upper Cretaceous and lower Tertiary strata in the Tethyan Himalayas of Tibet (Tingri area, China). *Geologische Rundschau*, 85(4):723–754.

Williams, H., Turner, S., Kelley, S., and Harris, N. (2001). Age and composition of dikes in Southern Tibet: New constraints on the timing of east-west extension and its relationship to postcollisional volcanism. *Geology*, 29(4):339–342.

Willis, B. (1933). The peneplains of East Africa. *The Geographical Journal*, 82(4):383–384.

Wolf, R. A., Farley, K. A., and Silver, L. T. (1996). Helium diffusion and low-temperature thermochronometry of apatite. *Geochimica et Cosmochimica Acta*, 60(21):4231–4240.

Wörner, G., Uhlig, D., Kohler, I., and Seyfried, H. (2002). Evolution of the West Andean Escarpment at 18°S (N. Chile) during the last 25 Ma: uplift, erosion and collapse through time. *Tectonophysics*, 345(1–4):183–198.

Wu, F. Y., Ji, W. Q., Liu, C. Z., and Chung, S. L. (2010). Detrital zircon U–Pb and Hf isotopic data from the Xigaze fore-arc basin: constraints on Transhimalayan magmatic evolution in southern Tibet. *Chemical Geology*, 271(1):13–25.

Xiao, L., Zhang, H. F., Clemens, J. D., Wang, Q. W., Kan, Z. Z., Wang, K. M., Ni, P. Z., and Liu, X. M. (2007). Late Triassic granitoids of the eastern margin of the Tibetan Plateau: Geochronology, petrogenesis and implications for tectonic evolution. *Lithos*, 96(3):436–452.

Xu, R. H., Schärer, U., and Allègre, C. J. (1985). Magmatism and metamorphism in the Lhasa block (Tibet): A geochronological study. *The Journal of Geology*, 93(1):41–57.

Xu, Z. and Lee, K. Y. (1984). *Tertiary system and its petroleum potential in the Lunpola Basin, Xizang (Tibet)*. USGS Open File Rep.

Yang, K., Li, J. W., Li, Z., and Wang, Z. R. (1975). On the Tertiary sporo-pollen assemblages from Lunpola Basin of Xizang, China and their palaeogeographic significance. *Scientia Geologica Sinica*, 4:366–374.

Yi, H., Wang, C., Shi, Z., Lin, J., and Zhu, L. (2008). Early uplift history of the Tibetan plateau: Records from paleocurrents and paleodrainage in the Hoh Xil basin. *Acta Geologica Sinica–English Edition*, 82(1):206–213.

Yin, A. and Harrison, T. M. (2000). Geologic evolution of the Himalayan-Tibetan orogen. *Annual Review of Earth and Planetary Sciences*, 28(1):211–280.

Yin, A., Kapp, P. A., and Murphy, M. A. (1999). Evidence for significant Late Cenozoic east-west extension in North Tibet. *Geology*, 27(9):787–790.

Yin, J., Xu, J., Liu, C., and Li, H. (1988). The Tibetan plateau: regional stratigraphic context and previous work. *Philosophical Transactions of the Royal Society of London, Series A*, 327(11):5–52.

Zadeh, L. A. (1968). Fuzzy algorithms. *Information and Control*, 12(2):94–102.

Zeitler, P. K., Herczeg, A. L., McDougall, I., and Honda, M. (1987). U-Th-He dating of apatite: A potential thermochronometer. *Geochimica et Cosmochimica Acta*, 51(10):2865–2868.

Zevenbergen, L. W. and Thorne, C. R. (1987). Quantitative analysis of land surface topography. *Earth Surface Processes and Landforms*, 12(1):47–56.

Zeyen, H., Novak, O., Landes, M., Prodehl, C., Driad, L., and Hirn, A. (1997). Refraction-seismic investigations of the northern Massif Central (France). *Tectonophysics*, 275(1):99–117.

Zhai, Q., Jahn, B., Su, L., Wang, J., Mo, X., Lee, H., Wang, K., and Tang, S. (2012). Triassic arc magmatism in the Qiangtang area, northern Tibet: Zircon U-Pb ages, geochemical and Sr-Nd-Hf isotopic characteristics, and tectonic implications. *Journal of Asian Earth Sciences*, 63:162–178.

Zhang, K. J. (2000). Cretaceous palaeogeography of Tibet and adjacent areas (China): Tectonic implications. *Cretaceous Research*, 21(1):23–33.

Zhang, K. J., Xia, B. D., Wang, G. M., Li, Y. T., and Ye, H. F. (2004). Early Cretaceous stratigraphy, depositional environments, sandstone provenance, and tectonic setting of central Tibet, western China. *Bulletin of the Geological Society of America*, 116(9-10):1202–1222.

Zhang, Q., Ding, L., Cai, F., Xu, X., Zhang, L., Xu, Q., and Willems, H. (2011). Early Cretaceous Gangdese retroarc foreland basin evolution in the Selin Co basin, central Tibet: evidence from sedimentology and detrital zircon geochronology. *Geological Society, London, Special Publications*, 353(1):27–44.

Zhang, Q., Willems, H., Ding, L., Gräfe, K. U., and Appel, E. (2012). Initial India-Asia continental collision and foreland basin evolution in the Tethyan Himalaya of Tibet: Evidence from stratigraphy and paleontology. *The Journal of Geology*, 120(2):175–189.

A Appendix

A.1 Tables related to “Peneplain formation in southern Tibet predates the India-Asia collision and plateau uplift”

Table A.1: (related to chapter 2a “Peneplain formation in southern Tibet”): Zrn U-Pb age dataset; sample H-23

H-23	U	Pb		RATIOS							AGES (Ma)				Cc[g]
spot#	(ppm)[a]	(ppm)[a]	Th/U[a]	$^{207}Pb/^{235}U$[b]	2 σ[d]	$^{206}Pb/^{238}U$[b]	2 σ[d]	rho[c]	$^{207}Pb/^{206}Pb$[e]	2 σ[d]	$^{207}Pb/^{235}U$	2 σ	$^{206}Pb/^{238}U$	2 σ	%
1	166	3	0.69	0.132	0.010	0.01853	0.00047	0.35	0.0515	0.0035	126	9	118	3	94
2	88	2	0.66	0.138	0.014	0.01981	0.00046	0.22	0.0507	0.0052	132	13	126	3	96
3	352	6	0.22	0.121	0.007	0.01750	0.00023	0.22	0.0499	0.0029	116	6	112	1	97
4	134	2	0.58	0.133	0.008	0.01820	0.00027	0.24	0.0529	0.0031	126	7	116	2	92
5	114	2	0.61	0.135	0.013	0.01916	0.00037	0.19	0.0511	0.0050	128	12	122	2	95
6	92	2	0.50	0.137	0.013	0.01968	0.00052	0.28	0.0506	0.0046	131	12	126	3	96
7	1216	22	0.07	0.125	0.002	0.01808	0.00016	0.52	0.0501	0.0007	120	2	116	1	97
8	134	3	0.47	0.142	0.011	0.01994	0.00042	0.27	0.0516	0.0039	135	10	127	3	95
9	105	2	0.53	0.135	0.016	0.01889	0.00034	0.15	0.0519	0.0062	129	14	121	2	94
10	134	3	0.56	0.134	0.012	0.01957	0.00052	0.29	0.0496	0.0043	127	11	125	3	98
11	968	19	0.09	0.135	0.004	0.01976	0.00025	0.42	0.0496	0.0013	129	4	126	2	98
12	485	9	0.27	0.132	0.009	0.01800	0.00038	0.33	0.0533	0.0033	126	8	115	2	91
13	172	3	0.88	0.145	0.021	0.01995	0.00034	0.12	0.0526	0.0076	137	19	127	2	93
14	847	18	0.24	0.151	0.007	0.02180	0.00030	0.31	0.0503	0.0021	143	6	139	2	97
15	3010	52	0.06	0.115	0.002	0.01731	0.00011	0.35	0.0482	0.0008	111	2	111	1	100
16	493	9	0.39	0.121	0.004	0.01829	0.00040	0.66	0.0479	0.0012	116	4	117	3	101
17	396	8	0.22	0.137	0.006	0.01976	0.00034	0.36	0.0503	0.0022	130	6	126	2	97
18	1535	37	0.08	0.164	0.004	0.02413	0.00018	0.27	0.0494	0.0013	155	4	154	1	99
19	1020	21	0.08	0.142	0.006	0.02012	0.00025	0.29	0.0513	0.0021	135	5	128	2	95
20	630	10	0.38	0.116	0.006	0.01620	0.00017	0.21	0.0519	0.0026	111	5	104	1	93
21	1752	35	0.06	0.138	0.004	0.02017	0.00023	0.39	0.0498	0.0014	132	4	129	1	98
22	129	2	0.57	0.125	0.010	0.01746	0.00025	0.19	0.0521	0.0040	120	9	112	2	93
23	113	2	0.69	0.142	0.014	0.01862	0.00026	0.14	0.0554	0.0056	135	13	119	2	88
24	621	12	0.09	0.133	0.008	0.01890	0.00029	0.25	0.0512	0.0030	127	7	121	2	95
25	693	13	0.37	0.127	0.007	0.01824	0.00017	0.17	0.0506	0.0027	122	6	117	1	96
											$^{206}Pb/^{238}U$	2 σ	n[f]	rej.[h]	
										Weighted mean age (Ma)	**117.0**	**2.8**	**23**	**1**	

Table A.2: Zrn U-Pb age dataset

H-29	U	Pb		RATIOS							AGES (Ma)				Cc[g]
spot#	(ppm)[a]	(ppm)[a]	Th/U[a]	$^{207}Pb/^{235}U$[b]	2 σ[d]	$^{206}Pb/^{238}U$[b]	2 σ[d]	rho[c]	$^{207}Pb/^{206}Pb$[e]	2 σ[d]	$^{207}Pb/^{235}U$	2 σ	$^{206}Pb/^{238}U$	2 σ	%
2	401	7	0.56	0.120	0.008	0.0179	0.0008	0.68	0.0486	0.0025	115	7	114	5	99
3	544	16	0.39	0.227	0.017	0.0289	0.0010	0.45	0.0569	0.0039	208	14	184	6	88
4	770	13	0.42	0.117	0.004	0.0171	0.0004	0.58	0.0496	0.0015	112	4	109	2	97
5	99	2	0.55	0.133	0.017	0.0185	0.0005	0.22	0.0521	0.0064	127	15	118	3	93
6	246	5	0.27	0.123	0.007	0.0183	0.0005	0.47	0.0488	0.0024	118	6	117	3	99
7	232	4	0.32	0.113	0.008	0.0176	0.0006	0.45	0.0466	0.0030	109	8	113	4	103
8	339	6	0.25	0.113	0.010	0.0169	0.0007	0.44	0.0485	0.0038	109	9	108	4	99
9	216	4	0.31	0.125	0.009	0.0183	0.0004	0.33	0.0495	0.0032	120	8	117	3	98
10	381	7	0.13	0.125	0.008	0.0179	0.0003	0.24	0.0506	0.0030	119	7	114	2	96
11	1123	43	0.11	0.270	0.010	0.0382	0.0008	0.57	0.0513	0.0016	243	8	242	5	99
12	394	7	0.18	0.131	0.008	0.0187	0.0006	0.46	0.0508	0.0029	125	8	119	3	96
13	432	7	0.12	0.117	0.007	0.0172	0.0002	0.16	0.0494	0.0029	112	6	110	1	98
14	313	6	0.32	0.121	0.007	0.0178	0.0004	0.37	0.0492	0.0026	116	6	114	2	98
15	547	9	0.17	0.114	0.004	0.0168	0.0002	0.31	0.0490	0.0017	109	4	108	1	98
16	741	14	0.14	0.132	0.009	0.0186	0.0003	0.24	0.0514	0.0034	126	8	119	2	95
17	238	4	0.39	0.121	0.007	0.0182	0.0004	0.35	0.0484	0.0027	116	6	116	2	100
18	153	3	0.28	0.118	0.007	0.0166	0.0002	0.24	0.0518	0.0030	114	6	106	2	93
20	397	7	0.18	0.120	0.007	0.0176	0.0006	0.52	0.0496	0.0026	115	7	112	4	98
21	191	3	0.32	0.122	0.010	0.0174	0.0003	0.23	0.0510	0.0041	117	9	111	2	95
22	131	2	0.34	0.122	0.012	0.0174	0.0003	0.19	0.0508	0.0048	117	11	111	2	95
23	486	9	0.22	0.124	0.007	0.0183	0.0003	0.35	0.0492	0.0024	119	6	117	2	98
24	305	6	0.35	0.135	0.013	0.0203	0.0007	0.35	0.0481	0.0043	128	12	130	4	101
25	1040	18	0.61	0.120	0.003	0.0175	0.0001	0.28	0.0495	0.0012	115	3	112	1	98
26	87	2	0.66	0.139	0.016	0.0199	0.0006	0.25	0.0509	0.0057	133	14	127	4	96
27	125	2	0.63	0.132	0.016	0.0181	0.0004	0.19	0.0528	0.0064	126	15	116	3	92
											$^{206}Pb/^{238}U$	2 σ	n[f]	rej.[h]	
									Weighted mean age (Ma)		**111.7**	**1.6**	**23**	**2**	

Table A.3: Zrn U-Pb age dataset

H-30	U	Pb		RATIOS							AGES (Ma)				Cc[g]
spot#	(ppm)[a]	(ppm)[a]	Th/U[a]	$^{207}Pb/^{235}U$[b]	2 σ[d]	$^{206}Pb/^{238}U$[b]	2 σ[d]	rho[c]	$^{207}Pb/^{206}Pb$[e]	2 σ[d]	$^{207}Pb/^{235}U$	2 σ	$^{206}Pb/^{238}U$	2 σ	%
1	275	5	0.16	0.121	0.007	0.0175	0.0003	0.27	0.0501	0.0028	116	6	112	2	97
4	186	3	0.29	0.124	0.008	0.0178	0.0002	0.20	0.0508	0.0032	119	7	114	1	95
5	876	15	0.15	0.115	0.009	0.0171	0.0002	0.18	0.0490	0.0036	111	8	109	1	98
6	207	4	0.32	0.124	0.009	0.0177	0.0004	0.27	0.0508	0.0036	119	8	113	2	95
7	113	3	0.22	0.195	0.014	0.0261	0.0014	0.78	0.0543	0.0024	181	12	166	9	92
8	335	6	0.41	0.129	0.010	0.0185	0.0003	0.22	0.0507	0.0038	124	9	118	2	96
9	242	4	0.47	0.122	0.010	0.0175	0.0005	0.33	0.0505	0.0040	117	9	112	3	96
11	442	15	0.28	0.236	0.009	0.0334	0.0007	0.51	0.0512	0.0017	215	8	212	4	98
14	386	16	0.26	0.309	0.019	0.0417	0.0007	0.27	0.0538	0.0031	274	14	263	4	96
15	658	12	0.21	0.133	0.008	0.0188	0.0006	0.52	0.0512	0.0025	126	7	120	4	95
16	442	8	0.16	0.123	0.010	0.0175	0.0004	0.29	0.0509	0.0040	118	9	112	3	95
18	66	4	1.75	0.525	0.027	0.0659	0.0017	0.50	0.0578	0.0025	429	18	412	10	96
19	327	6	0.21	0.126	0.009	0.0179	0.0005	0.36	0.0509	0.0035	120	8	114	3	95
21	648	44	0.40	0.523	0.020	0.0676	0.0014	0.54	0.0561	0.0018	427	13	422	8	99
23	344	14	0.55	0.288	0.014	0.0400	0.0007	0.38	0.0522	0.0023	257	11	253	5	98
24	432	9	0.40	0.152	0.008	0.0216	0.0005	0.45	0.0510	0.0025	144	7	138	3	96
											$^{206}Pb/^{238}U$	**2 σ**	**n[f]**	**rej.[h]**	
									Weighted mean age (Ma)		**112.8**	**2.3**	**11**	**2**	

Table A.4: Zrn U-Pb age dataset

DC-33	U	Pb		RATIOS							AGES (Ma)				Cc[g]
spot#	(ppm)[a]	(ppm)[a]	Th/U[a]	$^{207}Pb/^{235}U$[b]	2 σ[d]	$^{206}Pb/^{238}U$[b]	2 σ[d]	rho[c]	$^{207}Pb/^{206}Pb$[e]	2 σ[d]	$^{207}Pb/^{235}U$	2 σ	$^{206}Pb/^{238}U$	2 σ	%
1	76	1	0.67	0.117	0.012	0.0169	0.0005	0.28	0.0501	0.0048	112	11	108	3	96
2	50	1	0.56	0.127	0.015	0.0175	0.0005	0.25	0.0526	0.0060	121	14	112	3	92
3	95	2	0.82	0.122	0.007	0.0174	0.0003	0.31	0.0512	0.0028	117	6	111	2	95
4	64	1	0.65	0.118	0.014	0.0170	0.0003	0.13	0.0505	0.0061	114	13	109	2	96
5	108	2	0.63	0.118	0.011	0.0176	0.0003	0.17	0.0486	0.0045	113	10	113	2	99
6	48	1	0.68	0.127	0.016	0.0176	0.0005	0.22	0.0526	0.0065	122	14	112	3	92
7	75	1	0.67	0.121	0.014	0.0170	0.0005	0.23	0.0518	0.0058	116	13	109	3	93
8	55	1	0.59	0.124	0.020	0.0171	0.0005	0.17	0.0523	0.0083	118	18	110	3	93
9	128	2	0.65	0.122	0.008	0.0175	0.0003	0.27	0.0506	0.0033	117	7	112	2	96
10	111	2	0.68	0.124	0.010	0.0175	0.0006	0.39	0.0514	0.0040	119	9	112	4	94
11	73	1	0.80	0.129	0.014	0.0177	0.0005	0.27	0.0529	0.0055	123	13	113	3	92
12	90	2	0.69	0.123	0.009	0.0176	0.0004	0.30	0.0510	0.0037	118	8	112	3	95
13	93	2	0.45	0.125	0.016	0.0174	0.0003	0.14	0.0522	0.0065	120	14	111	2	93
14	81	1	0.43	0.112	0.014	0.0171	0.0006	0.30	0.0473	0.0057	108	13	110	4	102
15	43	1	0.66	0.118	0.016	0.0173	0.0005	0.20	0.0496	0.0066	113	15	110	3	97
16	100	2	0.74	0.118	0.011	0.0171	0.0004	0.28	0.0503	0.0045	114	10	109	3	96
17	48	1	0.49	0.131	0.023	0.0177	0.0006	0.18	0.0534	0.0092	125	21	113	4	91
18	144	3	0.52	0.121	0.008	0.0177	0.0003	0.27	0.0496	0.0033	116	8	113	2	98
19	135	2	0.44	0.119	0.008	0.0175	0.0004	0.32	0.0491	0.0032	114	7	112	2	98
20	91	2	0.83	0.118	0.014	0.0176	0.0004	0.19	0.0489	0.0059	114	13	112	3	99
21	133	2	0.97	0.123	0.008	0.0176	0.0003	0.27	0.0508	0.0034	118	8	112	2	95
22	115	2	0.59	0.135	0.023	0.0176	0.0003	0.11	0.0557	0.0094	129	21	112	2	87
23	64	1	0.42	0.120	0.014	0.0176	0.0004	0.21	0.0494	0.0056	115	12	112	3	98
24	123	2	0.51	0.120	0.008	0.0176	0.0005	0.43	0.0494	0.0029	115	7	112	3	98
25	236	4	0.33	0.117	0.007	0.0174	0.0005	0.44	0.0486	0.0027	112	6	111	3	99
26	321	6	0.28	0.151	0.073	0.0176	0.0004	0.05	0.0622	0.0299	143	64	112	3	79
27	190	3	0.33	0.124	0.006	0.0180	0.0002	0.23	0.0502	0.0023	119	5	115	1	96
28	138	2	0.47	0.117	0.014	0.0176	0.0005	0.25	0.0485	0.0055	113	13	112	3	100
29	136	2	0.91	0.120	0.010	0.0176	0.0005	0.35	0.0494	0.0037	115	9	112	3	98
											$^{206}Pb/^{238}U$	**2 σ**	**n[f]**	**rej.[h]**	
									Weighted mean age (Ma)		**111.6**	**0.5**	**29**	**2**	

Table A.5: Zrn U-Pb age dataset

DC-31	U	Pb		RATIOS							AGES (Ma)				Cc[g]
spot#	(ppm)[a]	(ppm)[a]	Th/U[a]	$^{207}Pb/^{235}U$[b]	2 σ[d]	$^{206}Pb/^{238}U$[b]	2 σ[d]	rho[c]	$^{207}Pb/^{206}Pb$[e]	2 σ[d]	$^{207}Pb/^{235}U$	2 σ	$^{206}Pb/^{238}U$	2 σ	%
1	521	10	0.15	0.129	0.006	0.0189	0.0004	0.42	0.0494	0.0020	123	5	121	2	98
2	235	4	0.36	0.125	0.004	0.0178	0.0002	0.30	0.0508	0.0017	119	4	114	1	95
4	497	10	0.11	0.136	0.006	0.0199	0.0004	0.45	0.0494	0.0020	129	6	127	3	98
7	674	49	0.54	0.564	0.015	0.0731	0.0008	0.39	0.0559	0.0014	454	10	455	5	100
9	553	10	0.18	0.120	0.008	0.0177	0.0006	0.51	0.0494	0.0029	115	7	113	4	98
10	227	13	0.35	0.511	0.016	0.0585	0.0009	0.52	0.0634	0.0017	419	11	366	6	87
11	482	27	0.46	0.443	0.020	0.0565	0.0013	0.48	0.0569	0.0023	373	14	354	8	95
12	131	13	0.82	0.856	0.037	0.0956	0.0018	0.44	0.0649	0.0025	628	20	589	11	94
14	357	23	0.40	0.505	0.021	0.0639	0.0016	0.61	0.0574	0.0019	415	14	399	10	96
16	867	16	0.07	0.122	0.011	0.0180	0.0003	0.20	0.0490	0.0044	117	10	115	2	99
19	343	7	0.49	0.154	0.009	0.0194	0.0005	0.44	0.0575	0.0029	145	8	124	3	85
20	449	12	0.47	0.186	0.010	0.0266	0.0003	0.24	0.0507	0.0026	173	8	169	2	98
21	298	18	0.68	0.483	0.026	0.0603	0.0015	0.46	0.0582	0.0028	400	18	377	9	94
23	359	7	0.40	0.135	0.008	0.0197	0.0005	0.40	0.0498	0.0026	129	7	126	3	98
24	404	8	0.32	0.138	0.008	0.0194	0.0005	0.47	0.0518	0.0025	132	7	124	3	94
25	332	6	0.32	0.125	0.005	0.0182	0.0004	0.50	0.0496	0.0018	119	5	116	2	98
											$^{206}Pb/^{238}U$	2 σ	n[f]	rej.[h]	
										Weighted mean age (Ma)	**117.5**	**3.9**	**10**	**1**	

[a] U and Pb concentrations and Th/U ratios are calculated relative to GJ-1 reference zircon.

[b] Corrected for background and within-run Pb/U fractionation and normalised to reference zircon GJ-1 (ID-TIMS values/measured value); $^{207}Pb/^{235}U$ calculated using ($^{207}Pb/^{206}Pb$)/($^{238}U/^{206}Pb$ * 1/137.88).

[c] Rho is the error correlation defined as the quotient of the propagated errors of the $^{206}Pb/^{238}U$ and the $^{207}/^{235}U$ ratio.

[d] Quadratic addition of within-run errors (2 SD) and daily reproducibility of GJ-1 (2 SD).

[e] Corrected for mass-bias by normalising to GJ-1 reference zircon (~0.6 per a.m.u.) and common Pb using the model of Stacey & Kramers (1975).

[f] Number of spots used for calculation.

[g] Concordance of $^{206}Pb/^{238}U$ and $^{207}Pb/^{235}U$.

[h] rej.: number of rejected acquisitions using isoplot (Ludwig, 2003).

Gray-dyed data were rejected, because the ages reflect an older zircon population or show inheritance.

Samples DC-31, H-29 and H-30 also yield a cluster of inherited zircons (>900 Ma) not listed in this table.

References

Ludwig, K.R., 2003, User's manual for Isoplot 3.00: a geochronological toolkit for Microsoft Excel. *Berkeley Geochronology Center Special Publication* 4, 70p.

Stacey, J.S., Kramers, J.D., 1975, Approximation of terrestrial lead isotope evolution by a two-stage model: *Earth and Planetary Science Letters,* 26, 207–221.

Table A.6: Zrn (U-Th)/He age dataset

sample number	aliq.	He vol. (ncc)	He ±1σ (ncc)	U-238 mass (ng)	U-238 ±1σ (ng)	U-238 conc. (ppm)	Th-232 mass (ng)	Th-232 ±1σ (ng)	Th-232 conc. (ppm)	Th/U ratio	Sm mass (ng)	Sm ±1σ (ng)	Sm conc. (ppm)	Ejection correction (Ft)[a]	*Uncorr. He age (Ma)*	**Ft-corr. age (Ma)**	**±1σ (Ma)**	**Sample age[b] (Ma)**	**±1σ (Ma)**
H-23	#1	3.314	0.055	0.464	0.009	373	0.138	0.004	116	0.30	0.004	0.001	4	0.62	*55.0*	**89.2**	**±2.1**		
	#2	13.344	0.219	2.674	0.048	1576	0.130	0.003	80	0.05	0.005	0.001	4	0.66	*40.7*	**62.2**	**±1.5**		
	#3	11.802	0.194	1.740	0.031	878	0.231	0.006	117	0.13	0.006	0.001	3	0.68	*54.2*	**79.9**	**±1.9**	**77.1**	**±7.9**
H-24	#1	3.796	0.063	0.489	0.009	116	0.285	0.007	69	0.58	0.011	0.001	3	0.74	*56.3*	**76.5**	**±1.8**		
	#2	32.316	0.529	3.948	0.071	886	0.658	0.016	149	0.17	0.016	0.001	4	0.72	*64.9*	**90.2**	**±2.1**		
	#3	4.307	0.071	0.623	0.011	191	0.296	0.007	91	0.47	0.014	0.003	4	0.69	*51.3*	**74.0**	**±1.7**	**80.2**	**±5.0**
H-29	#1	9.584	0.158	1.690	0.031	1167	0.253	0.006	175	0.15	0.018	0.002	12	0.63	*45.2*	**71.3**	**±1.7**		
	#2	5.070	0.084	0.655	0.012	254	0.107	0.003	41	0.16	0.005	0.001	2	0.70	*61.5*	**88.0**	**±2.1**		
	#3	9.415	0.157	1.769	0.032	1140	0.163	0.004	105	0.09	0.012	0.002	8	0.65	*43.0*	**65.9**	**±1.6**	**75.1**	**±6.6**
H-30	#1	15.472	0.254	2.061	0.037	432	0.187	0.005	39	0.09	0.035	0.015	7	0.77	*60.6*	**78.9**	**±1.9**		
	#2	38.639	0.633	4.324	0.078	806	0.449	0.011	84	0.10	0.014	0.001	3	0.77	*71.8*	**93.0**	**±2.2**		
	#3	16.875	0.277	1.700	0.031	485	0.051	0.001	15	0.03	0.011	0.001	3	0.74	*81.1*	**110.3**	**±2.6**	**94.1**	**±9.1**
H-31	#1	15.807	0.260	2.921	0.053	1896	0.260	0.006	169	0.09	0.049	0.003	32	0.62	*43.8*	**71.0**	**±1.7**		
	#2	19.860	0.326	3.282	0.059	1107	0.234	0.006	79	0.07	0.057	0.003	19	0.72	*49.1*	**68.5**	**±1.6**		
	#3	23.931	0.392	4.613	0.083	2080	0.199	0.005	90	0.04	0.222	0.008	100	0.70	*42.4*	**60.5**	**±1.4**	**66.7**	**±3.2**
DC-31	#1	17.341	0.284	2.202	0.040	1064	0.495	0.012	239	0.22	0.059	0.011	29	0.68	*61.6*	**91.3**	**±2.1**		
	#2	8.313	0.137	1.303	0.024	836	0.126	0.003	81	0.10	0.007	0.001	4	0.64	*51.5*	**80.2**	**±1.9**		
	#3	6.803	0.112	1.043	0.019	810	0.233	0.006	181	0.22	0.030	0.003	23	0.51	*51.1*	**99.7**	**±2.3**		
	#4	26.202	0.429	3.873	0.070	1366	1.140	0.027	402	0.29	0.030	0.003	10	0.64	*52.2*	**81.8**	**±1.9**		
	#5	6.332	0.107	1.054	0.019	399	0.298	0.007	113	0.28	0.071	0.006	27	0.64	46.5	**72.4**	**±1.7**	**85.1**	**±4.7**
DC-33	#1	5.481	0.091	0.694	0.013	136	0.437	0.011	85	0.63	0.011	0.001	2	0.74	*56.7*	**76.5**	**±1.7**		
	#2	3.799	0.063	0.564	0.010	185	0.144	0.003	47	0.25	0.090	0.003	30	0.72	*52.3*	**73.1**	**±1.7**	**74.8**	**±1.7**

[a] alpha-ejection correction factor (Ft) after Farley et al. (1996).

[b] unweighted average age of each single Ft-corrected (U-Th)/He age.

Reference

Farley, K.A., Wolf, R.A., and Silver, L.T., 1996, The effects of long alpha-stopping distances on (U-Th)/He ages: Geochimica Cosmochimica Acta, v. 60, p. 4223–4229.

Table A.7: Zrn (U-Th)/He age dataset

		He		U-238			Th-232				Sm			Ejection	*Uncorr.*	**Ft-corr.**		**Sample**	
sample number	aliq.	vol. (ncc)	±1σ (ncc)	mass (ng)	±1σ (ng)	conc. (ppm)	mass (ng)	±1σ (ng)	conc. (ppm)	Th/U ratio	mass (ng)	±1σ (ng)	conc. (ppm)	correction (Ft)[a]	*He age (Ma)*	**He age (Ma)**	**±1σ (Ma)**	**age[b] (Ma)**	**±1σ (Ma)**
H-23	#1	4.454	0.074	0.735	0.013	114	0.102	0.003	16	0.14	2.221	0.230	344	0.86	*47.3*	**55.1**	**±1.4**		
	#2	4.040	0.067	0.661	0.012	110	0.081	0.002	13	0.12	2.258	0.238	377	0.88	*47.7*	**54.4**	**±1.4**		
	#3	2.750	0.046	0.474	0.009	128	0.055	0.002	15	0.12	1.300	0.141	352	0.78	*45.6*	**58.6**	**±1.5**		
	#4	1.833	0.031	0.327	0.006	100	0.044	0.001	14	0.14	0.968	0.106	296	0.75	*43.8*	**58.1**	**±1.5**		
	#5	1.107	0.019	0.212	0.004	176	0.034	0.001	28	0.16	0.488	0.057	404	0.74	*40.7*	**54.9**	**±1.5**	**56.2**	**±0.9**
H-24	#1	0.622	0.011	0.092	0.002	20	0.045	0.001	10	0.49	1.553	0.150	343	0.81	*44.6*	**54.9**	**±1.6**		
	#2	0.454	0.009	0.066	0.001	23	0.034	0.001	12	0.51	1.074	0.105	376	0.79	*45.3*	**57.3**	**±1.7**		
	#3	0.230	0.005	0.042	0.001	16	0.021	0.001	8	0.50	0.510	0.052	195	0.65	*36.8*	**56.6**	**±1.9**	**56.3**	**±0.7**
H-29	#1	0.471	0.009	0.097	0.002	31	0.033	0.001	11	0.34	0.946	0.088	302	0.65	*34.4*	**52.7**	**±1.4**		
	#2	0.580	0.010	0.114	0.002	27	0.014	0.001	3	0.12	0.650	0.058	154	0.72	*39.2*	**55.9**	**±1.6**		
	#3	0.952	0.017	0.182	0.003	29	0.011	0.001	2	0.06	0.962	0.085	153	0.78	*40.7*	**52.2**	**±1.5**	**53.6**	**±1.2**
H-30	#1	0.260	0.005	0.054	0.001	45	0.005	0.001	4	0.09	0.344	0.017	280	0.62	*37.0*	**59.7**	**±1.8**		
	#2	0.095	0.003	0.011	0.001	4	0.005	0.001	2	0.47	0.457	0.023	188	0.78	*50.3*	**64.9**	**±3.8**		
	#3	0.715	0.013	0.126	0.002	5	0.010	0.001	1	0.08	1.087	0.054	43	0.82	*43.1*	**52.5**	**±1.4**	**59.0**	**±3.6**
H-31	#1	0.141	0.003	0.031	0.001	41	0.004	0.001	5	0.13	0.258	0.013	345	0.56	*34.3*	**61.0**	**±2.3**		
	#2	0.268	0.005	0.058	0.001	36	0.011	0.001	7	0.19	0.594	0.029	373	0.68	*33.8*	**49.7**	**±1.5**	**55.4**	**±5.7**
DC-31	#1	0.797	0.006	0.145	0.003	114	0.025	0.001	19	0.17	0.632	0.065	499	0.76	*42.2*	**55.7**	**±1.2**		
	#2	0.425	0.005	0.093	0.002	79	0.028	0.001	23	0.30	0.511	0.056	431	0.79	*33.8*	**42.6**	**±1.0**		
	#3	0.690	0.012	0.152	0.003	118	0.013	0.001	10	0.08	0.435	0.035	337	0.58	*35.9*	**61.4**	**±1.9**		
	#4	2.975	0.050	0.487	0.009	95	0.036	0.001	7	0.07	1.661	0.135	325	0.81	*48.2*	**59.3**	**±1.6**		
	#5	1.223	0.021	0.229	0.004	84	0.025	0.001	9	0.11	0.941	0.077	344	0.74	*41.7*	**56.3**	**±1.4**	**55.1**	**±3.3**
DC-33	#1	2.834	0.013	0.551	0.010	93	0.119	0.003	20	0.22	2.228	0.102	377	0.76	*39.2*	**51.8**	**±0.9**		
	#2	2.669	0.012	0.518	0.009	129	0.090	0.002	22	0.17	1.546	0.069	385	0.77	*39.9*	**51.6**	**±0.9**		
	#3	2.192	0.011	0.422	0.008	87	0.132	0.003	27	0.31	2.293	0.106	470	0.74	*38.4*	**51.9**	**±0.9**		
	#4	1.265	0.008	0.257	0.005	77	0.030	0.001	9	0.12	1.133	0.056	339	0.73	*38.3*	**52.7**	**±0.9**	**52.0**	**±0.2**

[a] alpha-ejection correction factor (Ft) after Farley et al. (1996).

[b] unweighted average age of each single Ft-corrected (U-Th)/He age.

Reference

Farley, K.A., Wolf, R.A., and Silver, L.T., 1996, The effects of long alpha-stopping distances on (U-Th)/He ages: Geochimica Cosmochimica Acta, v. 60, p. 4223–4229.

Table A.8: Ap fission track age dataset and goodness of fit values from thermal modeling

sample	number of	spontaneous		induced		dosimeter		chi-square[d]	dispersion[e]	**central age[f]**	**±1σ**	U	Dpar	±1σ	GOF[g]	GOF[g]	GOF[g]
number	crystals	Rho[a]	(N)[b]	Rho[a]	(N)[b]	Rho[c]	(N)[c]	P (%)		**(Ma)**	**(Ma)**	(ppm)	(µm)	(µm)	(age)	(length)	(AHe)
H-23	24	40.0	(1918)	77.7	(3726)	7.13	(6715)	79	0.00	**59.4**	**±2.3**	129	2.90	±0.15	0.75	0.33	0.25
H-24	23	11.0	(648)	21.7	(1279)	7.14	(6715)	99	0.00	**58.5**	**±3.3**	35	2.49	±0.16	0.18	0.17	0.19
H-29	26	15.3	(943)	31.1	(1921)	7.15	(6715)	100	0.00	**56.8**	**±2.8**	51	2.59	±0.18	0.97	0.37	0.44
H-31	23	12.7	(632)	21.5	(1073)	7.18	(6715)	95	0.00	**68.4**	**±3.9**	35	2.47	±0.18	–	–	–
DC-31	24	14.1	(802)	28.5	(1621)	7.35	(6680)	96	0.00	**58.8**	**±3.0**	48	2.09	±0.20	0.27	0.28	0.26
DC-33	28	21.2	(1694)	45.0	(3589)	7.80	(7096)	92	0.00	**59.6**	**±2.4**	70	2.37	±0.18	–	–	–

[a] Track densities (Rho) are as measured ($x10^5$ tr/cm^2).

[b] Number of tracks counted is shown in brackets.

[c] Rho and N are track densities of the CN5 detector.

[d] Chi-square P(%): probability obtaining Chi-square value for n degree of freedom (where n = no. crystals – 1).

[e] Dispersion was determined according to Galbraith and Laslett (1993).

[f] Central ages were calculated using dosimeter glass CN5.

[g] Goodness of fit (GOF) values obtained from the thermal modeling with the HeFTy software (see Data Repository for details)

Reference

Galbraith, R.F., and Laslett, G.M., 1993, Statistical models for mixed fission track ages: International Journal of Radiation Applications and Instrumentation, Part D, Nuclear Tracks and Radiation Measurements, v. 21(4), p. 459–470.

Table A.9: Sample locations, ^{10}Be concentrations, and erosion rates

sample number	latitude (°N)	longitude (°E)	elevation (m)	mean elevation (m)	sample thickness (cm)	^{10}Be concentration[a] (10^4 at g^{-1})	production rate (muons) (at g^{-1} a^{-1})	production rate (spallation) (at g^{-1} a^{-1})	**Erosion rate[b] (m Ma^{-1})**	internal 1σ error (m Ma^{-1})	external 1σ error (m Ma^{-1})	time scale[c] (ka)
Grus samples[d]												
08T10	31.2690	90.0759	5306	-	-	912 ± 27	0.829	93.14	**6.58**	±0.21	±0.62	91
08T12	31.2741	90.0842	5351	-	-	906 ± 27	0.838	94.99	**6.76**	±0.21	±0.63	89
08T13	31.2703	90.0852	5358	-	-	951 ± 29	0.840	95.26	**6.44**	±0.20	±0.60	93
08T20	31.2747	89.8416	5109	-	-	534 ± 16	0.792	85.42	**10.54**	±0.33	±0.96	57
08T24	31.4293	89.9033	5203	-	-	838 ± 25	0.810	89.55	**6.91**	±0.22	±0.64	87
Bedrock samples												
08T16	31.4548	89.9809	4916	-	3.5	714 ± 21	0.738	78.85	**6.97**	±0.22	±0.65	86
08T25	31.4293	89.9033	5203	-	5.0	709 ± 21	0.783	89.55	**7.90**	±0.25	±0.73	76
Stream sediment samples[d]												
08T21	31.4854	89.9299	4688	5070	-	346 ± 10	0.785	84.30	**16.29**	±0.50	±1.5	37
08T23	31.4009	90.0009	4734	4921	-	487 ± 15	0.758	78.52	**10.66**	±0.33	±0.97	56
08T26	31.4475	89.8987	4893	5054	-	441 ± 13	0.782	83.66	**12.61**	±0.39	±1.1	48
09T21	31.3534	89.8542	4783	5193	-	408 ± 12	0.808	88.74	**14.47**	±0.45	±1.3	41
09T26	31.3224	90.0513	4804	5202	-	479 ± 14	0.810	88.96	**12.30**	±0.38	±1.1	49
09T27	31.3450	90.0392	4776	5169	-	522 ± 16	0.804	87.70	**11.09**	±0.34	±1.0	54

[a] Blank-corrected ^{10}Be concentrations. Propagated analytical errors (1σ) include the error based on counting statistics and the error of the blank correction.

[b] Erosion rates were calculated with the CRONUS-Earth ^{10}Be - ^{26}Al calculator, version 2.2.1 (Balco et al., 2008; http://hess.ess.washington.edu) assuming a rock density of 2.7 g cm^{-3} and using the constant production rate scaling model of Lal (1991) - Stone (2000). Internal uncertainties include errors from the counting statistics and the blank correction, whereas external uncertainties also include the error of the production rate introduced by the scaling model. For calculating catchment-wide denudation rates we used the mean elevation of the respective catchments, which is reported in column 5. Topographic shielding of all samples was negligible.

[c] The time over which the erosion rate integrates is calculated by dividing the absorption depth scale of 60 cm with the erosion rate.

[d] For determining local and catchment-wide erosion rates from grus and stream sediment samples we used the 0.5–2 mm and 0.25–0.5 mm grain size fractions, respectively. To correct for the topographic shielding of the catchments we calculated a shielding factor for each catchment from a 30 m digital elevation model with the Matlab script of Greg Balco (http://depts.washington.edu/cosmolab/P_by_GIS.html).

A.2 Tables related to “Cretaceous to Cenozoic evolution of the northern Lhasa Terrane and the Early Paleogene development of peneplains at Nam Co, Tibetan Plateau”

Table A.10: Zrn U-Pb age dataset

				Ratios				Ages (Ma)				Conc[c]
Sample	**Spot #**	**Th/U[a]**	**$^{208}Pb/^{206}Pb$**	**$^{207}Pb/^{235}U$[a]**	**2 s[b]**	**$^{206}Pb/^{238}U$[a]**	**2 s[b]**	**$^{207}Pb/^{235}U$**	**2 s**	**$^{206}Pb/^{238}U$**	**2 s**	**%**
DC-23												
Tukey's Biweight robust sample mean:												
119.0 ± 2.3 [1.9%]												
	#1	0.48	0.24	0.1129	0.0071	0.0184	0.0006	120.4	8.7	115.1	4.5	0.96
	#2	0.48	0.24	0.1404	0.0059	0.0190	0.0008	133.4	7.1	121.2	5.8	0.91
	#3	0.49	0.24	0.1429	0.0051	0.0189	0.0005	133.6	6.0	122.2	3.8	0.91
	#4	0.44	0.22	0.1473	0.0031	0.0197	0.0006	139.5	3.8	126.0	4.5	0.90
	#5	0.48	0.23	0.1463	0.0063	0.0184	0.0003	132.4	7.1	118.7	2.5	0.90
	#6	0.77	0.37	0.1346	0.0074	0.0180	0.0005	128.0	8.4	115.5	3.6	0.90
	#7	0.66	0.31	0.1400	0.0043	0.0192	0.0004	133.2	5.2	120.9	3.4	0.91
	#8	0.80	0.38	0.1306	0.0044	0.0178	0.0005	125.0	5.0	113.3	3.3	0.91
	#9	0.61	0.31	0.1376	0.0048	0.0183	0.0005	129.3	5.6	118.0	3.5	0.91
	#10	0.51	0.29	0.1229	0.0289	0.0181	0.0007	118.3	31.5	116.0	5.0	0.98
	#11	0.44	0.22	0.1501	0.0053	0.0201	0.0003	139.9	6.4	130.2	2.9	0.93
	#12	0.55	0.27	0.1374	0.0049	0.0187	0.0005	129.0	5.7	119.0	4.0	0.92
	#13	0.46	0.22	0.1396	0.0053	0.0185	0.0004	129.5	6.0	118.4	2.7	0.91
	#14	0.54	0.28	0.1497	0.0148	0.0187	0.0006	127.0	15.1	118.3	4.6	0.93
	#15	0.27	0.13	0.1314	0.0068	0.0175	0.0005	127.0	7.9	116.0	3.9	0.91
	#16	0.55	0.26	0.1444	0.0059	0.0191	0.0006	134.2	7.0	121.6	4.4	0.91
DC-24												
Tukey's Biweight robust sample mean:												
111.8 ± 2.4 [2.2%]												
	#1	0.32	0.17	0.1212	0.0042	0.0160	0.0005	115.8	4.4	105.5	3.4	0.91
	#2	0.24	0.12	0.1338	0.0032	0.0177	0.0005	127.5	3.7	116.8	4.2	0.92
	#3	0.34	0.18	0.1272	0.0057	0.0175	0.0005	109.1	5.1	111.8	3.7	1.02
	#4	0.39	0.20	0.1276	0.0037	0.0172	0.0004	122.1	4.0	112.3	3.3	0.92
	#5	0.40	0.20	0.1300	0.0125	0.0169	0.0002	113.6	11.8	106.9	1.5	0.94
	#6	0.28	0.13	0.1284	0.0050	0.0172	0.0005	122.1	5.5	111.5	3.9	0.91
	#7	0.46	0.30	0.1252	0.0360	0.0180	0.0008	119.7	39.6	115.0	6.0	0.96
	#8	0.50	0.25	0.1378	0.0039	0.0189	0.0004	134.3	4.7	120.3	3.0	0.90
	#9	0.23	0.11	0.1383	0.0053	0.0182	0.0006	132.2	6.2	119.2	4.6	0.90
	#10	0.47	0.28	0.1149	0.0170	0.0161	0.0006	103.2	15.1	103.5	3.9	1.00
	#11	0.21	0.11	0.1244	0.0036	0.0172	0.0006	116.2	3.7	109.1	4.3	0.94
	#12	0.36	0.18	0.1324	0.0048	0.0172	0.0005	125.7	5.4	113.5	3.9	0.90
	#13	0.16	0.08	0.1215	0.0044	0.0166	0.0006	117.4	4.7	109.4	4.0	0.93
	#14	0.42	0.21	0.1338	0.0041	0.0182	0.0005	125.1	4.6	112.3	3.1	0.90
	#15	0.43	0.20	0.1814	0.0083	0.0233	0.0007	139.9	8.4	131.7	5.3	0.94
	#16	0.38	0.18	0.1599	0.0042	0.0206	0.0006	149.9	5.4	135.6	5.2	0.90
	#17	0.29	0.15	0.1240	0.0053	0.0165	0.0008	118.3	5.7	111.6	5.9	0.94
	#18	0.31	0.16	0.1313	0.0050	0.0175	0.0004	123.2	5.4	114.6	3.2	0.93
	#19	0.53	0.31	0.0936	0.0206	0.0165	0.0003	105.2	23.4	104.8	2.1	1.00
	#20	0.29	0.14	0.1335	0.0051	0.0177	0.0006	125.5	5.6	114.5	4.5	0.91

Table A.11: Zrn U-Pb age dataset

Sample	Spot #	Th/U[a]	$^{208}Pb/^{206}Pb$	Ratios: $^{207}Pb/^{235}U$[a]	2 s[b]	$^{206}Pb/^{238}U$[a]	2 s[b]	Ages (Ma): $^{207}Pb/^{235}U$	2 s	$^{206}Pb/^{238}U$	2 s	Conc[c] %
DC-28												
Tukey's Biweight robust sample mean:												
124.0 ± 3.6 [2.9%]												
	#1	0.38	0.17	0.1455	0.0070	0.0182	0.0011	129.3	7.5	122.3	8.8	0.95
	#2	0.51	0.25	0.1400	0.0140	0.0179	0.0010	129.5	15.8	118.5	7.8	0.91
	#3	0.36	0.16	0.2321	0.0167	0.0289	0.0016	197.5	25.7	185.9	19.5	0.94
	#4	0.39	0.17	0.1685	0.0130	0.0237	0.0018	165.4	19.5	149.8	16.5	0.91
	#5	0.22	0.10	0.1443	0.0094	0.0202	0.0010	135.6	11.3	125.9	7.6	0.93
	#6	0.37	0.17	0.1407	0.0059	0.0188	0.0006	133.3	7.1	120.8	4.5	0.91
	#7	0.48	0.23	0.1745	0.0101	0.0206	0.0005	151.9	12.5	137.6	4.8	0.91
	#8	0.38	0.18	0.1399	0.0059	0.0189	0.0005	131.9	6.9	118.3	3.9	0.90
	#9	0.50	0.24	0.1469	0.0082	0.0191	0.0005	138.9	10.1	120.8	3.5	0.87
	#10	0.49	0.26	0.1379	0.0058	0.0199	0.0006	128.0	6.5	125.4	4.5	0.98
	#11	0.48	0.23	0.1342	0.0039	0.0180	0.0005	128.0	4.5	114.8	3.6	0.90
	#12	0.48	0.22	0.1524	0.0052	0.0219	0.0007	146.0	6.7	137.2	5.6	0.94
	#13	0.24	0.12	0.1344	0.0070	0.0181	0.0006	128.0	8.1	115.5	4.5	0.90
	#14	0.40	0.19	0.1424	0.0070	0.0192	0.0004	135.3	8.4	122.4	3.4	0.90
	#15	0.54	0.27	0.1527	0.0257	0.0194	0.0007	118.2	22.3	121.1	5.0	1.02
	#16	0.50	0.22	0.1276	0.0070	0.0192	0.0008	129.1	8.6	120.1	6.0	0.93
	#17	0.36	0.17	0.1501	0.0131	0.0195	0.0007	135.2	15.0	125.4	5.4	0.93
	#18	0.60	0.26	0.1348	0.0090	0.0199	0.0008	134.9	11.5	126.7	6.1	0.94
	#19	0.07	0.03	0.1455	0.0051	0.0199	0.0004	136.0	6.1	124.9	3.1	0.92
	#20	0.50	0.23	0.1351	0.0062	0.0190	0.0005	133.2	7.7	123.2	4.1	0.93
DC-38												
Tukey's Biweight robust sample mean:												
58.3 ± 1.9 [3.3%]												
	#1	0.46	0.22	0.0747	0.0040	0.0090	0.0003	75.6	2.9	58.5	1.3	0.77
	#2	0.50	0.26	0.0580	0.0066	0.0082	0.0004	57.2	3.7	52.4	1.4	0.92
	#3	0.52	0.25	0.0647	0.0029	0.0090	0.0002	63.3	1.8	57.8	0.8	0.91
	#4	0.56	0.28	0.0656	0.0029	0.0087	0.0003	62.7	1.7	57.0	1.0	0.91
	#5	0.44	0.21	0.0700	0.0042	0.0098	0.0004	68.7	2.7	63.0	1.4	0.92
	#6	0.43	0.23	0.0605	0.0044	0.0086	0.0002	58.1	2.4	54.7	0.8	0.94
	#7	0.44	0.23	0.0753	0.0048	0.0091	0.0002	73.7	3.4	58.1	0.9	0.79
	#8	0.41	0.20	0.0618	0.0024	0.0088	0.0002	62.6	1.5	57.3	0.7	0.92
	#9	0.67	0.35	0.0797	0.0060	0.0093	0.0003	80.3	4.7	59.6	1.1	0.74
	#10	0.48	0.24	0.0688	0.0030	0.0088	0.0002	68.4	2.0	55.9	0.7	0.82
	#11	0.48	0.24	0.0725	0.0040	0.0091	0.0003	71.1	2.7	58.3	1.0	0.82
	#12	0.52	0.27	0.0702	0.0032	0.0089	0.0002	67.5	2.0	55.9	0.6	0.83
	#13	0.68	0.34	0.0688	0.0030	0.0096	0.0004	67.5	2.0	61.6	1.6	0.91
	#14	0.46	0.22	0.0726	0.0037	0.0091	0.0003	76.8	2.9	58.1	1.0	0.76
	#15	0.89	0.44	0.0653	0.0039	0.0089	0.0002	59.7	2.1	58.2	0.8	0.97
	#16	0.70	0.36	0.0732	0.0035	0.0088	0.0003	75.1	2.6	57.0	1.0	0.76
	#17	0.42	0.21	0.0635	0.0085	0.0087	0.0002	56.2	4.1	55.1	0.7	0.98
	#18	0.67	0.33	0.0772	0.0061	0.0093	0.0003	82.8	5.2	59.4	1.1	0.72
	#19	0.66	0.32	0.0724	0.0041	0.0099	0.0003	70.9	2.7	63.5	1.0	0.90
	#20	0.65	0.33	0.0678	0.0029	0.0097	0.0001	64.4	1.7	61.5	0.4	0.96
	#21	0.31	0.16	0.0637	0.0024	0.0085	0.0002	60.2	1.3	54.9	0.5	0.91

Table A.12: Zrn U-Pb age dataset

Sample	Spot #	Th/U[a]	$^{208}Pb/^{206}Pb$	Ratios: $^{207}Pb/^{235}U$[a]	2 s[b]	$^{206}Pb/^{238}U$[a]	2 s[b]	Ages (Ma): $^{207}Pb/^{235}U$	2 s	$^{206}Pb/^{238}U$	2 s	Conc[c] %
	#22	0.45	0.25	0.0817	0.0058	0.0089	0.0003	80.2	4.4	57.1	0.9	0.71
	#23	0.51	0.26	0.0621	0.0054	0.0090	0.0002	60.4	3.1	58.1	0.6	0.96
	#24	0.50	0.25	0.0679	0.0039	0.0085	0.0003	68.8	2.7	54.7	1.0	0.79
	#25	0.54	0.27	0.0666	0.0039	0.0087	0.0002	80.9	3.7	56.2	0.8	0.69
	#26	0.47	0.22	0.0626	0.0019	0.0087	0.0002	63.6	1.2	57.1	0.6	0.90
	#27	0.57	0.28	0.0687	0.0024	0.0091	0.0003	68.0	1.6	58.6	1.1	0.86
	#28	0.75	0.51	0.0843	0.0214	0.0087	0.0003	95.6	22.4	55.2	1.0	0.58
	#29	0.39	0.20	0.0741	0.0036	0.0101	0.0003	73.6	2.5	65.9	1.3	0.90
	#30	0.42	0.22	0.0685	0.0039	0.0088	0.0004	69.5	2.6	57.0	1.4	0.82
	#31	0.50	0.25	0.0654	0.0029	0.0083	0.0002	64.3	1.8	54.3	0.9	0.84
	#32	0.59	0.28	0.0724	0.0043	0.0090	0.0002	64.5	2.5	58.4	0.9	0.91
	#33	0.68	0.32	0.0626	0.0024	0.0085	0.0003	62.2	1.4	55.7	1.0	0.90
DC-40 Tukey's Biweight robust sample mean: **123.3 ± 4.2 [3.4%]**												
	#1	0.49	0.25	0.1306	0.0042	0.0180	0.0004	124.6	4.7	114.9	3.0	0.92
	#2	0.50	0.26	0.1464	0.0067	0.0188	0.0005	131.1	7.5	121.8	4.3	0.93
	#3	0.45	0.23	0.1385	0.0064	0.0190	0.0005	131.7	7.5	121.6	3.6	0.92
	#4	0.62	0.30	0.1495	0.0055	0.0204	0.0004	139.5	6.7	127.5	3.6	0.91
	#5	0.51	0.24	0.1565	0.0095	0.0197	0.0005	134.0	10.3	123.4	3.9	0.92
	#6	0.30	0.15	0.1297	0.0054	0.0175	0.0007	123.8	6.1	111.9	5.0	0.90
	#7	0.55	0.27	0.1395	0.0063	0.0183	0.0009	131.7	7.4	117.9	6.5	0.90
	#8	0.59	0.29	0.1508	0.0084	0.0200	0.0009	142.3	10.7	127.9	7.3	0.90
	#9	0.42	0.21	0.1427	0.0044	0.0190	0.0005	135.4	5.3	121.3	3.5	0.90
	#10	0.56	0.28	0.1873	0.0058	0.0225	0.0008	163.6	7.7	152.3	8.2	0.93
	#11	0.52	0.25	0.1473	0.0060	0.0192	0.0006	144.0	7.9	129.4	5.4	0.90
	#13	0.57	0.28	0.1425	0.0047	0.0211	0.0006	139.7	6.0	138.7	5.5	0.99
	#14	0.61	0.30	0.1495	0.0040	0.0199	0.0005	139.2	4.9	128.9	4.0	0.93
	#15	0.52	0.31	0.1432	0.0040	0.0195	0.0005	136.1	4.9	124.7	4.4	0.92
	#16	0.19	0.10	0.1489	0.0054	0.0197	0.0005	140.5	6.6	127.2	4.2	0.91
	#17	0.49	0.23	0.1542	0.0059	0.0210	0.0006	143.4	7.3	129.9	4.7	0.91
	#18	0.53	0.26	0.1417	0.0041	0.0188	0.0006	133.8	4.8	120.6	4.7	0.90
	#19	0.60	0.30	0.1237	0.0068	0.0183	0.0005	113.0	6.7	114.2	3.3	1.01
	#20	0.53	0.23	0.1167	0.0124	0.0163	0.0014	111.3	12.5	106.2	9.9	0.95
	#21	0.45	0.21	0.1348	0.0036	0.0185	0.0005	129.3	4.3	117.5	3.4	0.91
DC-41 Tukey's Biweight robust sample mean: **124.8 ± 4.2 [3.4%]**												
	#1	0.43	0.22	0.1454	0.0089	0.0191	0.0005	135.7	10.6	121.7	3.7	0.90
	#2	0.65	0.33	0.1490	0.0048	0.0204	0.0006	142.1	6.1	129.5	4.7	0.91
	#3	0.44	0.23	0.1701	0.0216	0.0187	0.0006	132.1	21.0	118.4	4.7	0.90
	#4	0.59	0.30	0.1387	0.0055	0.0189	0.0005	132.0	6.6	119.9	3.8	0.91
	#5	0.43	0.22	0.1552	0.0048	0.0221	0.0005	147.5	6.3	136.2	3.8	0.92
	#6	0.42	0.21	0.1418	0.0044	0.0190	0.0005	134.7	5.3	122.3	3.8	0.91
	#7	0.29	0.15	0.1685	0.0035	0.0216	0.0006	158.0	4.9	141.6	5.4	0.90
	#8	0.21	0.16	0.1529	0.0052	0.0202	0.0007	150.8	7.2	135.5	6.5	0.90

Table A.13: Zrn U-Pb age dataset

Sample	Spot #	Th/U[a]	$^{208}Pb/^{206}Pb$	Ratios: $^{207}Pb/^{235}U$[a]	2 s[b]	$^{206}Pb/^{238}U$[a]	2 s[b]	Ages (Ma): $^{207}Pb/^{235}U$	2 s	$^{206}Pb/^{238}U$	2 s	Conc[c] %
	#9	0.57	0.31	0.1331	0.0071	0.0188	0.0005	129.3	8.4	122.2	4.2	0.95
	#10	0.33	0.39	0.1190	0.0156	0.0183	0.0005	114.2	16.2	116.8	3.5	1.02
	#11	0.48	0.23	0.2083	0.0254	0.0197	0.0005	136.8	21.5	135.1	4.5	0.99
	#12	0.27	0.23	0.1454	0.0052	0.0192	0.0006	135.5	6.2	122.3	4.8	0.90
	#13	0.35	0.17	0.1195	0.0054	0.0167	0.0006	114.7	5.6	106.9	4.3	0.93
	#14	0.31	0.16	0.1498	0.0046	0.0190	0.0004	137.0	5.5	123.9	2.8	0.90
	#15	0.43	0.22	0.1434	0.0042	0.0189	0.0004	136.2	5.0	122.0	3.3	0.90
	#16	0.06	0.06	0.1438	0.0029	0.0190	0.0003	133.4	3.3	121.6	2.4	0.91
	#17	0.61	0.31	0.1535	0.0066	0.0204	0.0007	140.1	7.8	130.8	5.6	0.93
	#18	0.17	0.13	0.1408	0.0038	0.0190	0.0006	133.7	4.5	121.3	5.0	0.91
H-7 Tukey's Biweight robust sample mean: **127.0 ± 1.6 [1.2%]**												
	#1	0.43	0.23	0.1976	0.0091	0.0194	0.0004	189.3	15.1	124.2	3.4	0.66
	#2	0.43	0.21	0.1564	0.0048	0.0208	0.0004	147.4	6.3	133.0	3.2	0.90
	#3	0.53	0.24	0.1475	0.0043	0.0199	0.0003	139.5	5.3	126.8	2.3	0.91
	#4	0.50	0.23	0.1637	0.0036	0.0205	0.0003	158.9	5.1	129.3	2.8	0.81
	#5	0.25	0.12	0.1459	0.0067	0.0196	0.0005	138.2	8.3	125.4	4.4	0.91
	#6	0.28	0.13	0.1495	0.0030	0.0195	0.0004	141.3	3.7	124.3	2.9	0.88
	#7	0.29	0.14	0.1421	0.0054	0.0192	0.0004	133.2	6.4	121.8	3.4	0.91
	#8	1.15	0.50	0.1410	0.0051	0.0192	0.0007	134.0	6.0	122.8	5.4	0.92
	#9	0.34	0.16	0.1562	0.0042	0.0201	0.0004	147.3	5.5	128.2	3.1	0.87
	#10	0.36	0.17	0.1460	0.0036	0.0198	0.0005	137.4	4.4	126.5	3.8	0.92
	#11	0.50	0.23	0.1513	0.0051	0.0195	0.0005	144.1	6.6	125.3	3.8	0.87
	#12	0.29	0.14	0.1580	0.0070	0.0213	0.0007	151.3	9.4	140.0	6.6	0.93
	#13	0.51	0.24	0.1490	0.0067	0.0207	0.0006	146.0	8.9	135.4	5.1	0.93
	#14	0.34	0.16	0.1431	0.0059	0.0195	0.0004	135.4	7.0	124.1	2.9	0.92
	#15	0.49	0.25	0.1425	0.0118	0.0199	0.0003	135.0	14.2	127.0	2.4	0.94
	#16	0.81	0.39	0.1673	0.0127	0.0198	0.0003	121.2	10.5	121.3	2.4	1.00
	#17	0.25	0.12	0.1490	0.0036	0.0198	0.0003	140.1	4.3	126.0	2.5	0.90
	#19	0.49	0.23	0.1570	0.0053	0.0196	0.0003	149.1	7.0	125.5	2.4	0.84
	#20	0.35	0.16	0.1449	0.0036	0.0194	0.0004	137.0	4.4	124.6	3.1	0.91
	#21	0.47	0.22	0.1469	0.0066	0.0197	0.0006	139.1	8.2	125.5	5.0	0.90
	#22	0.15	0.07	0.1551	0.0039	0.0212	0.0005	144.8	4.9	135.7	4.3	0.94
	#23	0.33	0.16	0.1534	0.0041	0.0193	0.0005	145.1	5.4	124.9	3.7	0.86
	#24	0.29	0.14	0.1524	0.0079	0.0203	0.0003	142.0	9.8	129.1	2.8	0.91
	#25	0.28	0.24	0.1413	0.0973	0.0202	0.0008	139.4	131.0	129.2	6.5	0.93
	#26	0.31	0.14	0.1646	0.0069	0.0204	0.0005	159.2	9.9	130.8	4.2	0.82
	#27	0.29	0.13	0.1493	0.0025	0.0197	0.0003	142.9	3.3	128.0	2.8	0.90
	#28	0.20	0.10	0.1610	0.0061	0.0210	0.0005	152.1	8.2	136.9	4.8	0.90
	#29	0.29	0.13	0.1452	0.0032	0.0193	0.0003	138.5	4.0	124.7	2.4	0.90
	#30	0.57	0.28	0.1431	0.0044	0.0194	0.0004	135.8	5.3	123.6	3.5	0.91
	#31	0.16	0.07	0.1420	0.0045	0.0194	0.0005	134.7	5.4	123.9	3.6	0.92
	#32	0.31	0.16	0.1498	0.0057	0.0194	0.0004	136.5	6.7	123.6	2.8	0.91
	#33	0.36	0.17	0.1539	0.0040	0.0195	0.0005	145.4	5.1	124.0	4.1	0.85

Table A.14: Zrn U-Pb age dataset

				Ratios				Ages (Ma)				Conc[c]
Sample	**Spot #**	**Th/U[a]**	**$^{208}Pb/^{206}Pb$**	**$^{207}Pb/^{235}U^{a}$**	**2 s[b]**	**$^{206}Pb/^{238}U^{a}$**	**2 s[b]**	**$^{207}Pb/^{235}U$**	**2 s**	**$^{206}Pb/^{238}U$**	**2 s**	%
H-10												
Tukey's Biweight robust sample mean:												
130.4 ± 1.0 [0.8%]												
	#1	0.38	0.19	0.1450	0.0029	0.0205	0.0004	137.8	3.6	131.6	3.4	0.96
	#2	0.60	0.30	0.1413	0.0049	0.0209	0.0006	134.4	5.9	133.4	5.1	0.99
	#3	0.46	0.23	0.1467	0.0063	0.0207	0.0005	141.9	8.1	131.9	3.8	0.93
	#4	0.69	0.37	0.1473	0.0094	0.0207	0.0007	143.7	12.4	129.9	6.0	0.90
	#5	0.46	0.24	0.1538	0.0069	0.0208	0.0005	141.5	8.5	131.5	4.5	0.93
	#6	0.50	0.25	0.1452	0.0073	0.0214	0.0005	143.0	9.6	136.2	4.6	0.95
	#7	0.38	0.19	0.1362	0.0054	0.0187	0.0006	134.0	6.7	122.3	4.4	0.91
	#8	0.18	0.09	0.1490	0.0076	0.0216	0.0012	141.0	9.4	137.7	10.5	0.98
	#9	0.44	0.23	0.1517	0.0053	0.0207	0.0005	145.1	6.8	133.1	4.4	0.92
	#10	0.62	0.32	0.1417	0.0112	0.0204	0.0006	133.1	13.2	131.5	5.3	0.99
	#11	0.30	0.18	0.1370	0.0119	0.0198	0.0006	130.4	14.0	126.1	4.9	0.97
	#12	0.47	0.24	0.1432	0.0049	0.0205	0.0004	137.8	6.1	130.2	3.1	0.95
	#13	0.49	0.25	0.1542	0.0059	0.0208	0.0006	145.6	7.6	132.4	5.2	0.91
	#14	0.50	0.26	0.1305	0.0608	0.0207	0.0005	133.5	80.1	131.8	4.3	0.99
	#15	0.65	0.34	0.1393	0.0077	0.0203	0.0010	137.2	9.7	129.9	8.6	0.95
	#16	0.56	0.28	0.1383	0.0102	0.0206	0.0007	131.5	12.1	131.4	5.7	1.00
	#17	0.61	0.29	0.1389	0.0035	0.0205	0.0003	133.1	4.1	130.7	2.7	0.98
	#18	0.56	0.30	0.1353	0.0145	0.0200	0.0004	127.5	16.4	127.0	3.6	1.00
	#19	0.69	0.35	0.1431	0.0043	0.0200	0.0006	134.1	5.1	129.0	5.2	0.96
	#20	0.42	0.22	0.1344	0.0071	0.0203	0.0004	131.2	8.5	130.3	3.0	0.99
	#21	0.62	0.30	0.1348	0.0055	0.0204	0.0005	132.5	6.8	130.1	4.6	0.98
	#22	0.42	0.20	0.1400	0.0097	0.0203	0.0004	143.2	13.3	130.3	3.0	0.91
	#23	0.67	0.33	0.1333	0.0103	0.0202	0.0004	126.5	11.6	128.8	3.1	1.02
	#24	0.48	0.24	0.1509	0.0057	0.0208	0.0004	142.1	7.2	131.9	2.9	0.93
	#25	0.52	0.25	0.1420	0.0051	0.0206	0.0003	134.7	6.2	130.3	2.7	0.97
	#26	0.54	0.26	0.1444	0.0064	0.0205	0.0005	145.5	8.7	130.6	3.7	0.90
	#27	0.47	0.23	0.1426	0.0066	0.0197	0.0005	142.7	8.7	129.1	3.7	0.90
	#28	0.80	0.39	0.1396	0.0031	0.0200	0.0004	134.0	3.8	127.7	3.1	0.95
	#29	0.42	0.20	0.1428	0.0050	0.0203	0.0004	137.6	6.2	129.8	3.4	0.94
	#30	0.77	0.38	0.1357	0.0038	0.0193	0.0004	129.2	4.4	123.1	3.3	0.95
H-11												
Tukey's Biweight robust sample mean:												
63.1 ± 2.5 [3.9%]												
	#1	0.57	0.28	0.0826	0.0160	0.0100	0.0003	66.5	8.4	62.9	1.3	0.95
	#2	0.30	0.13	0.0785	0.0050	0.0112	0.0006	77.5	3.7	72.6	2.9	0.94
	#3	0.43	0.20	0.0935	0.0049	0.0133	0.0005	90.8	4.1	85.3	2.6	0.94
	#4	0.42	0.21	0.0622	0.0035	0.0092	0.0004	60.6	2.0	58.4	1.5	0.96
	#5	0.56	0.28	0.0708	0.0030	0.0100	0.0003	69.3	2.0	64.0	1.2	0.92
	#6	0.52	0.28	0.0623	0.0046	0.0089	0.0004	61.7	2.7	57.3	1.7	0.93
	#7	0.19	0.10	0.0647	0.0043	0.0097	0.0005	63.6	2.6	62.4	2.2	0.98
	#8	0.50	0.26	0.0754	0.0062	0.0105	0.0004	73.8	4.4	67.4	1.9	0.91
	#9	0.32	0.17	0.0642	0.0046	0.0091	0.0004	64.5	2.8	59.4	1.7	0.92
	#10	0.45	0.24	0.0618	0.0035	0.0092	0.0003	60.9	2.0	58.7	1.2	0.96
	#11	0.35	0.18	0.0831	0.0049	0.0117	0.0005	79.9	3.6	73.8	2.4	0.92

Table A.15: Zrn U-Pb age dataset

Sample	Spot #	Th/U[a]	$^{208}Pb/^{206}Pb$	Ratios $^{207}Pb/^{235}U$[a]	2 s[b]	$^{206}Pb/^{238}U$[a]	2 s[b]	Ages (Ma) $^{207}Pb/^{235}U$	2 s	$^{206}Pb/^{238}U$	2 s	Conc[c] %
	#12	0.40	0.20	0.0765	0.0031	0.0107	0.0003	71.9	2.0	65.6	1.3	0.91
	#13	0.47	0.26	0.0636	0.0035	0.0095	0.0004	62.6	2.1	60.6	1.6	0.97
	#14	0.52	0.29	0.0708	0.0037	0.0101	0.0004	70.5	2.5	65.4	1.5	0.93
	#15	0.79	0.40	0.0734	0.0045	0.0101	0.0003	71.9	3.1	65.0	1.1	0.90
	#16	0.43	0.22	0.0646	0.0042	0.0096	0.0005	63.8	2.6	62.0	1.9	0.97
	#17	0.53	0.27	0.0628	0.0037	0.0093	0.0005	62.4	2.2	60.5	1.9	0.97
	#18	0.70	0.36	0.0636	0.0041	0.0096	0.0004	62.7	2.4	61.8	1.6	0.99
	#19	0.64	0.33	0.0638	0.0046	0.0093	0.0006	63.3	2.8	59.9	2.2	0.95
	#20	0.14	0.07	0.0614	0.0031	0.0094	0.0004	60.7	1.8	60.4	1.6	1.00
	#21	0.43	0.22	0.0774	0.0038	0.0117	0.0005	78.5	2.9	77.6	2.5	0.99
	#22	0.52	0.28	0.0636	0.0032	0.0091	0.0003	62.6	1.9	58.4	1.2	0.93
	#23	0.69	0.38	0.0600	0.0052	0.0089	0.0004	60.2	3.1	58.4	1.4	0.97
	#24	0.56	0.29	0.0597	0.0031	0.0088	0.0004	60.1	1.8	57.8	1.4	0.96
H-14 Tukey's Biweight robust sample mean: **117.4 ± 1.3 [1.1%]**												
	#1	0.66	0.30	0.1932	0.0133	0.0243	0.0013	163.6	17.2	154.4	12.2	0.94
	#2	0.54	0.26	0.1379	0.0073	0.0178	0.0006	133.2	8.8	114.7	4.7	0.86
	#3	0.37	0.18	0.1557	0.0065	0.0187	0.0007	148.1	8.6	121.0	5.3	0.82
	#4	0.40	0.19	0.1328	0.0052	0.0181	0.0004	121.5	5.5	114.9	2.6	0.95
	#5	0.40	0.19	0.1356	0.0046	0.0185	0.0005	128.8	5.3	117.6	3.5	0.91
	#6	0.40	0.21	0.1370	0.0079	0.0178	0.0017	129.7	9.2	116.9	12.7	0.90
	#7	0.68	0.31	0.1351	0.0055	0.0182	0.0007	128.8	6.4	116.8	4.9	0.91
	#8	0.53	0.25	0.1334	0.0080	0.0183	0.0008	127.1	9.2	116.8	5.8	0.92
	#9	0.45	0.22	0.1344	0.0070	0.0185	0.0007	128.9	8.1	116.8	5.4	0.91
	#10	0.29	0.14	0.1340	0.0042	0.0182	0.0007	125.8	4.7	115.8	4.9	0.92
	#11	0.37	0.19	0.1390	0.0131	0.0174	0.0007	118.2	12.4	111.9	5.3	0.95
	#12	0.66	0.32	0.1389	0.0057	0.0190	0.0005	131.6	6.7	119.2	3.6	0.91
	#13	0.71	0.22	0.1438	0.0078	0.0191	0.0010	136.4	9.4	122.5	7.6	0.90
	#14	0.22	0.11	0.1344	0.0069	0.0182	0.0008	128.1	7.9	116.4	5.6	0.91
	#15	0.66	0.31	0.1275	0.0050	0.0180	0.0006	122.2	5.5	116.2	4.3	0.95
	#16	0.40	0.19	0.1315	0.0054	0.0181	0.0004	122.3	5.7	114.4	3.0	0.94
	#17	0.24	0.15	0.1600	0.0067	0.0222	0.0006	150.7	8.9	141.8	5.1	0.94
	#18	0.37	0.18	0.1361	0.0035	0.0181	0.0005	128.5	4.0	116.7	3.4	0.91
	#19	0.41	0.21	0.1377	0.0083	0.0188	0.0005	131.0	9.7	120.3	3.8	0.92
	#20	0.66	0.32	0.1386	0.0053	0.0177	0.0005	135.1	6.5	113.9	3.8	0.84
	#21	0.37	0.18	0.1488	0.0070	0.0193	0.0006	137.3	8.4	123.6	4.7	0.90
	#22	0.55	0.26	0.1315	0.0041	0.0178	0.0005	124.4	4.5	113.8	3.4	0.92
	#23	0.30	0.14	0.1334	0.0039	0.0183	0.0004	128.4	4.5	116.1	2.7	0.90
	#24	0.32	0.15	0.1428	0.0063	0.0189	0.0008	132.5	7.3	120.5	5.8	0.91
	#25	0.36	0.18	0.1319	0.0053	0.0180	0.0005	125.2	5.9	115.3	3.3	0.92
	#26	0.37	0.18	0.1234	0.0080	0.0174	0.0008	121.9	9.1	109.9	5.4	0.90
	#27	0.51	0.28	0.1350	0.0035	0.0176	0.0010	133.4	4.4	128.1	9.1	0.96
	#28	0.26	0.13	0.1392	0.0050	0.0185	0.0007	133.5	6.0	120.2	5.2	0.90
	#29	0.43	0.20	0.1330	0.0057	0.0182	0.0005	126.0	6.4	117.1	4.0	0.93
	#30	0.45	0.22	0.1355	0.0034	0.0187	0.0004	127.2	3.8	118.0	3.0	0.93
	#31	0.49	0.24	0.1375	0.0047	0.0182	0.0005	133.2	5.7	119.2	4.1	0.90
	#32	0.42	0.20	0.1452	0.0038	0.0196	0.0004	137.1	4.5	124.7	2.7	0.91

Table A.16: Zrn U-Pb age dataset

Sample	Spot #	Th/U[a]	$^{208}Pb/^{206}Pb$	Ratios $^{207}Pb/^{235}U$[a]	2 s[b]	$^{206}Pb/^{238}U$[a]	2 s[b]	Ages (Ma) $^{207}Pb/^{235}U$	2 s	$^{206}Pb/^{238}U$	2 s	Conc[c] %
	#33	0.56	0.26	0.1370	0.0051	0.0179	0.0006	126.6	5.6	116.0	4.3	0.92
	#34	0.36	0.18	0.1236	0.0098	0.0181	0.0004	118.1	10.4	118.4	3.1	1.00
	#35	0.31	0.15	0.1372	0.0104	0.0177	0.0004	125.2	11.3	112.7	2.9	0.90
H-19 Tukey's Biweight robust sample mean: **85.5 ± 1.5 [1.8%]**												
	#1	0.36	0.19	0.0857	0.0040	0.0122	0.0005	83.4	3.2	78.0	2.3	0.94
	#2	0.38	0.18	0.0834	0.0042	0.0124	0.0005	81.8	3.2	80.0	2.6	0.98
	#3	0.58	0.28	0.0834	0.0045	0.0124	0.0006	81.3	3.4	79.4	2.9	0.98
	#4	0.57	0.26	0.0988	0.0054	0.0136	0.0004	95.7	4.8	87.4	2.0	0.91
	#5	0.43	0.23	0.0867	0.0052	0.0124	0.0005	86.4	4.3	81.6	2.6	0.95
	#6	0.53	0.28	0.0819	0.0045	0.0123	0.0005	79.5	3.3	78.5	2.5	0.99
	#7	0.52	0.27	0.0828	0.0047	0.0121	0.0006	80.8	3.6	77.7	2.9	0.96
	#8	1.23	0.61	0.1043	0.0042	0.0143	0.0002	99.9	3.8	90.5	1.2	0.91
	#9	0.89	0.46	0.0895	0.0053	0.0129	0.0005	86.9	4.3	82.6	2.5	0.95
	#10	0.43	0.23	0.0917	0.0028	0.0135	0.0003	89.3	2.3	87.1	1.6	0.98
	#11	0.26	0.31	0.0969	0.0049	0.0136	0.0004	86.3	3.6	87.3	2.0	1.01
	#12	0.64	0.33	0.0938	0.0035	0.0140	0.0004	93.5	3.1	90.7	2.1	0.97
	#13	0.52	0.32	0.0890	0.0025	0.0131	0.0004	84.6	1.9	86.3	2.3	1.02
	#14	0.38	0.20	0.0869	0.0021	0.0135	0.0004	84.9	1.7	86.0	2.2	1.01
	#15	0.77	0.39	0.0953	0.0019	0.0133	0.0003	94.6	1.7	85.4	1.4	0.90
	#16	1.13	0.70	0.0932	0.0147	0.0133	0.0005	90.6	12.5	86.8	3.0	0.96
	#17	0.34	0.19	0.0989	0.0061	0.0141	0.0003	100.2	5.9	90.8	1.5	0.91
	#18	0.42	0.21	0.0970	0.0039	0.0137	0.0004	93.9	3.4	87.8	2.0	0.93
	#19	0.40	0.29	0.0959	0.0215	0.0135	0.0006	93.0	18.7	86.3	3.3	0.93
	#20	0.29	0.16	0.0878	0.0023	0.0133	0.0004	85.3	1.8	85.2	2.0	1.00
	#21	0.40	0.20	0.0908	0.0017	0.0132	0.0003	88.2	1.4	84.4	1.5	0.96
	#22	0.48	0.25	0.1001	0.0069	0.0136	0.0003	96.6	6.2	88.2	1.7	0.91
	#23	0.41	0.21	0.0927	0.0023	0.0137	0.0002	91.1	2.0	87.0	1.2	0.96
	#24	0.33	0.18	0.0912	0.0026	0.0135	0.0004	89.5	2.1	86.1	2.1	0.96
	#25	0.35	0.18	0.0945	0.0028	0.0135	0.0004	91.6	2.4	87.2	2.1	0.95
	#26	0.40	0.20	0.0912	0.0024	0.0132	0.0003	88.7	2.0	84.7	1.8	0.95
	#27	0.74	0.40	0.0901	0.0037	0.0133	0.0003	86.1	2.9	83.7	1.6	0.97
H-20 Tukey's Biweight robust sample mean: **83.7 ± 1.1 [1.3%]**												
	#1	0.88	0.42	0.0921	0.0085	0.0133	0.0005	95.6	8.0	86.4	3.0	0.90
	#2	0.98	0.47	0.0898	0.0037	0.0130	0.0003	86.6	2.9	82.3	1.6	0.95
	#3	0.37	0.18	0.0884	0.0019	0.0127	0.0002	85.8	1.5	81.3	1.0	0.95
	#4	0.78	0.37	0.0939	0.0037	0.0131	0.0003	89.5	3.0	82.4	1.5	0.92
	#5	0.60	0.29	0.0841	0.0046	0.0129	0.0003	79.6	3.3	81.3	1.8	1.02
	#6	0.35	0.18	0.0930	0.0033	0.0131	0.0002	90.6	2.7	84.8	1.4	0.94
	#7	0.56	0.29	0.0911	0.0129	0.0128	0.0002	87.6	10.5	81.7	1.2	0.93
	#8	0.82	0.40	0.0932	0.0049	0.0133	0.0004	92.0	4.3	86.0	2.2	0.94
	#9	0.59	0.33	0.0935	0.0376	0.0136	0.0005	93.3	34.1	87.4	2.6	0.94
	#10	0.49	0.24	0.0879	0.0037	0.0127	0.0003	81.6	2.7	81.7	1.5	1.00

Table A.17: Zrn U-Pb age dataset

Sample	Spot #	Th/U[a]	$^{208}Pb/^{206}Pb$	Ratios: $^{207}Pb/^{235}U$[a]	2 s[b]	$^{206}Pb/^{238}U$[a]	2 s[b]	Ages (Ma): $^{207}Pb/^{235}U$	2 s	$^{206}Pb/^{238}U$	2 s	Conc[c] %
	#11	0.69	0.33	0.0971	0.0076	0.0136	0.0005	95.4	6.8	88.2	3.0	0.93
	#12	0.36	0.36	0.0903	0.0052	0.0131	0.0003	94.5	4.9	84.9	1.7	0.90
	#13	0.20	0.09	0.0882	0.0022	0.0129	0.0002	85.9	1.8	82.6	1.2	0.96
	#14	0.34	0.17	0.0884	0.0044	0.0130	0.0005	86.7	3.6	83.6	2.7	0.96
	#15	1.03	0.51	0.0826	0.0067	0.0126	0.0004	80.5	5.1	80.7	1.9	1.00
	#16	0.23	0.12	0.0866	0.0020	0.0129	0.0004	85.4	1.6	82.5	2.0	0.97
	#17	0.38	0.19	0.0944	0.0034	0.0132	0.0004	90.8	2.8	83.2	2.0	0.92
	#18	0.96	0.46	0.0964	0.0055	0.0139	0.0007	98.2	5.3	90.1	3.9	0.92
	#20	0.97	0.50	0.0869	0.0049	0.0120	0.0004	84.4	3.8	78.3	2.0	0.93
	#21	0.83	0.41	0.0922	0.0035	0.0129	0.0004	91.0	3.0	82.8	2.1	0.91
	#22	1.09	0.52	0.0878	0.0041	0.0134	0.0005	85.4	3.3	85.7	2.7	1.00
	#24	0.64	0.31	0.0920	0.0062	0.0135	0.0006	87.2	4.9	83.7	3.0	0.96
	#25	0.45	0.24	0.0934	0.0048	0.0130	0.0003	90.7	4.0	83.3	1.4	0.92
	#26	0.94	0.46	0.0946	0.0040	0.0128	0.0004	86.7	3.0	83.0	2.1	0.96
	#27	0.82	0.43	0.0885	0.0131	0.0134	0.0006	87.4	10.9	87.9	3.4	1.01
H-33 Tukey's Biweight robust sample mean: **123.3 ± 3.2 [2.6%]**												
	#1	0.53	0.23	0.1405	0.0076	0.0191	0.0006	133.5	9.1	122.1	4.6	0.91
	#2	0.07	0.03	0.1286	0.0072	0.0173	0.0008	122.4	8.0	109.6	5.8	0.90
	#3	0.48	0.22	0.1629	0.0137	0.0188	0.0008	128.9	13.1	117.9	5.5	0.91
	#4	0.46	0.22	0.1556	0.0110	0.0192	0.0005	147.8	14.5	137.2	4.7	0.93
	#5	0.50	0.25	0.1414	0.0102	0.0215	0.0006	139.4	13.1	134.2	4.7	0.96
	#6	0.38	0.18	0.1386	0.0090	0.0187	0.0007	129.7	10.2	114.6	4.7	0.88
	#7	0.70	0.34	0.1605	0.0059	0.0202	0.0003	161.7	8.9	133.0	2.4	0.82
	#8	0.15	0.07	0.1401	0.0053	0.0194	0.0005	136.3	6.7	124.3	3.7	0.91
	#9	0.68	0.31	0.1362	0.0040	0.0193	0.0004	129.7	4.5	123.5	3.5	0.95
	#10	0.50	0.24	0.1449	0.0119	0.0202	0.0006	137.4	14.6	129.0	4.9	0.94
	#11	0.62	0.30	0.1380	0.0068	0.0191	0.0003	128.0	7.6	120.1	2.0	0.94
	#12	0.59	0.27	0.1707	0.0273	0.0218	0.0012	141.4	30.1	134.2	9.4	0.95
	#13	0.46	0.21	0.1352	0.0046	0.0187	0.0004	128.7	5.3	119.6	2.9	0.93
	#14	0.48	0.34	0.1640	0.0146	0.0218	0.0020	140.2	16.4	125.7	14.2	0.90
	#15	0.39	0.21	0.1421	0.0055	0.0196	0.0003	139.4	7.1	126.2	2.7	0.91
	#16	0.60	0.29	0.1485	0.0117	0.0191	0.0006	134.4	13.4	123.0	4.8	0.92
	#17	0.39	0.19	0.1398	0.0032	0.0191	0.0003	135.6	3.9	121.7	2.3	0.90
	#18	0.46	0.23	0.1408	0.0046	0.0184	0.0004	132.6	5.4	120.0	3.0	0.90
	#19	0.39	0.18	0.1449	0.0046	0.0196	0.0006	138.5	5.8	126.5	4.9	0.91
	#20	0.63	0.30	0.1354	0.0045	0.0195	0.0006	132.5	5.4	126.4	5.2	0.95
	#21	0.32	0.16	0.1345	0.0078	0.0183	0.0008	128.4	9.0	117.1	5.6	0.91
	#22	0.69	0.31	0.1150	0.0168	0.0171	0.0017	110.5	17.0	109.2	11.5	0.99
	#23	0.38	0.18	0.1355	0.0103	0.0189	0.0005	130.5	12.1	120.7	3.6	0.92
H-35 Tukey's Biweight robust sample mean: **120.8 ± 1.5 [2.2%]**												
	#1	0.32	0.17	0.1408	0.0038	0.0190	0.0003	132.0	4.4	119.9	2.5	0.91
	#2	0.26	0.13	0.1355	0.0028	0.0183	0.0003	129.7	3.4	116.8	2.2	0.90

Table A.18: Zrn U-Pb age dataset

				Ratios				Ages (Ma)				Conc[c]
Sample	**Spot #**	**Th/U[a]**	**$^{208}Pb/^{206}Pb$**	**$^{207}Pb/^{235}U$[a]**	**2 s[b]**	**$^{206}Pb/^{238}U$[a]**	**2 s[b]**	**$^{207}Pb/^{235}U$**	**2 s**	**$^{206}Pb/^{238}U$**	**2 s**	**%**
	#3	0.39	0.19	0.1403	0.0052	0.0187	0.0005	134.2	6.3	120.8	4.1	0.90
	#4	0.52	0.24	0.1426	0.0083	0.0187	0.0012	130.9	9.3	119.2	9.2	0.91
	#6	0.46	0.21	0.1301	0.0052	0.0175	0.0006	126.8	6.1	114.5	4.5	0.90
	#7	0.55	0.27	0.1389	0.0081	0.0178	0.0007	126.6	8.7	118.4	5.6	0.93
	#8	0.34	0.16	0.1350	0.0046	0.0182	0.0003	128.7	5.3	118.0	2.5	0.92
	#9	0.37	0.17	0.1379	0.0047	0.0187	0.0005	131.1	5.5	120.4	3.6	0.92
	#10	0.42	0.20	0.1374	0.0048	0.0190	0.0003	130.8	5.6	121.1	2.7	0.93
	#11	0.38	0.18	0.1266	0.0078	0.0175	0.0005	121.1	8.6	111.3	3.7	0.92
	#12	0.40	0.19	0.1404	0.0074	0.0195	0.0005	133.7	9.0	122.0	4.1	0.91
	#13	0.29	0.14	0.1425	0.0070	0.0189	0.0010	128.6	7.6	121.9	7.8	0.95
	#14	0.53	0.24	0.1799	0.0216	0.0190	0.0006	130.0	19.2	119.1	4.8	0.92
	#15	0.35	0.18	0.1321	0.0098	0.0182	0.0005	126.1	11.1	117.0	3.4	0.93
	#16	0.30	0.21	0.1467	0.0183	0.0206	0.0019	130.8	20.3	121.4	13.6	0.93
	#17	0.29	0.14	0.1468	0.0094	0.0192	0.0012	137.6	11.4	124.2	9.7	0.90
	#18	0.52	0.25	0.1359	0.0052	0.0187	0.0006	134.9	6.5	121.2	4.4	0.90
	#19	0.62	0.29	0.1418	0.0157	0.0185	0.0012	135.0	19.0	122.4	9.9	0.91
	#20	0.20	0.09	0.1449	0.0107	0.0192	0.0009	133.5	12.4	121.5	6.9	0.91
	#21	0.16	0.08	0.1491	0.0089	0.0199	0.0010	139.7	11.0	126.3	8.0	0.90
	#22	0.38	0.19	0.1432	0.0139	0.0188	0.0008	129.4	15.4	121.6	6.2	0.94
	#23	0.50	0.25	0.1467	0.0182	0.0191	0.0012	136.1	21.6	129.0	10.6	0.95
	#24	0.34	0.16	0.1390	0.0053	0.0188	0.0008	132.9	6.2	123.3	6.0	0.93
	#25	0.59	0.28	0.1455	0.0074	0.0197	0.0006	137.9	9.1	125.7	5.0	0.91
H-49												
Tukey's Biweight robust sample mean:												
103.3 ± 2.0 [1.9%]												
	#1	0.41	0.24	0.1012	0.0054	0.0152	0.0006	99.5	5.0	98.6	3.8	0.99
	#2	0.29	0.17	0.1046	0.0054	0.0156	0.0006	101.0	5.1	99.5	3.9	0.99
	#3	0.32	0.19	0.1033	0.0059	0.0159	0.0007	100.3	5.5	102.3	4.4	1.02
	#4	0.36	0.21	0.1128	0.0085	0.0161	0.0010	106.8	8.1	101.6	6.2	0.95
	#5	0.38	0.22	0.1045	0.0046	0.0158	0.0006	101.0	4.2	101.3	3.5	1.00
	#6	0.36	0.22	0.1072	0.0058	0.0161	0.0007	103.4	5.5	102.7	4.8	0.99
	#7	0.20	0.12	0.1155	0.0055	0.0174	0.0007	111.0	5.7	111.1	4.8	1.00
	#8	0.32	0.21	0.1009	0.0075	0.0151	0.0009	98.8	6.9	97.8	5.5	0.99
	#9	0.33	0.20	0.1250	0.0069	0.0180	0.0006	119.6	7.4	114.7	4.0	0.96
	#10	0.27	0.16	0.1044	0.0057	0.0157	0.0007	101.1	5.4	100.8	4.6	1.00
	#11	0.43	0.25	0.1033	0.0064	0.0154	0.0008	100.2	5.9	99.0	4.9	0.99
	#12	0.26	0.15	0.1086	0.0065	0.0164	0.0007	105.3	6.3	105.4	5.0	1.00
	#13	0.41	0.25	0.1047	0.0051	0.0158	0.0006	101.1	4.8	100.8	3.5	1.00
	#14	0.48	0.29	0.1118	0.0108	0.0159	0.0006	107.2	10.6	101.1	3.5	0.94
	#15	0.33	0.20	0.1161	0.0048	0.0175	0.0006	110.2	4.7	110.6	3.9	1.00
	#16	0.27	0.17	0.1103	0.0066	0.0161	0.0007	106.4	6.5	103.2	4.9	0.97
	#17	0.18	0.10	0.1071	0.0061	0.0160	0.0007	103.1	5.8	102.3	4.8	0.99
	#18	0.29	0.17	0.1056	0.0054	0.0161	0.0007	101.1	5.0	101.9	4.4	1.01
	#19	0.42	0.26	0.1175	0.0108	0.0166	0.0006	112.7	11.2	105.7	3.9	0.94
	#20	0.29	0.17	0.1177	0.0051	0.0177	0.0004	114.7	5.4	114.8	3.2	1.00
	#21	0.37	0.23	0.1141	0.0043	0.0166	0.0005	110.9	4.4	107.1	3.4	0.97
	#22	0.39	0.23	0.1063	0.0070	0.0156	0.0006	101.8	6.5	98.9	3.6	0.97
	#23	0.34	0.20	0.1053	0.0066	0.0161	0.0007	101.7	6.2	103.1	4.8	1.01

Table A.19: Zrn U-Pb age dataset

				Ratios				Ages (Ma)				Conc[c]
Sample	Spot #	Th/U[a]	$^{208}Pb/^{206}Pb$	$^{207}Pb/^{235}U$[a]	2 s[b]	$^{206}Pb/^{238}U$[a]	2 s[b]	$^{207}Pb/^{235}U$	2 s	$^{206}Pb/^{238}U$	2 s	%
	#24	0.29	0.17	0.1071	0.0063	0.0162	0.0007	103.3	6.0	103.5	4.8	1.00
H-72												
Tukey's Biweight robust sample mean:												
108.9 ± 0.8 [0.8%]												
	#1	0.30	0.19	0.1061	0.0067	0.0161	0.0006	103.1	6.4	103.6	3.7	1.00
	#2	0.37	0.22	0.1156	0.0098	0.0171	0.0008	111.1	10.0	109.5	5.8	0.99
	#3	0.25	0.15	0.1122	0.0064	0.0169	0.0007	108.0	6.4	107.9	4.7	1.00
	#4	0.27	0.16	0.1147	0.0087	0.0171	0.0009	110.8	8.9	110.1	6.2	0.99
	#5	0.34	0.19	0.1153	0.0074	0.0172	0.0009	110.4	7.4	109.7	6.4	0.99
	#6	0.42	0.24	0.1145	0.0079	0.0171	0.0008	110.0	7.9	109.0	5.8	0.99
	#7	0.39	0.23	0.1137	0.0078	0.0171	0.0008	109.7	7.9	109.8	5.7	1.00
	#8	0.39	0.23	0.1167	0.0075	0.0174	0.0009	112.1	7.6	111.0	6.0	0.99
	#9	0.25	0.17	0.1113	0.0089	0.0168	0.0007	106.5	8.6	106.8	4.9	1.00
	#10	0.32	0.19	0.1112	0.0103	0.0166	0.0011	109.1	10.6	108.1	7.7	0.99
	#11	0.34	0.19	0.1118	0.0077	0.0171	0.0009	108.0	7.7	109.9	5.9	1.02
	#12	0.40	0.23	0.1134	0.0074	0.0167	0.0007	111.0	7.7	108.8	4.7	0.98
	#13	0.34	0.20	0.1089	0.0073	0.0163	0.0009	107.0	7.3	106.7	6.3	1.00
	#14	0.30	0.18	0.1127	0.0068	0.0169	0.0008	108.5	6.7	108.2	5.4	1.00
	#15	0.54	0.31	0.1141	0.0081	0.0168	0.0008	109.2	8.1	106.9	5.2	0.98
	#16	0.18	0.16	0.1142	0.0085	0.0170	0.0010	109.9	8.5	108.7	7.1	0.99
	#17	0.37	0.23	0.1111	0.0081	0.0166	0.0009	107.0	7.9	105.9	6.0	0.99
	#18	0.36	0.21	0.1096	0.0064	0.0172	0.0006	107.0	6.3	111.7	4.6	1.04
	#19	0.33	0.19	0.1191	0.0075	0.0172	0.0007	114.9	7.9	110.2	4.6	0.96
	#20	0.36	0.21	0.1123	0.0060	0.0169	0.0007	110.7	6.2	110.7	4.8	1.00
	#21	0.54	0.31	0.1122	0.0075	0.0170	0.0008	108.0	7.5	108.8	5.8	1.01
	#22	0.37	0.21	0.1189	0.0077	0.0173	0.0009	111.3	7.7	107.5	5.7	0.97
	#23	0.43	0.25	0.1218	0.0100	0.0175	0.0010	116.7	10.6	111.8	7.3	0.96
	#24	0.29	0.17	0.1125	0.0071	0.0174	0.0009	109.3	7.1	112.2	6.7	1.03
	#25	0.45	0.26	0.1074	0.0058	0.0166	0.0007	104.5	5.6	107.2	4.8	1.03
H-87												
Tukey's Biweight robust sample mean:												
114.6 ± 1.8 [1.6%]												
	#1	0.36	0.21	0.1147	0.0069	0.0172	0.0009	111.4	7.0	111.0	6.4	1.00
	#2	0.36	0.21	0.1211	0.0067	0.0180	0.0009	116.0	7.0	114.9	6.5	0.99
	#3	0.40	0.24	0.1186	0.0072	0.0180	0.0010	113.8	7.5	115.0	6.9	1.01
	#4	0.35	0.23	0.1432	0.0077	0.0191	0.0004	135.9	9.4	121.8	3.3	0.90
	#5	0.55	0.32	0.1219	0.0057	0.0180	0.0007	116.8	6.1	115.2	5.3	0.99
	#6	0.37	0.23	0.1158	0.0072	0.0174	0.0008	110.8	7.2	111.0	5.9	1.00
	#7	0.36	0.22	0.1247	0.0091	0.0183	0.0011	120.0	10.0	117.6	8.0	0.98
	#8	0.42	0.25	0.1225	0.0072	0.0183	0.0008	117.6	7.8	116.9	6.0	0.99
	#9	0.56	0.32	0.1241	0.0072	0.0183	0.0009	118.8	7.7	116.7	6.5	0.98
	#10	0.34	0.20	0.1338	0.0124	0.0195	0.0015	127.6	14.3	124.4	11.9	0.98
	#11	0.44	0.27	0.1276	0.0091	0.0181	0.0006	121.2	9.8	114.7	4.5	0.95
	#12	0.36	0.22	0.1187	0.0071	0.0179	0.0009	113.1	7.2	113.4	6.8	1.00
	#13	0.52	0.38	0.1129	0.0059	0.0170	0.0007	108.5	5.9	108.4	4.8	1.00
	#15	0.50	0.28	0.1193	0.0070	0.0179	0.0009	111.8	7.0	111.2	6.0	1.00

Table A.20: Zrn U-Pb age dataset

Sample	Spot #	Th/U[a]	$^{208}Pb/^{206}Pb$	Ratios: $^{207}Pb/^{235}U$[a]	2 s[b]	$^{206}Pb/^{238}U$[a]	2 s[b]	Ages (Ma): $^{207}Pb/^{235}U$	2 s	$^{206}Pb/^{238}U$	2 s	Conc[c] %
	#16	0.30	0.18	0.1187	0.0070	0.0177	0.0009	113.9	7.3	113.1	6.3	0.99
	#17	0.43	0.25	0.1162	0.0073	0.0174	0.0008	110.1	7.3	109.5	5.6	0.99
	#18	0.42	0.24	0.1213	0.0079	0.0182	0.0010	115.7	8.2	115.9	7.1	1.00
	#19	0.40	0.24	0.1187	0.0082	0.0181	0.0011	113.8	8.5	115.8	8.0	1.02
	#20	0.58	0.34	0.1161	0.0068	0.0177	0.0008	111.5	6.9	112.8	6.0	1.01
	#21	0.48	0.28	0.1189	0.0079	0.0179	0.0008	114.3	8.2	114.3	5.8	1.00
	#22	0.52	0.31	0.1156	0.0061	0.0174	0.0007	110.1	6.1	109.9	5.2	1.00

[a] Corrected for background and within-run Pb/U fractionation and normalised to reference zircon GJ-1 (ID-TIMS values/measured value); $^{207}Pb/^{235}U$ calculated using ($^{207}Pb/^{206}Pb$)/($^{238}U/^{206}Pb$ × 1/137.88).

[b] Quadratic addition of within-run errors (2 sd) and daily reproducibility of GJ-1 (2 sd).

[c] Concordance of $^{206}Pb/^{238}U$ and $^{207}Pb/^{235}U$.

Table A.21: Zircon (U-Th)/He age dataset

		He		U238			Th232				Sm			Sphere	Ejection	Uncorr.	Ft-Corr.		Average	
Sample	aliq.	vol. [ncc]	r.s.e. [%]	mass [ng]	r.s.e. [%]	conc. [ppm]	mass [ng]	r.s.e. [%]	conc. [ppm]	Th/U ratio	mass [ng]	r.s.e. [%]	conc. [ppm]	radius [µm]	correct. (Ft)[a]	He-age [Ma]	He-age [Ma]	±1s [Ma]	age[b] [Ma]	±1s [Ma]
DC-23	#1	**15.57**	1.7	**1.830**	1.8	203	**1.107**	2.4	123	0.60	**0.035**	23	4	65	0.81	61.3	**76.0**	2.8		
	#2	**32.32**	1.6	**3.013**	1.8	269	**1.605**	2.4	143	0.53	**0.012**	24	1	69	0.82	78.4	**95.8**	3.4		
	#3	**23.70**	1.6	**2.407**	1.8	233	**1.688**	2.4	163	0.70	**0.023**	24	2	68	0.82	69.6	**85.3**	3.0	**85.7**	**5.7**
DC-29	#1	**16.10**	1.6	**2.016**	1.8	690	**0.718**	2.4	246	0.36	**0.017**	19	6	40	0.70	60.7	**86.4**	4.3		
	#2	**10.76**	1.6	**1.479**	1.8	310	**0.867**	2.4	182	0.59	**0.023**	19	5	50	0.76	52.7	**69.8**	3.0	**78.1**	**8.3**
DC-41	#1	**52.05**	1.6	**5.710**	1.8	357	**3.498**	2.4	219	0.61	**0.019**	25	1	77	0.84	65.6	**78.5**	2.6		
	#2	**195.68**	1.6	**16.323**	1.8	788	**7.316**	2.4	353	0.45	**0.059**	25	3	87	0.86	89.1	**104.2**	3.3		
	#3	**19.38**	1.6	**1.941**	1.8	145	**1.292**	2.4	97	0.67	**0.022**	26	2	73	0.83	71.1	**85.9**	3.0	**89.5**	**7.6**
H-7	#1	**75.99**	1.6	**10.718**	1.8	908	**4.036**	2.4	342	0.38	**0.036**	10	3	68	0.82	53.7	**65.7**	2.3		
	#2	**57.37**	1.6	**7.743**	1.8	662	**3.752**	2.4	321	0.48	**0.104**	9	9	77	0.84	54.8	**65.5**	2.2		
	#3	**5.78**	1.7	**0.862**	1.8	468	**0.512**	2.4	278	0.59	**0.017**	10	9	37	0.68	48.5	**71.8**	3.9	**67.7**	**2.1**
H-13	#1	**22.87**	1.6	**2.463**	1.8	430	**0.780**	2.4	136	0.32	**0.035**	19	6	54	0.77	71.1	**92.1**	3.8		
	#2	**15.42**	1.6	**1.676**	1.8	291	**0.630**	2.4	109	0.38	**0.012**	19	2	53	0.77	69.6	**90.5**	3.8		
	#3	**38.62**	1.6	**5.289**	1.8	611	**1.422**	2.4	164	0.27	**0.020**	19	2	63	0.80	56.6	**70.5**	2.7	**84.4**	**6.9**
H-16	#1	**17.27**	1.7	**2.281**	1.8	787	**0.286**	2.4	99	0.13	**0.028**	4	10	45	0.73	60.6	**83.0**	3.9		
	#2	**20.34**	1.6	**2.367**	1.8	1213	**0.271**	2.4	139	0.11	**0.025**	4	13	39	0.70	68.9	**99.0**	5.1	**91.0**	**8.0**
H-19	#1	**22.74**	1.6	**3.807**	1.8	1452	**2.208**	2.4	842	0.58	**0.045**	11	17	44	0.73	43.4	**59.8**	2.8		
	#2	**13.09**	1.7	**1.947**	1.8	755	**1.767**	2.4	685	0.91	**0.018**	11	7	43	0.72	45.7	**63.8**	3.1	**61.8**	**2.8**
H-20	#2	**6.66**	1.7	**0.890**	1.8	451	**0.732**	2.4	371	0.82	**0.015**	11	8	37	0.68	51.7	**76.4**	4.1		
	#3	**11.61**	1.7	**1.838**	1.8	1044	**1.085**	2.4	616	0.59	**0.012**	12	7	36	0.67	45.8	**68.2**	3.7	**72.3**	**5.8**
H-33	#1	**23.15**	1.6	**3.187**	1.8	659	**1.108**	2.4	229	0.35	**0.014**	4	3	53	0.77	55.4	**72.0**	3.0		
	#2	**2.25**	1.7	**0.365**	1.9	178	**0.210**	2.4	103	0.58	**0.005**	5	2	40	0.70	44.9	**64.4**	3.3		
	#3	**6.30**	1.6	**0.916**	1.8	113	**0.330**	2.4	41	0.36	**0.017**	11	2	63	0.80	52.3	**65.1**	2.4		
	#4	**36.67**	1.6	**3.878**	1.8	658	**3.254**	2.4	552	0.84	**0.025**	9	4	55	0.77	65.0	**84.0**	3.4		
	#5	**29.56**	1.6	**2.865**	1.8	275	**0.863**	2.4	83	0.30	**0.024**	9	2	63	0.80	79.3	**98.6**	3.7	**76.8**	**6.5**
H-34	#1	**16.51**	1.6	**2.385**	1.8	527	**0.441**	2.4	98	0.19	**0.017**	11	4	51	0.76	54.7	**71.9**	3.1		
	#2	**7.06**	1.6	**0.832**	1.8	203	**0.236**	2.4	58	0.28	**0.012**	10	3	52	0.76	65.5	**85.7**	3.6		
	#3	**6.21**	1.7	**1.078**	1.8	341	**0.275**	2.4	87	0.25	**0.016**	10	5	43	0.72	44.9	**62.1**	3.0	**73.3**	**6.8**
H-35	#1	**14.72**	1.6	**1.768**	1.8	432	**0.869**	2.4	212	0.49	**0.009**	4	2	49	0.75	61.5	**82.1**	3.6		

Table A.22: Zircon (U-Th)/He age dataset

		He		U238			Th232				Sm						Ft-Corr.		Average	
Sample	aliq.	vol. [ncc]	r.s.e. [%]	mass [ng]	r.s.e. [%]	conc. [ppm]	mass [ng]	r.s.e. [%]	conc. [ppm]	Th/U ratio	mass [ng]	r.s.e. [%]	conc. [ppm]	Sphere radius [µm]	Ejection correct. (Ft)[a]	Uncorr. He-age [Ma]	He-age [Ma]	±1s [Ma]	age[b] [Ma]	±1s [Ma]
	#2	**4.41**	2.0	**0.683**	1.8	284	**0.234**	2.4	97	0.34	**0.004**	5	2	40	0.70	49.2	**70.7**	3.7		
	#3	**6.12**	1.7	**0.904**	1.8	153	**0.436**	2.4	74	0.48	**0.009**	5	1	55	0.78	50.1	**64.6**	2.6		
	#4	**85.89**	1.6	**12.98**	1.8	677	**4.270**	2.4	223	0.33	**0.195**	3	10	82	0.85	50.7	**59.8**	1.9	**69.3**	**4.8**
H-72	#1	**13.11**	1.7	**1.442**	1.8	337	**1.117**	2.4	261	0.77	**0.017**	26	4	51	0.76	63.3	**83.4**	3.5		
	#2	**7.20**	1.7	**0.939**	1.8	212	**0.815**	2.4	184	0.87	**0.006**	28	1	52	0.76	52.5	**69.0**	2.9		
	#3	**10.50**	1.7	**1.237**	1.8	291	**0.845**	2.4	199	0.68	**0.011**	27	2	50	0.75	60.3	**80.1**	3.5	**77.5**	**4.4**
H-87	#1	**26.79**	1.6	**3.112**	1.8	402	**2.030**	2.4	262	0.65	**0.043**	28	5	62	0.80	61.5	**76.9**	2.9		
	#2	**25.51**	1.6	**3.433**	1.8	328	**1.991**	2.4	190	0.58	**0.136**	28	13	68	0.82	53.9	**66.0**	2.4		
	#3	**8.68**	1.7	**1.249**	1.8	204	**0.651**	2.4	106	0.52	**0.013**	30	2	60	0.79	51.0	**64.4**	2.5	**69.1**	**3.9**

Amount of helium is given in nano-cubic-cm in standard temperature and pressure.
Amount of radioactive elements are given in nanograms.
Ejection correct. (Ft): correction factor for alpha-ejection (according to Farley et al., 1996 and Hourigan et al., 2005).
Uncertainties of helium and the radioactive element contents are given as 1 sigma, in relative error %.
Uncertaintiy of the single grain age is given as 2 sigma in % (or in Ma) and it includs both the analytical uncertanity and the estimated uncertanity of the Ft.
Uncertainty of the sample average age is 2 standard error, as (SD)/(n)1/2; where SD=standard deviation of the age replicates and n =number of age determinations.

The raw data of samples DC-31, 33 and H-23, 24, 29, 30, 31 were published in Hetzel et al. (2011).

Table A.23: Apatite (U-Th)/He age dataset

		He		U238			Th232				Sm			Sphere	Ejection	Uncorr.	Ft-Corr.		Average	
		vol.	r.s.e.	mass	r.s.e.	conc.	mass	r.s.e.	conc.	Th/U	mass	r.s.e.	conc.	radius	correct.	He-age	He-age	±1s	age	±1s
Sample	aliq.	[ncc]	[%]	[ng]	[%]	[ppm]	[ng]	[%]	[ppm]	ratio	[ng]	[%]	[ppm]	[µm]	(Ft)^c	[Ma]	[Ma]	[Ma]	[Ma]	[Ma]
DC-23	#2	0.099	2.1	0.020	4.4	33	0.059	2.7	96	2.90	0.215	11	350	30	0.65	22.5	34.5	2.1		
	#3	0.093	2.0	0.023	4.1	44	0.058	2.7	111	2.50	0.230	10	436	25	0.59	19.7	33.7	2.4		
	#4	0.114	1.8	0.025	3.8	20	0.077	2.6	62	3.07	0.247	10	200	28	0.62	20.7	33.1	2.1		
	#5	0.182	1.6	0.033	3.1	39	0.097	2.6	115	2.98	0.281	11	332	33	0.68	26.0	38.0	2.0	34.8	1.1
DC-25	#1	0.312	1.2	0.050	2.5	37	0.093	2.6	69	1.87	0.615	13	456	37	0.71	33.4	46.9	2.3		
	#2	0.422	1.0	0.106	2.0	103	0.070	2.7	68	0.66	0.469	13	453	31	0.65	27.5	42.3	2.4		
	#3	0.815	0.8	0.162	1.9	101	0.131	2.5	82	0.81	0.692	13	430	33	0.67	33.8	50.5	2.7		
	#4	0.979	0.7	0.169	1.9	87	0.228	2.5	117	1.35	0.964	13	495	36	0.70	35.0	49.7	2.4	47.3	1.8
DC-28	#1	0.755	0.8	0.129	1.9	12	0.074	2.6	7	0.57	2.758	4	255	48	0.77	36.7	47.6	1.8		
	#2	0.115	2.0	0.031	2.8	26	0.016	3.5	13	0.52	0.393	4	332	26	0.58	25.3	43.4	3.0	45.5	2.1
DC-29	#1	0.128	1.9	0.021	4.9	6	0.044	2.9	13	2.14	1.073	6	326	44	0.76	26.6	35.0	1.7		
	#3	0.067	2.3	0.011	9.2	7	0.024	3.3	15	2.24	0.474	7	287	34	0.70	27.3	39.2	2.8		
	#4	0.133	1.8	0.020	5.0	7	0.037	2.9	12	1.84	0.874	6	285	42	0.76	30.1	39.6	2.0		
	#5	0.189	1.5	0.027	3.8	7	0.055	2.8	15	2.02	1.114	6	298	46	0.78	31.7	40.7	1.8		
	#6	0.065	2.5	0.010	9.8	7	0.020	3.5	15	1.97	0.325	6	236	36	0.70	30.4	43.1	3.3	39.5	1.3
DC-38	#1	0.100	1.9	0.012	7.3	13	0.063	2.7	63	5.03	0.506	13	510	47	0.70	26.2	37.3	2.2		
	#2	0.207	1.4	0.022	4.7	8	0.104	2.6	39	4.72	0.777	9	292	45	0.77	32.1	41.9	1.9		
	#3	0.169	1.6	0.020	4.8	10	0.098	2.6	50	4.90	0.947	6	489	35	0.70	27.5	39.1	2.1		
	#4	0.313	1.2	0.056	2.4	45	0.121	2.5	97	2.15	0.484	6	389	35	0.70	29.2	41.8	2.1	40.0	1.1
DC-40	#1	0.248	1.2	0.055	2.2	41	0.077	2.6	58	1.41	0.373	3	278	30	0.64	27.0	42.2	2.4		
	#2	0.233	4.9	0.068	2.1	46	0.135	2.5	93	2.00	0.451	3	310	31	0.65	18.6	28.6	2.1		
	#3	0.243	1.3	0.054	2.2	49	0.082	2.6	75	1.53	0.285	3	261	25	0.58	26.5	45.7	3.0	38.8	5.2
DC-41	#1	1.144	0.6	0.165	1.9	33	0.307	2.5	61	1.86	2.028	3	401	48	0.78	37.1	47.8	1.8		
	#2	0.614	0.9	0.074	2.1	30	0.213	2.5	86	2.89	0.950	3	384	34	0.69	38.4	55.8	2.8		
	#3	0.604	0.9	0.085	2.0	26	0.227	2.5	69	2.67	1.130	3	341	38	0.72	33.7	46.4	2.1	50.0	2.9
H-7	#1	0.108	1.9	0.019	3.8	8	0.058	2.7	24	2.97	1.086	4	459	29	0.66	21.3	32.3	1.9		
	#2	0.131	1.9	0.019	3.8	14	0.052	2.7	39	2.70	0.769	4	571	25	0.58	28.5	49.3	3.4		
	#4	0.348	2.0	0.030	2.8	13	0.114	2.6	50	3.74	1.267	9	561	35	0.70	42.4	60.6	3.2		
	#5	0.100	2.8	0.012	7.4	17	0.042	2.9	59	3.56	0.459	14	654	41	0.65	32.7	50.5	3.6		
	#6	0.106	2.7	0.016	4.8	12	0.056	2.7	43	3.50	0.723	9	553	26	0.59	25.0	42.1	3.0	47.0	4.7

Table A.24: Apatite (U-Th)/He age dataset

		He		U238			Th232				Sm			Sphere	Ejection	Uncorr.	Ft-Corr.		Average	
		vol.	r.s.e.	mass	r.s.e.	conc.	mass	r.s.e.	conc.	Th/U	mass	r.s.e.	conc.	radius	correct.	He-age	He-age	±1s	age	±1s
Sample	aliq.	[ncc]	[%]	[ng]	[%]	[ppm]	[ng]	[%]	[ppm]	ratio	[ng]	[%]	[ppm]	[µm]	$(Ft)^c$	[Ma]	[Ma]	[Ma]	[Ma]	[Ma]
H-12	#1	2.361	1.7	0.492	1.8	80	0.029	3.1	5	0.06	1.423	8	233	44	0.75	38.2	51.2	2.3		
	#2	2.351	1.7	0.464	1.8	73	0.030	3.0	5	0.07	1.480	8	233	45	0.75	40.2	53.3	2.4		
	#3	1.784	1.7	0.329	1.8	72	0.021	3.3	5	0.06	1.084	8	239	39	0.71	43.0	60.1	3.0		
	#4	2.080	1.7	0.404	1.8	72	0.021	3.4	4	0.05	1.493	8	267	42	0.73	40.8	55.8	2.6	55.1	1.9
H-13	#1	0.490	1.8	0.078	1.9	30	0.170	2.4	66	2.19	1.536	18	591	34	0.69	30.9	44.7	2.4		
	#2	0.708	1.8	0.116	1.9	19	0.189	2.4	30	1.64	1.998	18	321	42	0.75	33.1	44.2	2.1		
	#3	0.580	1.8	0.120	1.9	18	0.092	2.5	14	0.77	1.549	19	228	44	0.76	31.0	40.9	1.9	43.3	1.2
H-14	#1	1.077	1.7	0.184	1.8	38	0.345	2.4	71	1.87	1.908	6	392	57	0.72	31.6	44.2	2.1		
	#2	1.306	1.7	0.211	1.8	33	0.430	2.4	66	2.03	1.833	6	282	74	0.78	32.9	41.9	1.6		
	#3	0.571	1.8	0.091	1.9	28	0.133	2.5	41	1.46	0.763	6	234	49	0.67	36.6	54.6	3.0		
	#4	0.504	1.8	0.072	2.0	24	0.112	2.5	38	1.56	0.817	6	276	47	0.66	39.6	60.2	3.4	50.2	4.3
H-19	#2	0.383	1.0	0.044	2.4	25	0.180	2.5	101	4.12	0.559	5	313	34	0.71	34.8	49.0	2.3	49.0	4.7
H-20	#2	0.746	1.8	0.068	2.0	14	0.268	2.5	47	3.97	0.844	5	149	33	0.69	44.6	65.0	3.4		
	#3	0.153	2.4	0.020	3.5	18	0.063	2.7	21	3.10	0.250	5	184	25	0.59	34.1	57.5	4.0	61.2	5.3
H-21	#1	0.247	2.1	0.029	2.7	21	0.132	2.5	30	4.61	0.461	5	354	45	0.69	32.1	46.8	2.5		
	#2	0.225	2.1	0.024	4.0	15	0.100	2.6	18	4.20	0.121	7	108	30	0.65	38.4	59.1	3.6		
	#3	0.066	3.2	0.008	11.9	11	0.042	2.9	19	5.02	0.051	6	111	56	0.74	29.0	39.5	2.9		
	#4	0.082	3.0	0.014	4.9	13	0.044	2.8	42	3.20	0.110	5	105	29	0.65	27.2	41.8	2.8	46.8	4.4
H-22B	#1	0.295	2.0	0.032	2.5	15	0.168	2.4	77	5.27	0.845	6	388	46	0.66	31.0	46.9	2.7		
	#3	0.218	2.1	0.024	2.9	14	0.111	2.5	66	4.62	0.532	6	314	39	0.57	33.0	57.8	4.0		
	#5	0.244	2.4	0.027	2.6	23	0.126	2.5	108	4.70	0.331	7	286	42	0.59	34.1	57.9	4.0	54.2	3.7
H-33	#1	0.049	3.4	0.014	4.8	17	0.017	3.5	21	1.25	0.163	5	196	23	0.53	20.9	39.4	3.4		
	#2	0.147	2.4	0.034	2.6	26	0.056	2.7	44	1.66	0.414	5	320	24	0.55	24.0	43.6	3.2		
	#3	0.312	2.0	0.059	2.2	25	0.071	2.6	30	1.20	0.648	5	274	34	0.68	32.0	46.9	2.5		
	#4	0.183	2.3	0.034	2.6	16	0.047	2.8	22	1.36	0.567	5	271	30	0.64	30.1	47.0	2.9		
	#5	0.463	1.9	0.077	2.0	38	0.130	2.5	63	1.68	0.730	5	354	32	0.66	33.5	50.7	2.8		
	#6	0.177	2.2	0.040	2.4	34	0.056	2.7	46	1.37	0.339	5	282	25	0.58	26.0	44.9	3.1	45.4	1.5
H-34	#1	0.176	2.2	0.042	2.4	36	0.031	3.0	26	0.73	0.486	12	408	32	0.66	27.1	41.3	2.5		
	#2	0.310	1.9	0.073	1.9	28	0.044	2.6	17	0.61	0.896	9	350	54	0.73	28.4	38.8	1.8		
	#3	0.141	2.5	0.037	2.6	31	0.025	3.2	21	0.68	0.370	12	310	27	0.60	25.4	42.0	2.9		
	#4	0.156	2.1	0.037	2.2	34	0.022	2.7	21	0.60	0.379	9	355	36	0.59	28.6	48.6	3.3		

Table A.25: Apatite (U-Th)/He age dataset

		He		U238			Th232				Sm			Sphere	Ejection	Uncorr.	Ft-Corr.		Average	
		vol.	r.s.e.	mass	r.s.e.	conc.	mass	r.s.e.	conc.	Th/U	mass	r.s.e.	conc.	radius	correct.	He-age	He-age	±1s	age	±1s
Sample	aliq.	[ncc]	[%]	[ng]	[%]	[ppm]	[ng]	[%]	[ppm]	ratio	[ng]	[%]	[ppm]	[µm]	(Ft)[c]	[Ma]	[Ma]	[Ma]	[Ma]	[Ma]
	#5	**0.123**	2.5	**0.033**	2.8	34	**0.022**	3.3	23	0.66	**0.308**	13	321	31	0.64	25.0	**38.9**	2.5		
	#7	**0.229**	2.3	**0.055**	2.2	32	**0.036**	2.9	21	0.66	**0.584**	13	339	32	0.66	27.5	**41.5**	2.4		
	#8	**0.253**	2.0	**0.052**	2.0	11	**0.033**	2.6	7	0.64	**0.818**	9	179	46	0.68	31.4	**46.2**	2.5		
	#9	**0.244**	2.0	**0.058**	2.0	14	**0.047**	2.6	11	0.80	**0.641**	9	152	42	0.65	27.0	**41.7**	2.5	**42.4**	**1.2**
H-35	#1	**0.857**	1.7	**0.115**	1.8	2	**0.228**	2.4	4	1.99	**3.311**	9	59	52	0.72	36.1	**50.2**	2.5		
	#2	**0.449**	1.9	**0.058**	2.1	44	**0.105**	2.6	79	1.81	**0.590**	8	443	31	0.65	42.2	**64.6**	3.7		
	#3	**1.469**	1.7	**0.203**	1.8	3	**0.387**	2.4	6	1.91	**3.353**	9	56	58	0.75	37.7	**50.2**	2.2		
	#4	**1.102**	1.7	**0.135**	1.9	3	**0.263**	2.4	6	1.95	**1.603**	9	35	63	0.77	43.2	**56.0**	2.3		
	#5	**1.009**	1.7	**0.127**	1.9	4	**0.239**	2.4	7	1.89	**1.275**	9	38	53	0.73	43.0	**59.2**	2.8		
	#6	**1.121**	1.7	**0.162**	1.8	23	**0.285**	2.4	41	1.76	**3.670**	9	525	58	0.75	35.7	**47.4**	2.1		
	#7	**0.884**	1.8	**0.117**	1.9	13	**0.223**	2.4	25	1.90	**2.761**	9	315	56	0.74	37.9	**51.1**	2.3	**54.1**	**2.3**
H-45	#1	**0.527**	1.8	**0.081**	1.9	34	**0.179**	2.4	75	2.22	**0.981**	6	410	43	0.63	33.1	**52.3**	3.1		
	#2	**0.392**	1.8	**0.077**	2.0	27	**0.160**	2.4	56	2.08	**1.002**	6	353	42	0.62	26.3	**42.7**	2.7		
	#3	**0.238**	2.0	**0.047**	2.2	25	**0.100**	2.5	52	2.11	**0.623**	6	324	44	0.62	25.9	**41.6**	2.6		
	#4	**0.560**	1.8	**0.098**	1.9	33	**0.199**	2.4	68	2.04	**1.167**	6	396	41	0.61	30.0	**49.1**	3.1	**46.4**	**2.6**
H-50	#1	**0.934**	1.7	**0.083**	1.9	12	**0.189**	2.4	28	2.27	**3.605**	4	538	65	0.75	48.9	**65.2**	2.9		
	#2	**0.119**	2.5	**0.016**	3.1	16	**0.027**	2.7	26	1.68	**0.603**	4	583	55	0.77	35.7	**46.7**	2.2		
	#5	**0.185**	26.4	**0.020**	2.7	16	**0.063**	2.5	49	3.08	**0.574**	4	447	42	0.63	38.4	**61.4**	16.6	**57.7**	**5.6**
H-51	#1	**0.292**	2.0	**0.021**	2.4	14	**0.071**	2.5	47	3.30	**0.925**	4	616	44	0.63	52.6	**83.1**	5.0		
	#2	**0.363**	1.9	**0.047**	2.0	18	**0.085**	2.5	32	1.82	**1.933**	4	728	55	0.71	36.4	**51.3**	2.6	**67.2**	**15.9**
H-70	#1	**1.679**	1.7	**0.261**	1.8	38	**0.456**	2.4	66	1.74	**1.386**	4	200	61	0.73	36.4	**49.6**	2.3		
	#2	**2.752**	1.7	**0.402**	1.8	39	**0.812**	2.4	78	2.02	**2.598**	4	251	80	0.81	36.9	**45.7**	1.7		
	#3	**0.801**	1.8	**0.123**	1.9	40	**0.269**	2.4	87	2.19	**0.787**	5	253	47	0.65	34.2	**52.4**	3.0		
	#4	**0.777**	1.8	**0.133**	1.8	42	**0.227**	2.4	72	1.70	**0.751**	5	238	54	0.70	33.3	**47.7**	2.4	**48.9**	**1.4**
H-71B	#2	**0.757**	1.8	**0.094**	1.9	21	**0.271**	2.4	60	2.89	**1.377**	5	304	49	0.67	36.9	**55.2**	3.0		
	#3	**0.239**	2.0	**0.041**	2.2	16	**0.093**	2.5	37	2.27	**0.581**	5	232	39	0.58	29.3	**50.7**	3.5		
	#4	**0.203**	2.1	**0.042**	2.1	11	**0.067**	2.5	17	1.58	**0.711**	5	184	46	0.65	26.2	**40.5**	2.4		
	#5	**0.601**	1.8	**0.082**	1.9	17	**0.190**	2.4	39	2.32	**1.413**	6	287	58	0.72	35.9	**49.9**	2.4		
	#6	**0.315**	1.9	**0.047**	2.2	20	**0.141**	2.5	61	2.97	**0.662**	6	285	50	0.68	30.2	**44.5**	2.4	**48.2**	**2.6**
H-72	#1	**1.150**	1.8	**0.185**	1.8	18	**0.357**	2.4	35	1.93	**2.221**	5	219	67	0.76	33.0	**43.3**	1.8		
	#2	**2.138**	1.7	**0.343**	1.8	46	**0.673**	2.4	90	1.96	**2.269**	5	304	70	0.77	33.9	**43.8**	1.8		

Table A.26: Apatite (U-Th)/He age dataset

		He		U238			Th232				Sm			Sphere	Ejection	Uncorr.	Ft-Corr.		Average	
		vol.	r.s.e.	mass	r.s.e.	conc.	mass	r.s.e.	conc.	Th/U	mass	r.s.e.	conc.	radius	correct.	He-age	He-age	±1s	age	±1s
Sample	aliq.	[ncc]	[%]	[ng]	[%]	[ppm]	[ng]	[%]	[ppm]	ratio	[ng]	[%]	[ppm]	[µm]	(Ft)[c]	[Ma]	[Ma]	[Ma]	[Ma]	[Ma]
	#4	**1.828**	1.7	**0.300**	1.8	37	**0.557**	2.4	70	1.86	**2.059**	5	257	68	0.76	33.7	**44.2**	1.9	**43.8**	**0.3**
H-85	#2	**0.301**	2.0	**0.067**	2.0	33	**0.020**	2.8	10	0.30	**0.714**	6	348	45	0.64	32.1	**50.0**	3.0		
	#3	**1.207**	1.7	**0.167**	1.9	52	**0.060**	2.5	19	0.36	**1.362**	6	427	64	0.78	51.8	**66.8**	2.7	**58.4**	**11.9**
H-86	#1	**0.269**	2.0	**0.044**	2.2	19	**0.048**	2.6	21	1.10	**0.995**	6	430	43	0.63	34.9	**55.4**	3.4		
	#2	**0.560**	1.8	**0.078**	1.9	22	**0.148**	2.5	41	1.89	**1.093**	6	304	54	0.70	37.9	**54.4**	2.8	**54.9**	**0.7**
H-87	#1	**1.750**	1.7	**0.389**	1.8	195	**0.074**	2.5	37	0.19	**0.843**	5	423	47	0.68	35.0	**51.7**	2.8		
	#2	**1.097**	1.7	**0.258**	1.8	262	**0.093**	2.5	94	0.36	**0.518**	6	525	37	0.59	31.9	**54.4**	3.6	**53.0**	**1.8**
H-90	#3	**0.615**	1.8	**0.080**	1.9	18	**0.243**	2.4	56	3.03	**1.130**	5	260	62	0.73	34.5	**47.1**	2.2		
	#4	**0.413**	1.9	**0.068**	2.0	19	**0.100**	2.5	28	1.47	**0.927**	5	260	75	0.81	34.4	**42.6**	1.6	**44.9**	**3.1**
H-105	#1	**0.909**	1.8	**0.163**	1.8	59	**0.271**	2.4	98	1.66	**0.765**	5	276	50	0.68	32.1	**47.3**	2.5		
	#2	**0.275**	2.2	**0.062**	2.0	35	**0.069**	2.5	39	1.11	**0.191**	6	108	39	0.59	28.5	**47.9**	3.2		
	#3	**0.263**	2.2	**0.051**	2.1	38	**0.074**	2.5	56	1.47	**0.187**	6	141	38	0.59	31.0	**52.8**	3.6		
	#4	**1.028**	1.8	**0.183**	1.8	51	**0.288**	2.4	80	1.57	**1.176**	5	325	46	0.65	32.6	**50.1**	2.9	**49.5**	**1.2**

[a] Amount of helium is given in nano-cubic-cm in standard temperature and pressure.

[b] Amount of radioactive elements are given in nanograms.

[c] Ejection correct. (Ft): correction factor for alpha-ejection (according to Farley et al., 1996 and Hourigan et al., 2005).

[d] Uncertainties of helium and the radioactive element contents are given as 1 sigma, in relative error %.

[e] Uncertaintiy of the single grain age is given as 2 sigma in % (or in Ma) and it includs both the analytical uncertanity and the estimated uncertanity of the Ft.

[f] Uncertainty of the sample average age is 2 standard error, as (SD)/(n)1/2; where SD=standard deviation of the age replicates and n=number of age determinations.

The raw data of samples DC-31, 33 and H-23, 24, 29, 30, 31 were published in Hetzel et al. (2011).

Table A.27: Ap fission track age dataset

sample number	number of crystals	spontaneous Rho[a]	spontaneous (N)[b]	induced Rho[a]	induced (N)[b]	dosimeter Rho[c]	dosimeter (N)[c]	chi-square[d] P (%)	disp.[e]	**central age (Ma)**	error (±1s)	U ppm	Dpar µm	Dpar (±1s)
DC-26B	30	12.6	1524	19.9	2416	7.00	6680	9	0.1	**72.8**	3.2	41	1.92	0.16
DC-28	30	10.4	976	20.6	1928	7.00	7096	22	0.1	**58.8**	2.9	34	2.12	0.21
DC-40	25	21.2	1391	34.6	2271	7.00	6680	0	0.2	**71.7**	4.0	63	2.12	0.21
DC-41	25	15.4	1476	20.1	1925	7.21	6680	0	0.2	**88.5**	5.5	33	1.99	0.16
H-4	30	10.3	568	18.0	992	6.74	7370	19	0.1	**64.1**	3.9	31	2.69	0.31
H-7	23	6.5	335	12.5	640	7.09	6715	96	0.0	**61.7**	4.4	21	2.39	0.21
H-12	30	33.2	1717	70.6	3652	7.00	6641	2	0.1	**54.6**	2.4	119	2.36	0.27
H-16	27	19.0	1357	41.0	2932	6.78	7370	65	0.0	**52.2**	2.1	68	1.93	0.19
H-19	30	5.5	470	9.2	783	6.52	7370	58	0.1	**65.0**	4.2	17	2.91	0.27
H-20	30	8.0	669	13.7	1146	7.00	6715	6	0.2	**68.4**	4.3	23	2.65	0.21
H-21	30	7.6	546	11.5	832	7.00	6715	21	0.1	**76.6**	4.9	20	2.67	0.21
H-30	31	9.5	759	18.9	1513	7.17	6715	87	0.0	**59.8**	3.0	30	2.52	0.29
H-33	31	8.1	630	16.0	1252	7.17	6715	34	0.1	**60.1**	3.3	26	2.73	0.18
H-34	30	7.2	636	12.5	1107	7.00	6715	92	0.0	**66.9**	3.6	21	2.97	0.22
H-45	30	10.5	939	18.2	1635	6.00	6433	60	0.1	**57.3**	2.8	35	2.86	0.37
H-49	31	4.5	350	10.0	779	6.00	6433	13	0.2	**45.0**	3.6	20	2.34	0.31
H-70	30	7.3	615	14.9	1254	7.13	6925	33	0.0	**58.2**	3.2	25	1.98	0.17
H-71B	40	7.5	802	12.3	1309	7.00	6433	2	0.2	**72.0**	4.3	21	3.13	0.39
H-72	17	6.2	307	13.1	643	7.24	6925	71	0.0	**57.5**	4.2	20	2.35	0.20
H-85	30	14.5	783	28.1	1512	7.11	6433	99	0.0	**61.3**	3.0	44	3.57	0.31
H-86	30	6.4	396	14.3	882	7.13	6433	99	0.0	**53.3**	3.4	22	3.28	0.44
H-90	30	7.8	478	15.3	937	7.18	6433	60	0.0	**61.0**	3.7	26	3.52	0.71
H-105	30	11.2	705	24.5	1539	6.00	6002	22	0.0	**45.8**	2.4	51	4.05	0.40

[a] Track densities (Rho) are as measured (x10^5 tr/cm^2.)
[b] Number of tracks counted is shown in brackets.
[c] Rho and N are track densities of the CN5 detector.
[d] Chi-sq P(%): probability obtaining Chi-square value for n degree of freedom (where n = no. crystals – 1)
[e] Dispersion was determined according to Galbraith and Laslett (1993).

Table A.28: Electron microprobe data of amphiboles of sample H-14

Wt %		SiO_2	Na_2O	CaO	K_2O	FeO	Al_2O_3	MgO	TiO_2	MnO	Total
	Rim#1	45.34	1.12	11.25	0.81	18.46	8.34	10.32	1.06	0.71	97.4
	Rim#2	46.24	1.05	11.63	0.81	18.09	8.05	10.16	0.75	0.68	97.45
	Rim#3	47.32	0.90	11.79	0.58	18.23	7.12	10.47	0.39	0.71	97.5
	Rim#4	46.71	1.23	11.20	0.67	17.60	7.52	11.14	0.97	0.68	97.71
	Rim#5	46.92	0.89	11.57	0.68	18.13	7.23	10.57	0.57	0.77	97.32
	Rim#6	46.42	1.08	11.24	0.72	17.94	7.76	10.70	0.97	0.76	97.61
	Rim#7	47.13	0.83	11.51	0.71	17.87	7.20	10.72	0.64	0.69	97.31
	Rim#8	46.31	0.96	11.61	0.78	18.47	7.84	10.18	0.77	0.66	97.57
	Rim#9	46.08	1.00	11.38	0.79	18.59	7.85	9.99	0.80	0.78	97.26
	Rim#10	46.84	0.95	11.63	0.75	17.41	7.62	10.80	0.72	0.67	97.39
	Rim#11	46.51	0.92	11.49	0.72	18.43	7.61	10.23	0.71	0.78	97.4
	Core#1	46.95	1.22	11.18	0.68	16.71	7.43	11.54	1.27	0.67	97.66
	Core#2	46.21	1.19	11.08	0.70	17.20	7.87	10.81	1.34	0.63	97.03

13 cation normed		Si	Ti	Al	Fe	Mg	Ca	Na	K	Mn
	Rim#1	5.74	0.10	1.24	1.96	1.95	1.53	0.28	0.13	0.08
	Rim#2	5.86	0.07	1.20	1.92	1.92	1.58	0.26	0.13	0.07
	Rim#3	6.00	0.04	1.06	1.93	1.98	1.60	0.22	0.09	0.08
	Rim#4	5.87	0.09	1.11	1.85	2.09	1.51	0.30	0.11	0.07
	Rim#5	5.96	0.05	1.08	1.92	2.00	1.57	0.22	0.11	0.08
	Rim#6	5.86	0.09	1.16	1.89	2.01	1.52	0.27	0.12	0.08
	Rim#7	5.98	0.06	1.08	1.90	2.03	1.56	0.20	0.11	0.07
	Rim#8	5.87	0.07	1.17	1.96	1.92	1.58	0.24	0.13	0.07
	Rim#9	5.86	0.08	1.18	1.98	1.89	1.55	0.25	0.13	0.08
	Rim#10	5.92	0.07	1.14	1.84	2.04	1.57	0.23	0.12	0.07
	Rim#11	5.91	0.07	1.14	1.96	1.94	1.56	0.23	0.12	0.08
	Core#1	5.89	0.12	1.10	1.75	2.16	1.50	0.30	0.11	0.07
	Core#2	5.85	0.13	1.17	1.82	2.04	1.50	0.29	0.11	0.07

Instrument: JEOL JXA-8900RL microprobe of Geowissenschaftliches Zentrum Universitaet Goettingen
Voltage: 15.0 kV

A.3 Tables related to “Assessment of single-grain age signature from sediments and their potential source rocks: provenance of post-Jurassic sediments from northern Lhasa Terrane, Tibetan Plateau”

Table A.29: Zrn U-Pb age dataset

Zircon U-Pb data

Sample	Spot #	Th/U[a]	$^{208}Pb/^{206}Pb$	Ratios				Ages (Ma)				Cc[c]
				$^{207}Pb/^{235}U$[a]	2 σ[b]	$^{206}Pb/^{238}U$[a]	2 σ[b]	$^{207}Pb/^{235}U$	2 σ	$^{206}Pb/^{238}U$	2 σ	%
Lumpola south												
H-27	#1	0.86	1.51	3.0500	0.6649	0.0543	0.0064	1544.9	112.3	290.8	33.6	19
H-27	#2	0.82	0.33	0.1825	0.0099	0.0227	0.0005	143.5	7.5	124.6	3.1	87
H-27	#3	0.31	0.18	0.1283	0.0051	0.0196	0.0005	108.0	4.0	106.5	2.6	99
H-27	#4	0.20	0.11	5.5076	0.1873	0.3702	0.0137	1782.2	34.2	1803.1	60.0	101
H-27	#5	0.54	0.29	0.6305	0.0252	0.0799	0.0029	426.8	15.5	423.8	15.2	99
H-27	#6	0.03	1.46	7.3568	0.5370	0.0940	0.0061	2092.8	64.0	498.2	31.2	24
H-27	#7	0.24	0.13	0.3977	0.0286	0.0515	0.0025	285.5	14.8	277.7	13.3	97
H-27	#8	0.54	0.38	0.1755	0.0082	0.0260	0.0014	139.6	8.2	140.4	7.5	101
H-27	#9	2.88	1.87	2.7304	0.2130	0.0424	0.0025	1189.8	50.3	228.7	13.7	19
H-27	#10	0.15	0.08	6.0865	0.2313	0.3771	0.0147	1818.3	40.6	1794.2	63.0	99
H-27	#11	0.46	0.25	0.1266	0.0070	0.0187	0.0006	103.3	4.5	101.7	3.1	98
H-27	#12	0.38	0.21	0.1263	0.0059	0.0190	0.0007	102.7	4.7	103.2	4.0	100
H-27	#13	0.09	0.04	1.4437	0.0837	0.1555	0.0065	809.3	26.0	799.6	32.4	99
H-27	#14	0.09	0.08	0.4614	0.0540	0.0499	0.0034	213.3	20.0	192.8	12.9	90
H-27	#15	0.38	0.21	0.1405	0.0072	0.0191	0.0009	107.4	7.0	103.9	5.2	97
H-27	#16	0.89	0.32	0.1559	0.0095	0.0211	0.0009	113.5	6.6	109.5	4.9	96
H-27	#17	0.08	0.04	0.1469	0.0098	0.0206	0.0005	117.6	7.0	110.0	2.9	94
H-27	#18	0.27	0.14	0.3139	0.0100	0.0445	0.0009	244.2	6.8	239.4	5.2	98
H-27	#19	0.20	0.12	0.1351	0.0051	0.0190	0.0005	111.1	4.5	103.1	2.9	93
H-27	#20	0.55	0.30	0.1362	0.0039	0.0199	0.0006	111.2	4.2	108.7	3.3	98
H-27	#21	0.21	0.12	0.1445	0.0058	0.0200	0.0007	118.2	5.4	113.9	3.8	96
H-27	#22	0.22	0.06	0.1714	0.0199	0.0182	0.0009	107.3	7.3	98.5	4.8	92
H-27	#23	0.34	0.16	0.5510	0.0331	0.0711	0.0036	385.2	18.1	383.3	18.6	100
H-27	#24	0.89	0.47	0.2296	0.0152	0.0309	0.0009	220.5	16.0	168.3	5.2	76
H-27	#25	0.24	0.13	0.1326	0.0064	0.0206	0.0007	112.3	5.0	110.2	3.7	98
H-27	#26	0.23	0.04	5.7516	0.1438	0.3682	0.0099	1768.4	25.4	1731.6	42.7	98
H-27	#27	0.37	0.20	0.1485	0.0040	0.0203	0.0003	120.6	4.7	110.3	1.9	91
H-27	#28	0.35	0.15	0.1565	0.0136	0.0200	0.0009	129.5	10.6	106.0	4.6	82
H-27	#29	0.52	0.18	1.5412	0.0863	0.1475	0.0053	882.5	28.1	823.9	28.7	93
H-27	#30	0.39	0.23	0.2089	0.0100	0.0278	0.0011	162.1	7.2	151.3	6.0	93
H-27	#31	1.23	0.62	1.6054	0.0690	0.1635	0.0069	871.0	30.3	857.8	34.6	98
H-27	#32	0.71	0.35	0.1434	0.0103	0.0206	0.0012	116.5	8.2	111.4	6.5	96
H-27	#33	0.70	0.24	0.1809	0.0092	0.0220	0.0008	124.6	6.6	113.5	4.2	91
H-27	#34	0.21	0.12	0.1676	0.0085	0.0214	0.0004	126.7	6.1	114.7	2.3	91
H-27	#35	0.39	0.22	0.1231	0.0064	0.0182	0.0009	97.9	5.5	98.8	4.8	101
H-27	#36	0.20	0.09	3.1786	0.6580	0.3427	0.0315	1692.6	84.1	1636.8	134.4	97
H-27	#37	0.67	0.24	0.1419	0.0114	0.0205	0.0007	119.7	6.1	109.2	3.6	91
H-27	#39	0.21	0.62	0.1806	0.0038	0.0267	0.0006	144.2	3.8	143.7	3.1	100
H-27	#40	0.02	0.25	13.9423	2.4399	0.5800	0.0238	2726.0	52.4	2565.6	89.5	94
H-27	#41	0.58	1.45	28.8899	8.7825	0.2348	0.0169	2933.2	81.8	1216.4	80.3	41
H-27	#42	0.10	0.05	0.1329	0.0025	0.0203	0.0005	111.6	4.3	108.3	2.9	97
H-27	#43	0.25	0.13	0.1332	0.0033	0.0202	0.0005	112.8	3.2	111.7	2.8	99
H-27	#44	0.38	1.53	0.1522	3.3455	0.0190	0.0264	658.7	1232.9	145.2	202.4	22
H-27	#45	0.35	0.19	0.1208	0.0066	0.0181	0.0007	96.8	4.7	97.7	4.1	101
H-27	#47	0.44	0.23	0.1734	0.0121	0.0252	0.0016	135.5	8.7	135.4	8.7	100
H-27	#48	0.44	0.24	0.1252	0.0080	0.0184	0.0006	99.3	5.3	101.3	3.4	102
H-27	#49	0.55	0.30	0.3071	0.0175	0.0435	0.0022	233.3	11.7	234.0	11.5	100
H-27	#50	0.47	0.26	0.1244	0.0065	0.0179	0.0008	99.5	4.7	97.5	4.2	98
H-27	#51	0.47	0.15	1.2039	0.0361	0.1356	0.0023	730.6	11.5	695.7	11.9	95
H-27	#52	0.54	0.28	1.8368	0.0845	0.1814	0.0073	939.4	30.5	918.2	34.3	98
H-27	#53	0.44	0.16	0.2069	0.0103	0.0270	0.0012	166.5	9.1	151.5	6.4	91
H-27	#54	0.23	0.13	0.1292	0.0087	0.0183	0.0008	101.1	6.2	98.3	4.2	97
H-27	#55	0.23	0.13	0.3312	0.0384	0.0420	0.0037	242.6	25.1	227.5	19.5	94
H-27	#56	0.63	0.32	1.5569	0.1199	0.1707	0.0090	883.7	36.7	864.9	43.0	98
H-27	#57	0.23	0.12	0.2705	0.0133	0.0388	0.0016	211.7	9.4	206.9	8.4	98
H-27	#58	0.48	0.26	0.1258	0.0067	0.0188	0.0008	98.3	4.6	100.5	4.0	102
H-27	#59	0.64	0.33	0.3757	0.0150	0.0386	0.0010	219.0	14.7	205.7	5.5	94
H-27	#60	0.57	0.31	0.1315	0.0091	0.0195	0.0010	105.6	6.6	105.3	5.5	100
H-27	#61	0.97	0.60	0.2135	0.0147	0.0280	0.0013	164.0	10.7	148.6	7.1	91

Table A.30: Zrn U-Pb age dataset

Zircon U-Pb data

Sample	Spot #	Th/U[a]	$^{208}Pb/^{206}Pb$	Ratios				Ages (Ma)				Cc[c]
				$^{207}Pb/^{235}U$[a]	2 σ[b]	$^{206}Pb/^{238}U$[a]	2 σ[b]	$^{207}Pb/^{235}U$	2 σ	$^{206}Pb/^{238}U$	2 σ	%
H-27	#62	0.32	0.15	11.2907	0.4178	0.4892	0.0157	2344.2	34.4	2222.4	62.3	95
H-27	#63	0.27	0.13	0.1850	0.0154	0.0264	0.0020	147.8	10.9	141.5	10.5	96
H-27	#64	0.38	0.14	0.5730	0.0229	0.0743	0.0025	401.2	13.7	397.3	13.5	99
H-27	#65	0.56	0.35	0.1234	0.0048	0.0183	0.0006	95.9	4.1	95.8	3.3	100
H-27	#66	0.40	0.20	1.6498	0.0825	0.1708	0.0087	873.6	32.7	867.5	41.5	99
H-27	#67	0.42	0.19	2.0996	0.1197	0.2137	0.0115	1045.0	37.2	1053.8	52.7	101
H-27	#68	0.15	0.07	0.1445	0.0085	0.0209	0.0007	121.5	5.6	112.0	4.0	92
H-27	#69	0.64	0.30	0.1641	0.0098	0.0210	0.0010	123.7	7.1	112.5	5.4	91
H-27	#70	0.60	0.32	2.3132	0.0810	0.2142	0.0051	1115.9	22.6	1058.8	24.5	95
H-27	#71	0.12	0.01	4.3381	0.1475	0.2827	0.0051	1569.1	19.4	1375.1	23.6	88
H-27	#72	0.37	0.20	0.1653	0.0056	0.0248	0.0007	131.6	5.1	133.4	4.0	101
H-27	#73	0.71	0.38	0.1342	0.0083	0.0191	0.0006	103.7	5.3	103.9	3.4	100
H-27	#74	0.47	0.25	0.1351	0.0082	0.0196	0.0010	111.4	5.9	110.3	5.4	99
H-27	#75	0.25	0.13	0.6073	0.0279	0.0772	0.0033	414.7	16.5	410.0	17.1	99
H-27	#76	0.31	0.14	0.1249	0.0062	0.0176	0.0007	100.4	4.5	99.0	3.8	99
H-27	#77	0.06	0.04	0.1378	0.0156	0.0185	0.0007	99.0	11.9	96.4	3.8	97
H-27	#78	0.13	0.07	0.7799	0.0437	0.0949	0.0044	504.1	20.5	496.9	22.0	99
H-27	#79	0.58	0.21	0.1436	0.0056	0.0199	0.0006	118.2	4.9	111.7	3.4	95
H-27	#80	0.35	0.20	0.9509	0.0723	0.1054	0.0032	610.4	21.8	565.6	16.8	93
H-27	#81	0.39	0.21	0.6513	0.0247	0.0843	0.0032	439.2	16.2	442.0	16.3	101
H-27	#82	0.14	0.07	0.1349	0.0090	0.0185	0.0007	109.5	5.7	102.6	4.1	94
H-27	#83	0.76	0.34	0.1431	0.0080	0.0199	0.0009	117.3	5.9	110.2	5.0	94
H-27	#84	0.18	0.10	0.7254	0.0254	0.0932	0.0022	480.9	17.0	475.9	11.5	99
H-27	#85	0.31	0.16	0.9205	0.0359	0.1099	0.0040	589.1	19.9	581.1	20.0	99
H-27	#86	0.12	0.06	6.9574	0.4592	0.3664	0.0183	1905.5	57.5	1768.7	77.8	93
H-27	#87	0.22	0.11	0.3703	0.0104	0.0502	0.0010	269.1	5.9	260.3	5.4	97
H-27	#88	0.12	0.07	0.1243	0.0061	0.0182	0.0009	100.0	5.7	99.2	4.8	99
H-27	#89	0.46	0.10	2.6497	0.2438	0.1313	0.0104	1183.4	59.7	678.7	51.1	57
H-27	#90	0.60	0.24	0.2033	0.0053	0.0195	0.0004	111.2	6.4	104.8	2.4	94
H-27	#91	0.30	0.16	0.1667	0.0105	0.0219	0.0004	130.9	4.3	117.7	2.0	90
H-27	#92	0.78	0.86	1.0028	0.1103	0.0274	0.0021	611.7	47.5	150.2	11.4	25
H-27	#93	0.04	1.04	3.4083	0.3340	0.0589	0.0032	1390.8	50.5	314.6	16.9	23
H-27	#94	0.40	0.21	0.1282	0.0063	0.0192	0.0008	102.7	4.6	104.3	4.1	102
H-27	#95	0.50	0.27	0.1245	0.0067	0.0184	0.0008	101.0	4.9	100.3	4.1	99
H-27	#96	0.25	0.13	0.1255	0.0058	0.0186	0.0007	99.9	4.8	100.8	4.0	101
H-27	#97	0.35	0.17	0.2605	0.0182	0.0371	0.0020	200.4	10.8	198.6	10.4	99
H-27	#98	0.37	0.21	0.2161	0.0138	0.0262	0.0010	172.9	9.3	141.1	5.4	82
H-27	#99	0.25	0.13	1.4287	0.0643	0.1537	0.0055	802.0	25.8	786.1	26.7	98
H-27	#100	0.30	0.17	0.1221	0.0054	0.0179	0.0005	99.8	3.6	97.0	2.8	97
H-27	#101	0.12	0.06	0.5684	0.0347	0.0730	0.0028	388.0	14.3	384.8	14.2	99
H-27	#102	0.23	0.12	0.3116	0.0143	0.0432	0.0017	234.5	9.9	231.0	8.9	99
H-27	#103	0.24	0.16	0.1875	0.0109	0.0273	0.0012	150.1	7.7	146.7	6.2	98
H-38A	#1	0.31	0.16	9.3390	0.4763	0.4299	0.0155	2481.9	37.8	2538.2	76.0	102
H-38A	#2	0.65	0.37	0.1847	0.0072	0.0265	0.0009	194.3	7.6	186.8	6.1	96
H-38A	#3	0.26	0.08	5.3603	0.1769	0.3382	0.0078	1951.7	21.9	1991.7	41.3	102
H-38A	#4	0.04	0.02	0.7414	0.0297	0.0900	0.0034	609.2	19.4	613.3	22.3	101
H-38A	#5	0.21	1.17	1.8907	0.7657	0.0400	0.0066	1267.8	227.1	342.0	55.5	27
H-38A	#6	0.77	0.31	0.6432	0.0341	0.0787	0.0032	548.9	18.8	540.4	21.3	98
H-38A	#7	0.13	0.10	0.4155	0.0237	0.0395	0.0021	378.5	19.5	277.3	14.4	73
H-38A	#8	0.32	0.17	9.2650	0.5281	0.4113	0.0189	2430.5	46.2	2426.9	93.7	100
H-38A	#9	0.14	0.74	0.6437	0.1242	0.0271	0.0015	551.5	57.3	191.6	10.6	35
H-38A	#10	0.39	0.12	4.7639	0.1715	0.2777	0.0106	1888.5	35.8	1805.0	60.1	96
H-38A	#11	1.17	1.66	22.7273	1.2273	0.2740	0.0123	3292.7	49.0	1737.1	68.9	53
H-38A	#12	0.15	0.61	0.2620	0.1279	0.0255	0.0011	376.7	91.1	181.0	7.7	48
H-38A	#13	0.44	0.27	0.2099	0.0061	0.0288	0.0005	213.6	4.8	203.1	3.4	95
H-38A	#14	0.57	0.37	0.1396	0.0046	0.0198	0.0005	147.4	4.5	140.4	3.8	95
H-38A	#15	0.52	0.23	0.2082	0.0077	0.0291	0.0005	210.7	9.6	200.3	3.6	95
H-38A	#16	0.32	0.18	0.5388	0.0291	0.0664	0.0036	469.7	21.7	462.3	24.1	98
H-38A	#17	0.55	0.32	0.6131	0.0270	0.0750	0.0031	523.8	18.6	521.6	20.6	100
H-38A	#18	0.43	0.23	9.7913	0.3917	0.4180	0.0163	2489.0	39.7	2470.6	80.5	99
H-38A	#19	0.26	0.13	0.3016	0.0106	0.0388	0.0008	303.1	9.5	274.7	5.7	91

Table A.31: Zrn U-Pb age dataset

Zircon U-Pb data

Sample	Spot #	Th/U[a]	$^{208}Pb/^{206}Pb$	Ratios				Ages (Ma)				Cc[c]
				$^{207}Pb/^{235}U$[a]	2 σ[b]	$^{206}Pb/^{238}U$[a]	2 σ[b]	$^{207}Pb/^{235}U$	2 σ	$^{206}Pb/^{238}U$	2 σ	%
H-38A	#20	0.31	0.20	0.2677	0.0166	0.0355	0.0017	265.8	14.6	251.4	11.8	95
H-38A	#21	0.12	0.07	0.2000	0.0096	0.0267	0.0012	202.6	9.2	190.4	8.4	94
H-38A	#22	0.48	0.43	0.2198	0.0086	0.0285	0.0009	223.0	8.2	203.5	6.6	91
H-38A	#23	0.62	0.37	0.2336	0.0086	0.0301	0.0009	237.6	8.9	213.2	6.5	90
H-38A	#24	0.16	0.09	1.8110	0.0398	0.1375	0.0030	1122.6	16.4	913.1	19.6	81
H-38A	#25	0.40	0.23	0.1994	0.0074	0.0261	0.0010	203.1	8.9	186.3	7.3	92
H-38A	#26	0.20	0.18	0.7006	0.0462	0.0627	0.0036	568.8	31.8	443.7	24.5	78
H-38A	#27	0.43	0.21	0.2358	0.0177	0.0264	0.0012	254.6	17.3	217.2	9.8	85
H-38A	#28	0.13	0.04	4.7037	0.1552	0.1995	0.0056	1885.8	36.6	1301.9	34.3	69
H-38A	#29	0.22	0.16	0.2030	0.0081	0.0278	0.0006	211.5	9.6	198.4	4.3	94
H-38A	#30	0.30	0.18	0.6200	0.0267	0.0777	0.0031	533.5	18.8	536.3	20.6	101
H-38A	#31	0.31	0.13	4.3369	0.2515	0.2909	0.0140	1829.1	45.1	1883.9	78.9	103
H-38A	#32	0.38	0.23	0.5854	0.0222	0.0718	0.0027	511.7	17.0	501.0	18.3	98
H-38A	#33	0.24	0.14	0.1477	0.0062	0.0213	0.0008	151.7	5.8	152.9	5.4	101
H-38A	#34	0.80	0.47	0.7445	0.0342	0.0850	0.0032	597.0	19.6	589.6	21.4	99
H-38A	#35	0.35	0.22	0.5273	0.0248	0.0644	0.0030	464.5	19.2	451.7	20.1	97
H-38A	#36	0.29	0.16	0.3002	0.0153	0.0398	0.0019	288.7	12.9	282.5	13.0	98
H-38A	#37	0.20	0.07	5.0770	0.2640	0.3140	0.0148	1910.1	44.0	1953.3	79.7	102
H-38A	#38	0.25	0.14	4.8653	0.2335	0.3032	0.0100	1884.5	34.0	1895.8	56.1	101
H-38A	#39	0.35	0.21	0.2749	0.0124	0.0370	0.0012	268.5	9.5	263.3	8.8	98
H-38A	#40	0.31	0.10	4.6244	0.1850	0.2876	0.0106	1837.6	34.5	1811.3	58.7	99
H-38A	#41	0.30	0.19	0.2688	0.0126	0.0365	0.0017	260.7	12.3	259.4	11.7	100
H-38A	#42	0.39	0.23	0.6533	0.0261	0.0801	0.0030	571.3	19.4	571.8	20.8	100
H-38A	#43	0.38	0.21	0.1965	0.0086	0.0256	0.0011	201.1	8.4	186.8	7.7	93
H-38A	#44	0.36	0.22	2.6156	0.1439	0.2076	0.0087	1376.3	35.3	1358.3	51.6	99
H-38A	#45	0.17	0.08	1.6229	0.0600	0.1459	0.0055	1047.4	27.2	983.6	34.8	94
H-38A	#46	0.23	0.19	0.5781	0.0324	0.0547	0.0025	483.0	21.4	376.7	16.9	78
H-38A	#47	0.40	0.17	0.2739	0.0156	0.0329	0.0014	275.4	12.6	242.4	10.5	88
H-38A	#48	0.57	0.32	0.2012	0.0131	0.0260	0.0013	210.0	12.2	195.9	9.5	93
H-38A	#49	0.08	0.03	5.2165	0.2400	0.3237	0.0139	1937.5	40.6	2010.7	74.7	104
H-38A	#50	0.08	0.05	1.5686	0.0627	0.1515	0.0064	1034.6	29.6	1019.8	39.7	99
H-38A	#51	0.09	0.05	4.6120	0.2490	0.2868	0.0152	1838.2	47.8	1812.4	84.3	99
H-38A	#52	0.32	0.18	0.6127	0.0270	0.0750	0.0037	525.1	22.0	525.3	24.8	100
H-38A	#53	0.15	0.12	0.3677	0.0199	0.0380	0.0018	349.8	17.0	272.9	12.8	78
H-38A	#54	0.37	0.20	6.3387	0.3423	0.3486	0.0136	2100.3	38.9	2144.7	73.4	102
H-38A	#55	0.73	0.44	0.7093	0.0383	0.0820	0.0034	590.3	21.3	585.1	24.1	99
H-38A	#56	0.16	0.08	1.4959	0.0643	0.1500	0.0074	995.0	34.2	1021.2	46.4	103
H-38A	#57	0.35	0.23	9.6370	0.3373	0.3726	0.0101	2514.2	34.0	2296.6	54.3	91
H-38A	#58	0.60	0.36	1.8887	0.0812	0.1743	0.0054	1148.6	25.8	1162.1	34.1	101
H-38A	#59	0.07	0.04	3.9282	0.1925	0.2514	0.0111	1700.3	39.5	1616.2	64.6	95
H-38A	#60	0.49	0.29	0.2567	0.0108	0.0358	0.0014	261.1	10.4	257.2	9.8	99
H-38A	#61	0.08	0.05	1.4086	0.0648	0.1420	0.0054	961.3	27.1	979.4	35.5	102
H-38A	#62	0.43	0.26	0.1808	0.0080	0.0254	0.0010	184.5	8.0	183.3	7.4	99
H-38A	#63	0.12	0.06	3.6041	0.0901	0.2350	0.0061	1662.2	24.8	1539.5	37.1	93
H-38A	#64	0.14	0.08	1.3412	0.0604	0.1373	0.0060	950.3	30.1	963.0	40.4	101
H-38A	#65	0.36	0.20	1.5252	0.0610	0.1492	0.0058	995.0	27.6	1007.9	37.4	101
H-38A	#66	0.88	0.51	0.7600	0.0433	0.0852	0.0035	617.7	22.9	594.8	23.9	96
H-38A	#67	0.12	0.22	0.3852	0.0119	0.0255	0.0010	433.8	18.2	221.4	8.9	51
H-38A	#68	0.43	0.28	1.1796	0.0436	0.1223	0.0053	840.0	29.0	835.4	34.6	99
H-38A	#69	0.28	0.15	4.8574	0.2186	0.2953	0.0118	1852.9	40.0	1863.3	66.7	101
H-38A	#70	0.20	0.11	5.4128	0.3085	0.2942	0.0100	1981.5	45.4	1891.9	57.6	95
H-38A	#71	0.44	0.28	0.5552	0.0267	0.0671	0.0030	503.0	22.5	476.6	20.7	95
H-38A	#72	0.32	0.17	0.6194	0.0427	0.0733	0.0053	527.1	30.9	515.0	35.7	98
H-38A	#73	0.79	0.37	0.1924	0.0092	0.0251	0.0010	193.1	8.8	177.8	7.2	92
H-38A	#74	0.63	0.32	0.2333	0.0159	0.0268	0.0013	241.2	13.4	200.1	9.5	83
H-38A	#75	0.53	0.31	0.5834	0.0309	0.0695	0.0026	503.3	17.2	495.5	18.1	98
H-38A	#76	0.33	0.14	0.7786	0.0413	0.0849	0.0042	634.2	26.8	593.5	28.4	94
H-38A	#77	0.25	0.13	3.9317	0.1966	0.2277	0.0116	1741.3	46.9	1559.7	72.4	90
H-38A	#78	0.43	0.26	0.2569	0.0121	0.0347	0.0012	251.4	9.6	248.9	9.0	99
H-38A	#79	0.56	0.32	0.1897	0.0091	0.0251	0.0010	197.6	8.8	187.3	7.8	95
H-38A	#80	0.48	0.17	0.9078	0.0418	0.0967	0.0046	728.4	27.4	690.2	32.2	95
H-38A	#81	0.72	0.43	0.8226	0.0271	0.0895	0.0027	651.2	20.4	623.1	18.4	96

Table A.32: Zrn U-Pb age dataset

Zircon U-Pb data

Sample	Spot #	Th/U[a]	$^{208}Pb/^{206}Pb$	Ratios				Ages (Ma)				Cc[c]
				$^{207}Pb/^{235}U$[a]	2 σ[b]	$^{206}Pb/^{238}U$[a]	2 σ[b]	$^{207}Pb/^{235}U$	2 σ	$^{206}Pb/^{238}U$	2 σ	%
H-38A	#82	0.23	0.08	0.4454	0.0196	0.0559	0.0023	409.1	15.6	397.0	16.6	97
H-38A	#83	0.10	0.13	1.7899	0.0501	0.0981	0.0032	1145.2	30.0	684.9	22.1	60
H-38A	#84	0.68	0.39	1.2907	0.0684	0.1300	0.0064	894.4	34.5	890.6	41.7	100
H-38A	#85	0.26	0.14	3.8306	0.1494	0.2692	0.0100	1679.8	35.1	1719.7	57.6	102
H-38A	#86	0.18	0.14	0.7384	0.0111	0.0902	0.0004	614.6	6.5	613.5	5.3	100
H-38A	#87	0.44	0.30	0.3483	0.0212	0.0337	0.0013	311.0	15.4	241.9	9.7	78
H-38A	#88	0.13	0.07	4.8295	0.2560	0.2977	0.0158	1862.1	49.8	1874.1	88.4	101
H-38A	#89	0.19	0.11	4.2735	0.2179	0.2845	0.0122	1759.6	41.8	1804.3	69.6	103
H-38A	#90	0.36	0.17	0.5741	0.0385	0.0610	0.0030	506.9	25.0	445.4	22.0	88
H-38A	#91	0.57	0.72	0.2389	0.0086	0.0283	0.0003	230.4	8.5	203.7	2.8	88
H-38A	#92	0.13	0.09	4.3435	0.1781	0.2287	0.0087	1797.2	36.9	1488.0	52.0	83
H-38A	#93	0.23	0.13	0.5731	0.0229	0.0695	0.0026	493.4	16.5	489.7	18.4	99
H-38A	#94	0.46	0.19	1.1737	0.0563	0.1198	0.0055	837.6	28.9	821.9	36.4	98
H-38A	#95	0.13	0.10	0.2044	0.0213	0.0275	0.0008	219.0	16.7	198.4	5.7	91
H-38A	#96	0.39	0.22	0.2678	0.0375	0.0320	0.0030	250.2	29.2	229.7	21.2	92
H-38A	#97	0.04	0.02	0.1816	0.0082	0.0253	0.0010	186.9	7.9	186.7	7.7	100
H-38A	#98	0.21	0.12	2.4791	0.0967	0.2051	0.0070	1334.7	28.6	1348.6	42.7	101
H-38A	#99	0.28	0.19	0.1911	0.0034	0.0269	0.0008	197.4	6.8	194.0	5.7	98
H-38A	#100	0.41	0.23	0.5680	0.0312	0.0695	0.0034	500.4	21.2	489.3	23.6	98
H-38A	#101	0.12	0.06	1.2357	0.0556	0.1262	0.0053	868.3	27.2	861.9	34.8	99
H-38A	#102	0.08	0.04	1.3243	0.0689	0.1321	0.0053	904.1	27.3	899.7	34.5	100
H-38A	#103	0.34	0.11	1.6805	0.1160	0.1606	0.0074	1094.0	34.7	1078.3	46.8	99
H-38A	#104	0.55	0.33	0.1251	0.0059	0.0179	0.0008	130.9	6.4	129.2	6.0	99
H-38A	#105	0.12	0.07	0.3023	0.0184	0.0368	0.0007	268.7	6.6	263.6	5.2	98
H-38A	#106	0.15	0.27	0.3067	0.0138	0.0251	0.0010	293.0	12.6	180.8	7.5	62
H-38A	#107	0.79	0.42	0.6769	0.0447	0.0732	0.0031	547.5	21.0	515.2	21.3	94
H-38A	#108	0.05	0.30	0.3416	0.0116	0.0260	0.0012	347.3	21.1	187.4	8.7	54
H-38A	#109	0.18	0.18	0.3954	0.0838	0.0423	0.0013	423.2	51.8	302.8	9.2	72
H-38A	#110	0.39	0.23	1.1706	0.0562	0.1238	0.0050	850.0	26.2	845.7	32.6	99
H-38A	#111	0.24	0.26	0.1431	0.0063	0.0200	0.0007	146.3	5.9	144.5	5.4	99
H-38A	#112	0.11	0.44	0.3809	0.0339	0.0235	0.0008	320.5	33.2	171.0	5.9	53
H-38A	#113	0.09	0.11	0.2830	0.0108	0.0336	0.0017	283.9	15.5	240.3	12.5	85
H-38A	#114	0.24	0.15	0.2899	0.0125	0.0384	0.0015	280.2	10.8	273.8	10.7	98
H-38A	#115	0.30	0.19	0.4531	0.0208	0.0560	0.0020	405.7	14.1	395.8	14.2	98
Nagqu												
H-41A	#1	0.55	0.26	5.0364	0.2417	0.3236	0.0084	1851.4	26.7	1845.8	41.9	100
H-41A	#2	0.37	0.19	5.4672	0.3116	0.3324	0.0083	1883.1	25.1	1891.5	41.1	100
H-41A	#3	0.54	0.31	0.5182	0.0104	0.0633	0.0020	447.3	14.6	413.6	12.4	92
H-41A	#4	0.14	0.07	0.1308	0.0068	0.0191	0.0007	127.4	5.8	124.4	4.7	98
H-41A	#5	0.08	0.04	1.4634	0.0629	0.1443	0.0049	899.3	22.9	888.7	28.3	99
H-41A	#6	0.45	0.22	0.1297	0.0070	0.0172	0.0006	130.2	7.9	111.3	3.6	85
H-41A	#7	1.02	0.55	0.6758	0.0331	0.0802	0.0030	533.0	18.4	524.6	19.2	98
H-41A	#8	0.03	0.02	0.6693	0.0274	0.0799	0.0018	533.0	10.8	510.9	10.8	96
H-41A	#9	0.01	0.00	0.2546	0.0359	0.0330	0.0015	220.0	17.0	215.3	9.5	98
H-41A	#10	0.31	0.30	0.3192	0.0306	0.0189	0.0008	232.9	37.7	122.4	5.0	53
H-41A	#11	0.54	0.28	9.4582	0.2837	0.4190	0.0117	2369.4	29.8	2305.0	54.5	97
H-41A	#12	0.37	0.20	0.4456	0.0245	0.0570	0.0016	365.7	13.6	365.5	10.0	100
H-41A	#13	0.22	0.09	1.6535	0.0645	0.1633	0.0054	998.1	24.4	996.8	30.6	100
H-41A	#14	0.28	0.17	0.1179	0.0045	0.0166	0.0005	116.8	5.0	108.7	3.4	93
H-41A	#15	0.18	0.09	5.6730	0.2723	0.3466	0.0118	1892.4	32.2	1940.0	57.2	103
H-41A	#16	0.28	0.14	0.6868	0.0543	0.0820	0.0045	536.9	25.3	519.6	27.5	97
H-41A	#17	0.09	0.07	0.3213	0.0148	0.0409	0.0017	290.1	12.7	267.2	11.0	92
H-41A	#18	0.35	0.17	14.3522	0.5167	0.5284	0.0153	2762.3	32.8	2797.7	66.2	101
H-41A	#19	0.48	0.26	0.1329	0.0041	0.0189	0.0006	125.1	4.1	123.7	3.8	99
H-41A	#20	0.31	0.16	8.2767	0.5876	0.3845	0.0242	2274.7	64.6	2173.3	117.3	96
H-41A	#21	0.18	0.09	5.0343	0.1863	0.3050	0.0092	1817.9	29.2	1767.7	46.5	97
H-41A	#22	0.33	0.18	1.5322	0.0751	0.1466	0.0059	939.4	26.7	901.5	33.7	96
H-41A	#23	0.32	0.14	5.3849	0.2585	0.3351	0.0117	1886.2	34.0	1901.2	57.9	101
H-41A	#24	0.78	0.43	0.3755	0.0244	0.0486	0.0018	317.4	14.0	312.7	11.6	99
H-41A	#25	0.44	0.23	6.4607	0.2455	0.3640	0.0095	2040.9	27.6	2042.0	45.7	100

Table A.33: Zrn U-Pb age dataset

Zircon U-Pb data

Sample	Spot #	Th/U[a]	$^{208}Pb/^{206}Pb$	Ratios				Ages (Ma)				Cc[c]
				$^{207}Pb/^{235}U^{a}$	2 σ[b]	$^{206}Pb/^{238}U^{a}$	2 σ[b]	$^{207}Pb/^{235}U$	2 σ	$^{206}Pb/^{238}U$	2 σ	%
H-41A	#26	0.31	0.17	0.7235	0.0289	0.0892	0.0024	565.7	14.4	563.3	14.6	100
H-41A	#27	0.28	0.11	1.9386	0.0485	0.1786	0.0050	1103.2	22.4	1093.7	28.2	99
H-41A	#28	0.09	0.07	0.6010	0.0228	0.0653	0.0016	482.7	13.9	415.4	10.1	86
H-41A	#29	0.24	0.13	1.5320	0.0582	0.1524	0.0061	937.7	26.7	934.5	34.9	100
H-41A	#30	0.28	0.16	0.1153	0.0047	0.0171	0.0006	111.8	5.0	111.5	4.2	100
H-41A	#31	0.02	0.02	0.6461	0.0142	0.0757	0.0014	528.2	9.5	485.7	8.4	92
H-41A	#32	0.79	0.46	0.2051	0.0084	0.0287	0.0009	188.6	7.1	186.4	6.1	99
H-41A	#33	0.35	0.18	0.8318	0.0241	0.0996	0.0021	623.2	12.7	625.5	12.5	100
H-41A	#34	0.31	0.17	0.1710	0.0103	0.0225	0.0007	160.2	6.8	149.3	4.7	93
H-41A	#36	0.37	0.21	1.1960	0.0706	0.1250	0.0068	784.5	31.1	776.5	39.6	99
H-41A	#37	0.34	0.19	0.1612	0.0077	0.0226	0.0008	149.1	5.6	147.5	5.0	99
H-41A	#38	0.20	0.12	1.3524	0.0663	0.1356	0.0057	865.9	26.6	837.9	33.1	97
H-41A	#39	0.33	0.19	0.1237	0.0046	0.0177	0.0006	116.9	4.9	115.9	4.0	99
H-41A	#40	0.25	0.13	0.5563	0.0217	0.0700	0.0023	444.3	13.8	445.8	14.2	100
H-41A	#41	0.39	0.19	11.5330	0.6343	0.4693	0.0136	2553.4	32.2	2529.6	61.0	99
H-41A	#42	0.06	0.05	0.7096	0.0220	0.0850	0.0023	548.4	13.7	538.0	14.0	98
H-41A	#43	0.46	0.35	0.2144	0.0195	0.0254	0.0010	207.6	18.0	164.1	6.3	79
H-41A	#44	0.14	0.07	1.4609	0.1329	0.1495	0.0051	936.0	24.8	919.3	29.2	98
H-41A	#45	0.34	0.19	1.1809	0.0543	0.1269	0.0039	806.2	20.2	798.9	23.3	99
H-41A	#46	0.24	0.13	2.8908	0.2197	0.2234	0.0132	1327.1	52.4	1328.1	71.2	100
H-41A	#47	0.36	0.19	0.6361	0.0223	0.0758	0.0024	490.1	14.5	481.2	14.9	98
H-41A	#48	0.42	0.22	7.0713	0.2546	0.3780	0.0129	2107.4	34.3	2109.6	61.5	100
H-41A	#49	0.25	0.14	0.7443	0.0305	0.0882	0.0032	559.6	18.2	558.8	19.3	100
H-41A	#50	0.12	0.05	1.8204	0.0746	0.1646	0.0058	1049.4	25.8	1023.9	33.2	98
H-41A	#51	0.39	0.23	0.1097	0.0039	0.0163	0.0005	105.6	4.0	106.8	3.2	101
H-41A	#52	0.25	0.13	7.6887	0.3921	0.3964	0.0111	2188.2	29.1	2197.2	52.3	100
H-41A	#53	0.08	0.06	5.9381	0.1900	0.3394	0.0112	1963.7	35.4	1903.3	54.6	97
H-41A	#54	0.57	0.31	1.2448	0.0610	0.1287	0.0051	811.9	25.5	801.5	30.2	99
H-41A	#55	0.29	0.15	4.6247	0.3099	0.2943	0.0094	1741.1	30.4	1698.7	48.0	98
H-41A	#56	0.23	0.13	0.5409	0.0222	0.0679	0.0019	436.7	12.1	433.7	11.8	99
H-41A	#57	0.24	0.14	0.2695	0.0078	0.0369	0.0010	241.3	6.9	239.1	6.6	99
H-41A	#58	0.34	0.18	3.7181	0.1599	0.2665	0.0080	1571.8	27.6	1556.6	41.6	99
H-41A	#59	0.40	0.20	5.8048	0.2612	0.3414	0.0113	1934.0	32.5	1933.8	55.4	100
H-41A	#60	0.64	0.35	0.8228	0.0313	0.0956	0.0028	600.4	14.6	602.3	16.7	100
H-41A	#61	0.31	0.16	1.7221	0.0809	0.1663	0.0058	1002.0	25.1	1015.0	33.0	101
H-41A	#62	0.43	0.24	1.0486	0.0388	0.1163	0.0038	732.4	20.0	725.9	22.7	99
H-41A	#63	0.81	0.48	0.1177	0.0054	0.0174	0.0003	118.0	4.0	114.8	1.8	97
H-41A	#64	0.37	0.20	2.2770	0.0797	0.2047	0.0051	1217.9	21.5	1226.2	28.0	101
H-41A	#65	0.30	0.17	1.3446	0.0645	0.1383	0.0055	876.5	25.6	855.7	32.1	98
H-41A	#66	0.21	0.12	0.6904	0.0214	0.0832	0.0025	527.8	14.9	527.7	15.2	100
H-41A	#67	0.40	0.23	0.1235	0.0061	0.0176	0.0007	117.4	5.1	115.5	4.4	98
H-41A	#68	0.55	0.33	13.5884	0.5571	0.4209	0.0114	2763.4	30.8	2309.3	52.6	84
H-41A	#69	0.12	0.06	0.3582	0.0577	0.0481	0.0036	325.8	25.1	312.9	22.6	96
H-41A	#70	0.34	0.18	4.9752	0.1741	0.3181	0.0076	1814.0	23.9	1820.1	38.2	100
H-41A	#71	0.36	0.21	0.5084	0.0198	0.0648	0.0030	423.7	17.5	409.4	18.7	97
H-41A	#72	0.22	0.11	0.4963	0.0377	0.0688	0.0013	457.7	20.1	434.9	8.0	95
H-41A	#73	0.18	0.09	1.6624	0.0781	0.1562	0.0048	1001.0	25.1	958.5	27.7	96
H-41A	#74	0.52	0.30	0.9633	0.0559	0.1122	0.0036	740.0	18.6	709.5	21.5	96
H-41A	#75	0.51	0.27	4.2934	0.3349	0.2904	0.0183	1690.9	55.0	1669.3	93.3	99
H-41A	#76	0.21	0.12	0.1215	0.0040	0.0176	0.0004	115.9	3.6	115.2	2.9	99
H-41A	#77	0.59	0.31	9.5364	0.4864	0.4282	0.0081	2432.1	23.3	2350.2	37.5	97
H-41A	#78	0.54	0.29	1.1031	0.0563	0.1172	0.0036	748.7	19.2	740.6	21.7	99
H-41A	#79	0.21	0.16	4.4848	0.0897	0.2827	0.0057	1648.6	34.8	1642.6	29.1	100
H-41A	#80	0.38	0.21	1.3067	0.0823	0.1280	0.0038	840.6	27.2	794.9	22.5	95
H-41A	#81	0.30	0.17	0.5918	0.0207	0.0758	0.0026	482.3	15.1	483.0	15.8	100
H-41A	#82	0.41	0.22	0.5344	0.0224	0.0687	0.0021	454.8	26.0	440.7	12.8	97
H-41A	#83	0.30	0.17	0.1827	0.0108	0.0248	0.0008	166.5	8.0	162.1	5.1	97
H-41A	#84	0.19	0.10	1.5449	0.0572	0.1500	0.0040	944.5	19.9	928.4	23.4	98
H-41A	#85	0.47	0.23	9.9493	0.7064	0.4343	0.0135	2423.4	32.8	2378.4	62.0	98
H-41A	#86	0.35	0.20	1.4913	0.1417	0.1469	0.0123	899.3	56.4	906.3	71.4	101
H-41A	#87	0.69	0.39	0.2652	0.0117	0.0372	0.0015	248.4	10.4	242.1	9.3	97
H-41A	#88	0.02	0.01	1.8407	0.0828	0.1717	0.0053	1050.6	23.2	1047.4	30.0	100

Table A.34: Zrn U-Pb age dataset

Zircon U-Pb data

Sample	Spot #	Th/U[a]	$^{208}Pb/^{206}Pb$	Ratios				Ages (Ma)				Cc[c]
				$^{207}Pb/^{235}U$[a]	2 σ[b]	$^{206}Pb/^{238}U$[a]	2 σ[b]	$^{207}Pb/^{235}U$	2 σ	$^{206}Pb/^{238}U$	2 σ	%
H-41A	#89	0.25	0.15	0.1295	0.0097	0.0176	0.0006	121.4	6.5	115.2	4.1	95
H-41A	#90	0.48	0.26	0.4679	0.0370	0.0598	0.0019	391.7	12.4	385.6	11.6	98
H-41A	#91	0.15	0.08	0.3351	0.0101	0.0432	0.0012	296.7	10.9	280.1	7.4	94
H-41A	#92	0.43	0.24	0.1353	0.0087	0.0190	0.0006	136.3	9.7	124.8	4.2	92
H-41A	#93	0.24	0.14	0.2574	0.0167	0.0308	0.0014	224.4	11.3	201.3	8.9	90
H-41A	#94	0.13	0.08	0.1600	0.0072	0.0220	0.0009	152.6	6.4	148.2	5.9	97
H-41A	#95	0.54	0.26	3.0219	0.1571	0.2363	0.0120	1423.3	42.2	1402.9	64.6	99
H-41A	#96	0.37	0.16	0.1873	0.0084	0.0259	0.0012	179.6	8.4	174.3	8.1	97
H-41A	#97	0.40	0.46	0.1877	0.0084	0.0265	0.0010	175.0	7.1	173.3	6.5	99
H-41A	#98	0.47	0.27	0.1314	0.0068	0.0173	0.0006	118.8	5.6	111.5	4.1	94
H-41A	#99	0.28	0.16	0.9444	0.0331	0.1064	0.0041	683.2	21.6	667.9	24.8	98
H-41A	#100	0.38	0.20	1.4680	0.0719	0.1472	0.0034	927.5	22.8	909.6	20.4	98
H-41A	#101	0.46	0.27	0.3018	0.0115	0.0401	0.0008	281.3	9.9	260.6	5.6	93
H-41A	#102	0.17	0.09	13.1699	1.2906	0.4736	0.0426	2654.7	94.6	2567.7	193.5	97
H-41A	#103	0.71	0.33	1.2068	0.0350	0.1279	0.0024	849.3	20.9	785.7	14.8	93
H-41A	#104	0.44	0.23	0.7110	0.0220	0.0889	0.0017	569.1	9.6	565.2	10.8	99
H-41A	#105	0.27	0.16	0.6058	0.0109	0.0757	0.0010	505.0	8.0	484.4	6.5	96
H-41A	#106	0.76	0.42	0.7064	0.0226	0.0854	0.0022	556.3	12.1	543.6	13.6	98
H-41A	#107	0.32	0.28	1.3444	0.0229	0.1445	0.0027	876.5	14.2	888.0	16.6	101
H-41A	#108	0.28	0.16	1.2064	0.0434	0.1274	0.0022	807.7	12.9	795.6	13.5	99
H-41A	#109	0.39	0.22	0.1348	0.0030	0.0192	0.0003	132.8	2.9	126.4	2.0	95
H-41A	#110	0.31	0.18	0.1346	0.0096	0.0183	0.0006	123.8	6.1	120.1	3.9	97
H-41A	#111	0.76	0.42	0.7025	0.0344	0.0836	0.0025	543.5	17.8	533.4	15.9	98
H-41A	#112	0.53	0.30	0.6558	0.0374	0.0767	0.0021	511.4	15.8	491.0	13.7	96
H-41A	#113	0.68	0.36	4.9881	0.3392	0.3050	0.0146	1800.0	43.9	1764.5	74.5	98
H-41A	#114	0.07	0.05	4.5038	0.2072	0.2255	0.0106	1722.3	44.1	1395.8	59.3	81
H-41A	#115	0.17	0.10	1.4086	0.0507	0.1417	0.0034	886.3	17.3	880.7	20.6	99
H-42A	#1	0.35	0.21	0.1127	0.0047	0.0160	0.0007	107.5	4.8	105.4	4.4	98
H-42A	#2	0.28	0.18	0.1233	0.0074	0.0161	0.0007	116.1	6.9	108.0	4.7	93
H-42A	#3	0.24	0.15	0.1126	0.0048	0.0157	0.0005	106.4	4.6	103.4	3.3	97
H-42A	#4	0.14	0.09	0.1131	0.0077	0.0170	0.0007	119.1	6.1	112.0	5.0	94
H-42A	#5	0.24	0.14	0.1221	0.0038	0.0179	0.0006	126.2	6.8	118.1	3.9	94
H-42A	#6	0.29	0.16	0.1584	0.0108	0.0229	0.0011	149.6	9.6	148.1	7.2	99
H-42A	#7	0.39	0.22	0.1163	0.0040	0.0170	0.0005	111.9	4.1	111.7	3.4	100
H-42A	#8	0.26	0.15	0.1256	0.0051	0.0180	0.0003	127.2	4.9	118.0	2.3	93
H-42A	#9	1.00	0.49	10.2960	0.6075	0.4382	0.0149	2466.5	35.8	2403.5	70.6	97
H-42A	#10	0.24	0.14	0.1124	0.0055	0.0166	0.0005	113.0	4.8	109.4	3.7	97
H-42A	#11	0.25	0.14	0.1154	0.0033	0.0171	0.0006	113.0	5.3	112.5	3.9	100
H-42A	#12	0.38	0.22	0.1192	0.0061	0.0170	0.0005	117.1	4.4	112.7	3.2	96
H-42A	#13	0.25	0.18	0.1657	0.0123	0.0227	0.0012	155.3	9.4	145.0	7.9	93
H-42A	#14	0.40	0.22	0.3260	0.0173	0.0443	0.0019	285.2	12.5	285.5	11.7	100
H-42A	#15	0.98	0.55	0.2435	0.0139	0.0341	0.0013	228.8	10.1	226.5	8.5	99
H-42A	#16	0.55	0.39	0.1817	0.0124	0.0243	0.0009	167.0	8.0	152.4	5.4	91
H-42A	#17	0.37	0.21	0.1169	0.0055	0.0170	0.0008	116.0	6.0	114.2	5.3	98
H-42A	#18	0.25	0.16	0.1213	0.0065	0.0151	0.0005	113.1	4.7	99.1	3.4	88
H-42A	#19	0.09	0.05	0.1173	0.0041	0.0171	0.0005	112.3	3.9	112.2	3.7	100
H-42A	#20	0.47	0.26	0.1200	0.0067	0.0174	0.0006	118.3	5.1	114.5	3.9	97
H-42A	#21	0.28	0.16	0.1197	0.0038	0.0170	0.0005	114.1	3.7	111.5	3.1	98
H-42A	#22	0.33	0.19	0.1221	0.0060	0.0173	0.0005	117.5	4.8	114.1	3.4	97
H-42A	#23	0.26	0.15	0.1216	0.0039	0.0173	0.0003	115.0	3.0	113.6	2.0	99
H-42A	#24	0.25	0.14	0.1222	0.0072	0.0172	0.0005	115.6	5.1	111.3	3.5	96
H-42A	#25	0.21	0.12	0.1274	0.0080	0.0172	0.0006	127.0	8.0	113.2	4.0	89
H-42A	#26	0.32	0.18	0.0572	0.0029	0.0085	0.0003	57.2	3.2	55.8	2.3	98
H-42A	#27	0.15	0.09	0.1161	0.0050	0.0170	0.0006	111.9	4.4	111.4	3.9	100
H-42A	#28	0.25	0.14	0.1170	0.0037	0.0166	0.0005	112.1	4.4	108.9	3.5	97
H-42A	#29	0.24	0.14	0.1171	0.0050	0.0167	0.0005	114.3	4.3	109.9	3.4	96
H-42A	#30	0.15	0.11	0.1486	0.0088	0.0200	0.0010	138.6	7.3	131.1	6.6	95
H-42A	#31	0.05	0.03	0.3181	0.0690	0.0359	0.0048	307.9	39.0	239.8	31.6	78
H-42A	#32	0.25	0.14	0.1223	0.0050	0.0175	0.0005	115.0	4.6	115.2	3.5	100
H-42A	#33	0.24	0.12	6.8855	0.2823	0.3693	0.0126	2099.5	34.3	2093.8	61.1	100
H-42A	#34	0.53	0.31	0.1167	0.0058	0.0172	0.0006	119.3	6.0	113.5	3.7	95

Table A.35: Zrn U-Pb age dataset

Zircon U-Pb data

Sample	Spot #	Th/U[a]	$^{208}Pb/^{206}Pb$	Ratios				Ages (Ma)				Cc[c]
				$^{207}Pb/^{235}U$[a]	2 σ[b]	$^{206}Pb/^{238}U$[a]	2 σ[b]	$^{207}Pb/^{235}U$	2 σ	$^{206}Pb/^{238}U$	2 σ	%
H-42A	#35	0.27	0.16	0.1190	0.0044	0.0172	0.0006	114.5	4.1	113.3	3.6	99
H-42A	#36	0.38	0.20	2.0637	0.0702	0.1892	0.0062	1137.6	24.9	1144.5	34.7	101
H-42A	#37	0.28	0.16	0.1762	0.0058	0.0240	0.0008	164.5	5.8	157.2	5.1	96
H-42A	#38	0.12	0.06	5.5485	0.1554	0.3381	0.0101	1902.8	30.5	1920.9	50.0	101
H-42A	#39	0.32	0.19	0.0643	0.0044	0.0086	0.0003	62.3	3.6	57.6	1.8	92
H-42A	#40	0.07	0.04	0.1216	0.0044	0.0177	0.0007	117.0	5.3	116.5	4.8	100
H-42A	#41	0.08	0.05	0.1229	0.0059	0.0179	0.0006	118.3	4.6	117.2	3.8	99
H-42A	#42	0.61	0.35	0.1563	0.0058	0.0233	0.0008	151.2	6.5	152.2	5.0	101
H-42A	#43	0.26	0.15	0.1201	0.0055	0.0173	0.0007	114.0	5.3	112.3	4.3	99
H-42A	#44	0.83	0.47	0.1064	0.0051	0.0155	0.0006	107.0	5.2	105.2	4.1	98
H-42A	#45	0.08	0.05	0.1148	0.0040	0.0172	0.0007	110.3	4.3	113.5	4.3	103
H-42A	#46	0.11	0.06	0.1207	0.0040	0.0174	0.0005	115.6	4.0	114.5	3.4	99
H-42A	#47	0.42	0.25	0.1188	0.0045	0.0173	0.0006	115.4	4.6	113.5	3.8	98
H-42A	#48	0.31	0.18	0.1150	0.0072	0.0165	0.0006	113.4	6.3	109.9	4.3	97
H-42A	#49	0.31	0.18	0.1143	0.0057	0.0169	0.0005	112.4	4.6	110.9	3.3	99
H-42A	#50	0.23	0.16	0.2761	0.0080	0.0322	0.0010	247.4	10.4	203.9	6.0	82
H-42A	#51	0.29	0.16	0.1184	0.0051	0.0171	0.0005	114.1	4.3	111.8	3.3	98
H-42A	#52	0.27	0.15	0.1185	0.0062	0.0167	0.0007	113.5	7.2	109.2	4.9	96
H-42A	#53	0.31	0.17	0.1969	0.0093	0.0268	0.0008	182.9	7.1	175.2	5.4	96
H-42A	#54	0.38	0.22	0.1954	0.0088	0.0289	0.0007	188.4	6.7	187.5	4.4	100
H-42A	#55	0.26	0.14	0.6344	0.0197	0.0784	0.0020	501.7	11.9	499.6	12.0	100
H-42A	#56	0.33	0.18	2.0012	0.0861	0.1777	0.0069	1203.1	30.0	1223.3	43.6	102
H-42A	#57	0.27	0.16	0.1170	0.0060	0.0167	0.0007	126.4	6.2	123.9	5.2	98
H-42A	#58	0.30	0.18	0.1151	0.0055	0.0160	0.0007	123.8	6.2	118.1	5.5	95
H-42A	#59	0.34	0.22	0.5353	0.0182	0.0656	0.0024	475.6	14.9	472.7	16.4	99
H-42A	#60	0.26	0.16	0.1143	0.0082	0.0165	0.0006	126.2	5.1	124.7	4.2	99
H-42A	#61	0.30	0.18	0.1184	0.0054	0.0167	0.0006	123.9	5.3	122.6	4.0	99
H-42A	#62	0.26	0.16	0.1282	0.0090	0.0165	0.0007	136.0	7.5	127.1	5.7	93
H-42A	#63	0.24	0.14	0.1170	0.0073	0.0168	0.0008	124.5	6.6	125.2	6.0	101
H-42A	#64	0.26	0.16	0.1228	0.0056	0.0173	0.0007	131.4	5.4	128.5	4.8	98
H-42A	#65	0.52	0.31	0.0613	0.0035	0.0087	0.0004	66.4	3.2	65.3	2.9	98
H-42A	#66	0.25	0.15	0.1082	0.0057	0.0158	0.0009	118.5	7.1	117.2	6.7	99
H-42A	#67	0.45	0.29	0.1173	0.0062	0.0164	0.0006	128.3	5.8	122.3	4.6	95
H-42A	#68	0.26	0.16	0.1133	0.0076	0.0160	0.0007	126.1	5.7	121.3	5.2	96
H-42A	#69	0.24	0.15	0.1108	0.0053	0.0163	0.0008	121.2	6.4	121.1	5.6	100
H-42A	#70	0.24	0.15	0.1157	0.0054	0.0176	0.0003	141.1	4.9	131.0	2.2	93
H-42A	#71	0.16	0.10	0.1161	0.0049	0.0164	0.0006	124.4	5.2	122.0	4.7	98
H-42A	#72	0.26	0.16	0.1146	0.0055	0.0166	0.0007	127.2	5.8	123.4	5.0	97
H-42A	#73	0.23	0.14	0.1086	0.0046	0.0163	0.0007	123.7	6.7	121.0	4.8	98
H-42A	#74	0.15	0.08	0.3664	0.0136	0.0468	0.0016	361.0	11.6	342.3	11.7	95
H-42A	#75	0.15	0.05	1.8400	0.0699	0.1194	0.0035	1146.9	25.8	842.1	23.7	73
H-42A	#76	0.25	0.15	0.1157	0.0052	0.0162	0.0007	123.1	5.5	121.1	5.2	98
H-42A	#77	0.23	0.15	0.1241	0.0056	0.0175	0.0005	139.0	5.5	130.6	3.7	94
H-42A	#78	0.25	0.15	0.1156	0.0083	0.0163	0.0007	126.4	6.8	121.7	5.5	96
H-42A	#79	0.22	0.78	0.2107	0.0084	0.0252	0.0006	208.2	6.2	187.1	4.4	90
H-42A	#80	0.12	0.08	0.3932	0.0185	0.0378	0.0009	383.3	15.4	279.3	7.1	73
H-42A	#81	0.38	0.22	1.1793	0.0672	0.1235	0.0051	848.2	27.4	869.0	34.2	102
H-42A	#82	0.26	0.16	0.1130	0.0058	0.0159	0.0007	123.7	6.0	118.6	5.4	96
H-42A	#83	0.41	0.29	5.6251	0.2419	0.2486	0.0087	2036.6	35.8	1633.6	52.2	80
H-42A	#84	0.25	0.18	0.1239	0.0084	0.0158	0.0007	138.1	9.3	119.2	5.3	86
H-42A	#85	0.32	0.20	0.2424	0.0097	0.0327	0.0011	246.4	10.1	242.0	8.6	98
H-42A	#86	0.30	0.43	0.4956	0.1145	0.0188	0.0014	521.5	89.9	211.2	16.0	40
H-42A	#87	0.25	0.16	0.1248	0.0055	0.0176	0.0007	135.0	6.0	131.8	5.6	98
H-42A	#88	0.14	0.08	0.5020	0.0241	0.0637	0.0026	456.5	17.4	456.2	18.5	100
H-42A	#89	0.18	0.12	0.4425	0.0239	0.0562	0.0026	422.5	18.1	418.4	19.1	99
H-42A	#90	0.29	0.18	0.1071	0.0050	0.0154	0.0007	117.7	5.8	117.7	5.4	100
H-42A	#91	0.37	0.23	0.1108	0.0061	0.0155	0.0008	121.4	7.0	117.9	5.7	97
H-42A	#92	0.33	0.21	0.1112	0.0049	0.0157	0.0006	120.8	5.1	117.2	4.8	97
H-42A	#93	0.10	0.06	0.1823	0.0082	0.0223	0.0008	195.3	8.0	165.8	6.1	85
H-42A	#94	0.67	0.31	0.1420	0.0048	0.0191	0.0004	162.8	6.6	145.9	3.3	90
H-42A	#95	0.32	0.20	0.1063	0.0058	0.0149	0.0006	115.9	5.8	111.7	4.9	96
H-42A	#96	0.55	0.33	0.1093	0.0049	0.0160	0.0007	121.0	5.9	119.7	5.5	99

Table A.36: Zrn U-Pb age dataset

Zircon U-Pb data

Sample	Spot #	Th/U[a]	$^{208}Pb/^{206}Pb$	Ratios				Ages (Ma)				Cc[c]
				$^{207}Pb/^{235}U$[a]	2 σ[b]	$^{206}Pb/^{238}U$[a]	2 σ[b]	$^{207}Pb/^{235}U$	2 σ	$^{206}Pb/^{238}U$	2 σ	%
H-42A	#97	0.26	0.18	0.1093	0.0077	0.0154	0.0007	128.0	9.9	117.4	5.5	92
H-42A	#98	0.24	0.15	0.1076	0.0059	0.0159	0.0006	117.3	5.6	119.1	4.7	102
H-42A	#99	0.24	0.15	0.1095	0.0045	0.0157	0.0007	118.2	5.5	117.2	5.2	99
H-42A	#100	0.27	0.16	0.1084	0.0046	0.0159	0.0006	120.4	4.8	120.2	4.5	100
H-42A	#101	0.26	0.16	0.1077	0.0060	0.0157	0.0006	120.9	5.6	120.0	5.0	99
H-42A	#102	0.29	0.18	0.1125	0.0059	0.0153	0.0006	122.2	5.3	117.7	4.7	96
H-42A	#103	0.23	0.15	0.1099	0.0055	0.0155	0.0007	119.0	5.7	117.4	5.5	99
H-42A	#104	0.18	0.11	0.1533	0.0075	0.0214	0.0009	162.9	7.7	159.5	7.1	98
H-42A	#105	0.13	5.81	0.1108	0.0055	0.0156	0.0008	121.2	6.0	116.7	5.8	96
H-42A	#106	0.24	0.15	0.1061	0.0050	0.0156	0.0005	118.9	4.7	117.7	4.2	99
H-42A	#107	0.21	0.13	0.1133	0.0046	0.0161	0.0006	123.7	5.5	120.3	4.4	97
H-42A	#108	0.28	0.18	0.5954	0.0316	0.0711	0.0034	535.5	27.8	516.7	24.4	96
H-42A	#109	0.25	0.15	1.4977	0.0659	0.1458	0.0055	1028.6	28.2	1042.7	37.7	101
H-42A	#110	0.23	0.17	0.4966	0.0228	0.0525	0.0022	453.9	17.7	384.7	16.1	85
H-42A	#111	0.31	0.20	0.1138	0.0042	0.0162	0.0006	124.4	5.0	121.0	4.4	97
H-42A	#112	0.19	0.09	5.2354	0.2199	0.3049	0.0125	1936.3	40.6	1936.2	70.6	100
H-42A	#113	0.23	0.15	0.1111	0.0048	0.0159	0.0006	121.5	4.9	119.3	4.6	98
H-42A	#114	0.39	0.57	0.3429	0.0168	0.0444	0.0019	337.9	13.9	337.9	14.2	100
H-42A	#115	3.97	2.12	9.8701	1.1055	0.4159	0.0191	2528.8	49.6	2591.8	101.1	102
H-42A	#116	0.35	0.21	0.1127	0.0047	0.0160	0.0007	120.9	5.4	119.4	5.0	99
H-42A	#117	0.28	0.17	0.1008	0.0048	0.0146	0.0009	117.5	7.9	116.1	7.0	99
H-42A	#118	0.24	0.15	0.1126	0.0048	0.0157	0.0005	119.7	5.1	117.2	3.7	98
H-42A	#119	0.14	0.16	0.1230	0.0076	0.0177	0.0007	139.0	5.9	132.0	5.1	95
H-42A	#120	0.25	0.15	0.1227	0.0033	0.0180	0.0005	147.5	7.0	134.6	3.7	91
H-42A	#121	0.29	0.16	0.1584	0.0108	0.0229	0.0011	167.9	10.9	167.8	8.3	100
H-42A	#122	0.39	0.22	0.1163	0.0040	0.0170	0.0005	125.9	4.6	126.5	3.9	100
H-42A	#123	0.26	0.14	0.1288	0.0040	0.0180	0.0004	141.4	5.8	134.2	3.5	95
H-42A	#124	1.00	0.49	10.2960	0.6075	0.4382	0.0149	2582.6	36.2	2667.9	76.9	103
H-42A	#125	0.24	0.14	0.1124	0.0055	0.0166	0.0005	127.1	5.4	124.0	4.2	98
Bangoin North												
H-15B	#1	0.09	0.05	1.6344	0.0719	0.1678	0.0057	951.3	25.0	941.8	30.7	99
H-15B	#2	0.58	0.32	2.2909	0.2016	0.2085	0.0071	1207.4	61.9	1150.8	37.0	95
H-15B	#3	0.13	0.07	5.6255	0.2531	0.3547	0.0174	1860.1	46.2	1850.5	80.9	99
H-15B	#4	0.54	0.32	0.2184	0.0074	0.0301	0.0011	197.6	9.0	179.4	6.7	91
H-15B	#5	0.64	0.32	9.8615	0.4832	0.4603	0.0184	2353.4	42.1	2312.5	80.2	98
H-15B	#6	0.25	0.19	0.1434	0.0252	0.0179	0.0007	147.1	19.9	107.3	4.3	73
H-15B	#7	0.33	0.18	0.2506	0.0090	0.0362	0.0015	216.6	9.4	215.2	9.1	99
H-15B	#8	0.23	0.13	1.4974	0.1078	0.1568	0.0099	904.9	41.6	884.2	53.1	98
H-15B	#9	0.18	0.10	0.1265	0.0056	0.0186	0.0006	112.6	4.5	111.3	3.9	99
H-15B	#10	0.30	0.17	0.1847	0.0089	0.0261	0.0011	158.9	7.8	155.8	6.6	98
H-15B	#11	0.57	0.32	0.1329	0.0084	0.0195	0.0008	117.6	6.0	117.0	4.6	99
H-15B	#12	0.39	0.21	0.7581	0.0500	0.0952	0.0035	541.2	19.5	551.3	20.1	102
H-15B	#13	0.24	0.13	2.0536	0.1171	0.1959	0.0088	1089.8	34.7	1087.1	46.2	100
H-15B	#14	0.44	0.14	0.2915	0.0577	0.0376	0.0063	242.5	37.8	223.4	37.0	92
H-15B	#15	0.36	0.20	1.6134	0.1081	0.1704	0.0092	959.4	40.5	955.6	49.0	100
H-15B	#16	0.20	0.11	13.1693	0.7638	0.4990	0.0140	2630.4	32.4	2474.4	59.9	94
H-15B	#17	0.49	0.28	0.1240	0.0060	0.0193	0.0008	116.4	5.8	115.9	4.6	100
H-15B	#18	0.28	0.17	0.3773	0.0875	0.0306	0.0038	278.5	42.8	182.3	22.1	65
H-15B	#19	0.27	0.15	2.3923	0.1005	0.2181	0.0072	1190.9	27.0	1199.5	37.3	101
H-15B	#20	0.81	0.47	0.1428	0.0093	0.0214	0.0006	129.5	6.1	127.8	3.9	99
H-15B	#21	0.28	0.15	3.4667	0.1317	0.2690	0.0097	1459.2	33.0	1450.2	48.2	99
H-15B	#22	0.55	0.30	0.1249	0.0065	0.0186	0.0007	111.3	5.3	111.5	4.3	100
H-15B	#23	0.29	0.19	0.3628	0.0475	0.0473	0.0019	316.5	26.2	280.0	11.2	88
H-15B	#24	0.55	0.35	0.1466	0.0164	0.0204	0.0011	141.8	12.1	122.0	6.3	86
H-15B	#25	0.17	0.10	1.5957	0.0702	0.1670	0.0068	949.5	29.4	937.9	36.8	99
H-15B	#26	0.42	0.20	0.2979	0.0569	0.0287	0.0031	204.9	37.4	171.5	18.3	84
H-15B	#27	0.40	0.20	5.5463	0.2662	0.3511	0.0126	1862.1	37.4	1834.9	59.4	99
H-15B	#28	0.78	0.43	2.2881	0.1373	0.2098	0.0096	1149.6	35.0	1157.7	50.0	101
H-15B	#29	0.34	0.17	9.6554	0.8014	0.4322	0.0203	2344.8	53.5	2193.8	89.9	94
H-15B	#30	0.35	0.18	5.2109	0.2762	0.3359	0.0128	1811.8	37.9	1765.3	60.5	97

Table A.37: Zrn U-Pb age dataset

Zircon U-Pb data

Sample	Spot #	Th/U[a]	$^{208}Pb/^{206}Pb$	Ratios				Ages (Ma)				Cc[c]
				$^{207}Pb/^{235}U^{a}$	2 σ[b]	$^{206}Pb/^{238}U^{a}$	2 σ[b]	$^{207}Pb/^{235}U$	2 σ	$^{206}Pb/^{238}U$	2 σ	%
H-15B	#31	0.14	0.09	5.6038	0.2578	0.3286	0.0398	1963.2	167.7	1731.7	186.4	88
H-15B	#32	0.47	0.26	0.1416	0.0091	0.0216	0.0009	130.2	6.4	129.2	5.5	99
H-15B	#33	0.28	0.17	0.1441	0.0073	0.0202	0.0007	124.5	6.2	120.8	4.3	97
H-15B	#34	0.40	0.09	0.5070	0.0882	0.0507	0.0071	402.2	51.1	299.4	41.1	74
H-15B	#35	0.15	0.09	0.2803	0.0112	0.0390	0.0015	235.4	9.1	231.4	8.9	98
H-15B	#36	0.33	0.18	0.6543	0.0262	0.0852	0.0021	499.7	12.7	495.8	12.4	99
H-15B	#37	0.32	0.16	9.1655	0.4308	0.4301	0.0185	2295.4	44.6	2184.8	82.1	95
H-15B	#38	0.35	0.19	2.2393	0.0985	0.2092	0.0077	1148.4	29.3	1154.9	40.3	101
H-15B	#39	0.59	0.34	0.1329	0.0081	0.0204	0.0007	122.8	5.3	122.0	4.4	99
H-15B	#40	0.50	0.27	0.5698	0.0234	0.0733	0.0024	434.2	14.6	428.7	14.1	99
H-15B	#41	0.36	0.21	0.0551	0.0023	0.0083	0.0004	50.7	2.7	50.2	2.4	99
H-15B	#42	0.42	0.24	0.1268	0.0056	0.0189	0.0007	115.2	4.9	113.2	4.3	98
H-15B	#43	0.22	0.12	0.1895	0.0064	0.0279	0.0010	167.9	7.0	166.4	5.9	99
H-15B	#44	0.51	0.26	9.0990	0.5186	0.4508	0.0158	2319.0	37.1	2273.9	69.4	98
H-15B	#45	0.36	0.20	0.7293	0.0328	0.0910	0.0032	526.0	16.6	528.2	18.3	100
H-15B	#46	0.29	0.14	0.2107	0.0089	0.0302	0.0012	181.3	7.3	180.3	6.9	99
H-15B	#47	0.58	0.29	5.0348	0.2568	0.3325	0.0120	1787.0	43.8	1750.5	55.4	98
H-15B	#48	0.70	0.40	0.1418	0.0087	0.0202	0.0009	125.7	6.4	121.0	5.4	96
H-15B	#49	0.33	1.28	0.1304	1.7441	0.0194	0.0155	455.1	461.4	116.1	92.6	26
H-15B	#50	0.50	0.27	0.1480	0.0099	0.0216	0.0012	132.2	8.0	129.1	7.0	98
H-15B	#51	0.38	0.22	0.1299	0.0084	0.0191	0.0008	115.0	5.9	114.6	4.7	100
H-15B	#52	0.45	0.25	2.2080	0.1038	0.1999	0.0072	1127.7	29.0	1108.1	36.8	98
H-15B	#53	0.14	0.08	0.1304	0.0067	0.0190	0.0007	116.5	5.9	114.0	4.3	98
H-15B	#54	0.26	0.15	0.1314	0.0095	0.0185	0.0009	115.8	7.9	110.9	5.6	96
H-15B	#55	0.53	0.26	11.3330	0.5667	0.5092	0.0285	2504.3	56.4	2517.6	117.8	101
H-15B	#56	0.40	0.21	5.4968	0.3793	0.3558	0.0142	1865.7	40.9	1857.3	64.9	100
H-15B	#57	0.51	0.29	0.1319	0.0057	0.0195	0.0009	120.7	6.2	117.0	5.6	97
H-15B	#58	0.29	0.18	0.2660	0.0114	0.0384	0.0016	228.2	9.7	228.0	9.4	100
H-15B	#59	0.47	0.27	0.1303	0.0056	0.0190	0.0007	118.2	5.9	113.9	4.2	96
H-15B	#60	0.31	0.18	0.1199	0.0222	0.0184	0.0009	120.5	18.8	110.1	5.5	91
H-15B	#61	0.46	0.27	0.1483	0.0129	0.0194	0.0006	127.5	8.5	116.5	3.7	91
H-15B	#62	0.71	0.39	0.2748	0.0162	0.0392	0.0017	233.3	13.8	232.8	10.1	100
H-15B	#63	0.34	0.20	0.1247	0.0066	0.0185	0.0009	112.6	5.9	111.2	5.1	99
H-15B	#64	0.17	0.07	0.1336	0.0194	0.0198	0.0027	124.2	16.4	118.7	15.8	96
H-15B	#65	0.19	0.12	7.0970	0.5110	0.3526	0.0208	2000.4	62.2	1842.8	95.3	92
H-15B	#66	0.31	0.17	0.1249	0.0081	0.0184	0.0006	110.4	5.4	110.1	3.9	100
H-15B	#67	0.02	0.01	0.7905	0.0332	0.0976	0.0035	570.3	18.1	564.9	19.5	99
H-15B	#68	0.50	0.37	0.2457	0.0192	0.0355	0.0027	220.1	16.0	211.4	15.8	96
H-15B	#69	0.56	0.32	0.0575	0.0044	0.0084	0.0003	52.2	3.4	50.6	2.0	97
H-15B	#70	0.49	0.26	2.0063	0.0863	0.1948	0.0078	1102.0	30.7	1082.4	40.0	98
H-15B	#71	0.42	0.24	0.7314	0.0395	0.0889	0.0036	532.7	20.1	516.7	20.4	97
H-15B	#72	0.27	0.15	0.1180	0.0057	0.0180	0.0007	110.5	5.5	108.0	4.0	98
H-15B	#73	0.19	0.12	0.1331	0.0071	0.0183	0.0008	120.8	7.0	109.6	4.8	91
H-15B	#74	0.23	0.14	0.1102	0.0054	0.0157	0.0007	101.7	5.4	94.1	4.2	93
H-15B	#75	0.91	0.49	0.6708	0.0382	0.0840	0.0043	493.9	24.5	489.3	24.1	99
H-15B	#76	0.69	0.42	0.1474	0.0233	0.0193	0.0009	133.7	17.8	115.5	5.2	86
H-15B	#77	0.08	0.05	0.3814	0.0141	0.0520	0.0018	312.2	11.4	307.2	10.5	98
H-15B	#78	0.15	0.08	0.8200	0.0426	0.1001	0.0048	589.2	24.4	579.0	26.6	98
H-15B	#79	0.34	0.20	0.1296	0.0079	0.0185	0.0008	114.1	6.2	111.2	4.7	97
H-15B	#80	0.40	0.22	0.1386	0.0103	0.0193	0.0008	121.4	7.9	115.6	4.7	95
H-15B	#81	0.41	0.23	1.4032	0.0758	0.1528	0.0063	874.0	28.5	864.4	33.3	99
H-15B	#82	0.45	0.26	0.2620	0.0107	0.0368	0.0014	222.6	9.0	218.8	8.2	98
H-15B	#83	0.43	0.24	0.1212	0.0071	0.0185	0.0007	112.5	6.6	110.8	4.4	98
H-15B	#84	0.27	0.15	1.2716	0.0521	0.1384	0.0058	796.9	25.7	787.5	31.2	99
H-15B	#85	0.08	0.05	1.9238	0.1462	0.1749	0.0107	1004.4	51.0	980.2	55.7	98
H-15B	#86	0.36	0.19	8.9874	0.5213	0.4179	0.0221	2279.8	53.1	2133.9	97.0	94
H-15B	#87	0.29	0.19	1.4207	0.0810	0.1422	0.0078	848.6	35.1	807.9	41.9	95
H-15B	#88	0.42	0.23	0.2784	0.0125	0.0385	0.0020	236.8	11.9	228.7	11.5	97
H-15B	#89	0.36	1.61	0.3112	1.0087	0.0209	0.0067	678.7	326.5	125.0	39.7	18
H-15B	#90	0.11	0.06	10.3278	0.4131	0.4551	0.0250	2433.3	65.8	2293.5	107.0	94
H-15B	#91	0.09	0.05	3.1090	0.1213	0.2334	0.0098	1397.0	37.9	1277.7	48.9	91
H-15B	#92	0.34	0.47	0.1200	0.2067	0.0180	0.0018	294.3	104.0	108.1	10.5	37

Table A.38: Zrn U-Pb age dataset

Zircon U-Pb data

Sample	Spot #	Th/U[a]	$^{208}Pb/^{206}Pb$	Ratios				Ages (Ma)				Cc[c]
				$^{207}Pb/^{235}U^a$	2 σ[b]	$^{206}Pb/^{238}U^a$	2 σ[b]	$^{207}Pb/^{235}U$	2 σ	$^{206}Pb/^{238}U$	2 σ	%
H-15B	#93	0.54	0.31	0.1258	0.0065	0.0186	0.0009	113.0	6.0	111.3	5.2	98
H-15B	#94	0.66	0.36	1.5283	0.0825	0.1542	0.0069	902.8	31.6	871.6	36.8	97
H-15B	#95	0.41	0.21	12.4459	0.8090	0.5089	0.0285	2580.4	57.7	2518.1	117.8	98
H-15B	#96	0.45	0.33	0.1282	0.0064	0.0144	0.0009	115.3	10.0	86.6	5.4	75
H-15B	#97	0.12	0.07	0.5444	0.0261	0.0703	0.0028	423.6	16.4	412.2	16.0	97
H-15B	#98	0.63	0.37	0.1450	0.0093	0.0211	0.0009	131.0	6.7	126.4	5.5	96
H-15B	#99	0.51	0.29	0.7217	0.0447	0.0892	0.0036	531.7	20.5	518.7	20.0	98
H-15B	#100	0.32	0.16	1.5149	0.2045	0.1311	0.0149	896.5	72.8	748.4	81.1	83
H-15B	#101	0.79	0.43	1.6977	0.0781	0.1721	0.0079	966.0	32.9	965.8	41.4	100
H-15B	#102	0.05	0.03	2.8100	0.1377	0.1875	0.0058	1306.6	27.6	1045.4	30.0	80
H-15B	#103	0.30	0.17	0.1715	0.0166	0.0209	0.0012	137.2	11.9	125.4	7.3	91
H-15B	#104	0.27	0.14	5.0609	0.2075	0.3358	0.0118	1788.5	33.3	1767.3	54.3	99
H-15B	#105	0.50	0.28	0.1305	0.0083	0.0187	0.0008	116.3	6.3	112.1	4.8	96
H-15B	#106	0.25	0.14	0.1230	0.0065	0.0180	0.0008	108.9	5.3	108.1	4.9	99
H-15B	#107	0.53	0.30	0.1223	0.0053	0.0193	0.0008	114.2	6.2	115.6	4.5	101
H-15B	#108	0.52	0.29	0.1490	0.0080	0.0219	0.0008	133.3	5.5	131.5	4.6	99
H-15B	#109	0.35	0.19	0.1408	0.0072	0.0208	0.0009	125.7	6.5	124.8	5.6	99
H-15B	#110	0.22	0.11	4.9785	0.3385	0.3199	0.0138	1778.7	41.1	1693.7	64.4	95
H-15B	#111	0.16	0.04	0.4533	0.1092	0.0385	0.0066	366.5	66.4	229.1	38.8	63
H-15B	#112	0.17	0.10	1.4307	0.0944	0.1487	0.0089	861.2	37.9	842.7	47.6	98
H-15B	#113	0.31	0.16	4.4035	0.1761	0.3104	0.0124	1686.2	37.7	1649.2	58.5	98
H-15B	#114	0.46	0.28	0.1316	0.0072	0.0188	0.0011	122.0	8.8	112.6	6.6	92
H-15B	#115	0.25	0.14	0.1338	0.0047	0.0200	0.0007	120.1	5.1	120.0	4.4	100
H-37A	#1	0.62	0.36	0.9717	0.0360	0.1120	0.0039	663.3	19.7	645.2	21.5	97
H-37A	#2	0.26	0.15	0.2313	0.0093	0.0337	0.0012	209.2	8.5	201.1	6.9	96
H-37A	#3	0.65	0.37	0.1327	0.0062	0.0182	0.0011	115.3	7.6	109.5	6.7	95
H-37A	#4	0.38	0.21	0.1263	0.0061	0.0187	0.0009	113.2	5.9	112.3	5.2	99
H-37A	#5	0.40	0.22	0.1260	0.0050	0.0191	0.0007	114.5	5.1	114.7	4.3	100
H-37A	#6	0.12	0.08	1.5804	0.0537	0.1564	0.0055	926.3	23.4	883.6	29.0	95
H-37A	#7	0.48	0.38	0.1305	0.0103	0.0180	0.0014	123.2	14.3	108.4	8.4	88
H-37A	#8	0.52	0.30	0.1279	0.0047	0.0187	0.0008	119.9	6.0	112.0	4.7	93
H-37A	#9	0.46	0.25	0.2814	0.0180	0.0413	0.0015	245.6	9.9	245.6	8.7	100
H-37A	#10	0.07	0.04	0.1248	0.0049	0.0188	0.0005	113.9	3.7	113.1	3.0	99
H-37A	#11	0.60	0.34	0.1626	0.0073	0.0245	0.0008	146.1	6.0	146.9	4.9	101
H-37A	#12	0.79	0.43	0.0446	0.0053	0.0063	0.0004	40.0	6.0	38.0	2.3	95
H-37A	#13	0.36	0.21	0.1384	0.0083	0.0196	0.0006	123.4	6.5	117.5	3.8	95
H-37A	#14	0.37	0.26	1.1924	0.1646	0.0949	0.0121	706.1	80.4	550.8	67.4	78
H-37A	#15	0.52	0.34	0.1365	0.0550	0.0194	0.0008	159.3	37.9	116.2	4.8	73
H-37A	#16	0.42	0.26	0.1649	0.0176	0.0196	0.0009	142.4	13.6	117.4	5.2	82
H-37A	#17	0.34	0.19	0.1195	0.0071	0.0177	0.0007	108.2	5.1	106.5	4.0	98
H-37A	#18	0.48	0.31	0.0405	0.0017	0.0061	0.0003	37.8	2.2	37.0	1.9	98
H-37A	#19	0.29	0.16	0.1261	0.0045	0.0184	0.0006	114.0	4.0	110.7	3.5	97
H-37A	#20	0.48	0.26	0.6836	0.0273	0.0860	0.0023	504.6	13.2	500.9	13.0	99
H-37A	#21	0.34	0.19	0.1264	0.0052	0.0190	0.0007	115.9	4.9	114.3	4.2	99
H-37A	#22	0.18	0.10	1.5325	0.0582	0.1589	0.0043	907.8	19.4	897.4	22.7	99
H-37A	#23	0.68	0.38	0.1259	0.0062	0.0189	0.0008	117.0	6.2	113.6	4.6	97
H-37A	#24	0.41	0.21	5.3626	0.2306	0.3422	0.0147	1841.9	39.9	1798.0	67.8	98
H-37A	#25	0.72	0.41	0.1273	0.0048	0.0186	0.0009	115.2	6.0	111.4	5.1	97
H-37A	#26	0.10	0.06	0.1253	0.0044	0.0188	0.0006	114.5	4.2	112.7	3.7	98
H-37A	#27	0.28	0.16	0.1363	0.0087	0.0194	0.0011	119.1	8.1	116.6	6.4	98
H-37A	#28	0.44	0.23	5.6575	0.1980	0.3495	0.0094	1855.6	27.6	1831.5	43.2	99
H-37A	#29	0.28	0.17	0.1342	0.0062	0.0192	0.0011	120.0	7.3	115.3	6.7	96
H-37A	#30	0.29	0.16	0.1286	0.0067	0.0194	0.0006	116.8	5.0	116.6	3.7	100
H-37A	#31	0.49	0.27	0.1242	0.0053	0.0181	0.0007	109.3	4.6	108.8	3.9	100
H-37A	#32	0.29	0.15	0.1717	0.0117	0.0252	0.0018	153.0	11.0	150.8	10.9	99
H-37A	#33	0.31	0.17	0.1260	0.0065	0.0182	0.0007	111.7	4.6	109.4	4.0	98
H-37A	#34	0.38	0.21	0.1299	0.0106	0.0186	0.0008	116.7	7.3	111.9	4.5	96
H-37A	#35	0.44	0.24	0.1189	0.0062	0.0177	0.0005	107.1	4.2	106.4	3.3	99
H-37A	#36	0.12	0.07	0.1206	0.0048	0.0178	0.0005	108.9	3.8	107.2	3.2	98
H-37A	#37	0.26	0.14	0.1174	0.0063	0.0181	0.0007	109.2	5.7	108.5	4.2	99
H-37A	#38	0.19	0.11	0.4507	0.0185	0.0603	0.0021	361.4	12.5	355.6	12.1	98

Table A.39: Zrn U-Pb age dataset

Zircon U-Pb data

Sample	Spot #	Th/U[a]	$^{208}Pb/^{206}Pb$	Ratios				Ages (Ma)				Cc[c]
				$^{207}Pb/^{235}U$[a]	2 σ[b]	$^{206}Pb/^{238}U$[a]	2 σ[b]	$^{207}Pb/^{235}U$	2 σ	$^{206}Pb/^{238}U$	2 σ	%
H-37A	#39	0.76	0.43	0.1544	0.0068	0.0230	0.0010	141.0	6.9	137.8	5.7	98
H-37A	#40	0.36	0.20	0.1205	0.0064	0.0177	0.0007	109.8	4.9	106.2	4.1	97
H-37A	#41	0.06	0.04	0.1416	0.0055	0.0209	0.0007	128.4	5.1	125.5	4.1	98
H-37A	#42	0.44	0.36	0.2263	0.0763	0.0198	0.0010	234.9	47.6	119.1	5.7	51
H-37A	#43	0.51	0.29	0.1283	0.0059	0.0190	0.0008	116.7	5.4	114.0	4.9	98
H-37A	#44	0.42	0.24	0.1120	0.0080	0.0176	0.0007	108.5	5.9	105.8	4.4	98
H-37A	#45	0.38	0.21	0.1234	0.0086	0.0193	0.0006	116.1	5.9	116.0	3.8	100
H-37A	#46	0.33	0.18	0.1360	0.0063	0.0190	0.0008	119.2	5.6	114.2	4.9	96
H-37A	#47	0.22	0.13	0.4084	0.0172	0.0542	0.0020	327.6	11.8	320.5	11.6	98
H-37A	#48	0.65	0.34	0.7305	0.0321	0.0908	0.0030	533.2	16.7	528.3	17.3	99
H-37A	#49	0.40	0.22	0.1238	0.0059	0.0181	0.0007	113.1	5.4	109.0	4.1	96
H-37A	#50	0.57	0.32	0.1177	0.0066	0.0169	0.0006	103.4	4.7	101.9	3.6	99
H-37A	#51	0.16	0.09	0.2943	0.0121	0.0419	0.0015	253.6	9.7	249.1	8.8	98
H-37A	#52	0.37	0.21	0.1325	0.0057	0.0196	0.0006	119.3	4.4	117.8	3.9	99
H-37A	#53	0.17	0.09	5.6875	0.2218	0.3595	0.0119	1874.0	33.9	1877.7	55.6	100
H-37A	#54	0.20	0.11	0.1245	0.0052	0.0182	0.0005	112.7	4.5	109.6	3.4	97
H-37A	#55	0.55	0.30	0.1269	0.0060	0.0192	0.0008	117.3	5.8	115.4	5.0	98
H-37A	#56	0.17	0.09	0.1237	0.0066	0.0181	0.0006	113.3	5.6	109.1	3.9	96
H-37A	#57	0.27	0.15	0.1252	0.0086	0.0186	0.0008	112.4	7.2	111.6	5.0	99
H-37A	#58	0.02	0.04	0.3985	0.0143	0.0507	0.0036	379.1	43.0	300.0	21.1	79
H-37A	#59	0.38	0.21	0.1313	0.0064	0.0194	0.0009	121.2	5.8	116.6	5.1	96
H-37A	#60	0.31	0.17	0.1231	0.0068	0.0180	0.0009	112.4	5.9	107.9	5.4	96
H-37A	#61	0.60	0.33	0.1231	0.0065	0.0184	0.0007	112.0	5.3	110.3	4.3	98
H-37A	#62	0.30	0.14	13.0833	0.4841	0.5314	0.0197	2639.7	39.3	2613.3	80.0	99
H-37A	#63	0.30	0.17	0.1219	0.0063	0.0181	0.0005	110.0	4.6	108.8	3.3	99
H-37A	#64	0.26	0.14	0.1291	0.0056	0.0187	0.0007	116.6	4.9	112.6	4.4	97
H-37A	#65	0.38	0.21	0.1307	0.0042	0.0190	0.0007	116.9	5.0	114.1	4.1	98
H-37A	#66	0.23	0.13	0.1143	0.0088	0.0181	0.0008	109.0	5.4	108.9	5.0	100
H-37A	#67	0.34	0.18	0.2786	0.0134	0.0403	0.0015	243.3	9.3	239.9	9.0	99
H-37A	#68	0.08	0.04	0.1224	0.0040	0.0183	0.0006	110.6	4.0	109.8	3.7	99
H-37A	#69	0.43	0.21	9.5898	0.2877	0.4443	0.0133	2341.6	31.6	2251.2	59.2	96
H-37A	#70	0.34	0.19	0.1215	0.0051	0.0179	0.0007	108.2	4.8	107.4	4.3	99
H-37A	#71	0.37	0.21	0.1274	0.0051	0.0192	0.0007	116.7	5.1	115.5	4.2	99
H-37A	#72	0.44	0.24	0.1308	0.0068	0.0194	0.0007	119.7	5.2	116.3	4.3	97
H-37A	#73	0.23	0.13	0.1162	0.0044	0.0173	0.0006	105.3	4.0	104.0	3.6	99
H-37A	#74	0.27	0.14	2.8944	0.1013	0.2338	0.0063	1331.0	24.0	1281.6	32.6	96
H-37A	#75	0.15	0.08	0.1269	0.0093	0.0185	0.0007	118.8	6.9	111.3	4.1	94
H-37A	#76	0.37	0.21	0.1231	0.0062	0.0186	0.0007	111.3	5.1	111.6	4.2	100
H-37A	#77	0.31	0.17	0.1197	0.0072	0.0174	0.0007	106.6	5.1	104.7	4.4	98
H-37A	#78	0.30	0.15	4.5769	0.2243	0.3166	0.0108	1708.3	31.9	1680.8	52.0	98
H-37A	#79	0.41	0.24	2.7447	0.0906	0.2116	0.0063	1295.4	29.0	1170.5	33.3	90
H-37A	#80	0.56	0.28	9.8559	0.6603	0.4376	0.0254	2340.6	57.3	2223.0	110.0	95
H-37A	#81	0.33	0.18	0.1225	0.0074	0.0181	0.0008	110.8	6.4	109.1	4.9	98
H-37A	#82	0.43	0.25	0.1222	0.0046	0.0180	0.0006	110.7	4.3	108.2	3.8	98
H-37A	#83	0.26	0.13	5.1603	0.3561	0.3363	0.0185	1775.8	49.9	1772.3	85.8	100
H-37A	#84	0.23	0.14	0.1557	0.0223	0.0214	0.0009	145.6	16.0	128.7	5.6	88
H-37A	#85	0.56	0.32	0.1238	0.0131	0.0186	0.0007	122.9	12.7	112.0	4.4	91
H-37A	#86	0.34	0.20	0.1301	0.0072	0.0193	0.0007	122.3	6.0	115.7	4.4	95
H-37A	#87	0.42	0.24	0.1934	0.0095	0.0271	0.0010	166.2	6.8	162.0	6.1	97
H-37A	#88	0.28	0.16	0.1225	0.0070	0.0176	0.0007	113.1	5.5	105.7	4.3	93
H-37A	#89	0.45	0.25	0.1288	0.0085	0.0192	0.0009	120.8	7.9	115.3	5.4	95
H-37A	#90	0.21	0.11	0.1173	0.0040	0.0180	0.0006	108.8	4.2	108.3	3.4	100
H-37A	#91	0.33	0.24	0.8019	0.1540	0.0897	0.0114	590.9	62.4	522.7	64.1	88
H-37A	#92	0.35	0.20	2.1570	0.4336	0.1488	0.0274	1121.7	146.6	845.0	147.4	75
H-37A	#93	0.56	0.31	0.1247	0.0080	0.0180	0.0006	111.5	5.8	108.2	3.9	97
H-37A	#94	0.40	0.22	0.1232	0.0078	0.0182	0.0008	111.8	5.9	109.3	4.8	98
H-37A	#95	0.52	0.29	0.1337	0.0074	0.0194	0.0008	119.6	5.5	116.6	4.9	97
H-37A	#96	0.19	0.10	1.6188	0.0583	0.1675	0.0052	956.4	23.8	943.5	28.1	99
H-37A	#97	0.24	0.13	0.3208	0.0135	0.0444	0.0015	268.4	10.0	264.0	9.1	98
H-37A	#98	0.38	0.21	0.1242	0.0075	0.0189	0.0008	116.4	5.7	113.9	4.7	98
H-37A	#99	0.38	0.20	0.1769	0.0069	0.0258	0.0007	155.7	5.1	154.7	4.1	99
H-37A	#100	0.32	0.18	0.1286	0.0100	0.0183	0.0006	118.4	6.9	109.9	3.5	93

Table A.40: Zrn U-Pb age dataset

Zircon U-Pb data

Sample	Spot #	Th/U[a]	$^{208}Pb/^{206}Pb$	Ratios				Ages (Ma)				Cc[c]
				$^{207}Pb/^{235}U$[a]	2 σ[b]	$^{206}Pb/^{238}U$[a]	2 σ[b]	$^{207}Pb/^{235}U$	2 σ	$^{206}Pb/^{238}U$	2 σ	%
H-37A	#101	0.55	0.30	0.1162	0.0045	0.0174	0.0007	108.0	4.7	104.5	4.0	97
H-37A	#102	0.40	0.22	0.1640	0.0057	0.0241	0.0008	148.0	5.9	144.7	5.2	98
H-37A	#103	0.33	0.18	0.1182	0.0065	0.0181	0.0007	109.0	5.1	109.1	4.0	100
H-37A	#104	0.12	0.07	0.5439	0.0343	0.0701	0.0022	421.6	13.2	411.9	13.2	98
H-37A	#105	0.12	0.07	0.1236	0.0040	0.0185	0.0006	113.2	4.5	111.0	3.6	98
H-37A	#106	0.05	0.03	0.1420	0.0053	0.0208	0.0007	126.2	4.6	124.7	4.2	99
H-37A	#107	0.39	0.25	0.1476	0.0335	0.0191	0.0007	154.0	28.5	115.0	4.2	75
H-37A	#108	0.25	0.14	0.1344	0.0083	0.0194	0.0008	117.9	7.5	116.6	5.1	99
H-37A	#109	0.31	0.16	0.1315	0.0100	0.0196	0.0010	117.4	7.9	117.8	6.0	100
H-37A	#110	0.43	0.24	0.1311	0.0064	0.0195	0.0007	119.2	5.2	117.1	4.2	98
H-37A	#111	0.34	0.19	0.1224	0.0045	0.0183	0.0005	111.8	4.4	110.3	3.4	99
H-37A	#112	0.52	0.28	0.6745	0.0277	0.0869	0.0036	508.4	20.2	506.8	20.5	100
H-37A	#113	0.45	0.25	0.1339	0.0058	0.0195	0.0007	120.5	5.2	117.3	4.5	97
H-37A	#114	0.35	0.20	0.1345	0.0108	0.0194	0.0009	122.5	7.8	116.6	5.2	95
H-39A	#1	0.02	0.01	0.8738	0.0253	0.1059	0.0031	613.4	15.3	617.4	17.7	101
H-39A	#2	0.34	0.18	0.0881	0.0044	0.0127	0.0005	81.3	4.5	77.7	2.9	96
H-39A	#3	0.13	0.07	0.0850	0.0042	0.0126	0.0005	79.5	4.0	77.1	2.8	97
H-39A	#4	0.57	0.30	0.0724	0.0041	0.0102	0.0002	69.6	4.1	62.1	1.4	89
H-39A	#5	0.76	0.38	0.1420	0.0070	0.0200	0.0007	128.7	6.9	123.6	4.4	96
H-39A	#6	0.38	0.19	0.1348	0.0065	0.0193	0.0008	122.4	6.5	117.2	5.2	96
H-39A	#7	0.44	0.23	0.1304	0.0082	0.0195	0.0011	119.6	8.5	119.4	6.4	100
H-39A	#8	0.55	0.27	0.1648	0.0074	0.0183	0.0008	150.7	10.1	132.8	5.5	88
H-39A	#9	0.18	0.09	0.1307	0.0061	0.0196	0.0009	120.5	6.4	119.8	5.3	99
H-39A	#10	0.88	0.44	0.1451	0.0086	0.0209	0.0009	132.0	7.5	127.0	5.2	96
H-39A	#11	0.40	0.19	0.2749	0.0179	0.0386	0.0024	241.3	16.0	233.1	14.0	97
H-39A	#12	0.20	0.06	0.6404	0.1428	0.0613	0.0118	511.8	83.8	402.1	75.7	79
H-39A	#13	0.45	0.25	0.1518	0.0115	0.0198	0.0010	136.5	9.8	122.3	6.2	90
H-39A	#14	0.90	0.46	0.1657	0.0056	0.0229	0.0006	142.3	5.9	134.8	3.6	95
H-39A	#15	0.50	0.26	0.1439	0.0052	0.0205	0.0005	132.7	5.4	124.8	3.3	94
H-39A	#16	0.09	0.19	0.3149	0.0309	0.0191	0.0008	252.3	22.4	117.0	5.0	46
H-39A	#17	0.24	0.13	0.2846	0.0077	0.0390	0.0015	252.0	10.8	235.7	8.8	94
H-39A	#18	0.51	0.27	0.1346	0.0044	0.0199	0.0012	128.2	8.7	121.0	7.1	94
H-39A	#19	0.59	0.32	0.1318	0.0066	0.0192	0.0008	119.5	6.1	117.2	4.6	98
H-39A	#20	0.45	0.25	0.0726	0.0051	0.0094	0.0007	63.6	8.0	57.9	4.2	91
H-39A	#21	0.29	0.15	0.1259	0.0042	0.0183	0.0006	116.2	4.6	112.5	3.5	97
H-39A	#22	0.45	0.23	0.1433	0.0089	0.0210	0.0009	131.0	7.9	127.9	5.7	98
H-39A	#23	0.42	0.19	11.4105	0.3423	0.4982	0.0169	2523.5	36.0	2532.7	71.6	100
H-39A	#24	0.03	0.02	0.2698	0.0043	0.0379	0.0007	238.4	5.1	229.0	4.3	96
H-39A	#25	0.36	0.17	9.6626	0.3962	0.4496	0.0184	2377.5	43.1	2326.5	80.6	98
H-39A	#26	0.19	0.08	6.6236	0.2186	0.4016	0.0092	2109.2	35.2	2094.1	43.1	99
H-39A	#27	0.30	0.15	1.4863	0.0193	0.1585	0.0024	907.7	12.7	907.4	13.6	100
H-39A	#28	0.37	0.19	0.2990	0.0078	0.0388	0.0011	249.1	10.7	238.9	6.8	96
H-39A	#29	0.88	0.44	0.7956	0.0366	0.0950	0.0036	573.7	23.0	562.0	20.5	98
H-39A	#30	0.35	0.15	13.2324	0.5822	0.5419	0.0217	2645.3	44.2	2659.6	87.8	101
H-39A	#31	0.34	0.16	4.1144	0.1769	0.2979	0.0137	1650.5	42.5	1673.2	68.2	101
H-39A	#32	0.87	0.43	1.6225	0.0730	0.1637	0.0074	963.6	32.2	961.9	40.3	100
H-39A	#33	0.68	0.34	0.1409	0.0059	0.0197	0.0006	133.8	5.0	122.5	3.8	92
H-39A	#34	0.73	0.41	0.3309	0.0139	0.0479	0.0034	318.0	27.4	289.0	20.1	91
H-39A	#35	0.80	0.40	0.1571	0.0057	0.0226	0.0005	151.9	6.1	140.6	3.2	93
H-39A	#36	0.32	0.16	0.2725	0.0074	0.0382	0.0012	235.6	7.8	226.8	6.9	96
H-39A	#37	0.09	0.05	2.9170	0.1138	0.1974	0.0075	1404.5	30.9	1134.7	39.7	81
H-39A	#38	0.57	0.30	0.1624	0.0242	0.0215	0.0015	159.9	17.3	141.4	9.5	88
H-39A	#39	0.75	0.43	0.4149	0.2659	0.0247	0.0057	502.8	166.8	190.3	43.3	38
H-39A	#40	0.32	0.15	0.2113	0.0137	0.0280	0.0014	190.4	9.8	171.7	8.6	90
H-39A	#41	0.44	0.22	0.1261	0.0053	0.0184	0.0006	116.4	4.8	112.8	3.9	97
H-39A	#42	0.40	0.21	0.1395	0.0085	0.0196	0.0007	126.0	8.0	120.5	4.5	96
H-39A	#43	0.76	0.38	0.2268	0.0098	0.0247	0.0010	168.0	10.3	150.8	6.0	90
H-39A	#44	0.43	0.23	0.3492	0.0119	0.0458	0.0016	308.0	18.8	277.0	9.5	90
H-39A	#45	0.54	0.26	4.2127	0.1685	0.3020	0.0109	1652.3	34.0	1659.8	52.9	100
H-39A	#46	0.30	0.13	31.6979	1.3313	0.7098	0.0220	3476.8	58.6	3343.4	81.4	96
H-39A	#47	0.51	0.24	1.3900	0.0417	0.1490	0.0046	841.7	22.0	837.6	24.4	100

Table A.41: Zrn U-Pb age dataset

Zircon U-Pb data

Sample	Spot #	Th/U[a]	^{208}Pb/^{206}Pb	Ratios				Ages (Ma)				Cc[c]
				^{207}Pb/^{235}U[a]	2 σ[b]	^{206}Pb/^{238}U[a]	2 σ[b]	^{207}Pb/^{235}U	2 σ	^{206}Pb/^{238}U	2 σ	%
H-39A	#48	0.18	0.08	5.7069	0.1769	0.3635	0.0109	1872.7	29.5	1883.2	49.2	101
H-39A	#49	1.32	0.65	0.6965	0.0251	0.0878	0.0033	509.9	18.6	508.1	18.6	100
H-39A	#50	0.40	0.20	1.3665	0.0506	0.1490	0.0046	837.2	22.5	838.5	24.4	100
H-39A	#51	0.22	0.10	10.6303	0.4040	0.4816	0.0169	2430.5	37.6	2390.8	70.3	98
H-39A	#52	0.27	0.13	0.1277	0.0061	0.0191	0.0007	113.8	5.5	113.8	4.2	100
H-39A	#53	0.06	0.03	4.2291	0.0930	0.2793	0.0073	1601.2	25.3	1459.9	34.1	91
H-39A	#54	0.12	0.06	0.7278	0.0109	0.0922	0.0021	555.7	12.1	553.4	12.2	100
H-39A	#55	0.42	0.19	10.1229	0.2126	0.4852	0.0107	2490.5	28.2	2461.6	45.2	99
H-39A	#56	0.38	0.18	2.3304	0.0466	0.2219	0.0047	1214.5	15.7	1230.6	23.6	101
H-39A	#57	0.44	0.20	3.2400	0.0713	0.2678	0.0080	1468.8	28.3	1486.2	39.9	101
H-39A	#58	0.12	0.05	2.0014	0.0741	0.1859	0.0072	1095.8	25.1	1091.2	39.3	100
H-39A	#59	0.10	0.04	6.6073	0.2709	0.3391	0.0376	2023.3	36.6	1814.5	178.0	90
H-39A	#60	0.94	0.45	1.7196	0.0533	0.1727	0.0048	989.1	19.8	987.6	25.7	100
H-39A	#61	0.50	0.26	0.1349	0.0074	0.0198	0.0008	126.3	6.6	121.6	5.1	96
H-39A	#62	0.32	0.16	5.2164	0.1617	0.3301	0.0106	1832.2	26.6	1801.1	50.5	98
H-39A	#63	0.51	0.27	0.1667	0.0067	0.0235	0.0004	153.6	5.7	142.1	2.2	93
H-39A	#64	0.59	0.31	0.1731	0.0043	0.0235	0.0005	151.3	3.5	138.9	3.0	92
H-39A	#65	0.35	0.18	0.1469	0.0031	0.0215	0.0003	135.8	2.8	133.1	2.1	98
H-39A	#66	0.61	0.49	0.7269	0.0574	0.0543	0.0031	563.9	34.8	342.3	19.0	61
H-39A	#67	0.38	0.21	0.1423	0.0080	0.0204	0.0010	129.9	6.9	124.6	6.3	96
H-39A	#68	0.69	0.38	0.1565	0.0069	0.0218	0.0008	145.7	6.0	134.6	5.2	92
H-39A	#69	0.76	0.40	0.1483	0.0062	0.0213	0.0008	137.5	5.4	131.9	5.1	96
H-39A	#70	0.87	0.45	0.1433	0.0069	0.0211	0.0008	135.0	6.1	129.4	5.0	96
H-39A	#71	0.47	0.23	0.1511	0.0038	0.0230	0.0004	150.5	3.5	140.3	2.4	93
H-39A	#72	0.32	0.18	0.1370	0.0086	0.0196	0.0010	127.2	7.6	120.0	6.1	94
H-39A	#73	0.48	0.26	0.1530	0.0060	0.0214	0.0007	139.1	5.1	131.1	4.2	94
H-39A	#74	0.46	0.27	0.1893	0.0199	0.0203	0.0010	211.7	20.3	131.9	6.3	62
H-39A	#75	0.63	0.33	0.1689	0.0059	0.0236	0.0005	152.5	5.0	144.5	3.4	95
H-39A	#76	0.49	0.25	0.1915	0.0048	0.0272	0.0007	174.6	4.2	169.0	4.2	97
H-39A	#77	0.18	0.09	0.1422	0.0065	0.0217	0.0008	128.2	5.6	129.8	4.6	101
H-39A	#78	0.57	0.29	0.1560	0.0045	0.0220	0.0006	143.8	4.0	138.7	3.8	96
H-39A	#79	0.33	0.18	0.1388	0.0039	0.0201	0.0005	127.7	3.5	124.1	3.1	97
H-39A	#80	0.16	0.08	1.2398	0.0360	0.1356	0.0030	795.5	16.7	792.1	17.2	100
H-39A	#81	0.76	0.39	0.1742	0.0085	0.0238	0.0005	161.9	7.4	146.9	3.2	91
H-39A	#82	0.37	0.19	0.1491	0.0036	0.0220	0.0005	138.4	3.2	135.0	2.9	98
H-39A	#83	0.41	0.21	0.1442	0.0049	0.0223	0.0004	133.3	4.4	134.0	2.3	101
H-39A	#84	0.39	0.20	0.1486	0.0037	0.0215	0.0005	135.4	3.3	131.6	3.1	97
H-39A	#85	0.62	0.31	0.1552	0.0029	0.0216	0.0002	140.8	2.6	134.5	1.6	96
H-39A	#86	0.23	0.12	0.2899	0.0061	0.0418	0.0010	251.4	4.9	253.5	6.0	101
H-39A	#87	0.84	0.40	2.3699	0.0616	0.2178	0.0052	1204.8	19.2	1224.0	27.9	102
H-39A	#88	0.58	0.31	0.2862	0.0112	0.0412	0.0019	246.5	8.6	249.8	11.3	101
H-39A	#89	0.24	0.12	0.8265	0.0306	0.1014	0.0043	593.3	17.2	598.8	24.6	101
H-39A	#90	0.65	0.32	1.5792	0.0442	0.1629	0.0047	937.1	17.9	936.9	26.2	100
H-39A	#91	0.15	0.07	1.7140	0.0891	0.1728	0.0079	997.4	33.6	1004.2	43.9	101
H-39A	#92	0.16	0.08	2.6515	0.0981	0.2320	0.0081	1285.4	28.1	1296.8	42.4	101
H-39A	#93	0.36	0.17	1.6554	0.0546	0.1707	0.0058	963.7	21.4	974.8	31.7	101
H-39A	#94	0.65	0.18	4.9411	0.1779	0.3100	0.0115	1785.2	31.6	1709.4	57.3	96
H-39A	#95	0.92	0.47	0.8312	0.0332	0.1013	0.0034	595.9	18.7	598.4	20.0	100
H-39A	#96	0.54	0.26	1.6357	0.0589	0.1677	0.0062	976.1	23.5	983.4	34.8	101
H-39A	#97	0.62	0.32	0.4345	0.0209	0.0612	0.0016	350.6	14.6	360.2	9.5	103
H-39A	#98	0.10	0.04	6.4784	0.1296	0.3647	0.0084	1995.7	18.5	1884.3	39.3	94
H-39A	#99	0.67	0.32	2.4632	0.0961	0.2193	0.0096	1250.7	29.2	1262.5	51.8	101
H-39F	#1	0.23	0.12	4.3714	0.3410	0.2884	0.0147	1663.1	44.3	1592.3	73.8	96
H-39F	#2	0.57	0.33	0.1362	0.0064	0.0195	0.0005	124.7	4.8	121.5	3.5	97
H-39F	#3	0.43	0.25	0.1360	0.0057	0.0192	0.0005	127.7	5.3	122.8	3.6	96
H-39F	#4	0.46	0.27	0.1245	0.0047	0.0176	0.0003	111.2	3.9	110.1	2.3	99
H-39F	#5	1.57	0.83	0.1651	0.0135	0.0185	0.0010	126.1	12.3	117.1	6.3	93
H-39F	#6	0.30	0.17	0.1402	0.0060	0.0194	0.0003	123.6	4.4	121.0	2.5	98
H-39F	#7	0.41	0.22	0.1329	0.0060	0.0180	0.0004	117.6	4.3	110.6	2.7	94
H-39F	#8	0.07	0.10	0.6508	0.0221	0.0548	0.0019	429.8	18.7	330.1	11.6	77
H-39F	#9	0.53	0.31	0.1437	0.0047	0.0210	0.0004	133.5	4.1	130.6	3.0	98

Table A.42: Zrn U-Pb age dataset

Zircon U-Pb data

Sample	Spot #	Th/U[a]	$^{208}Pb/^{206}Pb$	Ratios				Ages (Ma)				Cc[c]
				$^{207}Pb/^{235}U$[a]	2 σ[b]	$^{206}Pb/^{238}U$[a]	2 σ[b]	$^{207}Pb/^{235}U$	2 σ	$^{206}Pb/^{238}U$	2 σ	%
H-39F	#10	0.73	0.55	0.5694	0.1367	0.0243	0.0014	318.3	90.2	159.2	9.0	50
H-39F	#11	0.42	0.24	0.2749	0.0212	0.0376	0.0012	229.2	9.3	234.0	7.6	102
H-39F	#12	0.15	0.06	2.6354	0.1081	0.2029	0.0081	1259.2	36.0	1169.1	44.0	93
H-39F	#13	0.32	0.19	0.2679	0.0099	0.0363	0.0004	240.2	8.4	227.0	3.1	95
H-39F	#14	0.14	0.08	0.3327	0.0113	0.0451	0.0011	287.1	9.5	279.4	7.1	97
H-39F	#15	0.58	0.32	0.6914	0.0366	0.0852	0.0018	526.4	10.7	521.0	11.5	99
H-39F	#16	0.20	0.12	0.7093	0.0383	0.0882	0.0041	532.6	20.9	535.1	24.2	100
H-39F	#17	0.28	0.15	0.1272	0.0033	0.0183	0.0004	116.1	3.1	114.2	2.5	98
H-39F	#18	0.25	0.23	7.6555	0.3828	0.3438	0.0107	2036.4	68.1	1874.5	53.9	92
H-39F	#19	0.41	0.23	0.1321	0.0071	0.0194	0.0005	124.5	4.8	120.6	3.1	97
H-39F	#20	0.61	0.34	0.1439	0.0043	0.0204	0.0004	126.8	4.5	127.2	2.6	100
H-39F	#21	0.33	0.19	0.1319	0.0045	0.0193	0.0004	126.3	3.9	122.7	2.9	97
H-39F	#22	0.58	0.31	2.3714	0.0640	0.2032	0.0041	1189.8	17.0	1174.9	23.7	99
H-39F	#23	0.13	0.15	0.1686	0.0362	0.0184	0.0005	199.8	25.3	117.6	3.6	59
H-39F	#24	0.13	0.07	0.1295	0.0049	0.0186	0.0004	118.1	3.9	116.7	2.8	99
H-39F	#25	0.32	0.19	0.1435	0.0093	0.0197	0.0003	130.8	6.2	121.7	2.4	93
H-39F	#26	0.23	0.13	0.1314	0.0038	0.0183	0.0006	122.8	5.1	115.4	4.0	94
H-39F	#27	0.30	0.18	0.1306	0.0070	0.0180	0.0005	125.8	7.2	115.4	3.2	92
H-39F	#28	0.33	0.19	0.1297	0.0043	0.0189	0.0004	122.5	3.8	119.4	2.8	97
H-39F	#29	0.34	0.22	0.1243	0.0097	0.0183	0.0004	142.4	12.2	114.1	2.9	80
H-39F	#30	0.40	0.22	0.7316	0.0124	0.0875	0.0016	532.0	10.4	533.6	10.8	100
H-39F	#31	0.52	0.30	0.1378	0.0037	0.0190	0.0004	124.5	4.0	119.9	2.6	96
H-39F	#32	0.39	0.22	0.1435	0.0037	0.0205	0.0004	134.6	4.3	129.0	2.7	96
H-39F	#33	0.31	0.18	0.1344	0.0062	0.0192	0.0004	125.3	3.9	121.9	3.0	97
H-39F	#34	0.22	0.14	0.5755	0.0253	0.0720	0.0020	451.6	13.2	440.9	12.8	98
H-39F	#35	0.42	0.24	0.1347	0.0053	0.0195	0.0003	128.3	3.5	124.9	2.4	97
H-39F	#36	0.09	0.05	0.6573	0.0158	0.0811	0.0016	502.6	10.8	499.8	11.1	99
H-39F	#37	0.39	0.22	0.5729	0.0195	0.0715	0.0017	449.2	10.9	443.2	11.1	99
H-39F	#38	0.37	0.21	0.1367	0.0075	0.0197	0.0006	128.9	5.3	123.9	3.7	96
H-39F	#39	0.48	0.23	0.9168	0.0348	0.0717	0.0022	456.3	50.5	441.5	14.1	97
H-39F	#40	0.28	0.16	0.1203	0.0051	0.0178	0.0005	113.6	4.3	112.4	3.5	99
H-39F	#41	0.43	0.23	0.1275	0.0101	0.0176	0.0010	121.9	7.3	115.4	6.8	95
H-39F	#42	0.21	0.12	0.1293	0.0043	0.0182	0.0005	115.4	4.8	113.2	3.6	98
H-39F	#43	0.17	0.10	0.1696	0.0061	0.0225	0.0007	150.4	5.0	144.1	4.6	96
H-39F	#44	0.31	0.18	0.1435	0.0079	0.0207	0.0006	137.2	6.6	130.6	4.1	95
H-39F	#45	0.33	0.19	0.3181	0.0124	0.0431	0.0009	277.7	6.8	271.2	6.4	98
H-39F	#46	0.49	0.29	0.1378	0.0070	0.0199	0.0007	127.4	4.9	126.5	4.4	99
H-39F	#47	0.73	0.39	1.7048	0.0682	0.1693	0.0044	1019.0	23.4	1004.9	26.1	99
H-39F	#48	0.29	0.17	0.0915	0.0055	0.0122	0.0003	81.1	5.1	78.4	2.1	97
H-39F	#49	0.24	0.13	0.3152	0.0082	0.0422	0.0007	268.2	5.9	262.5	4.9	98
H-39F	#50	0.36	0.21	0.1242	0.0060	0.0183	0.0003	117.4	3.7	115.1	2.4	98
H-39F	#51	0.31	0.17	1.7639	0.0670	0.1688	0.0051	1000.8	22.5	998.9	29.7	100
H-39F	#52	0.26	0.14	0.5873	0.0141	0.0704	0.0018	443.4	11.6	435.8	12.2	98
H-39F	#53	0.11	0.04	1.5111	0.1148	0.1476	0.0092	974.9	42.2	882.5	52.2	91
H-39F	#54	0.27	0.34	0.1088	0.0095	0.0169	0.0009	112.6	6.5	106.6	5.7	95
H-39F	#55	0.20	0.12	0.1913	0.0061	0.0250	0.0008	165.3	5.8	158.5	5.0	96
H-39F	#56	0.15	0.08	2.1629	0.0584	0.1969	0.0043	1158.4	19.5	1153.2	26.5	100
H-39F	#57	0.31	0.18	0.1508	0.0069	0.0207	0.0003	132.6	3.6	133.1	2.4	100
H-39F	#58	0.24	0.14	0.1254	0.0039	0.0182	0.0005	118.8	4.3	116.0	3.4	98
H-39F	#59	1.46	0.78	1.3056	0.0627	0.1292	0.0043	795.1	24.6	789.3	26.1	99
H-39F	#60	0.42	0.25	0.1527	0.0084	0.0190	0.0005	133.0	7.5	122.0	3.6	92
H-39F	#61	0.39	0.23	0.1267	0.0028	0.0177	0.0002	116.7	2.2	111.7	1.9	96
H-39F	#62	0.60	0.34	0.1624	0.0063	0.0202	0.0005	134.3	7.1	128.5	3.3	96
H-39F	#63	0.42	0.24	0.2896	0.0119	0.0393	0.0006	249.3	6.7	245.5	4.8	98
H-39F	#64	0.47	0.25	2.2809	0.0730	0.2045	0.0035	1199.8	17.0	1197.9	23.0	100
H-39F	#65	0.63	0.33	2.2543	0.0992	0.1964	0.0039	1162.2	21.0	1156.0	25.4	99
H-39F	#66	0.25	0.14	0.1213	0.0039	0.0185	0.0002	118.2	3.7	116.8	2.1	99
H-39F	#67	0.16	0.09	0.1333	0.0037	0.0184	0.0004	121.3	4.8	117.6	2.8	97
H-39F	#68	0.30	0.15	5.5209	0.2540	0.3556	0.0043	1937.7	18.3	1972.0	30.7	102
H-39F	#69	0.24	0.14	0.2525	0.0088	0.0346	0.0008	221.2	6.2	219.1	5.6	99
H-39F	#70	0.14	0.08	0.1261	0.0040	0.0178	0.0005	119.1	4.5	111.8	3.2	94
H-39F	#71	0.63	0.36	0.1525	0.0061	0.0203	0.0005	136.2	5.1	130.5	3.5	96

Table A.43: Zrn U-Pb age dataset

Zircon U-Pb data

Sample	Spot #	Th/U[a]	$^{208}Pb/^{206}Pb$	Ratios				Ages (Ma)				Cc[c]
				$^{207}Pb/^{235}U$[a]	2 σ[b]	$^{206}Pb/^{238}U$[a]	2 σ[b]	$^{207}Pb/^{235}U$	2 σ	$^{206}Pb/^{238}U$	2 σ	%
H-39F	#72	0.88	0.51	0.1446	0.0036	0.0201	0.0005	137.6	4.6	131.5	3.6	96
H-39F	#73	0.10	0.06	0.2615	0.0089	0.0361	0.0010	232.4	7.1	230.1	6.8	99
H-39F	#74	0.36	0.21	0.1308	0.0054	0.0186	0.0005	119.8	4.8	118.9	3.3	99
H-39F	#75	0.19	0.10	0.5903	0.0218	0.0723	0.0017	474.6	13.4	455.3	11.4	96
H-39F	#76	0.40	0.23	0.2955	0.0174	0.0401	0.0014	260.9	10.6	252.2	9.2	97
H-39F	#77	0.25	0.14	0.2592	0.0104	0.0352	0.0007	227.6	7.8	221.3	5.2	97
H-39F	#78	0.29	0.17	0.1298	0.0038	0.0189	0.0006	123.2	4.3	121.0	4.0	98
H-39F	#79	0.34	0.15	1.2596	0.0567	0.1226	0.0034	810.5	20.3	749.8	22.0	93
H-39F	#80	0.12	0.08	3.4976	0.0665	0.2599	0.0036	1520.5	19.1	1495.1	26.7	98
H-39F	#81	0.54	0.31	0.1513	0.0053	0.0203	0.0005	136.0	4.7	129.5	3.8	95
H-39F	#82	0.08	0.05	2.4395	0.1220	0.2081	0.0069	1268.3	30.1	1246.7	40.9	98
H-39F	#83	0.36	0.20	0.1343	0.0063	0.0196	0.0006	128.1	5.1	122.3	3.9	95
H-39F	#84	0.24	0.14	0.1343	0.0063	0.0185	0.0006	125.8	4.9	120.3	3.9	96
H-39F	#85	0.33	0.18	2.3637	0.0827	0.2033	0.0033	1210.9	17.1	1214.0	23.3	100
H-39F	#86	0.35	0.18	9.8667	0.2664	0.4534	0.0104	2433.1	28.1	2422.2	54.7	100
H-39F	#87	0.22	0.13	0.1446	0.0036	0.0196	0.0005	127.7	4.3	124.2	3.6	97
H-39F	#88	0.08	0.05	0.1288	0.0036	0.0180	0.0004	116.5	3.3	114.5	3.1	98
H-39F	#89	0.29	0.17	1.2663	0.0519	0.1301	0.0025	809.8	18.0	791.9	17.9	98
H-39F	#90	0.26	0.13	24.0633	0.7460	0.6750	0.0108	3284.3	23.7	3339.6	57.6	102
H-39F	#91	0.46	0.28	0.5407	0.0270	0.0609	0.0036	416.9	22.5	384.2	22.8	92
H-39F	#92	0.24	0.14	1.5545	0.0839	0.1422	0.0054	914.7	36.2	857.2	33.0	94
H-39F	#93	0.46	0.26	0.1229	0.0073	0.0171	0.0007	114.1	6.1	111.0	4.8	97
H-39F	#94	0.35	0.20	0.1314	0.0054	0.0191	0.0009	123.6	6.2	123.5	5.8	100
H-39F	#95	0.20	0.12	0.3051	0.0116	0.0421	0.0013	282.8	10.2	267.2	8.9	94
H-39F	#96	0.17	0.12	0.2950	0.0136	0.0351	0.0015	255.4	11.8	224.0	10.1	88
H-39F	#97	0.45	0.26	0.1195	0.0054	0.0167	0.0007	107.6	5.6	106.6	4.9	99
H-39F	#98	0.34	0.19	0.1731	0.0081	0.0244	0.0009	157.7	7.0	156.9	6.4	99
H-39F	#99	0.55	0.32	0.1325	0.0085	0.0188	0.0008	123.8	7.7	121.2	5.2	98
H-39F	#100	0.29	0.16	0.1209	0.0065	0.0175	0.0005	115.3	5.0	115.9	3.8	101
H-39F	#101	0.04	0.04	0.1880	0.0203	0.0232	0.0021	170.9	16.0	158.6	14.3	93
H-39F	#102	0.31	0.17	0.1362	0.0079	0.0182	0.0005	120.2	10.3	117.3	3.5	98
H-39F	#103	0.46	0.24	3.9391	0.2048	0.2639	0.0095	1552.1	34.8	1527.4	53.3	98
H-39F	#104	0.32	0.19	0.1147	0.0071	0.0164	0.0007	108.9	5.9	106.3	4.7	98
H-39F	#105	0.37	0.21	0.1272	0.0268	0.0170	0.0008	120.6	14.4	110.9	5.3	92
H-39F	#106	0.15	0.08	0.1247	0.0047	0.0178	0.0004	118.5	3.8	114.4	2.9	97
H-39F	#107	0.74	0.42	0.1240	0.0053	0.0183	0.0007	120.2	5.7	119.7	4.9	100
H-39F	#108	0.19	0.10	1.4761	0.0723	0.1455	0.0060	895.3	30.2	887.5	36.6	99
H-39F	#109	0.30	0.17	0.1161	0.0087	0.0174	0.0006	108.3	6.7	106.8	3.9	99
H-39F	#110	0.57	0.32	0.1286	0.0085	0.0186	0.0008	121.9	6.8	120.6	5.3	99
H-39F	#111	0.16	0.10	0.5417	0.0238	0.0661	0.0025	431.2	17.4	419.1	17.1	97
H-39F	#112	0.36	0.20	1.5652	0.0876	0.1494	0.0064	923.3	31.4	911.8	39.2	99
H-39F	#113	0.62	0.36	0.1377	0.0081	0.0186	0.0007	127.5	6.1	120.8	4.7	95
H-39F	#114	0.55	0.32	0.2205	0.0207	0.0262	0.0011	192.4	15.7	173.5	7.5	90
H-39F	#115	0.63	0.36	0.6011	0.0277	0.0736	0.0024	470.0	15.5	466.5	16.2	99
H-102A	#1	0.02	0.01	0.8186	0.0360	0.0986	0.0037	611.8	19.5	613.6	22.9	100
H-102A	#2	0.50	0.29	0.1272	0.0048	0.0180	0.0004	120.2	3.9	116.5	3.1	97
H-102A	#3	0.46	0.26	0.1246	0.0062	0.0174	0.0006	121.0	5.6	117.7	4.4	97
H-102A	#4	0.46	0.26	0.6896	0.0262	0.0824	0.0027	528.9	17.9	519.0	17.0	98
H-102A	#5	0.23	0.13	1.4161	0.0510	0.1451	0.0044	900.3	21.7	888.8	25.8	99
H-102A	#6	0.36	0.21	0.1402	0.0032	0.0190	0.0002	137.7	3.4	123.5	2.0	90
H-102A	#7	0.23	0.13	0.1263	0.0085	0.0168	0.0006	113.6	5.8	110.2	4.0	97
H-102A	#8	0.38	0.22	0.1214	0.0062	0.0178	0.0007	119.7	5.9	116.5	4.5	97
H-102A	#9	0.49	0.28	0.1231	0.0064	0.0172	0.0006	116.7	5.0	113.3	4.3	97
H-102A	#10	0.29	0.16	0.1279	0.0041	0.0189	0.0003	123.8	3.9	123.5	2.1	100
H-102A	#11	0.33	0.18	0.1217	0.0102	0.0175	0.0009	120.5	9.1	114.6	6.0	95
H-102A	#12	0.33	0.18	0.1130	0.0062	0.0161	0.0005	107.8	4.3	106.4	3.1	99
H-102A	#13	0.51	0.27	0.0526	0.0061	0.0072	0.0005	50.7	4.7	47.9	3.2	94
H-102A	#14	0.39	0.22	0.1241	0.0102	0.0177	0.0006	118.3	6.9	117.1	3.9	99
H-102A	#15	0.06	0.04	0.1507	0.0083	0.0206	0.0007	144.3	7.2	136.3	4.6	94
H-102A	#16	0.20	0.11	0.1340	0.0072	0.0194	0.0006	129.8	4.9	129.0	3.8	99
H-102A	#17	0.19	0.11	0.1407	0.0090	0.0200	0.0007	137.0	6.0	132.6	4.9	97

Table A.44: Zrn U-Pb age dataset

Zircon U-Pb data

Sample	Spot #	Th/U[a]	$^{208}Pb/^{206}Pb$	Ratios				Ages (Ma)				Cc[c]
				$^{207}Pb/^{235}U$[a]	2 σ[b]	$^{206}Pb/^{238}U$[a]	2 σ[b]	$^{207}Pb/^{235}U$	2 σ	$^{206}Pb/^{238}U$	2 σ	%
H-102A	#18	0.52	0.28	0.1349	0.0080	0.0190	0.0007	129.6	5.6	127.1	4.7	98
H-102A	#19	0.09	0.12	1.1728	0.1525	0.0668	0.0062	746.6	70.6	433.8	39.1	58
H-102A	#20	0.13	0.08	0.1810	0.0047	0.0249	0.0005	170.9	4.7	165.2	3.6	97
H-102A	#21	0.38	0.21	0.1127	0.0045	0.0160	0.0006	112.9	4.7	108.9	4.1	96
H-102A	#22	0.33	0.19	0.1337	0.0092	0.0175	0.0006	129.5	6.3	116.7	4.0	90
H-102A	#23	0.36	0.20	0.1344	0.0035	0.0191	0.0004	133.8	5.7	127.9	2.9	96
H-102A	#24	0.44	0.25	0.1257	0.0054	0.0175	0.0005	120.8	4.3	115.4	3.4	96
H-102A	#25	0.27	0.15	0.1249	0.0055	0.0179	0.0006	119.6	5.1	119.6	3.9	100
H-102A	#26	0.08	0.04	0.1424	0.0048	0.0201	0.0004	141.6	4.4	137.2	3.1	97
H-102A	#27	0.09	0.09	0.1764	0.0069	0.0193	0.0010	193.2	17.2	130.0	6.7	67
H-102A	#28	0.24	0.13	0.8079	0.0210	0.0958	0.0015	616.4	9.3	622.6	10.1	101
H-102A	#29	0.18	0.11	0.1432	0.0052	0.0198	0.0007	139.2	5.2	134.5	4.5	97
H-102A	#30	0.27	0.16	0.1186	0.0065	0.0177	0.0008	124.4	6.6	120.2	5.2	97
H-102A	#31	0.60	0.29	10.6521	0.3835	0.4683	0.0159	2537.8	37.0	2609.0	75.5	103
H-102A	#32	0.06	0.04	0.1436	0.0065	0.0206	0.0009	140.9	6.5	137.5	6.0	98
H-102A	#33	0.29	0.17	0.1306	0.0067	0.0188	0.0008	137.2	6.6	135.9	6.1	99
H-102A	#34	0.48	0.28	0.1341	0.0067	0.0198	0.0008	135.6	6.8	136.3	5.7	101
H-102A	#35	0.43	0.25	0.1461	0.0076	0.0205	0.0009	143.0	6.7	139.5	5.9	98
H-102A	#36	0.27	0.16	0.1405	0.0055	0.0201	0.0008	139.3	6.1	137.5	5.6	99
H-102A	#37	0.25	0.14	0.1338	0.0091	0.0194	0.0007	137.4	7.4	133.3	4.9	97
H-102A	#38	0.30	0.17	0.1171	0.0102	0.0166	0.0010	121.4	8.3	119.4	7.0	98
H-102A	#39	0.24	0.14	0.1269	0.0055	0.0183	0.0007	127.4	5.5	125.5	5.0	99
H-102A	#40	0.23	0.13	0.4931	0.0192	0.0439	0.0017	330.8	32.7	298.0	11.1	90
H-102A	#41	0.15	0.09	0.1291	0.0048	0.0192	0.0007	136.4	6.3	132.1	4.8	97
H-102A	#42	0.45	0.28	0.1671	0.0127	0.0261	0.0007	190.9	13.7	178.1	4.6	93
H-102A	#43	0.05	0.03	0.1444	0.0069	0.0200	0.0010	140.4	6.7	139.3	6.6	99
H-102A	#44	0.29	0.18	0.1786	0.0082	0.0226	0.0004	169.8	8.6	154.6	2.9	91
H-102A	#45	0.29	0.21	0.1450	0.0087	0.0193	0.0011	145.8	8.3	133.0	7.2	91
H-102A	#46	0.34	0.18	0.9190	0.0312	0.0846	0.0024	692.5	17.7	567.7	15.8	82
H-102A	#47	0.09	0.06	0.2131	0.0132	0.0293	0.0016	202.2	10.5	193.5	10.1	96
H-102A	#48	0.45	0.27	0.1527	0.0055	0.0213	0.0007	151.3	5.5	148.0	4.7	98
H-102A	#49	0.38	0.24	0.0571	0.0022	0.0087	0.0002	64.5	3.9	61.4	1.4	95
H-102A	#50	0.49	0.31	0.1364	0.0065	0.0191	0.0007	141.5	6.2	135.3	4.7	96
H-102A	#51	0.47	0.28	0.1401	0.0083	0.0197	0.0010	147.0	8.4	141.2	7.0	96
H-102A	#52	0.14	0.09	0.1308	0.0044	0.0194	0.0005	136.3	4.5	135.2	3.3	99
H-102A	#53	0.06	0.04	0.1444	0.0075	0.0210	0.0009	148.9	7.2	146.6	6.5	98
H-102A	#54	0.17	0.10	1.4947	0.0837	0.1526	0.0067	968.2	30.4	997.4	40.8	103
H-102A	#55	0.03	0.02	0.1510	0.0072	0.0213	0.0008	151.3	6.1	149.9	5.3	99
H-102A	#56	0.39	0.25	0.2691	0.0137	0.0355	0.0014	255.2	10.9	249.9	9.8	98
H-102A	#57	0.41	0.64	0.1111	0.0053	0.0162	0.0006	114.1	5.5	115.4	4.6	101
H-102A	#58	0.26	0.15	0.1229	0.0053	0.0178	0.0007	125.1	5.5	125.4	5.2	100
H-102A	#59	0.61	0.35	0.1351	0.0064	0.0195	0.0010	137.9	7.1	135.7	6.7	98
H-102A	#60	0.29	0.30	0.1338	0.0054	0.0195	0.0007	136.4	5.2	136.7	5.0	100
H-102A	#61	0.06	0.03	0.1365	0.0063	0.0198	0.0008	138.5	6.2	136.9	5.7	99
H-102A	#62	0.24	0.14	0.1289	0.0110	0.0192	0.0009	135.0	8.0	135.7	6.3	101
H-102A	#63	0.04	0.03	0.1411	0.0069	0.0199	0.0008	147.1	7.1	142.7	5.8	97
H-102A	#64	0.29	0.17	0.0812	0.0036	0.0118	0.0005	85.6	4.1	84.7	3.7	99
H-102A	#65	0.44	0.26	0.1270	0.0065	0.0180	0.0008	129.9	7.0	127.6	5.4	98
H-102A	#66	0.49	0.30	0.1437	0.0072	0.0199	0.0008	149.5	8.0	142.3	5.6	95
H-102A	#67	0.07	0.04	0.1473	0.0215	0.0206	0.0016	159.8	13.7	144.8	11.2	91
H-102A	#68	0.05	0.03	0.1302	0.0049	0.0190	0.0009	135.0	6.2	134.5	6.1	100
H-102A	#69	0.02	0.01	0.1393	0.0052	0.0206	0.0008	145.4	6.1	146.7	5.8	101
H-102A	#70	0.35	0.20	0.1363	0.0055	0.0194	0.0007	138.8	5.6	137.7	5.0	99
H-102A	#71	0.54	0.31	0.1341	0.0064	0.0195	0.0009	143.1	7.9	140.7	6.7	98
H-102A	#72	0.40	0.23	0.1294	0.0074	0.0193	0.0009	139.2	7.2	138.4	6.4	99
H-102A	#73	0.29	0.17	0.1287	0.0067	0.0181	0.0006	133.2	6.0	128.7	4.3	97
H-102A	#74	0.57	0.33	0.1309	0.0081	0.0190	0.0007	136.5	7.7	136.1	5.1	100
H-102A	#75	0.38	0.22	0.1200	0.0120	0.0179	0.0008	134.7	8.2	131.0	5.5	97
H-102A	#76	0.35	0.21	0.1280	0.0073	0.0184	0.0008	135.6	7.0	133.8	5.8	99
H-102A	#77	0.06	0.03	0.1389	0.0060	0.0203	0.0009	146.0	6.4	145.4	6.0	100
H-102A	#78	0.06	0.04	0.1471	0.0085	0.0203	0.0012	150.4	9.1	147.3	8.3	98
H-102A	#79	0.26	0.18	0.1752	0.0102	0.0246	0.0013	177.0	9.3	174.7	8.8	99

Table A.45: Zrn U-Pb age dataset

Zircon U-Pb data

Sample	Spot #	Th/U[a]	$^{208}Pb/^{206}Pb$	Ratios				Ages (Ma)				Cc[c]
				$^{207}Pb/^{235}U$[a]	2 σ[b]	$^{206}Pb/^{238}U$[a]	2 σ[b]	$^{207}Pb/^{235}U$	2 σ	$^{206}Pb/^{238}U$	2 σ	%
H-102A	#80	0.17	0.10	0.1252	0.0058	0.0184	0.0008	131.9	6.1	132.4	5.8	100
H-102A	#81	0.30	0.28	0.2447	0.0254	0.0194	0.0010	269.3	23.9	143.0	7.4	53
H-102A	#82	0.13	0.08	0.1322	0.0083	0.0195	0.0011	142.2	8.1	143.2	7.9	101
H-102A	#83	0.13	0.10	0.1668	0.0088	0.0196	0.0009	164.7	9.0	142.1	6.7	86
H-102A	#84	0.07	0.04	1.6252	0.1008	0.1583	0.0103	1016.3	44.0	1035.2	62.5	102
H-102A	#85	0.63	0.39	0.1275	0.0065	0.0190	0.0008	141.1	6.7	141.1	6.1	100
H-102A	#86	0.38	0.24	0.1346	0.0098	0.0182	0.0009	137.9	8.5	133.1	6.6	97
H-102A	#87	0.41	0.26	0.1505	0.0157	0.0218	0.0007	165.7	16.8	157.5	5.0	95
H-102A	#88	0.06	0.04	0.1370	0.0079	0.0201	0.0010	146.9	7.8	146.1	7.5	99
H-102A	#89	0.56	0.35	0.1405	0.0083	0.0189	0.0008	141.0	8.5	136.4	5.9	97
H-102A	#90	0.26	0.16	0.1205	0.0088	0.0171	0.0007	129.4	7.2	124.3	5.0	96
H-102A	#91	0.06	0.04	0.1348	0.0066	0.0195	0.0009	146.8	6.6	145.2	6.3	99
H-102A	#92	0.05	0.03	0.1275	0.0054	0.0188	0.0008	137.1	6.2	136.7	5.5	100
H-102A	#93	0.05	0.03	0.1305	0.0051	0.0190	0.0009	140.7	7.1	139.2	6.6	99
H-102A	#94	0.04	0.02	4.3236	0.1556	0.2743	0.0099	1780.2	35.0	1755.6	55.6	99
H-102A	#95	0.83	0.50	0.1374	0.0077	0.0187	0.0009	142.1	7.9	136.4	6.3	96
H-102A	#96	0.26	0.15	1.4143	0.0707	0.1444	0.0059	957.9	29.6	958.4	36.6	100
H-102A	#97	0.20	0.13	0.1306	0.0054	0.0187	0.0007	140.2	7.0	136.0	5.4	97
H-102A	#98	0.36	0.23	0.1282	0.0069	0.0187	0.0006	139.0	6.9	136.8	4.5	98
H-102A	#99	0.25	0.16	0.1182	0.0096	0.0176	0.0006	128.9	6.3	128.5	4.5	100
H-102A	#100	0.04	0.03	0.2116	0.0176	0.0264	0.0016	223.2	15.1	191.9	11.4	86
H-102A	#101	0.82	0.49	0.5165	0.0248	0.0649	0.0027	462.1	17.6	461.6	18.3	100
H-102A	#102	0.09	0.08	0.1674	0.0089	0.0188	0.0008	162.3	7.8	135.0	5.3	83
H-102A	#103	0.16	0.28	0.3763	0.0594	0.0217	0.0012	363.0	40.2	158.6	8.5	44
H-102A	#104	0.54	0.36	0.1461	0.0142	0.0209	0.0003	160.5	12.1	152.7	2.1	95
H-102A	#105	0.39	0.24	0.1395	0.0088	0.0193	0.0010	141.9	8.0	141.4	7.0	100
H-102A	#106	0.35	0.23	0.1612	0.0135	0.0217	0.0007	172.8	10.9	157.7	4.8	91
H-102A	#107	0.51	0.31	0.1316	0.0063	0.0188	0.0009	141.5	7.4	139.2	6.8	98
H-102A	#108	0.22	0.16	0.1583	0.0103	0.0193	0.0007	169.1	8.4	143.7	5.4	85
H-102A	#109	0.24	0.15	0.1306	0.0034	0.0186	0.0007	138.7	5.2	134.1	4.6	97
H-102A	#110	0.28	0.17	0.1211	0.0076	0.0165	0.0008	129.6	7.6	125.2	6.1	97
H-102A	#111	0.26	0.16	0.1159	0.0066	0.0171	0.0006	127.8	6.0	125.9	4.6	99
H-102A	#112	0.06	0.04	0.1398	0.0076	0.0199	0.0010	149.7	7.7	147.7	7.0	99
H-102A	#113	0.16	0.27	3.7534	0.1389	0.1662	0.0035	1640.8	21.4	1130.9	22.9	69
H-103	#1	0.02	0.01	0.8150	0.0269	0.0970	0.0026	568.6	15.8	570.9	17.5	100
H-103	#2	0.46	0.26	3.6364	0.1673	0.2678	0.0099	1517.3	36.1	1467.4	54.0	97
H-103	#3	0.36	0.22	0.1400	0.0062	0.0196	0.0008	125.1	6.3	119.9	5.1	96
H-103	#4	0.12	0.08	0.1756	0.0097	0.0236	0.0013	151.4	8.5	143.7	8.1	95
H-103	#5	0.61	0.35	0.2974	0.0113	0.0416	0.0012	258.4	9.4	251.2	8.1	97
H-103	#6	0.19	0.11	0.1346	0.0070	0.0189	0.0005	122.4	5.2	115.5	3.7	94
H-103	#7	0.23	0.14	0.1946	0.0066	0.0262	0.0007	165.6	5.5	157.9	4.8	95
H-103	#8	0.43	0.26	0.1329	0.0065	0.0189	0.0006	122.2	6.2	115.9	4.4	95
H-103	#9	0.25	0.15	0.1428	0.0066	0.0208	0.0005	129.5	5.0	126.6	3.8	98
H-103	#10	0.29	0.18	0.1532	0.0121	0.0213	0.0012	133.4	8.4	130.0	7.6	97
H-103	#11	0.74	0.44	0.1359	0.0082	0.0193	0.0008	119.7	6.5	117.3	5.5	98
H-103	#12	0.13	0.07	0.5027	0.0161	0.0629	0.0015	378.3	11.1	377.9	10.7	100
H-103	#13	0.30	0.19	0.1439	0.0066	0.0211	0.0008	133.0	6.3	128.2	5.5	96
H-103	#14	0.41	0.25	0.1379	0.0070	0.0184	0.0004	124.9	7.6	112.6	3.1	90
H-103	#15	0.07	0.04	0.1488	0.0046	0.0210	0.0004	130.5	3.9	126.8	3.4	97
H-103	#16	0.55	0.32	5.4148	0.1462	0.3269	0.0082	1807.7	30.0	1753.1	46.2	97
H-103	#17	0.24	0.13	4.2595	0.2002	0.2827	0.0110	1556.9	38.1	1536.1	59.0	99
H-103	#18	0.39	0.24	0.1373	0.0088	0.0192	0.0008	121.8	6.7	117.6	5.4	97
H-103	#19	0.23	0.14	0.1365	0.0085	0.0197	0.0005	121.7	6.3	118.7	3.8	98
H-103	#20	0.47	0.28	0.1427	0.0064	0.0191	0.0005	122.0	5.2	117.9	3.4	97
H-103	#21	0.55	0.29	0.1483	0.0113	0.0200	0.0006	128.4	6.5	120.3	3.8	94
H-103	#22	0.63	0.36	0.0774	0.0145	0.0082	0.0004	65.2	9.0	50.6	2.5	78
H-103	#23	0.33	0.20	0.1480	0.0038	0.0210	0.0004	129.9	3.8	127.4	3.3	98
H-103	#24	0.33	0.19	0.1473	0.0068	0.0202	0.0004	134.4	6.8	122.3	3.2	91
H-103	#25	0.30	0.17	0.1495	0.0055	0.0207	0.0004	133.2	5.0	126.1	3.2	95
H-103	#26	0.26	0.15	0.1885	0.0070	0.0248	0.0008	157.5	6.6	151.5	5.2	96
H-103	#27	0.26	0.15	0.1315	0.0078	0.0194	0.0006	119.1	5.9	116.4	4.3	98

Table A.46: Zrn U-Pb age dataset

Zircon U-Pb data

Sample	Spot #	Th/U[a]	$^{208}Pb/^{206}Pb$	Ratios				Ages (Ma)				Cc[c]
				$^{207}Pb/^{235}U$[a]	2 σ[b]	$^{206}Pb/^{238}U$[a]	2 σ[b]	$^{207}Pb/^{235}U$	2 σ	$^{206}Pb/^{238}U$	2 σ	%
H-103	#28	0.26	0.16	0.1582	0.0090	0.0186	0.0005	126.2	8.7	113.6	3.5	90
H-103	#29	0.42	0.27	0.1659	0.0058	0.0207	0.0012	156.3	11.8	127.1	7.3	81
H-103	#30	0.36	0.20	0.6250	0.0313	0.0789	0.0017	470.9	11.7	463.5	12.1	98
H-103	#31	0.32	0.19	0.1370	0.0044	0.0196	0.0003	121.3	3.9	116.9	2.7	96
H-103	#32	0.51	0.28	0.8922	0.0286	0.1001	0.0028	593.7	19.5	593.3	18.2	100
H-103	#33	0.54	0.33	0.1793	0.0113	0.0228	0.0004	153.7	9.0	136.1	3.1	89
H-103	#34	0.34	0.20	0.1454	0.0044	0.0200	0.0005	125.2	5.0	121.8	3.7	97
H-103	#35	0.08	0.04	0.9742	0.0331	0.1107	0.0030	656.9	17.6	650.2	19.2	99
H-103	#36	0.33	0.20	0.2294	0.0094	0.0318	0.0009	201.8	6.6	192.9	5.9	96
H-103	#37	0.25	0.15	0.6778	0.0366	0.0825	0.0018	503.6	17.2	490.5	12.8	97
H-103	#38	0.15	0.10	6.0331	0.3077	0.3917	0.0157	2058.4	56.2	2056.0	76.1	100
H-103	#39	0.11	0.06	2.1995	0.0726	0.1935	0.0052	1140.4	25.0	1126.7	32.1	99
H-103	#40	0.56	0.31	0.1495	0.0079	0.0215	0.0008	134.5	6.6	131.5	5.1	98
H-103	#41	0.29	0.16	0.1589	0.0064	0.0209	0.0007	137.0	5.9	126.2	4.5	92
H-103	#42	0.15	0.09	0.7447	0.0424	0.0862	0.0051	524.2	26.1	509.0	29.9	97
H-103	#43	0.34	0.19	0.1486	0.0040	0.0205	0.0005	128.8	4.8	125.2	3.7	97
H-103	#44	0.30	0.18	0.1277	0.0050	0.0185	0.0006	117.0	5.0	112.2	3.7	96
H-103	#45	0.27	0.15	0.1642	0.0057	0.0210	0.0005	135.8	7.3	129.6	3.9	95
H-103	#46	0.06	0.04	0.1516	0.0036	0.0213	0.0003	136.8	3.6	131.1	2.5	96
H-103	#47	0.34	0.20	0.1619	0.0087	0.0212	0.0006	143.5	6.2	130.6	4.3	91
H-103	#48	0.17	0.10	5.1135	0.1176	0.3114	0.0072	1795.6	26.4	1687.1	40.2	94
H-103	#49	0.20	0.11	0.1305	0.0057	0.0184	0.0006	116.7	5.5	114.0	3.8	98
H-103	#50	0.45	0.22	12.2551	0.8824	0.5038	0.0111	2493.8	33.0	2542.2	54.9	102
H-103	#51	0.01	0.01	0.8851	0.0204	0.1002	0.0020	606.9	15.2	591.2	13.6	97
H-103	#52	0.28	0.16	0.1335	0.0055	0.0185	0.0005	116.1	4.8	113.7	3.6	98
H-103	#53	0.38	0.23	0.1370	0.0051	0.0186	0.0003	122.2	5.1	113.9	2.3	93
H-103	#54	0.18	0.11	0.2009	0.0143	0.0262	0.0009	179.1	10.7	170.6	6.4	95
H-103	#55	0.38	0.23	0.1531	0.0064	0.0200	0.0005	133.6	7.3	122.7	3.3	92
H-103	#56	0.60	0.36	0.1582	0.0070	0.0210	0.0010	142.3	8.3	129.8	6.2	91
H-103	#57	0.08	0.09	0.7638	0.0336	0.0788	0.0039	521.2	31.5	474.5	23.4	91
H-103	#58	0.19	0.11	0.2199	0.0101	0.0309	0.0010	197.7	8.8	189.2	6.5	96
H-103	#59	0.25	0.15	0.1386	0.0086	0.0183	0.0008	119.6	7.0	113.7	5.3	95
H-103	#60	0.55	0.26	0.1281	0.0061	0.0177	0.0009	111.2	5.9	108.9	5.4	98
H-103	#61	0.28	0.16	0.1378	0.0055	0.0190	0.0006	116.5	5.2	116.3	3.8	100
H-103	#62	0.63	0.37	0.1462	0.0060	0.0206	0.0006	124.6	5.3	123.5	4.0	99
H-103	#63	0.34	0.20	0.1277	0.0070	0.0200	0.0005	121.7	6.0	120.5	3.6	99
H-103	#64	0.07	0.04	1.6521	0.0578	0.1624	0.0041	949.7	21.8	941.2	24.6	99
H-103	#65	0.35	0.22	0.1435	0.0056	0.0203	0.0006	132.3	5.1	126.1	4.0	95
H-103	#66	0.07	0.05	0.1643	0.0110	0.0217	0.0010	138.4	8.7	130.9	6.1	95
H-103	#67	0.30	0.18	0.1930	0.0106	0.0261	0.0010	168.8	7.7	156.1	6.0	92
H-103	#68	0.39	0.21	5.3499	0.2300	0.3317	0.0083	1839.7	31.1	1810.5	44.4	98
H-103	#69	0.37	0.23	0.0917	0.0040	0.0117	0.0003	77.0	5.1	72.1	1.8	94
H-103	#70	0.45	0.23	0.1707	0.0179	0.0194	0.0016	159.3	20.6	120.8	10.2	76
H-103	#71	0.39	0.24	1.4293	0.0457	0.1461	0.0034	844.1	18.5	853.0	20.8	101
H-103	#72	0.30	0.17	1.7192	0.0516	0.1706	0.0041	975.3	22.2	975.6	24.5	100
H-103	#73	0.13	0.08	1.0425	0.0354	0.1067	0.0034	677.9	18.5	630.3	20.4	93
H-103	#74	0.46	0.25	0.1372	0.0074	0.0208	0.0009	127.4	6.6	124.2	5.3	97
H-103	#75	0.80	0.43	0.1818	0.0075	0.0231	0.0008	150.0	9.0	142.5	4.9	95
H-103	#76	0.59	0.23	5.2104	0.2761	0.3352	0.0077	1859.3	22.4	1871.1	40.7	101
H-103	#77	0.35	0.20	0.1294	0.0058	0.0191	0.0004	116.2	4.5	117.9	2.9	101
H-103	#78	0.27	0.16	0.1510	0.0077	0.0189	0.0005	125.0	7.6	114.2	3.1	91
H-103	#79	0.68	0.36	1.5039	0.0632	0.1523	0.0032	886.1	17.3	884.8	19.9	100
H-103	#80	0.37	0.20	4.7520	0.2186	0.3265	0.0104	1769.2	39.3	1778.5	53.1	101
H-103	#81	0.16	0.10	1.8841	0.0659	0.1808	0.0052	1023.0	25.5	1042.1	29.9	102
H-103	#82	0.60	0.32	2.2525	0.0878	0.1993	0.0044	1141.3	22.2	1136.6	26.1	100
H-103	#83	0.40	0.23	0.0522	0.0025	0.0078	0.0003	48.6	2.5	47.5	2.0	98
H-103	#84	0.27	0.15	2.5150	0.0855	0.2149	0.0062	1252.7	24.0	1229.9	34.8	98
H-103	#85	0.23	0.14	0.7516	0.0301	0.0911	0.0015	559.7	12.1	545.9	10.5	98
H-103	#86	0.01	0.01	0.4700	0.0136	0.0588	0.0019	363.9	12.3	356.0	12.1	98
H-103	#87	0.52	0.30	0.1591	0.0075	0.0213	0.0007	131.6	6.9	131.9	4.7	100
H-103	#88	0.43	0.23	2.6979	0.0809	0.2231	0.0022	1269.0	19.7	1259.1	17.2	99
H-103	#89	0.31	0.16	0.1406	0.0063	0.0178	0.0024	118.4	17.2	119.3	16.2	101

Table A.47: Zrn U-Pb age dataset

Zircon U-Pb data

Sample	Spot #	Th/U[a]	^{208}Pb/^{206}Pb	Ratios				Ages (Ma)				Cc[c]
				^{207}Pb/^{235}U[a]	2 σ[b]	^{206}Pb/^{238}U[a]	2 σ[b]	^{207}Pb/^{235}U	2 σ	^{206}Pb/^{238}U	2 σ	%
H-103	#90	0.35	0.20	0.1412	0.0069	0.0195	0.0008	130.0	5.6	120.9	5.0	93
H-103	#91	0.07	0.06	1.4656	0.1436	0.1366	0.0117	931.2	57.0	835.6	68.5	90
H-103	#92	0.22	0.13	6.0933	0.3229	0.3624	0.0127	2015.7	42.9	1951.0	60.9	97
H-103	#93	0.06	0.04	0.1606	0.0040	0.0223	0.0003	140.4	3.9	137.8	2.2	98
H-103	#94	0.28	0.16	0.1391	0.0064	0.0196	0.0004	124.0	4.0	121.1	2.9	98
H-103	#95	0.30	0.12	5.4418	0.1741	0.3382	0.0108	1851.5	34.6	1829.9	54.4	99
H-103	#96	0.53	0.29	0.1477	0.0058	0.0207	0.0007	130.9	5.4	128.2	4.4	98
H-103	#97	0.25	0.14	1.6618	0.0565	0.1579	0.0039	934.9	24.7	919.4	23.2	98
H-103	#98	0.27	0.16	0.1462	0.0094	0.0194	0.0005	124.7	5.3	120.4	3.5	97
H-103	#99	0.44	0.26	0.1631	0.0113	0.0198	0.0006	134.6	9.6	122.5	3.9	91
H-103	#100	0.16	0.09	0.6987	0.0328	0.0794	0.0033	502.6	20.4	479.2	19.9	95
H-103	#101	0.61	0.35	0.1391	0.0083	0.0189	0.0007	121.8	6.3	119.6	4.7	98
H-103	#102	0.23	0.13	0.5915	0.0154	0.0741	0.0014	446.1	10.5	447.3	9.1	100
H-103	#103	0.24	0.21	0.4302	0.0710	0.0430	0.0015	417.0	42.2	282.6	9.7	68
H-103	#104	0.25	0.15	0.1699	0.0066	0.0226	0.0004	145.6	4.5	140.0	2.6	96
H-103	#105	0.30	0.17	0.6528	0.0287	0.0784	0.0027	502.7	17.2	474.2	16.0	94
H-103	#106	0.40	0.22	0.1257	0.0039	0.0174	0.0006	110.8	5.2	109.2	3.8	99
H-103	#107	0.20	0.12	0.1377	0.0040	0.0183	0.0006	115.8	4.6	111.8	3.9	97
H-103	#108	0.04	0.03	0.1632	0.0038	0.0224	0.0006	147.2	4.4	140.7	3.9	96
H-103	#109	0.29	0.17	0.1500	0.0103	0.0188	0.0007	131.4	7.7	119.3	4.3	91
H-103	#110	0.36	0.20	0.3362	0.0128	0.0438	0.0011	278.3	8.1	270.9	6.9	97
H-103	#111	0.51	0.28	0.3107	0.0140	0.0422	0.0009	267.0	8.7	262.1	6.2	98
H-103	#112	0.55	0.33	0.1502	0.0063	0.0207	0.0005	130.3	5.6	124.1	3.4	95
H-103	#113	0.56	0.32	0.1563	0.0059	0.0216	0.0005	140.7	6.2	133.2	3.6	95
H-103	#114	0.31	0.19	0.1407	0.0077	0.0200	0.0005	133.5	6.3	123.7	3.6	93
H-104A	#1	0.02	0.01	0.8769	0.0167	0.1036	0.0019	620.1	13.5	614.4	14.7	99
H-104A	#2	0.34	0.22	0.1477	0.0103	0.0190	0.0006	122.4	6.9	117.3	4.1	96
H-104A	#3	0.53	0.36	0.1668	0.0052	0.0226	0.0003	145.5	5.0	139.3	3.2	96
H-104A	#4	0.11	0.07	0.1386	0.0073	0.0196	0.0007	122.5	5.4	123.7	5.0	101
H-104A	#5	0.39	0.30	0.2127	0.0155	0.0165	0.0011	163.4	16.7	93.2	6.4	57
H-104A	#6	0.41	0.24	0.1367	0.0122	0.0187	0.0010	120.5	7.8	114.4	6.2	95
H-104A	#7	0.19	0.11	0.1477	0.0072	0.0213	0.0010	134.4	7.5	132.7	6.3	99
H-104A	#8	0.23	0.13	0.1239	0.0061	0.0183	0.0006	111.3	5.1	113.2	4.0	102
H-104A	#9	0.39	0.23	0.1365	0.0068	0.0189	0.0007	119.5	6.1	117.0	4.9	98
H-104A	#10	0.06	0.04	0.1386	0.0062	0.0198	0.0008	121.3	5.6	121.4	5.4	100
H-104A	#11	0.31	0.16	0.1461	0.0064	0.0205	0.0007	128.8	5.3	125.7	4.6	98
H-104A	#12	0.42	0.25	0.1329	0.0089	0.0181	0.0005	116.1	5.6	113.5	3.8	98
H-104A	#13	0.26	0.13	1.8388	0.0975	0.1684	0.0081	992.7	34.1	970.4	46.1	98
H-104A	#14	0.06	0.04	0.1477	0.0059	0.0210	0.0010	132.1	7.2	129.0	6.4	98
H-104A	#16	0.43	0.35	0.1465	0.0054	0.0208	0.0006	131.5	5.9	127.8	4.1	97
H-104A	#17	0.42	0.25	0.1508	0.0080	0.0206	0.0007	133.8	7.0	127.0	4.8	95
H-104A	#18	0.06	0.04	0.1365	0.0083	0.0201	0.0007	125.0	6.7	123.9	4.5	99
H-104A	#19	0.45	0.27	0.1301	0.0061	0.0186	0.0006	115.5	4.9	115.9	4.4	100
H-104A	#20	0.08	0.05	0.1465	0.0054	0.0204	0.0006	126.1	5.0	125.3	4.3	99
H-104A	#21	0.05	0.03	0.1450	0.0054	0.0206	0.0007	127.5	5.2	126.5	4.5	99
H-104A	#22	0.22	0.14	0.1529	0.0090	0.0208	0.0008	131.9	7.3	127.8	5.1	97
H-104A	#23	0.34	0.21	0.1394	0.0047	0.0197	0.0005	133.2	6.5	121.6	3.5	91
H-104A	#24	0.13	0.07	0.1719	0.0107	0.0230	0.0009	147.7	7.6	141.5	5.6	96
H-104A	#25	0.27	0.17	0.1341	0.0067	0.0190	0.0006	125.1	7.3	117.1	4.4	94
H-104A	#26	0.16	0.10	0.1478	0.0064	0.0207	0.0005	128.6	4.6	127.2	3.5	99
H-104A	#27	0.20	0.12	0.3642	0.0149	0.0485	0.0016	302.6	13.7	293.6	10.9	97
H-104A	#28	0.32	0.20	0.1504	0.0045	0.0211	0.0005	135.6	5.3	129.6	4.0	96
H-104A	#29	0.35	0.20	0.1565	0.0108	0.0213	0.0010	144.9	8.8	129.9	6.3	90
H-104A	#30	0.51	0.23	0.1407	0.0110	0.0187	0.0006	120.7	7.4	112.3	4.2	93
H-104A	#31	0.32	0.18	0.1201	0.0078	0.0177	0.0008	108.5	6.9	107.2	5.0	99
H-104A	#32	0.30	0.17	0.1948	0.0074	0.0196	0.0004	132.4	10.0	123.6	3.4	93
H-104A	#33	0.20	0.12	0.1260	0.0068	0.0181	0.0007	115.4	5.8	114.7	4.5	99
H-104A	#34	0.15	0.09	0.1520	0.0079	0.0207	0.0007	140.0	6.2	127.4	4.5	91
H-104A	#35	0.26	0.13	2.1286	0.0979	0.1878	0.0083	1109.8	35.0	1072.3	46.6	97
H-104A	#36	0.50	0.30	0.1433	0.0079	0.0199	0.0009	126.0	6.5	122.0	5.7	97
H-104A	#37	0.06	0.04	0.1405	0.0055	0.0202	0.0007	125.7	5.3	125.3	4.7	100

Table A.48: Zrn U-Pb age dataset

Zircon U-Pb data

Sample	Spot #	Th/U[a]	$^{208}Pb/^{206}Pb$	Ratios				Ages (Ma)				Cc[c]
				$^{207}Pb/^{235}U$[a]	2 σ[b]	$^{206}Pb/^{238}U$[a]	2 σ[b]	$^{207}Pb/^{235}U$	2 σ	$^{206}Pb/^{238}U$	2 σ	%
H-104A	#38	0.20	0.12	0.1276	0.0051	0.0188	0.0007	127.5	6.6	120.5	5.0	95
H-104A	#39	0.52	0.31	0.0999	0.0042	0.0141	0.0005	88.5	3.7	86.3	3.0	98
H-104A	#40	0.04	0.03	0.1517	0.0023	0.0226	0.0004	137.4	3.6	136.6	3.0	99
H-104A	#41	0.29	0.18	0.1345	0.0073	0.0184	0.0006	115.8	5.6	114.5	4.1	99
H-104A	#42	0.05	0.03	0.1458	0.0055	0.0205	0.0005	130.1	4.5	126.0	3.7	97
H-104A	#43	0.08	0.05	0.1433	0.0043	0.0207	0.0006	127.9	5.1	127.2	4.3	99
H-104A	#44	0.50	0.31	0.2063	0.0091	0.0279	0.0009	179.6	7.8	172.2	6.0	96
H-104A	#45	0.05	0.03	0.1453	0.0042	0.0217	0.0003	134.9	5.3	133.2	2.8	99
H-104A	#46	0.06	0.04	0.1499	0.0058	0.0210	0.0008	133.7	6.4	133.0	5.3	99
H-104A	#47	0.24	0.14	0.2018	0.0032	0.0250	0.0003	156.6	6.0	149.8	2.7	96
H-104A	#48	0.29	0.19	0.1309	0.0386	0.0165	0.0020	108.6	20.7	101.3	12.1	93
H-104A	#49	0.44	0.25	0.1276	0.0074	0.0180	0.0005	118.8	6.6	112.7	3.6	95
H-104A	#50	0.07	0.04	0.1446	0.0045	0.0203	0.0005	126.2	4.5	124.4	3.6	99
H-104A	#51	0.06	0.03	0.1443	0.0071	0.0203	0.0008	128.6	6.3	125.5	5.2	98
H-104A	#52	0.21	0.12	0.1482	0.0071	0.0211	0.0008	131.5	6.3	130.2	5.2	99
H-104A	#53	0.20	0.12	0.1289	0.0044	0.0188	0.0007	115.9	5.3	115.8	4.5	100
H-104A	#54	0.11	0.07	0.1469	0.0065	0.0209	0.0007	132.7	6.5	131.3	4.7	99
H-104A	#55	0.31	0.20	0.1638	0.0105	0.0215	0.0004	146.3	12.2	132.2	3.1	90
H-104A	#56	0.12	0.07	0.1499	0.0178	0.0219	0.0008	147.4	11.9	134.2	5.2	91
H-104A	#57	0.18	0.11	0.1273	0.0051	0.0185	0.0005	112.8	4.4	113.5	3.4	101
H-104A	#58	0.23	0.14	0.1302	0.0059	0.0184	0.0003	121.6	4.9	113.3	2.7	93
H-104A	#59	0.12	0.07	0.1636	0.0072	0.0206	0.0006	141.8	6.2	127.3	4.0	90
H-104A	#60	0.06	0.04	0.1515	0.0052	0.0209	0.0007	132.9	5.1	128.1	4.4	96
H-104A	#61	0.04	0.07	0.1924	0.0079	0.0231	0.0006	153.6	15.1	142.0	4.2	92
H-104A	#62	0.41	0.23	0.1863	0.0108	0.0246	0.0006	166.0	6.8	151.6	4.5	91
H-104A	#63	0.57	0.34	0.1012	0.0054	0.0142	0.0004	89.7	4.2	87.1	2.9	97
H-104A	#64	0.28	0.18	0.1409	0.0073	0.0202	0.0006	123.4	5.9	124.3	4.3	101
H-104A	#65	0.44	0.46	0.2012	0.0080	0.0277	0.0007	175.0	6.6	171.2	5.1	98
H-104A	#66	0.30	0.17	0.7477	0.0247	0.0924	0.0008	574.9	22.2	553.7	9.0	96
H-104A	#67	0.32	0.19	0.1272	0.0056	0.0187	0.0006	112.4	5.1	115.0	3.9	102
H-104A	#68	0.39	0.24	0.1341	0.0095	0.0191	0.0005	124.3	7.0	117.5	3.4	95
H-104A	#69	0.12	0.07	0.1553	0.0067	0.0219	0.0004	139.8	5.6	134.2	3.2	96
H-104A	#70	0.15	0.09	0.1524	0.0081	0.0222	0.0010	142.3	7.9	136.3	6.3	96
H-104A	#71	0.39	0.24	0.1234	0.0054	0.0174	0.0005	108.0	4.3	107.0	3.3	99
H-104A	#72	0.29	0.17	0.1324	0.0101	0.0189	0.0007	117.7	7.0	115.7	4.6	98
H-104A	#73	0.09	0.08	0.1651	0.0153	0.0201	0.0005	149.5	9.9	127.5	3.5	85
H-104A	#74	0.97	0.54	1.6089	0.0804	0.1581	0.0041	907.7	20.6	901.7	24.4	99
H-104A	#75	0.05	0.03	0.1404	0.0039	0.0203	0.0006	121.5	4.6	121.6	3.9	100
H-104A	#76	0.03	0.04	0.1678	0.0049	0.0214	0.0005	148.1	4.8	130.4	3.6	88
H-104A	#77	0.27	0.12	0.7373	0.0288	0.0909	0.0035	560.6	22.7	533.4	20.5	95
H-104A	#78	0.53	0.25	0.1981	0.0153	0.0230	0.0005	166.4	7.6	141.1	3.6	85
H-104A	#79	0.35	0.24	1.3065	0.0340	0.1149	0.0030	795.2	17.8	736.1	20.2	93
H-104A	#80	0.42	0.25	0.1009	0.0033	0.0142	0.0004	90.2	3.7	89.3	3.0	99
H-104A	#81	0.45	0.26	0.1416	0.0058	0.0198	0.0007	134.6	6.3	121.8	4.5	90
H-104A	#82	0.23	0.15	0.1437	0.0057	0.0197	0.0004	126.5	3.8	121.1	2.6	96
H-104A	#83	0.08	0.05	0.1520	0.0040	0.0228	0.0004	142.3	5.2	139.5	3.2	98
H-104A	#84	0.27	0.17	0.1321	0.0045	0.0182	0.0002	118.7	4.6	111.5	1.8	94
H-104A	#85	0.25	0.14	0.1509	0.0198	0.0204	0.0015	136.4	10.7	124.1	8.9	91
H-104A	#86	0.08	0.05	0.1423	0.0064	0.0206	0.0006	126.4	4.5	126.0	4.1	100
H-104A	#87	0.37	0.25	0.1327	0.0049	0.0188	0.0006	115.0	4.5	115.1	4.1	100
H-104A	#88	0.04	0.03	0.1460	0.0051	0.0205	0.0008	127.6	5.4	125.8	5.0	99
H-104A	#89	0.22	0.13	0.1340	0.0056	0.0193	0.0007	117.5	6.6	117.1	4.5	100
H-104A	#90	0.27	0.17	0.1292	0.0062	0.0185	0.0006	114.8	4.7	114.7	3.9	100
H-104A	#91	0.82	0.43	0.7331	0.0323	0.0924	0.0023	545.2	15.7	549.7	14.8	101
H-104A	#92	0.05	0.03	0.1456	0.0067	0.0208	0.0007	130.7	5.4	129.4	4.7	99
H-104A	#93	0.05	0.03	0.1448	0.0051	0.0204	0.0007	125.5	5.1	125.1	4.3	100
H-104A	#94	0.22	0.14	0.1228	0.0055	0.0176	0.0007	115.5	6.5	110.7	4.4	96
H-104A	#95	0.66	0.35	0.1741	0.0207	0.0213	0.0006	158.5	11.7	130.5	4.1	82
H-104A	#96	0.07	0.05	0.1586	0.0133	0.0222	0.0007	163.9	17.4	134.9	4.7	82
H-104A	#97	0.32	0.19	0.1320	0.0063	0.0189	0.0006	115.2	5.0	116.5	4.0	101
H-104A	#98	0.24	0.16	0.0851	0.0026	0.0117	0.0003	79.6	4.3	71.6	2.1	90
H-104A	#99	0.09	0.05	0.1475	0.0066	0.0206	0.0006	129.2	4.9	128.4	3.9	99

Table A.49: Zrn U-Pb age dataset

Zircon U-Pb data

Sample	Spot #	Th/U[a]	$^{208}Pb/^{206}Pb$	Ratios				Ages (Ma)				Cc[c]
				$^{207}Pb/^{235}U$[a]	2 σ[b]	$^{206}Pb/^{238}U$[a]	2 σ[b]	$^{207}Pb/^{235}U$	2 σ	$^{206}Pb/^{238}U$	2 σ	%
H-104A	#100	0.08	0.07	0.1406	0.0174	0.0202	0.0005	139.4	14.7	125.0	3.6	90
H-104A	#101	0.10	0.07	0.1430	0.0074	0.0204	0.0005	134.1	7.4	125.2	3.3	93
H-104A	#102	0.03	0.02	0.6247	0.0194	0.0773	0.0022	455.6	12.6	460.6	13.8	101
H-104A	#103	0.27	0.16	0.1422	0.0054	0.0201	0.0006	122.8	4.9	123.1	4.1	100
H-104A	#104	0.32	0.19	0.1494	0.0084	0.0214	0.0007	129.2	6.1	129.5	4.7	100
H-104A	#105	0.06	0.04	0.1484	0.0042	0.0210	0.0004	128.6	4.0	128.6	2.8	100
H-104A	#106	0.19	0.11	0.1522	0.0081	0.0214	0.0007	132.6	5.5	131.3	4.6	99
H-104A	#107	0.50	0.31	0.1360	0.0076	0.0189	0.0006	117.7	5.2	116.0	3.7	99
H-104A	#108	0.07	0.04	0.1521	0.0038	0.0216	0.0005	135.9	4.7	132.8	3.5	98
H-104A	#109	0.66	0.40	0.1283	0.0058	0.0180	0.0004	118.0	5.1	111.7	2.7	95
H-104A	#110	0.25	0.14	0.1475	0.0094	0.0213	0.0007	140.0	7.9	133.7	4.8	96
H-104A	#111	0.41	0.34	0.3414	0.0277	0.0443	0.0020	281.1	12.4	268.5	12.1	96
H-104A	#112	0.08	0.05	0.1424	0.0043	0.0206	0.0004	124.8	3.8	126.6	3.0	101
H-104A	#113	0.06	0.04	0.1559	0.0062	0.0218	0.0005	137.5	4.6	131.3	3.2	95
H-104A	#114	0.05	0.03	0.1384	0.0080	0.0197	0.0005	126.5	7.0	122.1	3.5	97
Mendanxiang												
H-9	#1	0.42	0.23	0.7168	0.0401	0.0909	0.0027	541.0	18.2	540.9	15.6	100
H-9	#2	0.35	0.20	0.1394	0.0065	0.0206	0.0009	128.8	7.3	126.7	5.5	98
H-9	#3	0.21	0.12	0.1326	0.0066	0.0199	0.0008	124.2	6.1	122.6	4.6	99
H-9	#4	0.36	0.22	0.1529	0.0132	0.0221	0.0008	140.4	7.9	135.6	4.7	97
H-9	#5	0.14	0.08	1.7453	0.1798	0.1638	0.0052	935.9	27.9	921.3	27.5	98
H-9	#6	0.45	0.26	0.1377	0.0070	0.0199	0.0007	123.3	5.0	119.1	4.0	97
H-9	#7	0.46	0.28	0.1698	0.0138	0.0181	0.0007	141.3	11.5	111.5	4.4	79
H-9	#8	0.39	0.23	0.1354	0.0072	0.0195	0.0006	123.7	6.2	120.0	3.8	97
H-9	#9	0.23	0.13	0.1474	0.0046	0.0213	0.0005	133.4	4.1	130.8	2.8	98
H-9	#10	0.16	0.10	1.1397	0.0422	0.1288	0.0036	761.6	18.4	754.7	20.0	99
H-9	#11	0.07	0.04	2.0492	0.0861	0.1980	0.0071	1111.3	28.1	1126.5	37.3	101
H-9	#12	0.19	0.10	16.4904	1.3192	0.5839	0.0169	2848.4	33.0	2815.2	66.5	99
H-9	#13	0.25	0.13	1.5293	0.0719	0.1556	0.0036	922.4	19.0	901.6	19.4	98
H-9	#14	0.35	0.22	0.1777	0.0140	0.0221	0.0008	156.8	11.5	136.1	5.1	87
H-9	#15	0.23	0.13	0.1320	0.0065	0.0191	0.0006	114.9	5.2	110.8	3.5	96
H-9	#16	0.31	0.50	0.4424	0.1075	0.0195	0.0011	376.1	49.6	120.0	6.9	32
H-9	#17	0.36	0.21	0.1259	0.0064	0.0187	0.0006	119.0	5.3	115.4	3.8	97
H-9	#18	0.04	0.04	0.2486	0.0291	0.0311	0.0013	211.8	14.8	183.4	7.4	87
H-9	#19	0.29	0.17	0.1288	0.0120	0.0189	0.0008	130.2	9.2	116.5	4.6	89
H-9	#20	0.22	0.13	0.1246	0.0102	0.0191	0.0007	124.8	9.6	117.8	4.1	94
H-9	#21	0.15	0.08	0.1462	0.0066	0.0221	0.0008	133.4	5.4	132.7	4.9	99
H-9	#22	0.39	0.21	0.1249	0.0065	0.0190	0.0008	117.5	6.6	114.5	5.0	97
H-9	#23	0.78	0.42	1.7832	0.2354	0.1813	0.0056	1044.4	23.8	1012.8	29.1	97
H-9	#24	0.32	0.18	0.1301	0.0072	0.0192	0.0007	121.4	5.7	118.6	4.1	98
H-9	#25	0.10	0.06	0.1326	0.0107	0.0197	0.0008	125.6	8.5	121.8	5.1	97
H-9	#26	0.24	0.13	0.7729	0.0340	0.0953	0.0026	584.4	15.7	568.3	14.7	97
H-9	#27	0.37	0.21	0.1207	0.0087	0.0183	0.0008	110.9	6.9	110.2	4.6	99
H-9	#28	0.60	0.34	0.1294	0.0078	0.0191	0.0007	119.7	5.3	115.3	3.9	96
H-9	#29	0.12	0.07	0.1317	0.0045	0.0195	0.0006	122.0	4.4	120.7	3.8	99
H-9	#30	0.25	0.14	0.1335	0.0068	0.0194	0.0007	126.5	6.1	119.8	4.4	95
H-9	#31	0.31	0.18	0.1215	0.0050	0.0180	0.0006	109.4	4.2	108.4	3.5	99
H-9	#32	0.40	0.23	0.1293	0.0045	0.0184	0.0006	115.8	4.9	110.6	3.4	96
H-9	#33	0.46	0.26	0.4569	0.0260	0.0611	0.0019	370.1	12.2	370.3	11.2	100
H-9	#34	0.33	0.20	0.6179	0.0241	0.0775	0.0036	502.9	26.5	466.2	20.7	93
H-9	#35	0.17	0.09	1.4294	0.0700	0.1526	0.0064	890.7	27.0	888.4	35.0	100
H-9	#36	0.10	0.07	0.1532	0.0052	0.0225	0.0008	143.8	5.9	139.0	4.8	97
H-9	#37	0.09	0.05	1.5993	0.0592	0.1625	0.0062	941.0	26.1	942.2	33.4	100
H-9	#38	0.34	0.18	0.1261	0.0053	0.0190	0.0006	117.9	4.8	117.5	3.8	100
H-9	#39	0.20	0.11	0.1192	0.0049	0.0179	0.0007	110.9	4.7	110.6	4.3	100
H-9	#40	0.42	0.25	0.1298	0.0086	0.0187	0.0008	118.9	7.3	115.9	5.1	97
H-9	#41	0.36	0.20	0.1374	0.0078	0.0191	0.0007	122.9	5.2	118.3	4.1	96
H-9	#42	0.12	0.09	0.5780	0.0410	0.0618	0.0021	426.3	24.3	375.0	12.4	88
H-9	#43	0.08	0.06	0.1724	0.0121	0.0211	0.0007	147.0	10.0	130.8	4.3	89
H-9	#44	0.03	0.02	0.1427	0.0056	0.0211	0.0009	133.9	6.3	130.6	5.8	98

Table A.50: Zrn U-Pb age dataset

Zircon U-Pb data

Sample	Spot #	Th/U[a]	$^{208}Pb/^{206}Pb$	Ratios				Ages (Ma)				Cc[c]
				$^{207}Pb/^{235}U$[a]	2 σ[b]	$^{206}Pb/^{238}U$[a]	2 σ[b]	$^{207}Pb/^{235}U$	2 σ	$^{206}Pb/^{238}U$	2 σ	%
H-9	#45	0.31	0.18	0.1237	0.0069	0.0180	0.0007	115.9	5.7	111.8	4.3	96
H-9	#46	0.31	0.19	0.1391	0.0118	0.0191	0.0008	125.5	9.5	118.2	5.2	94
H-9	#47	0.22	0.12	0.4075	0.0139	0.0535	0.0018	310.0	10.2	293.8	9.8	95
H-9	#48	0.18	0.10	5.0833	0.2440	0.3290	0.0105	1795.6	32.5	1785.9	50.1	99
H-9	#49	0.32	0.17	1.5678	0.1019	0.1593	0.0048	936.1	23.5	926.3	25.9	99
H-9	#50	0.35	0.18	1.1804	0.0472	0.1305	0.0051	775.0	23.0	768.8	28.3	99
H-9	#51	0.38	0.22	0.1305	0.0073	0.0188	0.0006	118.5	5.7	116.5	3.7	98
H-9	#52	0.39	0.21	0.1282	0.0069	0.0188	0.0008	119.4	5.2	116.8	4.6	98
H-9	#53	0.24	0.13	10.8049	0.8428	0.4808	0.0250	2445.5	59.0	2469.9	107.6	101
H-9	#54	0.23	0.13	0.1423	0.0064	0.0199	0.0007	131.7	5.1	123.5	4.0	94
H-9	#55	0.34	0.20	0.1491	0.0106	0.0194	0.0009	129.4	9.8	117.1	5.1	90
H-9	#56	0.36	0.21	0.3256	0.0163	0.0454	0.0012	309.0	12.3	305.3	7.8	99
H-9	#57	0.49	0.27	0.1321	0.0061	0.0189	0.0007	133.1	6.5	128.4	4.8	96
H-9	#58	0.41	0.23	0.1280	0.0064	0.0193	0.0007	121.1	5.1	119.7	4.3	99
H-9	#59	0.46	0.26	0.1281	0.0074	0.0190	0.0008	118.8	6.0	118.0	5.1	99
H-9	#60	0.55	0.30	0.6695	0.0315	0.0832	0.0031	515.9	17.1	510.8	18.2	99
H-9	#61	0.16	0.09	1.2096	0.0423	0.1354	0.0050	790.3	22.2	797.0	27.8	101
H-9	#62	0.43	0.25	0.1691	0.0069	0.0243	0.0004	164.4	5.3	150.8	2.4	92
H-9	#63	0.15	0.09	0.1552	0.0068	0.0224	0.0008	158.3	6.8	155.2	5.7	98
H-9	#64	0.31	0.17	1.9032	0.1066	0.1835	0.0062	1069.5	26.8	1058.5	33.3	99
H-9	#65	0.26	0.15	0.1233	0.0088	0.0179	0.0006	116.0	5.9	113.0	4.0	97
H-9	#66	0.19	0.11	0.1223	0.0043	0.0182	0.0006	114.9	4.4	113.3	3.6	99
H-9	#67	0.34	0.20	0.1279	0.0054	0.0191	0.0006	119.1	4.4	118.5	3.8	99
H-9	#68	0.16	0.09	2.2229	0.0756	0.2001	0.0066	1167.4	25.3	1147.1	34.8	98
H-9	#69	0.33	0.18	0.1419	0.0092	0.0193	0.0007	126.3	6.8	120.2	4.5	95
H-9	#70	0.13	0.21	0.4085	0.0780	0.0221	0.0008	253.1	53.6	136.6	5.1	54
H-9	#71	0.02	0.01	1.5444	0.0865	0.1590	0.0049	986.3	22.3	1005.1	28.9	102
H-9	#72	0.18	0.10	0.4409	0.0150	0.0581	0.0017	359.3	11.0	354.5	10.0	99
H-9	#73	0.19	0.11	2.0324	0.0732	0.1940	0.0068	1121.8	26.1	1115.5	36.0	99
H-9	#74	0.54	0.32	0.1302	0.0035	0.0192	0.0004	124.4	3.4	119.1	2.2	96
H-9	#75	0.06	0.05	0.2635	0.0084	0.0370	0.0007	252.9	6.5	232.9	4.1	92
H-9	#76	0.25	0.13	13.0129	0.2733	0.5309	0.0080	2688.5	17.1	2682.9	33.0	100
H-9	#77	0.20	0.11	2.1375	0.1411	0.1983	0.0056	1249.7	26.2	1258.6	32.1	101
H-9	#78	0.21	0.10	0.1432	0.0135	0.0210	0.0010	135.8	8.3	130.5	6.5	96
H-9	#79	0.37	0.22	0.1034	0.0049	0.0147	0.0006	94.5	5.0	91.8	3.9	97
H-9	#80	0.25	0.13	1.6216	0.0632	0.1696	0.0073	970.7	30.5	986.4	39.4	102
H-9	#81	0.24	0.14	0.1360	0.0091	0.0192	0.0008	121.7	7.3	116.6	4.7	96
H-9	#82	0.35	0.19	3.7416	0.2544	0.2742	0.0101	1559.9	34.0	1527.6	50.5	98
H-9	#83	0.27	0.14	2.6917	0.1803	0.2273	0.0082	1308.1	34.4	1291.0	42.3	99
H-9	#84	0.03	0.02	5.1479	0.2059	0.3355	0.0104	1829.1	29.2	1824.9	49.5	100
H-9	#85	0.33	0.20	0.1396	0.0156	0.0188	0.0008	121.6	7.6	119.0	5.1	98
H-9	#86	0.27	0.15	0.2451	0.0115	0.0339	0.0012	216.0	7.8	209.8	7.0	97
H-9	#87	0.15	0.09	0.1127	0.0066	0.0161	0.0006	104.8	4.4	100.2	3.6	96
H-9	#88	0.18	0.10	0.4966	0.0184	0.0659	0.0019	407.6	12.5	401.9	11.3	99
H-9	#89	0.24	0.13	0.1254	0.0049	0.0182	0.0006	114.8	4.1	113.4	3.7	99
H-9	#90	0.97	0.53	0.1146	0.0073	0.0173	0.0006	106.6	5.0	105.4	3.9	99
H-9	#91	0.28	0.16	0.1339	0.0110	0.0192	0.0011	125.3	8.6	120.2	6.8	96
H-9	#92	0.29	0.16	0.1382	0.0098	0.0200	0.0008	127.8	6.5	124.6	5.1	97
H-9	#93	0.21	0.12	0.2730	0.0117	0.0382	0.0015	237.8	9.6	236.0	8.8	99
H-9	#94	0.11	0.06	1.8485	0.0850	0.1790	0.0059	1054.4	25.2	1038.8	31.7	99
H-9	#95	0.29	0.16	0.1254	0.0045	0.0183	0.0004	112.9	3.4	110.5	2.5	98
H-9	#96	0.27	0.14	12.9699	0.3113	0.4786	0.0048	2625.6	18.0	2488.3	20.7	95
H-9	#97	0.43	0.24	0.1367	0.0075	0.0204	0.0005	134.0	5.3	131.5	3.3	98
H-9	#98	0.16	0.09	0.1265	0.0048	0.0188	0.0007	119.3	5.3	115.8	4.5	97
H-9	#99	0.06	0.03	0.1580	0.0070	0.0224	0.0011	144.6	6.9	139.6	6.5	97
H-9	#100	0.47	0.27	0.3210	0.0161	0.0417	0.0014	269.4	10.7	257.4	8.6	96
H-9	#101	0.32	0.16	6.3163	0.2211	0.3778	0.0136	2052.8	35.9	2026.6	62.9	99
H-9	#102	0.28	0.16	2.9149	0.1341	0.2304	0.0090	1423.5	31.9	1348.4	47.6	95
H-9	#103	0.46	0.26	0.1455	0.0106	0.0212	0.0009	131.5	7.3	131.4	5.7	100
H-9	#104	0.41	0.24	0.1165	0.0044	0.0176	0.0005	109.9	4.2	110.0	3.4	100
H-9	#105	0.42	0.22	4.1547	0.2368	0.2979	0.0086	1662.8	28.2	1648.5	42.3	99
H-9	#106	0.40	0.22	1.5093	0.0528	0.1533	0.0048	913.0	21.3	900.8	26.1	99

Table A.51: Zrn U-Pb age dataset

Zircon U-Pb data

Sample	Spot #	Th/U[a]	^{208}Pb/^{206}Pb	Ratios				Ages (Ma)				Cc[c]
				^{207}Pb/^{235}U[a]	2 σ[b]	^{206}Pb/^{238}U[a]	2 σ[b]	^{207}Pb/^{235}U	2 σ	^{206}Pb/^{238}U	2 σ	%
H-9	#107	0.08	0.08	0.5565	0.0456	0.0589	0.0041	430.9	26.7	360.9	24.6	84
H-9	#108	0.24	0.14	0.1955	0.0111	0.0279	0.0010	177.2	7.5	171.4	6.3	97
H-9	#109	0.37	0.22	0.1325	0.0058	0.0188	0.0007	126.2	6.0	114.3	4.1	91
H-9	#110	0.09	0.04	0.3251	0.0179	0.0419	0.0019	281.4	12.9	262.4	11.8	93
H-9	#111	0.24	0.19	0.2082	0.0587	0.0213	0.0010	199.2	38.1	135.8	6.2	68
H-9	#112	0.43	0.24	0.1762	0.0053	0.0219	0.0006	137.4	8.6	134.6	3.6	98
H-9	#113	0.35	0.20	0.1286	0.0076	0.0188	0.0008	121.6	6.1	117.4	4.7	97
H-9	#114	0.18	0.10	1.4434	0.0592	0.1476	0.0055	908.3	24.9	892.5	30.9	98
H-9	#115	0.25	0.13	4.2121	0.1643	0.2969	0.0104	1668.0	33.3	1665.5	51.6	100
H-17A	#1	0.06	0.04	0.1501	0.0036	0.0212	0.0004	143.0	5.6	133.9	2.5	94
H-17A	#2	0.51	0.23	0.1153	0.0056	0.0168	0.0007	113.8	6.2	108.4	4.6	95
H-17A	#3	0.36	0.16	0.1311	0.0085	0.0185	0.0008	126.1	5.6	116.8	4.7	93
H-17A	#4	0.19	0.11	1.2372	0.1126	0.1278	0.0101	810.9	46.9	768.7	57.5	95
H-17A	#5	0.10	0.05	0.1408	0.0062	0.0196	0.0006	134.2	5.7	125.3	4.0	93
H-17A	#6	0.28	0.13	0.1277	0.0049	0.0189	0.0006	128.2	4.5	119.3	3.7	93
H-17A	#7	0.33	0.17	0.1356	0.0052	0.0188	0.0003	130.1	5.3	118.5	2.2	91
H-17A	#8	0.50	0.26	0.1424	0.0046	0.0205	0.0004	137.9	4.8	130.8	2.8	95
H-17A	#9	0.15	0.08	0.7637	0.0199	0.0941	0.0025	575.8	14.2	570.0	14.7	99
H-17A	#10	0.07	0.10	0.1925	0.0110	0.0231	0.0003	217.0	15.8	145.7	2.0	67
H-17A	#11	0.45	0.24	0.1371	0.0063	0.0205	0.0004	135.9	3.8	130.3	2.6	96
H-17A	#12	0.42	0.22	0.1377	0.0040	0.0198	0.0006	135.4	7.5	125.2	4.0	92
H-17A	#13	0.42	0.23	0.1368	0.0079	0.0201	0.0003	134.1	4.2	127.6	2.1	95
H-17A	#14	0.09	0.05	0.2844	0.0205	0.0360	0.0022	259.4	16.8	226.8	13.6	87
H-17A	#15	0.21	0.12	0.1363	0.0136	0.0194	0.0007	141.8	13.5	123.4	4.3	87
H-17A	#16	0.26	0.12	0.1279	0.0082	0.0180	0.0005	122.7	5.1	113.4	3.0	92
H-17A	#17	0.28	0.11	0.1494	0.0142	0.0204	0.0011	142.3	9.9	130.7	6.9	92
H-17A	#18	0.29	0.15	0.1245	0.0105	0.0180	0.0010	121.7	8.1	115.2	6.6	95
H-17A	#19	0.20	0.10	5.3519	0.4763	0.3240	0.0110	1822.2	61.1	1801.1	53.6	99
H-17A	#20	0.32	0.14	0.1353	0.0050	0.0201	0.0005	135.2	4.1	127.6	3.3	94
H-17A	#21	0.30	0.16	0.1219	0.0083	0.0174	0.0008	119.3	6.6	114.4	5.1	96
H-17A	#22	0.63	0.30	1.2217	0.0562	0.1295	0.0044	799.6	21.2	781.7	25.1	98
H-17A	#23	0.49	0.18	0.0535	0.0344	0.0179	0.0021	189.1	21.6	179.3	20.5	95
H-17A	#24	0.53	0.27	0.1242	0.0051	0.0189	0.0007	122.1	6.2	120.6	4.5	99
H-17A	#25	0.59	0.31	0.1260	0.0065	0.0192	0.0007	123.3	5.7	122.0	4.1	99
H-17A	#26	0.05	0.03	0.1404	0.0083	0.0208	0.0007	135.1	5.1	132.4	4.7	98
H-17A	#27	0.25	0.13	0.1235	0.0051	0.0181	0.0006	116.0	4.5	115.1	3.8	99
H-17A	#28	0.28	0.14	0.1293	0.0088	0.0190	0.0008	127.3	6.1	122.4	4.9	96
H-17A	#29	0.36	0.19	0.1314	0.0045	0.0190	0.0005	125.7	4.6	120.9	3.1	96
H-17A	#30	0.36	0.15	0.1251	0.0058	0.0183	0.0009	123.1	6.2	120.1	5.6	98
H-17A	#31	0.42	0.19	0.1398	0.0073	0.0194	0.0010	135.3	7.9	125.4	6.6	93
H-17A	#32	0.49	0.25	0.1355	0.0073	0.0199	0.0006	133.1	6.0	126.0	4.0	95
H-17A	#33	0.62	0.32	1.5962	0.1053	0.1339	0.0082	955.0	43.0	840.6	48.3	88
H-17A	#34	0.28	0.16	0.1513	0.0077	0.0215	0.0005	152.8	11.7	137.0	2.8	90
H-17A	#35	0.24	0.13	0.1226	0.0094	0.0184	0.0009	124.0	7.5	117.3	5.6	95
H-17A	#36	0.62	0.33	0.1380	0.0131	0.0196	0.0009	139.0	9.4	125.1	5.6	90
H-17A	#37	0.44	0.24	0.1316	0.0067	0.0193	0.0008	124.5	5.6	123.5	5.0	99
H-17A	#38	0.50	0.26	0.1456	0.0082	0.0198	0.0009	138.1	7.4	125.8	6.0	91
H-17A	#39	0.37	0.18	3.4531	0.1727	0.2462	0.0086	1537.8	32.2	1418.6	44.7	92
H-17A	#40	0.31	0.17	0.1171	0.0052	0.0172	0.0008	115.4	5.7	112.1	5.0	97
H-17A	#41	0.27	0.14	0.1129	0.0060	0.0174	0.0008	113.3	5.6	112.9	5.3	100
H-17A	#42	0.32	0.18	0.1308	0.0064	0.0189	0.0009	125.7	6.6	121.6	5.9	97
H-17A	#43	0.62	0.29	0.1307	0.0072	0.0182	0.0008	121.9	6.5	116.3	5.1	95
H-17A	#44	0.43	0.31	0.1282	0.0067	0.0182	0.0008	124.5	5.8	117.8	5.1	95
H-17A	#45	0.18	0.09	0.1401	0.0052	0.0203	0.0008	131.5	5.4	129.3	4.9	98
H-17A	#46	0.42	0.23	0.1689	0.0103	0.0195	0.0010	156.9	9.1	127.0	6.2	81
H-17A	#47	0.32	0.16	0.1407	0.0075	0.0198	0.0010	132.6	7.7	125.9	6.5	95
H-17A	#48	0.21	0.10	2.5043	0.1453	0.2133	0.0113	1249.2	40.3	1244.5	60.3	100
H-17A	#49	0.47	0.26	0.1348	0.0089	0.0203	0.0006	131.9	5.7	129.7	4.1	98
H-17A	#50	0.53	0.26	0.1317	0.0079	0.0185	0.0007	124.1	5.9	118.1	4.4	95
H-17A	#51	0.33	0.18	0.1309	0.0080	0.0193	0.0008	125.4	6.7	124.1	5.0	99
H-17A	#52	0.41	0.20	0.7013	0.0224	0.0881	0.0028	542.1	16.1	543.6	16.7	100

Table A.52: Zrn U-Pb age dataset

Zircon U-Pb data

Sample	Spot #	Th/U[a]	^{208}Pb/^{206}Pb	Ratios				Ages (Ma)				Cc[c]
				^{207}Pb/^{235}U[a]	2 σ[b]	^{206}Pb/^{238}U[a]	2 σ[b]	^{207}Pb/^{235}U	2 σ	^{206}Pb/^{238}U	2 σ	%
H-17A	#53	0.06	0.03	0.3962	0.0147	0.0550	0.0020	344.1	12.0	344.9	12.4	100
H-17A	#54	0.06	0.03	0.3994	0.0176	0.0541	0.0020	344.3	12.3	345.2	12.4	100
H-17A	#55	0.05	0.03	0.3966	0.0151	0.0541	0.0019	338.7	11.6	339.5	11.9	100
H-17A	#56	0.08	0.05	0.4092	0.0168	0.0550	0.0023	348.3	13.4	344.5	13.8	99
H-17A	#57	0.08	0.04	0.4052	0.0182	0.0550	0.0023	343.5	12.9	344.5	13.8	100
H-17A	#58	0.40	0.22	0.1233	0.0081	0.0191	0.0009	131.9	7.1	131.0	6.2	99
H-17A	#59	0.18	0.10	0.1242	0.0065	0.0184	0.0009	124.4	6.5	126.1	6.2	101
H-17A	#60	0.07	0.04	0.1398	0.0064	0.0206	0.0008	144.7	6.2	141.3	5.5	98
H-17A	#61	0.70	0.33	0.2009	0.0241	0.0198	0.0007	184.8	16.9	138.8	4.5	75
H-17A	#62	0.39	0.22	0.1568	0.0053	0.0215	0.0006	161.1	6.0	147.0	4.1	91
H-17A	#63	0.15	0.07	0.1474	0.0050	0.0201	0.0007	148.2	9.0	137.1	4.7	93
H-17A	#64	0.50	0.18	0.1479	0.0178	0.0191	0.0014	144.3	12.7	132.3	10.0	92
H-17A	#65	0.52	0.28	0.1385	0.0104	0.0180	0.0009	131.8	9.3	124.2	6.2	94
H-17A	#66	0.44	0.23	0.1244	0.0056	0.0182	0.0008	128.2	5.7	125.2	5.2	98
H-17A	#67	0.38	0.22	0.1286	0.0086	0.0192	0.0012	130.4	8.9	132.4	8.0	102
H-17A	#68	0.06	0.03	0.4356	0.0144	0.0574	0.0016	390.9	10.4	388.1	10.6	99
H-17A	#69	0.44	0.24	0.1122	0.0047	0.0165	0.0007	115.6	5.6	114.1	5.1	99
H-17A	#70	0.43	0.21	0.1249	0.0060	0.0184	0.0005	136.4	5.0	129.6	3.6	95
H-17A	#71	0.41	0.18	0.5128	0.1790	0.0759	0.0037	611.2	107.9	509.3	24.0	83
H-17A	#72	0.40	0.25	0.1328	0.0084	0.0203	0.0005	152.2	7.4	140.0	3.7	92
H-17A	#73	0.70	0.29	0.1788	0.0125	0.0224	0.0004	188.4	11.6	154.6	3.2	82
H-17A	#74	0.66	0.29	0.1042	0.0094	0.0138	0.0009	105.9	11.3	95.8	6.3	90
H-17A	#75	0.47	0.24	0.1206	0.0083	0.0184	0.0007	127.9	6.1	126.6	5.0	99
H-17A	#76	0.36	0.18	0.1287	0.0072	0.0184	0.0007	136.2	6.4	127.3	4.7	93
H-17A	#77	0.41	0.24	2.2820	0.4085	0.1964	0.0084	1320.1	93.6	1253.7	49.2	95
H-17A	#78	1.08	0.40	1.6703	0.0818	0.1672	0.0040	1100.4	31.4	1078.6	24.9	98
H-17A	#79	0.35	0.16	0.1577	0.0047	0.0205	0.0004	158.1	6.0	142.3	3.1	90
H-17A	#80	0.54	0.25	0.1479	0.0040	0.0222	0.0005	157.4	3.9	153.0	3.3	97
H-17A	#81	0.19	0.12	0.1472	0.0032	0.0199	0.0005	145.6	4.9	138.3	3.4	95
H-17A	#82	0.52	0.24	0.1569	0.0115	0.0208	0.0004	186.7	15.3	144.7	3.0	78
H-17A	#83	0.16	0.06	0.1503	0.0092	0.0208	0.0008	155.7	6.8	152.4	5.6	98
H-17A	#84	0.53	0.21	0.1254	0.0046	0.0191	0.0005	161.1	7.3	144.5	3.7	90
H-17A	#85	0.45	0.25	0.1321	0.0063	0.0188	0.0006	134.3	5.3	131.1	4.0	98
H-17A	#86	0.53	0.25	0.1525	0.0229	0.0176	0.0008	123.4	8.2	118.1	5.3	96
H-17A	#87	0.19	0.11	0.1292	0.0075	0.0192	0.0008	136.0	6.6	134.6	5.6	99
H-17A	#88	0.30	0.12	1.2132	0.0837	0.1284	0.0077	836.9	37.2	848.2	47.9	101
H-17A	#89	0.21	0.13	0.1905	0.0190	0.0188	0.0007	198.6	20.0	130.2	5.0	66
H-17A	#90	0.32	0.19	0.1265	0.0106	0.0175	0.0007	135.1	9.7	122.0	4.7	90
H-17A	#91	0.25	0.15	0.1161	0.0052	0.0173	0.0006	122.2	5.0	121.7	4.5	100
H-17A	#92	0.45	0.22	0.0958	0.0116	0.0123	0.0007	95.1	8.2	86.3	5.1	91
H-17A	#93	0.40	0.22	0.1212	0.0065	0.0178	0.0006	127.4	6.0	124.9	4.5	98
H-17A	#94	0.40	0.19	0.1204	0.0095	0.0180	0.0006	135.1	8.3	129.7	4.5	96
H-17A	#95	0.67	0.42	0.1263	0.0062	0.0172	0.0008	135.0	7.6	122.0	5.3	90
H-17A	#96	0.07	0.04	0.1446	0.0059	0.0211	0.0009	152.2	7.2	148.6	6.6	98
H-17A	#97	0.48	0.26	0.1228	0.0060	0.0182	0.0007	131.0	5.3	127.7	4.6	97
H-17A	#98	0.42	0.21	0.3306	0.0205	0.0340	0.0013	314.4	15.0	238.8	9.2	76
H-17A	#99	0.23	0.14	0.1168	0.0048	0.0166	0.0007	127.6	6.5	118.4	5.0	93
H-17A	#100	0.46	0.19	0.1358	0.0081	0.0202	0.0004	166.2	7.5	143.0	3.0	86
H-17A	#101	0.38	0.16	0.1690	0.0096	0.0206	0.0005	147.2	6.7	120.2	3.0	82
H-17A	#102	0.52	0.24	0.1338	0.0056	0.0175	0.0006	141.2	5.6	122.6	4.0	87
H-17A	#103	0.54	0.35	0.1720	0.0108	0.0173	0.0006	190.1	15.0	122.6	4.1	64
H-17A	#104	0.64	0.26	0.1601	0.0115	0.0182	0.0006	165.1	8.7	130.0	4.5	79
H-17A	#105	0.19	0.09	0.1286	0.0058	0.0167	0.0006	140.5	7.0	121.0	4.2	86
H-17A	#106	0.46	0.27	0.1204	0.0064	0.0170	0.0007	125.1	5.5	119.8	5.0	96
H-17A	#107	0.29	0.17	0.1210	0.0038	0.0185	0.0004	144.3	6.5	133.1	3.2	92
H-17A	#108	0.19	0.11	0.1132	0.0053	0.0166	0.0007	118.3	5.6	116.6	5.2	99
H-17A	#109	0.35	0.16	0.1320	0.0082	0.0176	0.0008	138.4	7.1	126.6	5.4	91
H-17A	#110	0.49	0.18	0.8600	0.0387	0.0959	0.0029	690.3	19.7	663.4	19.6	96
H-17A	#111	0.67	0.26	0.1243	0.0051	0.0168	0.0007	134.8	6.2	124.3	5.2	92
H-17A	#112	0.28	0.13	0.1251	0.0059	0.0171	0.0007	131.2	6.3	120.1	4.6	92
H-17A	#113	0.32	0.18	0.1238	0.0045	0.0180	0.0005	130.0	4.3	126.9	3.6	98
H-17A	#115	0.23	0.27	0.1292	0.0057	0.0185	0.0005	138.7	7.3	131.1	3.6	95

Table A.53: Zrn U-Pb age dataset

Zircon U-Pb data

Sample	Spot #	Th/U[a]	$^{208}Pb/^{206}Pb$	Ratios				Ages (Ma)				Cc[c]
				$^{207}Pb/^{235}U$[a]	2 σ[b]	$^{206}Pb/^{238}U$[a]	2 σ[b]	$^{207}Pb/^{235}U$	2 σ	$^{206}Pb/^{238}U$	2 σ	%
H-17A	#116	0.16	0.09	0.1109	0.0048	0.0166	0.0007	117.8	5.1	117.3	4.8	100
H-17A	#117	0.06	0.05	0.1465	0.0045	0.0215	0.0005	169.0	11.7	152.1	3.8	90
H-17A	#118	0.51	0.23	0.1153	0.0056	0.0168	0.0007	127.5	6.9	121.4	5.3	95
H-17A	#119	0.36	0.16	0.1311	0.0085	0.0185	0.0008	141.2	6.2	130.8	5.4	93
H-17A	#120	0.19	0.11	1.2372	0.1126	0.1278	0.0101	880.1	49.5	855.9	63.6	97
H-17A	#121	0.10	0.05	0.1408	0.0062	0.0196	0.0006	150.2	6.3	140.3	4.4	93
H-18	#1	0.33	0.17	0.1332	0.0089	0.0196	0.0007	123.2	6.5	123.9	4.4	101
H-18	#2	0.46	0.24	0.1292	0.0068	0.0196	0.0007	126.0	6.5	121.9	4.7	97
H-18	#3	0.28	0.15	0.1307	0.0064	0.0196	0.0007	124.0	5.7	121.9	4.7	98
H-18	#4	0.33	0.18	0.1235	0.0058	0.0189	0.0005	121.2	4.9	118.6	3.3	98
H-18	#5	0.34	0.19	0.1364	0.0075	0.0196	0.0012	131.2	9.1	125.3	7.7	96
H-18	#6	0.44	0.23	0.1377	0.0059	0.0190	0.0004	125.7	5.1	119.8	2.8	95
H-18	#7	0.35	0.19	0.1475	0.0069	0.0218	0.0006	131.8	5.2	131.6	3.9	100
H-18	#8	0.36	0.19	0.1380	0.0055	0.0199	0.0007	130.4	5.8	125.3	4.7	96
H-18	#9	0.32	0.17	0.1398	0.0109	0.0190	0.0005	127.1	6.6	119.6	3.6	94
H-18	#10	0.36	0.18	0.1364	0.0080	0.0193	0.0007	125.6	6.4	120.6	4.4	96
H-18	#11	0.21	0.10	0.8083	0.0420	0.0986	0.0025	608.3	16.6	597.1	14.8	98
H-18	#12	0.57	0.30	0.1272	0.0066	0.0191	0.0007	123.0	6.0	120.5	4.3	98
H-18	#13	0.51	0.26	0.1317	0.0082	0.0188	0.0006	125.5	7.0	118.6	4.1	95
H-18	#14	0.55	0.26	1.7957	0.0557	0.1748	0.0035	1036.5	18.4	1025.7	19.9	99
H-18	#15	0.11	0.05	0.1410	0.0066	0.0211	0.0009	134.6	6.3	133.5	5.6	99
H-18	#16	0.58	0.30	0.1358	0.0100	0.0186	0.0006	122.4	6.2	117.4	4.0	96
H-18	#17	0.38	0.19	0.1323	0.0054	0.0193	0.0006	122.5	4.5	122.3	3.8	100
H-18	#18	0.30	0.15	0.1314	0.0074	0.0196	0.0007	125.0	5.4	123.9	4.5	99
H-18	#19	0.11	0.06	0.1586	0.0189	0.0224	0.0003	151.8	5.8	143.1	2.3	94
H-18	#20	0.37	0.19	0.1450	0.0119	0.0193	0.0007	136.5	8.2	124.7	4.7	91
H-18	#21	0.30	0.15	0.1259	0.0076	0.0185	0.0005	120.8	5.6	117.8	3.4	98
H-18	#22	0.39	0.20	0.1367	0.0094	0.0196	0.0006	127.9	6.5	124.8	4.2	98
H-18	#23	0.41	0.21	0.1248	0.0057	0.0183	0.0006	119.6	5.2	119.3	3.9	100
H-18	#24	0.35	0.18	0.1301	0.0072	0.0184	0.0006	124.8	6.0	117.0	4.2	94
H-18	#25	0.31	0.16	0.1275	0.0079	0.0187	0.0007	121.8	7.3	118.9	4.6	98
H-18	#26	0.07	0.04	0.1534	0.0089	0.0227	0.0005	162.8	8.6	145.8	3.2	90
H-18	#27	0.35	0.18	0.1234	0.0059	0.0187	0.0005	120.4	4.6	119.1	3.5	99
H-18	#28	0.35	0.17	0.1246	0.0074	0.0186	0.0007	123.1	6.4	119.8	4.6	97
H-18	#29	0.36	0.19	0.1253	0.0074	0.0187	0.0007	122.9	5.9	119.9	4.4	98
H-18	#30	0.35	0.18	0.1272	0.0066	0.0188	0.0007	121.8	6.1	120.3	4.3	99
H-18	#31	0.22	0.12	0.1304	0.0077	0.0197	0.0007	129.4	6.5	123.4	4.5	95
H-18	#32	0.54	0.28	0.6717	0.0282	0.0833	0.0024	523.5	14.4	518.7	14.5	99
H-18	#33	0.35	0.18	0.1288	0.0076	0.0184	0.0006	123.9	5.9	118.4	3.6	96
H-18	#34	0.32	0.17	0.1341	0.0071	0.0190	0.0007	128.3	6.4	122.4	4.5	95
H-18	#35	0.39	0.20	0.1232	0.0048	0.0185	0.0006	116.5	5.0	115.9	3.9	99
H-18	#36	0.08	0.04	0.1447	0.0058	0.0213	0.0006	138.3	5.4	137.0	4.1	99
H-18	#37	0.35	0.18	0.1284	0.0071	0.0187	0.0007	124.5	6.2	120.2	4.5	97
H-18	#38	0.22	0.13	0.5396	0.0302	0.0692	0.0030	428.9	16.9	418.6	17.9	98
H-18	#39	0.38	0.20	0.4582	0.0664	0.0352	0.0029	543.7	56.3	319.7	25.9	59
H-18	#40	0.11	0.06	0.1324	0.0057	0.0202	0.0006	133.1	5.6	130.5	3.9	98
H-18	#42	0.06	0.03	0.1417	0.0045	0.0209	0.0006	137.6	4.9	135.3	4.2	98
H-18	#43	0.02	0.26	2.0628	0.5982	0.1157	0.0093	1320.1	156.2	722.3	54.9	55
H-18	#44	0.49	0.26	0.1262	0.0062	0.0187	0.0007	129.9	6.2	124.7	4.4	96
H-18	#46	0.54	0.30	0.1325	0.0073	0.0190	0.0008	127.3	5.9	125.0	5.1	98
H-18	#47	0.39	0.22	0.1233	0.0057	0.0193	0.0007	124.5	5.4	125.5	4.6	101
H-18	#48	0.25	0.14	0.1291	0.0071	0.0184	0.0006	125.5	5.9	119.9	3.8	96
H-18	#49	0.24	0.14	0.1338	0.0098	0.0191	0.0008	135.7	6.9	127.7	5.3	94
H-18	#50	0.05	0.03	0.1454	0.0054	0.0219	0.0009	145.8	7.1	142.7	5.8	98
H-18	#51	0.29	0.16	0.1324	0.0099	0.0195	0.0008	127.4	6.0	127.2	5.3	100
H-18	#52	0.29	0.15	0.1226	0.0048	0.0186	0.0008	123.4	5.4	121.7	4.9	99
H-18	#53	0.38	0.20	0.1298	0.0058	0.0203	0.0008	129.1	6.4	132.6	5.4	103
H-18	#54	0.23	0.13	0.1337	0.0080	0.0202	0.0008	132.7	6.0	132.4	5.0	100
H-18	#55	0.44	0.24	0.1316	0.0071	0.0196	0.0009	128.5	6.7	128.4	6.1	100
H-18	#56	0.43	0.24	0.1391	0.0081	0.0195	0.0007	138.0	6.7	129.4	4.7	94
H-18	#57	0.09	0.06	0.1473	0.0062	0.0217	0.0010	145.3	7.3	142.0	6.6	98

Table A.54: Zrn U-Pb age dataset

Zircon U-Pb data

Sample	Spot #	Th/U[a]	$^{208}Pb/^{206}Pb$	Ratios $^{207}Pb/^{235}U$[a]	2 σ[b]	$^{206}Pb/^{238}U$[a]	2 σ[b]	Ages (Ma) $^{207}Pb/^{235}U$	2 σ	$^{206}Pb/^{238}U$	2 σ	Cc[c] %
H-18	#58	0.34	0.18	0.1320	0.0077	0.0199	0.0011	131.5	8.0	134.6	7.1	102
H-18	#59	0.11	0.06	0.1370	0.0104	0.0214	0.0009	141.2	6.6	140.7	5.8	100
H-18	#60	0.33	0.18	0.1310	0.0097	0.0191	0.0008	126.0	6.9	125.9	5.4	100
H-18	#61	0.54	0.26	0.1887	0.0098	0.0193	0.0008	181.2	8.5	129.5	5.3	71
H-18	#62	0.30	0.16	0.1258	0.0068	0.0185	0.0008	124.8	6.1	122.1	5.1	98
H-18	#63	0.42	0.22	0.1345	0.0052	0.0201	0.0008	132.7	5.7	132.6	5.3	100
H-18	#64	0.11	0.06	0.7519	0.0481	0.0901	0.0036	585.7	20.7	574.4	22.0	98
H-18	#65	0.38	0.20	0.1388	0.0092	0.0203	0.0008	136.3	6.7	133.7	5.0	98
H-18	#66	0.06	0.04	0.1671	0.0092	0.0246	0.0013	164.4	8.5	162.4	8.3	99
H-18	#67	0.10	0.05	5.9206	0.3493	0.3613	0.0130	2030.7	35.7	2031.7	63.0	100
H-18	#68	0.29	0.16	0.1259	0.0076	0.0197	0.0009	131.2	7.7	130.0	5.7	99
H-18	#69	0.81	0.39	2.5801	0.3019	0.2015	0.0153	1282.4	64.6	1225.4	85.4	96
H-18	#70	0.40	0.20	0.1298	0.0066	0.0193	0.0008	131.0	6.0	129.1	5.2	99
H-18	#71	0.40	0.27	0.2139	0.0199	0.0184	0.0007	203.4	19.2	139.4	5.1	69
H-18	#72	0.41	0.22	0.1293	0.0069	0.0191	0.0007	131.2	6.5	127.0	4.8	97
H-18	#73	0.07	0.03	0.1425	0.0060	0.0215	0.0008	141.2	5.8	142.6	5.5	101
H-18	#74	0.34	0.18	0.1340	0.0080	0.0203	0.0008	134.9	6.3	134.8	5.1	100
H-18	#75	0.33	0.18	0.1243	0.0062	0.0191	0.0006	127.3	6.0	126.9	4.1	100
H-18	#76	0.42	0.21	0.1309	0.0063	0.0195	0.0007	131.4	6.7	130.2	4.9	99
H-18	#77	0.49	0.26	0.1304	0.0089	0.0192	0.0007	131.9	6.5	127.9	4.3	97
H-18	#78	0.33	0.18	0.1304	0.0068	0.0191	0.0007	131.2	6.2	127.3	4.8	97
H-18	#79	0.21	0.10	2.2078	0.1016	0.2068	0.0077	1226.3	29.6	1264.3	42.6	103
H-18	#80	0.04	0.02	0.1384	0.0072	0.0208	0.0008	139.9	5.9	138.8	5.5	99
H-18	#81	0.50	0.26	0.1209	0.0044	0.0180	0.0006	122.4	4.9	120.8	4.3	99
H-18	#82	0.32	0.16	0.1438	0.0060	0.0209	0.0004	143.0	6.2	137.1	2.3	96
H-18	#83	0.31	0.16	0.1340	0.0064	0.0196	0.0008	133.0	5.8	131.1	5.1	99
H-18	#84	0.26	0.13	0.1457	0.0063	0.0211	0.0007	143.3	5.5	140.9	4.6	98
H-18	#85	0.62	0.33	0.1277	0.0075	0.0196	0.0008	132.3	7.1	131.8	5.4	100
H-18	#86	0.14	0.14	1.9725	0.1124	0.1253	0.0066	1137.9	38.4	798.0	39.9	70
H-18	#87	0.33	0.18	0.1376	0.0063	0.0198	0.0011	136.7	7.8	132.9	7.1	97
H-18	#88	0.30	0.17	0.1284	0.0064	0.0189	0.0008	129.1	6.7	127.1	5.7	98
H-18	#89	0.30	0.17	0.2189	0.0131	0.0259	0.0006	191.7	12.0	172.9	4.3	90
H-18	#90	0.32	0.18	0.1310	0.0076	0.0196	0.0010	134.6	7.2	132.0	6.4	98
H-18	#91	0.37	0.21	0.1304	0.0091	0.0190	0.0008	132.6	6.5	128.2	5.3	97
H-18	#92	0.31	0.17	0.1275	0.0085	0.0182	0.0009	138.3	8.0	133.4	6.5	96
H-18	#93	0.30	0.17	0.1380	0.0094	0.0203	0.0008	139.8	7.1	136.6	5.5	98
H-18	#94	0.23	0.13	0.1452	0.0071	0.0210	0.0010	142.6	7.9	138.5	6.9	97
H-18	#95	0.31	0.18	0.1438	0.0070	0.0200	0.0010	141.3	7.5	135.6	6.4	96
H-18	#96	0.36	0.20	0.1414	0.0158	0.0195	0.0010	138.2	12.5	131.7	6.8	95
H-18	#97	0.24	0.14	0.1568	0.0080	0.0234	0.0004	148.6	5.5	142.4	2.7	96
H-18	#98	0.30	0.30	0.2687	0.0330	0.0199	0.0009	262.8	21.3	135.1	5.8	51
H-18	#99	0.38	0.26	0.1886	0.0183	0.0210	0.0010	188.6	11.8	142.5	6.8	76
H-18	#100	0.39	0.22	0.1290	0.0092	0.0187	0.0007	133.3	8.3	129.6	5.0	97
H-18	#101	0.18	0.10	0.1257	0.0078	0.0187	0.0004	126.3	4.5	122.6	2.9	97
H-18	#102	0.30	0.17	0.1201	0.0077	0.0182	0.0008	126.0	6.7	123.9	5.4	98
H-18	#103	0.23	0.14	0.1352	0.0085	0.0181	0.0009	138.1	7.6	128.3	6.5	93
H-18	#104	0.30	0.19	0.9335	0.0439	0.1095	0.0038	712.4	20.7	712.2	23.6	100
H-18	#105	0.40	0.23	0.1292	0.0105	0.0195	0.0009	134.4	7.3	132.5	5.9	99
H-18	#106	0.36	0.21	0.1402	0.0153	0.0183	0.0009	134.8	12.3	128.1	6.5	95
H-18	#107	0.20	0.11	0.1366	0.0068	0.0194	0.0008	136.8	6.3	130.9	5.2	96
H-18	#108	0.28	0.16	0.1343	0.0130	0.0196	0.0009	143.1	13.2	133.7	6.1	93
H-18	#109	0.24	0.14	0.1227	0.0080	0.0188	0.0008	127.9	6.3	128.4	5.5	100
H-74B	#1	0.26	0.86	1.6717	0.1454	0.0332	0.0022	918.6	57.8	198.6	12.9	22
H-74B	#2	0.50	0.20	0.3426	0.0175	0.0416	0.0020	270.0	13.4	247.9	11.9	92
H-74B	#3	0.34	0.15	1.4037	0.3958	0.0719	0.0160	910.2	199.3	697.3	148.4	77
H-74B	#4	0.32	0.17	0.1362	0.0065	0.0196	0.0006	121.7	4.9	118.3	3.5	97
H-74B	#5	0.38	0.21	0.1575	0.0083	0.0220	0.0007	138.1	6.9	133.3	4.2	97
H-74B	#6	0.17	0.10	0.1497	0.0022	0.0217	0.0002	137.5	2.6	131.7	1.4	96
H-74B	#7	0.44	0.23	0.0891	0.0092	0.0201	0.0007	130.6	7.3	121.2	4.0	93
H-74B	#8	0.26	0.19	0.2591	0.0228	0.0202	0.0013	210.8	18.1	119.8	7.5	57
H-74B	#9	0.37	0.21	0.1392	0.0074	0.0206	0.0007	124.6	5.5	124.0	4.3	100

Table A.55: Zrn U-Pb age dataset

Zircon U-Pb data

Sample	Spot #	Th/U[a]	$^{208}Pb/^{206}Pb$	Ratios $^{207}Pb/^{235}U$[a]	2 σ[b]	$^{206}Pb/^{238}U$[a]	2 σ[b]	Ages (Ma) $^{207}Pb/^{235}U$	2 σ	$^{206}Pb/^{238}U$	2 σ	Cc[c] %
H-74B	#10	1.66	1.23	1.1051	0.1437	0.0274	0.0023	791.9	80.7	177.3	14.9	22
H-74B	#11	0.22	0.13	0.1341	0.0098	0.0198	0.0007	127.3	7.8	120.2	3.9	94
H-74B	#12	0.07	0.91	1.9172	0.1246	0.0351	0.0017	1164.4	38.8	249.0	12.0	21
H-74B	#13	0.49	0.30	1.1355	0.0806	0.1263	0.0083	746.2	37.1	726.3	45.5	97
H-74B	#14	0.11	0.06	0.1720	0.0189	0.0246	0.0010	156.9	7.6	148.2	6.2	94
H-74B	#15	0.11	0.08	0.6076	0.0358	0.0757	0.0048	460.7	24.7	445.3	27.2	97
H-74B	#16	0.16	0.87	1.5970	0.0703	0.0322	0.0014	1033.0	32.9	219.0	9.0	21
H-74B	#17	0.21	0.11	0.1621	0.0311	0.0213	0.0027	142.7	19.6	128.4	16.4	90
H-74B	#18	0.17	0.08	0.1579	0.0096	0.0231	0.0008	143.9	5.4	138.0	4.5	96
H-74B	#19	0.14	0.07	0.4664	0.0443	0.0601	0.0046	375.1	25.1	356.5	26.4	95
H-74B	#20	0.36	0.15	0.1882	0.0107	0.0255	0.0007	170.4	6.3	155.3	4.0	91
H-74B	#21	0.52	0.25	0.1821	0.0246	0.0214	0.0068	147.4	47.6	125.3	39.6	85
H-74B	#22	0.09	0.06	0.1562	0.0091	0.0231	0.0006	157.3	9.2	139.4	3.4	89
H-74B	#23	0.57	0.24	0.2583	0.0726	0.0216	0.0022	232.7	55.8	140.6	14.5	60
H-74B	#24	0.16	0.07	0.1754	0.0207	0.0245	0.0008	153.0	11.3	145.2	4.9	95
H-74B	#25	0.10	0.05	0.8125	0.3136	0.0607	0.0146	477.5	134.2	291.6	68.8	61
H-74B	#26	0.39	0.22	0.1879	0.0180	0.0187	0.0003	160.2	12.1	116.3	2.0	73
H-74B	#27	0.07	0.03	1.2454	0.0212	0.1239	0.0024	699.6	28.2	714.7	13.5	102
H-74B	#28	0.48	0.13	2.0249	0.1073	0.1831	0.0040	1070.6	22.1	1025.8	21.8	96
H-74B	#29	0.18	0.10	0.1837	0.0152	0.0225	0.0011	168.9	11.6	136.5	6.6	81
H-74B	#30	0.47	0.21	0.1674	0.0152	0.0233	0.0011	154.2	9.9	141.0	6.4	91
H-74B	#31	0.34	0.19	0.1533	0.0067	0.0219	0.0004	144.1	5.5	133.8	2.4	93
H-74B	#32	0.43	0.14	0.5075	0.0665	0.0643	0.0026	390.1	79.1	381.3	15.2	98
H-74B	#33	0.19	0.09	0.1703	0.0111	0.0227	0.0006	151.9	6.2	137.1	3.5	90
H-74B	#34	0.74	0.44	0.2142	0.0253	0.0228	0.0012	204.6	19.3	159.0	8.0	78
H-74B	#35	0.16	0.09	0.1406	0.0038	0.0209	0.0006	125.9	3.8	124.5	3.5	99
H-74B	#36	0.46	0.26	0.1506	0.0059	0.0222	0.0010	143.8	8.6	134.3	6.3	93
H-74B	#37	0.11	0.06	0.1422	0.0071	0.0196	0.0006	135.3	5.5	118.7	3.5	88
H-74B	#38	0.57	0.29	0.2127	0.0198	0.0251	0.0009	198.2	18.4	154.0	5.2	78
H-74B	#39	0.29	0.30	0.3133	0.0398	0.0190	0.0016	291.0	32.6	124.4	10.6	43
H-74B	#40	0.02	0.59	1.0367	0.0560	0.0276	0.0015	752.8	34.1	182.2	10.1	24
H-74B	#41	0.84	1.34	2.9140	0.2885	0.0446	0.0029	1361.9	54.7	267.4	17.0	20
H-74B	#42	0.27	0.14	0.1504	0.0236	0.0210	0.0045	151.3	33.6	139.2	29.4	92
H-74B	#43	0.51	0.28	0.1397	0.0092	0.0191	0.0006	126.5	6.8	119.6	3.6	95
H-74B	#44	0.27	0.13	0.1700	0.0087	0.0221	0.0009	146.9	7.4	133.9	5.3	91
H-74B	#45	0.17	0.09	0.1220	0.0275	0.0187	0.0012	116.1	8.6	111.6	6.9	96
H-74B	#46	0.43	0.25	0.1781	0.0057	0.0215	0.0003	146.4	8.4	132.3	2.1	90
H-74B	#47	0.29	0.16	0.1358	0.0080	0.0197	0.0007	123.7	6.5	119.9	4.0	97
H-74B	#48	0.17	0.09	0.1613	0.0071	0.0231	0.0007	148.6	5.8	140.4	4.0	94
H-74B	#49	0.19	1.25	3.2785	0.2000	0.0470	0.0027	1547.4	53.0	319.5	17.8	21
H-74B	#50	0.73	0.41	0.1207	0.0074	0.0179	0.0005	116.0	5.9	109.8	2.8	95
H-74B	#51	0.18	0.08	0.1566	0.0088	0.0212	0.0006	141.5	5.3	129.8	3.9	92
H-74B	#52	0.13	0.07	0.1506	0.0060	0.0213	0.0008	135.3	5.5	129.6	4.7	96
H-74B	#53	0.21	0.11	0.1549	0.0071	0.0219	0.0009	139.9	6.7	133.7	5.3	96
H-74B	#54	0.26	0.16	0.1328	0.0074	0.0194	0.0005	131.6	6.2	118.1	2.8	90
H-74B	#55	0.46	0.26	0.1316	0.0089	0.0195	0.0008	122.4	7.2	119.2	5.1	97
H-74B	#56	0.28	0.12	0.1688	0.0113	0.0240	0.0007	146.3	5.9	141.4	4.3	97
H-74B	#57	0.52	0.27	0.1344	0.0075	0.0195	0.0007	127.4	5.8	119.3	4.3	94
H-74B	#58	0.18	0.09	0.1886	0.0238	0.0245	0.0055	161.4	37.1	144.6	32.0	90
H-74B	#59	0.90	0.49	0.0554	0.0037	0.0083	0.0003	51.5	3.4	49.9	1.9	97
H-74B	#60	0.06	0.04	0.1592	0.0084	0.0214	0.0007	139.8	5.6	130.8	4.4	94
H-74B	#61	0.42	0.23	0.1327	0.0085	0.0197	0.0008	117.9	6.4	118.6	4.9	101
H-74B	#62	0.17	0.14	0.1780	0.0110	0.0238	0.0004	159.1	9.8	143.6	2.3	90
H-74B	#63	0.32	0.18	0.1183	0.0058	0.0175	0.0006	107.9	4.6	108.1	3.6	100
H-74B	#64	0.41	0.22	0.1318	0.0083	0.0196	0.0009	124.1	7.7	119.3	5.7	96
H-74B	#65	0.54	0.30	0.1338	0.0102	0.0190	0.0008	130.7	7.9	122.3	5.2	94
H-74B	#66	0.15	0.10	0.2487	0.0400	0.0246	0.0019	338.7	35.2	245.2	18.3	72
H-74B	#67	0.32	0.18	0.1291	0.0081	0.0185	0.0007	123.9	6.6	115.6	4.1	93
H-74B	#68	0.07	0.03	0.1397	0.0050	0.0210	0.0009	131.0	6.0	129.5	5.3	99
H-74B	#69	0.28	0.15	0.1316	0.0076	0.0191	0.0007	121.1	6.0	118.3	4.5	98
H-74B	#70	0.23	0.12	0.1308	0.0056	0.0195	0.0007	120.5	5.6	119.2	4.3	99
H-74B	#71	0.55	0.27	0.1349	0.0090	0.0194	0.0006	130.5	6.5	120.7	3.9	92

Table A.56: Zrn U-Pb age dataset

Zircon U-Pb data

Sample	Spot #	Th/U[a]	^{208}Pb/^{206}Pb	Ratios				Ages (Ma)				Cc[c]
				^{207}Pb/^{235}U[a]	2 σ[b]	^{206}Pb/^{238}U[a]	2 σ[b]	^{207}Pb/^{235}U	2 σ	^{206}Pb/^{238}U	2 σ	%
H-74B	#72	0.44	0.25	0.1406	0.0129	0.0197	0.0009	129.9	9.1	123.2	5.9	95
H-74B	#73	0.22	0.20	0.1467	0.0207	0.0156	0.0007	145.5	13.5	96.9	4.2	67
H-74B	#74	0.09	0.05	0.1803	0.0200	0.0239	0.0020	166.0	14.2	145.7	12.3	88
H-74B	#75	0.17	0.10	0.1453	0.0068	0.0218	0.0009	138.8	6.6	136.9	5.8	99
H-74B	#76	0.12	0.07	0.1382	0.0073	0.0201	0.0006	126.6	4.7	122.3	3.9	97
H-74B	#77	0.44	0.25	0.1302	0.0096	0.0190	0.0008	119.0	7.2	115.9	4.8	97
H-74B	#78	0.37	0.20	0.1293	0.0162	0.0182	0.0008	121.2	9.1	116.9	5.2	96
H-74B	#79	0.28	0.16	0.1355	0.0068	0.0197	0.0007	122.3	5.4	120.2	4.0	98
H-74B	#80	0.05	1.28	3.4749	0.2293	0.0463	0.0027	1462.4	53.3	282.4	16.0	19
H-74B	#81	0.08	0.05	0.1454	0.0048	0.0210	0.0008	131.6	5.1	128.6	4.7	98
H-74B	#82	0.17	0.09	0.1320	0.0070	0.0194	0.0006	118.5	4.6	118.9	3.9	100
H-74B	#83	0.35	0.18	0.1339	0.0076	0.0197	0.0008	124.9	7.1	121.5	4.7	97
H-74B	#84	0.25	0.14	0.1245	0.0081	0.0193	0.0007	118.2	5.8	118.3	4.5	100
H-74B	#85	0.07	0.04	0.1462	0.0063	0.0213	0.0006	132.1	4.5	130.7	3.9	99
H-74B	#86	0.44	0.24	0.1305	0.0068	0.0195	0.0007	119.4	5.9	118.5	4.2	99
H-74B	#87	0.33	0.18	0.1315	0.0072	0.0195	0.0008	119.9	6.0	120.6	5.0	101
H-74B	#88	0.47	0.27	0.1221	0.0188	0.0164	0.0008	105.2	11.7	103.0	5.0	98
H-74B	#89	0.29	0.16	0.1208	0.0060	0.0178	0.0006	114.1	5.1	110.7	3.6	97
H-74B	#90	0.41	0.23	0.1490	0.0085	0.0226	0.0008	141.9	6.5	141.2	5.2	100
H-74B	#91	0.44	0.24	0.1399	0.0108	0.0200	0.0009	130.4	8.6	122.5	5.3	94
H-74B	#92	0.16	0.09	0.1351	0.0077	0.0205	0.0007	122.3	5.2	125.3	4.2	102
H-74B	#93	0.39	0.21	0.1389	0.0143	0.0198	0.0007	126.2	7.5	121.3	4.3	96
H-74B	#94	0.43	0.23	0.1238	0.0124	0.0204	0.0009	127.1	11.1	124.8	5.3	98
H-74B	#95	0.44	0.23	0.1261	0.0096	0.0197	0.0008	120.8	8.6	120.6	5.1	100
H-74B	#96	0.30	0.16	0.1336	0.0090	0.0197	0.0007	119.7	5.5	117.6	4.1	98
H-74B	#97	0.34	0.18	0.1410	0.0075	0.0199	0.0008	127.0	6.2	122.0	4.6	96
H-74B	#98	0.27	0.15	0.1513	0.0077	0.0224	0.0008	129.7	4.8	126.5	4.3	98
H-74B	#99	0.15	0.08	0.1500	0.0081	0.0222	0.0007	127.1	5.5	125.1	4.1	98
H-74B	#100	0.43	0.24	0.1389	0.0124	0.0195	0.0007	119.6	6.3	116.3	3.9	97
H-74B	#101	0.47	0.25	0.2281	0.1610	0.0194	0.0007	175.8	113.4	119.0	4.2	68
H-74B	#102	0.31	0.17	0.1244	0.0097	0.0194	0.0006	118.7	5.5	119.4	3.8	101
H-74B	#103	0.43	0.24	0.2593	0.1343	0.0192	0.0008	174.7	113.5	118.2	4.7	68
H-75	#1	0.06	0.03	0.1420	0.0062	0.0208	0.0008	133.1	5.4	129.4	4.7	97
H-75	#2	0.05	0.03	0.1395	0.0080	0.0207	0.0012	128.1	7.2	126.4	7.0	99
H-75	#3	0.07	0.04	0.1484	0.0094	0.0211	0.0010	136.8	7.6	132.2	6.4	97
H-75	#4	0.07	0.04	0.1405	0.0073	0.0211	0.0008	132.8	6.0	131.7	5.2	99
H-75	#5	0.08	0.05	0.1392	0.0061	0.0208	0.0009	132.6	5.9	130.2	5.5	98
H-75	#6	0.07	0.05	0.4155	0.0465	0.0538	0.0055	345.5	31.8	329.8	32.9	95
H-75	#7	0.16	0.12	0.1771	0.0129	0.0219	0.0009	190.2	20.7	136.8	5.3	72
H-75	#8	0.06	0.04	0.1396	0.0064	0.0201	0.0009	128.1	5.9	125.8	5.5	98
H-75	#9	0.08	0.05	0.1466	0.0073	0.0217	0.0009	137.6	6.7	136.1	5.8	99
H-75	#10	0.12	0.08	1.0287	0.1286	0.0816	0.0090	722.5	60.7	503.0	53.4	70
H-75	#11	0.43	0.25	0.3690	0.0140	0.0516	0.0012	289.3	7.8	277.4	6.2	96
H-75	#12	0.05	0.03	0.1466	0.0057	0.0210	0.0007	138.9	5.5	134.0	4.6	96
H-75	#13	0.05	0.03	0.2016	0.0097	0.0287	0.0010	186.6	8.6	179.1	6.4	96
H-75	#14	0.05	0.03	0.1436	0.0078	0.0208	0.0010	144.3	7.2	142.5	6.5	99
H-75	#15	0.06	0.04	0.1420	0.0078	0.0206	0.0008	131.5	5.6	128.2	5.0	97
H-75	#16	0.20	0.12	0.1496	0.0090	0.0214	0.0009	140.0	7.5	133.8	5.3	96
H-75	#17	0.03	0.02	0.1391	0.0078	0.0201	0.0009	128.9	6.7	126.2	5.8	98
H-75	#18	0.09	0.06	0.1448	0.0071	0.0211	0.0008	136.7	6.4	132.4	5.0	97
H-75	#19	0.06	0.04	0.1475	0.0069	0.0212	0.0006	140.5	6.7	132.8	3.9	95
H-75	#20	0.07	0.04	0.1418	0.0060	0.0204	0.0009	131.8	6.6	129.0	5.9	98
H-75	#21	0.04	0.02	0.1376	0.0067	0.0204	0.0011	129.9	7.1	128.3	6.9	99
H-75	#22	0.06	0.03	0.1391	0.0067	0.0204	0.0009	132.1	6.5	128.0	5.5	97
H-75	#23	0.25	0.16	0.3876	0.0171	0.0512	0.0017	328.2	11.3	316.4	10.5	96
H-75	#24	0.10	0.06	0.1668	0.0310	0.0232	0.0012	162.3	21.8	145.6	7.5	90
H-75	#25	0.04	0.03	0.1213	0.0042	0.0175	0.0011	114.9	9.5	109.8	6.9	96
H-75	#26	0.06	0.04	0.1432	0.0053	0.0210	0.0009	136.4	6.1	133.6	5.6	98
H-75	#27	0.06	0.05	0.1551	0.0194	0.0205	0.0008	150.2	9.5	128.5	4.7	86
H-75	#28	0.35	0.21	0.7573	0.0136	0.0720	0.0022	448.8	20.9	440.8	12.8	98
H-75	#29	0.05	0.03	0.1403	0.0062	0.0208	0.0007	129.7	5.1	129.6	4.4	100

Table A.57: Zrn U-Pb age dataset

Zircon U-Pb data

Sample	Spot #	Th/U[a]	$^{208}Pb/^{206}Pb$	Ratios $^{207}Pb/^{235}U$[a]	2 σ[b]	$^{206}Pb/^{238}U$[a]	2 σ[b]	Ages (Ma) $^{207}Pb/^{235}U$	2 σ	$^{206}Pb/^{238}U$	2 σ	Cc[c] %
H-75	#30	0.32	0.21	0.0751	0.0067	0.0092	0.0004	81.0	6.4	63.2	2.8	78
H-75	#31	0.06	0.04	0.1418	0.0060	0.0210	0.0008	133.4	5.5	131.9	4.8	99
H-75	#32	0.84	0.48	0.0665	0.0039	0.0092	0.0003	64.4	4.4	57.9	2.2	90
H-75	#33	0.24	0.48	0.0536	0.0026	0.0081	0.0003	53.6	3.0	54.3	2.1	101
H-75	#34	0.05	0.03	0.1540	0.0066	0.0214	0.0006	140.5	5.8	134.2	3.9	96
H-75	#35	0.06	0.03	0.1454	0.0068	0.0214	0.0008	134.5	5.8	134.6	5.2	100
H-75	#36	0.05	0.03	0.1412	0.0061	0.0206	0.0008	131.6	5.6	129.3	4.9	98
H-75	#37	0.07	0.07	0.2930	0.0211	0.0303	0.0008	269.9	9.5	193.3	5.3	72
H-75	#38	0.03	0.01	0.1520	0.0067	0.0234	0.0007	143.6	5.2	142.3	4.4	99
H-75	#39	0.14	0.09	16.9195	0.5922	0.4964	0.0139	2614.0	75.9	2565.4	59.5	98
H-75	#40	0.22	0.40	0.0520	0.0022	0.0079	0.0003	51.7	2.3	50.3	1.9	97
H-75	#41	0.15	0.06	0.1602	0.0067	0.0226	0.0008	145.9	5.3	141.6	4.8	97
H-75	#42	0.05	0.03	0.1361	0.0073	0.0197	0.0008	127.4	5.5	124.2	5.0	97
H-75	#43	0.05	0.03	0.1432	0.0062	0.0213	0.0008	134.4	6.1	134.1	4.8	100
H-75	#44	0.10	0.17	0.4123	0.1245	0.0240	0.0020	196.5	53.2	102.6	8.7	52
H-75	#45	0.11	0.06	0.1458	0.0051	0.0220	0.0006	143.8	3.9	137.5	3.5	96
H-75	#46	0.14	0.08	0.1420	0.0043	0.0218	0.0005	141.3	4.2	137.0	3.4	97
H-75	#47	0.20	0.13	0.1824	0.0159	0.0212	0.0011	174.0	12.9	148.4	7.5	85
H-75	#48	0.05	0.03	0.1357	0.0050	0.0201	0.0006	129.5	4.5	128.2	4.1	99
H-75	#49	0.36	0.21	0.1395	0.0067	0.0203	0.0007	131.6	5.8	129.5	4.4	98
H-75	#50	0.04	0.02	0.1406	0.0049	0.0207	0.0006	132.0	4.6	130.7	3.5	99
H-75	#51	0.05	0.03	0.1447	0.0051	0.0213	0.0007	135.6	4.8	134.2	4.5	99
H-75	#52	0.11	0.09	0.2306	0.0081	0.0329	0.0009	222.4	7.6	208.9	5.8	94
H-75	#53	0.04	0.03	0.1646	0.0115	0.0218	0.0009	158.0	7.9	147.7	5.8	93
H-75	#54	0.06	0.05	0.1876	0.0053	0.0247	0.0007	153.8	5.3	138.1	3.7	90
H-75	#55	0.06	0.03	0.1451	0.0181	0.0208	0.0011	138.2	9.7	131.5	7.2	95
H-75	#56	0.05	0.03	0.1420	0.0054	0.0207	0.0007	134.0	5.2	130.3	4.5	97
H-75	#57	0.22	0.12	0.1415	0.0061	0.0212	0.0007	134.1	5.5	133.6	4.4	100
H-75	#58	0.71	0.41	0.0539	0.0025	0.0078	0.0003	53.1	2.7	50.0	1.9	94
H-75	#59	0.15	0.09	0.1613	0.0021	0.0226	0.0005	147.0	4.5	142.2	3.4	97
H-75	#60	0.03	0.02	0.1563	0.0064	0.0230	0.0007	151.1	5.1	144.6	4.4	96
H-75	#61	0.08	0.04	0.1375	0.0077	0.0202	0.0007	136.7	6.8	130.8	4.3	96
H-75	#62	0.05	0.03	0.1509	0.0065	0.0212	0.0007	141.7	5.6	133.4	4.6	94
H-75	#63	0.07	0.13	0.2189	0.0219	0.0208	0.0006	219.4	21.9	131.7	3.5	60
H-75	#64	0.16	0.36	0.4105	0.1252	0.0234	0.0011	446.8	92.7	151.2	7.3	34
H-75	#65	0.08	0.05	0.1486	0.0062	0.0213	0.0007	140.1	6.2	134.7	4.7	96
H-75	#66	0.13	0.09	0.2002	0.0042	0.0272	0.0007	181.5	5.7	170.0	4.5	94
H-75	#67	0.07	0.08	1.9585	0.1312	0.1082	0.0053	1433.4	44.7	993.4	45.3	69
H-75	#68	0.06	0.03	0.1516	0.0105	0.0208	0.0008	138.5	6.9	131.4	4.9	95
H-75	#69	0.10	0.07	0.2105	0.0076	0.0282	0.0006	197.6	6.7	178.9	3.9	91
H-75	#70	0.19	0.12	0.1549	0.0053	0.0220	0.0006	143.5	4.3	138.4	3.7	96
H-75	#71	0.11	0.07	0.1581	0.0081	0.0231	0.0010	151.0	6.9	147.2	6.3	97
H-75	#72	0.44	0.24	0.1306	0.0080	0.0190	0.0013	127.4	10.0	125.8	8.6	99
H-75	#73	0.05	0.03	0.1586	0.0030	0.0229	0.0003	146.0	3.3	141.5	2.0	97
H-75	#74	0.16	0.09	0.1560	0.0041	0.0223	0.0003	150.9	3.2	144.0	2.0	95
H-75	#75	0.52	0.30	0.1457	0.0066	0.0220	0.0002	142.8	4.5	139.3	1.5	98
H-75	#76	0.25	0.24	2.6262	0.0499	0.2130	0.0036	1241.2	40.2	1231.3	19.1	99
H-75	#77	0.09	0.06	0.1747	0.0066	0.0229	0.0005	158.6	6.5	144.1	3.3	91
H-75	#78	0.49	0.27	0.1348	0.0071	0.0189	0.0005	122.8	4.9	119.5	3.4	97
H-75	#79	0.27	0.16	0.1455	0.0052	0.0213	0.0007	136.2	4.9	134.5	4.3	99
H-75	#80	0.05	0.03	0.1416	0.0061	0.0208	0.0007	132.3	5.0	131.7	4.6	100
H-75	#81	0.08	0.05	0.1412	0.0058	0.0211	0.0007	136.2	5.2	133.7	4.4	98
H-75	#82	0.06	0.04	0.1430	0.0060	0.0212	0.0008	134.5	5.6	133.6	5.0	99
H-75	#83	0.07	0.05	0.1758	0.0040	0.0231	0.0003	160.2	5.1	148.1	2.2	92
H-75	#84	0.07	0.05	0.1786	0.0100	0.0232	0.0010	161.0	7.6	146.4	5.9	91
H-75	#85	0.17	0.10	0.1461	0.0074	0.0208	0.0007	139.7	6.3	131.2	4.2	94
H-75	#86	0.16	0.10	0.1665	0.0058	0.0231	0.0003	156.0	5.4	144.9	2.0	93
H-75	#87	0.05	0.03	0.1405	0.0041	0.0212	0.0008	135.4	5.5	133.9	4.8	99
H-75	#88	0.06	0.04	0.1419	0.0060	0.0204	0.0006	136.0	4.7	129.2	3.8	95
H-75	#89	0.15	0.23	0.4541	0.0872	0.0346	0.0031	274.8	62.0	109.6	9.9	40
H-75	#90	0.06	0.04	0.1476	0.0055	0.0211	0.0009	136.4	5.9	133.6	5.6	98
H-75	#91	0.34	0.25	0.2457	0.0260	0.0217	0.0008	218.4	19.4	139.5	5.0	64

Table A.58: Zrn U-Pb age dataset

Zircon U-Pb data

Sample	Spot #	Th/U[a]	$^{208}Pb/^{206}Pb$	Ratios				Ages (Ma)				Cc[c]
				$^{207}Pb/^{235}U$[a]	2 σ[b]	$^{206}Pb/^{238}U$[a]	2 σ[b]	$^{207}Pb/^{235}U$	2 σ	$^{206}Pb/^{238}U$	2 σ	%
H-75	#92	0.04	0.02	0.1380	0.0048	0.0199	0.0007	128.9	4.9	125.6	4.5	97
H-75	#93	0.18	0.13	0.2112	0.0494	0.0230	0.0008	211.7	21.2	157.4	5.6	74
H-75	#94	0.49	0.34	0.0537	0.0024	0.0082	0.0003	52.0	2.2	52.0	2.0	100
H-75	#95	0.08	0.06	0.1467	0.0085	0.0209	0.0006	149.7	9.1	134.7	3.7	90
H-75	#96	0.15	0.08	0.1504	0.0093	0.0195	0.0007	130.9	9.3	120.1	4.4	92
H-75	#97	0.06	0.03	0.1535	0.0077	0.0220	0.0009	141.7	6.0	135.9	5.5	96
H-75	#98	0.08	0.04	0.1808	0.0054	0.0244	0.0003	165.2	4.9	155.0	2.1	94
H-75	#99	0.27	0.18	0.3220	0.0283	0.0305	0.0009	255.8	24.3	191.3	5.7	75
H-75	#100	0.12	0.07	0.1773	0.0094	0.0247	0.0005	164.7	4.7	153.8	3.3	93
H-75	#101	0.05	0.03	0.1456	0.0077	0.0211	0.0008	140.5	7.1	135.4	5.1	96
H-75	#102	0.04	0.03	0.1487	0.0061	0.0214	0.0007	143.1	5.5	138.5	4.5	97
H-75	#103	0.53	0.34	0.1809	0.0143	0.0220	0.0008	177.2	12.9	139.4	5.0	79
H-75	#104	0.14	0.11	0.1887	0.0047	0.0274	0.0006	175.4	4.8	172.9	3.8	99
H-75	#105	0.05	0.03	0.1704	0.0051	0.0223	0.0008	152.2	5.4	145.2	5.3	95
H-75	#106	0.05	0.03	0.1351	0.0095	0.0207	0.0006	132.5	4.6	131.0	3.6	99
H-75	#107	0.05	0.03	0.1431	0.0054	0.0211	0.0006	135.3	4.7	133.3	4.0	99
H-75	#108	0.05	0.04	0.1657	0.0081	0.0213	0.0009	153.8	7.2	134.8	5.5	88
H-75	#109	0.22	0.13	0.1524	0.0093	0.0218	0.0007	145.6	6.4	138.6	4.1	95
H-75	#110	0.07	0.04	0.1498	0.0049	0.0218	0.0006	142.2	4.8	138.0	4.0	97
H-75	#111	0.05	0.08	0.2951	0.0516	0.0359	0.0041	274.8	30.8	226.1	25.2	82
Mangrexian												
H-66	#1	0.41	0.24	0.5008	0.0175	0.0641	0.0013	350.1	9.2	340.3	7.0	97
H-66	#2	0.45	0.24	0.1329	0.0089	0.0193	0.0008	106.6	5.7	104.2	4.1	98
H-66	#3	0.35	0.19	0.1449	0.0059	0.0207	0.0007	118.1	8.3	111.7	3.7	95
H-66	#4	0.48	0.17	0.1635	0.0123	0.0224	0.0006	98.6	4.6	90.6	2.3	92
H-66	#5	0.40	0.20	0.1279	0.0061	0.0190	0.0007	103.6	4.7	103.0	3.7	99
H-66	#6	0.40	0.21	0.1349	0.0069	0.0201	0.0008	110.7	5.4	108.5	4.2	98
H-66	#7	0.36	0.19	0.1217	0.0062	0.0185	0.0006	101.3	4.7	102.8	3.5	101
H-66	#8	0.26	0.15	0.5482	0.0143	0.0712	0.0019	381.7	10.2	377.1	9.9	99
H-66	#9	0.35	0.19	0.1223	0.0082	0.0189	0.0009	102.1	5.7	103.1	5.0	101
H-66	#10	0.41	0.21	0.1368	0.0088	0.0195	0.0008	106.7	5.8	105.7	4.3	99
H-66	#11	0.35	0.20	0.1537	0.0108	0.0202	0.0008	120.8	10.4	109.2	4.2	90
H-66	#12	0.50	0.26	0.1272	0.0070	0.0197	0.0009	102.9	5.6	107.2	4.7	104
H-66	#13	0.41	0.22	0.1238	0.0094	0.0190	0.0008	103.4	6.8	103.3	4.4	100
H-66	#14	0.32	0.14	0.1310	0.0054	0.0200	0.0008	119.2	5.6	108.4	4.1	91
H-66	#15	0.44	0.24	0.1349	0.0101	0.0222	0.0004	122.7	4.5	121.5	2.0	99
H-66	#16	0.64	0.33	0.1253	0.0060	0.0188	0.0007	102.1	4.5	103.1	3.9	101
H-66	#17	0.37	0.19	0.1317	0.0084	0.0199	0.0008	105.4	5.0	108.1	4.4	103
H-66	#18	0.41	0.22	0.1323	0.0073	0.0191	0.0009	105.8	5.4	103.1	4.7	97
H-66	#19	0.38	0.19	0.1331	0.0137	0.0195	0.0009	109.5	8.7	107.8	5.0	98
H-66	#20	0.34	0.19	0.1220	0.0060	0.0180	0.0007	101.6	4.7	100.8	4.1	99
H-66	#21	0.46	0.24	0.1259	0.0078	0.0189	0.0008	103.9	5.2	102.6	4.2	99
H-66	#22	0.39	0.20	0.1305	0.0060	0.0192	0.0008	105.3	4.7	104.2	4.1	99
H-66	#23	0.25	0.13	0.1284	0.0067	0.0195	0.0007	105.1	4.9	106.0	4.0	101
H-66	#24	0.42	0.14	0.1490	0.0082	0.0252	0.0005	151.6	8.1	136.9	2.8	90
H-66	#25	0.48	0.24	0.1701	0.0194	0.0205	0.0011	143.5	13.3	112.3	6.0	78
H-66	#26	0.44	0.23	0.1291	0.0057	0.0191	0.0007	105.7	4.9	104.0	3.5	98
H-66	#27	0.54	0.28	0.1237	0.0083	0.0189	0.0008	102.4	5.0	102.6	4.2	100
H-66	#28	0.54	0.30	0.1242	0.0050	0.0187	0.0007	99.0	4.5	102.0	4.0	103
H-66	#29	0.44	0.23	0.1241	0.0081	0.0187	0.0009	101.3	5.5	102.0	4.9	101
H-66	#30	0.50	0.26	0.1335	0.0077	0.0191	0.0007	107.6	4.4	104.2	3.7	97
H-66	#31	0.47	0.25	0.1930	0.0060	0.0195	0.0007	116.2	7.5	106.3	3.8	91
H-66	#32	0.38	0.18	0.1238	0.0131	0.0191	0.0011	108.9	9.1	104.4	5.7	96
H-66	#33	0.40	0.20	0.1328	0.0062	0.0192	0.0009	107.1	5.8	105.7	5.0	99
H-66	#34	0.50	0.26	0.1291	0.0076	0.0193	0.0009	105.3	5.5	105.1	4.8	100
H-66	#35	0.64	0.33	0.1323	0.0079	0.0186	0.0009	106.3	7.0	101.6	5.0	96
H-66	#36	0.69	0.82	0.8600	0.1075	0.0253	0.0020	500.8	39.1	117.3	9.4	23
H-66	#37	0.37	0.20	0.1312	0.0083	0.0193	0.0010	107.7	7.3	105.1	5.6	98
H-66	#38	0.30	0.16	0.1224	0.0076	0.0189	0.0010	101.4	6.2	103.1	5.3	102
H-66	#39	0.28	0.15	0.1275	0.0102	0.0190	0.0009	102.0	5.8	103.7	5.0	102

Table A.59: Zrn U-Pb age dataset

Zircon U-Pb data

Sample	Spot #	Th/U[a]	^{208}Pb/^{206}Pb	Ratios				Ages (Ma)				Cc[c]
				^{207}Pb/^{235}U[a]	2 σ[b]	^{206}Pb/^{238}U[a]	2 σ[b]	^{207}Pb/^{235}U	2 σ	^{206}Pb/^{238}U	2 σ	%
H-66	#40	0.38	0.20	0.1217	0.0054	0.0189	0.0007	101.5	4.4	103.4	3.9	102
H-66	#41	0.49	0.24	0.1374	0.0092	0.0198	0.0009	109.2	6.1	108.1	4.8	99
H-66	#42	0.44	0.23	0.1246	0.0090	0.0192	0.0006	107.7	6.3	104.7	3.4	97
H-66	#43	0.44	0.23	0.1558	0.0056	0.0210	0.0005	117.6	5.9	113.9	2.9	97
H-66	#44	0.36	0.20	0.1388	0.0165	0.0190	0.0010	109.7	10.8	106.0	5.4	97
H-66	#45	0.36	0.19	0.1256	0.0075	0.0188	0.0009	102.1	5.2	102.6	4.9	100
H-66	#46	0.52	0.28	0.1286	0.0069	0.0189	0.0008	104.2	5.2	103.8	4.4	100
H-66	#47	0.26	0.14	0.1308	0.0056	0.0192	0.0007	105.3	4.9	105.0	4.1	100
H-66	#48	0.44	0.25	0.1335	0.0071	0.0196	0.0006	108.2	4.3	106.9	3.3	99
H-66	#49	0.24	0.09	0.4445	0.0773	0.0430	0.0059	330.9	44.1	232.6	31.6	70
H-66	#50	0.44	0.22	0.1282	0.0058	0.0192	0.0008	105.1	4.8	107.3	4.3	102
H-66	#51	0.38	0.22	0.1436	0.0079	0.0206	0.0006	119.6	6.2	112.6	3.4	94
H-66	#52	0.42	0.22	0.1287	0.0086	0.0191	0.0007	106.6	6.4	106.5	3.8	100
H-66	#53	0.38	0.20	0.1414	0.0081	0.0208	0.0005	114.2	5.8	114.0	2.8	100
H-66	#54	0.28	0.14	0.1393	0.0089	0.0207	0.0006	110.9	5.4	112.1	3.1	101
H-66	#55	0.33	0.17	0.1330	0.0072	0.0195	0.0008	106.7	5.1	106.9	4.1	100
H-66	#56	0.25	0.15	0.1435	0.0099	0.0195	0.0007	114.1	6.3	106.9	3.9	94
H-66	#57	0.19	0.10	0.8257	0.0421	0.1005	0.0049	537.1	23.2	533.5	25.1	99
H-66	#58	0.30	0.16	0.1310	0.0073	0.0190	0.0009	106.9	5.1	105.1	4.7	98
H-66	#59	0.38	0.20	0.1328	0.0078	0.0202	0.0006	108.9	5.1	111.4	3.2	102
H-66	#60	0.35	0.19	0.1318	0.0082	0.0190	0.0009	108.4	7.2	104.2	4.8	96
H-66	#61	0.29	0.16	0.1927	0.0071	0.0152	0.0013	90.1	8.1	82.7	7.0	92
H-66	#62	0.44	0.19	0.1770	0.0050	0.0246	0.0002	149.0	4.9	134.5	1.5	90
H-66	#63	0.46	0.24	0.1323	0.0094	0.0205	0.0004	116.0	5.5	115.5	2.3	100
H-66	#64	0.49	0.26	0.1332	0.0040	0.0211	0.0006	118.8	5.2	114.2	3.2	96
H-66	#65	0.37	0.19	0.1442	0.0048	0.0210	0.0004	119.1	3.7	116.6	2.4	98
H-66	#66	0.55	0.28	0.1372	0.0102	0.0210	0.0005	116.1	5.2	114.9	2.5	99
H-66	#67	0.60	0.32	0.1513	0.0057	0.0215	0.0003	121.7	3.3	118.1	1.9	97
H-66	#68	0.37	0.19	0.1340	0.0044	0.0204	0.0004	113.8	3.6	111.9	2.3	98
H-66	#69	0.42	0.22	0.1363	0.0049	0.0209	0.0003	116.2	3.3	113.6	1.7	98
H-66	#70	0.19	0.11	0.2195	0.0070	0.0252	0.0005	144.8	7.7	133.9	2.8	92
H-66	#71	0.11	0.05	4.9461	0.1583	0.3583	0.0125	1746.3	32.2	1732.7	53.4	99
H-66	#72	0.16	0.08	0.1231	0.0052	0.0186	0.0006	102.8	5.0	104.1	3.2	101
H-66	#73	0.38	0.20	3.9535	0.1384	0.2792	0.0070	1506.6	23.8	1388.4	31.3	92
H-66	#74	0.26	0.13	0.1615	0.0099	0.0237	0.0009	133.6	5.4	132.9	5.0	99
H-66	#75	0.30	0.16	0.1300	0.0077	0.0193	0.0006	104.8	4.7	106.3	3.5	101
H-66	#76	0.32	0.15	0.1408	0.0106	0.0211	0.0007	121.5	9.5	116.3	3.9	96
H-66	#77	0.43	0.22	0.1332	0.0085	0.0190	0.0008	106.9	4.9	105.4	4.2	99
H-66	#78	0.42	0.23	0.1272	0.0084	0.0189	0.0006	111.0	7.2	105.2	3.3	95
H-66	#79	0.32	0.17	0.1445	0.0074	0.0204	0.0005	122.7	8.4	112.3	2.8	92
H-66	#80	0.38	0.20	0.1244	0.0072	0.0188	0.0007	101.8	5.0	103.6	3.8	102
H-66	#81	0.58	0.31	0.1318	0.0071	0.0191	0.0008	107.1	5.1	105.4	4.4	98
H-66	#82	0.32	0.17	0.1303	0.0065	0.0191	0.0007	105.9	4.8	105.3	3.8	99
H-66	#83	0.49	0.25	0.1249	0.0110	0.0187	0.0007	102.2	7.0	103.1	3.6	101
H-66	#84	0.34	0.18	0.1315	0.0068	0.0196	0.0007	109.9	5.2	108.9	3.9	99
H-66	#85	0.45	0.25	0.1267	0.0075	0.0189	0.0007	104.2	5.2	104.2	3.9	100
H-66	#86	0.41	0.22	0.1231	0.0047	0.0188	0.0007	101.3	4.2	103.3	3.7	102
H-66	#87	0.46	0.24	0.1474	0.0102	0.0215	0.0007	122.4	5.4	119.0	4.0	97
H-66	#88	0.25	0.14	0.1375	0.0077	0.0207	0.0004	114.3	5.4	113.5	2.3	99
H-66	#89	0.22	0.11	0.1399	0.0048	0.0212	0.0007	111.9	4.8	116.8	4.1	104
H-66	#90	0.40	0.21	0.1481	0.0056	0.0210	0.0005	121.1	4.9	114.9	2.5	95
H-66	#91	0.45	0.25	0.1390	0.0082	0.0202	0.0005	117.6	6.6	111.8	2.5	95
H-66	#92	0.42	0.23	0.1457	0.0099	0.0202	0.0004	114.2	6.1	111.6	2.3	98
H-66	#93	0.74	0.40	0.1440	0.0072	0.0209	0.0004	118.5	4.8	115.3	2.3	97
H-66	#94	0.38	0.21	0.1339	0.0130	0.0211	0.0004	120.4	3.8	116.6	2.1	97
H-66	#95	0.35	0.18	0.1396	0.0050	0.0208	0.0004	115.6	3.9	114.9	2.4	99
H-66	#96	0.33	0.17	0.1348	0.0053	0.0212	0.0004	119.5	3.6	117.3	2.3	98
H-66	#97	0.21	0.12	0.1490	0.0060	0.0219	0.0006	126.4	4.9	120.9	3.1	96
H-66	#98	0.43	0.22	0.1792	0.0070	0.0229	0.0005	136.6	7.2	128.3	2.7	94
H-66	#99	0.46	0.25	0.1375	0.0092	0.0204	0.0005	117.3	6.0	112.5	3.0	96
H-66	#101	0.48	0.26	0.1440	0.0081	0.0189	0.0007	116.2	5.4	106.7	3.8	92
H-66	#102	0.56	0.30	0.1433	0.0069	0.0210	0.0004	122.4	5.2	116.7	2.4	95

Table A.60: Zrn U-Pb age dataset

Zircon U-Pb data

Sample	Spot #	Th/U[a]	$^{208}Pb/^{206}Pb$	Ratios				Ages (Ma)				Cc[c]
				$^{207}Pb/^{235}U$[a]	2 σ[b]	$^{206}Pb/^{238}U$[a]	2 σ[b]	$^{207}Pb/^{235}U$	2 σ	$^{206}Pb/^{238}U$	2 σ	%
H-66	#103	0.25	0.13	0.1269	0.0104	0.0192	0.0008	102.0	6.2	102.0	4.3	100
H-66	#104	0.25	0.13	0.1326	0.0111	0.0210	0.0005	120.0	6.1	118.7	3.1	99
H-66	#105	0.35	0.18	0.1457	0.0054	0.0211	0.0005	117.9	4.3	116.5	3.0	99
H-66	#106	0.21	0.12	0.1444	0.0038	0.0214	0.0003	120.8	3.5	118.2	1.9	98
H-66	#107	0.35	0.19	0.1369	0.0034	0.0205	0.0003	116.2	2.9	113.2	1.8	97
H-66	#108	0.27	0.14	0.1369	0.0073	0.0213	0.0005	117.5	4.9	117.6	2.7	100
H-66	#109	0.38	0.20	0.1372	0.0082	0.0219	0.0005	124.5	6.2	120.8	2.8	97
H-66	#110	0.38	0.19	0.1430	0.0080	0.0212	0.0004	120.6	5.2	117.3	2.6	97
H-66	#111	0.29	0.15	0.1442	0.0091	0.0209	0.0004	122.0	5.6	115.8	2.5	95
H-66	#112	0.13	0.07	0.5788	0.0232	0.0749	0.0019	418.4	10.3	405.1	10.2	97
H-66	#113	0.26	0.14	0.1372	0.0069	0.0208	0.0005	117.9	3.2	114.9	2.7	97
H-66	#114	0.36	0.19	0.1328	0.0056	0.0208	0.0004	115.7	3.5	114.9	2.1	99
H-66	#115	0.42	0.22	0.1396	0.0050	0.0213	0.0005	119.1	3.9	118.0	2.8	99
H-66	#116	0.33	0.17	0.1452	0.0054	0.0207	0.0004	118.8	4.6	114.5	2.3	96
Namucuoxiang												
H-3A	#1	0.14	0.07	1.5997	0.0560	0.1591	0.0068	934.2	28.5	923.4	38.0	99
H-3A	#2	0.20	0.17	1.8391	0.0405	0.1642	0.0034	1019.8	20.1	937.7	21.0	92
H-3A	#3	0.46	0.23	1.5060	0.1009	0.1518	0.0056	908.1	26.1	886.7	32.4	98
H-3A	#4	0.25	0.09	3.1337	0.3228	0.2333	0.0236	1375.3	85.6	1316.9	122.7	96
H-3A	#5	0.36	0.19	1.0883	0.0566	0.1222	0.0062	732.4	29.1	724.0	35.7	99
H-3A	#6	0.15	0.07	2.6752	0.1685	0.2040	0.0108	1287.5	43.2	1168.6	58.0	91
H-3A	#7	0.41	0.18	1.6558	0.1176	0.1642	0.0108	947.6	43.4	945.5	59.2	100
H-3A	#8	0.39	0.19	1.3658	0.0505	0.1428	0.0054	854.9	25.2	841.4	31.6	98
H-3A	#9	0.10	0.03	0.8669	0.0659	0.0979	0.0062	613.7	31.3	591.7	36.3	96
H-3A	#10	0.43	0.21	0.6592	0.0316	0.0835	0.0024	519.7	17.2	506.7	15.1	97
H-3A	#11	1.47	0.73	1.8232	0.1039	0.1745	0.0063	1045.9	27.8	1021.5	35.0	98
H-3A	#12	0.15	0.07	1.5659	0.0470	0.1578	0.0047	948.7	22.4	931.7	27.8	98
H-3A	#13	0.19	0.07	7.5236	0.2031	0.3693	0.0114	2157.2	34.6	2002.4	57.1	93
H-3A	#14	0.51	0.24	3.0551	0.1436	0.2420	0.0106	1411.1	37.3	1381.5	56.2	98
H-3A	#15	0.14	0.06	5.4072	0.1676	0.3412	0.0106	1878.9	31.3	1874.1	53.9	100
H-3A	#16	0.32	0.16	1.5043	0.0677	0.1557	0.0061	929.5	27.2	923.9	34.5	99
H-3A	#17	0.60	0.27	10.2486	0.5227	0.4549	0.0209	2431.4	47.2	2399.0	94.8	99
H-3A	#18	0.29	0.13	9.8148	0.2650	0.4189	0.0054	2401.0	20.4	2245.2	30.4	94
H-3A	#19	1.12	0.56	0.6788	0.0400	0.0826	0.0031	517.2	19.2	510.9	18.7	99
H-3A	#20	0.33	0.16	2.8928	0.1070	0.2363	0.0076	1361.0	28.9	1360.7	41.8	100
H-3A	#21	0.26	0.12	8.0754	0.3715	0.3791	0.0144	2236.7	39.6	2070.9	69.5	93
H-3A	#22	0.23	0.12	1.3802	0.0511	0.1446	0.0048	874.9	22.5	870.8	27.8	100
H-3A	#23	0.38	0.13	8.4605	0.4399	0.3933	0.0197	2279.3	49.3	2143.1	93.7	94
H-3A	#24	0.61	0.30	1.9088	0.0840	0.1813	0.0053	1073.7	24.1	1076.7	29.8	100
H-3A	#25	0.74	0.39	0.7044	0.0479	0.0835	0.0028	536.7	20.6	519.1	17.5	97
H-3A	#26	0.77	0.42	1.4706	0.0676	0.1422	0.0051	893.7	25.3	861.0	29.9	96
H-3A	#27	0.91	0.42	1.0937	0.1356	0.1187	0.0055	741.6	31.5	727.2	32.4	98
H-3A	#28	0.12	0.06	1.8115	0.0797	0.1776	0.0064	1040.3	27.0	1061.1	36.3	102
H-3A	#29	0.24	0.13	2.5341	0.1292	0.1970	0.0150	1272.5	63.6	1168.2	82.8	92
H-3A	#30	0.48	0.22	1.7265	0.0691	0.1777	0.0027	1046.8	15.8	1054.2	16.6	101
H-3A	#31	0.69	0.17	15.8838	0.5559	0.4706	0.0122	2870.8	29.1	2609.0	60.4	91
H-3A	#32	1.52	0.19	8.2879	0.2984	0.3821	0.0111	2275.0	34.1	2112.6	54.3	93
H-3A	#33	0.20	0.11	1.3020	0.0820	0.1411	0.0072	867.8	33.2	877.7	42.8	101
H-3A	#34	0.37	0.17	9.1914	0.4688	0.4292	0.0223	2367.3	52.7	2335.2	104.7	99
H-3A	#35	0.18	0.09	1.5220	0.0685	0.1533	0.0058	957.6	27.0	949.6	34.5	99
H-3A	#36	0.24	0.11	12.6562	0.5189	0.4920	0.0207	2655.9	45.2	2620.1	93.2	99
H-3A	#37	0.83	0.32	3.2470	0.2468	0.2486	0.0174	1462.9	59.0	1457.5	93.3	100
H-3A	#38	0.20	0.10	1.5597	0.0655	0.1581	0.0058	965.2	25.9	978.2	34.6	101
H-3A	#39	0.32	0.16	1.6769	0.0721	0.1667	0.0055	1006.3	24.6	1014.4	32.0	101
H-3A	#40	0.45	0.22	9.9415	0.5269	0.4288	0.0202	2420.8	48.1	2352.2	95.3	97
H-3A	#41	0.06	0.02	1.2221	0.0599	0.1295	0.0063	820.6	29.7	805.5	38.0	98
H-3A	#42	0.53	0.21	10.5800	0.5184	0.4429	0.0204	2508.8	47.6	2419.8	95.5	96
H-3A	#43	1.82	0.90	1.5246	0.0899	0.1553	0.0054	952.7	25.7	956.2	32.1	100
H-3A	#44	0.55	0.19	9.5658	0.5835	0.4324	0.0285	2435.4	64.8	2375.7	132.5	98
H-3A	#45	0.11	0.05	1.4320	0.0487	0.1517	0.0052	932.1	24.1	937.3	30.6	101

Table A.61: Zrn U-Pb age dataset

Zircon U-Pb data

Sample	Spot #	Th/U[a]	$^{208}Pb/^{206}Pb$	Ratios $^{207}Pb/^{235}U$[a]	2σ[b]	$^{206}Pb/^{238}U$[a]	2σ[b]	Ages (Ma) $^{207}Pb/^{235}U$	2σ	$^{206}Pb/^{238}U$	2σ	Cc[c] %
H-3A	#46	1.96	0.99	0.8237	0.0552	0.0902	0.0055	621.5	35.0	568.1	33.8	91
H-3A	#47	0.18	0.08	1.7278	0.0708	0.1678	0.0049	1034.3	22.3	1030.8	28.6	100
H-3A	#48	0.44	0.23	1.2149	0.0377	0.1344	0.0050	817.9	23.9	831.6	29.7	102
H-3A	#49	0.30	0.16	1.3690	0.0534	0.1441	0.0048	892.8	22.8	896.7	28.5	100
H-3A	#50	0.87	0.44	1.4551	0.0800	0.1512	0.0062	927.9	29.0	938.7	36.8	101
H-3A	#51	0.26	0.16	1.3166	0.0882	0.1346	0.0065	879.7	34.1	845.1	38.9	96
H-3A	#52	0.82	0.24	2.5722	0.1106	0.2226	0.0087	1340.1	33.3	1344.0	48.7	100
H-3A	#53	0.29	0.13	9.9511	0.5274	0.4537	0.0254	2466.6	55.2	2496.5	117.0	101
H-3A	#54	0.35	0.16	1.3852	0.0665	0.1014	0.0047	910.4	37.3	651.3	29.2	72
H-3A	#55	0.12	0.06	4.6833	0.2342	0.3149	0.0167	1797.8	49.2	1832.9	85.1	102
H-3A	#56	0.32	0.15	10.0028	0.5201	0.4520	0.0185	2469.8	43.5	2494.4	87.5	101
H-3A	#57	0.45	0.20	2.1580	0.1144	0.1974	0.0083	1188.7	32.7	1210.3	47.6	102
H-3A	#58	1.36	0.59	1.1607	0.0963	0.1101	0.0095	785.0	51.0	681.4	55.8	87
H-3A	#59	0.26	0.09	3.5122	0.2353	0.1981	0.0099	1578.3	43.4	1243.9	56.8	79
H-3A	#60	0.49	0.18	2.9785	0.1787	0.2146	0.0131	1450.7	50.7	1334.1	73.9	92
H-3A	#61	0.56	0.10	1.8945	0.1042	0.1691	0.0073	1086.2	32.5	1056.0	43.0	97
H-3A	#62	0.31	0.16	2.0153	0.1169	0.1936	0.0093	1185.1	37.8	1196.5	53.7	101
H-3A	#63	0.67	0.36	1.4501	0.0856	0.1493	0.0058	941.1	26.7	942.5	35.2	100
H-3A	#64	0.66	0.19	1.4151	0.0467	0.1415	0.0040	918.3	18.9	897.1	24.3	98
H-3A	#65	0.44	0.24	1.4999	0.0750	0.1555	0.0068	976.6	30.6	980.2	41.1	100
H-3A	#66	0.61	0.35	0.6348	0.0336	0.0774	0.0036	513.4	21.2	507.1	23.4	99
H-3A	#67	0.33	0.07	1.2439	0.0647	0.1225	0.0042	850.1	22.7	798.9	26.4	94
H-3A	#68	0.64	0.19	2.7202	0.1333	0.2247	0.0101	1368.5	36.7	1374.2	57.2	100
H-3A	#69	0.20	0.10	1.1696	0.0725	0.1238	0.0059	809.1	31.1	794.4	36.7	98
H-3A	#70	0.79	0.11	1.4520	0.0682	0.1427	0.0064	948.1	30.7	908.5	39.1	96
H-3A	#71	0.86	0.11	2.3182	0.0301	0.1942	0.0012	1277.1	9.5	1210.2	8.8	95
H-3A	#72	0.11	0.10	1.4088	0.0268	0.1435	0.0020	990.1	10.8	956.1	13.3	97
H-3A	#73	0.36	0.12	1.7434	0.0663	0.1707	0.0061	1058.0	26.6	1084.6	36.0	103
H-3A	#74	0.50	0.11	1.8274	0.0731	0.1599	0.0061	1113.1	30.2	1031.1	36.3	93
H-3A	#75	0.39	0.97	1.8964	0.0815	0.1704	0.0080	1118.4	34.5	1077.1	46.8	96
H-3A	#76	0.54	0.10	1.7566	0.0668	0.1670	0.0018	1073.9	21.4	1046.8	12.6	97
H-3A	#77	0.20	0.10	1.4713	0.0603	0.1448	0.0054	972.5	26.6	939.1	32.4	97
H-3A	#78	0.26	0.14	2.1689	0.1171	0.1963	0.0090	1212.7	35.3	1228.6	51.7	101
H-3A	#79	0.52	0.07	15.0966	0.2868	0.4648	0.0051	2921.9	13.5	2593.3	27.8	89
H-3A	#80	0.26	0.14	6.5531	0.1573	0.3384	0.0037	2190.2	16.3	2007.4	22.5	92
H-3A	#81	0.35	0.19	2.1139	0.0846	0.1930	0.0073	1187.8	29.1	1217.3	42.3	102
H-3A	#82	0.32	0.18	1.5239	0.0671	0.1525	0.0066	979.2	30.0	981.3	39.3	100
H-3A	#83	0.41	0.06	1.7935	0.0735	0.1671	0.0084	1073.4	35.7	1065.5	49.3	99
H-3A	#84	0.18	0.05	1.9052	0.0686	0.1886	0.0058	1132.3	24.9	1194.2	35.0	105
H-3A	#85	0.66	0.37	0.4569	0.0251	0.0594	0.0029	397.9	18.9	400.1	18.6	101
H-3A	#86	1.76	0.99	0.7546	0.0475	0.0893	0.0038	610.5	23.2	612.8	25.2	100
H-3A	#87	0.41	0.24	1.4214	0.0611	0.1392	0.0054	922.0	27.0	901.7	32.9	98
H-3A	#88	0.40	0.21	1.4671	0.0866	0.1506	0.0045	956.9	21.9	970.9	28.0	101
H-3A	#89	0.12	0.41	1.2831	0.0629	0.1312	0.0060	874.1	29.1	854.5	36.9	98
H-3A	#90	0.26	0.15	1.1404	0.0901	0.1252	0.0039	815.0	23.8	818.5	24.6	100
H-3A	#91	0.05	0.02	0.7780	0.0615	0.0926	0.0044	634.5	24.8	632.8	29.0	100
H-3A	#92	0.37	0.21	1.5285	0.0673	0.1544	0.0065	981.5	28.7	998.1	39.0	102
H-3A	#93	0.14	0.06	8.5790	0.3946	0.3876	0.0163	2364.9	43.1	2263.7	80.7	96
H-3A	#94	0.69	0.15	12.0441	0.9033	0.4281	0.0283	2650.9	65.1	2461.1	136.5	93
H-3A	#95	0.27	0.13	1.6590	0.0664	0.1604	0.0064	1045.4	28.5	1035.8	38.4	99
H-3A	#96	0.30	0.17	0.8550	0.0393	0.0986	0.0041	657.4	23.0	656.3	26.3	100
H-3A	#97	0.10	0.05	4.4652	0.1741	0.2991	0.0108	1772.7	33.2	1816.1	57.2	102
H-3A	#98	0.85	0.33	2.0385	0.0999	0.1820	0.0075	1187.3	33.4	1165.2	43.9	98
H-3A	#99	0.15	0.08	0.8685	0.0426	0.1009	0.0046	678.7	25.6	672.2	29.4	99
H-3A	#100	0.28	0.14	28.0378	1.2617	0.6649	0.0279	3475.6	47.2	3513.8	114.8	101
H-3A	#101	0.41	0.23	0.7919	0.0317	0.0925	0.0031	634.4	19.0	620.8	20.2	98
H-3A	#102	0.48	0.28	1.2278	0.0614	0.1273	0.0057	861.2	28.9	840.1	35.5	98
H-3A	#103	0.30	0.15	14.3808	0.6471	0.5093	0.0204	2824.5	42.8	2855.0	92.9	101
H-3A	#104	0.25	0.15	5.2733	0.4166	0.3048	0.0213	1898.6	64.7	1855.8	113.9	98
H-3A	#105	0.67	0.18	3.4105	0.1262	0.2394	0.0072	1570.2	27.5	1500.9	40.3	96
H-3A	#106	1.27	0.67	0.6716	0.0343	0.0750	0.0032	546.5	22.2	516.5	21.4	95
H-3A	#107	0.32	0.12	1.4339	0.0516	0.1436	0.0049	950.6	23.7	942.3	29.9	99

Table A.62: Zrn U-Pb age dataset

Zircon U-Pb data

Sample	Spot #	Th/U[a]	$^{208}Pb/^{206}Pb$	Ratios				Ages (Ma)				Cc[c]
				$^{207}Pb/^{235}U$[a]	2 σ[b]	$^{206}Pb/^{238}U$[a]	2 σ[b]	$^{207}Pb/^{235}U$	2 σ	$^{206}Pb/^{238}U$	2 σ	%
H-3A	#108	1.25	0.55	1.2682	0.0495	0.1236	0.0042	858.6	22.3	809.8	25.9	94
H-3A	#109	0.51	0.28	2.1216	0.0976	0.1881	0.0077	1205.1	32.3	1209.8	45.4	100
H-3A	#110	0.50	0.10	1.3177	0.0369	0.1333	0.0039	916.8	20.7	880.5	23.9	96
H-3A	#111	0.38	0.11	1.5794	0.0758	0.1528	0.0066	1001.2	29.1	1002.1	40.0	100
H-3A	#112	0.20	0.07	1.2987	0.0481	0.1332	0.0048	905.2	24.2	882.1	29.7	97
H-3A	#113	0.21	0.09	1.4409	0.0447	0.1428	0.0046	955.4	23.2	941.9	28.1	99
H-3A	#114	0.40	0.22	3.0503	0.1281	0.2416	0.0087	1489.4	30.9	1522.1	49.0	102
H-3A	#115	0.34	0.18	1.5868	0.0571	0.1578	0.0063	1017.1	28.0	1034.1	38.3	102
H-3A	#116	0.29	0.16	1.3372	0.0548	0.1381	0.0046	901.7	22.4	914.5	28.2	101
H-3A	#117	0.34	0.17	9.6642	0.3576	0.4410	0.0163	2506.0	36.9	2557.0	78.6	102

[a] Corrected for background and within-run Pb/U fractionation and normalised to reference zircon GJ-1 (ID-TIMS values/measured value); $^{207}Pb/^{235}U$ calculated using $(^{207}Pb/^{206}Pb)/(^{238}U/^{206}Pb \times 1/137.88)$.
[b] Quadratic addition of within-run errors (2 sd) and daily reproducibility of GJ-1 (2 sd).
[c] Concordance of $^{206}Pb/^{238}U$ and $^{207}Pb/^{235}U$.

Table A.63: Zrn U-Pb age components

Epoch	Sample	mean [Ma]	s.d. [Ma]	w. [%]
Eocene	H-15B	50	---	2
		91	3	4
		112	4	49
		124	8	38
		166	7	7
	H-37A	37	2	2
		112	5	92
		147	7	6
	H-39A	62	3	2
		77	2	2
		121	4	25
		140	9	71
	H-39F	78	---	2
		119	7	92
		155	9	6
	H-102A	48	---	1
		61	---	1
		85	---	1
		115	3	13
		137	8	85
	H-103	49	---	3
		72	---	2
		119	6	64
		130	3	15
		139	13	16
	H-104A	72	---	1
		88	3	4
		114	2	20
		127	6	73
		171	2	2
	H-66	83	---	1
		91	---	1
		104	2	46
		115	5	47
		134	3	5
Upper Cretaceous	H-9	117	5	78
		136	5	19
		152	4	3
	H-17A	90	4	2
		121	6	56
		129	4	23
		144	7	19
	H-18	129	9	100
	H-74B	50	---	1
		106	4	5
		120	2	30
		130	13	64
	H-75	51	3	7
		132	4	72
		146	4	17
		174	5	4

Table A.64: Ap fission track age dataset

Sample	Cryst	Ns	Ni	A	spontaneous Rho	induced Rho	Age H-17A	error ± 1σ	U ppm
H-17A	1	11	9	8	13.988	11.445	144.91	65.2	18.08
H-17A	2	56	85	12	47.474	72.058	78.52	13.61	113.835
H-17A	3	24	54	8	30.519	68.667	53.07	13.06	108.478
H-17A	4	6	7	12	5.086	5.934	101.97	56.77	9.375
H-17A	5	51	108	20	25.941	54.934	56.38	9.65	86.782
H-17A	6	16	25	16	10.173	15.895	76.29	24.47	25.111
H-17A	7	11	11	12	9.325	9.325	118.81	50.72	14.732
H-17A	8	7	21	16	4.451	13.352	39.85	17.41	21.093
H-17A	9	11	7	24	4.663	2.967	185.73	89.88	4.687
H-17A	10	29	33	12	24.585	27.976	104.52	26.69	44.195
H-17A	11	25	16	24	10.597	6.782	184.69	59.25	10.714
H-17A	12	7	7	12	5.934	5.934	118.81	63.55	9.375
H-17A	13	6	7	12	5.086	5.934	101.97	56.77	9.375
H-17A	14	5	9	12	4.239	7.63	66.27	36.99	12.053
H-17A	15	21	32	16	13.352	20.346	78.21	22.02	32.142
H-17A	16	11	10	12	9.325	8.477	130.57	57.11	13.392
H-17A	17	7	20	24	2.967	8.477	41.83	18.39	13.392
H-17A	18	25	47	16	15.895	29.883	63.47	15.76	47.208
H-17A	19	33	51	20	16.785	25.941	77.12	17.3	40.981
H-17A	20	26	43	8	33.062	54.68	72.1	17.97	86.381
H-17A	21	12	32	12	10.173	27.128	44.81	15.2	42.855
H-17A	22	9	10	16	5.722	6.358	107.02	49.22	10.044
H-17A	23	43	93	16	27.34	59.13	55.2	10.24	93.412
H-17A	24	15	34	40	3.815	8.647	52.69	16.37	13.66
H-17A	25	15	42	12	12.716	35.605	42.68	12.87	56.248
H-17A	26	19	41	16	12.08	26.068	55.33	15.4	41.181
H-17A	27	6	9	24	2.543	3.815	79.45	41.9	6.027
H-17A	28	13	20	36	3.674	5.652	77.47	27.65	8.928
H-17A	29	10	30	24	4.239	12.716	39.85	14.57	20.088
H-17A	30	8	12	16	5.086	7.63	79.45	36.3	12.053
H-17A	31	8	12	16	5.086	7.63	79.45	36.3	12.053
H-17A	32	11	31	8	13.988	39.42	42.41	14.91	62.274
H-17A	33	39	62	12	33.062	52.56	74.99	15.4	83.032
H-17A	34	47	112	20	23.906	56.968	50.12	8.77	89.996
H-17A	35	52	129	16	33.062	82.019	48.16	7.97	129.571
H-17A	36	7	7	12	5.934	5.934	118.81	63.55	9.375
H-17A	37	40	71	16	25.432	45.142	67.2	13.36	71.314
H-17A	38	29	42	12	24.585	35.605	82.27	19.93	56.248
H-17A	39	10	10	20	5.086	5.086	118.81	53.19	8.035
H-17A	40	20	39	16	12.716	24.797	61.2	16.88	39.173
H-17A	41	50	105	12	42.387	89.013	56.85	9.84	140.619
H-17A	42	16	34	20	8.138	17.294	56.18	17.07	27.32
H-17A	43	10	19	12	8.477	16.107	62.8	24.57	25.445
H-17A	44	9	10	12	7.63	8.477	107.02	49.22	13.392
H-17A	45	11	17	12	9.325	14.412	77.12	29.88	22.767

Table A.65: Ap fission track age dataset

Sample	Cryst	Ns	Ni	A	spontaneous Rho	induced Rho	Age H-17A	error ± 1σ	U ppm
H-17A	46	4	4	12	3.391	3.391	118.81	84.04	5.357
H-17A	47	10	20	12	8.477	16.955	59.68	23.14	26.785
H-17A	48	54	99	36	15.259	27.976	65.08	11.09	44.195
H-17A	49	4	30	12	3.391	25.432	15.97	8.51	40.177
H-17A	50	10	146	16	6.358	92.828	8.21	2.69	146.646
H-17A	51	7	5	12	5.934	4.239	165.72	97.1	6.696
H-17A	52	7	8	16	4.451	5.086	104.08	53.91	8.035
H-17A	53	12	30	8	15.259	38.149	47.79	16.35	60.265
H-17A	54	38	56	12	32.214	47.474	80.86	17.07	74.997
H-17A	55	13	21	8	16.531	26.704	73.81	26.09	42.186
H-17A	56	6	5	8	7.63	6.358	142.31	86.22	10.044
H-17A	57	13	24	8	16.531	30.519	64.63	22.29	48.212
H-17A	58	6	32	16	3.815	20.346	22.44	10	32.142
H-17A	59	13	45	24	5.51	19.074	34.55	10.9	30.133
H-17A	60	24	31	24	10.173	13.14	92.17	25.13	20.758
H-17A	61	26	64	36	7.347	18.085	48.53	11.33	28.57
H-17A	62	19	56	16	12.08	35.605	40.56	10.8	56.248
H-17A	63	21	34	12	17.803	28.823	73.64	20.49	45.534
H-17A	64	34	20	24	14.412	8.477	200.69	56.7	13.392
H-17A	65	24	82	24	10.173	34.758	35	8.15	54.909
H-17A	66	15	34	36	4.239	9.608	52.69	16.37	15.178
H-17A	67	8	13	36	2.261	3.674	73.37	33	5.803
H-17A	68	12	32	36	3.391	9.043	44.81	15.2	14.285
H-17C	1	29	31	16	18.438	19.71	103.78	26.9	33.384
H-17C	2	14	21	36	3.956	5.934	74.13	25.62	10.051
H-17C	3	60	102	36	16.955	28.823	65.45	10.74	48.82
H-17C	4	12	14	12	10.173	11.868	95.16	37.49	20.102
H-17C	5	17	21	20	8.647	10.682	89.91	29.39	18.092
H-17C	6	6	6	12	5.086	5.086	110.88	64.06	8.615
H-17C	7	24	39	40	6.104	9.919	68.46	17.82	16.8
H-17C	8	31	66	60	5.256	11.19	52.32	11.44	18.954
H-17C	9	11	16	12	9.325	13.564	76.43	29.98	22.974
H-17C	10	27	49	24	11.445	20.77	61.33	14.75	35.179
H-17C	11	14	27	12	11.868	22.889	57.73	19.05	38.769
H-17C	12	6	14	24	2.543	5.934	47.75	23.32	10.051
H-17C	13	32	59	12	27.128	50.017	60.37	13.31	84.717
H-17C	14	62	106	12	52.56	89.861	65.09	10.49	152.203
H-17C	15	6	9	12	5.086	7.63	74.13	39.1	12.923
H-17C	16	6	2	12	5.086	1.695	327.07	267.14	2.872
H-17C	17	26	29	12	22.041	24.585	99.5	26.95	41.64
H-17C	18	43	45	40	10.936	11.445	105.99	22.71	19.384
H-17C	19	18	24	12	15.259	20.346	83.34	26.04	34.461
H-17C	20	60	108	24	25.432	45.778	61.83	10.04	77.537
H-17C	21	49	52	24	20.77	22.041	104.53	20.92	37.333
H-17C	22	27	42	12	22.889	35.605	71.5	17.7	60.307

Table A.66: Ap fission track age dataset

Sample	Cryst	Ns	Ni	A	spontaneous Rho	induced Rho	Age H-17A	error ± 1σ	U ppm
H-17C	23	16	29	8	20.346	36.877	61.41	19.17	62.461
H-17C	24	24	38	8	30.519	48.321	70.25	18.37	81.845
H-17C	25	13	28	24	5.51	11.868	51.72	17.39	20.102
H-17C	26	12	14	12	10.173	11.868	95.16	37.49	20.102
H-17C	27	76	132	16	48.321	83.927	64.07	9.32	142.152
H-17C	28	13	15	20	6.612	7.63	96.2	36.51	12.923
H-17C	29	18	29	24	7.63	12.292	69.05	20.77	20.82
H-17C	30	6	14	16	3.815	8.901	47.75	23.32	15.077
H-17C	31	16	23	12	13.564	19.498	77.33	25.23	33.025
H-17C	32	11	12	12	9.325	10.173	101.71	42.51	17.231
H-17C	33	6	4	12	5.086	3.391	165.61	106.96	5.744
H-17C	34	30	53	12	25.432	44.93	63	14.45	76.102
H-17C	35	11	28	8	13.988	35.605	43.79	15.61	60.307
H-17C	36	6	2	12	5.086	1.695	327.07	267.14	2.872
H-17C	37	81	126	12	68.667	106.816	71.5	10.29	180.921
H-17C	38	10	20	40	2.543	5.086	55.68	21.59	8.615
H-17C	39	22	21	12	18.65	17.803	116.11	35.5	30.153
H-17C	40	54	123	12	45.778	104.273	48.91	8.05	176.613
H-17C	41	11	17	16	6.994	10.809	71.96	27.89	18.307
H-17C	42	25	32	24	10.597	13.564	86.79	23.24	22.974
H-17C	43	21	36	20	10.682	18.311	64.91	17.87	31.015
H-17C	44	40	70	24	16.955	29.671	63.59	12.67	50.256
H-17C	45	45	44	24	19.074	18.65	113.38	24.15	31.589
H-17C	46	17	30	16	10.809	19.074	63.07	19.19	32.307
H-17C	47	48	101	12	40.692	85.622	52.93	9.34	145.024
H-17C	48	5	3	12	4.239	2.543	183.75	134.25	4.308
H-17C	49	40	38	24	16.955	16.107	116.66	26.54	27.282
H-17C	50	72	89	24	30.519	37.725	89.85	14.36	63.897
H-18	1	11	24	12	9.325	20.346	53.68	19.57	32.772
H-18	2	37	53	16	23.525	33.698	81.58	17.56	54.278
H-18	3	11	32	12	9.325	27.128	40.3	14.11	43.696
H-18	4	13	33	24	5.51	13.988	46.16	15.14	22.531
H-18	5	13	38	16	8.266	24.161	40.11	12.91	38.917
H-18	6	11	25	16	6.994	15.895	51.54	18.68	25.603
H-18	7	16	25	24	6.782	10.597	74.83	24.01	17.069
H-18	8	27	44	24	11.445	18.65	71.76	17.6	30.041
H-18	9	12	38	12	10.173	32.214	37.03	12.29	51.889
H-18	10	22	68	8	27.976	86.47	37.94	9.34	139.28
H-18	11	17	19	16	10.809	12.08	104.37	34.91	19.458
H-18	12	14	33	16	8.901	20.982	49.7	15.88	33.796
H-18	13	72	177	24	30.519	75.025	47.66	6.73	120.846
H-18	14	24	80	16	15.259	50.865	35.18	8.22	81.93
H-18	15	25	53	24	10.597	22.465	55.24	13.45	36.186
H-18	16	18	31	16	11.445	19.71	67.93	20.18	31.748

Table A.67: Ap fission track age dataset

Sample	Cryst	Ns	Ni	A	spontaneous Rho	induced Rho	Age H-17A	error ± 1σ	U ppm
H-27	1	28	29	16	17.803	18.438	104.74	27.83	31.936
H-27	2	6	8	16	3.815	5.086	81.51	44.05	8.81
H-27	3	6	17	36	1.695	4.804	38.49	18.29	8.32
H-27	4	3	3	12	2.543	2.543	108.45	88.58	4.405
H-27	5	23	23	60	3.9	3.9	108.45	32.06	6.754
H-27	6	12	30	16	7.63	19.074	43.6	14.92	33.037
H-27	7	21	35	60	3.561	5.934	65.29	18.07	10.278
H-27	8	24	61	8	30.519	77.569	42.89	10.37	134.351
H-27	9	12	43	36	3.391	12.151	30.45	9.96	21.046
H-27	10	3	27	12	2.543	22.889	12.14	7.39	39.645
H-27	11	19	39	36	5.369	11.021	53.06	14.89	19.088
H-27	12	34	46	6	57.647	77.993	80.33	18.24	135.085
H-27	13	12	36	16	7.63	22.889	36.35	12.14	39.645
H-27	14	23	24	12	19.498	20.346	103.97	30.41	35.24
H-27	15	8	23	24	3.391	9.749	37.93	15.59	16.886
H-27	16	12	24	32	3.815	7.63	54.45	19.28	13.215
H-27	17	25	16	24	10.597	6.782	168.66	54.11	11.747
H-27	18	59	81	24	25.008	34.334	79.17	13.65	59.467
H-27	19	12	18	12	10.173	15.259	72.5	27.06	26.43
H-27	20	5	10	16	3.179	6.358	54.45	29.85	11.012
H-27	21	17	34	24	7.206	14.412	54.45	16.21	24.961
H-27	22	8	16	16	5.086	10.173	54.45	23.61	17.62
H-27	23	17	15	24	7.206	6.358	122.77	43.56	11.012
H-27	24	14	44	24	5.934	18.65	34.71	10.67	32.303
H-27	25	82	135	24	34.758	57.223	66.09	9.35	99.111
H-27	26	33	35	24	13.988	14.836	102.3	24.91	25.696
H-27	27	56	30	40	14.242	7.63	200.99	45.66	13.215
H-27	28	32	40	24	13.564	16.955	86.91	20.69	29.366
H-27	29	42	44	12	35.605	37.301	103.56	22.44	64.606
H-27	30	7	7	24	2.967	2.967	108.45	58.01	5.139
H-27	31	23	4	12	19.498	3.391	600.05	325.3	5.873
H-37A	1	20	31	36	5.652	8.76	76.06	21.87	13.993
H-37A	2	13	44	24	5.51	18.65	34.94	11.05	29.791
H-37A	3	22	31	36	6.217	8.76	83.62	23.37	13.993
H-37A	4	41	75	24	17.379	31.79	64.51	12.6	50.779
H-37A	5	21	27	8	26.704	34.334	91.58	26.71	54.842
H-37A	6	21	72	12	17.803	61.038	34.5	8.58	97.496
H-37A	7	5	8	16	3.179	5.086	73.7	42.04	8.125
H-37A	8	8	9	12	6.782	7.63	104.56	50.85	12.187
H-37A	9	23	15	16	14.624	9.537	179.32	59.62	15.234
H-37A	10	22	18	12	18.65	15.259	143.34	45.65	24.374
H-37A	11	16	27	20	8.138	13.733	69.9	22.1	21.937
H-37A	12	7	20	12	5.934	16.955	41.37	18.19	27.082
H-37A	13	29	41	24	12.292	17.379	83.34	20.29	27.759
H-37A	14	15	20	12	12.716	16.955	88.34	30.23	27.082

Table A.68: Ap fission track age dataset

Sample	Cryst	Ns	Ni	A	spontaneous Rho	induced Rho	Age H-17A	error ± 1σ	U ppm
H-37A	15	15	18	20	7.63	9.156	98.08	34.35	14.624
H-37A	16	43	53	12	36.453	44.93	95.5	19.7	71.768
H-37A	17	22	49	36	6.217	13.847	53.03	13.65	22.117
H-37A	18	21	20	10	21.363	20.346	123.33	38.62	32.499
H-37A	19	31	20	36	8.76	5.652	181.24	52.11	9.027
H-37A	20	22	28	24	9.325	11.868	92.51	26.42	18.958
H-37A	21	29	33	18	16.39	18.65	103.38	26.4	29.791
H-37A	22	52	45	36	14.694	12.716	135.6	27.74	20.312
H-37A	23	15	21	36	4.239	5.934	84.16	28.5	9.479
H-37A	24	56	57	16	35.605	36.241	115.47	21.85	57.888
H-37A	25	13	13	12	11.021	11.021	117.51	46.15	17.603
H-37A	26	104	117	36	29.388	33.062	104.56	14.25	52.81
H-37A	27	5	15	12	4.239	12.716	39.41	20.37	20.312
H-37A	28	17	38	16	10.809	24.161	52.84	15.45	38.592
H-37A	29	13	36	12	11.021	30.519	42.68	13.84	48.748
H-37A	30	9	15	12	7.63	12.716	70.76	29.87	20.312
H-37A	31	55	94	24	23.313	39.844	69.02	11.8	63.643
H-37A	32	51	96	12	43.235	81.384	62.7	10.94	129.995
H-37A	33	12	15	12	10.173	12.716	94.18	36.53	20.312
H-37A	34	31	18	8	39.42	22.889	201.07	59.72	36.561
H-37A	35	18	16	12	15.259	13.564	132.05	45.45	21.666
H-37A	36	24	31	12	20.346	26.28	91.16	24.86	41.978
H-37A	37	16	31	8	20.346	39.42	60.92	18.79	62.966
H-37A	38	18	20	24	7.63	8.477	105.86	34.46	13.541
H-37A	39	25	12	24	10.597	5.086	242.45	85.29	8.125
H-37A	40	35	42	20	17.803	21.363	98.08	22.53	34.124
H-37A	41	28	22	12	23.737	18.65	149.19	42.61	29.791
H-37A	42	14	26	36	3.956	7.347	63.54	21.1	11.736
H-37A	43	12	25	12	10.173	21.194	56.67	19.94	33.853
H-37A	44	20	20	20	10.173	10.173	117.51	37.24	16.249
H-37A	45	29	45	36	8.195	12.716	75.98	18.16	20.312
H-37A	46	69	61	12	58.494	51.712	132.77	23.49	82.601
H-37A	47	12	11	12	10.173	9.325	128.09	53.53	14.895
H-37A	48	10	10	12	8.477	8.477	117.51	52.61	13.541
H-37A	49	4	6	12	3.391	5.086	78.58	50.75	8.125
H-39A	1	28	41	8	35.605	52.136	78.26	19.26	85.657
H-39A	2	8	8	16	5.086	5.086	114.28	57.19	8.357
H-39A	3	45	88	12	38.149	74.602	58.69	10.82	122.567
H-39A	4	22	25	16	13.988	15.895	100.67	29.5	26.115
H-39A	5	28	12	16	17.803	7.63	263.56	91.1	12.535
H-39A	6	12	9	12	10.173	7.63	151.92	67.07	12.535
H-39A	7	24	48	16	15.259	30.519	57.39	14.4	50.141
H-39A	8	43	117	24	18.227	49.593	42.24	7.58	81.479
H-39A	9	73	163	20	37.131	82.909	51.43	7.32	136.216
H-39A	10	13	24	12	11.021	20.346	62.15	21.44	33.427

Table A.69: Ap fission track age dataset

Sample	Cryst	Ns	Ni	A	spontaneous Rho	induced Rho	Age H-17A	error ± 1σ	U ppm
H-39A	11	22	28	12	18.65	23.737	89.96	25.7	38.998
H-39A	12	21	58	24	8.901	24.585	41.61	10.63	40.391
H-39A	13	19	55	8	24.161	69.939	39.71	10.6	114.906
H-39A	14	7	14	20	3.561	7.121	57.39	26.59	11.7
H-39A	15	29	31	12	24.585	26.28	106.97	27.72	43.177
H-39A	16	20	15	16	12.716	9.537	151.92	51.99	15.669
H-39A	17	20	12	8	25.432	15.259	189.35	69.25	25.07
H-39A	18	8	14	12	6.782	11.868	65.55	29.08	19.499
H-39A	19	12	15	12	10.173	12.716	91.58	35.52	20.892
H-39A	20	27	33	24	11.445	13.988	93.65	24.38	22.981
H-39A	21	34	26	24	14.412	11.021	149.04	38.95	18.106
H-42A	1	8	20	24	3.391	8.477	44.84	18.78	14.275
H-42A	2	8	13	20	4.069	6.612	68.86	30.98	11.134
H-42A	3	19	21	40	4.832	5.341	100.99	32.04	8.993
H-42A	4	15	20	20	7.63	10.173	83.83	28.68	17.13
H-42A	5	10	12	12	8.477	10.173	93.07	39.9	17.13
H-42A	6	12	12	16	7.63	7.63	111.53	45.59	12.847
H-42A	7	17	31	24	7.206	13.14	61.4	18.57	22.126
H-42A	8	14	26	24	5.934	11.021	60.29	20.03	18.557
H-42A	9	11	14	24	4.663	5.934	87.79	35.42	9.992
H-42A	10	11	12	20	5.595	6.104	102.31	42.76	10.278
H-42A	11	9	17	16	5.722	10.809	59.28	24.47	18.2
H-42A	12	5	3	24	2.119	1.272	184.82	135.03	2.141
H-42A	13	10	13	16	6.358	8.266	85.96	36.2	13.918
H-42A	14	5	10	8	6.358	12.716	56	30.7	21.412
H-42A	15	5	12	24	2.119	5.086	46.7	24.88	8.565
H-42A	16	10	20	24	4.239	8.477	56	21.72	14.275
H-42A	17	12	10	16	7.63	6.358	133.6	57.27	10.706
H-42A	18	8	10	12	6.782	8.477	89.38	42.43	14.275
H-42A	19	14	24	24	5.934	10.173	65.29	22	17.13
H-42A	20	10	30	40	2.543	7.63	37.39	13.67	12.847
H-42A	21	24	53	40	6.104	13.479	50.74	12.53	22.697
H-42A	22	35	30	40	8.901	7.63	129.93	32.44	12.847
H-42A	23	11	22	24	4.663	9.325	56	20.71	15.702
H-42A	24	27	22	36	7.63	6.217	136.61	39.34	10.468
H-42A	25	12	71	40	3.052	18.057	18.99	5.94	30.405
H-42A	26	23	13	24	9.749	5.51	196.02	68.14	9.279
H-42A	27	8	18	24	3.391	7.63	49.81	21.19	12.847
H-42A	28	12	21	24	5.086	8.901	63.97	23.19	14.988
H-42A	29	3	7	24	1.272	2.967	48.03	33.16	4.996
H-42A	30	14	17	40	3.561	4.323	91.99	33.25	7.28
H-42A	31	11	15	20	5.595	7.63	81.97	32.58	12.847
H-42A	32	7	4	12	5.934	3.391	193.92	121.61	5.71
H-42A	33	37	43	40	9.41	10.936	96.08	21.64	18.414
H-42A	34	9	18	40	2.289	4.578	56	22.89	7.708

Table A.70: Ap fission track age dataset

Sample	Cryst	Ns	Ni	A	spontaneous Rho	induced Rho	Age H-17A	error ± 1σ	U ppm
H-42A	35	11	25	40	2.798	6.358	49.31	17.87	10.706
H-42A	36	14	46	24	5.934	19.498	34.15	10.45	32.832
H-42A	37	15	22	12	12.716	18.65	76.25	25.58	31.404
H-42A	38	17	36	8	21.617	45.778	52.91	15.61	77.083
H-42A	39	4	17	24	1.695	7.206	26.42	14.69	12.133
H-42A	40	7	17	12	5.934	14.412	46.16	20.75	24.267
H-42A	41	6	14	8	7.63	17.803	48.03	23.46	29.977
H-42A	42	5	3	8	6.358	3.815	184.82	135.03	6.424
H-42A	43	5	24	24	2.119	10.173	23.39	11.51	17.13
H-42A	44	6	6	24	2.543	2.543	111.53	64.43	4.282
H-42A	45	17	28	24	7.206	11.868	67.94	20.94	19.985
H-42A	46	13	34	32	4.133	10.809	42.87	14.01	18.2
H-42A	47	6	18	24	2.543	7.63	37.39	17.64	12.847
H-42A	48	9	12	12	7.63	10.173	83.83	37	17.13
H-42A	49	6	11	12	5.086	9.325	61.07	31.02	15.702
H-42A	50	10	23	20	5.086	11.699	48.73	18.48	19.699
H-42A	51	6	7	24	2.543	2.967	95.71	53.29	4.996
H-42A	52	6	9	12	5.086	7.63	74.57	39.33	12.847
H-66	1	19	27	16	12.08	17.167	80.17	24.06	28.366
H-66	2	17	40	16	10.809	25.432	48.54	14.09	42.024
H-66	3	20	22	16	12.716	13.988	103.38	32.01	23.113
H-66	4	16	20	16	10.173	12.716	91.06	30.6	21.012
H-66	5	12	24	16	7.63	15.259	57.07	20.21	25.215
H-66	6	35	56	16	22.253	35.605	71.25	15.42	58.834
H-66	7	13	19	12	11.021	16.107	77.96	28.11	26.615
H-66	8	55	157	16	34.969	99.822	40.04	6.33	164.945
H-66	9	20	38	16	12.716	24.161	60.06	16.64	39.923
H-66	10	24	22	20	12.208	11.19	123.86	36.65	18.491
H-66	11	11	16	12	9.325	13.564	78.34	30.72	22.413
H-66	12	20	25	20	10.173	12.716	91.06	27.38	21.012
H-66	13	12	22	16	7.63	13.988	62.23	22.37	23.113
H-66	14	23	24	16	14.624	15.259	108.94	31.87	25.215
H-66	15	25	66	24	10.597	27.976	43.28	10.2	46.227
H-66	16	8	7	24	3.391	2.967	129.7	67.18	4.903
H-66	17	33	57	32	10.491	18.121	66.03	14.51	29.942
H-66	18	39	28	36	11.021	7.912	157.73	39.2	13.074
H-66	19	12	13	12	10.173	11.021	104.96	42.07	18.21
H-66	20	14	34	32	4.451	10.809	47.03	14.97	17.86
H-66	21	39	72	36	11.021	20.346	61.8	12.35	33.619
H-66	22	31	36	32	9.855	11.445	97.97	24.09	18.911
H-66	23	18	33	24	7.63	13.988	62.23	18.28	23.113
H-66	24	12	12	16	7.63	7.63	113.63	46.45	12.607
H-66	25	19	35	24	8.054	14.836	61.93	17.69	24.514
H-66	26	24	35	24	10.173	14.836	78.13	20.77	24.514
H-66	27	19	21	24	8.054	8.901	102.89	32.65	14.708

Table A.71: Ap fission track age dataset

Sample	Cryst	Ns	Ni	A	spontaneous Rho	induced Rho	Age H-17A	error ± 1σ	U ppm
H-66	28	14	21	12	11.868	17.803	75.98	26.26	29.417
H-66	29	11	13	16	6.994	8.266	96.28	39.49	13.658
H-66	30	26	39	20	13.225	19.837	75.98	19.3	32.779
H-66	31	34	63	36	9.608	17.803	61.57	13.16	29.417
H-66	32	20	37	24	8.477	15.683	61.67	17.16	25.915
H-66	33	23	25	40	5.849	6.358	104.61	30.3	10.506
H-66	34	19	36	24	8.054	15.259	60.22	17.12	25.215
H-66	35	21	28	24	8.901	11.868	85.41	24.72	19.611
H-66	36	24	36	36	6.782	10.173	75.98	20.08	16.81
H-66	37	24	38	12	20.346	32.214	72	18.83	53.231
H-66	38	23	25	20	11.699	12.716	104.61	30.3	21.012
H-66	39	10	20	16	6.358	12.716	57.07	22.13	21.012
H-66	40	21	28	36	5.934	7.912	85.41	24.72	13.074
H-66	41	17	25	12	14.412	21.194	77.49	24.41	35.02
H-66	42	37	68	36	10.456	19.216	62.08	12.75	31.752
H-66	43	71	128	16	45.142	81.384	63.28	9.45	134.477
H-66	44	24	41	24	10.173	17.379	66.76	17.21	28.717
H-66	45	32	30	16	20.346	19.074	121.14	30.88	31.518
H-66	46	50	70	40	12.716	17.803	81.37	15.16	29.417
H-66	47	44	79	36	12.434	22.324	63.53	12.02	36.888
H-66	48	33	55	24	13.988	23.313	68.42	15.13	38.522
H-66	49	15	17	36	4.239	4.804	100.37	35.61	7.938
H-66	50	62	131	16	39.42	83.291	54.03	8.4	137.629
H-66	51	46	61	36	12.999	17.237	85.87	16.86	28.483
H-66	52	18	37	40	4.578	9.41	55.53	16	15.549
H-66	53	23	40	32	7.312	12.716	65.58	17.21	21.012
H-66	54	23	23	24	9.749	9.749	113.63	33.59	16.109
H-66	55	50	84	36	14.129	23.737	67.88	12.2	39.223
H-66	56	12	17	24	5.086	7.206	80.42	30.37	11.907
H-66	57	30	29	24	12.716	12.292	117.51	30.7	20.312
H-66	58	54	79	30	18.311	26.789	77.89	13.84	44.266
H-66	59	22	30	24	9.325	12.716	83.52	23.51	21.012
H-66	60	27	47	24	11.445	19.922	65.52	15.88	32.919
H-66	61	22	25	24	9.325	10.597	100.1	29.33	17.51
H-66	62	22	42	36	6.217	11.868	59.77	15.78	19.611
H-66	63	23	31	24	9.749	13.14	84.5	23.32	21.713
H-66	64	28	44	24	11.868	18.65	72.54	17.6	30.818
H-66	65	15	36	40	3.815	9.156	47.59	14.66	15.129
H-66	66	20	37	24	8.477	15.683	61.67	17.16	25.915
H-66	67	30	99	12	25.432	83.927	34.65	7.26	138.68
H-66	68	22	34	16	13.988	21.617	73.75	20.24	35.721
H-66	69	49	94	12	41.54	79.688	59.48	10.55	131.676
H-66	70	6	16	12	5.086	13.564	42.85	20.53	22.413
H-66	71	16	20	16	10.173	12.716	91.06	30.6	21.012
H-66	72	15	20	16	9.537	12.716	85.41	29.23	21.012
H-66	73	14	18	16	8.901	11.445	88.55	31.61	18.911

Table A.72: Ap fission track age dataset

Sample	Cryst	Ns	Ni	A	spontaneous Rho	induced Rho	Age H-17A	error ± 1σ	U ppm
H-66	74	21	39	24	8.901	16.531	61.43	16.68	27.316
H-66	75	14	21	24	5.934	8.901	75.98	26.26	14.708
H-66	76	12	17	12	10.173	14.412	80.42	30.37	23.814
H-66	77	56	90	132	4.316	6.936	70.94	12.16	11.461
H-66	78	24	20	12	20.346	16.955	136.12	41.31	28.016
H-66	79	26	34	16	16.531	21.617	87.07	22.76	35.721
H-66	80	15	22	16	9.537	13.988	77.69	26.06	23.113
H-66	81	56	77	12	47.474	65.276	82.84	14.65	107.862
H-66	82	20	19	36	5.652	5.369	119.56	38.38	8.872
H-66	83	17	18	24	7.206	7.63	107.37	36.38	12.607
H-66	84	23	35	18	12.999	19.781	74.9	20.16	32.686
H-66	85	104	137	16	66.124	87.106	86.44	11.38	143.933
H-66	86	26	25	36	7.347	7.065	118.13	33.18	11.673
H-66	87	41	39	24	17.379	16.531	119.4	26.82	27.316
H-66	88	25	34	36	7.065	9.608	83.75	22.13	15.876
H-66	89	18	29	24	7.63	12.292	70.76	21.28	20.312
H-66	90	31	51	24	13.14	21.617	69.31	15.85	35.721
H-66	91	20	35	24	8.477	14.836	65.18	18.32	24.514
H-66	92	30	35	40	7.63	8.901	97.52	24.35	14.708
H-66	93	13	23	12	11.021	19.498	64.47	22.41	32.219
H-66	94	29	51	40	7.375	12.97	64.86	15.14	21.432
H-66	95	7	10	12	5.934	8.477	79.75	39.34	14.008
H-66	96	21	44	24	8.901	18.65	54.48	14.49	30.818
H-66	97	16	28	24	6.782	11.868	65.18	20.47	19.611
H-66	98	22	46	24	9.325	19.498	54.6	14.2	32.219
H-66	99	28	26	24	11.868	11.021	122.29	33.4	18.21
H-66	100	22	27	36	6.217	7.63	92.74	26.7	12.607
H-74A	1	12	45	12	10.173	38.149	30.94	10.07	62.143
H-74A	2	13	98	12	11.021	83.079	15.41	4.56	135.335
H-74A	3	23	62	12	19.498	52.56	42.99	10.53	85.62
H-74A	4	54	182	24	22.889	77.145	34.41	5.38	125.668
H-74A	5	15	24	8	19.074	30.519	72.27	23.83	49.715
H-74A	6	13	41	8	16.531	52.136	36.77	11.73	84.929
H-74A	7	20	52	8	25.432	66.124	44.57	11.76	107.715
H-74A	8	12	92	4	30.519	233.978	15.15	4.66	381.147
H-74A	9	14	50	12	11.868	42.387	32.48	9.84	69.048
H-74A	10	8	67	16	5.086	42.599	13.87	5.2	69.394
H-74A	11	22	37	4	55.951	94.1	68.77	18.57	153.287
H-74A	12	14	30	8	17.803	38.149	54.04	17.53	62.143
H-74A	13	19	68	16	12.08	43.235	32.41	8.44	70.429
H-74A	14	9	24	4	22.889	61.038	43.46	17.01	99.43
H-74A	15	20	44	12	16.955	37.301	52.64	14.24	60.762
H-74A	16	18	26	12	15.259	22.041	80.01	24.59	35.905
H-74A	17	6	7	16	3.815	4.451	98.91	55.07	7.25
H-74A	18	10	16	8	12.716	20.346	72.27	29.17	33.143

Table A.73: Ap fission track age dataset

Sample	Cryst	Ns	Ni	A	spontaneous Rho	induced Rho	Age H-17A	error ± 1σ	U ppm
H-74A	19	15	67	8	19.074	85.198	25.98	7.44	138.787
H-74A	20	74	94	16	47.05	59.766	90.9	14.25	97.358
H-74A	21	42	102	8	53.408	129.705	47.71	8.8	211.288
H-74A	22	18	35	8	22.889	44.507	59.53	17.31	72.501
H-74A	23	4	13	16	2.543	8.266	35.68	20.41	13.464
H-74A	24	10	32	8	12.716	40.692	36.24	13.15	66.286
H-74A	25	17	53	16	10.809	33.698	37.19	10.39	54.893
H-74A	26	31	49	16	19.71	31.155	73.15	16.85	50.75
H-74A	27	30	50	8	38.149	63.581	69.4	16.09	103.572
H-74A	28	36	82	12	30.519	69.515	50.85	10.22	113.239
H-74A	29	22	51	8	27.976	64.852	49.97	12.79	105.644
H-74A	30	23	46	12	19.498	38.996	57.88	14.83	63.524
H-74A	31	24	63	12	20.346	53.408	44.15	10.63	87.001
H-74A	32	8	17	4	20.346	43.235	54.49	23.39	70.429
H-74A	33	40	95	8	50.865	120.804	48.78	9.25	196.788
H-74A	34	16	33	12	13.564	27.976	56.14	17.14	45.572
H-74A	35	9	30	4	22.889	76.297	34.79	13.24	124.287
H-74A	36	29	64	8	36.877	81.384	52.48	11.8	132.573
H-74A	37	13	21	8	16.531	26.704	71.59	25.31	43.5
H-74A	38	27	53	8	34.334	67.396	58.97	14	109.787
H-74A	39	27	41	8	34.334	52.136	76.13	18.93	84.929
H-74A	40	12	17	12	10.173	14.412	81.57	30.8	23.476
H-74A	41	20	44	16	12.716	27.976	52.64	14.24	45.572
H-74A	42	39	83	16	24.797	52.772	54.41	10.62	85.965
H-74A	43	7	12	8	8.901	15.259	67.48	32.12	24.857
H-74A	44	10	21	8	12.716	26.704	55.14	21.21	43.5
H-74A	45	15	35	8	19.074	44.507	49.64	15.35	72.501
H-74A	46	21	47	12	17.803	39.844	51.75	13.62	64.905
H-74A	47	32	48	12	27.128	40.692	77.06	17.66	66.286
H-74A	48	16	139	8	20.346	176.755	13.37	3.54	287.931
H-74A	49	23	41	8	29.247	52.136	64.91	16.96	84.929
H-74A	50	12	38	12	10.173	32.214	36.62	12.15	52.477
H-102A	1	60	62	24	25.432	26.28	111.56	20.33	42.81
H-102A	2	61	129	20	31.027	65.615	54.75	8.58	106.887
H-102A	3	26	37	24	11.021	15.683	81.2	20.84	25.548
H-102A	4	14	17	12	11.868	14.412	95.06	34.36	23.476
H-102A	5	10	21	16	6.358	13.352	55.14	21.21	21.75
H-102A	6	66	156	24	27.976	66.124	49.01	7.26	107.715
H-102A	7	15	11	12	12.716	9.325	156.65	62.26	15.191
H-102A	8	15	23	24	6.358	9.749	75.4	25.07	15.881
H-102A	9	15	26	16	9.537	16.531	66.74	21.68	26.929
H-102A	10	28	34	24	11.868	14.412	95.06	24.34	23.476
H-102A	11	18	16	12	15.259	13.564	129.51	44.58	22.095
H-102A	12	71	131	16	45.142	83.291	62.72	9.33	135.68
H-102A	13	18	43	12	15.259	36.453	48.49	13.65	59.382

Table A.74: Ap fission track age dataset

Sample	Cryst	Ns	Ni	A	spontaneous Rho	induced Rho	Age H-17A	error ± 1σ	U ppm
H-102A	14	11	10	20	5.595	5.086	126.66	55.4	8.286
H-102A	15	14	14	24	5.934	5.934	115.25	43.62	9.667
H-102A	16	26	61	24	11.021	25.856	49.37	11.61	42.119
H-102A	17	43	77	12	36.453	65.276	64.61	12.37	106.334
H-102A	18	23	30	16	14.624	19.074	88.54	24.6	31.072
H-102A	19	11	16	24	4.663	6.782	79.45	31.16	11.048
H-102A	20	35	33	12	29.671	27.976	122.17	29.75	45.572
H-102A	21	37	43	16	23.525	27.34	99.29	22.36	44.536
H-102A	22	35	52	24	14.836	22.041	77.8	17.08	35.905
H-102A	23	11	15	16	6.994	9.537	84.72	33.67	15.536
H-102A	24	16	30	12	13.564	25.432	61.72	19.15	41.429
H-102A	25	19	23	16	12.08	14.624	95.35	29.62	23.822
H-102A	26	25	32	8	31.79	40.692	90.21	24.15	66.286
H-102A	27	41	108	12	34.758	91.556	43.99	8.12	149.144
H-102A	28	36	73	20	18.311	37.131	57.09	11.68	60.486
H-102A	29	44	51	12	37.301	43.235	99.55	20.58	70.429
H-102A	30	15	4	16	9.537	2.543	421.95	237.6	4.143
H-102A	31	25	36	16	15.895	22.889	80.25	20.96	37.286
H-102A	32	36	52	24	15.259	22.041	80.01	17.42	35.905
H-102A	33	9	3	8	11.445	3.815	339.74	226.6	6.214
H-102A	34	16	26	24	6.782	11.021	71.17	22.66	17.953
H-102A	35	13	51	8	16.531	64.852	29.57	9.21	105.644
H-102A	36	6	11	12	5.086	9.325	63.12	32.06	15.191
H-102A	37	89	137	24	37.725	58.071	75.1	10.34	94.596
H-102A	38	22	29	12	18.65	24.585	87.62	24.84	40.048
H-102A	39	4	6	12	3.391	5.086	77.06	49.77	8.286
H-102A	40	13	4	12	11.021	3.391	367.26	210.12	5.524
H-102A	41	66	157	36	18.65	44.365	48.7	7.21	72.271
H-102A	42	31	24	12	26.28	20.346	148.48	40.48	33.143
H-102A	43	8	23	12	6.782	19.498	40.32	16.57	31.762
H-102A	44	8	16	8	10.173	20.346	57.88	25.09	33.143
H-102A	45	7	9	16	4.451	5.722	89.82	45.3	9.322
H-102A	46	15	75	16	9.537	47.686	23.22	6.58	77.679
H-102A	47	6	6	4	15.259	15.259	115.25	66.58	24.857
H-102A	48	46	58	16	29.247	36.877	91.57	18.17	60.072
H-102A	49	7	11	12	5.934	9.325	73.58	35.61	15.191
H-102A	50	5	4	6	8.477	6.782	143.74	96.47	11.048
H-102A	51	21	17	16	13.352	10.809	142.07	46.44	17.607

Ns: *number of tracks counted (spontaneous)*
Ni: *number of tracks counted (induced)*
A: *counted area*

Table A.75: Ap (U-Th)/He age dataset

		He		U238			Th232				Sm			Sphere	Ejection	*Uncorr.*	Ft-Corr.		Average	
		vol.	1s	mass	1s	conc.	mass	1s	conc.	Th/U	mass	1s	conc.	radius	correct.	*He-age*	He-age	±1	age	±1
Sample	aliq.	[ncc]	[%]	[ng]	[%]	[ppm]	[ng]	[%]	[ppm]	ratio	[ng]	[%]	[ppm]	[µm]	(Ft)	*[Ma]*	[Ma]	[Ma]	[Ma]	[Ma]
H-17A	#1	**0.793**	2.0116155	**0.158**	1.9	41.74	**0.127**	2.5	33.41	0.80	**0.733**	14.6	193.54	62	**0.753**	*33.77*	**44.87**	4.04		
H-17A	#2	**0.186**	3.0532994	**0.033**	2.8	22.62	**0.034**	2.7	23.27	1.03	**0.268**	15.1	184.73	43	**0.628**	*35.79*	**57.00**	7.69		
H-17A	#3	**0.153**	3.5550076	**0.026**	3.6	13.70	**0.048**	2.6	25.37	1.85	**0.742**	7.0	394.36	42	**0.609**	*29.18*	**47.88**	6.95	**49.9**	**3.6**

Amount of helium is given in nano-cubic-cm in standard temperature and pressure.

Amount of radioactive elements are given in nanograms.

Ejection correct. (Ft): correction factor for alpha-ejection (according to Farley et al., 1996 and Hourigan et al., 2005).

Uncertainties of helium and the radioactive element contents are given as 1 sigma, in relative error %.

Uncertaintiy of the single grain age is given as 2 sigma in % (or in Ma) and it includs both the analytical uncertanity and the estimated uncertanity of the Ft.

Uncertainty of the sample average age is 2 standard error, as (SD)/(*n*)1/2; where SD=standard deviation of the age replicates and *n* =number of age determinations.

A.4 Python script for PAT

```
# ---------------------------------------------------------------------------
# PAT_script.py
# Created on: Fr Okt 18 2013 01:07:07
#   (generated by ArcGIS/ModelBuilder)
# ---------------------------------------------------------------------------

# Import system modules
import sys, string, os, arcgisscripting

# Create the Geoprocessor object
gp = arcgisscripting.create()

# Check out any necessary licenses
gp.CheckOutExtension("spatial")
gp.CheckOutExtension("3D")

# Load required toolboxes...
gp.AddToolbox("ROOT:/Program Files/ArcGIS/ArcToolbox/Toolboxes/
Spatial Analyst Tools.tbx")
gp.AddToolbox("ROOT:/Program Files/ArcGIS/ArcToolbox/Toolboxes/
Conversion Tools.tbx")
gp.AddToolbox("ROOT:/Program Files/ArcGIS/ArcToolbox/Toolboxes/
3D Analyst Tools.tbx")


# Local variables...
fill__2_ = "ROOT:\\RUN\\METAFILES\\fill"
Tibet_map_UTM_tif = "ROOT:\\RUN\\INPUT\\Tibet_map_UTM.tif"
sl1 = "ROOT:\\RUN\\METAFILES\\sl1"
Output_profile_curve_raster = ""
Output_plan_curve_raster = ""
cu1 = "ROOT:\\RUN\\METAFILES\\cu1"
cu2 = "ROOT:\\RUN\\METAFILES\\cu2"
tri2 = "ROOT:\\RUN\\METAFILES\\tri2"
Input_raster_or_constant_value_2 = "9"
tri4 = "ROOT:\\RUN\\METAFILES\\tri4"
tri3 = "ROOT:\\RUN\\METAFILES\\tri3"
tri7 = "ROOT:\\RUN\\METAFILES\\tri7"
tri8 = "ROOT:\\RUN\\METAFILES\\tri8"
tri9 = "ROOT:\\RUN\\METAFILES\\tri9"
tri10 = "ROOT:\\RUN\\METAFILES\\tri10"
tri6 = "ROOT:\\RUN\\METAFILES\\tri6"
tri5 = "ROOT:\\RUN\\METAFILES\\tri5"
tri1 = "ROOT:\\RUN\\METAFILES\\tri1"
Input_raster_or_constant_value_2__2_ = "2"
Output_drop_raster = ""
rh1 = "ROOT:\\RUN\\METAFILES\\rh1"
rh2 = "ROOT:\\RUN\\METAFILES\\rh2"
rh3 = "ROOT:\\RUN\\METAFILES\\rh3"
rh4 = "ROOT:\\RUN\\METAFILES\\rh4"
rh5_shp = "ROOT:\\RUN\\METAFILES\\rh5.shp"
rh6 = "ROOT:\\RUN\\METAFILES\\rh6"
rh7 = "ROOT:\\RUN\\METAFILES\\rh7"
rh8 = "ROOT:\\RUN\\METAFILES\\rh8"
sl2 = "ROOT:\\RUN\\METAFILES\\sl2"
T_FM = "ROOT:\\RUN\\METAFILES\\T_FM"
RcT_FM = "ROOT:\\RUN\\OUTPUT\\RcT_FM"
tim02 = "ROOT:\\RUN\\METAFILES\\tim02"
tim03 = "ROOT:\\RUN\\METAFILES\\tim03"
tim01 = "ROOT:\\RUN\\METAFILES\\tim01"
```

```
# Process: Fill...
gp.Fill_sa(Tibet_map_UTM_tif, fill__2_, "")

# Process: Curvature...
gp.Curvature_sa(fill__2_, cu1, "1", Output_profile_curve_raster,
Output_plan_curve_raster)

# Process: Flow Direction...
gp.FlowDirection_sa(fill__2_, rh1, "NORMAL", Output_drop_raster)

# Process: Times...
gp.Times_sa(fill__2_, fill__2_, tri2)

# Process: Focal Statistics (2)...
gp.FocalStatistics_sa(tri2, tri3, "Rectangle 3 3 CELL", "SUM", "DATA")

# Process: Times (2)...
gp.Times_sa(tri2, Input_raster_or_constant_value_2, tri4)

# Process: Plus...
gp.Plus_sa(tri3, tri4, tri7)

# Process: Focal Statistics...
gp.FocalStatistics_sa(fill__2_, tri1, "Rectangle 3 3 CELL", "SUM", "DATA")

# Process: Times (3)...
gp.Times_sa(fill__2_, tri1, tri5)

# Process: Times (4)...
gp.Times_sa(tri5, Input_raster_or_constant_value_2__2_, tri6)

# Process: Minus...
gp.Minus_sa(tri7, tri6, tri8)

# Process: Square Root...
gp.SquareRoot_sa(tri8, tri9)

# Process: Single Output Map Algebra (2)...
gp.SingleOutputMapAlgebra_sa("CON ((tri9) < 1, 0, (tri9) >= 1 AND (tri9) < 80, 1,
(tri9) >= 80 AND (tri9) <= 100, (100 - (tri9))  / 20, (tri9) > 100, 0 )

", tri101, "ROOT:\\RUN\\METAFILES\\tri9")

# Process: Single Output Map Algebra (3)...
gp.SingleOutputMapAlgebra_sa("CON ((cu1) < -1, 0, (cu1) >= -1 AND (cu1) < -0.14,
((cu1) + 1) / (0.86), (cu1) >= -0.14 AND (cu1) <= 0.14, 1,
(cu1) <= 1 AND (cu1) > 0.14, (1 - (cu1))  / 0.86, (cu1) > 1, 0 )",
cu2, "ROOT:\\RUN\\METAFILES\\cu1")

# Process: Times (11)...
gp.Times_sa(tri10, cu2, tim01)

# Process: Slope...
gp.Slope_sa(fill__2_, sl1, "DEGREE", "1")

# Process: Single Output Map Algebra (6)...
gp.SingleOutputMapAlgebra_sa("CON ((sl1) >= 0 AND (sl1) < 10, 1, (sl1) <= 30 AND
(sl1) >= 10, (30 - (sl1)) / 20,  (sl1) >30, 0)
", sl2, "ROOT:\\RUN\\METAFILES\\sl1")

# Process: Flow Accumulation...
gp.FlowAccumulation_sa(rh1, rh2, "", "FLOAT")

# Process: Extract by Attributes (3)...
gp.ExtractByAttributes_sa(rh2, "value >= 10000", rh3)
```

```
# Process: Extract by Mask (3)...
gp.ExtractByMask_sa(fill__2_, rh3, rh4)

# Process: Raster to Point (2)...
gp.RasterToPoint_conversion(rh4, rh5_shp, "Value")

# Process: Natural Neighbor (2)...
gp.NaturalNeighbor_3d(rh5_shp, "GRID_CODE", rh6, "90")

# Process: Minus (3)...
gp.Minus_sa(fill__2_, rh6, rh7)

# Process: Single Output Map Algebra (5)...
gp.SingleOutputMapAlgebra_sa("CON ((rh7) < 600 AND (rh7) > 100, 1,
(rh7) >= 0 AND (rh) <= 100, (rh7)  / 100 ,
(rh7) >= 600 AND (rh7) <= 2000, (2000 - (rh7)) / 1400,
(rh7) < 0 OR (rh7) > 2000, 0)", rh8, "ROOT:\\RUN\\METAFILES\\rh7")

# Process: Times (6)...
gp.Times_sa(sl2, rh8, tim02)

# Process: Times (7)...
gp.Times_sa(tim01, tim02, tim03)

# Process: Focal Statistics (9)...
gp.FocalStatistics_sa(tim03, T_FM, "Rectangle 22 22 CELL", "MEAN", "DATA")

# Process: Reclassify (8)...
gp.Reclassify_sa(T_FM, "VALUE", "0 0; 0,000001 0.010000 1;
0.010001 0.020000 2; 0.020001 0.030000 3; 0.030001 0.040000 4;
0.040001 0.050000 5; 0.050001 0.060000 6; 0.060001 0.070000 7;
0.070001 0.080000 8; 0.080001 0.090000 9; 0.090001 0.100000 10;
0.100001 0.110000 11; 0.110001 0.120000 12; 0.120001 0.130000 13;
0.130001 0.140000 14; 0.140001 0.150000 15; 0.150001 0.160000 16;
0.160001 0.170000 17; 0.170001 0.180000 18; 0.180001 0.190000 19;
0.190001 0.200000 20; 0.200001 0.210000 21; 0.210001 0.220000 22;
0.220001 0.230000 23; 0.230001 0.240000 24; 0.240001 0.250000 25;
0.250001 0.260000 26; 0.260001 0.270000 27; 0.270001 0.280000 28;
0.280001 0.290000 29; 0.290001 0.300000 30; 0.300001 0.310000 31;
0.310001 0.320000 32; 0.320001 0.330000 33; 0.330001 0.340000 34;
0.340001 0.350000 35; 0.350001 0.360000 36; 0.360001 0.370000 37;
0.370001 0.380000 38; 0.380001 0.390000 39; 0.390001 0.400000 40;
0.400001 0.410000 41; 0.410001 0.420000 42; 0.420001 0.430000 43;
0.430001 0.440000 44; 0.440001 0.450000 45; 0.450001 0.460000 46;
0.460001 0.470000 47; 0.470001 0.480000 48; 0.480001 0.490000 49;
0.490001 0.500000 50; 0.500001 0.510000 51; 0.510001 0.520000 52;
0.520001 0.530000 53; 0.530001 0.540000 54; 0.540001 0.550000 55;
0.550001 0.560000 56; 0.560001 0.570000 57; 0.570001 0.580000 58;
0.580001 0.590000 59; 0.590001 0.600000 60; 0.600001 0.610000 61;
0.610001 0.620000 62; 0.620001 0.630000 63; 0.630001 0.640000 64;
0.640001 0.650000 65; 0.650001 0.660000 66; 0.660001 0.670000 67;
0.670001 0.680000 68; 0.680001 0.690000 69; 0.690001 0.700000 70;
0.700001 0.710000 71; 0.710001 0.720000 72; 0.720001 0.730000 73;
0.730001 0.740000 74; 0.740001 0.750000 75; 0.750001 0.760000 76;
0.760001 0.770000 77; 0.770001 0.780000 78; 0.780001 0.790000 79;
0.790001 0.800000 80; 0.800001 0.810000 81; 0.810001 0.820000 82;
0.820001 0.830000 83; 0.830001 0.840000 84; 0.840001 0.850000 85;
0.850001 0.860000 86; 0.860001 0.870000 87; 0.870001 0.880000 88;
0.880001 0.890000 89; 0.890001 0.900000 90; 0.900001 0.910000 91;
0.910001 0.920000 92; 0.920001 0.930000 93; 0.930001 0.940000 94;
0.940001 0.950000 95; 0.950001 0.960000 96; 0.960001 0.970000 97;
0.970001 0.980000 98; 0.980001 0.990000 99; 0.990001 1 100;
NODATA 0", RcT_FM, "DATA")
```

Table A.76: Description and settings of the used toolboxes of ArcGis

Tool	Parameters	Explanation
Fill		All imperfections as sinks are removed in the DEM
Flow direction		Creates a raster of flow direction from each cell to its steepest downslope neighbour
Flow accumulation	Output data type: FLOAT	Creates a raster accumulated flow to each cell
Focal statistics	Neighborhood: Rectangle; Neighborhood settings: Height:3/Width:3, Cell units, Satistic type: SUM; NoData are ignored in calculations Neighborhood: Rectangle; Neighborhood settings: Height:3/Width:3, Cell units, Satistic type: SUM; NoData are ignored in calculations Neighborhood: Rectangle; Neighborhood settings: Height:22/Width:22, Cell units, Satistic type: MEAN; NoData are ignored in calculations	Calculates a statistic on a raster over a specified neighborhood
Extract by Attributes	value <= 10000	Extracts the cells of a raster based on a logical query
Extract by Mask	input mask data: rh3	Extracts the cells of a raster data correspond to the areas defined by a mask
Times	other raster or value	Multiplies the values of two rasters on a cell-by-cell basis
Plus	tri3 and	Adds the values of two rasters on a cell-by-cell basis within the Analysis window
Minus	tri7 and	Subtracts the value of the second input raster from the value of the first input raster on a cell-by-cell basis within the Analysis window
Square Root		Calculates the square root of cells in a raster
Raster to Point	Field Value	Converts a raster dataset to point features
Natural Neighbor	Z value field: GRID CODE; Output cell size: 90	Interpolates a surface from points using a natural neighbor technique
Curvature		Calculates the curvature of a raster surface
Slope	Output measurement: Degree, Z factor: 1	Identifies the rate of maximum change in z-value from each cell
Single Output Map Algebra	CON ((cu1) < -1, 0, (cu1) >= -1 AND (cu1) < -0.14, ((cu1) + 1) / (0.86), (cu1) >= -0.14 AND (cu1) <= 0.14, 1, (cu1) <= 1 AND (cu1) > 0.14, (1 - (cu1)) / 0.86, (cu1) > 1, 0) CON ((sl1) >= 0 AND (sl1) < 10, 1, (sl1) <= 30 AND (sl1) >= 10, (30 - (sl1)) / 20, (sl1) >30, 0) CON ((rh7) < 600 AND (rh7) > 100, 1, (rh7) >= 0 AND (rh7) <= 100, (rh7) / 100 , (rh7) >= 600 AND (rh7) <= 2000, (2000 - (rh7)) / 1400, (rh7) < 0 OR (rh7) > 2000, 0) CON ((tri9) < 1, 0, (tri9) >= 1 AND (tri9) < 80, 1, (tri9) >= 80 AND (tri9) <= 100, (100 - (tri9)) / 20, (tri9) > 100, 0)	Runs a single expression built with the Map Algebra language
Reclassify	Reclass field: Value; Reclassification: 0 - 100 (natural numbers)	Reclassifies the values in a raster

Acknowledgement

This thesis was realized with the financial support of the German Research Foundation (DFG), which funded this research in the framework of the priority programme 1372 entitled Tibetan Plateau: Formation - Climate Ecosystem (grant DU 373/5). I wish to thank all those who contributed to the completion of my thesis. First of all, I would like to express my sincere thanks to the member of the thesis commission, especially Prof. Dr. Jonas Kley for his constructive criticism. I am very grateful to Dr. István Dunkl for his inspiration, discussions, and guidance throughout the PhD project. *Nagyon közönöm!* I am very thankful to Prof. Dr. Hilmar von Eynatten for his support and encouragement, especially during the last period of this PhD project. This work would not have been possible without the intense commitment of drivers, technicians, and colleagues. Therefore, I am very grateful to: the Tibetan drivers Taba, Puchum and Nobu (Lhasa) for their help during the field work; Dr. Marcus Strobl, Prof. Dr. Ralf Hetzel, and Dr. Li Yun Zhang for the good time in the field and Marcus especially for his successful action of fixing my broken notebook amidst the Tibetan Plateau; the technicians Irina Ottenbacher and Ursula Grünewald for their invaluable support; Dr. Magdalena Banaszak for the calculations of the amphibole geobarometry; Dr. Balázs Székely (Budapest) for the helpful key discussion concerning the geomorphometrical part of the thesis; Dr. Jan Kropáček and Dr. Bianca Wagner for a very prolific collaboration; and last but not least Dr. Raimon Tolosana-Delgado for many valuable discussions about Linux, statistics, the powerful "R" software, and many more topics. Further, I wish to thank all my colleagues of the Department of Sedimentology and Environmental Geology for the warm and inspiring atmosphere. For constructive discussions, feedback and continuous motivation, I am very thankful to all of my supporting friends. Last but not least, I am very very grateful to my family for their continuous support.